



I. R. IRAN

ISSN: 1728-144X

e-ISSN: 1735-9244



International Journal of Engineering

Journal Homepage: www.ije.ir



TRANSACTIONS B: Applications

Volume 33, Number 11, November 2020

Materials and Energy Research Center

INTERNATIONAL JOURNAL OF ENGINEERING

Transactions B: Applications

DIRECTOR-IN-CHARGE

A. R. Khavandi

EDITOR IN CHIEF

G. D. Najafpour

ASSOCIATE EDITOR

A. Haerian

EDITORIAL BOARD

- | | | | |
|------|------------------------------------------------------------------|-------|----------------------------------------------------------|
| S.B. | Adeloju, Charles Sturt University, Wagga, Australia | A. | Mahmoudi, Bu-Ali Sina University, Hamedan, Iran |
| K. | Badie, Iran Telecomm. Research Center, Tehran, Iran | O.P. | Malik, University of Calgary, Alberta, Canada |
| M. | Balaban, Massachusetts Ins. of Technology (MIT), USA | G.D. | Najafpour, Babol Noshirvani Univ. of Tech., Babol, Iran |
| M. | Bodaghi, Nottingham Trent University, Nottingham, UK | F. | Nateghi-A, Int. Ins. Earthquake Eng. Seis., Tehran, Iran |
| E. | Clausen, Univ. of Arkansas, North Carolina, USA | S. E. | Oh, Kangwon National University, Korea |
| W.R. | Daud, University Kebangsaan Malaysia, Selangor, Malaysia | M. | Osanloo, Amirkabir Univ. of Tech., Tehran, Iran |
| M. | Ehsan, Sharif University of Technology, Tehran, Iran | M. | Pazouki, MERC, Karaj, Iran |
| J. | Faiz, Univ. of Tehran, Tehran, Iran | J. | Rashed-Mohassel, Univ. of Tehran, Tehran, Iran |
| H. | Farrahi, Sharif University of Technology, Tehran, Iran | S. K. | Sadrnezhaad, Sharif Univ. of Tech, Tehran, Iran |
| K. | Firoozbakhsh, Sharif Univ. of Technology, Tehran, Iran | R. | Sahraeian, Shahed University, Tehran, Iran |
| A. | Haerian, Sajad Univ., Mashhad, Iran | A. | Shokuhfar, K. N. Toosi Univ. of Tech., Tehran, Iran |
| H. | Hassanpour, Shahrood Univ. of Tech., Shahrood, Iran | R. | Tavakkoli-Moghaddam, Univ. of Tehran, Tehran, Iran |
| W. | Hogland, Linnaeus Univ, Kalmar Sweden | T. | Teng, Univ. Sains Malaysia, Gelugor, Malaysia |
| A.F. | Ismail, Univ. Tech. Malaysia, Skudai, Malaysia | L. J. | Thibodeaux, Louisiana State Univ, Baton Rouge, U.S.A |
| M. | Jain, University of Nebraska Medical Center, Omaha, USA | P. | Tiong, Nanyang Technological University, Singapore |
| M. | Keyanpour rad, Materials and Energy Research Center, Karaj, Iran | X. | Wang, Deakin University, Geelong VIC 3217, Australia |
| A. | Khavandi, Iran Univ. of Science and Tech., Tehran, Iran | | |

EDITORIAL ADVISORY BOARD

- | | | | |
|-------|------------------------------------------------------|-------|---------------------------------------------------------|
| S. T. | Akhavan-Niaki, Sharif Univ. of Tech., Tehran, Iran | A. | Kheyroddin, Semnan Univ., Semnan, Iran |
| M. | Amidpour, K. N. Toosi Univ of Tech., Tehran, Iran | N. | Latifi, Mississippi State Univ., Mississippi State, USA |
| M. | Azadi, Semnan university, Semnan, Iran | H. | Oraee, Sharif Univ. of Tech., Tehran, Iran |
| M. | Azadi, Semnan University, Semnan, Iran | S. M. | Seyed-Hosseini, Iran Univ. of Sc. & Tech., Tehran, Iran |
| F. | Behnamfar, Isfahan University of Technology, Isfahan | M. T. | Shervani-Tabar, Tabriz Univ., Tabriz, Iran |
| R. | Dutta, Sharda University, India | E. | Shirani, Isfahan Univ. of Tech., Isfahan, Iran |
| M. | Eslami, Amirkabir Univ. of Technology, Tehran, Iran | A. | Siadat, Arts et Métiers, France |
| H. | Hamidi, K.N.Toosi Univ. of Technology, Tehran, Iran | C. | Triki, Hamad Bin Khalifa Univ., Doha, Qatar |
| S. | Jafarmadar, Urmia Univ., Urmia, Iran | | |

TECHNICAL STAFF

M. Khavarpour; M. Mohammadi; V. H. Bazzaz, R. Esfandiar; T. Ebadi

DISCLAIMER

The publication of papers in International Journal of Engineering does not imply that the editorial board, reviewers or publisher accept, approve or endorse the data and conclusions of authors.

International Journal of Engineering *Transactions A: Basics* (ISSN 1728-1431) (EISSN 1735-9244)

International Journal of Engineering *Transactions B: Applications* (ISSN 1728-144X) (EISSN 1735-9244)

International Journal of Engineering *Transactions C: Aspects* (ISSN 2423-7167) (EISSN 1735-9244)

Web Sites: www.ije.ir & www.ijeir.info E-mails: ije.editor8@gmail.com, Tel: (+9821) 88771578, Fax: (+9821) 88773352
Materials and Energy Research Center (MERC)

CONTENTS:**Chemical Engineering**

- A. Abdul Rahman–
Al Ezzi** An Experimental Investigation of Synergistic Pulsation Bubble Column with Inverse Fluidized Loop Reactor for Removing Chloroform from Wastewater 2120-2126

Civil Engineering

- M. Ghamari;
M. S. Karimi;
A. AmirShahkarami** Effects of Lateral Constraints and Geometrical Characteristics on Deformation Capacity of the Persian Historic Unreinforced Masonry Shear Walls under Uncertainty Conditions 2127-2136

- B. H. Tran;
B. V. Le;
V. T. A. Phan;
H. M. Nguyen** In-situ Fine Basalt Soil Reinforced by Cement Combined with Additive DZ33 to Construct Rural Roads in Gia Lai Province, Vietnam 2137-2145

- A. H. Sadeghi Fazel;
J. Bolouri Bazaz** Behavior of Eccentrically Inclined Loaded Ring Footings Resting on Granular Soil 2146-2154

- A. K. Shadhar;
A. M. Raouf
Mahjoob** Pavement Maintenance Management Using Multi-objective Optimization: (Case Study: Wasit Governorate-Iraq) 2155-2161

- B. AlizadehKharazi;
A. Alvanchi;
H. Taghaddos** A Novel Building Information Modeling-based Method for Improving Cost and Energy Performance of the Building Envelope 2162-2173

Electrical & Computer Engineering

- H. B. Jond;
J. Platoša;
Z. Sadreddini** Autonomous Vehicle Convoy Formation Control with Size/Shape Switching for Automated Highways 2174-2180

- M. M. Fakharian** A Wideband Fractal Planar Monopole Antenna with a Thin Slot on Radiating Stub for Radio Frequency Energy Harvesting Applications 2181-2187

- S. Nageena Parveen;
P. Siddaiah** Reference Satellite Strategic Methods to Improve Position Accuracy of Rover with Resolved Integer Ambiguities Using Linear Combination in DIRNSS System 2188-2194

- İ Devecioğlu;
Ş. Ç. Yener;
R. Mutlu** Demonstration of Synaptic Connections with Unipolar Junction Transistor based Neuron Emulators 2195-2200

O. V. Chernoyarov; A. N. Glushkov; V. P. Lintvinenko; B. v. Matveev; A. N. Faulgaber	Digital Root-mean-square Signal Meter	2201-2208
J. G. Fantidis; G. E. Nicolaou	The Comparison of Neutron Beams through ${}^7\text{Li}(p,n)$ Reactions for the Design of a Thermal Neutron Radiography Facility using the MCNPX Code	2209-2214
N. Arunkumar; N. Senathipathi; S. Dhanasekar; P. Malin Bruntha; C. Priya	An Ultra-low-power Static Random-Access Memory Cell Using Tunneling Field Effect Transistor	2215-2221
S. Norouzi; H. Ghoreishy; A. Ale Ahmad; F. Tahami	A New Variable Frequency Zero Voltage Switching Control Method for Boost Converter Operating in Boundary Conduction Mode	2222-2232
Industrial Engineering		
I. Dadashpour; A. Bozorgi-Amiri	Evaluation and Ranking of Sustainable Third-party Logistics Providers using the D-Analytic Hierarchy Process	2233-2244
C. Jaqin; A. Rozak; H. Hardi Purba	Case Study in Increasing Overall Equipment Effectiveness on Progressive Press Machine Using Plan-do-check-act Cycle	2245-2251
S. Sajedi; A. H. Sarfaraz; S. Bamdad; K. Khalili-Damghani	Designing a Sustainable Reverse Logistics Network Considering the Conditional Value at Risk and Uncertainty of Demand under Different Quality and Market Scenarios	2252-2271
F. Delfani; A. Kazemi; S. M. Seyedhosseini; S. T. A. Niaki	A Green Hazardous Waste Location-routing Problem Considering the Risks Associated with Transportation and Population	2272-2284
L. Izadi; F. Ahmadizar; J. Arkat	A Hybrid Genetic Algorithm for Integrated Production and Distribution Scheduling Problem with Outsourcing Allowed	2285-2298
N. Maleki; M. Bagherifard; M. R. Gholamian	Application of Incomplete Analytic Hierarchy Process and Choquet Integral to Select the best Supplier and Order Allocation in Petroleum Industry	2299-2309

M. A. Farsi; E. Zio	Modeling and Analyzing Supporting Systems for Smart Manufacturing Systems with Stochastic, Technical and Economic Dependences	2310-2318
N. Ghaffarian; M. Hamed	Optimization of Rubber Compound Design Process Using Artificial Neural Network and Genetic Algorithm	2319-2326
Material Engineering		
H. Hasibi; A. Mahmoudian; G. R. Khayati	Modified Particle Swarm Optimization-Artificial Neural Network and Gene Expression Programming for Predicting High Temperature Oxidation Behavior of Ni-Cr-W-Mo Alloys	2327-2338
Mechanical Engineering		
M. S. EL-Wazery; M. EL-Kelity; R. A. Elsad	Effect of Water Absorption on the Tensile Characteristics of Natural/ Synthetic Fabrics Reinforced Hybrid Composites	2339-2346
M. A. Shahiri; A. R. Arshi; A. Kazemi; V. Cooper	Kinesiological Description of Hippotherapy as a Treatment Modality	2347-2355
S. M. Arabi; H. Ghadamian; M. Aminy; H. A. OZgoli; B. Ahmadi; M. Khodsiani	Simulation of a GEF5 Gas Turbine Power Plant Using Fog Advanced Cycle and a Systematic Approach to Calculate Critical Relative Humidity	2356-2364
A. Amrullah; A. Syarief; M. Saifudin	Combustion Behavior of Fuel Briquettes Made from Ulin Wood and Gelam Wood Residues	2365-2371
J. Roshanian; E. Rahimzadeh	A Generalization for Model Reference Adaptive Control and Robust Model Reference Adaptive Control Adaptive Laws for a Class of Nonlinear Uncertain Systems with Application to Control of Wing Rock Phenomenon	3272-3283
T. Saeheaw	Regression Modeling and Process Analysis of Plug and Spot Welds Used in Automotive Body Panel Assembly	2384-2398
M. Esmailian; K. Khalili	Prediction of Tool Force in Two Point Incremental Forming by Slab Analysis	2399-2407

Z. Sarparast; R. Abdoli; A. Rahbari; M. Varmazyar; K. Reza Kashyzadeh Mining Engineering	Experimental and Numerical Analysis of Permeability in Porous Media	2408-2415
J. Zhang; Z. Ai; L. Guo; X. Cui	Reliability Evaluation of a Disaster Airflow Emergency Control System Based on Bayesian Networks	2416-2424
A. H. Abdullah; M. A. Maoinsar; E. A. Rahim	Interaction Effect of Depth of Cut, Back Rake Angle and Rock Properties on Temperature of Single Polycrystalline Diamond Compact Cutter	2425-2435



An Experimental Investigation of Synergistic Pulsation Bubble Column with Inverse Fluidized Loop Reactor for Removing Chloroform from Wastewater

A. Abdul Rahman–Al Ezzi*

Department of Chemical Engineering, University of Technology, Baghdad, Iraq

PAPER INFO

Paper history:

Received 04 March 2020

Received in revised form 21 August 2020

Accepted 03 September 2020

Keywords:

Stripping

Oxidation

Pulsation Bubble Column

Adsorption

Inverse Fluidization Airlift Loop Reactor

Chloroform

ABSTRACT

In this study, the feasibility of using the developed design for the removal of organic pollutants from wastewater was examined. The design includes the integration of the work of both pulsation bubble column (PBC) and the inverse fluidization airlift loop reactor (IFALR). The experimental podium was fabricated and installed which that consists of a bubble column with a diameter of 5 cm and a height of 210 cm, contains at the top a solenoid valve which is electrically turned via at least two timers, and its connection with the loop reactor by a one-way valve. The loop reactor consists of an outer rectangular tube with dimensions (29 cm long x 15.5 cm wide x 150 cm high) and an internal draft tube with 9 cm diameter and 120 cm long as granular activated carbon is put as an adsorbent in the annulus region between the inner and outer tube. Experiments were conducted using one of the organic pollutants namely chloroform, with a work scenario that includes changing both the airflow rate (2-20) liters/minute, the total survival time of the treatment (5-60) minutes, the molar ratio of the chloroform pollutant to the oxidizing agent of hydrogen peroxide (1/10 - 1/20). The results showed removal efficiency near to 89%, and it gives an indication of the success of the proposed design, with the possibility of recycling the treated water and releasing it to the environment due to the low risk of the organic pollutant in it.

doi: 10.5829/ije.2020.33.11b.01

1. INTRODUCTION

It is known that there are trace amounts of chloroform accompanying water of all types whether, drinking water, surface water, tap water, and domestic sewage, cooling water in industrial plants, groundwater, as a side product in the chlorination stage during the remedy process for wastewater to decrease the hazard of diseases due to microorganisms or viruses [1]. Through the previous periods, chloroform was utilized as a doped for operations and in many products such as cough suppressants and toothpaste, in addition, that chloroform is used also in industrial processes producing many typically materials of various uses such as lubricating oils, cleaning solvents, bleaching paper, refrigerants, rubber, intermediate materials in the pharmaceutical industry for herbicides and fungicides [2]. Emission of

chloroform causes damage to the environment, in particular, the destruction of the ozone layer [3]. In addition to being toxic and carcinogenic; it represents a direct threat to health and a direct cause of kidney and liver cancer and damage that may affect the nervous and reproductive system [4, 5]. Several studies carried out regarding treatments methods used to remove hydrocarbon compounds of low molecular weights including chloroform have been classified into three methods, firstly the physical methods like adsorption via activated carbon or by many different other adsorbents (Nano adsorbents or zeolite) [6], agglomeration, Flotation's, abstraction, and ion exchange, [7-10] secondly the chemical methods, such as oxidation with many catalysts and finally, the conventional biological methods have failed to abstract poisonous compounds or recalcitrant organic pollutants [11-13]. Therefore, one of

*Corresponding Author Institutional Email:
ali.a.nsaif@uotechnology.edu.iq (A. Abdul Rahman–Al Ezzi)

the most important and dangerous challenges at the present time is to protect water resources via removing dangerous and toxic organic materials by unconventional, effective and inexpensive methods [14, 15]. Each of the three mentioned methods has advantages and at the same time has negative aspects, so the need has become necessary to find cheap and effective alternative methods that collecting the majority of the advantages of those operations with one device [16-28]. The aim of this research is to test the effectiveness of a proposed new design for treating water-contaminated organic compounds by combination of a bubble pulsed column with an internal air loop reactor with different operating conditions in terms of treatment time (5-60) minutes and various airflow rates (2-20) L/minute and the molar ratio of chloroform to hydrogen peroxide (1/10 - 1/20).

2. EXPERIMENTAL

2. 1. Materials and Methods

2. 1. 1. Materials The essential of prepared a stock chloroform solution by dissolving one gram of chloroform (Sigma-Aldrich, Inc.) chemical structure CHCl_3 , with more than 99.8% pureness, its molecular weight 119.4, while the dissolved amount in water is 0.005 mL/mL (v/v) in a liter of deionized water to create a stock solution with a concentration of 1000 mg chloroform/L, then prepare the required experimental concentrations of 10, 20, 50, 100 and 150 mg/L. The acidity of the stock solution was regulated to the desirable acidity (7.5-8) via using 0.1M for both HCl and NaOH solution. The trade granular activated carbon (GAC) with a surface area of 1050 square meters per gram and a solid density of 1.153 g/mL, 0.8–2 mm particle size, it's imported by Sigma (Chemicals CO.). It is treated prior before its uses, by means of washing it multiple times with deionized water and drying it in an oven at a temperature of 105 °C. The strong oxidizing agents which have a 35% concentration of hydrogen peroxide generating the shattered free radicals for dissolved organic pollutants in water was supplied by GmbH Germany.

2. 2. Experimental Setup

The integrative treatment system consists of two units, the first being the pulsation bubbles column (presented in Figure 1) which was made by using transparent acrylic material of an engineering dimensions embodied via the length of tube 210 cm, the inside diameter (ID) 5 cm, and thickness 0.3 cm, equipped with a solenoid valve located at the top end and it is working periodically opens and closes depending on the electrical timer. The stripping and oxidation processes are performed simultaneously when the wastewater mixture with hydrogen peroxide is fed to the column via a twin dosing pump (P1 and P2). The

compressed air is passed via the compressor (C1) through the air sparger located 50 cm above the base of the column to cause the violent mixing of polluted water with hydrogen peroxide this happens during the solenoid valve opens and given sufficient time for complemented the two processes of stripping and oxidation.

During the period of closing the valve, air will disperse the oxidized water resulting in a pressure difference between the pulse-bubble column and the reverse fluidizing reactor causing the flowing of oxidized water from the pulse- bubble column to the inverse Fluidizing reactor passes through a one-way valve located on a perforated pipe that connects them as shown in Figure 2a. The process of opening and closing the solenoid valve is repeated periodically to reach the stability condition where samples for the treated water are taken at the point of taking samples 1.

The second unit is the inverse fluidizing reactor that consists of a diaphanous rectangular outer column and a draft tube having specifications given in Figure 2b. The draft tube extends vertically from a center of the outer rectangular column leaving a distance allowing the oxidizing water to recirculate between the inner draft tube and the outer rectangular box, the space creating between the draft tube and the outer column was partially filled with a granular activated carbon to working as an adsorbent material.

To create a space between the draft pipe and the bottom of the outer box, three supports are distributed across the top, middle and end of the reactor fixed with screws placed on the outer sides of the reactor. Every support contains sixteen holes, each hole has a diameter of 1 mm, these holes allow water to pass through it and do not allow granulated carbon to pass due to its small size 1 mm compared to the size of the granulated carbon 3-4 mm.

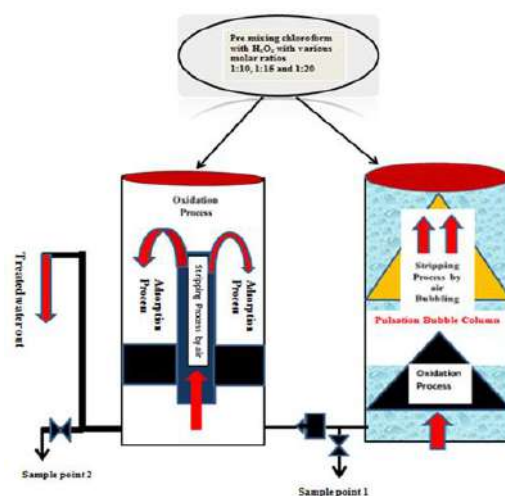


Figure 1. The integrative treatment system

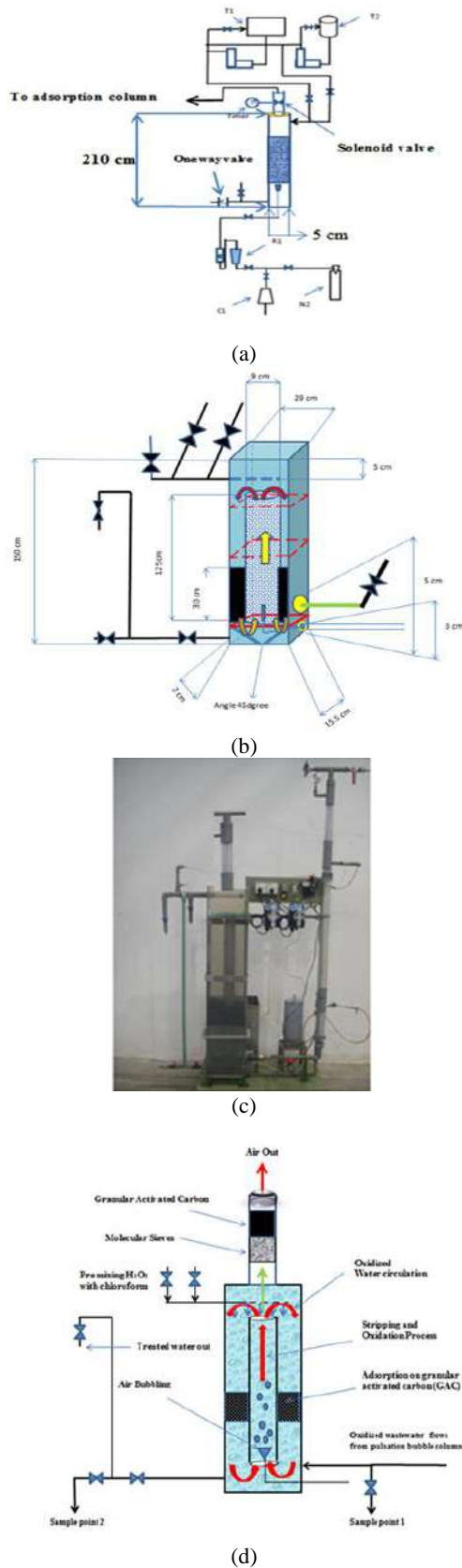


Figure 2. Planning and sequence of an integrated system (a, b, c and d)

Pillars cooperate on installing the inner tube from one side and loading the granulated carbon from another side. There is a port for inserting the polluted water mixture and hydrogen peroxide into the inverse fluidization loop reactor. P1 and P2 pumps (called SECO, chemical dosing type, country of origin China) use batches to feed the polluted water and hydrogen peroxide to both the pulsed bubble column and the reverse fluidizing reactor through the same duration as shown in Figure 3.

Valves	
R1	regulator
N2	nitrogen cylinder
P1, P2	Dosing pumps
RE	reactor
D1	distributor
T1	waste water tank
C1	compressor
F1	flow meter
T2	hydrogen peroxide tank

2. 3. Experimental Procedure

The operation process is carried out by the following steps - :

First: - Preparation of water contaminated with chloroform at a concentration of 150ppm, and an acidity ranging from 7-7.5 in the feed tank T1.

Second: - Preparing a solution of hydrogen peroxide-based on the molar ratio as an operational condition is required 20 moles of hydrogen peroxide to one-mole chloroform, where one liter of hydrogen peroxide is added to 8 liters of deionized water in tank T1.

Third: - The assign bed for the adsorption process is filled with 5 kg of granular activated carbon, equivalent to 4.5cm³ in size.

Fourth: - Determination of flow rates for each of the contaminated water pump P2 at 0.3 L/min, and the pump of hydrogen peroxide solution P1 at 0.2L/min, and the two pumps operate at a pressure of 2 bars.

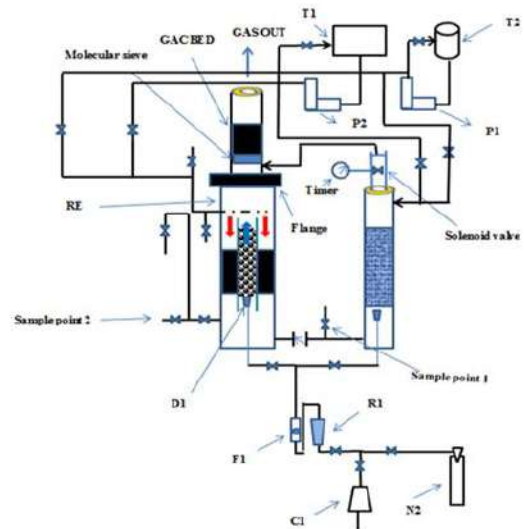


Figure 3. Schematic diagram of an experimental device

Fifth: - The system should be operational for an hour for reaching stability, prior to conducting the experiments.

Sixth: - The first experiment is being tested by installing the timer controlling the operation of the solenoid valve as follows, 30 seconds to open the valve + 5 seconds to close the valve.

Seventh: - Five samples of treated water are taken in the pulsed bullous column at a rate one sample each every six minutes at the point of withdrawal of samples No. 1, to measure the concentration of chloroform using the UV spectrophotometer (UV-1800, Hitachi, Japan) and at a wavelength of 254 nanometers.

Eighth: - After passing the treated water from the pulsed bubble column to the inverse fluidization reactor, and as a result of the difference in density due to the dispersion of the oxidized water via the flowing air between the draft tube and the outer box, the water recycling and forcing to pass through the granular carbon from the top to the bottom to cause adsorption process and give the entire opportunity to complete the abstraction and oxidation processes.

Ninth: - Five samples are taken at the rate of one sample every six minutes to measure the concentration of chloroform in the treated water at the point of drawing the samples No. 2.

Tenth: - The previous steps will be repeated by changing the following- :

a: The total time of the operation is (5-60) minutes

b: - Solenoid valve opening times (40, 50, 60,120,180) seconds while valve shutdown time remains 5 seconds for all experiments.

c: - Airflow rates range from (2-20) liters per minute.

d: - molar ratios of chloroform to hydrogen peroxide (1/10, 1/15, 1/20).

Eleventh: - The percentage of chloroform removal for the whole process is calculated by the following formula: -

$$\eta = \frac{C_{INPUT} - C_{SAMP2}}{C_{INPUT}} \times 100 \quad (1)$$

where η is CHCl_3 elimination efficiency (%), c_{input} and c_{samp2} are the primary and final concentrations of CHCl_3 in ppm, respectively.

3. RESULT AND DISCUSSION

Figure 4 illustrates the effect of the change in contact time due to the different timing of opening the solenoid valve which locates at the upper of the pulse-bubble column during the occurring of the stripping and oxidation processes on the percentage for the removal efficiency of chloroform at different concentrations for chloroform in the contaminated water which feeding the pulse-column.

The results indicate an increase in removal efficiency with increased contact time and get maximal removal rate

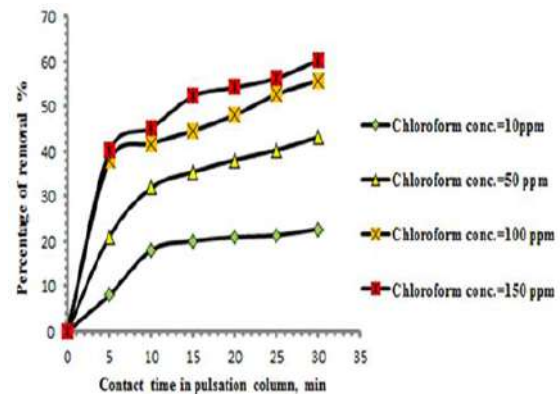


Figure 4. Impact of contact time on the proportion of abstraction of CHCl_3 with various initial concentrations of CHCl_3

at the highest concentration of polluted chloroform that feeding the pulsation column. The elimination rate of CHCl_3 in 30 minutes for, 10, 50, 100 and 150ppm were 22.7, 43.2, 55.8 and 60.3%, respectively. The explanation of this case is the high concentration of chloroform creates the highest rate of driving force for the mass transfer in the stripping process between the pollutant concentration in the liquid phase (water) and the concentration of chloroform in the gas phase (air) [29, 30]. At the same time, the longest contact time gives the complete opportunity to the free radical that produce from decomposing hydrogen peroxide to attack chloroform and decompose it into substances that are fewer hazards to the environment.

Figure 5 shows the effect of the retention time in the inverse fluidization reactor of the various concentrations of the pollutant that feeding the process during the occurring of stripping, oxidation and adsorption processes on the removal efficiency of chloroform. To enrich the process of removing and dismantling chloroform and increasing the efficiency of removal

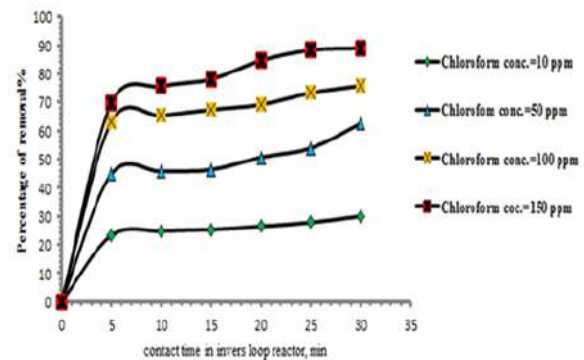


Figure 5. Impact of contact time on the percentage of removal of CHCl_3 with various initial concentrations of CHCl_3 during the occurring of stripping, oxidation, and adsorption processes in reverse fluidizing reactor

achieved in the pulsation bubble column. The inverse fluidization reactor is designed to ensure occurring the adsorption process of the pollutant or the compounds resulting from its dissociation in the oxidation processes that previously occurred in the pulsation bubble column.

The dispersed contaminated water in the reverse liquefaction reactor is forced to circulate as a result of the density difference between the contaminated water dispersed in the draft tube and the water that in outer box which will passing through the granular carbon layer to adsorb the chloroform or the remaining compounds from the disintegration of the chloroform by free radicals, reaching to reducing the hazard of pollutant on environmental and elevate the efficiency of removal chloroform, subsequently the removal rate of CHCl_3 in 30 minutes for, 10, 50, 100 and 150ppm were 30, 62.6, 75.8 and 89%, respectively.

The increasing removal efficiency of chloroform for all types of concentrations that fee to the reactor, with increasing contact time is due to three factors. The first is the continued presence of the driving force for mass transfer due to the difference in the concentration of the pollutant (chloroform) between the two phases, (contaminated water) liquid phase and (air) gaseous phase and thus cause continuity of stripping process [30]. The second factor, it is the availability of large numbers of free radicals resulting from the disintegration of hydrogen peroxide. Thus, the continuation of the oxidation reaction to the disintegration of chloroform [31, 32]. The third factor is the continuation of the recycling process of the contaminated water between the inner and outer tubes of the reverse fluidization reactor; which gives the opportunity to continue adsorption of chloroform occurs when it's passing through the granular carbon bed.

The oxidation reaction using hydrogen peroxide as an oxidized agent leads to an increase in the rate of oxidation depended on optimum molar ratio for the pollutant to oxidized agent, it became clear through Figure 6 that the highest removal rate of chloroform 60% was obtained in pulsation column when imposing the suitable ratio of hydrogen peroxide (twenty times more than chloroform) in the synthetic polluted water fed for pulse column with a treatment time of 30 minutes. The result shows that the percentage removal of CHCl_3 at 30 minutes for molar ratio 1:10, 1:15, 1:20 were 50.3, 54.4 and 60.3%, respectively. The availability of the optimum molar ratio for hydrogen peroxide to the pollutant is the key to successfully controlling the oxidation process due to the preparation of appropriate free radicals to obtain the highest removal rate. The low number of free radicals reduces the dissociation rate of chloroform and thus reducing the removal efficiency, while if the number of free radicals more than the optimum numbers this cause a phenomenon that is known as sweeping the free radicals that lead to a lower percentage of chloroform removal

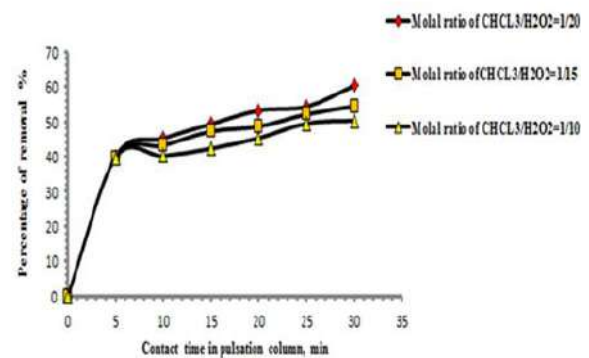


Figure 6. Influence of residence time on the proportion of removal at several molar ratios of CHCl_3 to hydrogen peroxide in the pulsation reactor

[33]. Figure 7 shows the efficacy of the adsorption process associated with enough time opportunity to complete the stripping and oxidation processes, on the removal percentage of chloroform from contaminated water in the loop reactor.

It is observed that the percentage of removal of chloroform at 30 min for molar ratio 1:20 is 89% however for rest molar ratio 1:10, 1:15 it was 73.2 and 79.9%, respectively.

Figure 7 shows that the removal rate reached 89% due to a scenario of synchronization of the best molar ratio (1/20) with the optimal amount of adsorbent activated carbon (5 kg) and the largest area and contact time for complete the adsorption process for chloroform and thus obtain the highest performance efficiency of the system and this matches the proposed design of the treatment system.

Figures 8 and 9 illustrate the effect of treatment time on removal efficiency when the airflow rate changes for three flows 5, 10 and 20 L/min and for both stages, the treatment via pulse bubble and the second stage of the treatment in the inverse fluidization reactor where the

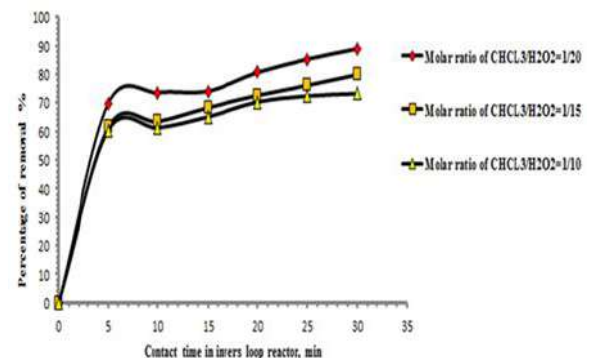


Figure 7. Effectiveness of retention time on the proportion of removal at various molar ratios of CHCl_3 to hydrogen peroxide in the inverse loop reactor

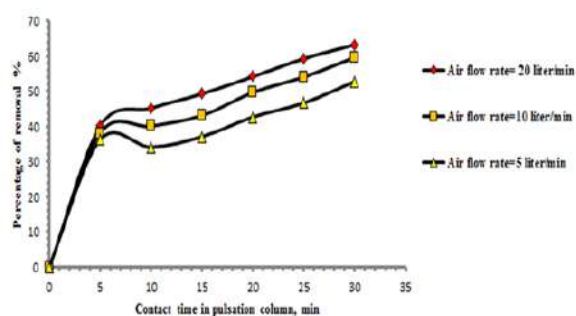


Figure 8. Impact of pulsation time on the percentage of removal with different airflow rates

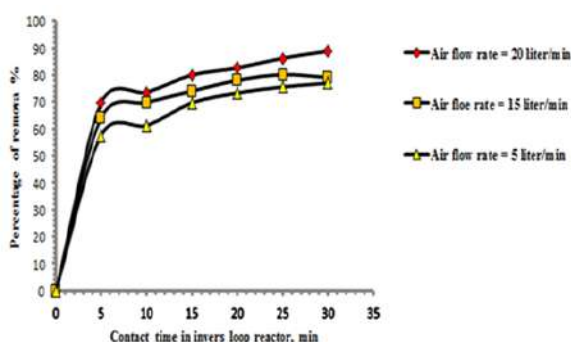


Figure 9. Effectiveness of retention time on the proportion of removal at various airflow rates in the inverse loop reactor

efficiency for the chloroform removal for two stages with total residence period 60 min were as follows: 77.1, 79.09, and 89%, respectively. No significant variation was observed for the effect of the volumetric flow rate of air on the percentage of removal where the difference did not exceed 10% in the removal percent when the range of airflow rate changed from 5 to 20 L/min for both phases, the pulse bubble column stage and the next stage of the reverse liquefaction reactor.

4. CONCLUSION

The removal of chloroform by 89% with treatment duration of one hour is evidence of the following:
 First: The success of the proposed design by combining the pulsating bubble column and the reverse fluidization reactor as a treatment system for water contaminated with hazard and toxic organic materials.
 Second: The success of using the solenoid valve to convey treated water from the bubble pulsating column to the inverse liquefaction reactor without using a pump.
 Third: - Determining the best conditions for the removal system to work, which is the airflow rate of 20 liters/minute, the molar ratio between the pollutant (CHCl_3) to the oxidizing agent (H_2O_2) is 1/20, and the residence time of one hour.

The system can be considered economically feasible for several considerations such, the cheap of construction materials that used in building the system (acrylic) and the simplicity of carrying out maintenance work in addition to the minimal space for the system occupied it makes the possibility for the use of a treatment system to minimize the risk of organic pollutants in wastewater and the possibility of recycling and release into the environment after treatment of a reality fact.

5. REFERENCES

- Grafton, R.Q., National primary drinking water regulations (NPDWR), in A dictionary of climate change and the environment. (2012), Edward Elgar Publishing Limited. <https://www.epa.gov/ground-water-and-drinking-water/national-primary-drinking-water-regulations>
- Li, J., Wu, F., Mailhot, G. and Deng, N., "Photodegradation of chloroform in aqueous solution: Impact of montmorillonite ksf particles", *Journal of Hazardous Materials*, Vol. 174, No. 1-3, (2010), 368-374. doi.org/10.1016/j.jhazmat.2009.09.061
- Gharbani, P., Tabatabaei, S., Dastmalchi, S., Ataie, S., Mosenharzandi, A. and Mehrizad, A., "Adsorption of chloroform from aqueous solution by nano-TiO₂", *International Journal of Nano Dimension*, Vol. 1, No. 4, (2011), 287-296
- Ahmad, R. and Kumar, R., "Kinetic and thermodynamic studies of brilliant green adsorption onto carbon/iron oxide nanocomposite", *Journal of the Korean Chemical Society*, Vol. 54, No. 1, (2010), 125-130. DOI 10.5012/jkcs.2010.54.01.125
- Kadirova, Z.C., Katsumata, K.-i., Isobe, T., Matsushita, N., Nakajima, A. and Okada, K., "Adsorption and photodegradation of methylene blue by iron oxide impregnated on granular activated carbons in an oxalate solution", *Applied Surface Science*, Vol. 284, (2013), 72-79. doi.org/10.1016/j.apsusc.2013.07.014
- Krishnaiah, D., Anisuzzaman, S., Bono, A. and Sarbatly, R., "Adsorption of 2,4,6-trichlorophenol (TCP) onto activated carbon", *Journal of King Saud University-Science*, Vol. 25, No. 3, (2013), 251-255. doi.org/10.1016/j.jksus.2012.10.001
- Liu, X., Li, X.-M., Yang, Q., Yue, X., Shen, T.-T., Zheng, W., Luo, K., Sun, Y.-H. and Zeng, G.-M., "Landfill leachate pretreatment by coagulation-flocculation process using iron-based coagulants: Optimization by response surface methodology", *Chemical Engineering Journal*, Vol. 200, (2012), 39-51. doi.org/10.1016/j.cej.2012.06.012
- Zinabu, T., "Gac adsorption processes for chloroform removal from drinking water", *Tajonas: Tanzania Journal of Natural and Applied Sciences*, Vol. 2, No. 1, (2012), 352-358.
- Samadi, M., Naseri, S., Mesdaghinia, A. and Alizadefard, M., "Removal of chloroform (CHCl_3) from tehran drinking water by gac and air stripping columns", *Iran Journal of Environmental Health Science Engineering*, Vol.1, (2004), 5-12.
- Tarpani, R.R.Z. and Azapagic, A., "A methodology for estimating concentrations of pharmaceuticals and personal care products (ppcps) in wastewater treatment plants and in freshwaters", *Science of The Total Environment*, Vol. 622, (2018), 1417-1430. doi.org/10.1016/j.scitotenv.2017.12.059
- Papageorgiou, M., Kosma, C. and Lambropoulou, D., "Seasonal occurrence, removal, mass loading and environmental risk assessment of 55 pharmaceuticals and personal care products in a municipal wastewater treatment plant in central greece", *Science of The Total Environment*, Vol. 543, (2016), 547-569. doi.org/10.1016/j.scitotenv.2015.11.047

12. Pérez, M.H., Peñuela, G., Maldonado, M.I., Malato, O., Fernández-Ibáñez, P., Oller, I., Gernjak, W. and Malato, S., "Degradation of pesticides in water using solar advanced oxidation processes", *Applied Catalysis B: Environmental*, Vol. 64, No. 3-4, (2006), 272-281. doi.org/10.1016/j.apcatb.2005.11.013
13. Martín, M.B., López, J.C., Oller, I., Malato, S. and Pérez, J.S., "A comparative study of different tests for biodegradability enhancement determination during aop treatment of recalcitrant toxic aqueous solutions", *Ecotoxicology and Environmental Safety*, Vol. 73, No. 6, (2010), 1189-1195.
14. Melo, S.A.S., Trovó, A.G., Bautitz, I.R. and Nogueira, R.F.P., "Degradation of residual pharmaceuticals by advanced oxidation processes", *Química Nova*, Vol. 32, No. 1, (2009), 188-197.
15. Oturan, M.A., Oturan, N., Edelahi, M.C., Podvorica, F.I. and El Kacemi, K., "Oxidative degradation of herbicide diuron in aqueous medium by fenton's reaction based advanced oxidation processes", *Chemical Engineering Journal*, Vol. 171, No. 1, (2011), 127-135.
16. Ali, I., "New generation adsorbents for water treatment", *Chemical Reviews*, Vol. 112, No. 10, (2012), 5073-5091. doi.org/10.1021/cr300133d
17. Ali, I., "Water treatment by adsorption columns: Evaluation at ground level", *Separation & Purification Reviews*, Vol. 43, No. 3, (2014), 175-205. doi.org/10.1080/15422119.2012.748671
18. Ali, I., Alharbi, O.M., Althman, Z.A., Badjah, A.Y. and Alwarthan, A., "Artificial neural network modelling of amido black dye sorption on iron composite nano material: Kinetics and thermodynamics studies", *Journal of Molecular Liquids*, Vol. 250, (2018), 1-8.
19. Burakova, E.A., Dyachkova, T.P., Rukhov, A.V., Tugolukov, E.N., Galunin, E.V., Tkachev, A.G. and Ali, I., "Novel and economic method of carbon nanotubes synthesis on a nickel magnesium oxide catalyst using microwave radiation", *Journal of Molecular Liquids*, Vol. 253, (2018), 340-346.
20. Ali, I., Gupta, V.K., Khan, T.A. and Asim, M., "Removal of arsenate from aqueous solution by electro-coagulation method using al-fe electrodes", *International Journal of Electrochemical Science*, Vol. 7, (2012), 1898-1907.
21. Meher, A.K., Das, S., Rayalu, S. and Bansiwala, A., "Enhanced arsenic removal from drinking water by iron-enriched aluminosilicate adsorbent prepared from fly ash", *Desalination and Water Treatment*, Vol. 57, No. 44, (2016), 20944-20956.
22. Ali, I., Khan, T.A. and Asim, M., "Removal of arsenate from groundwater by electrocoagulation method", *Environmental Science and Pollution Research*, Vol. 19, No. 5, (2012), 1668-1676.
23. Ali, I., AL-Othman, Z.A. and Alwarthan, A., "Molecular uptake of congo red dye from water on iron composite nano particles", *Journal of Molecular Liquids*, Vol. 224, (2016), 171-176. doi.org/10.1016/j.molliq.2016.09.108
24. Ali, I., AL-Othman, Z.A. and Sanagi, M.M., "Green synthesis of iron nano-impregnated adsorbent for fast removal of fluoride from water", *Journal of Molecular Liquids*, Vol. 211, (2015), 457-465. doi.org/10.1016/j.molliq.2015.07.034
25. Alharbi, O.M., Khattab, R.A. and Ali, I., "Health and environmental effects of persistent organic pollutants", *Journal of Molecular Liquids*, Vol. 263, (2018), 442-453. doi.org/10.1016/j.molliq.2018.05.029
26. Ali, I., Alharbi, O.M., Althman, Z.A. and Alwarthan, A., "Facile and eco-friendly synthesis of functionalized iron nanoparticles for cyanazine removal in water", *Colloids and Surfaces B: Biointerfaces*, Vol. 171, (2018), 606-613. doi.org/10.1016/j.colsurfb.2018.07.071
27. Kirsanov, M. and Shishkin, V., "Evaluating and improving the efficiency of the use of activated carbons for the extraction of organochlorine compounds in water treatment technology", *Foods and Raw Materials*, Vol. 4, No. 1, (2016).
28. Shiqian, L., Peijiang, Z. and Ling, D., "Adsorption application for removal of hazardous chloroform from aqueous solution by nanocomposites rectorite/chitosan adsorbent", *Journal of Water Resource and Protection*, Vol. 2011, (2011). DOI:10.4236/jwarp.2011.36055
29. Zareei, F. and Ghoreyshi, A., "Modeling of air stripping-vapor permeation hybrid process for removal of vocs from wastewater and vocs recovery", *World Applied Sciences Journal*, Vol. 13, No. 9, (2011), 2067-2074.
30. Zhang, Y., Wei, C. and Yan, B., "Emission characteristics and associated health risk assessment of volatile organic compounds from a typical coking wastewater treatment plant", *Science of The Total Environment*, Vol. 693, (2019), 133417. doi.org/10.1016/j.scitotenv.2019.07.223
31. Wang, B., Zhang, H., Wang, F., Xiong, X., Tian, K., Sun, Y. and Yu, T., "Application of heterogeneous catalytic ozonation for refractory organics in wastewater", *Catalysts*, Vol. 9, No. 3, (2019), 241. doi.org/10.3390/catal9030241
32. Aghaeinejad-Meybodi, A., Ebadi, A., Shafiei, S., Khataee, A. and Kiadehi, A.D., "Degradation of fluoxetine using catalytic ozonation in aqueous media in the presence of nano- γ -alumina catalyst: Experimental, modeling and optimization study", *Separation and Purification Technology*, Vol. 211, (2019), 551-563. doi.org/10.1016/j.seppur.2018.10.020
33. Rahman–Al Ezzi, A.A., "A modification of a trio effects portable water treatment system", *Science International*, Vol. 30, No. 4, (2018), 673-680.

Persian Abstract

چکیده

در این مطالعه امکان استفاده از طرح توسعه یافته برای حذف آلاینده های آلی از فاضلاب مورد بررسی قرار گرفته است که شامل ادغام کار هر دو ستون حباب پالس (PBC) و راکتور حلقه هوایی معکوس سیال سازی (IFALR) می باشد. تریبون آزمایشی ساخته شده و نصب شده است که از یک ستون حباب به قطر ۵ سانتی متر و ارتفاع ۲۱۰ سانتی متر تشکیل شده است. در قسمت بالا یک شیر الکتریکی وجود دارد که حداقل از طریق دو تایمر به صورت الکتریکی تبدیل می شود و اتصال آن با حلقه راکتور توسط سوپاپ یک طرفه راکتور حلقه شامل یک لوله مستطیل شکل بیرونی با ابعاد (۲۹ سانتی متر طول x 15.5 سانتی متر عرض x ۱۵۰ سانتی متر ارتفاع) و یک لوله پیش ساز داخلی با قطر ۹ سانتی متر و طول ۱۲۰ سانتی متر به عنوان کربن فعال شده دانه ای به عنوان جاذب در ناحیه آنولوس قرار می گیرد. بین لوله داخلی و خارجی. آزمایشات با استفاده از یکی از آلاینده های آلی یعنی کلروفرم انجام شد، با یک سناریوی کار که شامل تغییر هر دو سرعت جریان هوا (۲-۲۰) لیتر در دقیقه، زمان کل بقای تیمار (۵-۶۰) دقیقه، نسبت مولی از آلاینده کلروفرم به عامل اکسید کننده پراکسید هیدروژن (۱۰/۱ - ۲۰/۱). نتایج نشان داد راندمان حذف نزدیک ۸۹٪ است و نشانگر موفقیت در طرح پیشنهادی می باشد که احتمال بازیافت آب تصفیه شده و رها کردن آن به محیط زیست به دلیل کم خطر بودن آلاینده آلی موجود در آن است.



Effects of Lateral Constraints and Geometrical Characteristics on Deformation Capacity of the Persian Historic Unreinforced Masonry Shear Walls under Uncertainty Conditions

M. Ghamari^a, M. S. Karimi^{*a}, A. AmirShahkarami^b

^a Faculty of Civil Engineering, Semnan University, Semnan, Iran

^b Department of Civil & Environmental Engineering, Amirkabir University of Technology, Tehran, Iran

PAPER INFO

Paper history:

Received 14 March 2020

Received in revised form 27 April 2020

Accepted 04 August 2020

Keywords:

Unreinforced Masonry Shear Walls

Lateral Constraints

Aspect Ratio

Nonlinear Pushover Analysis

Partial Factor for Deformation Capacity

ABSTRACT

In the most structural codes, deformation capacity of the unreinforced masonry shear walls is estimated based on their structural behavior (failure mode) and aspect ratio. In this paper, deformation capacity was determined for the Persian historic brick masonry walls by considering the effects of various parameters such as lateral constraints, aspect ratio and thickness. Also, to take into account the uncertainties in material and geometry of the walls in their deformation capacity, partial factor γ_{du} was proposed, somehow, deformation capacity of masonry wall is determined by multiplying this factor in the computed deformation. Accordingly, the in-plane behavior of 48 different specimens of masonry walls with four lateral constraint configurations (contribution of transverse walls and also top slab), four distinct aspect ratios (height to length) of 0.5, 0.75, 1.0 and 1.5, three traditional wall thicknesses of 0.20, 0.35 and 0.50 m, under pre-compression load of 0.10 MPa were computed using nonlinear pushover analyses. Then, the obtained force-deformation curves were idealized by bilinear curves (linear elastic – perfectly plastic) to make them easier for comparison objectives as well as to be more adopted in practical purposes. The latter results indicated that deformation capacity of the shear walls decreases by stiffer lateral constraints, more thickening; and decrease in height-to-length aspect ratio. In addition, it was observed that the transverse walls (vertical constraints on two sides, and at two ends of the base shear walls) were more efficient in reducing deformation capacity than the top slab (horizontal constraint). As a result, according to the numerical calculations, the ultimate drift value for the Persian historic brick masonry walls determined between 1.3% and 2.7%. Eventually, the partial factor of γ_{du} to consider uncertainty in modulus of elasticity and thickness assessment in deformation capacity of the Persian historic masonry shear walls achieved in the range of 1.3 to 1.7.

doi: 10.5829/ije.2020.33.11b.02

1. INTRODUCTION

Masonry structures are one of the oldest and most widely used constructions. In Iran, many masonry structures were built using clay units walls and jack-arch top slab (ceiling). Seismic vulnerability is a serious matter for masonry structures and the most vulnerable members during earthquakes are the load-bearing shear walls [1]. One of the main factors in seismic assessment of the masonry shear walls is their deformation capacity, which so far, limited researches has been carried out on this

context [2]. Deformation capacity of masonry shear walls is affected by various factors such as; aspect ratio, thickness, and lateral constraints of the wall, as well as gravitational load level, in addition to the material properties. Because of limited knowledge on deformation capacity of the masonry walls and lack of reliable analytical model, directing a study on this area seemed inevitable. In recent years, some researchers have investigated on behavior of the masonry structures using finite element methods; in which, mostly adopted an identical homogenized properties for the units and

*Corresponding Author Institutional Email: mskarimi@semnan.ac.ir (M. S. Karimi)

mortar; which known as “macro modelling”. In addition, behavioral models of masonry materials with homogeneous properties were developed, ignoring the effects of mortar bonds (while are able to model local failures) [3]. This process led to suggest a nonlinear finite element model for the behavior of masonry materials based on biaxial experiments on masonry assemblages [4]. This model is capable to consider nonlinear effects of materials and also progressive local failures [5]. Loading on masonry walls is mainly applied in two forms of in-plane shear and out-of-plane bending. Due to multi-directionality of the earth motions during earthquake, accurate seismic modeling of the masonry structures should include both in-plane and out-of-plane loads, simultaneously. By locating shear walls perpendicularly, in-plane behavior dominantly controls response of the walls. However, the effect of simultaneous loadings was experimentally studied on smaller wall specimens than the real ones; with different aspect ratios. It was found that aspect ratio had significant effect on behavior of the masonry walls, especially on deformation capacity [6, 7]. This led to consider mainly the in-plane shear loading in numerical modellings, which these conditions was achieved by applying appropriate boundary conditions, laterally, to prevent out-of-plane failure [8]. Simplified equations have also been proposed for shear strength of the masonry walls under different loading conditions (concentrated, distributed and out-of-plane loading) [9]. By research progressing, more completed and simpler relations have been proposed to determine the shear strength of masonry walls on the finite element basis [10]. Furthermore, using analytical methods, behavioral force-deformation curve, based on an elastic-perfectly plastic behavior for masonry materials, was proposed [11, 12].

Transverse wall or flange were defined as part of the out-of-plane wall that participates with the shear wall to resist lateral (out-of-plane) loads [13]. The influence of transverse wall (flange) for unreinforced masonry building (URM) walls under in-plane (shear) loading has been investigated, too. Based on the report NZSEE [14], the in-plane response of URM walls is significantly influenced by the presence of transverse walls. Yi [15] indicated the effects of transverse walls (flanges) on the maximum strength of shear walls, and also noted that no experimental data were available to specifically investigate the URM shear walls with transverse wall. In these investigations, it was determined that the amount of drift depends on the locations of the transverse walls to the in-plane wall. It was also determined that the location of the transverse walls has a significant effect on shear strength of the wall. If the transverse wall is positioned closer to either ends of the wall, its shear strength increases, but when the transverse wall is in the middle of the in-plane wall, it has no effect on its shear strength [16].

The Eurocode 6 [17], Eurocode 8 [18], and several FEMA guidelines [19, 20] debated about drift capacity for URM walls. In Eurocode 8-Part 3 [18], deformation capacity of the masonry structures is dependent on the aspect ratio and the modes of failure. However, the deformation capacity of the shear walls is mainly influenced by their lateral constraints which define the stiffness and strength of the horizontal (top slab) and vertical (transverse wall) constraints. FEMA 306 [19] and FEMA 273 [20] distinguishes drift capacities for different damage levels. The drift capacities proposed by FEMA 306 [20] are very similar to those in Eurocode 8 [18]. Contrary to the aforementioned codes, the Swiss code considers drift capacity as a function of axial stress ratio of the masonry compressive strength [21]. The study on effect of the geometry and aspect ratio (height to length) showed that these parameters had a great effect on shear wall deformation capacity, which increased by decreasing size (i.e. its length) [6]. In recent years, deformation-based methods have been gradually developed for the seismic assessment of existing masonry structures. It is generally accepted that methods of evaluating structural damage based on materials deformation predicts the conditions of damages and their distributions, more realistically [22]. Thus, it would be vital to consider the deformation capacity of masonry structures on their assessing or design. In this regard, the in-plane behavior of several masonry walls with different modes of failure [2] and lateral constraints [23] has been investigated. On the one hand, the existence of significant variability in the experimental data and the lack of a reasonable conclusion for the displacement capacity of the URM shear walls based on the experimental data, and on the other hand, lack of valid analytical model, limits for either the displacement capacity or the force-displacement relationship of URM walls [2]. It should be noted that most of the researches has been done on the strength characteristics of the in-plane response of URM walls. Petri and Bayer [23] studied the effect of boundary conditions on displacement capacity by performing six series tests of static and/or cyclic shear loadings on unreinforced masonry shear walls. Tomazevic and Weiss [24] examined a set of samples with varying aspect ratios and in actual size by shaking table tests to determine the force-reduction factor for the URM structures.

2. RESEARCH APPROACH

In this study, shear walls with four different lateral constraint components were modelled to study the behavior of Persian historic masonry shear walls, influenced by the presence of transverse walls and of a top slab, as illustrated in Figure 1. In the first model, a shear wall was modeled without any lateral component, known as the base wall, as "W" (Figure 1a).

Subsequently, with the gradual increase of the neighboring members, other masonry specimens with different lateral constraints were created. Figure 1b, exposed a specimen with a horizontal component or top slab and is represented by the "H" index. The third set of specimens with transverse walls at two ends and on both sides of the wall is presented in Figure 1c as "V". In the fourth typologies, both the horizontal (top slab) and vertical (transverse walls on both sides) constraints are placed with the base shear wall specimen (Figure 1d), which is named "H+V".

For simulation purposes, masonry materials should be considered as quasi-brittle materials. The SOLID65 element (from the library elements of the ANSYS [25] program) was used to represent the properties of homogeneous composition of bricks and mortar. This is a dedicated three-dimensional solid iso-parametric element to model nonlinear response. The element is a hexahedron with eight nodes, with three degrees of freedom at each node (translations in x, y and z directions) and eight integration points. The walls are restricted by the conditions of presence of the connecting side elements. At borders of the specimens in which there is no connecting side constraint, nodes on those edges of the wall are only prevented from lateral movement. Transition at nodes located on edge borders of the vertical (transverse walls) and/or horizontal (top slab) constraints, are free along the directions located on the wall plane, and the lateral transition, perpendicular to the wall plane, was prevented. This was regarding the point that historic walls are not confined in a frame and are able to displace vertically. To apply support conditions at the base, all nodes of the masonry block elements, located at the base of the wall, were fully fixed.

In this research, the base walls with a constant height of 3.0 m, three thicknesses of 0.20, 0.35, and 0.50 m, and four lengths of 2.0, 3.0, 4.0, and 6.0 m (resulting in height-to-length aspect ratios of 1.5, 1.0, 0.75 and 0.5,

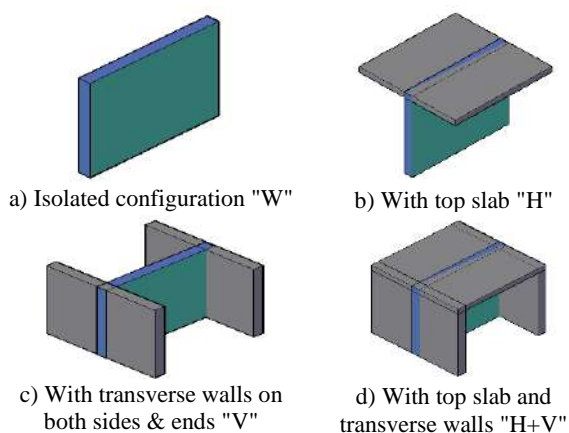


Figure 1. Masonry shear wall models with distinct lateral constraints

respectively) were modelled. The half-lengths of the horizontal component (top slab) and the transverse walls, attached to each side of the main shear wall, is equal to 3.0 m. This value was chosen according to definition of the effective loading span with the maximum distance of two masonry walls i.e. 6.0 m. Thickness of the transverse walls are the same as the base shear wall, in each model. The top slab is also selected from the Persian jack-arch with a thickness of 20 cm. The specimens were analyzed under corresponding gravity load of one floor, only. The gravity load was calculated according to the applied dead-load of 400 kg/m² and live-load of 200 kg/m², of one floor. Hence, the gravity load was 100 kN/m² (0.2 MPa), which applied on the top of the shear walls. In addition, monotonically increasing in-plane shear deformation was applied on the top of the wall, as the shear loading. Newton-Raphson iteration with deformation control and the convergence criterion with a tolerance of 10⁻⁴ was used to run the numerical analyses.

In this research, due to the lack of sufficient knowledge about the effective factors in deformation capacity of the masonry shear walls, it was attempted to determine a partial safety factor for their deformation capacity, using the protocols and techniques available in the structural codes. The partial safety factor for deformation capacity (γ_{du}) is a coefficient that can be used to model uncertainties. To evaluate the safety of historic masonry structures, this study is focused on two parameters, namely the modulus of elasticity and thickness of the wall as input parameters for uncertainty determination. The strength value of the masonry materials is affected by the modulus of elasticity, therefore a correlation with those properties is considered such that they would change accordingly to the changes of the modulus of elasticity. Thickness is another relevant factor in the stiffness and shear strength of the walls.

In this study, ANSYS software [25] was used for the masonry wall specimen analyses under in-plane loading. The characteristics of isotropic homogeneous masonry material used in this study; are presented in Table 1. This table indicates the mechanical properties for the assemblage of clay brick and clay-gypsum mortar; used in Persian historical buildings in Qazvin. These mechanical properties have been determined from the experimental tests [26], and also available in literature [27, 28].

TABLE 1. Mechanical properties for masonry assemblage [27-29]

Bulk density (kg/m ³)	1530
Modulus of elasticity (MPa)	2730
Poisson's ratio (-)	0.17
Compressive strength (f_c) (MPa)	2.73
Tensile strength (f_t) (MPa)	0.27

In general, description of failure criterion for the homogenized masonry material is a complicated task, and it needs to be investigated by the results of several tests, including biaxial tests. In here, the failure criterion used in FE modeling of the masonry materials is the Willam-Warnke failure criterion [29]. This failure criterion is expressed by the multi-axial stress conditions. In this theory, each stress is not individually compared to its limit state value; but, by combining the stresses with the stresses at the limit state; and considering their interactions, an ultimate value is obtained as the criterion of failure, as given in Equation (1):

$$\frac{F}{f_c} - S \geq 0 \quad (1)$$

where in, F is a function of the principal stresses state (σ_{xp} , σ_{yp} , σ_{zp}), f_c is characteristic compressive strength of masonry, S is the failure surface expressed in terms of principal stresses, and σ_{xp} , σ_{yp} , σ_{zp} are the principal stresses (in principal directions). The parameters of Willam-Warnke criterion (used in ANSYS [25]) for the masonry assemblage of clay brick and clay-gypsum mortar; were calculated from Equations (2) to (6) [27], and values for the parameters used in this study (for $f_c = 2.73$ MPa) are shown in Table 2.

$$f_t = 0.1f_c \quad (2)$$

$$f_{cb} = 1.2f_c \quad (3)$$

$$f_1 = 1.45f_c \quad (4)$$

$$f_2 = 1.725f_c \quad (5)$$

$$|\sigma_h^a| \leq 3^{0.5}f_c \quad (6)$$

where in, f_t is the uniaxial tensile strength, f_{cb} is the biaxial compressive strength, f_1 is the biaxial compressive strength for the case of hydrostatic pressure, f_2 is the uniaxial compressive strength for the case of hydrostatic pressure, $|\sigma_h^a|$ is the hydrostatic pressure, TCF is the stiffness multiplier for the cracked tensile condition, β_t is the shear transfer coefficient across the

TABLE 2. Parameters of Willam-Warnke failure criterion (used in ANSYS) [25, 29]

f_t (MPa)	0.27
f_{cb} (MPa)	3.28
f_1 (MPa)	3.96
f_2 (MPa)	4.71
$ \sigma_h^a $ (MPa)	4.73
TCF	0.6
β_t	0.15
β_c	0.75

open crack, and β_c is the shear transfer coefficient across the closed crack.

3. VALIDATION OF NUMERICAL MODELLING

To make sure about credibility of details in the way of making the walls numerical models, chosen failure criterion, assigned values for the input parameters, and also results to be obtained, initially, it is necessary to validate numerical results by the available data from the experimental specimens. This important was achieved by modelling of in-plane masonry shear walls with available experimental results [30]. This verification was performed on two wall specimens with different dimensions. The first specimen is in 250 cm height and 125 cm length (Figure 2a), and the second one is in both height and length of 250 cm (Figure 2b). The nominal thickness of the specimens is 32 cm. A constant gravity load of 0.2 MPa was applied on top of the walls, as pre-compression. The parameters of Willam-Warnke criterion was set in accordance with the available data from the experimental ones.

In Figure 3, the obtained numerical force-displacement curves were compared with the experimental ones. Due to the different number of experimental samples and easier perception, the experimental results are shown as a shading area. As shown in Figure 3, the numerical results are satisfactorily verified by the experimental ones, in their initial stiffness and the peak load. As it is shown, the numerical estimated of shear capacity reaches 86.4 kN and 223.3 kN for two specimens, which is within the limits of what achieved in experiments (grey area). Therefore, it can be concluded that further considered numerical models with the same procedure and details of modelling, failure criterion, and input data for the material parameters, will acceptably predict the real shear behavior of those real ones.

4. PARAMETRIC ANALYSIS

In this section, nonlinear pushover analyses results of 48 shear walls –similar to what were used for validation purpose- with the same details of modelling and material

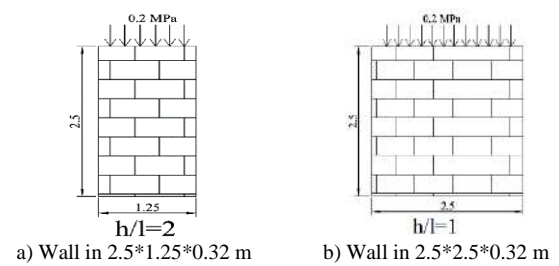


Figure 2. Shear wall specimens for validation [30]

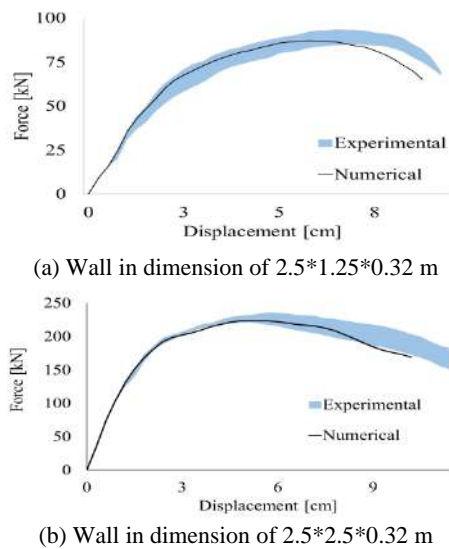


Figure 3. Comparison of the force-displacement diagrams for the validation models [31]

characteristics is presented. Behavior of the walls in distinct lateral constraints (shown in Figure 1), in height of 3.0 m and aspect ratios of 0.5, 0.75, 1.0 and 1.5, in thicknesses of 0.20, 0.35, and 0.50 m, under constant pre-compression level of 0.10 MPa, for the material characteristics (Table 2) are investigated. In all models, the top slab is in thickness of 20 cm; and the transverse walls are in the same thickness of the base shear wall, with 3.0 m length on each side of the shear wall. Figure 4 indicates the force-displacement behavioral curves for the specimens with different lateral constraints and aspect ratios; for the walls with a thickness of 0.20 m. The force-displacement curves for the specimens with an aspect ratio of 0.5 are shown in Figure 4a. In this figure, it is clear that the walls with more components of the lateral constraints had higher shear strength and less displacement capacity. The force-displacement curves of the walls with an aspect ratio of 0.75, 1.0 and 1.5 are also depicted in Figures 4b, 4c, and 4d, respectively. From the curves in Figure 4, it is apparent that the specimens with more lateral constraint components had lower ultimate displacement and higher shear strength. In addition, by increasing aspect ratio, the shear strength was reduced while the ultimate displacement was increased. It should be noted that the "H+V" wall with the aspect ratio of 0.5 and the "H" wall with the aspect ratio of 1.0 -in their post peak area- had a smaller shear strength than the specimens with lower lateral constraints, which is mainly due to the dependency of numerical results on the assumed geometric configuration and boundary conditions of the models, as well as meshing and non-real numerical parameters. Figures 5 and 6 illustrate the force-displacement curves for the specimens with 0.35 m and 0.50 m thicknesses, respectively. As it is evident,

increasing wall thickness led to higher shear strength and lower ultimate deformation. For instance, the ultimate deformations of specimens with 0.35 m and 0.50 m thicknesses are between 5.0 and 6.0 cm, while for the wall with 0.20 m thickness it is in range of 7.0 to 8.0 cm. Also, for the "H+V" wall with the aspect ratio of 0.5 -as a sample- with 20 cm thickness its shear strength is 675 kN (Figure 4a), while with 0.35 m and 0.50 m thicknesses, its shear strength is 852 kN and 1158 kN, respectively (Figures 5a and 6a).

Also, it can be concluded that the two transverse wall components were more efficient in confining and stiffening of the wall, than the top slab, which consequently affected in reduction of the ultimate displacement as well as increase in shear strength. Moreover, for a given aspect ratio, there was not significant changes in initial stiffness of the walls with distinct lateral constraints. It should be mentioned that difference in the end-point of the curves are due to the run termination by the program. To obtain the normalized ultimate displacement value, it is necessary to equate the results of these curves to idealized bilinear envelopes.

4. 1. Idealized Bilinear Envelopes

In this section, the aforementioned force-displacement curves are idealized by bilinear curves (linear elastic-perfectly plastic), to facilitate comparison objectives and driving desired numerical values. For idealization; the effective stiffness (K_{eff}), the ultimate deformation (d_u), and the normalized ultimate shear force (F_u) are the required parameters to define the bilinear curves. The modified ultimate deformation corresponds to the point with 80% reduction in the maximum shear force ($0.8 \times F_{max}$), after the peak point [31]. Figure 7 schematically illustrates the followed calculation method to extract aforementioned parameters. In more details, the effective stiffness is evaluated from the slope of the initial part of the curve up to 70% of maximum shear force ($0.7 F_{max}$), while F_{max} is the maximal shear force on the curve. Finally, by choosing the appropriate values for the normalized ultimate shear force (F_u) and drawing a horizontal line that represents perfect plastic yielding of the material, so that the area under the two curves become identical, the bilinear curve is obtained. Thus, the obtained idealized curves for investigated specimens with different lateral constraints, aspect ratios, and thicknesses are presented in Figures 8 to 10.

The linear elastic-perfectly plastic envelopes in Figure 8 is derived from the obtained responses presented in Figure 4; which were the result of specimens with thickness of 0.20 m. Ultimate deformation for the masonry walls with thickness of 0.20 m were obtained in range of 6 to 8 cm. The bilinear envelopes in Figures 9 and 10 are derived from the presented data in Figures 5 and 6; which are the result of specimens with thicknesses of 0.35 and 0.50 m, respectively. Figures 9 and 10 are

evidences of descending trend in deformation capacity (d_u) by increasing the lateral constraints components and reducing the aspect ratio.

4. 2. Ultimate Drift Values Values of ultimate relative deformation or ultimate drift representing the ratio of modified deformation capacity to the specimen height (d_u/H); are reported in Table 3. The outcomes were categorized based on lateral constraints, aspect ratio, and thickness. For an illustrating example, the results for the thickness variable are shown in Figure 11. As it can be inferred, increasing thickness of the masonry walls reduces their ultimate drift of d_u/H ; which varies in range of 1.3 to 2.6%.

4. 3. Derivation of Partial Factor Γ_{du} for Deformation Capacity under Uncertainty Conditions

Accurate modeling and input parameter estimation are significant to obtain reliable results from the actual nonlinear behavior of the structure, so, it is necessary to investigate the impact of variability on geometry and material properties. As stated, also, the three-dimensional finite element model for masonry material for both modes; the geometrical conditions and parameters of material properties; were evaluated. Two parameters are analyzed in this study, namely the modulus of elasticity and the thickness of the wall. In order to obtain a measure of uncertainty in drift capacity partial factor (γ_{du}) is proposed, somehow, deformation,

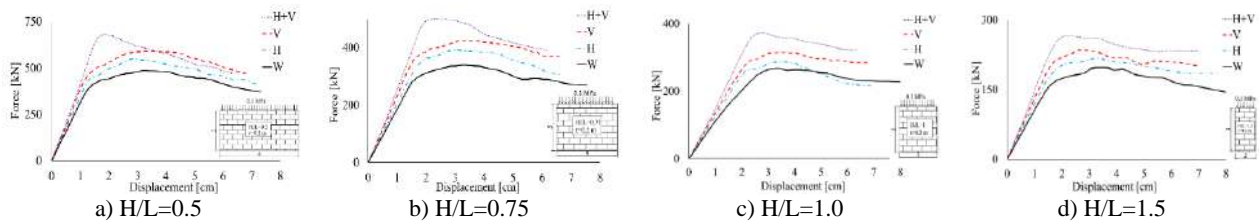


Figure 4. Force-displacement curves for masonry walls with distinct lateral constraints and aspect ratios, walls in thickness of 20cm

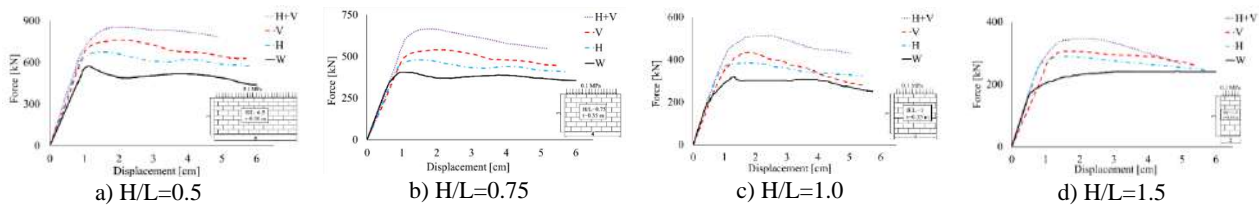


Figure 5. Force-displacement curves for masonry walls with distinct lateral constraints and aspect ratios, walls in thickness of 35cm

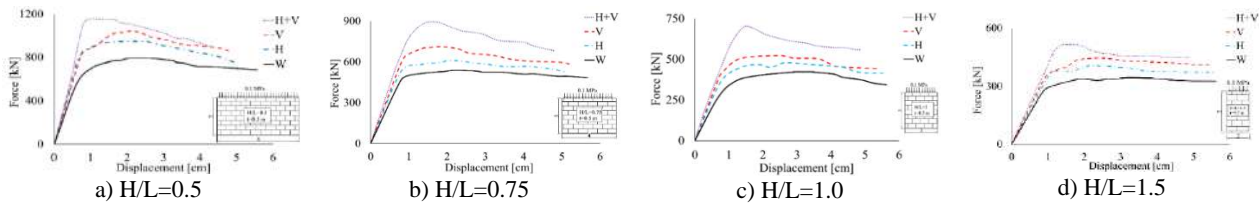


Figure 6. Force-displacement curves for masonry walls with distinct lateral constraints and aspect ratios, walls in thickness of 50cm

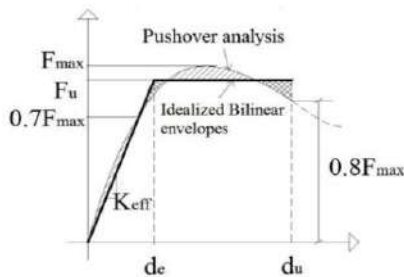


Figure 7. Definition of the parameters of the idealized bilinear envelope [31]

capacity of the wall is obtained by multiplying this factor in the modified deformation (obtained from bilinear F-d curves). In fact, to the aim of this study, the purpose of idealizing the results was to determine modified d_u characteristics (from bilinearization) to calculate the partial factor (γ_{du}). Studying the uncertainty effects was carried out using the utilities which are provided by the ANSYS program [24]. The probability distribution function of the variables (modulus of elasticity and thickness) and their covariance values are the input data given to the program.

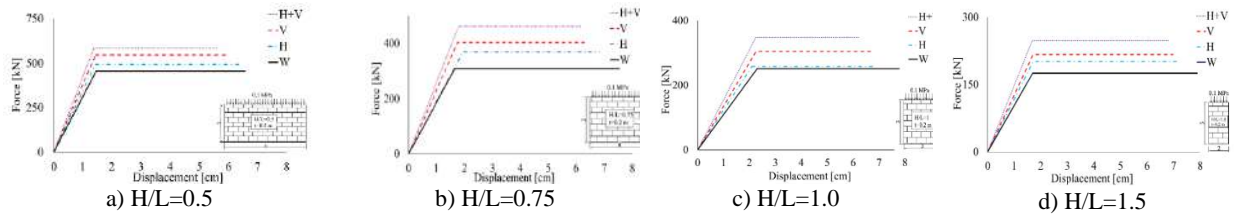


Figure 8. Idealized bilinear envelopes for masonry walls with distinct lateral constraints and aspect ratios, walls in 20cm thickness

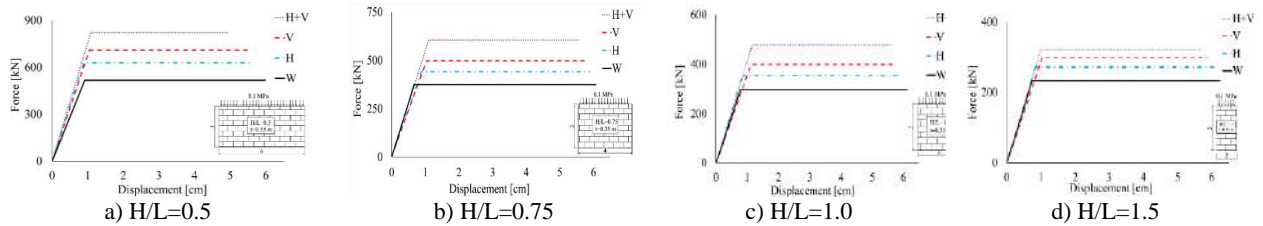


Figure 9. Idealized bilinear envelopes for masonry walls with distinct lateral constraints and aspect ratios, walls in 35cm thickness

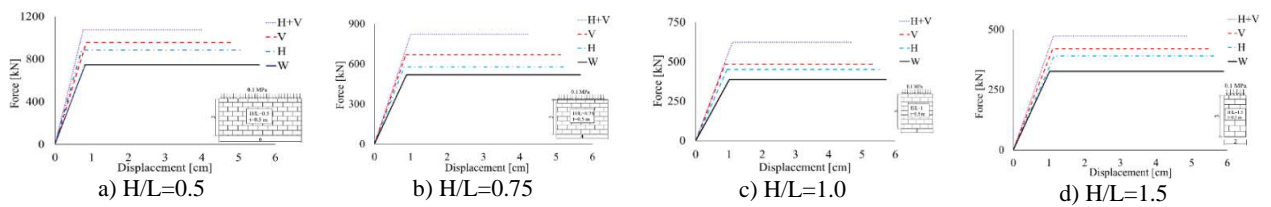


Figure 10. Idealized bilinear envelopes for masonry walls with distinct lateral constraints and aspect ratios, walls in 50cm thickness

For that purpose for each of the 48 individual studied specimens, thirty simulations were performed taking into account the consideration of modulus of elasticity and thickness; as random variables. The number of simulations (i.e. 30) was chosen so that the variation on the mean value of the response of the walls did not change more than 5% with the increase of more simulations. The force-displacement curves -which acquired from the analysis of each of the thirty specimens - were used by random variables wherein the modulus of elasticity was implemented by a log-normal probability distribution with a CoV of 0.25 [32], and the thickness was modeled by a normal probability distribution with CoV of 0.2 [33]. Then, the modified γ_{du} values for each specimen were accessed using the bilinear curves of each simulation. The partial factor (γ_{du}) for drift capacity was achieved by dividing the γ_{du} value of the specimen without any uncertainty analysis to the γ_{du} value obtained from the simulation of the thirty specimens with random properties. The γ_{du} value for each combination were attained according to the described procedure and summarized in Table 4 for all specimens with distinct variables.

The results in Table 4 to improve the perception of the relationships between variables in the value of the partial factor (γ_{du}) are plotted in Figure 12. From the

results in Figure 12, it can be concluded that by increasing the lateral constraint components of the wall, the value of the partial factor (γ_{du}) has decreased. In addition, by increasing the aspect ratio (height-to-length), the value of the γ_{du} factor has increased. For example, for a shear wall without any lateral constraints ("W"), with aspect ratio of 0.5 and thickness of 0.35 m, the γ_{du} value is 1.34; which is 7%, 9% and 14% smaller than the walls with aspect ratios of 0.75, 1.0 and 1.5, respectively. A similar trend can be noticed for other samples. Finally, according to Table 4, partial factor of deformation capacity (γ_{du}) for the Persian historic brick masonry was obtained between 1.3 and 1.7, depending on its lateral constraint, aspect ratio, and thickness conditions.

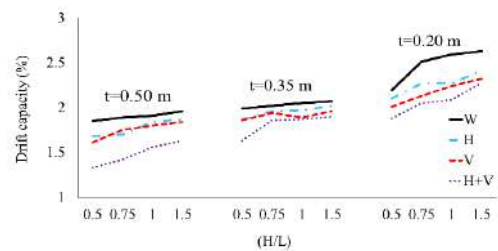


Figure 11. Ultimate drift vs. aspect ratio for the masonry walls with distinct thicknesses and lateral constraints

TABLE 3. Drift capacity values (d_u/H) for the masonry walls with distinct lateral constraints, aspect ratios, and thicknesses (in percentage)

Specimen	Lateral constraints	Wall thickness=20 cm				Wall thickness=35 cm				Wall thickness=50 cm			
		0.5	0.75	1	1.5	0.5	0.75	1	1.5	0.5	0.75	1	1.5
	H/L (aspect ratio)												
W	Original building wall	2.19	2.51	2.59	2.63	1.99	2.02	2.05	2.07	1.85	1.89	1.91	1.96
H	With top slab	2.10	2.27	2.27	2.41	1.87	1.96	1.97	2.02	1.68	1.70	1.84	1.87
V	With transverse walls on both sides	2.01	2.13	2.24	2.32	1.86	1.94	1.89	1.96	1.61	1.75	1.80	1.84
H+V	With top slab and transverse walls	1.88	2.05	2.08	2.27	1.63	1.86	1.87	1.90	1.33	1.42	1.56	1.63

TABLE 4. Partial factor γ_{du} for the masonry walls with distinct lateral constraints, aspect ratios, and thicknesses

Specimen	Lateral constraints	Wall thickness=20 cm				Wall thickness=35 cm				Wall thickness=50 cm			
		0.5	0.75	1	1.5	0.5	0.75	1	1.5	0.5	0.75	1	1.5
	H/L (aspect ratio)												
W	Original building wall	1.48	1.57	1.59	1.64	1.34	1.43	1.48	1.52	1.41	1.42	1.48	1.56
H	With top slab	1.43	1.46	1.53	1.58	1.29	1.41	1.42	1.45	1.38	1.36	1.45	1.52
V	With transverse walls on both sides	1.45	1.52	1.54	1.56	1.31	1.39	1.43	1.39	1.34	1.37	1.39	1.46
H+V	With top slab and transverse walls	1.36	1.43	1.48	1.51	1.27	1.34	1.39	1.41	1.30	1.38	1.36	1.39

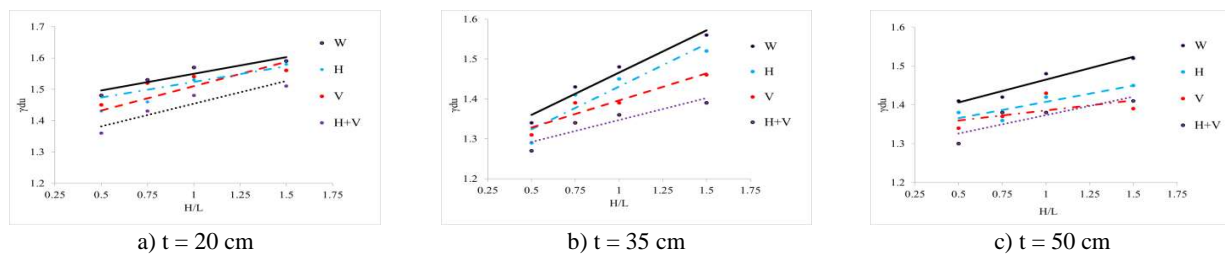


Figure 12. Partial factor γ_{du} for the masonry walls with distinct lateral constraints, aspect ratios, and thicknesses

5. SUMMARY AND CONCLUSION

In this study, it was attempted to investigate the deformation capacity for the Persian historic brick masonry under the influence of various variables under uncertainty conditions. The variety of lateral constraints, the height-to-length aspect ratio, and thickness of the wall have been investigated. For that aim, different combinations (48 different specimens) of masonry walls under in-plane loading were tested numerically in four different lateral constraints, four different height-to-length ratios, and three distinct thicknesses of the wall. The results indicated dependency of the deformation capacity to these variables. In addition, the effect of uncertainty on two parameters of modulus of elasticity (material parameter) and thickness of the specimens (geometry parameter) was investigated. As an outcome, it was tried to propose a partial factor (γ_{du}), to consider uncertainty effect in deformation capacity value (d_u), so that the deformation capacity is computed by multiplying the computed deformation capacity (d_u) by the (γ_{du}).

1. It was determined that increasing in lateral constraint components, and thickness of the wall, caused decrease in deformation capacity (d_u) of the wall.
2. The wall deformation capacity (d_u) increased by increasing its aspect ratio.
3. Evaluation to examine the effect of vertical and horizontal constraints, separately, showed that the effect of two vertical constraints (transverse walls at two ends and on both sides) on reduction of the wall drift capacity was more than the top slab.
4. Based on these numerical computations, the ultimate drift value of d_u/H ; for the shear walls with Persian historic material, obtained in range of 1.3 to 2.6%.
5. The results showed that by increasing lateral constraint components, and wall thickness, in contrary to the aspect ratio, the value of partial factors (γ_{du}) for deformation capacity was decreased.
6. The value of the partial factors for the wall deformation capacity (γ_{du}) based on the considered conditions in this study, is proposed in range of 1.3 to 1.7.

It was tried to delimit the results of this study only on specific governed conditions, assumptions and limitations including; walls typology, aspect ratio, thickness, protocols on numerical modelling and bilinearization technique, the method and parameters used in uncertainty studying, and especially the Persian historic masonry material properties. Definitely, to increase reliability on the results, it should study quite more experimentals as well as numerical specimens, with different conditions of historic masonry structures..

Finally, it should be mentioned that in cases of design purposes, the proposed values for (γ_{du}) should be magnified, by dividing γ_{du} on a less than one factor (This is an adaptation from the codes in computing the partial safety factor for materials (γ_M), using factor of 0.8).

6. REFERENCES

- Hamid, A.A., Mahmoud, A. and El Magd, S.A., "Strengthening and repair of unreinforced masonry structures: State-of-the-art", in Proc., 10th Int. Brick and Block Masonry Conf. Vol. 2, (1994), 485-497. DOI: 10.1061/(ASCE)1090-0268(2001)5:2(76)
- Salmanpour, A.H., Mojsilović, N. and Schwartz, J., "Displacement capacity of contemporary unreinforced masonry walls: An experimental study", *Engineering Structures*, Vol. 89, (2015), 1-16. DOI:10.1016/j.engstruct.2015.01.052
- Feba, S.T. and Kuriakose, B., "Nonlinear finite element analysis of unreinforced masonry walls", in Applied Mechanics and Materials, Trans Tech Publ. Vol. 857, (2017), 142-147. DOI: 10.4028/www.scientific.net/AMM.857.142
- Hendry, A., Samarasinghe, W., Page, A. And Poisson, "A finite element model for the in-plane behaviour of brickwork", *Proceedings of the Institution of Civil Engineers*, Vol. 73, No. 1, (1982), 171-178. DOI: 10.1680/iicep.1982.1878
- Laurenco, P., Rots, J.G. and Blaauwendraad, J., "Two approaches for the analysis of masonry structures: Micro and macro-modeling", *HERON*, Vol. 40, No. 4, (1995). <http://resolver.tudelft.nl/uuid:c39b29ab-3c75-47db-9cb5-bf2b1c678f1f> [Accessed 01. 01. 1995]
- Najafgholipour, M., Maheri, M.R. and Lourenço, P.B., "Capacity interaction in brick masonry under simultaneous in-plane and out-of-plane loads", *Construction and Building Materials*, Vol. 38, (2013), 619-626. DOI:10.1016/j.conbuildmat.2012.08.032Get rights and content
- Niasar, A.N., Alaei, F.J. and Zamani, S.M., "Experimental investigation on the performance of unreinforced masonry wall, retrofitted using engineered cementitious composites", *Construction and Building Materials*, Vol. 239, (2020), 117788. DOI: 10.1016/j.conbuildmat.2019.117788
- Howlader, M., Masia, M. and Griffith, M., "Numerical analysis and parametric study of unreinforced masonry walls with arch openings under lateral in-plane loading", *Engineering Structures*, Vol. 208, (2020), 110337. DOI: 10.1016/j.engstruct.2020.110337
- Howlader, M., Masia, M. and Griffith, M., "In-plane shear testing of unreinforced masonry walls and comparison with fea and nzsee predictions", *International Journal of Masonry Research and Innovation*, Vol. 5, No. 1, (2020), 47-66. DOI: 10.1504/IJMRI.2020.104845
- Roca, P., "Assessment of masonry shear-walls by simple equilibrium models", *Construction and Building Materials*, Vol. 20, No. 4, (2006), 229-238. DOI: 10.1016/j.conbuildmat.2005.08.023
- Giordano, A., De Luca, A., Mele, E. and Romano, A., "A simple formula for predicting the horizontal capacity of masonry portal frames", *Engineering Structures*, Vol. 29, No. 9, (2007), 2109-2123. DOI: 10.1016/j.engstruct.2006.10.011
- Howlader, M., Masia, M. and Griffith, M., "In-plane response of perforated unreinforced masonry walls under cyclic loading: Experimental study", *Journal of Structural Engineering*, Vol. 146, No. 6, (2020), 04020106. DOI: 10.1061/(ASCE)ST.1943-541X.0002657
- Moon, F.L., "Seismic strengthening of low-rise unreinforced masonry structures with flexible diaphragms", Georgia Institute of Technology, (2003), <http://hdl.handle.net/1853/5128>
- Engineering, N.Z.S.f.E., "Assessment and improvement of the structural performance of buildings in earthquakes: Prioritisation, initial evaluation, detailed assessment, improvement measures: Recommendations of a nzsee study group on earthquake risk buildings, New Zealand Society for Earthquake Engineering, (2014). <https://www.nzsee.org.nz/library/guidelines/>
- Yi, T., "Experimental investigation and numerical simulation of an unreinforced masonry structure with flexible diaphragms", Georgia Institute of Technology, (2004), <http://hdl.handle.net/1853/5149>
- Choudhury, T. and Kaushik, H.B., "Influence of individual wall strengths on lateral strength of urm buildings constructed using low-strength masonry", *Journal of Earthquake Engineering*, (2020), 1-28. DOI: 10.1080/13632469.2020.1742253
- Standard, B., "Eurocode 6—design of masonry structures—", British Standard Institution. London, Vol., No., (2005).
- Code, P., "Eurocode 8: Design of structures for earthquake resistance-part 1: General rules, seismic actions and rules for buildings", Brussels: European Committee for Standardization, (2005).
- Council, A.T. and Response, P.f., "Evaluation of earthquake damaged concrete and masonry wall buildings: Basic procedures manual, The Agency, (1999).
- Council, B.S.S., "Nehrp guidelines for the seismic rehabilitation of buildings", FEMA-273, Federal Emergency Management Agency, Washington, DC, (1997), 2-12.
- SIA, S., "266: Masonry", Swiss code, Swiss society of engineers and architects SIA, Zürich, Switzerland, (2005).
- ASCE, Fema 356-prestandard and commentary for the seismic rehabilitation of buildings. 2000.
- Petry, S. and Beyer, K., "Influence of boundary conditions and size effect on the drift capacity of urm walls", *Engineering Structures*, Vol. 65, (2014), 76-88. DOI: 10.1016/j.engstruct.2014.01.048
- Tomažević, M. and Weiss, P., "Displacement capacity of masonry buildings as a basis for the assessment of behavior factor: An experimental study", *Bulletin of Earthquake Engineering*, Vol. 8, No. 6, (2010), 1267-1294. DOI: 10.1007/s10518-010-9181-y
- ANSYS, A., 14, *ansys inc., basic analysis procedures guide release 14*.
- Hejazi, M.M. and Saradj, F.M., "Persian architectural heritage: Structure, WIT Press, (2014).
- Binda, L., Fontana, A. and Frigerio, G., "Mechanical behaviour of brick masonries derived from unit and mortar characteristics", Brick and Block Masonry (8 th IBMAC) London, Elsevier Applied Science, Vol. 1, (1988), 205-216. <http://www.hms.civil.uminho.pt/ibmac/1988/205.pdf>
- D'Altri, A.M., Sarhosis, V., Milani, G., Rots, J., Cattari, S., Lagomarsino, S., Sacco, E., Tralli, A., Castellazzi, G. and de Miranda, S., "Modeling strategies for the computational analysis

- of unreinforced masonry structures: Review and classification", *Archives of Computational Methods in Engineering*, (2019), 1-33. DOI: 10.1007/s11831-019-09351-x
29. Drobiec, L. and Jasiński, R., "Adoption of the willam-warnke failure criterion for describing behavior of ca-si hollow blocks", *Procedia Engineering*, Vol. 193, (2017), 470-477. DOI: 10.1016/j.proeng.2017.06.239
30. Magenes, G., Galasco, A., Penna, A. and Da Paré, M., "In-plane cyclic shear tests of undressed double leaf stone masonry panels", in Proceedings of the 14th European conference on earthquake engineering. Ohrid. (2010). <https://www.masonry.org.uk/downloads/volume-1-d-216>
31. Tomaževič, M., "Earthquake-resistant design of masonry buildings, World Scientific, (1999).
32. Code, J.P.M., "Joint committee on structural safety", URL: www.jess.ethz.ch, (2001).
33. Zhai, X. and Stewart, M., "Structural reliability of reinforced concrete block masonry walls in concentric compression", in 11th Canadian Masonry Symposium. Vol. 32, No. 1, (2009). DOI: 10.1016/j.engstruct.2009.08.020

Persian Abstract

چکیده

در اکثر آیین‌نامه‌های سازه‌ای، ظرفیت جابجایی در دیوارهای برشی بنایی، تخمینی از عملکرد رفتاری (و نوع شکست) و نسبت ابعادی ارتفاع به طول نمونه‌ها می‌باشد. این تحقیق، به منظور بررسی ظرفیت جابجایی دیوارهای برشی بنایی تاریخی ایرانی تحت تاثیر پارامترهایی نظیر قیودات جانبی، نسبت ابعادی و ضخامت دیوار انجام شده است. همچنین، برای مدل‌کردن اثر عدم قطعیت در مصالح و هندسه دیوار، ضریب جزئی γ_{du} پیشنهاد گردید، بطوریکه، جابجایی نهایی دیوار از حاصلضرب تغییر مکان محاسباتی در این ضریب جزئی بدست می‌آید. از این رو، ۴۸ نمونه مختلف از دیوارهای بنایی تحت بارگذاری برشی درون‌صفحه‌ای، برای چهار حالت مختلف از قیودات جانبی (ناشی از اثرات دیوارهای جانبی و سقف)، چهار نسبت ابعادی ارتفاع به طول ۰/۵، ۰/۷۵، ۱، و ۱/۵، با سه اندازه مرسوم برای ضخامت دیوار (۰/۲، ۰/۳۵، و ۰/۵ متر)، تحت بار پیش فشار ۰/۱ مگاپاسکال (متناظر بار یک سقف) مدل‌سازی گردیدند. پس از تهیه منحنی‌های رفتاری بار-تغییر مکان (منحنی ظرفیت)، به منظور ساده‌سازی پاسخ‌ها و نیز کاربردی‌تر کردن آنها، ایده‌آل‌سازی نتایج توسط منحنی‌های دوخطی الاستیک خطی-پلاستیک کامل، انجام گردید. نتایج ناشی از ایده‌آل‌سازی منحنی‌های رفتاری بار-تغییر مکان، مشخص نمود که با افزایش قیودات جانبی، افزایش ضخامت، و نیز کاهش نسبت ابعادی؛ ظرفیت جابجایی دیوارهای بنایی کاهش می‌یابد. ضمناً، مشاهده گردید که قید جانبی دیوارهای عرضی - اتصال‌یافته در هر دو انتها و در هر دو طرف دیوار برشی - نسبت به مولفه‌ی افقی (سقف تنها) در کاهش ظرفیت جابجایی و افزایش سختی دیوار برشی موثرتر می‌باشد. بر اساس این مدل‌سازی‌ها، نسبت تغییر مکان جانبی نهایی به ارتفاع (دریفت نهایی) برای دیوارهای برشی بنایی تاریخی ایرانی در بازه ۱/۳ تا ۲/۷ درصد بدست آمد. در نهایت، ضریب جزئی γ_{du} برای لحاظ نمودن عدم قطعیت در برآورد دو پارامتر مدول الاستیسیته مصالح و ضخامت دیوار در تعیین دریفت نهایی دیوار برشی با مصالح بنایی تاریخی ایرانی؛ در بازه ۱/۳ تا ۱/۷ حاصل گردید.



In-situ Fine Basalt Soil Reinforced by Cement Combined with Additive DZ33 to Construct Rural Roads in Gia Lai Province, Vietnam

B. H. Tran^a, B. V. Le^b, V. T. A. Phan^{*c}, H. M. Nguyen^d

^a Roads Management Center, Ho Chi Minh City, Vietnam

^b University of Transport and Communications, Ha Noi, Vietnam

^c Faculty of Civil Engineering, Ton Duc Thang University, Ho Chi Minh City, Vietnam

^d Research Institute of transportation Science & Roadway Laboratory 3, Ho Chi Minh City, Vietnam

PAPER INFO

Paper history:

Received 30 June 2020

Received in revised form 06 August 2020

Accepted 02 September 2020

Keywords:

Additive DZ33

Basalt

Rural Roads

Gia Lai Province

In-situ Soil

ABSTRACT

Today, the use of additives to enhance the load-bearing capacity of the soil has been applied to some rural roads in a number of provinces in Viet Nam, proving the outstanding advantages. This paper presents the results of research work and techno-application to rural road construction with on-spot fine basalt soil combined with adhesives including cement PCB40 and additive DZ33. The experimental results show that additive DZ33 has made it possible to increase the hydration ability with cement when effectively reacting with soil particles to reduce construction costs and environmental harms, improve the intensity of reinforced soil mix such as Elastic modulus of reinforced soil (E_s), splitting tensile strength (f_{st}), compressive strength (f'_s) and California Bearing Ratio (CBR). Successful application of additive DZ33 combined with cement in soil reinforcement to build rural transport works not only brings about economic efficiency but also, makes use of in-situ fine basalt soil to create a new material for the construction industry, humbly contributing to the study of rural road development in Gia Lai mountainous province in particular and Vietnamese transport infrastructures in general.

doi: 10.5829/ije.2020.33.11b.03

1. INTRODUCTION

Towards creating materials that reduce construction costs and environmental harms, there have been researches using natural pozzolan to strengthen the soil. This topic has been successfully studied and applied in the world. Some researchers have fruitfully studied the use of natural pozzolan combined with lime to reinforce weak clay, cohesive soil, etc. For instance, Harichane et al. [1], Harichane et al. [2], Harichane et al. [3], Malisa et al. [4], Al-Swaidani et al. [5], Mfinanga et al. (2008) [6] conducted experiments to find out the proper ratio of mixing natural pozzolan and lime with the soil for building foundation and pavement. The study result was soil mixed with 10-30% pozzolan (by weight) and 2% lime. Gypsum if added will significantly increase the

compressive strength. Sharpe et al. [7] made a report on the use of natural puzolan for building the low strength roadbed and pavement. Regarding the stabilized fine-grained soils, Javdanian [8] evaluated the compressive strength of fly ash and blast furnace slag based geopolymer clayey soil based on a large database and the results showed that the variation trends of the proposed UCS model are in reasonable agreement with the experimental result.

Rural roads play an important factor, constituting a high percentage of investment capital in practice of the criteria for new countryside in Viet Nam. Currently, most of the rural roads are made of cement concrete. However, the concrete road is limited by fracture due to its low compressive and tensile strength. Also, the continued exploitation and use of traditional materials will soon deplete the natural resources, affecting the environment. Using additive DZ33 to reinforce the soil is an option that contributes to reducing the total

*Corresponding Author Institutional Email:
phantoanhvu@tdtu.edu.vn (V. T. A. Phan)

construction cost of the building by allowing utilization of the local materials, lessening the need for aggregate materials and decreasing the total cost of road materials in general. Additive DZ33 is commonly used in construction of roadbeds with and without pavement, roads and shoulders, public roads, temporary roads into construction works, car parks with and without pavement, works foundation, farm roads, access to mines, foundation of airport runways, rural roads, and wherever technical improvement of road materials is in need. Additive DZ33 is capable of changing the physical and mechanical properties of the soil, thereby reducing the elasticity and permeability, increasing compactness and the load-bearing capacity of the soil.

The study of using local materials to replace traditional materials like sand, stone, etc. to build roads is extremely necessary and of high scientific significance. In this article, the authors would like to present the experimental results on effects of the ratio between cement and additive DZ33 on the soil hardening technology, those experiments done in laboratory and the practical application in a rural road section in Pleiop village, Hoa Lu ward, Pleiku city, Gia Lai province, Viet Nam.

2. MATERIALS USED

2. 1. Portland Cement Blended Portland cement Blended (Cement PCB) is commercially manufactured in Viet Nam. Cement PCB of grade 40 was used as a binder in this study. The specific gravity is 3.10 and specific surface area is 3550 cm²/g [9]. The chemical composition and basic physical properties of cement are presented in Tables 1 and 2, respectively.

TABLE 1. Chemical composition of cement PCB 40

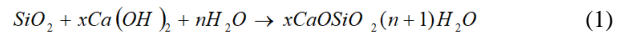
Component	Cement PCB (in weight %)
C ₃ S	52.19
C ₂ S	29.37
C ₃ A	6.36
C ₄ AF	10.62

TABLE 2. Physical properties of PCB

Component	Unit	Cement PCB
Specific gravity	g/cm ³	3.10
Fineness	(cm ² /g)	3550
Loss on ignition	(%)	0.90
Insolubility	(%)	0.10
Alkali content	(%)	0.54
Initial setting time	(min.)	142
Final setting time	(min.)	400

2. 2. Mechanism for Forming the Strength of Cement-reinforced Soil

Chemical process: This is the hydration process of cement particles, the ion exchange process of the double electric layer of clay and ions in the environment to make clay hard with a crystalline structure. The equation for the reaction is as follows:



The silicate calcification process and the aluminate calcification process above are very important in soil reinforcement, creating the crystalline structure for the soil and also enabling the particles in the soil to well bind. These processes slowly occur in the reinforced soil, hence cement, lime or fly ash must be well compacted and retain the best moisture for a given time.

Physical and chemical process: This is the process of exchanging ions between clay and ions in the environment, the absorption of molecules of substances from the liquids on the surface separating the phases, the coagulation of clay particles and colloidal particles, which creates stronger and more solid soil.

Physicochemical and mechanical process: Loosening the soil plays an important role to create gradation between soil, cement, lime or fly ash in the condition of compacting at the best moisture_ the smaller the soil particle, the more the particle surface is exposed to the binders, which increases linkability, thereby enhancing compaction and stability of the reinforced soil. Therefore, construction equipment that well loosens the soil plays a key role in the effectiveness of the reinforced soil.

2. 3. Additive DZ33

Additive DZ33 was supplied by MTV New Technology Application and Tourism Ltd Company (Newtatco), Vietnam. Additive DZ33 is a multi-Enzyme product specially developed as an effective aid to the workability, mix-ability, binding and compaction of soil. Also, additive DZ33 significantly improved stability in construction of roads and other infrastructure constructions. Especially, DZ33 has ionic actions, which bind dust particles together and cause dust-free environment. The physical and chemical properties are not provided by supplier due to a commercial and exclusive product.

Presence of additive DZ33 in the cement and soil mix enables water to penetrate farther into the cement particle core, which makes the reaction process of minerals C₃S and C₂S more thorough. During the reaction process, crystal lattices will be formed. These crystals penetrate and grow in the soil pores, which reduces permeability and increases intensity of the soil-cement mix. Pore reduction by increasing the number of

structural crystals will increase the compressive strength, elasticity and destruction resistance of the reinforced soil.

2. 4. Principle of Strength Formation in Reinforcing Basalt by Cement Combined with Additive DZ33

The working mechanism of additive DZ33 consists of the following steps [10].

3. CONSTRUCTION OF RURAL ROADS WITH IN-SITU BASALT REINFORCED BY ADDITIVE DZ33

3. 1. Introduction of the Works The road of Pleiup village, Hoa Lu ward, Pleiku city, Gia Lai province, Viet Nam has a cross-section of 3 meters and a total length of 1100 meters. The current state of the road pavement is seriously deteriorating, so transportation activities in the area face many difficulties.

3. 2. Content of the Experiment The experimental samples must meet the requirements for eliminating rough errors. Therefore, the uniformity, sample height, sample maintenance, and casting pattern were followed by the Vietnamese standard. Generally, the performance was carried out in principle:

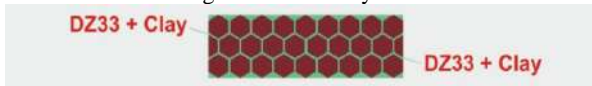
- Each group consists of 06 samples;
- Samples were cast on the automatic compactor;
- Test results were tested at curing age of 7, 14 and 28



Step 1. DZ33 introduces organic cations into the soil and neutralizes negative charges on the clay molecules



Step 2. The ionic reaction occurs by the participation of DZ33, weakening the molecular bonds between the naturally formed water film layer that envelops the clay molecule and making it easier to dehydrate



Step 3. Through the compaction process, the 'polymerization' between the soil molecules appears, pushing water and gas molecules present in the soil out, allowing the soil molecules reinforced with DZ33 to be uniformly arranged and closely linked together



Step 4. Multilateral bonding of the soil molecules forms a strong solid structure, greatly improving the load-bearing capacity and permeability coefficient of the material

days in two curing conditions: Moisturizing and water saturation. The specimens firstly were cured at room temperature and above 80% relative humidity for hydration to take place. For moisturizing condition, samples were tested after reaching sufficient days of moisturizing for moisturizing. For water saturation, samples were tested after reaching sufficient days of moisturizing and being soaked continuously for 48 hours. Survey criteria were tested as:

- + Elastic modulus E_s , (MPa);
- + Compressive strength R_n , (MPa);
- + Splitting strength f_{st} , (MPa);
- + California bearing capacity, CBR, (%).
- The cement content varied from 6%, 8% and 10%, respectively, by the dry soil weight. Additive DZ33 was mixed with water, performed at the moisturizing step to enable the reinforced soil mix to achieve the optimum moisture of W_{DZ33} . The mixing ratio is 1 liter of DZ33 for $30m^3$ of compacted soil. This is also the recommended dosage according to the guidance of supplier. When experimenting, all samples had control samples for comparison. The reinforced soil was cast as survey samples in two forms:
 - + Form 1: Reinforced basalt (cement + DZ33);
 - + Form 2: Cement-reinforced basalt as reference sample.

3. 3. Experimenting Methods Within the study scope, the researchers aim to use basalt in pavement construction, so first of all, it is necessary to test the physical and mechanical properties of the local basalt, including the particle composition test by TCVN 4198:1995 [11], the plasticity index by TCVN 4197:1995 [12], the load-bearing capacity index CBR by ASTM D1883-16 [13], the standard compaction to determine the maximum dry unit weight and optimum moisture content by 22 TCN 59-84 [14].

3. 4. Experiment Results

3. 4. 1. Physical Mechanical Properties of Basalt Soil

The fundamental physical properties of basalt in the western region, southwest of Gia Lai Province, Viet Nam, are illustrated in Item 3.5 for the selected section of Pleiup village road, Hoa Lu ward, Pleiku city, Gia Lai province, Viet Nam. The soil sample is dark brown as shown in Figure 1.



Figure 1. Basalt soil sample

* The tested properties of basalt soil are collected as follows.

- + Maximum dry unit weight: $\gamma_{kmax} = 1.371 \text{ g/cm}^3$;
- + Optimum water content: $W_{opt} = 30.52 \%$;
- + Liquid limit: $W_L = 64.20 \%$;
- + Plastic limit: $W_P = 40.64 \%$;
- + Plasticity index: $I_p = 23.56$;
- + CBR index at compact K = 0.98, CBR = 13.924 %;
- + CBR index at compact K = 0.95, CBR = 11.125 %;
- + Natural moisture: $W = 31.47 \%$.

3. 4. 2. Elastic Modulus of the Reinforced Soil E_s (MPa)

The reinforced basalt (cement+DZ33) gains E_s increasing by 6%, 8% and 10% cement in both states of moisturizing and water saturation, illustrated in Figures 2-4.

- * **Remarks:** The control basalt soil reinforced with 6%, 8% and 10% cement, all yield lower elastic modulus than the reinforced soil with cement + DZ33. In detail,
 - + 22.90% lower in the sample reinforced with 6% cement, moisturizing on curing age of 28 days, 26.15% lower in the saturated sample;
 - + 20.86% lower in the sample reinforced with 8% cement, moisturizing on curing age of 28 days, 25.61% lower in the saturated sample;
 - + 20.31% lower in the sample reinforced with 10% cement, moisturizing on curing age of 28 days, 19.61%



Figure 2. Elastic modulus test apparatus

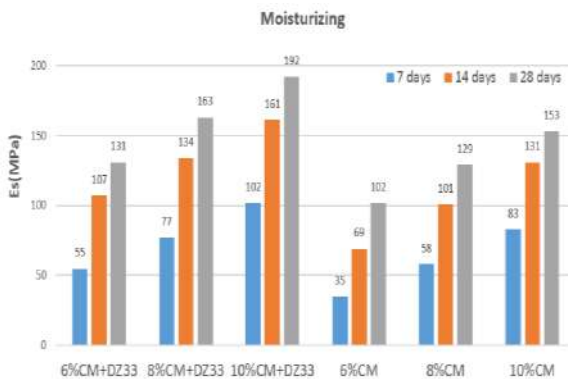


Figure 3. Elastic modulus of moisturizing sample

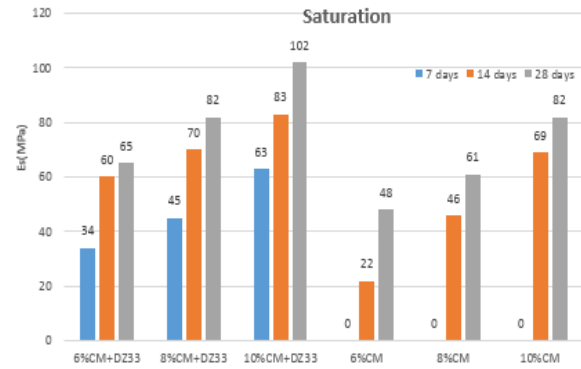


Figure 4. Elastic modulus of saturation sample

lower in the saturated sample. Looking the data presented in Figures 3-4, an increase in elastic modulus with adding additive DZ33 was to be found. The results also can be explained by the mechanism of additive DZ33 as presented in previous part and be described in the guidance of supplier.

3. 4. 3. Splitting Strength of the Reinforced Soil f_{st} (MPa)

This is an important norm of reinforced materials, indicating the ability to resist structural cracking of the road background in unfavorable conditions. There is forced basalt (cement+DZ33) gains f_{st} (MPa) increasing by 6%, 8% and 10% cement in both states of moisturizing and water saturation, illustrated in Figure 5 as experimental test setup and in Figures 6-7 as obtained results.

- * **Remarks:** The control basaltic soil reinforced with 6%, 8% and 10% cement, all yield lower splitting strength than the reinforced soil with cement + DZ33. In detail,
 - + 20.60% lower in the sample reinforced with 6% cement, moisturizing on Day 28, 29.71% lower in the saturated sample;
 - + 17.15% lower in the sample reinforced with 8% cement, moisturizing on Day 28, 39.94% lower in the saturated sample;



Figure 5. Splitting test apparatus

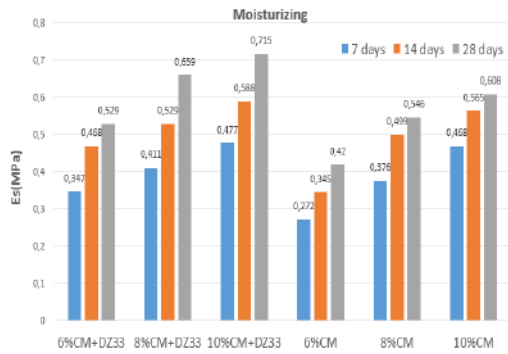


Figure 6. Splitting strength of moisturizing sample



Figure 8. Compressive strength test apparatus

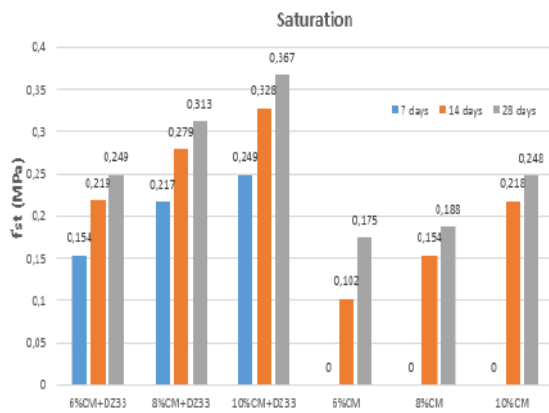


Figure 7. Splitting strength of saturation sample

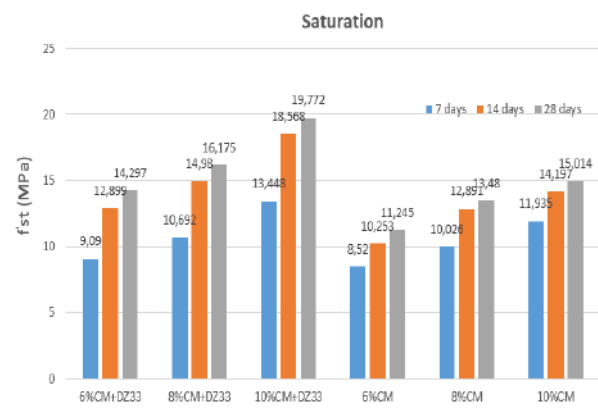


Figure 9. Compressive strength of moisturizing sample

+ 14.96% lower in the sample reinforced with 10% cement, moisturizing on Day 28, 32.43% lower in the saturated sample.

3. 4. 4. Compressive Strength of the Reinforced Soil f_{st} (Mpa)

The reinforced basalt (cement+DZ33) gains f_{st} (MPa) increasing by 6%, 8% and 10% cement in both states of moisturizing and water saturation, illustrated in Figure 8 as experimental test setup and in Figures 9-10 as obtained results.

* **Remarks:** The control basaltic soil reinforced with 6%, 8% and 10% cement, all yield lower compressive strength than the reinforced soil with cement + DZ33. In detail,

+ 21.34% lower in the sample reinforced with 6% cement, moisturizing on day 28, 38.48% lower in the saturated sample;

+ 16.66% lower in the sample reinforced with 8% cement, moisturizing on day 28, 30.22% lower in the saturated sample;

+ 24.06% lower in the sample reinforced with 10% cement, moisturizing on day 28, 38.80% lower in the saturated sample. As seen in Figures 9-10, adding

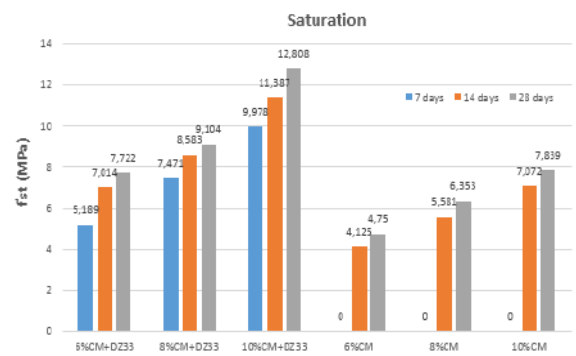


Figure 10. Compressive strength of saturation sample

additive DZ33 increased the compressive strength of the reinforced soil. This phenomenon can be explained by the way that the additive DZ33 allowed soil materials to become more easily wet and more densely compacted. Also, it improved the chemical bonding that helped to link the soil particles together and created a more permanent structure which increased the compressive strength of reinforced soil.

3. 4. 5. Load-bearing Index CBR The test on the in-situ soil reinforced with 6% cement + DZ33 15cm thick in the subbase clearly shows improved effectiveness and enhanced load-bearing capacity of the substrate via CBR index. Test equipments are shown in Figure 11. The results were obtained as at compaction of $K=0.98$ with $CBR=13.924\%$, increasing to 23.37% ; at a compaction $K=0.95$ with $CBR=11.125\%$, increasing to 17.72% . This finding is the same tendency with the research of Tolleson et al. [15] who studied the Enzyme Catalyst and indicated that CBR significantly increased with adding this Enzyme to the soil. This process is probably involved providing a surface for materials in the soil, which in this case is the enzyme, onto which they can easily be adsorbed, brought into closer proximity of each other and hence bind more easily.

3. 5. Application in Rural Road Reinforcement

The road Pleiop village, Hoa Lu ward, Pleiku city, Gia Lai province, Viet Nam is calculated for the single axle of 10 tons and the traffic flow in 24 hours on a single lane is not high. Elastic modulus is required at $E_{yc}=91$ MPa for rural roads according to current Vietnamese standard. Based on the experimental data such as compressive strength, elastic modulus, CBR value, and splitting strength, a recommended pavement structure is presented as follows, as shown in Figures 12-13.

- + Surface layer: Covered with asphalt mortar, $h=3\text{cm}$;
- + Base layer: In-situ soil reinforced with 6% cement and DZ33, with the thickness of 12cm;
- + Subbase layer: In-situ soil reinforced with 6% cement and DZ33, with a thickness of 15cm.

In site, to investigate the strength of pavement structure, the Benkelman beam deflection test was used in this project. The general modulus of base layer was obtained in range of 90-110 MPa in the site. These results indicated that the chosen thickness of layers was satisfied the requirement of rural roads according to current Vietnamese standard. Investigating the surface in site indicated that the hardened basalt after in-situ reinforcement does not disintegrate in water, opening new possibilities for soil reinforcement with cement and DZ33. For instance,



Figure 11. CBR test apparatus

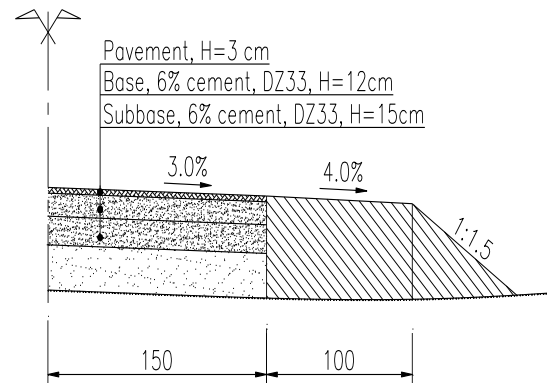


Figure 12. A half of cross-section



Figure 13. The road after covering the surface layer

- + Apart from making rural roads, such technology can be applied for construction of residential roads, green parks, parking areas, etc. ;
- + Building the foundation of national highways, provincial highways, water grooves, reinforced margins;
- + Taking advantage of local materials in some other rural areas of Vietnam's territory.

3. 6. Method of Reinforcing In-situ Fine Basalt with Cement and Additive DZ33

3. 6. 1. Ground Making

- Step 1: Levelling the Existing The soil to be reinforced for the substrate construction is required to be leveled at 3.5m wide and 15cm thick after compaction. The sponge coefficient for the soil is 1.4, illustrated in Figure 14.

- Step 2: Fine Milling the Soil to be Reinforced Using the agricultural milling machine of greater 30 horsepower for fine milling. The milling rig has a cover to ensure dust-proof and flat ground, illustrated in Figure 15.

- Step 3: Spreading Cement PCB40 String stretching to determine the boundary of the road substrate; Manual cement spreading; Weight conversion is 50 kg/bag; Allocating the bags by across and lengthwise distance, corresponding to the construction area, illustrated in Figure 16.



Figure 14. Bulldozer leveling the ground



Figure 15. Plowing machine stirring the soil



Figure 16. Spreading cement PCB40

- Step 4: Mixing Basaltic Soil with Cement PCB40
Using the agricultural milling machine to turn up cement PCB40 and the soil downward. Setting the slow milling speed for turning (2-3 turns/spot), then increasing the speed. Checking the even mixing level by taking a shovel of soil from a groove across the reinforced layer and then making comments on the color of cement PCB40 with the soil distributed on the

vertical walls of that horizontal groove. Testing to determine the moisture and uniformity of cement PCB40 according to the reinforcement ratio, illustrated in Figure 17.

- Step 5: Watering with Additive DZ33 Added and Wet Mixing

Determining the amount of water needed for one cubic meter of reinforced compacted soil; Preparing enough water in a truck or drum; Adding additive DZ33 to water and stirring up; Also spraying and mixing up 2-3 times /spot by a milling machine; Testing the moisture content of the soil reinforced by spraying additive DZ33, illustrated in Figure 18.

- Step 6: Levelling the Surface of the Reinforced Lane Using a dump truck to re-level the reinforced lane on the vertical and horizontal slopes according to the design requirements, illustrated in Figure 19.

- Step 7: Mixed Compacting the Reinforced Soil Using a hard wheel roller or a vibrating roller of >10 tons to roll from outside to the center with the later streak overlapping 30cm the former. Rolling starts about 30 cm from the margin. The number of rolls of about 12-18 times/spot meets the required compactness K. Testing to determine the compactness after rolling ($K \geq 0.95$), illustrated in Figure 20.



Figure 17. Milling machine to mix cement CB40 with basalt



Figure 18. Watering with additive DZ33 added



Figure 19. Leveling



Figure 20. Rolling

- **Step 8: Stapling Stones to Create Adhesion** After compaction rolling, spreading stones (2x4cm) on the reinforced lane, then using a hard wheel roller to press them into the surface for 'sticky feet' creation. The stone spreading area is 3.20m wide, 10cm larger than the road surface in each side, illustrated in Figure 21.

3. 6. 2. Making the Asphalt Mortar Surface

- Step 1: Making the Link Layer

+ Watering the asphalt emulsion over the surface the first time and spreading stones (1.0x2.0) cm and then well compacting the layer by a 10-ton hard wheel roller.



Figure 21. Stapling stones to create adhesion

+ Watering the asphalt emulsion over the layer the second time and spreading stones (0.5x1.0) cm and then well compacting it by a 10-ton hard wheel roller
+ The link layer should be 3.20m wide on the surface.

- Step 2: Making the Asphalt Mortar Layer

+ String stretching to determine the boundary of the road surface of 3.00m wide;
+ Making asphalt mortar of a group of aggregates, including stones (0.5x1.0) cm, dust stone and sand mixed with asphalt emulsion by a concrete mixer;
+ The formula for the mortar is adjusted corresponding to the aggregates arriving at site;
+ Placing the navigation bar and pouring the mortar mixture onto the site. Using a mortar wiper and a trowel to create flatness for the mortar mix following the navigation bar and then compacting with a vibration compactor;
+ Performing the same process, moving two navigation bars along the string that determines the boundary of the road surface to make the asphalt mortar layer.
- After the asphalt mortar layer making comes rolling for maintenance. Using a 10-ton static roller to roll about (3-5) times/spot, illustrated in Figure 22.



Figure 22. Making the asphalt mortar layer

4. CONCLUSIONS

The road surface making technology using in-situ fine basalt combined with cement + additive DZ33 soil has proved suitable for rural roads because local materials are taken advantage of. This method makes use of farm equipment and road construction machines available in the locality, so the investment costs are low, which is a good message to help localities implement the asphalt covering of rural roads, reduce the need for aggregate materials and lessen the total cost of materials for road construction.

Chemical additives used in soil reinforcement are capable of changing the physical and mechanical properties of soil, thereby reducing elasticity, permeability while increasing compactness and the load-bearing capacity of the soil.

The introduction of chemical additives soil reinforcement chemicals and their advantages as analyzed has opened up many hopes for beautiful, durable and clean rural roads, contributing to the renewal of rural appearance particularly in Pleiop village, Hoa Lu ward, Pleiku city, Gia Lai province and generally in Vietnam's territory on the motto "the State and the people work together" in the context of extremely difficult budget capital today.

Through this study/ article, the researchers/ authors also wish that the relevant and related agencies and industries promulgate properties, unit prices, technical standards and encourage localities to widely apply the study results to contribute to completing the infrastructures at minimal costs, succeeding the cause of national industrialization and modernization, creating rich people, a powerful country and a democratic, fair and civilized society.

5. REFERENCES

1. Harichane, K., Ghrici, M. and Kenai, S., "Effect of the combination of lime and natural pozzolana on the compaction and strength of soft clayey soils: A preliminary study", *Environmental Earth Sciences*, Vol. 66, No. 8, (2012), 2197-2205, <https://doi.org/2110.1007/s12665-12011-11441-x>.
2. Harichane, K., Ghrici, M., Kenai, S. and Grine, K., "Use of natural pozzolana and lime for stabilization of cohesive soils", *Geotechnical and Geological Engineering*, Vol. 29, No. 5, (2011), 759-769, <https://doi.org/710.1007/s10706-10011-19415-z>.
3. Harichane, K., Wiam, K., Ghrici, M. and Missoum, H., "Effect of the combination of lime and natural pozzolana on the durability of clayey soils", *Electronic Journal of Geotechnical Engineering*, Vol. 15, No., (2010), 1194-1210.
4. Malisa, A.S., Park, E. and Lee, J., "Effect of lime on physical properties of natural pozzolana from same, tanzania", *International Journal of Engineering Research & Technology*, Vol. 3, No. 11, (2014), 1357-1361.
5. Al-Swaidani, A., Hammoud, I. and Meziab, A., "Effect of adding natural pozzolana on geotechnical properties of lime-stabilized clayey soil", *Journal of Rock Mechanics and Geotechnical Engineering*, Vol. 8, No. 5, (2016), 714-725, <https://doi.org/710.1016/j.jrmge.2016.1004.1002>.
6. Mfinanga, D.A. and Kamuhabwa, M.L., "Use of natural pozzolan in stabilising lightweight volcanic aggregates for roadbase construction", *International Journal of Pavement Engineering*, Vol. 9, No. 3, (2008), 189-201, <https://doi.org/110.1080/10298430701303173>.
7. Sharpe, G.W., Deen, R.C., Southgate, H.F. and Anderson, M., "Pavement thickness designs utilizing low - strength (pozzolanic) base and subbase materials", 1984, Kentucky Transportation Center Research Report. 693.122-130, https://uknowledge.uky.edu/ktc_researchreports/693.
8. Javdanian, H., "The effect of geopolymerization on the unconfined compressive strength of stabilized fine-grained soils", *International Journal of Engineering*, Vol. 30, No. 11, (2017), 1673-1680, Doi: 1610.5829/ije.2017.1630.1611b.1607.
9. ASTM C150/ C150M-09, Standard Specification for Portland Cement, ASTM International, West Conshohocken, PA, 2009, www.astm.org. DOI: 10.1520/C0150_C0150M-1509.
10. <https://www.enchoices.com/vi/san-pham/dz33>.
11. TCVN 4198:1995, Soils - Laboratory Methods of Determination of Grain Size Distribution.
12. TCVN 4197-1995, Soils- Methods of Laboratory Determination of Plastic Limit and Liquid Limit.
13. ASTM D1883-16, Standard Test Method for California Bearing Ratio (CBR) of Laboratory-Compacted Soils, ASTM International, West Conshohocken, PA, 2016, www.astm.org. DOI: 10.1520/D1883-1516.
14. 22 TCN 59-84, Testing process of soil reinforced with cement-lime binder.
15. Tolleson, R.A., Mahdavian, E., Shatnawi, F.M. and Harman, E.N., "An evaluation of strength change on subgrade soils stabilized with an enzyme catalyst solution using CBR and SSG comparisons", 2003: Project No.R-03-Utc-Alterpave-Geo-01.

Persian Abstract

چکیده

امروزه استفاده از مواد افزودنی برای افزایش ظرفیت تحمل بار خاک در برخی از راههای روستایی تعدادی از استانهای ویتنام اعمال شده است و این مزایای برجسته را اثبات می کند. در این مقاله نتایج کار تحقیقاتی و کاربردهای فنی برای ساخت جاده های روستایی با خاک ریز بازالت درجا همراه با چسب از جمله سیمان PCB40 و افزودنی DZ33 ارائه شده است. نتایج تجربی نشان می دهد که ماده افزودنی DZ33 امکان افزایش توانایی هیدراتاسیون با سیمان را در هنگام واکنش موثر با ذرات خاک برای کاهش هزینه های ساخت و ساز و آسیب های محیطی، بهبود شدت مخلوط خاک تقویت شده مانند مدول الاستیک خاک تقویت شده فراهم کرده است. شکافتن مقاومت کششی، مقاومت فشاری و ضریب تحمل کالیفرنیا (CBR) استفاده موفقیت آمیز از افزودنی DZ33 همراه با سیمان در تقویت خاک برای ساخت کارهای حمل و نقل روستایی نه تنها باعث بهره وری اقتصادی می شود بلکه از خاک بازالت خوب درجا برای ایجاد ماده جدیدی برای صنعت ساخت، فروتنانه به مطالعه توسعه جاده های روستایی در استان کوهستانی جیالای به طور خاص و زیرساخت های حمل و نقل ویتنام به طور کلی استفاده گردید.



Behavior of Eccentrically Inclined Loaded Ring Footings Resting on Granular Soil

A. H. Sadeghi Fazel, J. Bolouri Bazaz*

Department of Civil Engineering, Faculty of Engineering, Ferdowsi University of Mashhad, Mashhad, Iran

PAPER INFO

Paper history:

Received 10 May 2020

Received in revised form 12 August 2020

Accepted 07 September 2020

Keywords:

Combined Loading

Experimental Modeling

Failure Envelope

Ring Footing

Sand

ABSTRACT

For civil engineers, the determination of ring footing bearing capacity subject to the combination of inclined and eccentric loading is a great topic of interest. In this paper, a novel approach is proposed to predict the behavior of ring footing subject to combinations of inclined and eccentric loading using the failure envelope approach, which can explain shallow footings behavior. Load eccentricity, inclination angle, and diameter ratio for ring footings are the most effective parameters on the failure envelope. In this regard, a series of experiments were conducted to investigate the behavior of ring footing subject to a possible form of eccentrically inclined loading. Three values of diameter ratio were considered, including $n = 0.2, 0.4,$ and $0.6,$ along with a circular footing ($n = 0$). According to the test results, the conical 3D failure envelope and its equation were developed for each type of footing model. With constant vertical load the failure envelopes show that when the eccentricity is increased, the possible inclination angle is decreased. Also, by increasing the vertical loading, the possible eccentricity and inclination angle is decreased. Based on the observations, and obtained failure envelopes for different diameter ratios, when a ring footing is subject to combined eccentric inclined loading, $n=0.4$ is optimum. In the following, by using the failure envelope, the concepts of critical eccentricity and critical inclination angle were defined in a way that is suitable for studying the stability of ring footings in the V-H-M/B space.

doi: 10.5829/ije.2020.33.11b.04

NOMENCLATURE

n	Ring footing diameter ratio	D_o	Outer diameter of ring footing
e	Vertical eccentricity	D_i	Inner diameter of ring footing
e_h	Horizontal eccentricity	V_{ult}	Ultimate vertical load
V	Vertical load	α	Inclination angel of inclined load
H	Horizontal load	R_f	Reduction factor of eccentric loading
M	Bending moment	H_{ult}	Ultimate horizontal load
B	Diameter of footing model	M_{ult}	Ultimate bending moment

1. INTRODUCTION

Foundations of structures may be subjected to inclined and eccentric loading depending on various design considerations. Ring footing is a special type of shallow foundation that is appropriate for telecommunication towers, silos, bridge piers, and advertisement boards. Classical researchers provided empirical coefficients when an eccentric or inclined load is applied on a footing

[1–3]. Several studies about ring footing using different methods have been performed. Using experimental model, the ring footing behavior, subject to vertical loading was investigated. The results showed that the behavior of ring footing would approach a strip footing for $n > 0.7$ [4]. The optimum value of ring footing bearing capacity occurred when the diameter ratio was 0.4 [5, 6]. The results of the behavior of small-scale ring footings subject to eccentric loading on reinforced soil reported

*Corresponding Author Institutional Email: bolouri@um.ac.ir
(J. Bolouri Bazaz)

that with an increase in eccentricity, the bearing capacity ratio of ring footing increased more than circular foundation. Also, for an optimum response of ring footing, the recommended diameter ratio is 0.39 [7]. Based on the limit equilibrium method, the solution was derived for the bearing capacity of a ring footing on soil beds [8]. Besides that, the bearing capacity factor, N_γ , was calculated by using the stress characteristic method [9]. After conducting in-situ tests, the bearing capacity of circular and ring plate was investigated in very dense calcareous sands using plate load tests. The results showed that the bearing capacity of ring footings is greater than that of circular footings with the same outer diameter in some situations [10]. In other work, researchers found that by increasing the diameter ratio, the bearing capacity of ring footings resting on clay was reduced [11]. In numerical simulations, the bearing capacity of a ring footing was assessed using a finite difference method on non-cohesive soil subject to eccentric load [12].

In the field of non-vertical-central loading on a shallow footing, the stability analysis of an eccentrically loaded footing supported by sand was proposed by using the slices method [13]. The theoretical limit equilibrium analysis was performed to determine the average ultimate bearing capacity of strip footing subject to eccentrically-inclined load [14]. About 120 laboratory test results have been reported regarding the ultimate bearing capacity of a strip footing subject to eccentrically-inclined load as a reduction factor [15]. There are many papers about the application of analytical and numerical approaches in the modeling of shallow footings subject to general loading [16–24].

Since the ring footing of many structures such as telecommunication towers and silos is subject to combination of eccentric inclined load, it is necessary experimentally to investigate the behavior of this type of footing. Besides that, most of the literature reviewed in the previous section focused on the effect of diameter ratio on the settlement and bearing capacity of ring footings subject to vertical load. Also, both experimental and theoretical research has been conducted on ring footings to find an optimum diameter ratio. However, to the best of the authors' knowledge, no attempt has been made to produce a model explaining the behavior of ring footings subject to a combination of inclined, eccentric, and vertical loading, which is useful for designing the structure subject to aforementioned loading. To this aim, six loading states were defined to investigate the behavior of ring footings resting on sand in $V/V_{ult}-\tan(\alpha)-e/B$ space. In this space, the instability conditions of footings, in addition to bearing capacities, subjected to inclined and eccentric loading under constant and variable inclination angles and eccentricity were studied.

2. PROGRAM DEFINITION

The combination of vertical, inclined, and eccentric loading was considered to investigate the effect of loading states on ring footing bearing capacity. The six loading states are defined as follows:

V state: The pure central vertical loading (Figure 1a) is applied to determine the ultimate bearing capacity, V_{ult} , of the ring footing.

αv state: The central vertical load is applied up to $0.2V_{ult}$, $0.3V_{ult}$, $0.5V_{ult}$, $0.7V_{ult}$, and $0.85V_{ult}$. While keeping the vertical load constant, the horizontal load is applied and gradually increased until reaching failure (H/V =variable) (Figure 1b).

αc state: Vertical and horizontal loads are applied to the center of the footing model with a constant ratio (H/V =constant). The result of this loading state is inclined load with a constant inclination angle of α (Figure 1c).

ev state: The eccentric loading with variable eccentricity is applied to the footing model. Similar to the V-H path, the central vertical load was increased until reaching $0.3V_{ult}$, $0.5V_{ult}$, and $0.7V_{ult}$, while keeping the vertical load constant, the moment was applied on the footing as a couple (Figure 1d).

ec state: The vertical loading with a constant eccentricity (e) is applied to the footing model (Figure 1-e).

$\alpha v-ev$ state: The inclined eccentric loading with a variable inclination angle and eccentricity is applied to the footing model. The central vertical load was increased until reaching $0.3V_{ult}$, $0.5V_{ult}$, and $0.7V_{ult}$, while keeping the vertical load constant, the bending moment by the horizontal load with a constant ratio was gradually applied to the ring footing until reaching failure (Figure 1f).

A load-displacement curve was drawn for all of the experiments, and the failure point was derived for each test. Since the sandy soil used in this study had a medium density, no peak was observed in the load-displacement

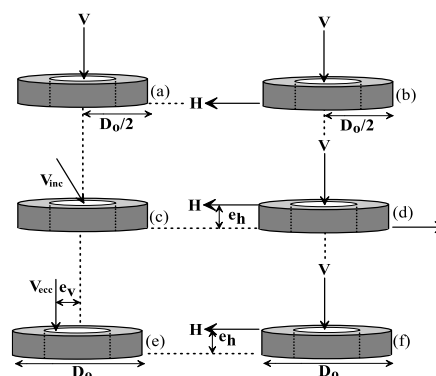


Figure 1. The position of loads in different loading states

curves. The failure criterion for whole loading states was considered when the slope load-displacement curve was approaching zero (i.e., the curve tends to become a straight line). For example, the load-displacement results of the e_c loading state for the ring footing $n=0.4$ is illustrated in Figure 2.

If all of the failure-relevant points are perceived, a failure envelope in $V/V_{ult}-\tan(\alpha)-e/B$ space is established, which is useful for design engineers. For instance, by considering constant and variable inclination angles and eccentricity, the influence of eccentricity and inclination can be observed simultaneously. A unique failure envelope obviously exists for each diameter ratio of ring footings with specific soil parameters. The purpose of this research is to obtain the equation of the failure envelope in $V/V_{ult}-\tan(\alpha)-e/B$ space and the parameters involved in it. The flowchart of this research methodology is illustrated in Figure 3. Based on the above explanation, the test details are summarized in Table 1.

3. LOADING SYSTEM

The loading system is suitable to apply precisely the combination of vertical load, horizontal load, and bending moment simultaneously. Since the vertical and horizontal loads are incrementally applied by filling the cylindrical tanks with constant water flow, the magnitude of the applied load was measured precisely by the water entered at the rate of 10 liters per minute. Additionally,

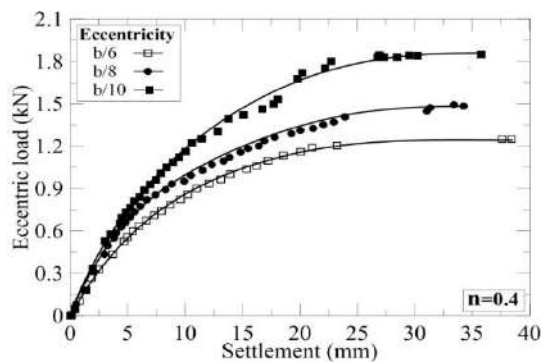


Figure 2. The typical load-displacement results of the e_c loading state for ring footing ($n=0.4$)

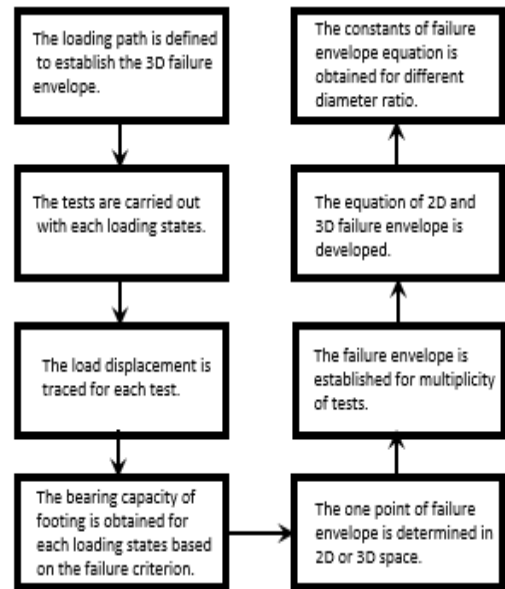


Figure 3. The flowchart of research methodology

two calibrated load cells were employed to measure and ensure no error was induced during load application. The schematic drawing of the apparatus is shown in Figure 4; the picture of loading system is illustrated in Figure 5. When the desired loading combination is achieved. It is of interest to apply horizontal load or a bending moment with either a constant or variable angle or eccentricity, respectively; which is achieved by the automated drain valves. Fully lubricated frictionless rolling bearings facilitate the movement of the reservoir tanks easily to create vertical and horizontal eccentricities [25].

3. 1. Sample Preparation

The experimental model tests were conducted in a steel tank made with 1000 mm high, 1100 mm inside dimension and 10 mm thickness. The loading system was firmly attached to the top of the tank. The tank diameter was larger than 5 times the footing diameter (20 cm) to avoid undesirable effect of the test tank boundary on the results [12].

3. 2. Soil Specifications

The soil used in this research was dry Firuzkuh sand (No. 161), which was taken from north of Iran. It is a uniform sand with a specific gravity of $G_s=2.71$ and maximum and minimum

TABLE 1. Main characteristics of tests program

Series	No. of tests	Loading State	V/V_{ult}	e	α (Degree)	e_n (mm)	n
1	4	V	-	-	-	-	0, 0.2, 0.4, 0.6
2	20	α_v	0.2, 0.3, 0.5, 0.7, 0.85	-	variable	-	0, 0.4, 0.4, 0.6
3	8	α_c	-	-	18,24	-	0, 0.2, 0.4, 0.6
4	20	e_v	0.2, 0.3, 0.5, 0.7, 0.85	variable	-	50	0, 0.2, 0.4, 0.6
5	12	e_c	-	B/10,B/8,B/6	-	-	0, 0.2, 0.4, 0.6
6	36	α_v-e_v	0.7, 0.5, 0.3	-	-	50,100,200	0, 0.2, 0.4, 0.6

dry unit weights of $\gamma_{max}=16.4 \text{ kN/m}^3$ and $\gamma_{min}=14.1 \text{ kN/m}^3$, respectively. A pluviation system that has been developed at Mashhad University was employed to prepare a sand bed with a medium relative density of 70%. The corresponding dry unit weight and internal friction angle were $\gamma=15.2 \text{ kN/m}^3$ $\phi=36^\circ$, respectively [26].

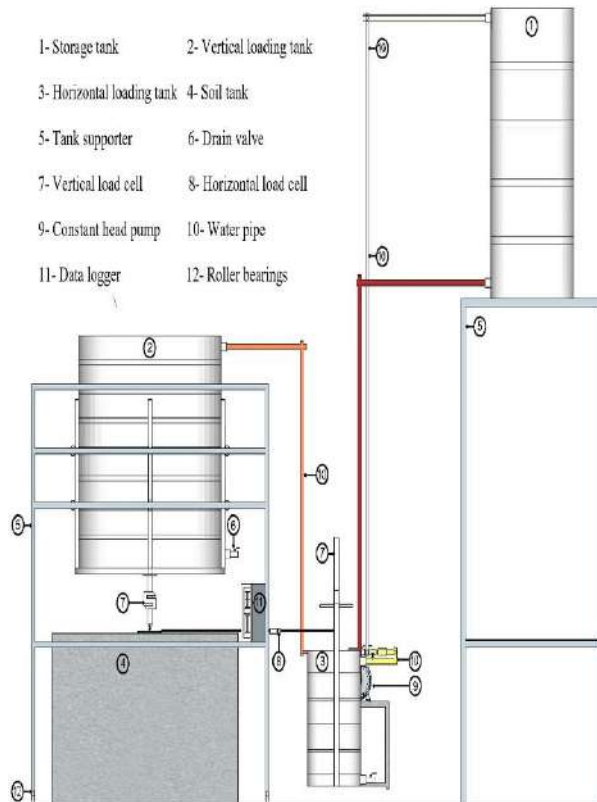


Figure 4. Schematic view of loading system



Figure 5. General photo of loading system

4. FAILURE ENVELOPE

4. 1. $\tan(\alpha)$ - V/V_{ult} Space ($e=0$)

The failure points corresponding to V , α_c and α_v loading states are gathered in V/V_{ult} - $\tan(\alpha)$ space as illustrated in Figure 6. Each point represents the failure condition of the relevant test. The trend of results shows a linear relationship between vertical load ratio (V/V_{ult}) and tangent of inclination angle. It has to be noted that, the α_c and α_v loading states are the loading paths parallel to horizontal and vertical axes, respectively. While the points below the failure envelope indicate the ordinary (possible) loading state and the points above that are the impossible state.

4. 2. e/B - V/V_{ult} Space

Tests with no inclination are considered for this space. The failure points of V , e_c , and e_v loading states are collected in the V/V_{ult} - e/B space as illustrated in Figure 7. The trend of results shows the linear relationship between vertical loads and eccentricity, which show the failure envelope in the V/V_{ult} - e/B space. It should be noted that the e_c and e_v loading states are the loading paths parallel to horizontal and vertical axes, respectively.

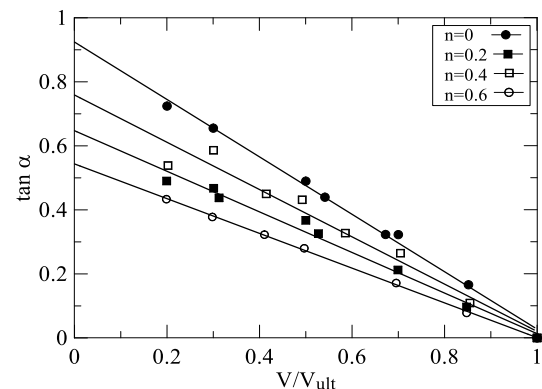


Figure 6. Failure envelopes of the ring footing in $\tan(\alpha)$ - V/V_{ult} space

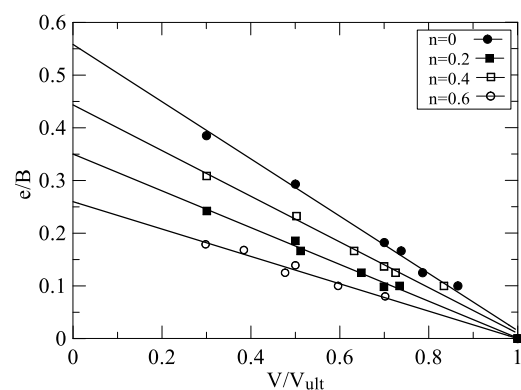


Figure 7. Failure envelopes of the ring footing in e/B - V/V_{ult} space

4. 3. $\tan(\alpha)$ - e/B Space The behavior of ring footings in the $\tan(\alpha)$ - e/B space, which has been investigated by providing data from the α_V - e_V state test results, indicates a nonlinear relationship between $\tan(\alpha)$ - e/B at any constant value of vertical load as illustrated in Figure 8.

The effect of the diameter ratio on the failure envelope in the $\tan(\alpha)$ - e/B space for $V= 0.5V_{ult}$ is illustrated in Figure 9. It can be observed that the results for $n=0.2$ appear to fall out of sequence with the other results. This could be explained by creating an additional shear failure surface, which develops from the internal edge of the ring footing and extends beyond the end of the wedge zone of the shear failure surface. However, additional shear failure surface causes the friction area of the active zone. This phenomenon is called the *edge effect*, which is also true for the optimum diameter ratio of a ring footing ($n=0.4$). When $n>0.4$, the bearing capacity is reduced because of the high interaction between both of the external and internal shear failure surfaces in the small zone (Figures 10 and 11) [27].

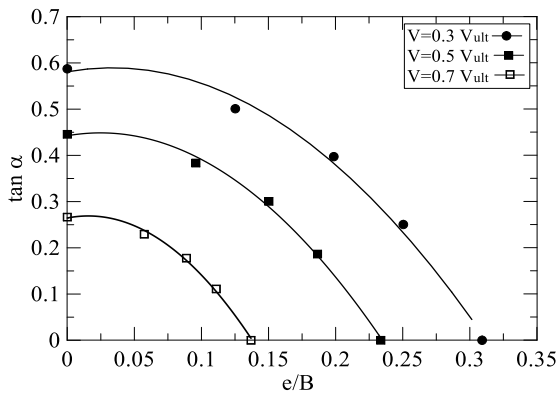


Figure 8. Failure envelopes of the ring footing in $\tan(\alpha)$ - e/B space for different magnitude of vertical load ($n=0.4$)

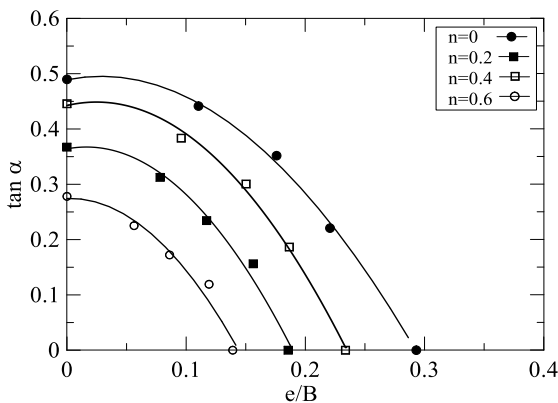


Figure 9. Failure envelopes of the ring footing in $\tan(\alpha)$ - e/B space

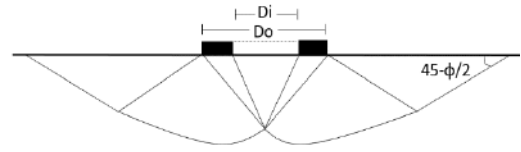


Figure 10. Ring footing edge effect ($0 < n \leq 0.4$)

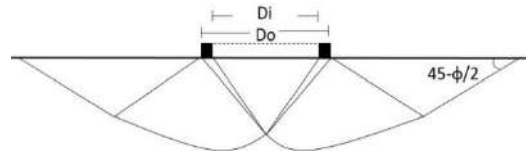


Figure 11. Ring footing edge effect ($n > 0.4$)

5. MODEL DEVELOPMENT

To predict the behavior of ring footing subject to eccentric inclined loading, an analytical model, based on experimental results and failure envelopes were developed and proposed as follows (see Equations (1)-(3)):

$$\text{In } \tan \alpha - V/V_{ult} \text{ space : } \tan \alpha = h(1 - \frac{V}{V_{ult}}) \tag{1}$$

$$\text{In } e/B - V/V_{ult} \text{ space : } \frac{e}{B} = m(1 - \frac{V}{V_{ult}}) \tag{2}$$

$$\text{In } \tan \alpha - e/B \text{ space: } (\frac{\tan \alpha}{h})^2 + (\frac{e}{mB})^2 + c \frac{\tan \alpha}{h} \frac{e}{mB} = D \tag{3}$$

where, V , V_{ult} , e , B , α are vertical load, ultimate vertical load, load eccentricity, the outer diameter of the footing model and the inclination angle, respectively. Also h , m and c are footing shape coefficients and D is a functional coefficient of V/V_{ult} ratio, i.e. (Equation (4)):

$$D = (1 - V/V_{ult})^2 \tag{4}$$

Combining Equations (1), (2) and (3), derived for the failure envelopes in 2D spaces, leads to Equation (5), which expresses the 3D shape of the failure in the V/V_{ult} - $\tan(\alpha)$ - e/B space:

$$(\frac{\tan \alpha}{h})^2 + (\frac{e}{mB})^2 + c \frac{\tan \alpha}{h} \frac{e}{mB} = (1 - V/V_{ult})^2 \tag{5}$$

Using the least square method, the constant coefficients, which are derived based on the test results, are summarized in Table 2.

TABLE 2. Parameters of the failure envelope for different diameter ratios

n	h	m	c
0	1	0.6	0.2
0.2	0.7	0.35	0.2
0.4	0.8	0.45	0.2
0.6	0.28	0.14	0.2

The 3D failure envelope of ring footing diagrams based on coefficient derived from Table 2 are shown in Figure 12.

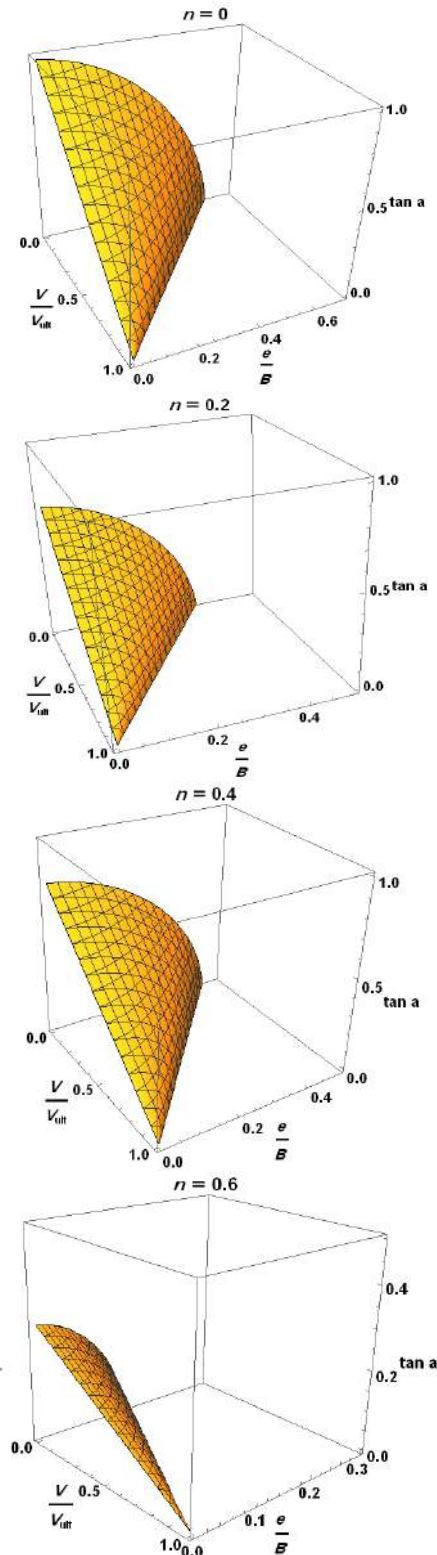


Figure 12. The 3D failure envelopes of ring footing

6. TEST RESULTS ANALYSIS

Shallow footings subjected to eccentric inclined loading can be analyzed as a combination of vertical load (V), horizontal load (H), and moment (M) simultaneously. Then, the failure envelope in V-H and M/D_o-V spaces are obtained. A noteworthy finding of this study is a new parameter called the *inclined load line*, which has a constant inclination angle in the V/V_{ult}-H/V_{ult} space and can be introduced to interpret the results as follows: Where α is the inclination angle of load with respect to the vertical direction, and the other parameters are as described earlier. When a ring footing is subjected to the inclined load with an inclination angle of α, the loading path in the V/V_{ult}-H/V_{ult} space is a line determined by Equation (6).

$$\frac{H}{V_{ult}} = \frac{V}{V_{ult}} \tan \alpha \tag{6}$$

The intersection of this line with the failure envelope in the V/V_{ult}-H/V_{ult} space represents the positions of failure points. This helps to predict the ring footing behavior subject to the inclined loading. In addition, an increase in the value of α causes the inclined load to get closer to the vertical axis in the V/V_{ult}-H/V_{ult} space until the line becomes tangent to the failure envelope. The inclination angle of loading, which results in tangency with the failure envelope, is called the *critical angle* (α_{cr}). In the case of α ≥ α_{cr}, the ring footing slid, and an instability condition occurred. Based on the test results, four inclined load lines were sketched (see Figure 13). For instance, the inclined load line with α=25° is tangent to the failure envelope of the ring footing with n=0.6. This indicates that it is not possible to apply an inclined load under these conditions. In other words, the ring footing with n=0.6 is not stable if α=25°.

Similarly, a new parameter in M/BV_{ult}-V/V_{ult} space can be defined as *eccentric load line*. This parameter is defined by Equation (7):

$$\frac{M}{BV_{ult}} = e \frac{V}{V_{ult}} \tag{7}$$

Equation (7) describes a line with a constant slope in the M/D_oV_{ult}-V/V_{ult} space. The intersection of this line with the failure envelope provides the ultimate bearing capacity of an eccentrically-loaded ring footing. As the load eccentricity increases, the line slope increases until it reaches the failure envelope. The load eccentricity in this situation is called the *critical eccentricity* (e_{cr}). When e ≥ e_{cr}, the ring footing is unstable and vibrates in the rocking mode. For instance, as shown in Figure 14, it is not possible to apply a load with e=D_o/4 on a ring footing with n=0.6. Also, as the diameter ratio becomes smaller, loads with larger eccentricity can be applied to the ring footing. Based on the test results, the magnitudes of critical angle and corresponding critical eccentricity are summarized in Table 3.

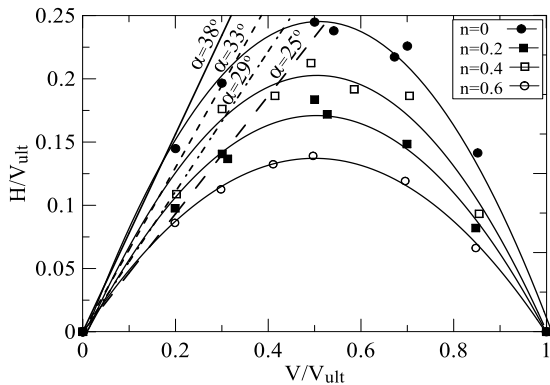


Figure 13. Inclined load lines in H/V_{ult} - V/V_{ult} space

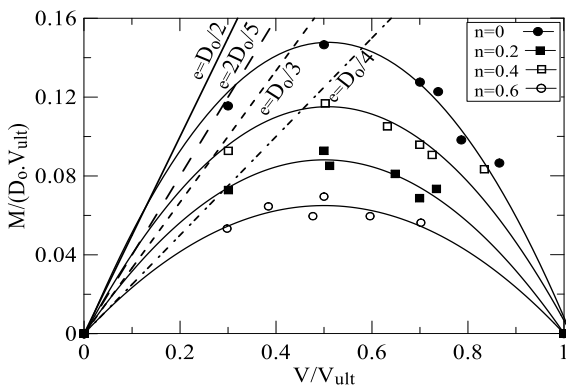


Figure 14. Eccentric load lines in $M/D_o V_{ult}$ - V/V_{ult} space

TABLE 3. Values of the critical angle and the critical eccentricity

n	α_{cr}	e_{cr}
0	38	$D_o/2$
0.2	29	$D_o/3$
0.4	33	$2D_o/5$
0.6	25	$D_o/4$

7. VERIFICATION

To the best of authors’ knowledge, no similar attempt was made to study the behavior of ring footings subject to combined loading. However, it is only possible to compare the results for vertical loading states for ring footing and combined loading state for other types of footing (such as circular and strip footings). This was conducted as follows:

7. 1. Footing Subject to Pure Vertical Loading

One method to verify the test results is to compare N_γ values of different studies using Equation (8) [12].

$$N_\gamma = \frac{q_u}{0.5B\gamma} \tag{8}$$

The obtained trend of N_γ seems to be comparable and reasonable with others findings (see Figure 15). However, the differences depend on the internal friction angle of soil as well as the approach employed in each study.

7. 2. Footing Subject to Eccentric Loading

Another way to validate the test results is to investigate the variation of a reduction factor, R_f , as expressed in Equation (9) [15].

$$R_f = \frac{q_{u,eccentric}}{q_{u,centric}} \tag{9}$$

where $q_{u,eccentric}$, $q_{u,centric}$ are the ultimate bearing capacity of the footing subject to eccentric and centric loading, respectively. As shown in Figure 16, the results of this study are generally in good agreement with those reported in other investigations.

7. 3. Footing Subject to Combined Loading

The proposed model of shallow footing subject to combined loading is presented in Equations (10) and (11) [28]. Figures 17 and 18 show the failure envelope obtained from the test results in a normalized H/H_{ult} - V/V_{ult} and

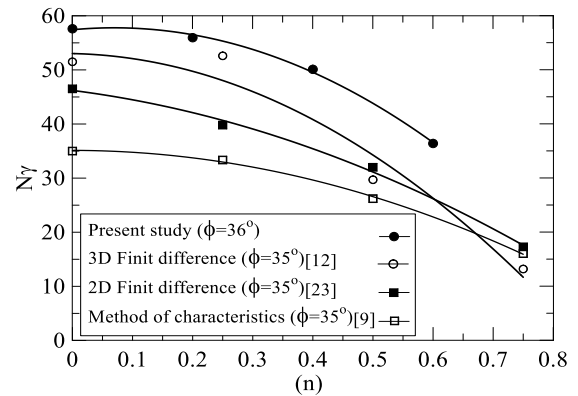


Figure 15. Variation of N_γ with the diameter ratio for a ring footing

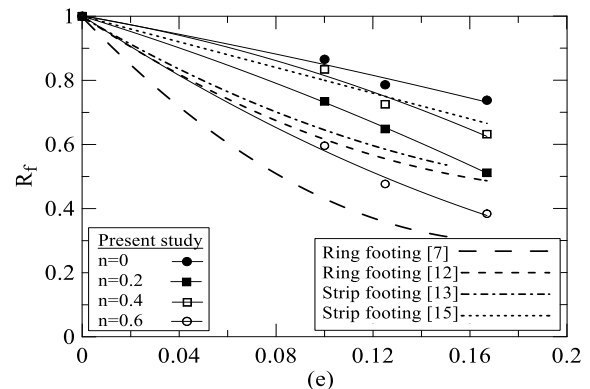


Figure 16. Variation of R_f with the eccentricity

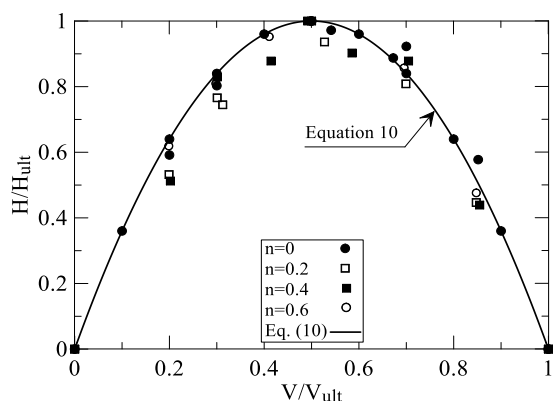


Figure 17. The failure envelope of a ring footing in H/H_{ult} - V/V_{ult} space

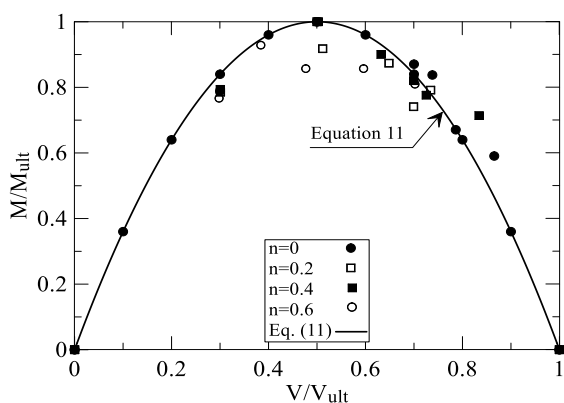


Figure 18. The failure envelope of the ring footing in M/M_{ult} - V/V_{ult} space

M/M_{ult} - V/V_{ult} space respectively, which is in a good agreement with the outputs of Equations (10) and (11).

$$\frac{H}{H_{ult}} = 4 \frac{V}{V_{ult}} \left(1 - \frac{V}{V_{ult}}\right) \quad (10)$$

$$\frac{M}{M_{ult}} = 4 \frac{V}{V_{ult}} \left(1 - \frac{V}{V_{ult}}\right) \quad (11)$$

where, all of parameters were introduced before.

8. CONCLUSION

In this study, 100 experimental tests were performed to investigate the behavior of ring footings resting on sandy soils subject to combined eccentric inclined loading. Since ring footings comprise less material than circular footings with the same outer diameter, ring footings are economically efficient in the engineering projects. In order to study the combined loading effect on the behavior of ring footings, six loading states were considered. The obtained results were described as follows:

The failure envelopes in the V/V_{ult} - $\tan(\alpha)$ and V/V_{ult} - e/B spaces are governed by a line. Therefore, as the vertical load decreases, loading with more eccentricity becomes possible. In the same manner, when vertical load decreases, loading with a higher inclination angle is possible. Moreover, the failure envelopes in the $\tan(\alpha)$ - e/B space are governed by a quarter ellipsoid, which is useful for the design of footings subject to eccentric inclined loading. When the eccentricity is increased, the possible inclination angle is decreased. In the same way, when the inclination angle is increased, the possible eccentricity is decreased. The constant coefficients of the failure envelope, n , m , and h , are introduced in terms of the ring footing diameter ratio. It is observed that the optimum ring footing diameter ratio is 0.4, subject to combined eccentric inclined loading. According to this result, it is more appropriate to use a ring footing with a diameter ratio of $n=0.4$. The geometrical shape of the 3D failure envelope in the V/V_{ult} - $\tan(\alpha)$ - e/B space is quite similar to a cone, and its size varies with the ring footing's diameter ratio. Another advantage of the failure envelope is the control of stability conditions subject to the desired loading state. In this research, by defining the critical eccentricity and critical inclined angle, it is possible to check the stability of ring footings in the V/V_{ult} - H/V_{ult} and M/BV_{ult} - V/V_{ult} spaces. The results show that a ring footing with diameter $n=0.4$ is more stable than other ring footings when subjected to inclined eccentric loading.

It is worth mentioning that the main limitation of this research is the small scale of ring footing and the soil bed which a special granular material. This research could be developed on cohesive and/or saturated soil. Also a numerical approach makes it possible to evaluate all diameter ratio of ring footings subject to combined loading.

9. REFERENCES

1. Meyerhof, G. G. "The Ultimate Bearing Capacity of Foundations on Slopes La Force Portante des Fondations sur Talus." In Proceedings of the Fourth International Conference on Soil Mechanics and Foundation Engineering, (1957), 384-386. Retrieved from https://www.academia.edu/download/48325191/docslide.us_ultimate-bearing-capacity-of-foundations-on-slopes-paper.pdf
2. Meyerhof, G. G. "Influence of Roughness of Base and Ground-Water Conditions On The Ultimate Bearing Capacity of Foundations." *Géotechnique*, Vol. 5, No. 3, (1955), 227-242. <https://doi.org/10.1680/geot.1955.5.3.227>
3. Hansen, J. B. "A revised and extended formula for bearing capacity." Bulletin No. 28, Copenhagen: Danish Geotechnical Institute, (1970), 5-11. Retrieved from <https://trid.trb.org/view/125129>
4. Egorov, K. E. "Calculation of bed for foundation with ring footing." In Proceeding 6 th International Conference of Soil Mechanics and Foundation Engineering (Vol. 2) (1965),41-45.

5. Hataf, N., and Razavi, M. R. "Model tests and finite element analysis of bearing capacity of ring footings on loose sand." *Iranian Journal of Science and Technology, Transaction B - Engineering*, Vol. 27, No. 1, (2003), 47–56. Retrieved from <https://www.sid.ir/en/Journal/ViewPaper.aspx?ID=14838>
6. Boushehrian, J. H., and Hataf, N. "Experimental and numerical investigation of the bearing capacity of model circular and ring footings on reinforced sand." *Geotextiles and Geomembranes*, Vol. 21, No. 4, (2003), 241–256. [https://doi.org/10.1016/S0266-1144\(03\)00029-3](https://doi.org/10.1016/S0266-1144(03)00029-3)
7. El Sawwaf, M., and Nazir, A. "Behavior of Eccentrically Loaded Small-Scale Ring Footings Resting on Reinforced Layered Soil." *Journal of Geotechnical and Geoenvironmental Engineering*, Vol. 138, No. 3, (2012), 376–384. [https://doi.org/10.1061/\(asce\)gt.1943-5606.0000593](https://doi.org/10.1061/(asce)gt.1943-5606.0000593)
8. Karaulov, A. M. "Static solution of the limiting-pressure problem for ring foundations on soil beds." *Soil Mechanics and Foundation Engineering*, Vol. 42, No. 6, (2005), 189–194. <https://doi.org/10.1007/s11204-006-0007-5>
9. Kumar, J., and Ghosh, P. "Bearing capacity factor N_γ for ring footings using the method of characteristics." *Canadian Geotechnical Journal*, Vol. 42, No. 5, (2005), 1474–1484. <https://doi.org/10.1139/t05-051>
10. Al-Sanad, H. A., Ismael, N. F., and Brenner, R. P. "Settlement of Circular and Ring Plates in Very Dense Calcareous Sands." *Journal of Geotechnical Engineering*, Vol. 119, No. 4, (1993), 622–638. [https://doi.org/10.1061/\(ASCE\)0733-9410\(1993\)119:4\(622\)](https://doi.org/10.1061/(ASCE)0733-9410(1993)119:4(622))
11. Laman, M., Yildiz, A., Ornek, M., and Demir, A. "Field Test of Circular Footings on Reinforced Granular Fill Layer Overlying a Clay Bed." *Geotechnical Testing Journal*, Vol. 35, No. 4, (2012), 575–585. <https://doi.org/10.1520/GTJ103512>
12. Sargazi, O., and Seyedi Hosseininia, E. "Bearing capacity of ring footings on cohesionless soil under eccentric load." *Computers and Geotechnics*, Vol. 92, (2017), 169–178. <https://doi.org/10.1016/j.compgeo.2017.08.003>
13. Purkayastha, R. D., and Char, A. N. "Stability analysis for eccentrically loaded footings." *Journal of Geotechnical and Geoenvironmental Engineering*, Vol. 103, No. GT-6, (1977), 647–651. Retrieved from <https://trid.trb.org/view/59977>
14. Saran, S., and Agarwal, R. K. "Bearing Capacity of Eccentrically Obliquely Loaded Footing." *Journal of Geotechnical Engineering*, Vol. 117, No. 11, (1991), 1669–1690. [https://doi.org/10.1061/\(ASCE\)0733-9410\(1991\)117:11\(1669\)](https://doi.org/10.1061/(ASCE)0733-9410(1991)117:11(1669))
15. Patra, C. R., Behara, R. N., Sivakugan, N., and Das, B. M. "Ultimate bearing capacity of shallow strip foundation under eccentrically inclined load, Part I." *International Journal of Geotechnical Engineering*, Vol. 6, No. 3, (2012), 343–352. <https://doi.org/10.3328/IJGE.2012.06.03.343-352>
16. Loukidis, D., Chakraborty, T., and Salgado, R. "Bearing capacity of strip footings on purely frictional soil under eccentric and inclined loads." *Canadian Geotechnical Journal*, Vol. 45, No. 6, (2008), 768–787. <https://doi.org/10.1139/T08-015>
17. Krabbenhoft, S., Damkilde, L., and Krabbenhoft, K. "Lower-bound calculations of the bearing capacity of eccentrically loaded footings in cohesionless soil." *Canadian Geotechnical Journal*, Vol. 49, No. 3, (2012), 298–310. <https://doi.org/10.1139/T11-103>
18. Gupta, R., and Trivedi, A. "behavior of model circular footings on silty soils with cellular supports." *International Journal of Engineering, Transactions B: Applications*, Vol. 23, No. 1, (2010), 21–35. Retrieved from http://www.ije.ir/article_71826.html
19. Safarzadeh, Z., and Aminfar, M. H. "Experimental and numerical modeling of the effect of groundwater table lowering on bearing capacity of shallow square footings." *International Journal of Engineering, Transactions A: Basics*, Vol. 32, No. 10, (2019), 1429–1436. <https://doi.org/10.5829/ije.2019.32.10a.12>
20. Azan, D., and Haddad, A. "Effect of Fuzzy Boundaries on the Bearing Capacity of Footings on Two-Layered Clay." *International Journal of Engineering, Transactions B: Applications*, Vol. 32, No. 5, (2019), 667–672. <https://doi.org/10.5829/ije.2019.32.05b.07>
21. Ibrahim, S. K., and Zakaria, W. A. "Effect of Vibrating Footing on a Nearby Static – Load Footing." *Civil Engineering Journal*, Vol. 5, No. 8, (2019), 1738–1752. <https://doi.org/10.28991/cej-2019-03091367>
22. Moffitt, C. J. "Footing Soil Pressure from Biaxial Loading." *Civil Engineering Journal*, Vol. 5, No. 11, (2019), 2423–2440. <https://doi.org/10.28991/cej-2019-03091421>
23. Jalili, M., Ghasemi, M. R., and Pifloush, A. R. "Stiffness and strength of granular soils improved by biological treatment bacteria microbial cements." *Emerging Science Journal*, Vol. 2, No. 4, (2018), 219–227. <https://doi.org/10.28991/esj-2018-01146>
24. Shadmand, A., Ghazavi, M., and Ganjian, N. "Scale Effects of Footings on Geocell Reinforced Sand Using Large-Scale Tests." *Civil Engineering Journal*, Vol. 4, No. 3, (2018), 497. <https://doi.org/10.28991/cej-0309110>
25. Tajari, S., Sadrossadat, E., and Bazaz, J. B. "Indirect estimation of the ultimate bearing capacity of shallow foundations resting on rock masses." *International Journal of Rock Mechanics and Mining Sciences*, Vol. 80, (2015), 107–117. <https://doi.org/10.1016/j.ijrmm.2015.09.015>
26. Abdollahi, M., and Bolouri Bazaz, J. "Reconstitution of Sand Specimens Using a Rainer System." *International Journal of Engineering, Transactions B: Applications*, Vol. 30, No. 10, (2017), 1451–1463. <https://doi.org/10.5829/ije.2017.30.10a.05>
27. Jumikis, A. Theoretical soil mechanics: With practical applications to soil mechanics and foundation engineering, Van Nostrand Reinhold Company, 1969.
28. Gottardi, G., Houslyby, G. T., and Butterfield, R. "Plastic response of circular footings on sand under general planar loading." *Géotechnique*, Vol. 49, No. 4, (1999), 453–469. <https://doi.org/10.1680/geot.1999.49.4.453>

Persian Abstract

چکیده

بررسی همه جانبه رفتار پی‌های حلقوی تحت بارگذاری مایل و خارج محور میخنی است که کمتر مورد توجه محققان قرار گرفته است. در این پژوهش با استفاده از مدل‌سازی آزمایشگاهی، رفتار پی حلقوی با نسبت‌های قطر ۰، ۰/۲، ۰/۴ و ۰/۶ تحت بارگذاری ترکیبی مایل و خارج محور مورد بررسی قرار گرفته است. حالت‌های مختلف بارگذاری تعریف و نقاط گسیختگی در هر آزمایش تعیین گردید. با جمع‌آوری مقادیر بدست آمده سطح گسیختگی پی در فضای $\tan(\alpha)-e/B-V/V_{ult}$ ترسیم و معادله سطح گسیختگی بدست آمد. سپس ضرایب رابطه سطح گسیختگی با توجه به نسبت‌های مختلف قطر پی حلقوی کالیبره گردید. نتایج نشان می‌دهد با افزایش مقدار بار قائم، زاویه انحراف و گریز از مرکز کمتر امکان پذیر است. همچنین افزایش خروج از محوری بار قائم امکان بارگذاری مایل با زاویه انحراف بار کمتر را ممکن می‌کند. در ادامه با استفاده از مفهوم سطح گسیختگی به بررسی پایداری پی تحت بارگذاری ترکیبی مایل و خارج محور پرداخته شده است.



Pavement Maintenance Management Using Multi-objective Optimization: (Case Study: Wasit Governorate-Iraq)

A. K. Shadhar^a, A. M. Raoof Mahjoob^{*b}

^a Department of Civil Engineering, College of Engineering, University of Wasit, Iraq

^b Department of Civil Engineering, College of Engineering, University of Baghdad, Iraq

PAPER INFO

Paper history:

Received: 16 March 2020

Received in revised form: 16 June 2020

Accepted 21 July 2020

Keywords:

Genetic Algorithms

Maintenance

Optimization

Pavement

Roadway

ABSTRACT

Limited resources and budget are the most important problem facing the road management sector; therefore, apportionment of maintenance and rehabilitation (M&R) requirements and priorities at the right time and logical are the most significant factors. Roadway will request continuous (M&R) works to avoid deterioration result from repetitive vehicle weight as well as other factors such as environmental factors. Whether, with the allocation budget that was allocated for roadway maintenance work; there is a necessity to efficiently used the obtainable funding. To execute this, a systematic approach for planning M-and-R process to reach optimum the benefits from roadway segment and minimize necessary funding and costs to repeat the pavement into first state. This process defined as the pavement maintenance management system (PMMS); thus, approach would enable agency to allotted funds, labors, equipment and other resources, most efficiently. This paper demonstrates the applying process of the maintenance program according to the genetic algorithm optimization. The aim of it was to obtain the optimal maintenance strategy alternative percent to reach best values for service life extended as well as increasing the pavement condition index (PCI) along with a specific budget that is not sufficient to restore the whole pavement to its previous state. After applying this program, it was found that it gives the road an additional service life (1.2 years), and at the same time it gives an increase in PCI value (3.8%), taking into consideration the limited resources allocated for maintenance.

doi: 10.5829/ije.2020.33.11b.05

NOMENCLATURE

X_i	Value between 0 and 1 represent the percent of segment of roadway under treatments	$i =$	Chosen segment number
n	Number of road segments	$j =$	Type of maintenance strategy options
C_i	Percent of funding or budget	$m =$	Total number of pavement maintenance options
UI	Useful service life extended index	X_{ij}	Value between 0 and 1 represent the percent of segment of roadway under treatments.
le	Maintenance options life extended in year	d_i	PCI rating for each road segment
mle	Maximum maintenance options life extended in year, usually taken 10 years	B_l	Budget allocated to road

1. INTRODUCTION

Appropriate management, study and planning are effective factors in maintaining the level of service provided by infrastructure projects and preventing possible deterioration through maintenance of the

integrity of such projects. Neglect or misuse and mismanagement of these public services can result in additional expenses and subversive alternatives as well as significant failures [1].

Decision-makers (DMs) need mathematical solutions and process research models to find appropriate

*Corresponding Author Institutional Email:
ahmed.mahjoob@coeng.uobaghdad.edu.iq (A. R. Mahjoob)

decisions in case of a number of conflicting goals that need to deal effectively and ideally to reach the optimal decision. As an example of this case when there is a desire to improve the level of performance of a particular project at the same time there are financial constraints through limited budget or lack of financial allocations available for maintenance work. Therefore, there is a need for a multi-objective decision support system (MODSS) to improve the effective use of available resources and to create a distinct cost-benefit ratio.

It is necessary to understand the nature of the infrastructure projects and the history of maintenance of its parts and study the mechanism of degradation of the project, as the process of optimal decision-making requires knowledge of the problem and determine its variables and what are the most important constraints that may hinder the achievement of the appropriate decision which in turn leads to the creation of an effective maintenance and rehabilitation program for the project under study.

In fact, the current state of the project and its future development are determinants of the effectiveness of any (DSS) [2]. In this paper, performance will be increased through benefiting from expertise in pavement engineering as well as information and knowledge available from other areas such as management science, decision support systems, mathematical modeling and artificial intelligence. Furthermore, this research is part of the study of the benefits of using multi-objective systems in the management of pavement maintenance.

2. RESEARCH METHODOLOGY

The methodology for this research is:

- Provides a brief review of existing optimization technique throughout related literature review.
- Define Genetic Algorithm technique.
- Determine project deterioration rate from data provided by bridges directorate of Wasit.
- Define optimization objective functions and constraints of the roadway.
- Applying the optimization tool for cost and the stable rehabilitation or maintenance required using Genetic Algorithm technique.

3. RELATED LITERATURE

In the field of pavement management, there are several mathematical models using step to reach optimum solution known as optimization technique, and usually used are linear programming (LP), dynamic programming (DP), integer programming (IP), nonlinear, and Multi-objective optimization (MO) [3]. Often, optimal solutions within the synthesis of the

infrastructure management problem determination and formulation caused from a well defined variables of mathematical models in optimization field.

Linear programming (LP) in road network domain commonly involves dividing the road into groups of pavement segment that have similar features, such as road class, pavement condition rating, traffic load road dimensions, distress type, etc. Based on this, M&R treatments varying and a resource allocation problem is formulated in order to find the optimal distribution of resources for the pavement groups under study. Accordingly, LP models are relatively manageable and allow users to test its modeling though perform sensitivity analyses for the output data and input factors [4].

In domain in which LP fails, the integer programming (IP) tactic prosper. IP models can provide precise facts regarding M&R strategy activities scheduling and individual segment selections to reach the optimum rating of the roadway network. However, IP models need to more calculation step, essentially when performing on huge networks [5].

Even for single-objective functions, the scheduling and planning model that has integer solution or resolving variables is a nondeterministic polynomial time (NP)-difficult problem [6]. Furthermore, dynamic programming (DP) can be used to solve separated problems having a clear construction and imbrication secondary problems. This means that the issue formulated should be solvable consecutive, and ingredient of the most favorable solution should also smooth the solving of sub-problem [7]. Else, DP is often used for searching the circumstance of uncertainty in defining the best M&R strategy in infrastructure [8-10]. Finally, nonlinear programming models usually have their objective and at sometimes one of their restriction formulated as nonlinear (curvilinear) [11]. Many studies that have used nonlinear programming proposed that it is more reflexive of the allocation of the chosen input variables, particularly for variables concerning with roadway performance [12, 13].

Thorough knowledge and survey of related study in the literature discover a high number of works using genetic algorithms (GAs) for solving infrastructure maintenance resource distribution problems as well as in structural building [14, 15].

Multi-objective optimization transacts with more complex scenarios where DMs need to reconcile between multiple and often incompatible goals with each other. In fact, systems optimized taking into account a single feature might not perform efficiently with consideration to other systems, and optimizing problems according to multiple concordant features becomes major requirements to achieve the best results. GA built in solving the multi-objective optimization [16].

4. PAVEMENT CONDITION INDEX CALCULATION

The rating of roadway is specified from a correlation that display roadway rating as a result of the PCI value calculation. Table 1 presents the PCI ratings limits.

When explaining data that was collected from field survey and visual inspection for road condition, three varied type of the collected data must have concerned: the traffic density, the type, density and severity of distress at survey time and at last the evolution of road deterioration. The PCI value presents a general conception of the pavement state and the nature of the work that will be wanted to maintain the pavement. Pavements at surface layer are more potential to require a simple repair and minor maintenance, while the lower layers of road are more suitable to be nomination for essential rehabilitation or reconstruction (Shahin 2005).

There are two methods for calculating PCI, which are the manual method, it depends on the use of equations and curves, while the second method uses the PAVER software.

5. MAINTENANCE STRATEGY ALTERNATIVE

The objective was addressed to this study is to select the optimum pavement maintenance strategy. This selection has been made based on maximum benefit to cost ratio. All the benefits and costs have been converted to monetary terms. Functional benefits have been estimated using PCI increase due to a maintenance treatment which is the key component of this study. Data [17], regarding the life extension of the pavement due to various treatments and their unit costs have been obtained from airport cooperative research program (ACRP), and it is shown in Table 2.

The PCI increase data has been obtained from a previous study. All treatments are applied over the whole area as surface treatment except the spray patching. It is assumed that 50% area should be patched where patching is required.

6. CASE STUDY

The proposed methodology aims to be implemented on any type of road. As an application, a case study is

TABLE 1. PCI rating scale

PCI Range	Rating Scale
71-100	Good
56-70	Fair
40-55	Poor
25-39	Very Poor
0-24	Failed

TABLE 2. Unit cost and life extension of different maintenance strategy [17]

Alternative	Maintenance	Unit Cost (\$/M ²)	Life Extension (Years)	PCI Rise
1	Crack Treatment	1.75	3	5
2	Patching	6.5	4	5
3	Slurry Seal	3.5	5	30
4	Thin Overlay	8.5	10	35

prepared to identify the best strategy option that will be done for the major road which connects the commercial capital of Iraq; Baghdad city with eastern south Kut city as well as with other major cities. This road is a significant entrance of south Iraq capital for transportation of people and goods as well. The percentage of total vehicles represents the big amount of heavy vehicles movement on this road.

Data collected from bridges directorate of Wasit, is discussed in Table 3.

According to official source the budget allocated to road *B1* for each last two years was equal to 15*10⁸ DI, and this funding must be distributed to all roadway segment according to priority determinate through optimization process with genetic algorithms.

7. GENETIC ALGORITHM FORMULATION

The variables of decision model are exemplifying in GAs by a string framework comparable to the chromosomes in natural growth. The decision variables relate to the choice of pavement sections chosen for maintenance. A suitable string framework is one that be formed of one cell for each pavement section as shown in Figures 1(a) and 1(b) [17]. Therefore, the number of roadway segments of the road chosen should be equal to number of cells (total length of the string framework).

TABLE 3. PCI rating

Segment NO.	1	2	3	4
PCI	31	12	36	57

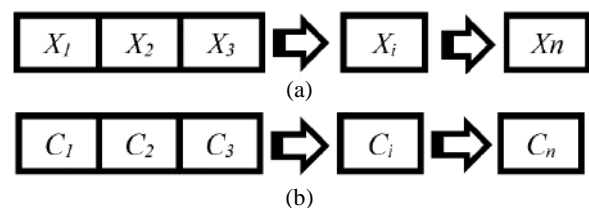


Figure 1. String of genes for (a) project level GA and (b) network level GA

The decision taken about value of each cell gives the percent of the road segment needed for maintenance that the cell represents.

The decision variables are plainly represented the percentage shares of funding allotment for the roadway. As shown in Figure 1(b). The genes values C1 represent percent of funding or budget (cost of treatment) that will be allotment for each X1 segment and so on. The following figure (Figure 2) shows the process flow chart for the genetic algorithm optimization [18].

8. USEFUL SERVICE LIFE EXTENDED INDEX

The best way to prioritize road repair is by determining the added service life that will be obtained through the adoption of the proposed maintenance option, provided that it does not conflict with the budget limits and the specific financial allocation.

The added service life coefficient (UI) will be adopted which can be obtained from the following equation:

$$UI = \frac{le}{mle} \tag{1}$$

where, UI is useful service life extended index; le is each maintenance options life extended in a year (Table 2). Also, mle is maximum maintenance options life extended in a year, usually taken 10.

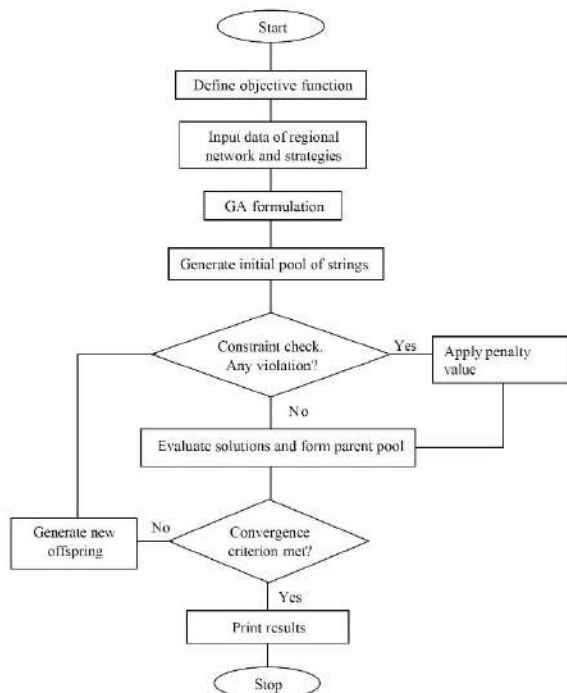


Figure 2. Flow chart for process of genetic algorithm optimization

In order to define the objective functions, there is need to collect suitable data. Table 3 in addition to the field survey information provided by the roads and bridges department in the region; data are shown in Table 2.

Accordingly, from precedence table can be reached to clarify the objective functions, and it defined by three objectives, which is the first one it to minimize the maintenance costs and the two other objectives are to maximize both the road rating and the service road life extended.

9. OBJECTIVE FUNCTIONS AND CONSTRAINTS

As the objective functions and constraints of the roadway, the GA formulation and optimization analysis are performed to evaluate the maintenance costs. When conducting the optimization process for the maintenance of road sections, we need to determine the most important goals to be reached, namely:

- Increase the road condition (road evaluation).
- Extending the service life of the road.
- Carry out maintenance work according to assigned costs and under budget limits.

9. 1. Objective Functions This section presents the mathematical expressions of objective function for Kut-Baghdad roadway:

- a. The objective function is to maximize the useful service life (USL) of the road through distressed road segments repaired, that is:

$$\text{Maximize} = \sum_{i=1}^n \sum_{j=1}^m X_{ij} * UI_{ij} \tag{2}$$

where, i is the chosen segment number ; j is type of maintenance strategy options; n is total number of pavement segment of the road; m is total number of pavement maintenance options; UIij is useful service life extended index of road segment; Xij is value between 0 and 1 represent the percent of segment of roadway under treatments.

The final formulation will be:

$$\text{Maximizing} = \{0.3*x_{11} + 0.4*x_{12} + 0.5*x_{13} + 1*x_{14} + 0.3*x_{21} + 0.4*x_{22} + 0.5*x_{23} + 1*x_{24} + 0.3*x_{31} + 0.4*x_{32} + 0.5*x_{33} + 1*x_{34} + 0.3*x_{41} + 0.4*x_{42} + 0.5*x_{43} + 1*x_{44}\}$$

- b. The objective function is to minimize the total maintenance expenditure, as given below:

$$\text{Minimize} = \sum_{i=1}^n \sum_{j=1}^m C_{ij} * X_{ij} \tag{3}$$

where, Cij is the maintenance costs incurred in road segment i with maintenance option j (Table 2). The final formulation will be as follows:

$$\text{Minimizing Cost} = \{1.75*x_{11} + 6.5*x_{12} + 3.5*x_{13} + 8.5*x_{14} + 1.75*x_{21} + 6.5*x_{22} + 3.5*x_{23} + 8.5*x_{24} +$$

$$1.75 * x_{31} + 6.5 * x_{32} + 3.5 * x_{33} + 8.5 * x_{34} + 1.75 * x_{41} + 6.5 * x_{42} + 3.5 * x_{43} + 8.5 * x_{44}$$

c. The objective function is to maximize the condition rating of the road through distressed road segments repaired, that is:

$$\text{Maximize} = \sum_{i=1}^n X_i * \frac{1}{d_i} \tag{4}$$

where di is the PCI rating for each road segment (Table 3). The final formulation will be:

$$\text{Maximizing PCI Rating} = \{3.57 * x_{11} + 3.57 * x_{12} + 3.57 * x_{13} + 3.57 * x_{14} + 8.33 * x_{21} + 8.33 * x_{22} + 8.33 * x_{23} + 8.33 * x_{24} + 3.26 * x_{31} + 3.26 * x_{32} + 3.26 * x_{33} + 3.26 * x_{34} + 1.89 * x_{41} + 1.89 * x_{42} + 1.89 * x_{43} + 1.89 * x_{44}\}$$

9. 2. Constraint of Objective Function The objective function is subject to the following constraints:

9. 2. 1. Maintenance Expenditure The total maintenance expenditure must not exceed the total budget allocated, as given by:

$$\sum_{i=1}^n \sum_{j=1}^m C_{ij} * X_{ij} \leq Bl \tag{5}$$

where, Bl the budget allocated to road. The final formulation will be:

$$1.75 * x_{11} + 6.5 * x_{12} + 3.5 * x_{13} + 8.5 * x_{14} + 1.75 * x_{21} + 6.5 * x_{22} + 3.5 * x_{23} + 8.5 * x_{24} + 1.75 * x_{31} + 6.5 * x_{32} + 3.5 * x_{33} + 8.5 * x_{34} + 1.75 * x_{41} + 6.5 * x_{42} + 3.5 * x_{43} + 8.5 * x_{44} \leq 15$$

9. 2. 2. Non Negative Value The value of variable X_{ij} should not to be negative value (between 0 and 1).

$$0 \leq X_{ij} \leq 1 \tag{6}$$

9. 2. 3. Select one Strategy The objective functions optimization should be selected one option of maintenance strategy as follow:

$$\sum_{j=1}^m X_j \leq 1 \tag{7}$$

10. RESULTS AND INTERPRETATION OF THE FINDINGS

The results of applying the genetic algorithms multi-objective explained in the next figure, the result are presented in Figures 3 and 4; which obviously shown that the Pareto interface can be obtained using the proposed approach and that a uniform allocation can be achieved by changing the different objective weights. Each point in the graph required independent operation with a defining number population and more than 100 iterations.

Figures 3 and 4 show the relation between the objective functions, where the Figure 3 clearly presented evidence to how the increase in the PCI will lead to extend the roadway useful life.

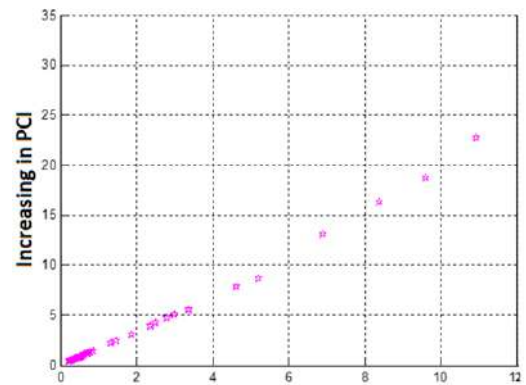


Figure 3. Relation between increasing in the PCI and useful life extend

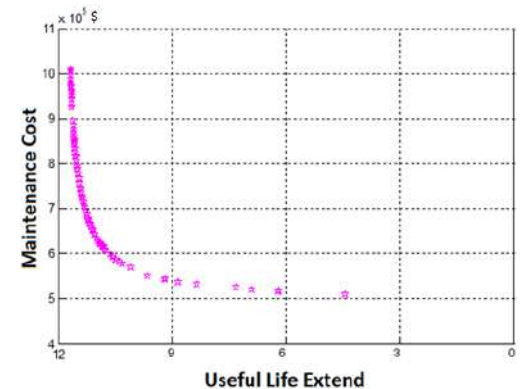


Figure 4. Effect of maintenance cost on extend of roadway useful life

While Figure 4 shows the effect of availability budget for funding the maintenance cost on extend of roadway useful life.

The followed Figure 5 displays the percent of each maintenance strategy option that will be applied to reach optimum benefit from allocated budget that lead to the best PCI and more fitness from the side of useful life extend. The main purpose of performing maintenance work is to either maintain the service provided, prevent the pavement from collapsing, or extend the service life of the road.

After applying the genetic algorithm optimization and taking into consideration the limited budget as a constraint, it was found that its used as a decision tool was suitable to reach an optimal distribution of maintenance work on all road sections according to the alternatives provided for the system.

Thus, the proportions of each of these alternatives are distributed in Table 3 for each road sections.

Depending on the values shown in Table 1, it is noted that the maintenance strategy described in Table 3 is applied. It will contribute to extend the service life of the road by 1.2 year. At the same time, it will increase PCI by 3.8 % for overall road rating.

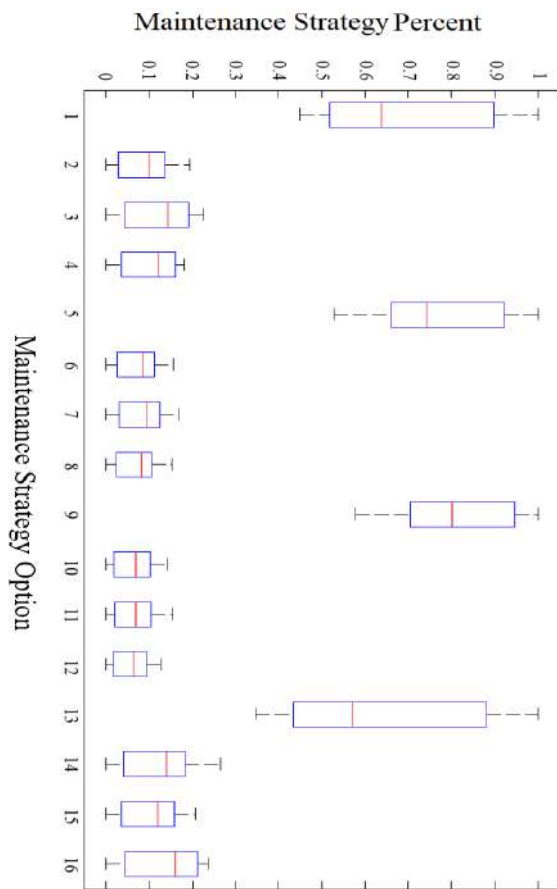


Figure 5. Percent for each maintenance strategy

TABLE 3. Maintenance strategy alternative for each road sections area percentage

Maintenance Strategy	Sec. 1	Sec. 2	Sec. 3	Sec. 4
Crack Treatment	0.38	0.26	0.24	0.42
Patching	0.12	0.09	0.07	0.19
Slurry Seal	0.17	0.12	0.09	0.14
Thin Overlay	0.14	0.09	0.07	0.24

Tables 4 and 5 show increasing in PCI percentage also the extended service life for each section according to the maintenance procedure taken.

TABLE 4. Maintenance strategy alternative contribution in extended service life for each road sections

Maintenance Strategy	Sec. 1	Sec. 2	Sec. 3	Sec. 4
Crack Treatment	1.14	0.78	0.72	1.26
Patching	0.48	0.36	0.28	0.76
Slurry Seal	0.85	0.60	0.45	0.70
Thin Overlay	1.40	0.90	0.70	2.40

TABLE 5. Maintenance strategy alternative contribution in pci increasing for each road sections

Maintenance Strategy	Sec. 1	Sec. 2	Sec. 3	Sec. 4
Crack Treatment (%)	1.9	1.3	1.2	2.1
Patching (%)	0.6	0.5	0.4	1.0
Slurry Seal (%)	5.1	3.6	2.7	4.2
Thin Overlay (%)	4.9	3.2	2.5	8.4

11. CONCLUSIONS

This paper presents optimization process with a multi-objective programming, used maximizing level of user comfortable through increasing PCI rating of roadway as measured. It examines the prioritizing optimization of the road segments that is needed for maintenance using the genetic algorithm based on useful service life and pavement condition as an objective function. The constraints faced is maintenance cost must not be exceeding the limited yearly financial (budget limit) as well as the non-negatively constraint. This research presents approach to find optimum maintenance alternative according ability limiting of funds allocated by Governorate to each project. The research reaches to the following recommendations:

1. The rapid deterioration in Iraqi roads in general has been observed due to negligence in regular and planned maintenance of the roads. So there is need to manage road maintenance in a systematic and continuous manner.
2. The adoption of this model by the bodies responsible for the maintenance of roads will be of great benefit by providing them with a clear vision of the behaviour of pavement and the extent of the deterioration. Thus, provide a basis for prioritizing the provision of funds to maintain road sections subject to failure.
3. Moreover, other studies can be developed using maintenance strategy with other option, overlooking from standard strategy that has been adopted in this work.
4. The adoption of optimization in decision-making, greatly helps decision makers in determining maintenance priorities and an optimal distribution of the budget, although it is limited, so, the project can be reached to the best rate of improvement in performance.
5. Available budget contributes to extend the service life of the road by 1.2 year. At the same time, it will increase PCI by 3.8 % for overall road rating, as a result of applying genetic algorithms optimization for each section according to the maintenance procedure taken.
6. It is possible to conduct additional studies comparing the different optimization methods and showing the difference between their results on increase in road rating and the value of service life extended.

12. ACKNOWLEDGEMENTS

Baghdad University, supported this project. Authors are

thankful to roads and bridges directorate of Wasit, who has provided the information related with budget limit allocated to maintenance work.

13. REFERENCES

- Farran, M. and Zayed, T., "Comparative analysis of life-cycle costing for rehabilitating infrastructure systems", *Journal of Performance of Constructed Facilities*, Vol. 23, No. 5, (2009), 320-326. doi.org/10.1061/(ASCE)CF.1943-5509.0000038
- Li, Z. and Sinha, K.C., "Methodology for multicriteria decision making in highway asset management", *Transportation Research Record*, Vol. 1885, No. 1, (2004), 79-87. doi.org/10.1061/(ASCE)CF.1943-5509.0000038
- Torres-Machí, C., Chamorro, A., Videla, C., Pellicer, E. and Yepes, V., "An iterative approach for the optimization of pavement maintenance management at the network level", *The Scientific World Journal*, Vol. 2014, No., (2014). doi.org/10.1155/2014/524329
- Jesus, M., Akyildiz, S., Bish, D.R. and Krueger, D.A., "Network-level optimization of pavement maintenance renewal strategies", *Advanced Engineering Informatics*, Vol. 25, No. 4, (2011), 699-712. doi.org/10.1016/j.aei.2011.08.002
- Gao, L. and Zhang, Z., "Management of pavement maintenance, rehabilitation, and reconstruction through network partition", *Transportation Research Record*, Vol. 2366, No. 1, (2013), 59-63. doi.org/10.3141/2366-07
- Gao, L., Xie, C., Zhang, Z. and Waller, S.T., "Network-level road pavement maintenance and rehabilitation scheduling for optimal performance improvement and budget utilization", *Computer-Aided Civil and Infrastructure Engineering*, Vol. 27, No. 4, (2012), 278-287. doi.org/10.1111/j.1467-8667.2011.00733.x
- Boyles, S.D., Zhang, Z. and Waller, S.T., "Optimal maintenance and repair policies under nonlinear preferences", *Journal of Infrastructure Systems*, Vol. 16, No. 1, (2010), 11-20. doi.org/10.1061/(ASCE)1076-0342(2010)16:1(11)
- Madanat, S., Park, S. and Kuhn, K., "Adaptive optimization and systematic probing of infrastructure system maintenance policies under model uncertainty", *Journal of Infrastructure Systems*, Vol. 12, No. 3, (2006), 192-198. doi.org/10.1061/(ASCE)1076-0342(2006)12:3(192)
- Medury, A. and Madanat, S., "Incorporating network considerations into pavement management systems: A case for approximate dynamic programming", *Transportation Research Part C: Emerging Technologies*, Vol. 33, (2013), 134-150. doi.org/10.1016/j.trc.2013.03.003
- Kuhn, K.D., "Network-level infrastructure management using approximate dynamic programming", *Journal of Infrastructure Systems*, Vol. 16, No. 2, (2010), 103-111. doi.org/10.1061/(ASCE)IS.1943-555X.0000019
- Bryce, J.M., Flintsch, G. and Hall, R.P., "A multi criteria decision analysis technique for including environmental impacts in sustainable infrastructure management business practices", *Transportation Research Part D: Transport and Environment*, Vol. 32, (2014), 435-445. doi.org/10.1016/j.trd.2014.08.019
- Abaza, K.A., "Iterative linear approach for nonlinear nonhomogenous stochastic pavement management models", *Journal of transportation engineering*, Vol. 132, No. 3, (2006), 244-256. doi.10.1061/(ASCE)0733-947X(2006)132:3(244)
- Gao, L., Chou, E.Y. and Wang, S., *Comparison of pavement network management tools based on linear and non-linear optimization methods*. 2013.
- Chootinan, P., Chen, A., Horrocks, M.R. and Bolling, D., "A multi-year pavement maintenance program using a stochastic simulation-based genetic algorithm approach", *Transportation Research Part A: Policy and Practice*, Vol. 40, No. 9, (2006), 725-743. doi.org/10.1016/j.tra.2005.12.003
- Jha, M.K. and Abdullah, J., "A markovian approach for optimizing highway life-cycle with genetic algorithms by considering maintenance of roadside appurtenances", *Journal of the Franklin Institute*, Vol. 343, No. 4-5, (2006), 404-419. doi.org/10.1016/j.jfranklin.2006.02.027
- Fakhrzad, M., Sadeghieh, A. and Emami, L., "A new multi-objective job shop scheduling with setup times using a hybrid genetic algorithm", *International Journal of Engineering, Transactions B: Applications*, Vol. 26, No. 2, (2013). doi: 10.5829/idosi.ije.2013.26.02b.11
- Fwa, T., Tan, C. and Chan, W., "Backcalculation analysis of pavement-layer moduli using genetic algorithms", *Transportation Research Record*, Vol. 1570, No. 1, (1997), 134-142. doi.org/10.3141/1570-16
- Yew, T.J., "Coordinated budget allocation in multi-district highway agencies", (2005), ISBN-13: 978-0387-23464-9

Persian Abstract

چکیده

منابع و بودجه محدود مهمترین مشکل در بخش مدیریت راه است، بنابراین تخصیص نیازها و اولویت های نگهداری و توانبخشی در زمان مناسب و منطقی مهمترین عوامل است. برای جلوگیری از نتیجه بدتر شدن در اثر تکرار وزن وسیله نقلیه و همچنین سایر عوامل مانند عوامل محیطی، جاده ها درخواست کار مداوم دارند. این که آیا با بودجه تخصیصی که برای کارهای مربوط به تعمیر و نگهداری جاده ها اختصاص داده شده است، لازم است که از بودجه به دست آمده استفاده بهینه استفاده شود. برای اجرای این روش، یک رویکرد منظم برای فرایند برنامه ریزی برای دستیابی بهینه از مزایای بخش جاده و به حداقل رساندن بودجه و هزینه های لازم برای تکرار روسازی در حالت اول. این فرآیند به عنوان سیستم مدیریت تعمیر و نگهداری پیاده رو تعریف شده است. بنابراین، رویکرد، مؤثرترین کارایی بودجه، کار، تجهیزات و سایر منابع را به آژانس اختصاص می دهد. در این مقاله روند استفاده از برنامه نگهداری با توجه به بهینه سازی الگوریتم ژنتیک نشان داده شده است. هدف از آن دستیابی به درصد جایگزین استراتژی تعمیر و نگهداری کم برای دستیابی به بهترین مقادیر برای عمر سرویس تمدید شده و همچنین افزایش شاخص وضعیت روسازی (PCI) به همراه بودجه مشخصی است که برای بازگرداندن کل پیاده رو به حالت قبلی خود کافی نیست. پس از استفاده از این برنامه، مشخص شد که طول عمر سرویس اضافی را به جاده (۱.۲ سال) می دهد و در عین حال با در نظر گرفتن منابع محدود اختصاص یافته برای نگهداری، مقدار (3.8) PCI را نیز افزایش می دهد.



A Novel Building Information Modeling-based Method for Improving Cost and Energy Performance of the Building Envelope

B. AlizadehKharazi, A. Alvanchi*, H. Taghaddos

Department of Civil Engineering, Sharif University of Technology, Tehran, Iran

PAPER INFO

Paper history:

Received 24 May 2020

Received in revised form 30 August 2020

Accepted 02 September 2020

Keywords:

Building Information Modeling

Building Envelope Materials

Energy Consumption

Life Cycle Cost

ABSTRACT

Building envelopes and regional conditions can significantly contribute to the cost and energy performance of the buildings. Structured methods that take into account the impacts of both the envelope materials and the regional conditions to find the most feasible envelope materials within a region, however, are still missing. This study responds to this need by proposing a novel method using the capabilities of Building Information Modeling (BIM). The proposed method is used for identifying cost- and energy-efficient building envelope materials within a region over the life cycle. First, commonly used envelope materials in a region are identified. Then, BIM is employed for simulating the energy performance and evaluating the life cycle cost of the materials. The method was implemented in Tehran, Iran. It was successfully utilized for improving the cost and energy performance of a nine-story residential building case. The achieved results indicated a potential energy performance enhancement of 31%, and the life cycle cost improvement of 28% by replacing conventionally used envelope materials with the available high-performance building materials. The proposed method can benefit various stakeholders in the building construction industry, including municipalities, owners, contractors, and consumers, by enhancing the cost and energy performance of the buildings.

doi: 10.5829/ije.2020.33.11b.06

1. INTRODUCTION

Selecting an appropriate type of building envelope can have a considerable impact on the cost and energy performance of buildings. It is estimated that more than 20% of a building's construction cost is spent on the building envelope [1, 2]. The building envelope forms the border between the interior and exterior of the building. Therefore, a majority of the building's heat exchange during the operation period occurs via the envelope. The high impact of the building envelope on the life cycle cost and energy performance of the buildings has inspired many researchers around the globe. Researchers have examined the impacts of different building envelope materials and insulators on the cost and energy performance of the buildings. Sawhney et al. [3] compared the cost efficiency of very energy-efficient (or Five Star) and super energy efficient (or Five Star Plus) materials. They found a shorter payback period for Five

Star materials in Michigan, USA. Cheung et al. [4] found a potential average energy consumption savings of 31% for high-rise apartments in the hot and humid climate of Hong Kong using extruded polystyrene (XPS) insulation layers. Hoseini et al. [5] found the use of fiberglass insulation in the brick walls and ceilings with the double-glazed windows results in a 49% reduction in the energy-saving in Tehran, Iran. Domínguez et al. [6] identified a potential energy saving of up to 27% with a proper selection of insulation materials in Seville, Spain. Sim and Sim [7] found energy performance deviations for different types of wall materials, including mud brick, cement brick, autoclaved light-weight concrete block, cellulose fiber reinforced cement board, and chaff charcoal, in traditional Korean buildings. Braulio-Gonzalo and Bovea [8] found the use of mineral and glass wool insulations highly effective in saving energy in the buildings in Spain. Echarri [9] reduced the annual energy consumption of a detached residential building in Spain

*Corresponding Author Institutional Email: alvanchi@sharif.edu
(A. Alvanchi)

by 10% using thermal ceramic panel walls. Pakand and Toufigh [10] found the energy efficiency of low-cost rammed earth wall materials comparable to the high-cost Expanded polystyrene insulation (EPS) and phase change materials. Rahbar and Saadati [11] showed the use of polystyrene insulation layers could improve the energy performance of the buildings by up to 6.5% in the hot and dry climate of Semnan, Iran. Song et al. [12] analyzed the impacts of EPS insulation materials on the energy consumption of an office building in Southern China. Hasan et al. [13] found phase change envelope materials can reduce the energy consumption of buildings.

Impacts of regional conditions on the cost and energy performance of the building envelope have also been investigated in past research. Masoso and Grobler [14] identified the use of 80 mm XPS insulation in buildings results in the energy-saving up to 26 degrees Celsius and the waste of energy beyond this temperature in a hot and dry climate. Pulselli et al. [15] examined the energy performance of three different types of building envelope materials in three regions in Europe. The study found the regional climate condition as the main factor affecting the performance of different building envelope materials. Additional building insulation resulted in different life cycle cost savings in four cities in Turkey [16]. Ramesh et al. [17] found that the use of insulation materials could result in a range of 10% to 30% energy savings in five different climate zones in India, depending on the climate conditions. Friess et al. [18] identified different impacts for insulation materials in typical office buildings across Malaga (Spain), Dubai (UAE), and El Dorado (USA). Climate condition was also identified as the main contributing factor to the energy performance of the buildings' envelope insulation materials in Greece by Charisi [19].

Since the emergence of Building Information Modeling (BIM), the employment of BIM for Building Energy Modeling (BEM) has become quite popular [20, 21]. BIM encompasses a detailed integrated multi-discipline design of the buildings to provide necessary input data for BEM in a cost and time-efficient manner [22–24]. BIM models can also provide foundations for capturing the regional and environmental impacts on the energy performance of the buildings [25]. Furthermore, material quantity takeoff and cost estimation is a frequently used application of BIM models in the building construction projects [26]. In the past, the low accuracy level of the building's cost estimation [27] and energy performance analysis [3] performed with traditional methods was a significant issue. BIM could considerably enhance the accuracy level of cost estimation [27] and life cycle energy performance analysis [25] and address this concern of the traditional methods.

The capabilities of BIM to facilitate and improve BEM development have encouraged many researchers to

apply BIM in their building performance improvement efforts. Niu et al. [28] developed a BIM-GIS (geographical information system) integrated web-based database of regional energy-efficient building design for urban development. More specifically, some researchers have utilized BIM for optimizing building design options. Jalaei and Jrade [29] proposed a BIM-based integrated life cycle assessment platform for analyzing the environment cost of buildings with different sustainable-certified building components. Oduyemi and Okoroh [30] employed BIM as a useful information-based tool for analyzing the effect of increasing insulation to roof and windows and occupancy level on the indoor environmental quality. Ahsan et al. [31] used BIM for the selection of most efficient insulation materials and their optimum thickness to improve the cost and energy performance of existing buildings in Pakistan. Lim et al. [32] developed a BIM-based method for automatically calculating the thermal values and construction costs of available building envelope choices. Shalabi and Turkan [33] developed a BIM-energy simulation method to identify building spaces with abnormal energy consumption behavior.

Past research identifies BIM as a powerful tool for comparing different aspects of the available building envelope materials. Nevertheless, the past research lacks a structured method that guides practitioners for identifying cost- and energy-efficient building envelope materials within a region over the life cycle. This research fills this gap by proposing a novel BIM-based method to assist building practitioners. The proposed method considers regional conditions affecting the performance of buildings, including weather conditions, availability of the energy carriers and construction materials in the region, energy carriers' costs, and construction materials' costs. First, different parts of the proposed method are outlined. Then, the capability of the proposed method is verified during its implementation for the buildings in Tehran, Iran. Finally, the results achieved in the research are discussed and concluded.

2. PROPOSED METHOD

Various regional conditions, including climate conditions, energy and material availability, cost, and construction method, contribute to the final cost and energy performance of the building envelope materials over the life cycle. Identified cost- or energy-efficient materials within a region are not necessarily efficient in another region. Therefore, in addition to the material properties, the proposed method needs to capture the regional conditions to accurately identify cost- and energy-efficient building envelope materials within a region. The use of efficient envelope materials that are not accessible in a region is not feasible. The proposed

method does not consider the creation of supply chains for the materials and new investments in capacity development for producing unavailable or new materials within the region. Therefore, in the first part of the proposed method, the commonly used and accessible building envelope materials and the alternative building envelope scenarios in the region are identified. In the next part, the BIM models of a sample building are developed for the rival envelope scenarios. The BIM models encompass detailed specifications of each scenario, including geometrical information of the building, type of materials, material density, and thermal conductivity of the material. This information can facilitate the life cycle cost estimation of the building's envelope in the next part of the proposed method.

In the third part of the proposed method, the BIM models are hired for extracting the material quantities and simulating the annual energy consumption of the building. Estimated material quantities are used for the cost estimation of the building envelope construction and maintenance using locally collected cost rates. Locally regulated cost of energy carriers, e.g., natural gas and electricity, are used for the estimation of the energy cost of the building over the operation years. In the last part of the proposed method, the life cycle cost of each scenario, considering the construction and maintenance cost of the building envelope, and the operational cost of the building is estimated. Here, the construction cost includes the building's envelope material cost, installation cost, and transportation cost, which occur during the construction period. The maintenance cost consists of the annual cost spent on preventive and corrective maintenance activities to maintain the required level of service during the operation period. The operational cost includes the overall building's energy consumption cost during the operation period. The accounted costs of each scenario occur during different periods of the building's life cycle. However, to compare the performance of different adopted scenarios, a single value representing each scenario is required. Net Present Value (NPV) represents the equivalent present value of a set of cash flows occurring in different periods. Here, the

calculated NPV of each scenario is proposed as the indicator of each scenario's performance. Figure 1 represents the resulting cash flow and the applicable calculation equation of each scenario's NPV. Figure 2 summarizes the different parts of the proposed method.

3. METHOD IMPLEMENTATION

Tehran is the capital and the most populated city in Iran. According to SCI [34], approximately one-fourth of new residential building areas within the country are built in Tehran. The significant impact of Tehran's residential building construction market in the country was the main contributing reason for selecting Tehran for the sample implementation of the proposed method. Approximately 95 percent of residential buildings in the city are multi-story buildings with five floors or more [34]. In multi-story buildings, the exterior walls have the highest thermal transfer surface area and consequently bear a significant share of the energy loss. As a result, the proposed method in this research was implemented for improving wall materials of multi-story buildings in Tehran. The proposed steps were followed to identify the most viable wall construction materials in the city. A more in-depth explanation of the various steps is provided in the remainder of the section.

3.1. Identifying Prevalent Materials The first step of implementing the proposed method for Tehran was to identify the frequency of various available materials in the region. At the time, no information was found regarding the frequency of different available building envelope materials in Tehran. Therefore, the research team directly performed a field survey on various building construction companies in Tehran for identifying common building envelope materials in the city. An inclusive list of materials used in three main components of the building envelope, including walls, façade, and windows, was created according to the reported articles from different sources [33–36]. According to Golabchi and Mazaherian [36], various

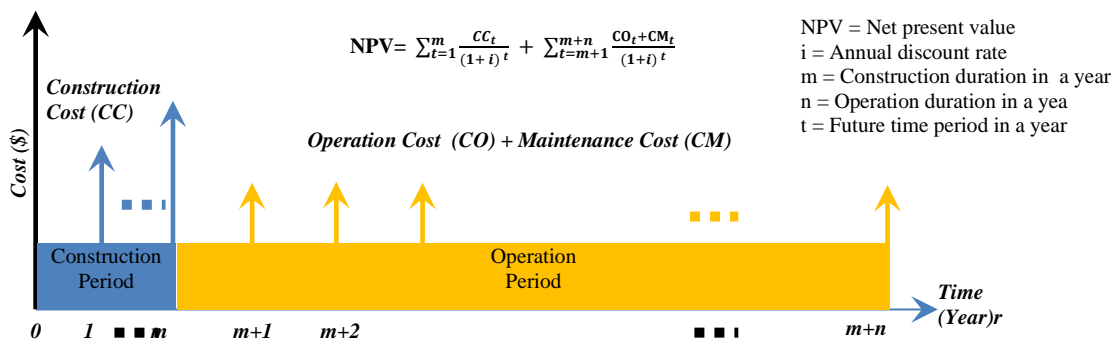


Figure 1. Schematic view of the life cycle cash flow related to the building envelope

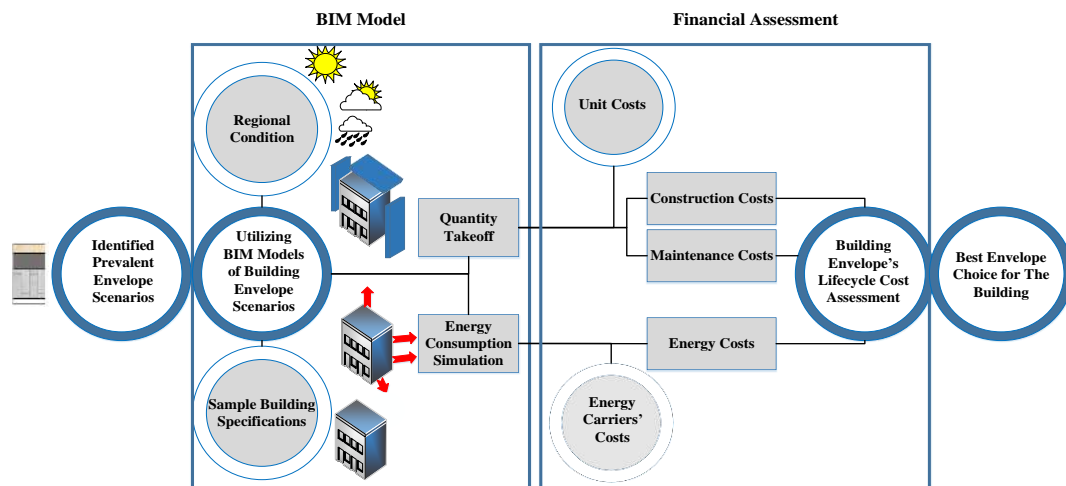


Figure 2. Different parts of the proposed method

exterior wall structures in the region could be divided into three main groups, including traditional, semi-industrial, and industrial. This approach could capture emerging building envelope materials. Table 1 presents the list of materials organized under the adopted categorization method. This material list was then utilized in the field survey to identify and rank the most common building envelope materials in Tehran.

3. 1. 1. Survey Design Building construction companies in Tehran were the target group of the statistical survey. A data sampling method using a questionnaire survey was adopted for ranking the frequency of the identified building envelope materials. The frequency of various building envelope materials was questioned using five-level Likert scale questions ranging from 1 to 5.

3. 1. 2. Questionnaire Distribution The 64 paper-form questionnaires were distributed and collected through an in-person questionnaire distribution method. IBM SPSS software was then employed to analyze the collected data. Cronbach's alpha value of 0.881 affirmed the reliability of the responses. The relational consumption frequency level of different materials was calculated as the average value of the responses received for each question. Table 1 presents the achieved average consumption frequency and the ranks of different identified envelope materials in the survey.

3. 1. 3. Survey Analysis The achieved results for the wall materials represent higher consumption frequency levels for the most traditional materials than the emerging semi-industrial and industrial materials. Among various wall materials, two traditional materials of clay block and expanded clay concrete block received the highest rank with the respective values of 3.87 and

TABLE 1. List of available residential building envelope materials and their achieved consumption frequency in Tehran

Component	Production method	Material	Frequency value (out of 5)	Rank in group
Wall	Traditional	Brick	2.05	7
		Clay Block	3.87	1
		Expanded Clay Concrete Block	3.47	2
		Sandcrete block	2.85	3
		Perlite Concrete Block	2.10	6
	Semi-Industrial	Aerated Block	1.40	9
		Cement board	1.72	8
		EPS Concrete Block	2.15	5
		Light-weight Concrete Panel	2.17	4
		3D Panel	2.17	4
Industrial	Precast Concrete Panel	1.40	9	
Façade		Granite Stone	2.65	4
		Travertine Stone	4.17	1
		Sandstone	1.47	14
		Limestone	2.22	6
		Sedimentary Stone	1.97	8
	Other Stones	Other Stones	0.22	16
		Brick	3.07	3
		Cement	3.37	2
		Aluminum Composite Panel	1.95	9
		Glass	2.50	5
Low-E Glazed	1.82	10		
Ceramics	2.00	7		

Window	Concrete Panel	1.60	12
	Stretch Metal	1.22	15
	HPL	1.57	13
	Fibre Cement Board	1.67	11
	Iron-Single Glazed	1.68	9
	Iron-Double Glazed	1.53	11
	Iron-Triple Glazed	1.15	14
	Iron-Low-E	1.09	15
	Iron-Reflex	1.56	10
	Aluminum-Single Glazed	1.78	7
	Aluminum-Double Glazed	2.84	2
	Aluminum-Triple Glazed	1.78	7
	Aluminum-Low-E	1.46	12
	Aluminum-Reflex	2.37	4
	UPVC-Single Glazed	2.09	5
	UPVC-Double Glazed	4.15	1
	UPVC-Triple Glazed	1.93	6
	UPVC-Low-E	1.28	13
UPVC-Reflex	2.59	3	

values for the two industrial wall materials of 3D panels and precast concrete panels were 2.17 and 1.40, respectively. Among different façade materials, travertine stone tiles were by far the most commonly used material with the consumption frequency value of 4.17. In the window systems, UPVC-double glazed was the dominant system with the consumption frequency level of 4.15. Subsequently, six different building envelope material scenarios were formed by choosing the two most common wall materials from the three production methods. Figure 3 presents the considered specifications in different scenarios. In all six scenarios, the UPVC-double glazed window was used since it was the most dominantly used window system. Travertine stone façade attached to the wall by cement mortar for the visible sides or the street-facing sides of the buildings was used in all scenarios. However, the concealed exterior sides of the building were only covered by cement mortar. Plaster and earth plaster (if required) were considered for leveling the interior side of the walls as a commonly used method. The performance of these six scenarios was analyzed and compared in the case of Tehran following the proposed method.

3. 2. Building Case Specification

An under-construction, nine-story residential building with a reinforced concrete structural system in Tehran was used for the case study. The area of each floor was 716 square meters. The cost estimation performed by the construction team indicated the share of the entire envelope construction cost exceeds 22% of the building construction cost. The air conditioning system was a two-pipe fan coil system using a central chiller with a 5.96 coefficient of performance for the cooling and a central boiler with an 84.5% efficiency rating for the heating.

3.47. Light-weight concrete panels and EPS concrete blocks scored the best ranks among the semi-industrial materials with the respective values of 2.17 and 2.15. The

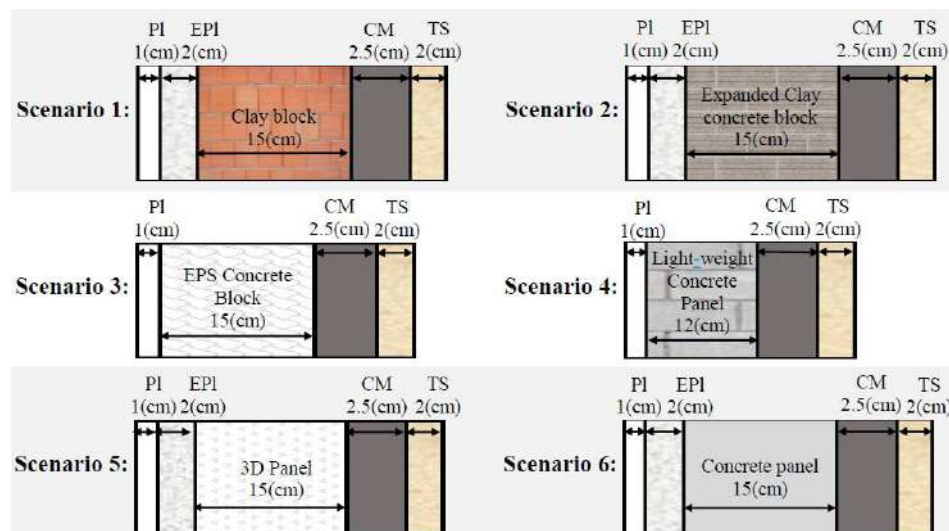


Figure 3. Specifications of different adopted building envelope scenarios, PI: Plaster; EPI: Earth Plaster; CM: Cement Mortar; TS: Travertine Stone; Sh: Shotcrete; EP: Expanded Polystyrene

3. 3. Wall Construction Cost BIM-based 3D models of different building scenarios were developed by the collaborating construction company using Autodesk Revit software. The developed models had a level of detail of 300 to encompass the material specification and air conditioning system of the building [37]. Figure 4 illustrates the floor plan and 3D view of the developed BIM model of the building. The BIM technology for the material quantity takeoff was used for extracting the volume of different envelope materials. Construction methods of three to four different past building projects were assessed for estimating the resource required and cost spent in each building envelope scenario. Unit prices of the transportation and construction costs of different parts of the building's envelope were collected from the corresponding subcontractors in the market. Overall, the construction costs of different adopted scenarios were estimated based on the extracted quantities and prices for different scenarios. Table 2 presents the estimated construction cost of the walls in different scenarios. Among different scenarios, Scenario 1 or the base scenario, which uses the clay block materials, is the most frequently consumed in Tehran, represents the lowest overall construction cost. Scenario 3 with EPS concrete blocks scored the highest construction cost, among other envelope materials.

3. 4. Energy Consumption Simulation Thermal specifications of the adopted construction materials were collected from the corresponding references and were

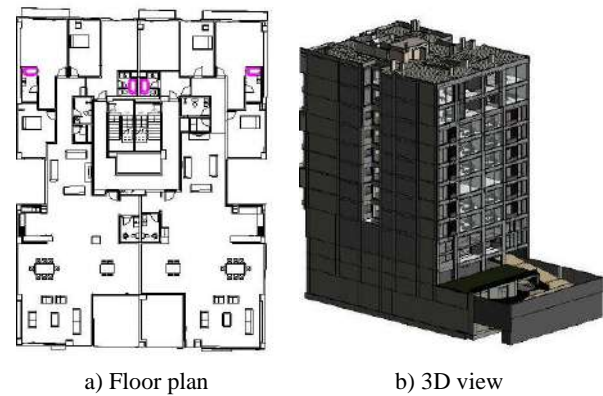


Figure 4. Floor plan and 3D view of the building

added to the BIM models. Autodesk® Green Building Studio software, which effectively works with BIM models to simulate the energy performance of the buildings, was selected in the research. The simulation software imported the thermal specification of the materials and the spatial dimensions of the building from the BIM model. The regional climate condition received from Mehrabad international airport's weather station in Tehran and the comfort temperature of 25 degrees Celsius was also directly introduced to the simulation software. The BIM-based energy simulation software was then used for estimating the monthly energy consumption of each building scenario during the operation phase. Table 3 presents the extracted thermal

TABLE 2. The estimated construction cost of the envelope materials in different scenarios

Scenario	Material purchase cost (\$)	Wall surface area (m ²)	Wall installation unit cost (\$/m ²)	Total installation cost (\$)	Transportation cost (\$)	Overall construction cost (\$)
1	54,514	2,862	1.67	4,770	1,726	61,010
2	64,736	2,862	1.67	4,770	1,908	71,414
3	106,984	2,862	1.19	3,407	3,082	113,473
4	57,921	2,862	11.90	34,071	1,629	93,622
5	88,586	2,862	3.57	10,221	1,671	100,478
6	68,143	2,862	11.90	34,071	236	102,450

TABLE 3. Thermal properties of different scenarios introduced to the BIM model

Production Method	Scenario	Thickness (m)	Overall Thermal Resistance (m ² · k/w)*	Source
Traditional	1	0.22	0.25	BHRC [35]
	2	0.22	1.37	BHRC [35]; Leca [38]
Semi-Industrial	3	0.20	1.11	BHRC [35]; Khane Irani Group [39]
	4	0.17	0.90	BHRC [35]; Bastanpol [40]
Industrial	5	0.17	2.62	BHRC [35]; Mohammad Kari and Ahmadi [41]
	6	0.18	0.16	BHRC [35];
Window	All		0.32	

specifications of the adopted construction materials from the corresponding references. Figures 5 and 6 present monthly and annual electricity and natural gas consumption estimated for different scenarios.

Interestingly enough, Scenario 1 with the clay block materials, represented the highest overall energy consumption among all six scenarios. The scenario with the light-weight concrete panels presented the lowest total energy consumption. The standing of different scenarios in the separate electricity and natural gas consumption, however, follows a different trend. Scenario 2, with the expanded clay concrete block materials, presented the highest electricity consumption. Scenario 6, with the precast concrete panels, consumed the least annual electricity. In a changing mood, Scenario 6 represented the highest natural gas consumption,

among other scenarios. Scenario 4, with the light-weight concrete panels, presented the lowest natural gas consumption. In general, semi-industrial and industrial scenarios considerably showed less overall energy consumption compared to the traditional scenarios.

3. 5. Energy Consumption Cost

Iran’s government regulates and controls the cost of electricity and natural gas in different parts of the country during different parts of the year. A portion of the energy price is subsidized, and incremental cost rates are applied when monthly electricity and natural gas consumption are increased [42]. Tables 4 and 5 present the incremental rates of electricity and natural gas costs set by the government in Tehran in 2018. Therefore, the estimated monthly energy consumption by BIM-based energy

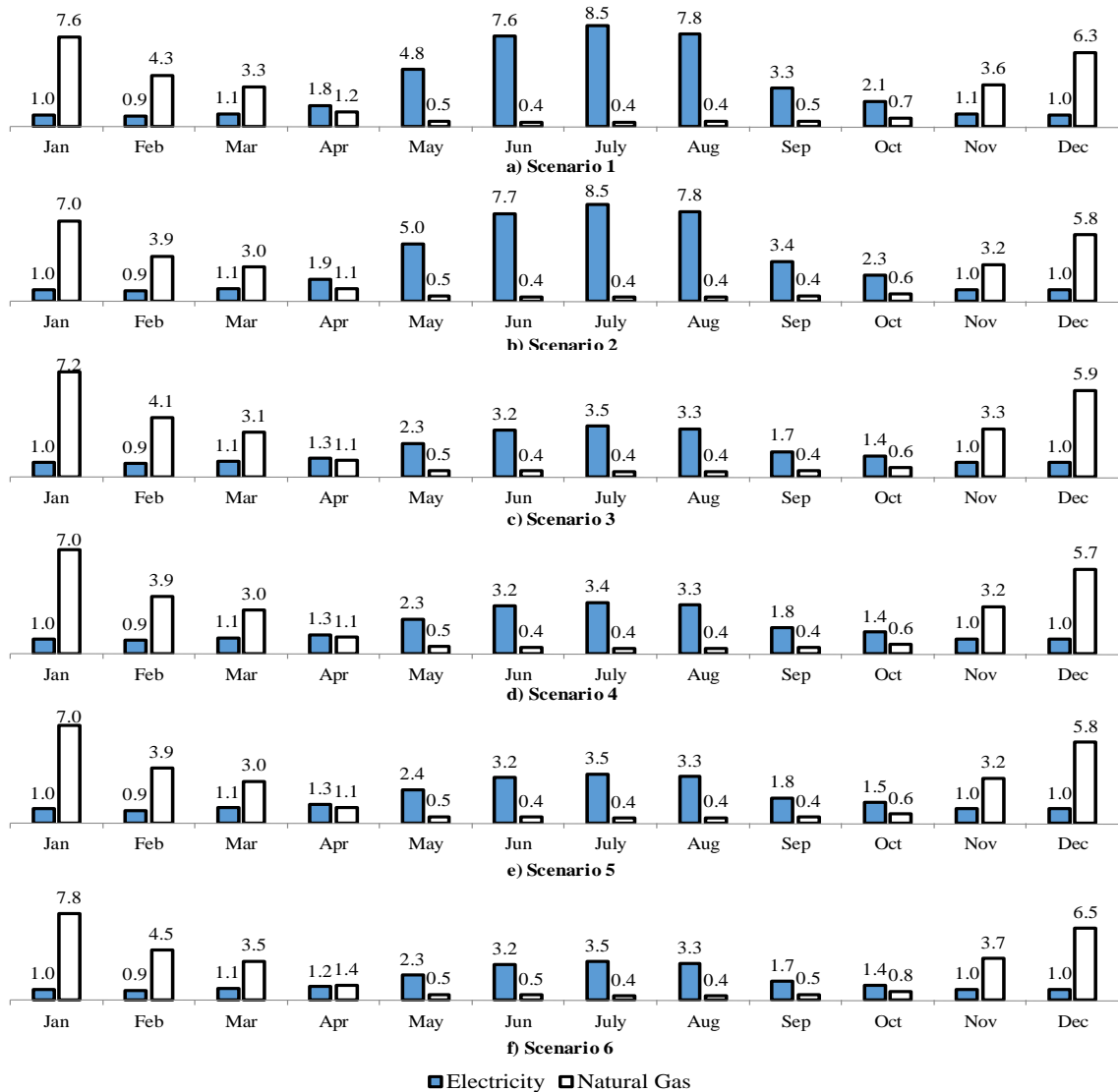


Figure 5. Monthly energy consumption distribution (GJ)

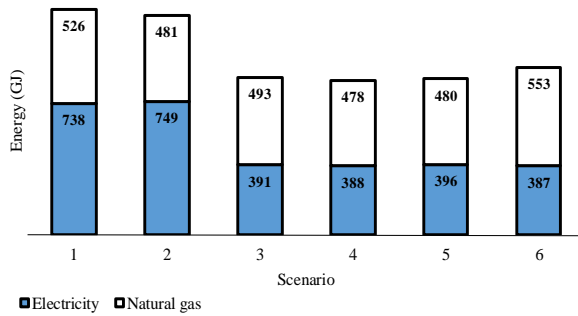


Figure 6. Estimated annual energy consumption by BIM-based energy simulation software in different scenarios

simulation software was used for estimating the building’s energy consumption cost. Table 6 presents the summary result of the annual energy consumption costs of different scenarios. Also, annual energy consumption by BIM-based energy simulation software is illustrated in Figure 6.

3. 6. Financial Assessment

Despite the high energy consumption of the traditional wall scenarios, these scenarios were most frequently consumed in the construction market of Tehran due to their low construction costs. The low construction cost of materials, however, does not necessarily result in an overall low cost. The operation cost of the building during the operation period can play a detrimental role as well. The life cycle cost of six different envelope scenarios was estimated by concurrently capturing construction, maintenance, and operating costs. The cash

flow of each scenario was formed by accounting the construction cost of walls, and annual energy consumption cost of the building during the 30 years of the building’s life cycle. According to the field study from different building construction and maintenance companies, the maintenance cost of the building envelope is trivial during the first ten years of the building construction. The main portion of the maintenance cost is spent on the building façade and the interior plaster. These two components of the envelope stay the same in all of the adopted envelope scenarios. Therefore, the maintenance cost in different scenarios was considered constant and was not added to the cash flow.

The net present value (NPV) was calculated with a discount rate of 15%, equal to the interest rate of a bank investment account [43], and the officially announced inflation rate of 9.5% [44]. Table 7 summarizes the financial calculation results in different scenarios. Figure 7 also presents the rank of different scenarios in various aspects. Among different scenarios, Scenario 4, with the light-weight concrete panels, resulted in the minimum life cycle cost. This scenario also represented the least energy consumption among all scenarios. It was ranked 3rd in the consumption frequency and the construction cost. Here, two traditional scenarios, the first and second, with the highest consumption frequency rates, showed the highest NPV of the building envelope’s life cycle cost and the lowest energy performance. The achieved results represented a potential of a 31% reduction in energy consumption during the operation phase and a 28% reduction in the envelope life cycle cost of the building.

TABLE 4. Electricity price in Tehran in different consumption ranges

Step	1	2	3	4	5	6	7
Consumption Range (KWh)	0-100	101-200	201-300	301-400	401-500	501-600	Over 600
Cost* (US¢ / KWh)	1.07	1.25	2.68	4.82	5.54	6.97	7.68

* Exchange rate of 42500 Iranian Rial per US dollar was considered according to CBI [45]

TABLE 5. Natural gas price in Tehran in different consumption ranges and seasons

Step	1	2	3	4	5	6	7	8	9	10	11	12	
Apr. – Oct.	Consumption Range (m ³)	0-45	46-95	96-145	146-195	196-245	246-295	296-345	346-395	396-445	446-495	496-545	Over 545
	Cost* (US¢ / m ³)	2.57	3.12	3.94	5.04	6.13	6.68	7.50	8.32	8.87	9.42	9.97	10.24
Nov. – Mar.	Consumption Range (m ³)	0-200	201-300	301-400	401-500	501-600	601-700	701-800	801-900	901-1000	1001-1100	1101-1200	Over 1200
	Cost* (US¢ / m ³)	0.99	1.64	2.25	2.96	3.61	5.50	6.24	7.23	8.21	9.20	10.51	11.50

* Exchange rate of 42500 Iranian Rial per US dollar was considered according to CBI [45]

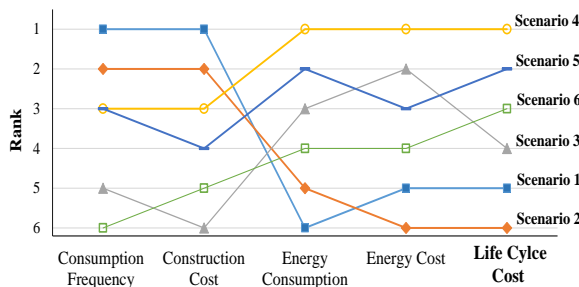
TABLE 6. Annual energy cost of different building envelope scenarios (USD)

Scenario	Electricity Cost	Natural Gas Cost	Total Energy Cost
1	\$17,085	\$2,598	\$19,683
2	\$18,136	\$2,283	\$20,420
3	\$8,391	\$2,371	\$10,762
4	\$8,350	\$2,260	\$10,611
5	\$8,640	\$2,275	\$10,915
6	\$8,334	\$2,769	\$11,104

TABLE 7. Cost and energy performance of scenarios over the building's life cycle (USD)

Scenario	Construction Cost	Annual Energy Cost	Life cycle NPV	Payback Period*
1	\$61,010	\$19,683	\$292,713	-
2	\$71,414	\$20,420	\$310,726	Never
3	\$113,473	\$10,762	\$229,715	8 Years
4	\$93,622	\$10,611	\$210,603	5 Years
5	\$100,478	\$10,915	\$220,277	6 Years
6	\$102,450	\$11,104	\$224,283	7 Years

* Payback period is calculated in comparison to Scenario 1 or the base scenario.

**Figure 7.** The rank of different scenarios in various aspects

The payback period of different scenarios in comparison to Scenario 1 (i.e., the base scenario) is presented in the last column of Table 7. Scenario 1 provides the lowest construction cost among the others. Therefore, project owners pay high construction costs when they opt for other wall construction scenario than the base scenario. In scenarios with lower operating costs than the base scenario, the additional construction cost is gradually paid off. Except Scenario 2, which provides both higher construction and operation costs than Scenario 1, additional construction costs are returned for the other four scenarios after a while. Expectedly, Scenario 4 represents the shortest payback period of 5 years among different scenarios.

4. RESULTS AND DISCUSSION

The survey results identified low-price and traditionally produced wall materials as the most commonly used materials in the residential building construction in Tehran, Iran. The achieved results show that building developers are more concerned about the initial construction costs than the energy consumption and the operating costs of buildings. Currently, many investors who are not the end-users of buildings invest their money in building construction projects. These investors, who make up the first group of builders, are not the ultimate consumers of the buildings and are not concerned by the high energy consumption nor the high operation cost.

On the other hand, residential building consumers are regular and non-technical clients of the buildings. They are generally not familiar with the construction cost of different types of wall materials, nor can they distinguish between the impacts of different types of materials on the building's energy consumption. Furthermore, a significant portion of the building envelope is covered when consumers visit the buildings for the first time. Concealed parts of the buildings attract less attention from the buyers compared to the visible parts. Therefore, the high cost of the concealed portions of the wall materials is barely paid off for the investors. In the current condition of the residential building market, these investors are not encouraged to change their approach in using low-cost and traditionally produced wall materials.

Based on the field observations, the use of traditional wall materials is also widespread among the second group of builders, i.e., builders who are ultimately going to occupy the building. To date, no prior research has been conducted to analyze the balance between the construction and the energy costs of the envelope materials in different parts of Iran. As a result, these builders are not knowledgeable regarding the cost balance of various building materials. Currently, guidelines provided by BHRC [37] are the primary reference for selecting energy-efficient materials. These guidelines, however, cover a limited number of wall materials. It only considers the energy performance but not the cost performance in its recommendations and follows the accept/reject approach for different materials. For example, among six different wall materials investigated in the research, BHRC [37] only covers two traditional wall materials included in Scenarios 1 and 2. Both these materials are accepted according to the BHRC [37] set criteria. Nevertheless, these two scenarios were identified with the lowest performance among the studied scenarios throughout the building's life cycle. Therefore, even in the cases where builders consider the concurrent energy and the cost performance of wall materials over the building's life cycle, no dependable source was available.

The current situation in the residential building construction market in the country can be changed when municipalities require the builders to reveal their envelope materials, e.g., in the building permits. Furthermore, municipalities need to research the high energy and the cost performance envelope materials in their regions. Presenting the impacts of different envelope materials, on the energy consumption of the building, to the building's consumers can further educate them. It can potentially increase the consumers' demands for the buildings with high cost and energy performance ratings. The increase in demand can hike the price of these buildings and motivate building developers to use high-performance envelope materials.

5. SUMMARY AND CONCLUSION

As the boundary between the interior and exterior of the building, the building envelope plays an essential role in the building's cost and energy performance over the building's life-cycle. This essential role has encouraged many researchers to investigate influential factors affecting the performance of the building envelope. The emergence of BIM in the recent decade has created an opportunity to facilitate the evaluation and improvement of the resulting performance of the building envelope. This research responded to the identified need for a structured method to guide practitioners in identifying the most viable building envelope materials within a region over the life cycle. The proposed method utilizes BIM capabilities to accurately capture detailed specifications of buildings, and evaluate the building's cost and energy performance considering influential regional factors. The sample implementation of the method in Tehran, Iran, indicated the current prevalent traditional wall materials are neither energy-efficient nor cost-efficient compared to the available industrial and semi-industrial wall materials. The proper selection of the building envelope materials, in this case, demonstrated a potential energy savings of 31% during the building's operation phase and the resulting envelope life cycle cost reduction of 28%. As a result of the sample implementation of the method, high-performance wall materials were identified for the building construction industry in Tehran. Furthermore, for the first time, prevalent building envelope materials used by building constructors in the city were identified.

Implementation of the proposed method in a region can benefit various stakeholders. Municipalities can use the method to identify and introduce a list of viable envelope materials to the builders as guidelines, or even instructions. The use of the recommended materials can increase the profit margin of the homebuilders. Building residents can see the benefits of their reduced utility bills. The entire society gains advantages due to reduced

energy consumption and green gas emission. In this research, the embodied energy of the envelope materials was not directly taken into account. The implied cost of the embodied energy was assumed in the purchase cost of the envelope materials. Incorporating the embodied energy of the envelope materials can be considered in future research to improve the resulting energy performance of the envelope materials. In the financial assessment of the building, only direct construction and operation costs were considered. Other influential factors might play a vital role in the performance evaluation of the buildings. For example, in different envelope scenarios, the thickness of the walls was different. It is assumed that the thin walls result in more building space than the thick walls improving the performance of the buildings. The implication of the adopted wall thickness on the building performance was not considered in this study.

6. REFERENCES

1. Ford, C., Cost of Constructing a Home. National Association of Home Builders Special Studies, 2017. Retrieved from <http://www.nahbclassic.org/generic.aspx>.
2. Doheny, M. Square Foot Costs with Rsmeans Data. *R S MEANS Company Incorporated*. R S MEANS Company Incorporated, (2019). Retrieved from https://books.google.com/books/about/Square_Foot_Costs_with_Rsmeans_Data.html?id=LGf7uWEACAAJ
3. Sawhney, A., Mund, A., and Syal, M. "Energy-Efficiency Strategies for Construction of Five Star Plus Homes." *Practice Periodical on Structural Design and Construction*, Vol. 7, No. 4, (2002), 174–181. [https://doi.org/10.1061/\(asce\)1084-0680\(2002\)7:4\(174\)](https://doi.org/10.1061/(asce)1084-0680(2002)7:4(174))
4. Cheung, C. K., Fuller, R. J., and Luther, M. B. "Energy-efficient envelope design for high-rise apartments." *Energy and Buildings*, Vol. 37, No. 1, (2005), 37–48. <https://doi.org/10.1016/j.enbuild.2004.05.002>
5. Hoseini, R., Jahangiri, P., and Bahmanpour, D. "Economic analysis of the use of thermal insulations and the use of a double glazed window in a residential unit" *Iranian Journal of Mechanical Engineering*, Vol. 13, No. 1, (2011), 2–31. (In Farsi)
6. Domínguez, S., Sendra, J. J., León, A. L., and Esquivias, P. M. "Towards Energy Demand Reduction in Social Housing Buildings: Envelope System Optimization Strategies." *Energies*, Vol. 5, No. 7, (2012), 2263–2287. <https://doi.org/10.3390/en5072263>
7. Sim, J., and Sim, J. "The effect of external walls on energy performance of a Korean traditional building." *Sustainable Cities and Society*, Vol. 24, (2016), 10–19. <https://doi.org/10.1016/j.scs.2016.04.003>
8. Braulio-Gonzalo, M., and Bovea, M. D. "Environmental and cost performance of building's envelope insulation materials to reduce energy demand: Thickness optimisation." *Energy and Buildings*, Vol. 150, (2017), 527–545. <https://doi.org/10.1016/j.enbuild.2017.06.005>
9. Echarri, V. "Thermal Ceramic Panels and Passive Systems in Mediterranean Housing: Energy Savings and Environmental Impacts." *Sustainability*, Vol. 9, No. 1613, (2017), 1–27. <https://doi.org/10.3390/su9091613>
10. Pakand, M., and Toufigh, V. "A multi-criteria study on rammed

- earth for low carbon buildings using a novel ANP-GA approach.” *Energy and Buildings*, Vol. 150, (2017), 466–476. <https://doi.org/10.1016/j.enbuild.2017.06.004>
11. Rahbar, N. and Saadati, S. E. “Investigating the effect of different building materials on the energy consumption of a case study - Modeling with Design Builder software in Semnan climate zone.” In 3rd Iran. Conf. Heat Mass Transf., Babol Noshirvani University of Technology, Babol, Iran, (2017). (In Farsi)
 12. Song, X., Ye, C., Li, H., Wang, X., and Ma, W. “Field study on energy economic assessment of office buildings envelope retrofitting in southern China.” *Sustainable Cities and Society*, Vol. 28, (2017), 154–161. <https://doi.org/10.1016/j.scs.2016.08.029>
 13. Hasan, M. L., Basher, H. O., and Shdhan, A. O. “Experimental investigation of phase change materials for insulation of residential buildings.” *Sustainable Cities and Society*, Vol. 36, (2018), 42–58. <https://doi.org/10.1016/j.scs.2017.10.009>
 14. Masoso, O. T., and Grobler, L. J. “A new and innovative look at anti-insulation behaviour in building energy consumption.” *Energy and Buildings*, Vol. 40, No. 10, (2008), 1889–1894. <https://doi.org/10.1016/j.enbuild.2008.04.013>
 15. Pulselli, R. M., Simoncini, E., and Marchettini, N. “Energy and energy based cost-benefit evaluation of building envelopes relative to geographical location and climate.” *Building and Environment*, Vol. 44, No. 5, (2009), 920–928. <https://doi.org/10.1016/j.buildenv.2008.06.009>
 16. Ucar, A., and Balo, F. “Determination of the energy savings and the optimum insulation thickness in the four different insulated exterior walls.” *Renewable Energy*, Vol. 35, No. 1, (2010), 88–94. <https://doi.org/10.1016/j.renene.2009.07.009>
 17. Ramesh, T., Prakash, R., and Shukla, K. K. “Life cycle energy analysis of a residential building with different envelopes and climates in Indian context.” *Applied Energy*, Vol. 89, No. 1, (2012), 193–202. <https://doi.org/10.1016/j.apenergy.2011.05.054>
 18. Friess, W. A., Rakhshan, K., and Davis, M. P. “A global survey of adverse energetic effects of increased wall insulation in office buildings: degree day and climate zone indicators.” *Energy Efficiency*, Vol. 10, No. 1, (2017), 97–116. <https://doi.org/10.1007/s12053-016-9441-z>
 19. Charisi, S. “The Role of the Building Envelope in Achieving Nearly-zero Energy Buildings (nZEBs).” *Procedia Environmental Sciences*, Vol. 38, No. 38, (2017), 115–120. <https://doi.org/10.1016/j.proenv.2017.03.092>
 20. Jalaee, F., and Jade, A. “Integrating Building Information Modeling (BIM) and Energy Analysis Tools with Green Building Certification System to Conceptually Design Sustainable Buildings.” *Journal of Information Technology in Construction*, Vol. 19, No. 29, (2014), 494–519. Retrieved from <https://itcon.org/paper/2014/29>
 21. Cho, Y. K., Ham, Y., and Golpavar-Fard, M. “3D as-is building energy modeling and diagnostics: A review of the state-of-the-art.” *Advanced Engineering Informatics*, Vol. 29, No. 2, (2015), 184–195. <https://doi.org/10.1016/j.aei.2015.03.004>
 22. Park, J., Park, J., Kim, J., and Kim, J. “Building information modelling based energy performance assessment system: An assessment of the Energy Performance Index in Korea.” *Construction Innovation*, Vol. 12, No. 3, (2012), 335–354. <https://doi.org/10.1108/14714171211244587>
 23. Ham, Y., and Golparvar-Fard, M. “Mapping actual thermal properties to building elements in gbXML-based BIM for reliable building energy performance modeling.” *Automation in Construction*, Vol. 49, (2015), 214–224. <https://doi.org/10.1016/j.autcon.2014.07.009>
 24. Gao, H., Koch, C., and Wu, Y. “Building information modelling based building energy modelling: A review.” *Applied Energy*, Vol. 238, (2019), 320–343. <https://doi.org/10.1016/j.apenergy.2019.01.032>
 25. Hollberg, A., Genova, G., and Habert, G. “Evaluation of BIM-based LCA results for building design.” *Automation in Construction*, Vol. 109, (2020), 102972. <https://doi.org/10.1016/j.autcon.2019.102972>
 26. Khosakitchalert, C., Yabuki, N., and Fukuda, T. “Improving the accuracy of BIM-based quantity takeoff for compound elements.” *Automation in Construction*, Vol. 106, (2019), 102891. <https://doi.org/10.1016/j.autcon.2019.102891>
 27. Bečvarovská, R., and Matějka, P. “Comparative Analysis of Creating Traditional Quantity Takeoff Method and Using a BIM Tool.” In Construction Maeconomics Conference, (2014), 1–4. Retrieved from http://www.conference-cm.com/podklady/history5/Prispevky/paper_becvarovska.pdf
 28. Niu, S., Pan, W., and Zhao, Y. “A BIM-GIS Integrated Web-based Visualization System for Low Energy Building Design.” *Procedia Engineering*, Vol. 121, (2015), 2184–2192. <https://doi.org/10.1016/j.proeng.2015.09.091>
 29. Jalaee, F., and Jade, A. “Integrating BIM with Green Building Certification System, Energy Analysis, and Cost Estimating Tools to Conceptually Design Sustainable Buildings.” In Construction Research Congress, (2014), 140–149. <https://doi.org/10.1061/9780784413517.015>
 30. Oduyemi, O., and Okoroh, M. “Building performance modelling for sustainable building design.” *International Journal of Sustainable Built Environment*, Vol. 5, No. 2, (2016), 461–469. <https://doi.org/10.1016/j.ijsbe.2016.05.004>
 31. Ahsan, M. M., Zulqernain, M., Ahmad, H., Ali Wajid, B., Shahzad, S., and Hussain, M. “Reducing the Operational Energy Consumption in Buildings by Passive Cooling Techniques using Building Information Modelling Tools.” *International Journal of Renewable Energy Research*, Vol. 9, No. 1, (2019), 1–11. Retrieved from <https://mail.ijrer.org/ijrer/index.php/ijrer/article/view/8951>
 32. Lim, Y.-W., Seghier, T. E., Harun, M. F., Ahmad, M. H., Samah, A. A., and Majid, H. A. “Computational BIM for Building Envelope Sustainability Optimization.” *MATEC Web of Conferences*, Vol. 278, (2019), 1–6. <https://doi.org/10.1051/mateconf/201927804001>
 33. Shalabi, F., and Turkan, Y. “BIM-energy simulation approach for detecting building spaces with faults and problematic behavior.” *Journal of Information Technology in Construction*, Vol. 25, (2020), 342–360. <https://doi.org/10.36680/j.itcon.2020.020>
 34. SCI, Statistical Center of Iran: Report of Building Permits Issued by the Country’s Municipalities, 2018. (In Farsi)
 35. BHRC, Building and Housing Research Center: 19th Code of General Building Requirements (3rd Edition), Tehran: Ministry of Road and Urban Development, 2011. (In Farsi)
 36. Golabchi, M. and Azaherian, H., New Architectural Technologies (6th Edition), University of Tehran, Tehran, 2014. (In Farsi)
 37. BIMForum, ‘Level Of Development (LOD) Specification Part I & Commentary for Building Information Models And Data’. BIMForum, May, 2020.
 38. Leca, Light Expanded Clay Aggregate Co.: Leca Blocks Product Specification, 2019.
 39. Khane Irani Group, Iran Wall Products, 2020. (In Farsi)
 40. Bastanpol Co, Wallcrete Panel Catalogue, 2018.
 41. Mohammad Kari, B. and Ahmadi, M. R., Lightweight Three Dimensional Sandwich Panels (2nd Edition), Tehran, 2000. (In Farsi)
 42. TEEDP, Tehran Electric Energy Distribution Portal: Rules and Electricity Prices, Tehran, 2018. (In Farsi)
 43. CBI, Central Bank of Iran: Minimum Acceptable Rate of Return, 2018. (In Farsi)
 44. CBI, Central Bank of Iran: Inflation Rate, Tehran, 2018. (In Farsi)
 45. CBI, Central Bank of Iran: Currency Exchange Rate, 2018. (In Farsi)

Persian Abstract

چکیده

شرایط محیطی و ترکیب مصالح استفاده شده در پوشش بیرونی ساختمان‌ها نقش زیادی در میزان مصرف انرژی و هزینه‌های ساخت و نگهداری ساختمان دارد. با این حال هنوز روش‌های مدون و ساخت‌یافته‌ای که با در نظر گرفتن تأثیر شرایط محیطی و نوع مصالح مورد استفاده در پوشش بیرونی ساختمان، مناسب‌ترین ترکیب مصالح مصرفی در پوشش بیرونی ساختمان را شناسایی نمایند و سازندگان ساختمان را در این زمینه یاری نماید، ارائه نشده است. این مطالعه با ارائه یک روش نوین با استفاده از قابلیت‌های مدل‌سازی اطلاعات ساختمان، به این نیاز پاسخ می‌دهد. در این روش با در نظر گرفتن شرایط محیطی صنعت ساخت، شرایط آب و هوایی منطقه و همچنین در نظر گرفتن هندسه و ابعاد ساختمان، مصالح مورد استفاده در پوشش ساختمان که هم از منظر هزینه و هم از نظر مصرف انرژی در طول چرخه عمر ساختمان به صرفه هستند شناسایی و پیشنهاد می‌شوند. ابتدا مصالح مرسوم مورد استفاده در ساخت ساختمان‌ها در منطقه شناسایی می‌شوند، سپس عملکرد مصرف انرژی آنها با استفاده از قابلیت‌های ارائه شده در مدلسازی اطلاعات ساختمان شبیه‌سازی می‌شود و در نهایت هزینه چرخه عمر آنها ارزیابی می‌گردد. به منظور بررسی قابلیت‌های این روش، این روش برای ساخت ساختمان‌ها در شهر تهران اجرا شد و با موفقیت برای کاهش هزینه و مصرف انرژی در یک نمونه موردی ساختمان مسکونی نه طبقه استفاده شد. نتیجه استفاده از روش پیشنهادی در نمونه موردی، پیشنهاد استفاده از مصالح جایگزین به منظور کاهش مصرف انرژی به میزان ۳۱٪ و کاهش هزینه در چرخه عمر ساختمان به میزان ۲۸٪ بود. روش پیشنهادی می‌تواند با کاهش هزینه و مصرف انرژی ساختمان‌ها، ذینفعان مختلف در صنعت ساختمان‌سازی از جمله شهرداری‌ها، مالکان، پیمانکاران و مصرف‌کنندگان را بهره‌مند سازد.



Autonomous Vehicle Convoy Formation Control with Size/Shape Switching for Automated Highways

H. B. Jond^{*a}, J. Platoš^a, Z. Sadreddini^b

^a Department of Computer Science, VSB – Technical University of Ostrava, Ostrava, Czech Republic

^b Department of Computer Engineering, Istanbul Arel University, Istanbul, Turkey

PAPER INFO

Paper history:

Received 15 April 2020

Received in revised form 03 September 2020

Accepted 03 September 2020

Keywords:

Automated Highway
Autonomous Vehicle
Formation Control
Receding Horizon Control
Size/Shape Switching

ABSTRACT

Today's semi-autonomous vehicles are gradually moving towards full autonomy. This transition requires developing effective control algorithms for handling complex autonomous tasks. Driving as a group of vehicles, referred to as a convoy, on automated highways is a highly important and challenging task that autonomous driving systems must deal with. This paper considers the control problem of a vehicle convoy modeled with linear dynamics. The convoy formation requirement is presented in terms of a quadratic performance index to minimize. The convoy formation control is formulated as a receding horizon linear-quadratic (LQ) optimal control problem. The receding horizon control law is innovatively defined via the solution to the algebraic Riccati equation. The solution matrix and therefore the receding horizon control law are obtained in the closed-form. A control architecture consisting of four algorithms is proposed to handle formation size/shape switching. The closed-form control law is at the core of these algorithms. Simulation results are provided to justify the models, solutions, and proposed algorithms.

doi: 10.5829/ije.2020.33.11b.07

1. INTRODUCTION

Soon, public roads will host the massive deployment of autonomous vehicles. An autonomous convoy is a group of networked autonomous vehicles maintaining a formation (Figure 1). The formation control is defined as designing control inputs for the vehicles so that they form and maintain a pre-defined geometric shape. The line (or linear) formation, so-called platooning, concerns only longitudinal coordinated control of networked autonomous vehicles [1]. Convoy formation control requires both longitudinal and lateral coordination of vehicles [2]. Convoy control algorithms are essential for vehicle maneuvers such as lane change and overtaking on automated highways. Intelligent Traffic Management Systems [3] can also use these algorithms for city traffic.

Many algorithms from multi-agent systems are used in autonomous vehicle convoy formation control. Classical approaches which include leader-follower [4], virtual-structure [5] and behavior-based [6, 7] comprise a

significant amount of research effort in multi-agent systems formation control.

While the leader-follower approach is a popular design for the formation control, there are limitations. The loss of the leader or the leader being perturbed by some disturbances causes the entire group formation to fail [8]. On the contrary, the formation control can be leaderless, where all agents have the same role within the team.

In this study, we intend to derive an optimality-based formation control strategy for a leaderless autonomous

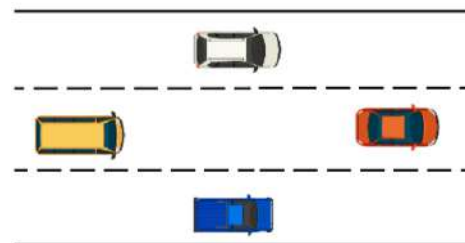


Figure 1. A convoy in a diamond formation

*Corresponding Author Institutional Email: hossein.barghi.jond@vsb.cz
(H. B. Jond)

convoy. The optimality-based approach has received attention in robotic car literature (see, e.g., [9, 10]). Particularly the LQ modeling of formation control is highly interesting due to the analytic tractability of LQ problems. In this approach, the formation objective, which is to drive multiple agents to achieve a prescribed constraint on their states, is implemented by using a quadratic performance index through the use of graph theory [11]. The multi-agent system dynamics is modeled as a controllable linear system.

Depending on the available information structure, open-loop [12], state-feedback [13] and receding horizon [14] control structures can be investigated for formation control. The receding horizon or model predictive controller uses the open-loop control signals to implement an online algorithm that predicts the system's output based on current states and system models. It has become the most popular feedback strategy in industrial applications.

In the operation field, when obstacles or boundaries are detected along the formation's path, the formation is able to squeeze through obstacles by switching to suited patterns that are chosen among a collection of formations. In some other cases, a safe formation control strategy scales the formation shape (by a size switching strategy). By adjusting the scale, the formation can grow and shrink as necessary to accommodate and avoid obstacles in its surrounding area. An illustrative example is given in [15], where a group of agents is to traverse a narrow passage while maintaining a desired triangular shape.

In this paper, the convoy formation control is addressed as a receding horizon LQ optimal control problem. Under this framework, the matrix Riccati equation must be solved. Obtaining a solution to this equation is not generally straightforward. This type of matrix equation has been discussed in detail in [16]. Innovatively, the receding horizon control law is constructed via the algebraic Riccati equation, which leads to obtaining the control law in the closed-form. Besides, a control scheme is developed to deal with the formation size/shape switching under the receding horizon LQ framework. This scheme consists of four control modes in which each control mode is run under an algorithm constructed via the closed-form control law.

The remainder of this paper is organized as follows. The system models and LQ optimal control formulation of the formation control problem are introduced in Section 2. The receding horizon control design is presented in Section 3. The control scheme and corresponding algorithms for formation size/shape switching are developed in Section 4. The simulation results are shown in Section 5. The conclusion is given in Section 6.

2. CONVOY FORMATION STATEMENT

Vehicle dynamics is highly nonlinear. Hierarchical control architectures at their top-level consider a simplified dynamics model of the system and shift the nonlinearity to their lower levels. An appropriate simple dynamical model for a vehicle is the double integrator model. It simplifies vehicle dynamics as a point mass governed by Newton's laws [17].

Consider a convoy of m networked vehicles, each of which is described by a double integrator dynamics. Let $\mathbf{q}_i, \mathbf{v}_i, \mathbf{u}_i \in \mathbb{R}^2$ be the coordinates, velocity and control input vectors for vehicle i ($i = 1, \dots, m$), respectively. Define $\mathbf{z} = [\mathbf{q}_1^T, \dots, \mathbf{q}_m^T, \mathbf{1}, \mathbf{v}_1^T, \dots, \mathbf{v}_m^T]^T$ and $\mathbf{u} = [\mathbf{u}_1^T, \dots, \mathbf{u}_m^T]^T$. Vectors $\mathbf{z} \in \mathbb{R}^{4m+1}$ and $\mathbf{u} \in \mathbb{R}^{2m}$ are system state and control input vectors, respectively. The system dynamics can be expressed as

$$\dot{\mathbf{z}} = \mathbf{A}\mathbf{z} + \mathbf{B}\mathbf{u} \quad (1)$$

where $\mathbf{A} = \begin{bmatrix} \mathbf{0} & \mathbf{I}_{2m} \\ \mathbf{0} & \mathbf{0} \end{bmatrix}$, $\mathbf{B} = [\mathbf{0}_{2m}, \mathbf{0}_{2m \times 1}, \mathbf{I}_{2m}]^T$, and \mathbf{I} is the identity matrix of appropriate dimension.

Networked systems such as a convoy of vehicles exchange information via a communication network. The information flow over the communication network can be modeled with graph theory. A directed graph $\mathcal{G} = (\mathcal{V}, \mathcal{E})$ consists of a set of vertices $\mathcal{V} = \{1, 2, \dots, m\}$ and a set of edges $\mathcal{E} \subseteq \{(i, j) : i, j \in \mathcal{V}\}$ containing ordered pairs of distinct vertices. For the formation control, the set of vertices \mathcal{V} corresponds to the vehicles and then the set of edges \mathcal{E} represents the interconnections. Each edge $(i, j) \in \mathcal{E}$ is assigned with a weight $\mu_{ij} > 0$.

Assumption 1. Formation graph \mathcal{G} is connected, i.e., for every pair of vertices $i, j \in \mathcal{V}$, from i to j for all $j = 1, \dots, m, j \neq i$, there exists a path of (undirected) edges from \mathcal{E} .

The graph Laplacian $\mathbf{L} \in \mathbb{R}^m$ is defined as

$$\mathbf{L} = \mathbf{D}\mathbf{W}\mathbf{D}^T \quad (2)$$

where $\mathbf{D} \in \mathbb{R}^{m \times |\mathcal{E}|}$ is the incidence matrix and $\mathbf{W} = \text{diag}(\mu_{ij}) \in \mathbb{R}^{|\mathcal{E}|}$ is a diagonal weight matrix. \mathbf{D} 's uv th element is 1 if the node u is the head of the edge v , -1 if the node u is the tail, and 0, otherwise.

The Kronecker product \otimes can be used to extend the dimension. The 2-dimensional graph Laplacian $\mathcal{L} \in \mathbb{R}^{2m}$ is defined as

$$\mathcal{L} = \mathbf{L} \otimes \mathbf{I}_2 \quad (3)$$

Based on the properties of the Kronecker product, \mathcal{L} can be rearranged as

$$\mathcal{L} = \mathbf{D}\mathbf{W}\mathbf{D}^T \otimes \mathbf{I}_2 = (\mathbf{D} \otimes \mathbf{I}_2)(\mathbf{W} \otimes \mathbf{I}_2)(\mathbf{D} \otimes \mathbf{I}_2)^T = \mathcal{D}\mathcal{W}\mathcal{D}^T \quad (4)$$

where $\mathcal{D} = \mathbf{D} \otimes \mathbf{I}_2$ and $\mathcal{W} = \mathbf{W} \otimes \mathbf{I}_2$.

The graph Laplacian is symmetric, positive semidefinite and holds the sum-of-squares property [18]:

$$\mathbf{z}^T \mathbf{Lz} = \sum_{(i,j) \in \mathcal{E}} \mu_{ij} \|\mathbf{q}_i - \mathbf{q}_j\|^2 \quad (5)$$

where $\|\cdot\|$ is the Euclidean norm in \mathbb{R}^2 .

The formation requirement according to the information graph can be expressed as

$$\sum_{(i,j) \in \mathcal{E}} \mu_{ij} \left(\|\mathbf{q}_i - \mathbf{q}_j - \mathbf{d}_{ij}\|^2 + \|\mathbf{v}_i - \mathbf{v}_j\|^2 \right) \rightarrow 0 \quad (6)$$

where $\mathbf{d}_{ij} \in \mathbb{R}^n$ is the desired distance vector between two neighbor vehicles i and j . Using the property of sum-of-squares, (6) can be transformed into the following matrix form

$$\sum_{(i,j) \in \mathcal{E}} \omega_{ij} \left(\|\mathbf{q}_i - \mathbf{q}_j\|^2 - 2(\mathbf{q}_i - \mathbf{q}_j)^T \mathbf{d}_{ij} + \|\mathbf{d}_{ij}\|^2 + \|\mathbf{v}_i - \mathbf{v}_j\|^2 \right) = \mathbf{q}^T \mathbf{Lq} - 2\mathbf{q}^T \mathbf{D}\mathbf{W}\mathbf{d} + \mathbf{d}^T \mathbf{W}\mathbf{d} + \mathbf{v}^T \mathbf{L}\mathbf{v} = \mathbf{z}^T \mathbf{Qz} \quad (7)$$

where $\mathbf{Q} = \begin{bmatrix} \mathbf{L} & -\mathbf{D}\mathbf{W}\mathbf{d} & \mathbf{0} \\ -(\mathbf{D}\mathbf{W}\mathbf{d})^T & \mathbf{d}^T \mathbf{W}\mathbf{d} & \mathbf{0} \\ \mathbf{0} & \mathbf{0} & \mathbf{L} \end{bmatrix}$, $\mathbf{d} = \text{col}(\mathbf{d}_{ij})$ and $\text{col}(\cdot)$ stands for "column vector". As $\mathbf{z}^T \mathbf{Qz} \geq 0$, matrix \mathbf{Q} is positive semidefinite.

A performance index for the convoy formation control is defined as

$$J = \mathbf{z}(t_f)^T \mathbf{Q}_f \mathbf{z}(t_f) + \int_0^{t_f} (\mathbf{z}^T \mathbf{Qz} + \mathbf{u}^T \mathbf{R}\mathbf{u}) dt \quad (8)$$

where $\mathbf{Q}_f = \begin{bmatrix} \mathcal{L}_f & -\mathbf{D}\mathbf{W}_f \mathbf{d} & \mathbf{0} \\ -(\mathbf{D}\mathbf{W}_f \mathbf{d})^T & \mathbf{d}^T \mathbf{W}_f \mathbf{d} & \mathbf{0} \\ \mathbf{0} & \mathbf{0} & \mathcal{L}_f \end{bmatrix}$, $\mathcal{L}_f = \mathbf{D}\mathbf{W}_f \mathbf{D}^T$, $\mathbf{W}_f = \mathbf{W}_f \otimes \mathbf{I}_n$, $\mathbf{W}_f = \text{diag}(\omega_{ij}) \in \mathbb{R}^{|\mathcal{E}|}$, $\omega_{ij} > 0$, t_f is the fixed finite horizon length and $\mathbf{R} \in \mathbb{R}^{2m}$ is diagonal positive definite ($\mathbf{R} > \mathbf{0}$). Matrices \mathbf{W} and \mathbf{R} represent the penalties on the formation-velocity errors and control effort during the entire formation control process, respectively. Matrix \mathbf{W}_f represents the penalty on the terminal formation-velocity errors.

The convoy formation control objective is to design the control input vector \mathbf{u} to minimize the performance index J for the underlying system dynamics (1). The formation control problem under the framework of LQ optimal control formulation converts to the symmetric Riccati differential equation problem, which is stated in the following theorem. The proof can be found in [19].

Theorem 1. For the formation control defined as the LQ optimal control problem (1) and (8), the open-loop solution is given by

$$\mathbf{u} = -\mathbf{R}^{-1} \mathbf{B}^T \mathbf{Pz} \quad (9)$$

where \mathbf{P} is the solution to the Riccati differential equation;

$$\dot{\mathbf{P}} + \mathbf{P}\mathbf{A} + \mathbf{A}^T \mathbf{P} - \mathbf{P}\mathbf{S}\mathbf{P} + \mathbf{Q} = \mathbf{0}, \quad \mathbf{P}(t_f) = \mathbf{Q}_f \quad (10)$$

and $\mathbf{S} = \mathbf{B}\mathbf{R}^{-1} \mathbf{B}^T$.

Matrix \mathbf{P} is symmetric positive semidefinite. In general, (10) must be solved numerically by using the terminal value and backward iteration.

3. RECEDING HORIZON CONTROL

Fixed horizon control problems suffer from the main drawback that unexpected changes in the system that may happen at a future time cannot be included in the model. This issue is addressed by the idea of receding horizon control [20]. Let $0 < \delta < t_f$ denote the sampling period. In the receding horizon control, the current control law \mathbf{u} is obtained by solving the open-loop optimal control problem (1) and (8) at each sampling instant t for the interval $[t, t + t_f]$. Then, \mathbf{u} and the corresponding system trajectory \mathbf{z} is used until the next sampling time $t + \delta$ arrives. In this method, at each time instant t the current state vector \mathbf{z} is considered as the initial state. The open-loop control signal \mathbf{u} minimizes the following receding horizon performance index

$$j = \mathbf{z}(t + t_f)^T \mathbf{Q}_f \mathbf{z}(t + t_f) + \int_t^{t+t_f} (\mathbf{z}^T \mathbf{Qz} + \mathbf{u}^T \mathbf{R}\mathbf{u}) dt \quad (11)$$

Following [14], the receding horizon control for the formation control problem is defined as

$$\bar{\mathbf{u}} = -\mathbf{R}^{-1} \mathbf{B}^T \mathbf{P}(0)\mathbf{z} \quad (12)$$

The closed-loop system is

$$\dot{\mathbf{z}} = \mathbf{A}_{cl}(0)\mathbf{z} \quad (13)$$

where $\mathbf{A}_{cl}(0) = \mathbf{A} - \mathbf{S}\mathbf{P}(0)$ is the closed-loop system matrix.

As it is seen from (12) calculation of the signal $\bar{\mathbf{u}}$ needs the solution matrix $\mathbf{P}(0)$ of the Riccati differential Equation (10). In a particular case in which $t_f \rightarrow \infty$, \mathbf{P} approaches a finite constant \mathbf{P} where it satisfies the algebraic Riccati equation (ARE)

$$\mathbf{P}\mathbf{A} + \mathbf{A}^T \mathbf{P} - \mathbf{P}\mathbf{S}\mathbf{P} + \mathbf{Q} = \mathbf{0} \quad (14)$$

In the system dynamics (1) if (\mathbf{A}, \mathbf{B}) is stabilizable then \mathbf{P} is a stabilizing solution to (10). Moreover, \mathbf{P} approaches to \mathbf{P} as $t \rightarrow -\infty$. Therefore, in this paper, we propose the idea that solution \mathbf{P} to the ARE (14) can be used in (12) instead of $\mathbf{P}(0)$. Consequently, the receding horizon control for the formation control problem in (1) and (11) is redefined as

$$\bar{\mathbf{u}} = -\mathbf{R}^{-1} \mathbf{B}^T \mathbf{Pz} \quad (15)$$

In the next theorem, the closed-form solution of the algebraic Riccati Equation (14) is presented. Before, the following definition is introduced.

Definition 1. Let the real symmetric matrix \mathbf{M} be positive semidefinite. The square root of \mathbf{M} is denoted by $\mathbf{M}^{\frac{1}{2}}$ and

satisfies $\mathbf{M} = \mathbf{M}^{\frac{1}{2}} \mathbf{M}^{\frac{1}{2}}$. Any symmetric, positive semidefinite matrix has a unique symmetric, semidefinite square root [21].

Theorem 2. The unique symmetric solution to the algebraic Riccati Equation (14) is in the following form:

$$\mathcal{P} = \begin{bmatrix} \mathbf{MR}^{-1}\mathbf{N} & -\mathbf{MN}^{-1}\mathcal{D}\mathcal{W}\mathbf{d} & \mathbf{N} \\ * & * & * \\ \mathbf{N} & -\mathbf{RN}^{-1}\mathcal{D}\mathcal{W}\mathbf{d} & \mathbf{M} \end{bmatrix} \quad (16)$$

where $\mathbf{M} = (\mathbf{2NR} + \mathbf{N}^2)^{\frac{1}{2}}$, $\mathbf{N} = (\mathcal{L}\mathbf{R})^{\frac{1}{2}}$ and * are the elements/blocks to be not concerned.

Proof. By ignoring the (artificially made) middle row of \mathbf{A} we see that (\mathbf{A}, \mathbf{B}) is stabilizable. As \mathbf{R} is positive definite, and \mathbf{Q} is symmetric positive semidefinite, there exists a unique symmetric solution to (14).

Assume that \mathcal{P} has the following form:

$$\mathcal{P} = \begin{bmatrix} \mathcal{P}_{11} & \mathcal{P}_{12} & \mathcal{P}_{13} \\ \mathcal{P}_{12}^T & \mathcal{P}_{22} & \mathcal{P}_{23} \\ \mathcal{P}_{13} & \mathcal{P}_{23}^T & \mathcal{P}_{33} \end{bmatrix} \quad (17)$$

Substituting \mathbf{A} , \mathbf{S} and \mathbf{Q} into (14) yields

$$\mathcal{P}_{13}\mathbf{R}^{-1}\mathcal{P}_{13} - \mathcal{L} = \mathbf{0} \quad (18)$$

$$2\mathcal{P}_{13} - \mathcal{P}_{33}\mathbf{R}^{-1}\mathcal{P}_{33} + \mathcal{L} = \mathbf{0} \quad (19)$$

$$\mathcal{P}_{11} - \mathcal{P}_{33}\mathbf{R}^{-1}\mathcal{P}_{13} = \mathbf{0} \quad (20)$$

$$\mathcal{P}_{23}\mathbf{R}^{-1}\mathcal{P}_{13} + (\mathcal{D}\mathcal{W}\mathbf{d})^T = \mathbf{0} \quad (21)$$

$$\mathcal{P}_{12} - \mathcal{P}_{33}\mathbf{R}^{-1}\mathcal{P}_{23}^T = \mathbf{0} \quad (22)$$

By solving these equations using the matrix square root definition we obtain (16). Finally, from (15) it can be seen that the calculation of $\bar{\mathbf{u}}$ is not dependent on the middle row elements/blocks of \mathcal{P} .

The closed-loop system matrix is redefined as $\bar{\mathbf{A}}_{cl} = \mathbf{A} - \mathbf{S}\mathcal{P}$. The system is asymptotically stable on the condition that all the eigenvalues of $\bar{\mathbf{A}}_{cl}$ have negative real parts. As $\bar{\mathbf{A}}_{cl}$ is a function of penalty matrices \mathbf{W} and \mathbf{R} , the asymptotic stability can be achieved by selecting appropriate \mathbf{W} and \mathbf{R} matrices.

Together with satisfying the asymptotic stability condition, matrices \mathbf{W} and \mathbf{R} should reflect the real-world requirements such as vehicle's energy consumption management. For example, if the vehicles have a sufficient amount of fuel in their tank or if they are near a gas station, a large \mathbf{W} and a small \mathbf{R} can be selected to emphasize the formation-velocity errors rather than the control effort. On the contrary, a small \mathbf{W} and a large \mathbf{R} can be selected for situations in which the vehicles are on an energy-saving policy. The best trade-off between the system performance (e.g. convoy formation) and control effort (e.g. energy consumption) should be taken.

4. SIZE/SHAPE SWITCHING

The receding horizon based controller calculates controls that drive each vehicle to acquire the desired relative position with respect to its neighbor(s) in the graph topology. During the process of acquiring a desired formation shape, at every time instant, there could be a change in the environment/system that might require a new desired formation shape to be acquired. For example, due to newly detected obstacles or failed vehicle(s) in the group, the initial formation topology would be subject to change in size/shape.

To handle size/shape switching a control architecture is presented in Figure 2. Based on the signal received from an external observer or a decision-maker vehicle equipped with appropriate sensors, a control mode is selected at each time instant. The control loop terminates when the formation control expectations are fulfilled.

Initially, the vehicle convoy is supposed to acquire the desired formation under the receding horizon control scheme. The receding horizon approach to the formation control problem is implemented using Algorithm 1. Here, the control commands are generated by the closed-form law in (15).

Algorithm 1. Receding Horizon Control

At each time instant t :

- 1: **Measure** the current state vector \mathbf{z}
- 2: **Calculate** \mathbf{u} and \mathbf{z} for $[t, t + t_f]$
- 3: **Apply** $\mathbf{u} = \bar{\mathbf{u}}$ for the period $[t, t + \delta]$
- 4: **Update** $t \leftarrow t + \delta$
- 5: **Repeat** the steps 1 to 4

Size switching is subject to change only at desired distances among neighboring vehicles. Within this control platform when a size switching signal is received the formation desired distances vector $\mathbf{d} = \text{col}(\mathbf{d}_{ij})$ is multiplied by a scalar α where α is the formation shape scale factor. In this case, recalculation of the open-loop

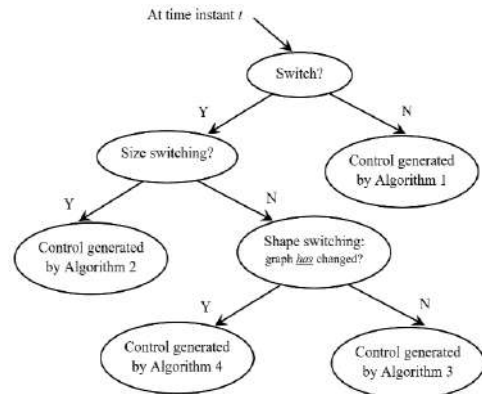


Figure 2. Proposed control structure

control \mathbf{u} for $[t, t + t_f]$ needs fewer computation resources. This is because the control signal can be rewritten as

$$\mathbf{u} = -\mathbf{R}^{-1}(\mathbf{N}\mathbf{q} - \mathbf{R}(\mathbf{N}^{-1})^T \mathbf{D}\mathbf{W}\mathbf{d} + \mathbf{M}\mathbf{v}) \quad (23)$$

and as it is seen only the middle term is subject to being multiplied by scalar α . The proposed size switching procedure is presented in Algorithm 2.

Algorithm 2. Size Switching

At each time instant t :

- 1: **Measure** the current state vector $\mathbf{z}(t)$
 - 2: **Update** \mathbf{d} as $\alpha\mathbf{d}$
 - 3: **Calculate** \mathbf{u} and \mathbf{z} for $[t, t + t_f]$
 - 4: **Apply** $\mathbf{u} = \bar{\mathbf{u}}$ for the period $[t, t + \delta]$
 - 5: **Update** $t \leftarrow t + \delta$
 - 6: **Repeat** the steps 1 to 5
-

In shape switching the vehicles might keep their neighbors but need to acquire different desired distances. In other words, formation graph \mathcal{G} does *not* change. In this case, similar to size switching only the middle term of the control signal is subject to the minor change of updating \mathbf{d} . The proposed shape switching procedure is presented in Algorithm 3.

Algorithm 3. Shape Switching (\mathcal{G} has *not* changed)

At each time instant t :

- 1: **Measure** the current state vector $\mathbf{z}(t)$
 - 2: **Update** \mathbf{d}
 - 3: **Calculate** \mathbf{u} and \mathbf{z} for $[t, t + t_f]$
 - 4: **Apply** $\mathbf{u} = \bar{\mathbf{u}}$ for the period $[t, t + \delta]$
 - 5: **Update** $t \leftarrow t + \delta$
 - 6: **Repeat** the steps 1 to 5
-

Shape switching might be subject to change on interconnections. Some vehicles might lose some of their immediate neighbors in the graph topology and some might acquire new neighbors (i.e., \mathcal{G} changes). Here, the \mathbf{D} , \mathbf{W} and \mathbf{d} parameters of the control signal must be updated. The proposed shape switching procedure when \mathcal{G} changes, is presented in Algorithm 4.

Algorithm 4. Shape Switching (\mathcal{G} has changed)

At each time instant t :

- 1: **Measure** the current state vector $\mathbf{z}(t)$
 - 2: **Update** \mathbf{D} , \mathbf{W} , \mathbf{d}
 - 3: **Calculate** \mathbf{u} and \mathbf{z} for $[t, t + t_f]$
 - 4: **Apply** $\mathbf{u} = \bar{\mathbf{u}}$ for the period $[t, t + \delta]$
 - 5: **Update** $t \leftarrow t + \delta$
 - 6: **Repeat** the steps 1 to 5
-

When designing the software interface of the control structure in Figure 2 (for example in Java), each different control mode can be addressed by using the abstract methods presented in Table 1.

TABLE 1. Abstract methods for different control procedures

Abstract method	Control generated by	Description
$control()$	Algorithm 1	Receding horizon control
$control(\alpha)$	Algorithm 2	Size switching, \mathbf{d} updates as $\alpha\mathbf{d}$
$control(\mathbf{d})$	Algorithm 3	Shape switching, \mathcal{G} has not changed, only \mathbf{d} updates
$control(\mathbf{D}, \mathbf{W}, \mathbf{d})$	Algorithm 4	Shape switching, \mathcal{G} has changed, \mathbf{D} , \mathbf{W} , \mathbf{d} update

5. SIMULATIONS

Simulations are carried out to analyze the proposed control architecture and algorithms. The experiments consist of five vehicles ($m = 5$). We consider a scenario in which at the time instants $t = 0s$ and $t = 7s$, the vehicles receive the signals $control()$ and $control(\mathbf{D}, \mathbf{W}, \mathbf{d})$, respectively. The corresponding information graphs are given in Figure 3, and their incidence matrices are, respectively:

$$\mathbf{D} = \begin{bmatrix} -1 & -1 & 0 & 0 \\ 1 & 0 & -1 & 0 \\ 0 & 0 & 1 & 0 \\ 0 & 1 & 0 & -1 \\ 0 & 0 & 0 & 1 \end{bmatrix}, \quad \mathbf{D} = \begin{bmatrix} 0 & -1 & 0 & 0 \\ 1 & 0 & -1 & 0 \\ 0 & 0 & 1 & 0 \\ -1 & 1 & 0 & -1 \\ 0 & 0 & 0 & 1 \end{bmatrix}$$

The weight matrices \mathbf{W} and \mathbf{R} are selected as the identity matrices. The desired offset vectors of the formation shape among the vehicles at $t = 0s$ are: $\mathbf{d}_{12} = \mathbf{d}_{23} = [-2, -4]^T$ and $\mathbf{d}_{14} = \mathbf{d}_{45} = [2, -4]^T$. These vectors mean that to form the desired shape; vehicle 1 and 2, as well as vehicle 2 and 3, have to achieve to relative distance -2 and -4 in the x and y position, respectively; vehicle 1 and 4, as well as vehicle 4 and 5, have to achieve to relative distance 2 and -4 in the x and y position, respectively. Moreover, all vehicles have to achieve zero relative velocities.

At time instant $t = 7s$, the communication link between vehicles 1 and 2 must break down and a new link between vehicles 2 and 4 must be built. The new desired offset vectors are: $\mathbf{d}_{24} = [2, 0]^T$, $\mathbf{d}_{14} = [2, -4]^T$, $\mathbf{d}_{23} = \mathbf{d}_{45} = [0, -4]^T$.

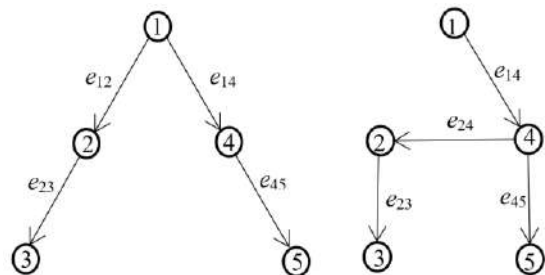


Figure 3. Information graph at $t = 0s$ (left) and $t = 7s$ (right)

The initial positions of the vehicles are set to: $\mathbf{q}_1 = [1,0]^T$, $\mathbf{q}_2 = [4,0]^T$, $\mathbf{q}_3 = [7,0]^T$, $\mathbf{q}_4 = [-1,0]^T$, $\mathbf{q}_5 = [-4,0]^T$. The initial velocities are set to: $\dot{\mathbf{q}}_1 = [0,2]^T$, $\dot{\mathbf{q}}_2 = [0,3]^T$, $\dot{\mathbf{q}}_3 = [0,1.5]^T$, $\dot{\mathbf{q}}_4 = [0,1]^T$, $\dot{\mathbf{q}}_5 = [0,2.5]^T$.

The finite horizon length is selected as $t_f = 7s$ and the sampling time for simulation/control is $0,1s$. The total running time of the control is $14s$. The vehicles' trajectories under signals $control()$ and $control(\mathbf{D}, \mathbf{W}, \mathbf{d})$ are shown in Figure 4. The vehicles are shown at $t = 0s$, $t = 5s$, and $t = 12s$. The results show that the desired formations among the vehicles are achieved under both signals at the end of their time interval. Time histories of the relative positions and velocities and also the control input of the individual vehicles are shown in Figure 5. It can be seen that all the formation control objectives are achieved.

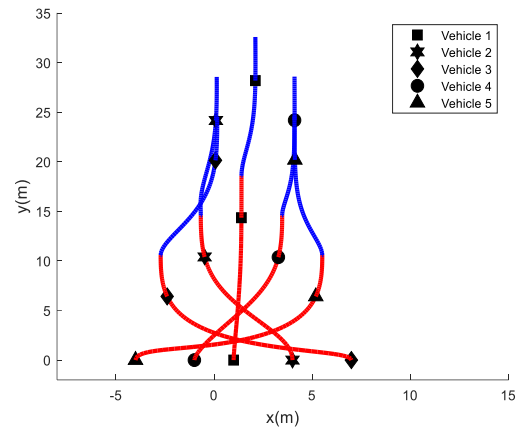


Figure 4. Vehicles' trajectories under $control()$ followed by $control(\mathbf{D}, \mathbf{W}, \mathbf{d})$ in red and blue, respectively

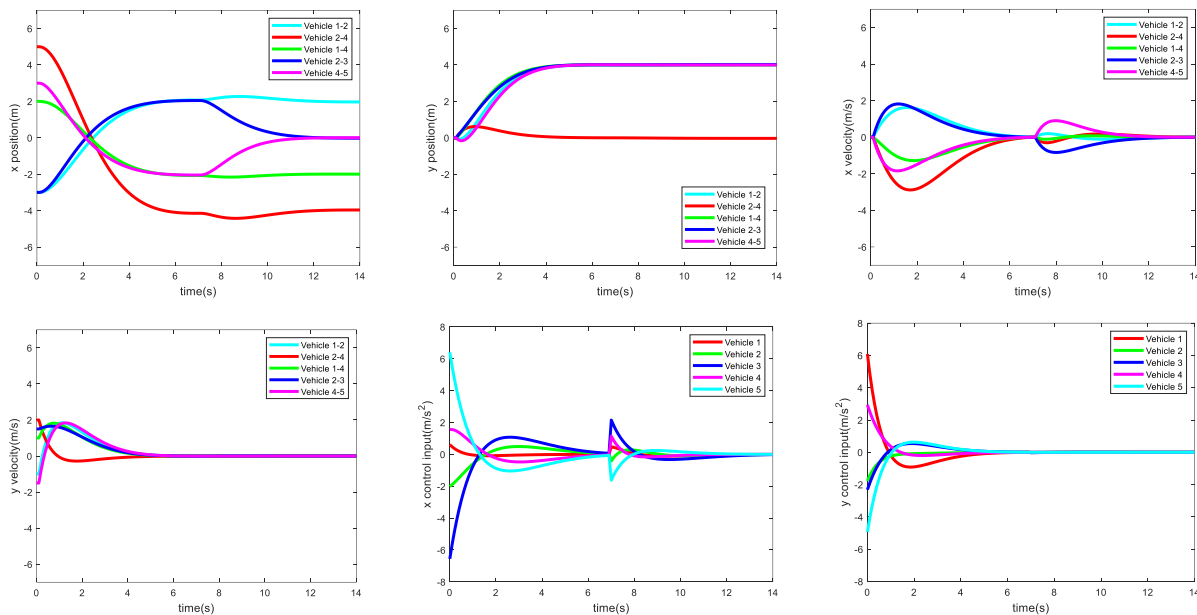


Figure 5. Time histories of the relative positions, velocities and control inputs under $control()$ followed by $control(\mathbf{D}, \mathbf{W}, \mathbf{d})$

6. CONCLUSION

In this paper, the convoy formation control problem was investigated under the receding horizon LQ optimal control framework. A closed-form solution was presented for the receding horizon LQ optimal formation control. The solution to the control law is a non-linear function of the graph Laplacian matrix and the formation desired distance vectors. A control architecture consisting of four control modes for formation size/shape switching problems was proposed. An algorithm based on the presented closed-form control law is developed for each control mode. The models, closed-form solution and proposed algorithms are approved by the simulations.

7. ACKNOWLEDGMENTS

This work was supported by the ESF in "Science without borders" project, reg. nr. CZ.02.2.69/0.0/0.0/16_027/0008463 within the Operational Programme Research, Development and Education.

8. REFERENCES

1. Chehardoli, H., and Homaienezhad, M. "Third-order Decentralized Safe Consensus Protocol for Inter-connected Heterogeneous Vehicular Platoons." *International Journal of Engineering - Transactions C: Aspects*, Vol. 31, No. 6, (2018),

- 967–972. <https://doi.org/10.5829/ije.2018.31.06c.14>
2. Qian, X., De La Fortelle, A., and Moutarde, F. "A hierarchical Model Predictive Control framework for on-road formation control of autonomous vehicles." In Proceedings IEEE Intelligent Vehicles Symposium, (Vol. 2016), 376–381. <https://doi.org/10.1109/IVS.2016.7535413>
 3. Sumia, L., and Ranga, V. "Intelligent Traffic Management System for Prioritizing Emergency Vehicles in a Smart City." *International Journal of Engineering - Transactions B: Applications*, Vol. 31, No. 2, (2018), 278–283. <https://doi.org/10.5829/ije.2018.31.02b.11>
 4. Liu, X., Ge, S. S., and Goh, C. H. "Vision-Based Leader-Follower Formation Control of Multiagents with Visibility Constraints." *IEEE Transactions on Control Systems Technology*, Vol. 27, No. 3, (2019), 1326–1333. <https://doi.org/10.1109/TCST.2018.2790966>
 5. Rabelo, M. F. S., Brandao, A. S., and Sarcinelli-Filho, M. "Centralized control for an heterogeneous line formation using virtual structure approach." In Proceedings - 15th Latin American Robotics Symposium, 6th Brazilian Robotics Symposium and 9th Workshop on Robotics in Education, LARS/SBR/WRE 2018, 141–146. <https://doi.org/10.1109/LARS/SBR/WRE.2018.00033>
 6. Balch, T., and Arkin, R. C. "Behavior-based formation control for multirobot teams." *IEEE Transactions on Robotics and Automation*, Vol. 14, No. 6, (1998), 926–939. <https://doi.org/10.1109/70.736776>
 7. Xu, D., Zhang, X., Zhu, Z., Chen, C., and Yang, P. "Behavior-based formation control of swarm robots." *Mathematical Problems in Engineering*, Vol. 2014, (2014), 1–13. <https://doi.org/10.1155/2014/205759>
 8. Ren, W., and Sorensen, N. "Distributed coordination architecture for multi-robot formation control." *Robotics and Autonomous Systems*, Vol. 56, No. 4, (2008), 324–333. <https://doi.org/10.1016/j.robot.2007.08.005>
 9. Wang, J., and Xin, M. "Integrated optimal formation control of multiple unmanned aerial vehicles." *IEEE Transactions on Control Systems Technology*, Vol. 21, No. 5, (2013), 1731–1744. <https://doi.org/10.1109/TCST.2012.2218815>
 10. Pourasad, Y. "Optimal Control of the Vehicle Path Following by Using Image Processing Approach." *International Journal of Engineering - Transactions C: Aspects*, Vol. 31, No. 9, (2018), 1559–1567. <https://doi.org/10.5829/ije.2018.31.09c.12>
 11. Hossein Barghi Jond, Vasif V. Nabiyev, and Dalibor Lukáš. "Linear Quadratic Differential Game Formulation for Leaderless Formation Control." *Journal of Industrial and Systems Engineering*, Vol. 11, (2017), 47–58. Retrieved from http://www.jise.ir/article_50882.html
 12. Lin, W. "Distributed UAV formation control using differential game approach." *Aerospace Science and Technology*, Vol. 35, No. 1, (2014), 54–62. <https://doi.org/10.1016/j.ast.2014.02.004>
 13. Meng, Y., Chen, Q., Chu, X., and Rahmani, A. "Maneuver guidance and formation maintenance for control of leaderless space-robot teams." *IEEE Transactions on Aerospace and Electronic Systems*, Vol. 55, No. 1, (2019), 289–302. <https://doi.org/10.1109/TAES.2018.2850382>
 14. Gu, D. "Receding Horizon Nash Approach to Formation Control." *SCIS & ISIS*, (2008), 1026–1031. <https://doi.org/10.14864/SOFTSCIS.2008.0.1026.0>
 15. Mesbahi, M., and Egerstedt, M. Graph theoretic methods in multiagent networks (Vol. 33). Princeton University Press.
 16. Engwerda, J. LQ dynamic optimization and differential games. John Wiley & Sons. Retrieved from
 17. George, C. E., and O'Brien, R. T. "Vehicle lateral control using a double integrator control strategy." In *Proceedings of the Annual Southeastern Symposium on System Theory* (Vol. 36, pp. 398–400). <https://doi.org/10.1109/ssst.2004.1295687>
 18. Olfati-Saber, R. "Flocking for multi-agent dynamic systems: Algorithms and theory." *IEEE Transactions on Automatic Control*, Vol. 51, No. 3, (2006), 401–420. <https://doi.org/10.1109/TAC.2005.864190>
 19. Naidu, D. Optimal control systems. CRC press.
 20. Sun, Z., and Xia, Y. "Receding horizon tracking control of unicycle-type robots based on virtual structure." *International Journal of Robust and Nonlinear Control*, Vol. 26, No. 17, (2016), 3900–3918. <https://doi.org/10.1002/mc.3555>
 21. Koeber, M., and Schäfer, U. "The unique square root of a positive semidefinite matrix." *International Journal of Mathematical Education in Science and Technology*, Vol. 37, No. 8, (2006), 990–992. <https://doi.org/10.1080/00207390500285867>

Persian Abstract

چکیده

وسایل نقلیه نیمه خودکار و هوشمند امروزی به تدریج به سمت خودمختاری کامل حرکت می‌کنند. این انتقال مستلزم ایجاد الگوریتم‌های کنترل موثر برای انجام وظایف مختلط پیچیده است. رانندگی به عنوان گروهی از وسایل نقلیه، که به آنها کاروان گفته می‌شود، در بزرگراه‌های خودکار وظیفه‌ای بسیار مهم و چالش برانگیز است که سیستم‌های رانندگی مستقل باید از پس آن برآیند. در این مقاله مشکل کنترل کاروان وسیله نقلیه مدل شده با پویایی خطی در نظر گرفته شده است. نیاز تشکیل کاروان از نظر شاخص عملکرد درجه دوم ارائه می‌شود تا به حداقل برسد. کنترل تشکیل کاروان به عنوان یک مسئله کنترل بهینه خطی-درجه دوم LQ برای افق عقب‌سازی فرموله شده است. قانون کنترل افق در حال عقب‌نشینی از طریق راه‌حل معادله جبری ریکاتی تعریف شده است. ماتریس راه‌حل و بنابراین قانون کنترل افق در حال عقب‌نشینی به صورت بسته به دست می‌آید. یک معماری کنترلی متشکل از چهار الگوریتم برای کنترل تغییر شکل اندازه / شکل تشکیل شده است. قانون کنترل فرم بسته در هسته اصلی این الگوریتم‌ها است. نتایج شبیه‌سازی برای توجیه مدل‌ها، راه‌حل‌ها و الگوریتم‌های پیشنهادی ارائه شده است.



A Wideband Fractal Planar Monopole Antenna with a Thin Slot on Radiating Stub for Radio Frequency Energy Harvesting Applications

M. M. Fakharian*

Faculty of Engineering, University of Garmsar, Garmsar, Iran

PAPER INFO

Paper history:

Received 23 January 2020

Received in revised form 18 August 2020

Accepted 25 August 2020

Keywords:

Wideband Monopole Antenna

Fractal Geometry

Slot on Radiating Stub

Radio Frequency Energy Harvesting

ABSTRACT

In this paper, for energy harvesting applications a design of a wideband planar monopole antenna is proposed using fractal geometry and inserting a thin slot on radiation patch. The proposed antenna is optimized at various stages during its design. Moreover, a parametric study is done for understanding sensitivity of important design parameters in the design process of the antenna. The designed antenna operates at 10-dB impedance bandwidth from 0.92 to 2.58 GHz (fractional bandwidth of 95%) with low profile structure and compact size of $65 \times 65 \times 0.8$ mm³, acceptable return losses, stable radiation characterizes and reasonable gains. A potential application of the antenna as a receiving antenna for harvesting systems has been carried out inside the laboratory as the harvested power from ambient radio-frequency (RF) energy. This wideband antenna has a good potential to harvest RF energy of available signals in the GSM-900, GSM-1800, and Wi-Fi bands, and can be used as a part in DC power supply modules of low power sensor networks.

doi: 10.5829/ije.2020.33.11b.08

1. INTRODUCTION

Nowadays, wideband antennas are used in various wireless applications such as in multimedia devices, smart phones etc. Apart from these applications, wideband antennas can be also used as an important component for radio frequency (RF) energy harvesting systems [1]. The RF energy harvesting can be applied as a power supply for a number of the low power electronic devices such as wireless sensor nodes, in order to either replace or even to recharge the the devices' battery. The wideband feature in the antennas in these systems helps in scavenging ambient RF energy from the incoming signal may come from different frequency channels from 0.8 to 2.5 GHz covering GSM900, GSM1800, and Wi-Fi bands of the surrounding environment [2]. Furthermore, the available RF energy can be from various powers and different directions. Hence, an appropriate wideband antenna with a single structure and an omni-directional pattern with stable radiation pattern is required for such

systems to have higher RF energy harvesting efficiency from the ambient.

In the last decade, ranges of antenna for energy harvesting applications have been proposed such as patch antenna [3], spiral antenna [4], dipole antenna [5], slot antenna [6], metamaterial antenna [7], and so on. These antenna designs have narrowband [5, 8], multiband [9, 10], or wideband [1-4, 11-14] operations. A single narrow band design produces low conversion efficiency for low-power levels of input power density and not very proper for wireless energy scavenging applications. A multiband or a wideband design can capture more power from the existing signals of different standards from RF energy sources in air and then produce more output power than that a narrowband antenna. But, it was already discussed in literature [15] that wideband antennas are desirable rather than multiband antennas, because they have easier design, and they are interoperable among countries, whose assignment plans of frequency can be diverse among them.

Corresponding Author Institutional Email: fakharian@fmgarmsar.ac.ir
(M. M. Fakharian)

Please cite this article as: M. M. Fakharian, A Wideband Fractal Planar Monopole Antenna with a Thin Slot on Radiating Stub for Radio Frequency Energy Harvesting Applications, International Journal of Engineering (IJE), IJE TRANSACTIONS B: Applications Vol. 33, No. 11, (November 2020) 2181-2187

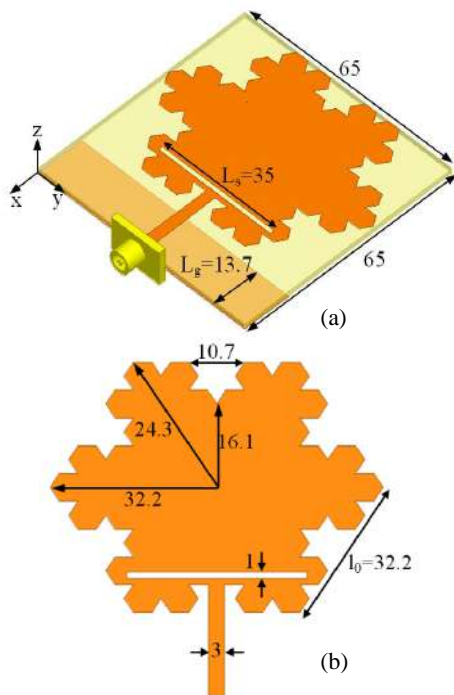


Figure 1. Structure of the proposed antenna (a) side view (b) radiating patch (dimension: mm)

So far, several planar wideband antennas are reported in the literature for RF energy harvesting applications [2-3, 12-14]. A wideband printed log periodic dipole array antenna is proposed by triangular shaped dipoles [2]. The antenna covers the 10-dB impedance bandwidth from 0.570 to 2.750 GHz, but the size of antenna is very large and the pattern is not omnidirectional. Di Carlo et al. [3] dealt with a circularly polarized (CP) microstrip monolithic antenna operating at 868 MHz with fractional bandwidth of 5% for wireless power transfer. But they achieved impedance bandwidth which is not adequate and its pattern is not uniform and omnidirectional. A wideband CP antenna is designed by Adam et al. [12]. The frequency band of this antenna is achieved from 1.73 to 2.61 GHz that is not very suitable for scavenging, furthermore the pattern is not uniform due to the asymmetric structure of the antenna. An antenna is presented by merging a 2×2 array with a tapered antenna [13]. The antenna has 6-dB impedance bandwidth of 720–1300 MHz and 1630–3630 MHz, but its pattern is not omnidirectional and uniform across the entire bandwidth. A wideband bent triangular monopole planar antenna is proposed for this application [14]. The antenna has a 10-dB impedance bandwidth from 0.85 to 1.94 GHz, but this bandwidth is not sufficient for harvesting application. Therefore, a simple and compact planar wideband antenna with uniform and omnidirectional radiation pattern necessities to be developed for wireless energy scavenging.

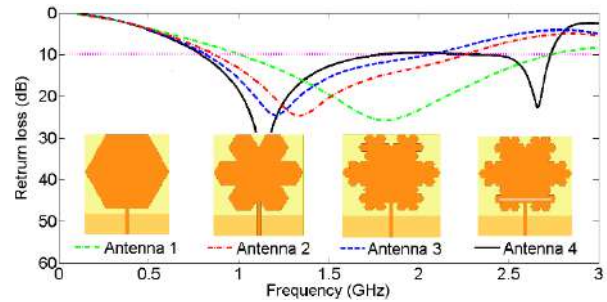


Figure 2. Development stages and the corresponding simulated return loss of the antenna

In this paper a wideband fractal planar monopole antenna is presented. The fractal geometry is based on an iterative Koch snowflake up to second iteration. The compact structure and ease configuration are the main advantage of this fractal monopole antenna [16-18]. In the proposed antenna, wideband function is expanded by inserting a rectangular thin slot on the fractal radiating stub, so a multiresonance characteristic can be produced, especially at the higher band. Good impedance bandwidth and uniform omnidirectional radiation pattern are acquired in the interest frequency band. Measured and simulated data are shown to validate the practicality of the proposed fractal antenna configuration for RF energy harvesting.

2. ANTENNA DESIGN AND SIMULATION

The proposed planar antenna based on a fractal structure with etching a thin slot on it is shown in Figure 1. The antenna is designed on a low-cost FR4 substrate with a relative permittivity of 4.4, thickness of 1.6 mm, and loss tangent ($\tan \delta$) of 0.02. A modified 2nd iteration of Koch snowflake fractal radiation patch with an embedded rectangular-shaped thin slot on it is fed by a 50- Ω microstrip line. The ground plane is modified to partial rectangular plane to enhance the desired impedance bandwidth and omnidirectional radiation pattern characteristics as a monopole antenna. The antenna performance is analyzed and optimized using 3D Ansoft HFSS EM software [19].

The development stages of the antenna are shown in Figure 2, and the corresponding simulated return loss curves are shown in same Figure 2. The 1st antenna consists of a radiator with a hexagon-shaped, a microstrip feed-line with 50 Ω impedance, and a rectangular ground plane. In the 2nd antenna, first fractal iteration is implemented to radiator of the 1st antenna, and also in the 3rd antenna, second fractal iteration is implemented to previous antenna. As shown in Figure 2, the resonant frequency of the fractal antenna decreases with the increase in the number of iterations, although it

reduces its impedance bandwidth. In order to understand the cause of this phenomenon, the following equations can be considered. The perimeter length (l_{perim}) and the effective area (A) of the proposed modified fractal patch geometry, at indentation angle 60° and at iteration n , are found in literature [20].

$$l_{perim}(n) = 4 \left[\frac{2}{3} \left(\frac{5}{3} - \cos 60 \right) \right]^n l_0, \tag{1}$$

$$A(n) = \left[1 - 4 \left(\sum_{i=1}^n \frac{4^{i-1}}{9^i} \right) \cos 60 \sin 60 \right] l_0^2. \tag{2}$$

As shown in these formulas, the perimeter or the overall electrical length of the antenna increases with increasing the number of iterations so the decrease in resonant frequency stems from that. On the other hand, the enclosed area of the fractal antenna decreases with iteration increasing. Therefore, the ratio of perimeter length to enclosed area is large when more iteration is implemented in the fractal geometry, so the impedance bandwidth decreases with this extending of iteration. Finally, at the 4th antenna, a thin rectangular slot is applied to the radiating patch. This technique increases bandwidth, especially at the end of the frequency band [21]. Indeed, this thin slot is used for the new resonance excitation function, and hence multi-resonance characteristics with wider impedance bandwidth can be created. As shown in Figure 2, the operating band of the antenna is improved and shifts from 1–2.73 GHz to 0.78–2.73 GHz as develops design of the antenna, so completely covering the RF energy scavenging interesting bands. Antenna 4 is the final proposed antenna. The optimized geometrical parameters of the final proposed antenna are illustrated in the same Figure 1.

To understand the operation theory of the proposed antenna at the wideband performance, the current distributions at three frequencies are shown in Figure 3. Figure 3(a) shows the surface current distributions at 0.95 GHz. As shown in this figure, the electric current is strengthened around the edges of the interior of the thin slot and on the entire feed line of the fractal-shaped radiating patch. Consequently, the antenna performance is dependent on these sections mainly near the resonance frequency at 0.95 GHz. It is observed in Figure 3(b) that the current distributions are more concentrated on the lower section of the feed line and around two sides of the thin slot at 1.85 GHz. Figure 3(c) shows that the current distributions are concentrated on the bottom part of the feed line and on the edges of the interior and exterior of the thin slot at 2.45 GHz.

To understand the influence of the antenna physical dimensions on the bandwidth characteristics. The return loss curves for two important parameters are shown in Figure 4. Figure 4(a) shows the effect of slot length (L_s) on the impedance matching of the proposed antenna. It is

indicate that by inserting the thin slot with suitable dimensions on the radiation stub, additional resonance is excited at the higher band. It is clear that with increasing of L_s from 33 to 36 mm, the upper resonance frequency decreases. On the other hand, it is shown in Figure 4(b) that by increasing rectangular ground length (L_g) from 11.7 to 15.7 mm, the lower frequency of the bandwidth decreases. This figure also shows that for smaller values of L_g , the antenna return loss deteriorates.

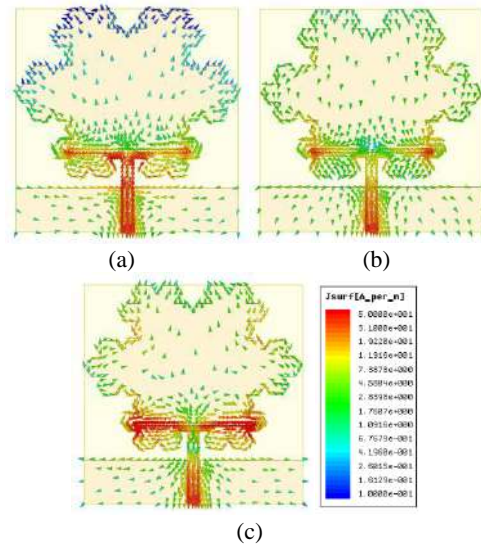


Figure 3. The simulated current distributions of the proposed antenna at three frequencies. (a) 0.95 GHz, (b) 1.85 GHz, and (c) 2.45 GHz

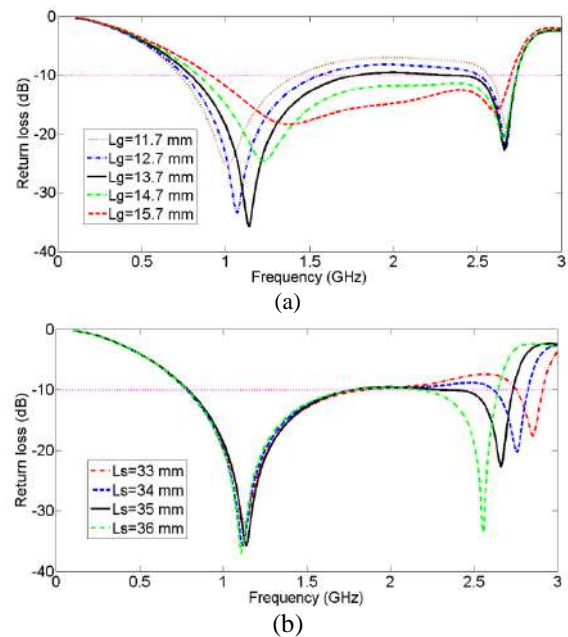


Figure 4. Effects of L_g and L_s on the antenna return loss of the antenna. (a) L_g and (b) L_s

3. ANTENNA FABRICATION AND MEASUREMENT RESULTS

In order to validate the simulated results, the proposed fractal monopole antenna is fabricated and its impedance bandwidth, radiation and power spectrum characteristics are measured. Figure 5 shows photographs of the fabricated prototype. In the following, the experimental results are given, discussed, and compared with the simulated results.

In Figure 6, it is presented a comparison between the simulated and measured return losses of the proposed antenna which appear to be in relatively good agreement. The discrepancies between the simulated data and measured result are almost due to fabrication tolerances and misalignments, including the dimensional error of the antenna and the nonconformity of the actual dielectric permittivity of the substrate. Moreover, it can be attributed to the calibration errors resulting from the vector network analyzer, measurement setup and connecting coaxial cables. Measured result shows that the proposed fractal antenna can cover a frequency range from 0.92 to 2.58 GHz (95%, 10-dB impedance bandwidth). Thus, it covers the most interest bands for harvesting application.

The measured radiation pattern along H(x-z) and E(y-z) planes for three different frequencies 0.95, 1.85, and 2.45GHz are presented in Figure 7. As seen in this figure, the radiation patterns are nearly stable and uniform at the different frequencies. As well as, it is also seen that the

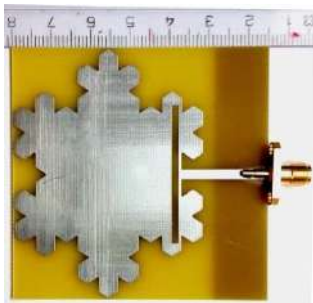


Figure 5. Prototype of the fractal monopole antenna

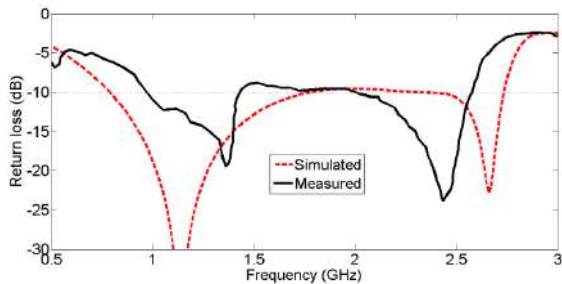


Figure 6. Simulated and measured return losses of the proposed antenna

antenna maintains omni-directional pattern in the H-plane and bi-directional pattern in the E-plane over the frequency band.

The increase in cross-polarization level at high frequencies is almost by reason of the excitation of hybrid current distribution on the antenna radiator patch. The measured gain and simulated radiation efficiency of the antenna are also shown in Figure 8. The antenna achieved an average gain of 0.9 dBi over the operating frequency, and the maximum value of 3.1 dBi which occurs at 2.7 GHz. It should be noted that the antenna gain is reasonable over the working band respecting the compact size and omnidirectional behavior of the proposed antenna. Besides, the efficiency of the antenna is almost stable with the growth of frequency, while the value of gain increases for higher frequencies. The following values of simulated efficiency are obtained of 84.8, 79.12 and 78.37% at 0.95, 1.85 and 2.45 GHz, respectively.

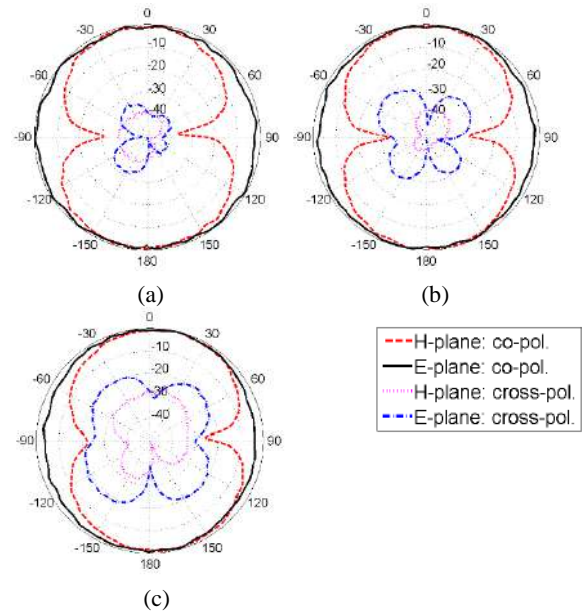


Figure 7. Radiation patterns of the proposed antenna in the H- and E-planes at a) 0.95 GHz, b) 1.85 GHz, and c) 2.45GHz

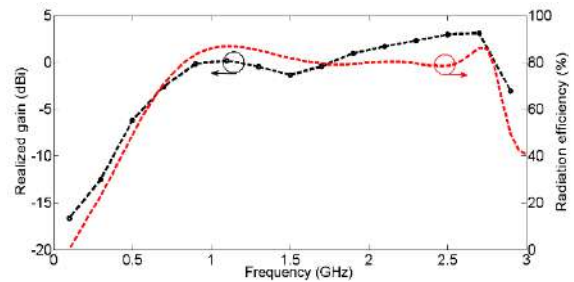


Figure 8. Measured gain and simulated radiation efficiency of the proposed design

To evaluate the performance of the proposed wideband antenna in a realistic measurement of the harvested power, a spectrum analyzer is connected to the antenna for integrating the power spectrum over bandwidth. An indoor laboratory environment is selected with a relatively low ambient RF power density to conduct the test. Nearest cell phone tower site is about 600 m away from the laboratory and a Wi-Fi router is near to the position of test. The received power in dBm in term of frequency is shown in Figure 9. It is clear that the power is mostly distributed at three frequency bands which are GSM-900, GSM-1800, and Wi-Fi with average power levels of -46, -32, and -33 dBm, respectively. It should be noted that the measured total power in the band received by antenna is variable as a function of time.

The performance comparison of the designed antenna with other relevant designs available in the literature is presented in Table 1. Antenna parameters such as Impedance Bandwidth, Electrical Size, Peak Gain, and Efficiency for given dielectric constant of substrate are

shown. It is obvious that the proposed antenna has design superiority over many designs in terms of compactness and bandwidth for the designed frequency bands. Compared to results reported by Alex-Amor et al. [4], impedance bandwidth of the antenna is reduced that it is because of reduction in the total area of the proposed antenna.

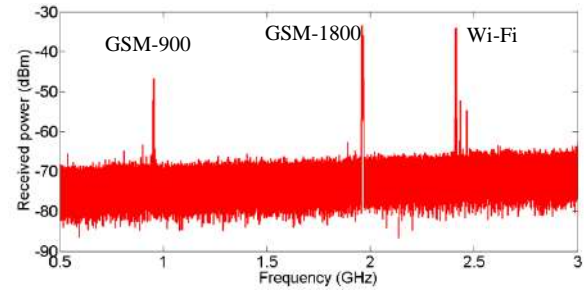


Figure 9. Measured power spectrum by the proposed antenna inside the laboratory

TABLE 1. Comparison of the designed antenna with related works in literature

Ref.	Description	Impedance Bandwidth (GHz), (%)	Electrical Size	Max. Rad. Efficiency (%)	Peak Gain (dBi)	Substrate, ϵ_r
Proposed	Fractal monopole with inserted slot	0.92-2.58, (95%)	$0.2 \times 0.2 \lambda_0$ (0.92 GHz)	83.3	3.1	FR4, 4.4
[4]	Archimedean spiral	0.35-16 (192%)	$0.23 \times 0.24 \lambda_0$ (0.35 GHz)	98	-	FR4, 4.7
[7]	Metamaterial with EBG structure	5.03- 6.04 (18%)	$0.83 \times 0.83 \lambda_0$ (5.03 GHz)	50.4	8.6	FR4, 4.2
[11]	Dual-polarized cross-dipole	1.8-2.5 (33%)	$0.42 \times 0.42 \lambda_0$ (1.8 GHz)	70	4.2	FR4, 4.4
[12]	Electromagnetically-fed CP	1.73-2.61 (40%)	$0.38 \times 0.38 \lambda_0$ (1.73 GHz)	-	8.7	FR4, 4.6
[14]	Bent triangular omnidirectional	0.85-1.94 (79%)	$0.31 \times 0.27 \lambda_0$ (0.85 GHz)	75	2	FR4, 4.4

The proposed wideband antenna is developed to array configuration based on a microstrip-to-slot-line transition feeding network in literature [22]. In this design, a wideband rectifying circuit using two-branch matching circuits by applying a full-wave rectifier circuit and an optimized coupled-line is presented to match with the ambient wireless signals in the low power density. A series-mounted Schottky diode HSMS-285C from Avago is applied for the rectifier circuit owing to its low turn-on voltage condition and small junction capacitance for a low input signal. Therefore, the proposed design can be used for efficiently harvesting RF energy from the ambient environment with appropriate RF-to-DC conversion efficiency.

4. CONCLUSION

A low-cost wideband fractal antenna with embedded a thin slot was proposed particularly for ambient RF energy

harvesting. The antenna is capable of operating in a wide range from 0.92 GHz to 2.58 GHz, as the measurement results. Using fractal structure in radiating patch causes miniaturized dimension of antenna and the thin slot in the radiating patch is applied for the bandwidth enhancement of the antenna. The designed monopole antenna shows omnidirectional radiation patterns and responsible gains for different frequencies over the bandwidth range. Moreover, in order to estimate the incoming power level, a test is carried out with the antenna inside the laboratory. These results cause the conclusion that the major role of the harvested power comes from the cellular bands and wi-Fi router, especially from 1.8 and 2.4 GHz.

5. ACKNOWLEDGMENT

The author gratefully acknowledge: experimental support by Sharif Center for Laboratory Services (Center Lab) at Sharif University of Technology and Antenna

Laboratory at Iran Telecommunication Research Center (ITRC). This research was also supported by Iran's National Elites Foundation (INEF).

6. REFERENCES

1. Simón, J., Flores-Gonzalez, J.R., González-Salas, J.S., Ordaz-Salazar, F.C. and Flores-Troncoso, J., "A log-periodic toothed trapezoidal antenna for rf energy harvesting", *Microwave and Optical Technology Letters*, Vol. 57, No. 12, (2015), 2765-2768. DOI: 10.1002/mop.29425
2. Kumar, H., Arrawatia, M. and Kumar, G., "Broadband planar log-periodic dipole array antenna based rf-energy harvesting system", *IETE Journal of Research*, Vol. 65, No. 1, (2019), 39-43. DOI: 10.1080/03772063.2017.1385427
3. Di Carlo, C., Di Donato, L., Mauro, G., La Rosa, R., Livreri, P. and Sorbello, G., "A circularly polarized wideband high gain patch antenna for wireless power transfer", *Microwave and Optical Technology Letters*, Vol. 60, No. 3, (2018), 620-625. DOI: 10.1002/mop.31022
4. Alex-Amor, A., Padilla, P., Fernández-González, J.M. and Sierra-Castañer, M., "A miniaturized ultrawideband archimedean spiral antenna for low-power sensor applications in energy harvesting", *Microwave and Optical Technology Letters*, Vol. 61, No. 1, (2019), 211-216. DOI: 10.1002/mop.31534
5. Sun, H., Guo, Y.-x., He, M. and Zhong, Z., "Design of a high-efficiency 2.45-GHz rectenna for low-input-power energy harvesting", *IEEE Antennas and Wireless Propagation Letters*, Vol. 11, (2012), 929-932. DOI: 10.1109/LAWP.2012.2212232
6. Monti, G., Tarricone, L. and Spartano, M., "X-band planar rectenna", *IEEE Antennas and Wireless Propagation Letters*, Vol. 10, No., (2011), 1116-1119. DOI: 10.1109/LAWP.2011.2171029
7. Olule, L.J., Gnanagurunathan, G. and Kasi, B., "Low-profile broadband metamaterial-based rf energy harvesting with mushroom ebg structure", in 2016 IEEE Asia-Pacific Conference on Applied Electromagnetics (APACE), IEEE, (2016), 229-233. DOI: 10.1109/APACE.2016.7916430
8. Palandöken, M., "Microstrip antenna with compact anti-spiral slot resonator for 2.4 GHz energy harvesting applications", *Microwave and Optical Technology Letters*, Vol. 58, No. 6, (2016), 1404-1408. DOI: 10.1002/mop.29824
9. Taghadosi, M., Albasha, L., Qaddoumi, N. and Ali, M., "Miniaturised printed elliptical nested fractal multiband antenna for energy harvesting applications", *IET Microwaves, Antennas & Propagation*, Vol. 9, No. 10, (2015), 1045-1053. DOI: 10.1049/iet-map.2014.0744
10. Singh, N., Kanaujia, B., Beg, M., Mainuddin, Kumar, S., Choi, H.C. and Kim, K.W., "Low profile multiband rectenna for efficient energy harvesting at microwave frequencies", *International Journal of Electronics*, Vol. 106, No. 12, (2019), 2057-2071. DOI: 10.1080/00207217.2019.1636302
11. Song, C., Huang, Y., Zhou, J., Zhang, J., Yuan, S. and Carter, P., "A high-efficiency broadband rectenna for ambient wireless energy harvesting", *IEEE Transactions on Antennas and Propagation*, Vol. 63, No. 8, (2015), 3486-3495. DOI: 10.1109/TAP.2015.2431719
12. Adam, I., M. Yasin, M.N., Soh, P.J., Kamardin, K., Jamlos, M.F., Lago, H. and Razalli, M.S., "A simple wideband electromagnetically fed circular polarized antenna for energy harvesting", *Microwave and Optical Technology Letters*, Vol. 59, No. 9, (2017), 2390-2397. DOI: 10.1002/mop.30746
13. Lee, C.H., Park, J.H. and Lee, J.H., "Wideband tapered monopole antenna with 2 by 2 resonant loop array for electromagnetic energy harvesting and microwave power transmission", *Microwave and Optical Technology Letters*, Vol. 59, No. 4, (2017), 797-802. DOI: 10.1002/mop.30387
14. Arrawatia, M., Baghini, M.S. and Kumar, G., "Broadband bent triangular omnidirectional antenna for rf energy harvesting", *IEEE Antennas and Wireless Propagation Letters*, Vol. 15, (2015), 36-39. DOI: 10.1109/LAWP.2015.2427232
15. Azadi, A., Rezaei, P., Fakharian, M.M. and Dadras, M.R., "A capacitive fed microstrip patch antenna with air gap for wideband applications (research note)", *International Journal of Engineering, Transactions B: Applications*, Vol. 27, No. 5, (2014), 715-722. DOI:10.5829/idosi.ije.2014.27.05b.06
16. Krishna, D.D., Gopikrishna, M., Aanandan, C., Mohanan, P. and Vasudevan, K., "Compact wideband koch fractal printed slot antenna", *IET Microwaves, Antennas & Propagation*, Vol. 3, No. 5, (2009), 782-789. DOI: 10.1049/iet-map.2008.0210
17. Fakharian, M.M. and Rezaei, P., "Parametric study of uc-pbg structure in terms of simultaneous amc and ebg properties and its applications in proximity-coupled fractal patch antenna", *International Journal of Engineering, Transactions A: Basics*, Vol. 25, No. 4, (2012), 347-354. DOI:10.5829/idosi.ije.2012.25.04a.05
18. Garg, R., "Antenna miniaturization using fractals (research note)", *International Journal of Engineering, Transactions C: Aspects*, Vol. 25, No. 1, (2012), 39-44. DOI: 10.5829/idosi.ije.2012.25.01c.05
19. Ansoft, H., "Ver. 12.0", Pittsburgh, PA, (2010).
20. Da Costa, K.Q. and Dmitriev, V., "Theoretical analysis of a modified koch monopole with reduced dimensions", *IEEE Proceedings-Microwaves, Antennas and Propagation*, Vol. 153, No. 5, (2006), 475-479. DOI: 10.1049/ip-map:20050046
21. Fakharian, M.M., Rezaei, P. and Orouji, A.A., "A novel slot antenna with reconfigurable meander-slot dgs for cognitive radio applications", *Applied Computational Electromagnetics Society Journal*, Vol. 30, No. 7, (2015), 748-753.
22. Fakharian, M.M., "A wideband rectenna using high gain fractal planar monopole antenna array for rf energy scavenging", *International Journal of Antennas and Propagation*, Vol. 2020, (2020). DOI: 10.1155/2020/3489323

Persian Abstract

چکیده

در این مقاله، یک آنتن مونوپل مسطح باندوسیع بر پایه هندسه فرکتال و تعبیه یک شکاف نازک بر روی پچ تشعشع‌کننده برای کاربردهای برداشت انرژی RF طراحی شده است. آنتن پیشنهاد شده در روند طراحی، در چندین مرحله بهینه شده است. علاوه بر این، یک مطالعه پارامتری به منظور درک حساسیت برخی پارامترهای مهم در روند طراحی آنتن، انجام شده است. آنتن طراحی شده دارای پهنای باند امپدانس 0.92 تا 2.58 گیگاهرتز (پهنای باند کسری 95%) با یک ساختار فشرده به اندازه $65 \times 65 \times 0.8$ میلی‌متر مکعب است. همچنین آنتن دارای بهره و مشخصات تشعشعی قابل قبول و پایداری است. قابلیت کاربردی آنتن به عنوان یک آنتن دریافت‌کننده برای سیستمهای برداشت انرژی، داخل محیط یک آزمایشگاه تست شده است. آنتن باندوسیع طراحی شده، قابلیت خوبی در برداشت انرژی باندهای در دسترس GSM-1800, GSM-900 و Wi-Fi دارد که میتواند به عنوان یک بخش در ماژول تغذیه توان DC در شبکه‌های حسگر کم‌توان به کار برده شود.



Reference Satellite Strategic Methods to Improve Position Accuracy of Rover with Resolved Integer Ambiguities Using Linear Combination in DIRNSS System

S. Nageena Parveen*, P. Siddaiah

Department of ECE, ANU College of Engineering and Technology, Acharya Nagarjuna University, Guntur, India

PAPER INFO

Paper history:

Received 21 June 2019
Received in revised form 28 May 2020
Accepted 03 September 2020

Keywords:

Dual Carrier Wide Lane
IRNSS
Integer Ambiguity Resolution
least Squares Modified Linear Combination
Measurement by Carrier Phases
Narrow Lane
Ionosphere Free
Baseline Error

ABSTRACT

IRNSS is a regional system designed to procure, an accurate user position in all circumstances with 24/7 coverage. This system is used in a wide range of applications with accuracy better than 20 meters in the primary service area. The IRNSS provided position, velocity, and timing services are useful for the Indian users and also the users 1500km from the Indian frontier. The accurate positioning in the phase measurement technique depends on the resolution of ambiguities. In this paper, the main focus is on the effective resolution of ambiguities and thereby position estimation. This paper proposes a Carrier Phase (CP) differencing based Wide Lane (WL) measurement. To resolve the ambiguities, estimate the position of the WL classified methods, Single Frequency Single Difference (SFSD), Single Frequency Double Difference (SFDD), Dual Frequency Single Difference (DFSD), and Dual Frequency Double Difference (DFDD) are used. These four types are processed through the Reference Base and Reference Satellite (RBARS) algorithm to estimate the position of the user/rover. In this paper, direct amalgamate of three estimations are utilized: WL, Narrow Lane (NL), and Ionosphere Free (IF) carrier phase estimations. Using this combination, the estimations of ambiguities are determined for individual satellites by utilizing WL and NL techniques. Thereby the user/rover position is computed, by assessing these real number ambiguities. In this work, every single condition is utilized and together with the least-squares modifications, the positional errors are computed in 3D plane. The computed root mean square errors are compared for all classified methods.

doi: 10.5829/ije.2020.33.11b.09

1. INTRODUCTION

The Indian Space Research Organization has started implementing India's indigenous regional (IRNSS) navigation system. The IRNSS system is designed to provide navigation services to the Indian geographical area. The basic idea behind this regional system is an alternative to the Global Positioning System, in any land, air, sea, and navigational type of applications. The main objective of the IRNSS system is, to provide an accurate position in all circumstances with 24/7 coverage.

The IRNSS provides two types of services to the users, such as Standard Positioning Services (SPS) and Restricted Services (RS) [1]. The regular civilian users

are serviced with SPS. The authorized (military) users are serviced with RS. In its primary service area, it is designed to provide accuracy better than 20 meters.

In the last few years, researchers have concentrated on India's indigenous IRNSS system. The positioning topic is high interest of the research communities for a newly added GNSS system i.e. IRNSS. The main intent of the positioning topic is, to determine the user/rover position by measuring the distance between the satellite and receiver (range). This range is calculated either by the travel time (pseudo-range) of the signal or in terms of a number of cycles (phase measurement). In this paper, the Carrier Phase (CP) measurement is used to estimate the position.

The IRNSS is a Dual Frequency (DF) receiver (L5/S1 bands), however, in most of the investigations solely Single Frequency (SF) (either L5 or S1) is considered. In IRNSS system depending on the adopted

*Corresponding Author Email: syednageena@gmail.com
(S. Nageena Parveen)

application either the SF or DF is selected. The adopted SF resulted in an inaccurate position and unstable ambiguities. However, the expensive DF receivers have an advantage of a shorter time for ambiguity resolution.

In this work, the ambiguities are fixed using WL, Wide Lane linear mix (Wide-Narrow-Lane, or WNL), and observed the reliability. The RBARS algorithm is developed to estimate the user position in WL technique. The convergent time is going to be reduced if these ambiguities are quickly fixed. This paper presents an amalgamate approach, to compute a 3D user/rover position. With this linear combination, the 3D RMS errors are computed and compared for WL classified measurements.

In Section 2, a detailed description of WL is presented. In Section 3, a detailed concept of position estimation using the RBARS algorithm is explained. In section 4, the results are discussed and concluded the paper in Section 5.

2. DESCRIPTION OF WIDE LANE TECHNIQUE

Differential IRNSS (DIRNSS) is the most acquainted and well-liked methodology that works based on correction information of Carrier Phase (CP) measurement and forwarding this correction to end-users. Figure 1 shows the setup of DIRNSS system for user/rover position estimation. The DIRNSS system consists of two receivers which simultaneously track the same IRNSS satellites. In the DIRNSS system with more than two satellites and two receivers, the CP measurement can achieve accuracy in a few centimeters.

In this work, the CP measurement is used to estimate the position. The CP based positioning technique provides a more accurate positioning solution compare to the code-based positioning technique [2]. But the CP measurement included with integer ambiguity as an extra parameter. In CP measurements, the ambiguities have to resolve for the desired accuracy in user position. Once the ambiguities are correctly fixed, the time required to determine the user position is decreased. The IRNSS navigation message file contains the data, included with the satellite positions, receiver-satellite range, ionosphere delay, satellite clock bias, and receiver position. The information of these parameters is collected either from a data file or from the video record. The data sets are noted and the proposed algorithm is practically implemented in MATLAB software. The estimated reference receiver positions are validated with respect to the survey location. The positional errors and their RMS values are calculated using the DIRNSS system. The obtained RMS errors are compared for SF and DF combinations.

The frequencies of L5 and S bands are considered as (1176.45 MHz and 2492.028 MHz). The corresponding

WL frequency is 1315.578 MHz and NL frequency is 3668.478 MHz [1].

Table 1 shows the various parameters of WL and NL techniques. The WL frequency is less compare to NL frequency therefore the WL wavelength is longer compare to NL wavelength. The better integer estimate is obtained with the longer wavelength (f_{WL}). Therefore, to resolve ambiguities the WL is best to compare to NL. It is harder to determine the Ambiguity Resolution (AR) in NL technique. In position estimation, the combination of WNL is used popularly known as WL linear mix [3]. This combination is very helpful for the determination of ambiguities. Therefore, with this combined technique more accurate results are obtained than individual measurements.

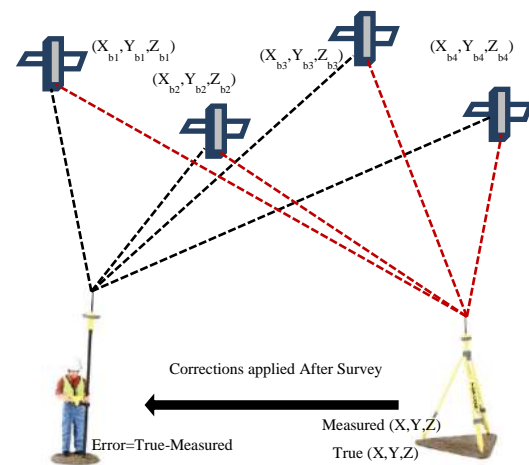


Figure 1. DIRNSS system setup

TABLE 1. Comparison of WL and NL calculations

Parameter	NL	WL
Frequency	$f_{NL} = f_{L5} + f_S$	$f_{WL} = f_{L5} - f_S$
Wavelength	$\lambda_{NL} = 81.8\text{cm}$	$\lambda_{WL} = 0.2280\text{m}$
Integer Ambiguity	$N_{NL} = N_{L5} + N_S$	$N_{WL} = N_{L5} - N_S$
CP	$\phi_{NL} = \phi_{L5} + \phi_S$ $= \left[\frac{r_{L5S}}{\lambda_{NL}} + N_{NL} \right]$	$\phi_{WL} = \phi_{L5} - \phi_S$ $= \left[\frac{r_{L5S}}{\lambda_{WL}} + N_{WL} \right]$
Integer (fixed)	$\hat{N}_{NL} = \left[\phi_{NL} - \frac{\rho_{L5S}}{\lambda_{NL}} \right]$	$\hat{N}_{WL} = \left[\phi_{WL} - \frac{\rho_{L5S}}{\lambda_{WL}} \right]$

where λ_{L5S} is the wavelength of L5 and S bands, r_{L5S} is the pseudo range of L5 and S signals, I_{L5S} and T_{L5S} is WL ionosphere, troposphere delay, N_{L5S} is the WL DD integer ambiguity, and $\epsilon_{\phi_{L5S}}$ is the effects due to multipath.

2. 1. Amalgamate of WL, NL and IF Mode

In this section to dispense with the ionosphere delay on estimations, the IF model straight amalgamate is used. In this combined linear technique, WL and NL are useful in ambiguity determination. The estimations of ambiguities are determined for individual satellites by utilizing WL and NL techniques. These obtained real number ambiguities are assessed to compute the user/rover position. To acquire centimeter precision, the precise IGS IRNSS satellite orbital parameters, satellite clock offsets, etc. are required. With this combined augmentations, the equipment delays, comparative offsets of receiver, satellites, and other different errors are reduced. In this amalgamate, the IF model is utilized to decrease the effect of the ionosphere and a WL linear mix is utilized, for ambiguity resolution. This combined amalgamate is termed as RBARS algorithm. This algorithm is used for position estimation. The required accuracy is achieved with this linear combination. Three amalgamations of WL, NL, and IF model are utilized for position estimation [3]. With the accurate IGS IRNSS satellite orbital parameters, the cm-level accuracy in the IRNSS system is achieved. To get the benefit of every one of these strategies, the three methods are combined and solved together with the least-squares modification [4]. Therefore, the ambiguities are resolved for the corresponding CP measurement, and the baseline solution is determined. When the ambiguities are settled, the carrier phase is expressed in the units of length for position estimation. The computed results of fixed ambiguities and the baseline errors are forwarded to the reference base position to get the precise user/rover position.

3. POSITION ESTIMATION USING RBARS ALGORITHM

In DIRNSS system, due to differential measurements, these errors are greatly reduced or eliminated. To reduce the impact of ionospheric delay in this paper IF linear combination is used [4]. In IF method, the first-order effect of the ionosphere is eliminated. In addition to the IF combination, the proposed RBARS algorithm eliminates the effects of multipath, receiver/satellite offsets etc. Due to the differentiation of two receivers, the hardware delays are also reduced. The convergent time is greatly reduced, and thereby the position accuracy is improved. Therefore, this is the advantage of using of RBARS algorithm. The following are the steps to determine the positional errors in RBARS algorithm.

a. Initially, the two IRNSS receivers (manufactured by Accord software Pvt limited) are kept a few meters distance away from each other at known coordinates. Measure the baseline length and collect the data sets in RINEX/CSV format from IGS IRNSS-GUI.

b. Select the WL classified type: SFSD/SFDD /DFSD/DFDD.

c. Apply the integer fixing using WL/WNL calculations and compute the fixed ambiguity and averaging of cycles (Table I). [5].

d. The carrier phase measurement also contains the hardware delay, phase bias, and receiver, satellite offsets. The WL phase observables of Single Difference (SD) between two receivers and a single satellite is written as

$$(\Phi_{L_5 S})_{iWIDE} = r_{L_5 S} + \lambda_{L_5 S} N_{L_5 S} - \frac{f_S I_S}{f_{WL}} + \frac{f_{L_5} I_{L_5}}{f_{WL}} + T_{L_5 S} + \varepsilon_{\theta, L_5 S} - c(\delta_{rx, clk} - \delta_{clk}^i) \quad (2)$$

where, I_{L_5} and I_S are the WL ionosphere delay in the

IF model, i represents the satellite number, c is the speed of light in m/s, $\delta_{rx, clk}$ is receiver offset and δ_{clk}^i is the satellite offset [6].

e. The straight mix of the WL, NL, and without ionosphere is used to fix the ambiguities (N_{WL} , N_{NL}). Here, for a couple of satellites, the position of user/rover is determined with these fixed ambiguities. The unknown state vector of size 13x1 is defined as

$$X = [x, y, z, N_{WL}, N_{NL}]_{13 \times 1}^T \quad (3)$$

where x , y , z are the unknown user/rover position in 3D plane.

f. The Line of sight vector of estimated rover position and satellites ephemeris for the design matrix is defined as:

$$U = \begin{bmatrix} (u_{xyz})_{ref, i (n-1) \times 3} & 0 & 0 \\ (u_{xyz})_{ref, i (n-1) \times 3} & I & 0 \\ (u_{xyz})_{ref, i (n-1) \times 3} & 0 & I \end{bmatrix}_{15 \times 13} \quad (4)$$

$$(u_{xyz})_i = \frac{[(x_{est} - x^i), (y_{est} - y^i), (z_{est} - z^i)]^T}{\sqrt{(x_{est} - x^i)^2 + (y_{est} - y^i)^2 + (z_{est} - z^i)^2}} \quad (5)$$

where n is the number of satellites.

The size of vector u_{xyz} is $(n-1) \times 3$ and identity matrix of size $(n-1) \times (n-1)$.

g. The refreshed covariance lattice at each epoch is given as

$$P(t_+) = U^T P U + P(t_-)^{-1} + \varepsilon_{noise} \quad (7)$$

where, P is a weight lattice for wide path mixes.

This designed weight lattice depends upon two factors like the correlation between satellite and receiver, and the standard deviation of WL/NL estimations. Therefore, the weight lattice is characterized as:

$$DRD = D\sigma_{WL}^2 ID^T \tag{8}$$

The D indicates the correlation between individual receivers and satellites. The size of D depends on the type of differencing technique (SD/DD). The $D = [-I]_{15 \times 15}$, is a unitary matrix of size (15x15) and σ_{WL} is the standard deviation of WL estimations. The characterization of NL weight grid is similar to WL. Therefore, by considering all these characteristics the weight grid is written as:

$$P = (DRD)^{-1} \tag{9}$$

h. The adjustment in the incremental rover position is characterized as:

$$\nabla X = [(U^T P U) + (P(t_-)^{-1})^{-1} U^T P L \tag{10}$$

where, $P(t_-)$ is the initial estimated covariance matrix and L is a miscellaneous vector obtained from WL, NL measurements.

i. Finally, the assessed rover position is equivalent to a steady position and prior positional vector. Therefore, the final rover position is estimated using the least square modified method as:

$$x = x_{est} + \nabla x, y = y_{est} + \nabla y, z = z_{est} + \nabla z \tag{11}$$

j. Similarly, for remaining cases DFSD/SFDD/SFSD estimated the position and compared the results.

Figure 2 represents the RBARS algorithmic steps. The first step in this algorithm includes the selection of frequency, selection of differentiation techniques, and correlation vector. The size of matrices depends on the type of differencing technique (SD/DD).

4. RESULTS AND DISCUSSIONS

The IF linear method eliminates the impact of the first-order ionosphere effect on the measurements. This linear combined IF method can stop the full ambiguity value determination. Therefore, to see the full ambiguity values and fixing these ambiguities as integers, the mixture of the WL and NL is used [7-8]. In this analysis, to fix the ambiguities the WNL is employed, and it doesn't have a direct impact on the positional error determinations [3].

In this section, the ambiguities are fixed by WL and WNL combination techniques. The uncorrelated estimations from many epochs would lessen the standard deviation of estimation [9]. These results are obtained using MATLAB software.

Table 2, represents the comparison of standard deviation with successive epochs for WL and WNL ambiguities (cycles). By averaging process, the deviation in ambiguities is decreased from SFSD to

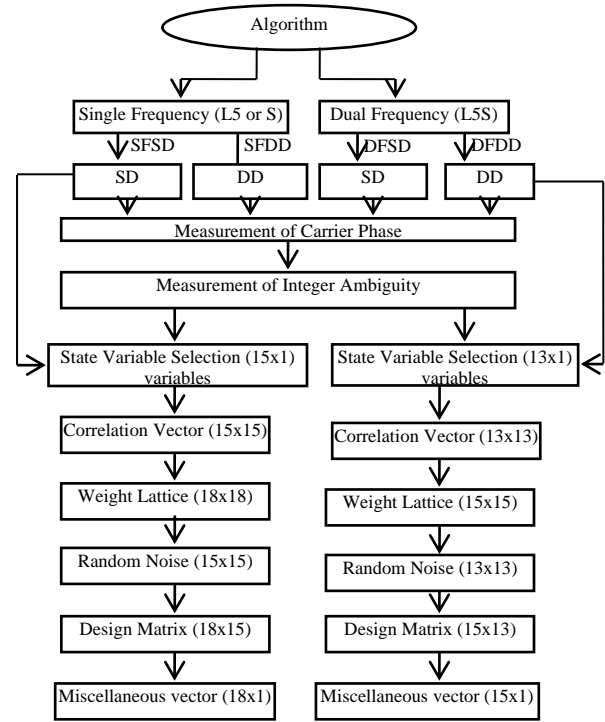


Figure 2. RBARS algorithmic steps

DFDD for both WL and WNL measurements. In WL the standard deviation is reduced from 4.7403 to 1.5749 cycles, whereas in WNL linear mix it is reduced from 1.3293 to 0.2354 cycles.

Figure 3 shows the baseline solution for SFSD (0.4 m), DFSD (0.7-0.8 m), SFDD (0.2-0.3 m), and DFDD (0.2 m). Figure 4 indicates the baseline solution in WL measurements with standard deviation. After fixing the WL ambiguities the distance error for four methods is calculated. With the fixed ambiguities, the baseline solution is better accurate compare to without averaging. It is in the range of 10-3 cm. The maximum error is obtained with SFSD and minimum error with DFDD measurement.

The main motto of WL is to generate the signal with a slightly longer wavelength; the WL can fix the ambiguities as integers in less than three minutes. In NL more than three minutes are required to fix the ambiguity because of shorter wavelength. Therefore, in a combinational mix, less than one minute is required to fix the ambiguities [10-11]. It is impossible for a single receiver to compute the initial full cycles for each

TABLE 2. Standard deviation of ambiguities in cycles

Parameter	SFSD	SFDD	DFSD	DFDD
WL (cycles)	4.7403	3.6934	3.578	1.5749
WNL (cycles)	1.3293	1.0024	0.6283	0.2354

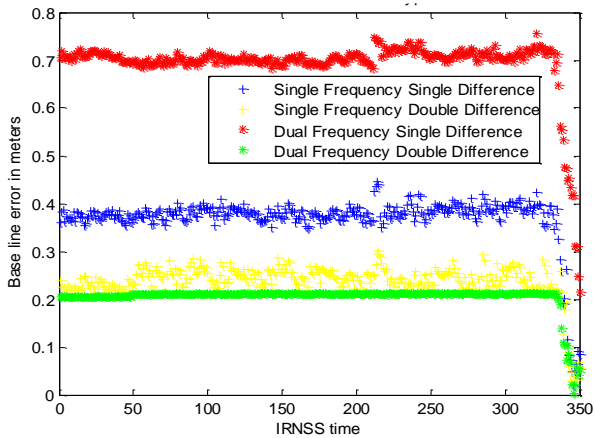


Figure 3. Baseline solutions for WL measurements without averaging

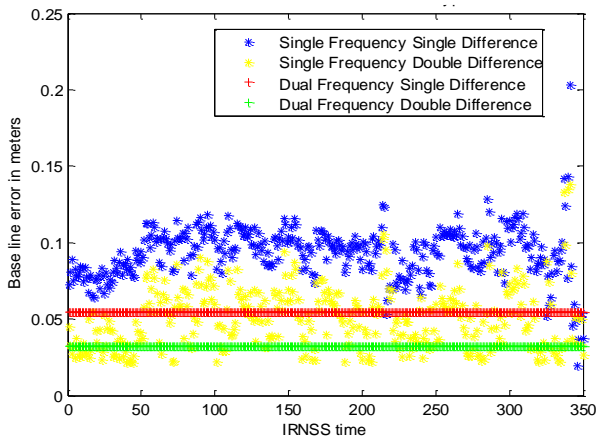


Figure 4. Baseline distance Δd with WL in meters with averaging

satellite. The RBARS algorithmic program is employed, to determine the integer value of the ambiguities by WNL combination. Using WNL linear combination the integer ambiguities are fixed. The fixed AR would have an immediate impact on position estimation. The fixing time is less in RBARS algorithm; therefore, more accurate results are obtained in position estimation. The best outcomes are obtained in the dual-carrier case.

Figure 5 indicates the estimated error in cycles. This error is calculated at every single epoch (nearly 350 epochs are taken). Here, continuous lines represent the estimated real values, and dots represent the corresponding rounding values (rounded-off integers).

From the Table 2 a succession of intervals the reduction in the standard deviation of carrier cycles ends up in higher position accuracy. At starting epochs, the utilization of RBARS algorithm ends up peak at maximum value and then stabilizes at minimum error. This stabilization is, because of the correlation between satellite, receiver, updated covariance, and state vector.

The rover position incremental values are assessed in 3D (X, Y, Z) using RBARS algorithm and forwarded this error to get the precise user/rover position [12-13]. The improvement in position occurred after fixing the ambiguities. In Table 3, the positional errors are calculated and compared for proposed WL classified methods. The RMS errors are listed in 3D (X, Y, Z) plane for a short baseline. The minimum RMS error is obtained in DFDD (50.32 cm).

From Figures 6-8, it is observed that about 30 seconds the error values are [1.5 1.2 -0.5] meters in 3D plane for DFDD, thereafter this error is diminished to

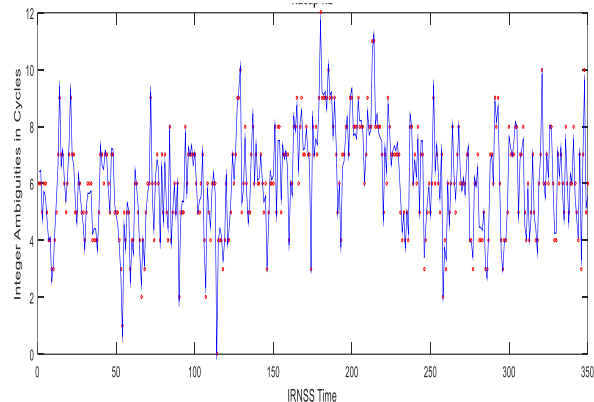


Figure 5. Resolved ambiguities and the estimated errors in cycles

TABLE 3. The RMS errors in 3D (X, Y, Z) directions of WNL four kinds

Type of WNL	RMS error (meters)			Average RMS error in 3D (meters)
	X	Y	Z	
SFSD	1.5825	1.0415	0.7575	1.1271
SFDD	0.6658	0.8278	0.3944	0.6293
DFSD	0.6700	0.8207	0.3715	0.6207
DFDD	0.7470	0.5287	0.2340	0.5032

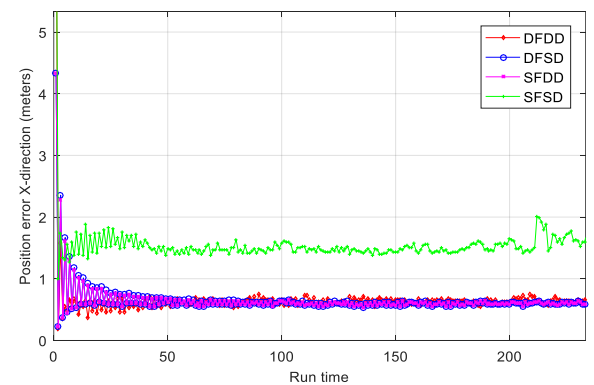


Figure 6. Positional error comparisons in four types using RBARS algorithm (X direction)

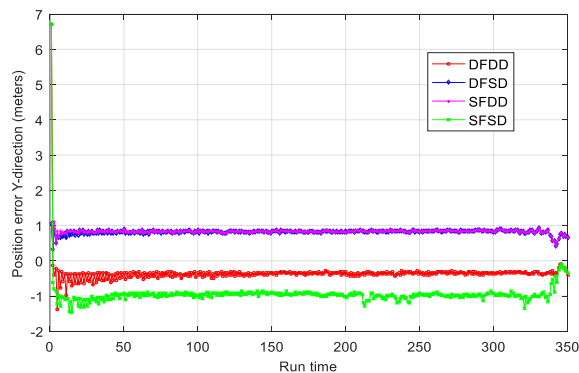


Figure 7. Positional error comparisons in four types using RBARS algorithm (Y direction)

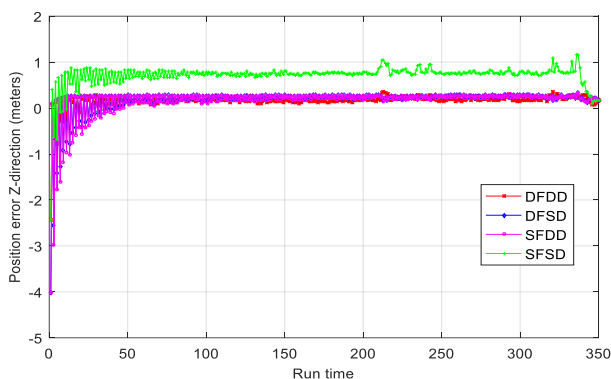


Figure 8. Positional error comparisons in four types using RBARS algorithm (Z direction)

[0.8 -0.5 0.2] meters and reaches to stable due to the correlation of measurements. Similarly, 3D positional errors are evaluated for SFSD, SFDD, DFSD, and DFDD with the least-squares modifications.

The linear combination of WNL and IF with CP measurements is implemented. These models help to resolve the ambiguities and to reduce the first-order ionosphere impact on measurements. Therefore, due to decreased convergent time the high reliable position is obtained for DF compare to SF.

5. CONCLUSION

In this paper, the WL and WNL techniques are used for AR. Using WL, WNL ambiguities are fixed, and their standard deviation is compared. The least standard deviation of 0.2354 cycles is obtained in DFDD using WNL linear mix. Therefore, a reduction in the standard deviation of carrier cycles ends up in higher position accuracy. With the averaging process, the least distance error ~3 cm is obtained for DFDD. To estimate the position combination of WL, NL, and IF CP estimations are utilized. Hence with direct amalgamate of the three methods, the incremental rover positional error in (x, y, z) 3D plane is resolved with modified least squares.

Thereby, the precise rover position in latitude, longitude, height is computed. Due to fewer error impacts in baseline solution and AR, the DFDD is reliable. This RBARS algorithm is implemented by the MATLAB software and this gives the user position at the highest accuracy. The average obtained RMS errors in the 3D position are compared for different types. Therefore, AR process, baseline solution, and position estimation (3D plane), the DFDD is reliable and best technique because of fewer error impacts.

6. REFERENCES

1. Wang Kan, Pei Chen, Safoora Zaminpardaz, and Peter J. G. Teunissen, "Precise regional L5 positioning with IRNSS and QZSS: stand-alone and combined", *GPS Solutions*, Vol. 23, No. 1, (2019), doi: 10.1007/s10291-018-0800-4
2. Ch. Rajasekhar, V. B. S. Srilatha Indira Dutt, and G. Sasibhushana Rao, "Investigation of Best Satellite-Receiver Geometry to Improve Positioning Accuracy Using GPS and IRNSS Combined Constellation over Hyderabad Region", *Springer, Wireless Personal Communications*, Vol. 88, No. 2, (2016), 385-393, doi: 10.1007/s11277-015-3126-3
3. M.R Mosavi, "Applying Genetic Algorithm to Fast and Precise Selection of GPS satellites", *Asian Journal of Applied Sciences*, Vol. 4, No. 3, (2011), 229-237, doi: 10.3923/ajaps.2011.229.237
4. Nykiel, Grzegorz, and Mariusz Figurski, "Precise point positioning method based on wide-lane and narrow-lane phase observations and between satellites single differencing", In Proceedings of the 2016 International Technical Meeting, ION ITM, (2016), 25-28, doi: 10.33012/2016.13494
5. Héroux, Pierre, and Jan Kouba, "GPS precise point positioning using IGS orbit products", *Physics and Chemistry of the Earth, Part A: Solid Earth and Geodesy*, Vol. 26, No. 6-8, (2001), 573-578, doi: 10.1016/S1464-1895(01)00103-X
6. S. N. Parveen and P. Siddaiah, "Ambiguity Resolution and Distance Error Analysis in DIRNSS System Using Dual carrier Wide Lane," 2020 International Conference on Artificial Intelligence and Signal Processing (AISP), Amaravati, India, (2020), 1-6, doi: 10.1109/AISP48273.2020.9073324
7. Ali Valizadeh and Hojatollah Hamidi, "Improvement of Navigation Accuracy using Tightly Coupled Kalman Filter," *International Journal of Engineering, Transactions B: Applications*, Vol. 30, No. 2, (2017), 215-223, doi: 10.5829/idosi.ije.2017.30.02b.08
8. Pratap Misra, and Per Enge, "Global Positioning System: Signals, Measurements, and Performance", Revised 2nd edition, 2012, doi: 10.1007/BF02106512
9. Oscar L. Colombo, Manuel Hernandez Pajares, J. Miguel Juan, and Jaime Sanz, "Wide-Area, Carrier-Phase Ambiguity Resolution Using a Tomographic Model of the Ionosphere", *Navigation*, Vol. 49, No. 1, (2002), 61-69, doi: 10.1002/j.2161-4296.2002.tb00255.x
10. Feng, Yanming, and Chris Rizos. "Network-based geometry-free three carrier ambiguity resolution and phase bias calibration." *GPS Solutions*, Vol. 13, No. 1, (2009), 43-56, doi: 10.1007/s10291-008-0098-8
11. Fabian de Ponte Muller, Diego Navarro Tapia, and Matthias Kranz, "Precise Relative Positioning of Vehicles with On-the-Fly Carrier Phase Resolution and Tracking", Hindawi Publishing Corporation, *International Journal of Distributed Sensor Networks*, Vol. 11, No. 11, (2015), doi: 10.1155/2015/459142

12. Feng Yanming, and LI Bo Feng, "Wide-area real-time kinematic decimeter positioning with multiple carrier GNSS signals", *Science China Earth Sciences*, Vol. 53, No. 5, (2010), 731-740, doi: 10.1007/s11430-010-0032-0
13. Temiissen, P. J. G, "The least-squares ambiguity decorrelation adjustment: a method for fast GPS integer ambiguity estimation", *Journal of Geodesy*, Vol. 70, (1995), 65-82, doi: 10.1007/BF00863419

Persian Abstract

چکیده

یک سیستم منطقه ای طراحی شده برای تهیه، موقعیت دقیق کاربر در هر شرایط با پوشش ۷/۲۴ است. این سیستم در طیف وسیعی از برنامه ها با دقت بهتر از ۲۰ متر در منطقه سرویس اولیه استفاده می شود. خدمات موقعیت، سرعت و زمان بندی IRNSS برای کاربران هندی و همچنین ۱۵۰۰ کیلومتری مرز هند برای کاربران مفید است. موقعیت یابی دقیق در تکنیک اندازه گیری فاز به حل ابهامات بستگی دارد. در این مقاله، تمرکز اصلی بر حل موثر ابهامات و در نتیجه تخمین موقعیت است. در این مقاله اندازه گیری Wide Lane (WL) مبتنی بر تفاوت فاز حامل (CP) پیشنهاد شده است. برای رفع ابهامات، موقعیت روشهای طبقه بندی شده WL، تخمین تک فرکانس (SFSD)، فرکانس دو فرکانس (SFDD)، اختلاف فرکانس دوگانه (DFSD) و دو فرکانس دو فرکانس (DFDD) را تخمین بزنید. این چهار نوع از طریق الگوریتم Reference Base و Reference Satellite (RBARS) برای تخمین موقعیت کاربر / مریخ نورد پردازش می شوند. در این مقاله، از آمیخته های مستقیم سه برآورد استفاده شده است WL، باریک باریک (NL) و برآورد فاز حامل آزاد یونوسفر (IF) با استفاده از این ترکیب، تخمین ابهامات برای ماهواره های جداگانه با استفاده از تکنیک های WL و NL تعیین می شود. بدین ترتیب با ارزیابی این ابهامات تعداد واقعی، موقعیت کاربر / مریخ نورد محاسبه می شود. در این کار، از تک تک شرایط استفاده شده و همراه با حداقل تغییرات مربع، خطاهای موقعیتی در صفحه سه بعدی محاسبه می شوند. میانگین خطاهای مربع ریشه محاسبه شده برای تمام روشهای طبقه بندی شده مقایسه می شود.



Demonstration of Synaptic Connections with Unipolar Junction Transistor based Neuron Emulators

İ. Devocioğlu^a, Ş. Ç. Yener^{*b,c}, R. Mutlu^d

^a Department of Biomedical Engineering, Tekirdag Namik Kemal University, Tekirdag, Turkey

^b Department of Electrical and Electronics Engineering, Sakarya University, Sakarya, Turkey

^c Electromagnetic Research Center, Sakarya University, Sakarya, Turkey

^d Department of Electronics and Telecommunication Engineering, Tekirdag Namik Kemal University, Tekirdag, Turkey

PAPER INFO

Paper history:

Received 20 October 2019

Received in revised form 02 September 2020

Accepted 03 September 2020

Keywords:

Unipolar Junction Transistor

Neuron Emulators

Artificial Neurons

Biomedical Engineering Education

ABSTRACT

Neuron emulator circuits can be used for teaching and proving concepts. Such emulators should be made with cheap and off-the-shelf components. There are bipolar and MOSFET transistor-based neuron emulator circuits heavily used in literature. Opamp-based neuron emulators are also commonly used. Such circuits provide simple and cheap solution instead of using microcontroller-based neuron emulators if many neurons are to be used in the studies such as showing circadian resonance. Unipolar junction transistor (UJT) is commonly used in industrial electronics applications. It provides a cheap timing circuit. Although there are a few UJT-based artificial neuron patents, we were unable to find research articles on UJT-based artificial neurons. In this study, we examined a simple network of UJT-based artificial neurons and show their spiking and bursting behavior with synaptic connections between neurons. It is shown that the firing rate of a UJT-neuron can be increased by utilizing spikes generated by another one with simulations. This behavior represents excitatory connectivity between two neurons.

doi: 10.5829/ije.2020.33.11b.10

NOMENCLATURE

R	Resistor	C	Capacitor
η	Intrinsic stand-off ratio of an UJT	B_1, B_2	Biases of UJT
V	Voltage	E	Emitter of UJT
f	Frequency	V_{TH}	Emitter threshold of UJT

1. INTRODUCTION

Hudgkin-Huxley neuron model have resulted in a Nobel prize [1, 2]. This model is quite complex to emulate with electronic circuits and that's why simplified neuron models are commonly used in artificial neural network studies [3, 4]. Fitzhugh-Nagumo model is a simplified neuron model whose circuit emulator is the first made historically [5, 6]. Neuron emulators are commonly used in neuroscience for education and studies [7-13]. As public awareness increases in life sciences, demand for easy-to-build and low-cost tools increases.

A unijunction transistor (UJT) is a three-terminal, semiconductor device which shows negative resistance and switching characteristics for use as a relaxation oscillator in phase control applications. Unipolar junction transistor is a commonly used component in triggering circuits of industrial electronics applications. They provide cheap timing circuits. There are a few UJT-based artificial neuron patents [14, 15]. In addition, some recent papers are presenting UJT-based neuron models where other transistor types were also used [16, 17]. Although these models generate action potentials very similar to a real neuron, their structure is complex (i.e. inductors were used) and how the inhibitory neurons could be built

*Corresponding Author Institutional Email: syener@sakarya.edu.tr
(Ş. Ç. Yener)

is not clear. It is important to show that a UJT-based neuron emulator circuit can be made using cheap and off-the-shelf circuit components. In this manner, how ensembles of neurons work together can be shown and experimented in low-budget laboratory environments. Furthermore, we aimed to provide simpler circuit structures for easier analyses and further experimentations on artificial neural networks on devices with low specifications. They have the potential to be used in system control [18].

In this study, we examined a UJT-based artificial neuron and show that it can produce spikes as well as receiving synaptic inputs. First, a UJT-based artificial neuron circuit is given, its operation is explained, and, using simulations, its spiking behavior is demonstrated. A single neuron may encode different sensory inputs, but neural systems mostly depend on the activity of an ensemble of neurons connected via synapses. Therefore, a neural emulator needs to demonstrate a synaptic connection between neural units in a plain concept. Using UJT-based neurons, excitatory or inhibitory neurons can be mimicked with a simple modification in the circuit. We simulated an excitatory synapse between two UJT-based neurons in OrCAD PSpice. The proposed neuron and synaptic connection models can be used for educational purposes when implemented in emulators.

This article is organized as follows. A brief introduction to UJT is made in the second section. A UJT-based neuron model is given and its operation is explained in the third section. The simulation results are given in the fourth section. The article is finished with the conclusion section.

2. UNIUNCTION TRANSISTOR

Unijunction Transistor symbol is shown in Figure 1a. It has three legs designated as B_1 , B_2 , and E. It is made of p and n type regions and it has only one p-n junction shown in Figure 1b. It has a different characteristic than Bipolar junction transistors (BJTs). They are not used to amplify signals like BJTs and MOSFETs. A simplified internal circuit model and circuit symbol of a UJT is given in Figure 1c. The diode models the p-n junction formed between the heavily doped p region (E) and the lightly doped n-type region and R_{BB1} and R_{BB2} resistors model the channel resistances of the n-type regions from the junction to bases B_1 and B_2 respectively. shown in the equivalent circuit. The UJTs have negative resistance property which results in their usage in triggering or timer circuits Its equivalent circuit is given in Figure 1c. Its emitter current- emitter voltage characteristic is depicted in Figure 2 and the intrinsic stand-off ratio of a UJT transistor which is used to calculate its firing frequency in oscillator applications is given as:

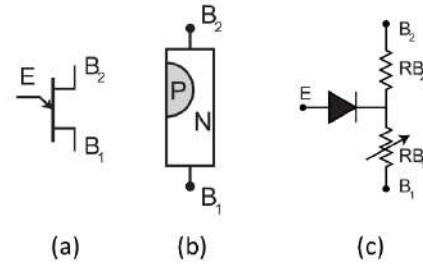


Figure 1. (a) UJT symbol (b) UJT topology and (c) UJT equivalent circuit

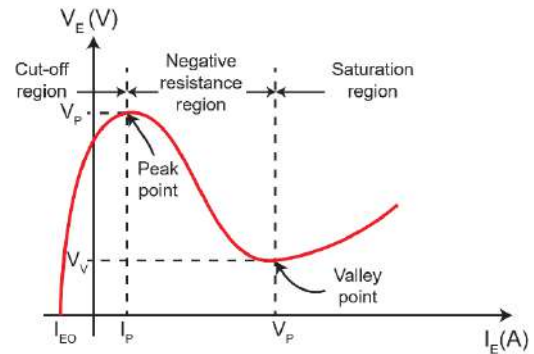


Figure 2. Static emitter current-voltage characteristic for a Unipolar Junction Transistor

$$\eta = R_{BB1} / (R_{BB1} + R_{BB2}) \quad (1)$$

where R_{BB1} and R_{BB2} base resistors. Typical values of η range from 0.4 to 0.8 for most common UJT's. The emitter threshold voltage of a UJT transistor with a silicon p-n junction called the firing voltage of UJT is given as:

$$V_{TH} = \eta V_{BB1-BB2} + V_D = \eta V_{BB1-BB2} + 0.7 \quad (2)$$

This is the minimum value of the emitter voltage V_E for which current starts flowing through the emitter. As V_E increases, so does the emitter current I_E . When V_E increases to a particular point called the peak voltage V_P . At this point, a significant amount of I_E flows and a substantial number of holes are injected into the junction.

These holes are attracted by B_1 and repelled by B_2 . Consequently, the region between E and B_1 terminal gets saturated by injected holes, and the electrical conductivity of this region increases. This increased conductivity reduces R_{BB1} and η . This results in a situation where I_E increases and V_E decreases. This condition is similar to a negative resistance scenario. In Figure 2, it can be seen that, If the emitter voltage reaches V_P , it starts operating in negative resistance region and its voltage falls to V_F . The curve between V_P and V_V (valley voltage) has a negative slope. This negative resistance characteristic makes the UJT employed in relaxation oscillators and in triggering circuits. Finally, I_E gets

increased to a point that no more increase in electrical conductivity is possible. This point is called the “Valley point”. The emitter current at valley point is represented as I_V . Beyond the valley point, the UJT is under complete saturation and the junction acts as a fully saturated p-n junction. When the breakdown occurs, The UJT resistance between B_1 and E falls from R_{BB1} down to R_{BB1sat} . That’s why the R_{BB1} is shown as a potentiometer.

3. UNIUNCTION TRANSISTOR-BASED NEURON EMULATOR

A commonly used UJT-based relaxation oscillator is shown in Figure 3. This UJT transistor-based neuron emulator circuit used also in this paper. It is made of one UJT, three resistors, and a capacitor. More information about UJT and its usage in triggering circuits can be found in textbooks [19, 20]. Its frequency is determined by R_3 and C with Equation (3).

$$f = 1 / (R_3 C \ln(1 / (1 - \eta))) \tag{3}$$

The UJT transistor-based neurons used in this paper are similar to those shown in Figure 4. It is simulated in OrCAD PSpice and the neuron emulator waveforms are shown in Figure 5.

We aimed to model synaptic connections between different UJT-neurons in a simplified context, rather than firing behavior of a single UJT-neuron. Therefore, we preferred a plain version of the UJT-neuron compared to [15].

4. SIMULATION RESULTS OF TWO NEURONS WITH SYNAPTIC CONNECTION

In this section, we used the emulator circuit given in the previous section to show the synaptic connection between two neurons. The circuit is given in Figure 6 to show how a synaptic connection can be modeled between two neurons. The circuit has two UJTs, each one of which

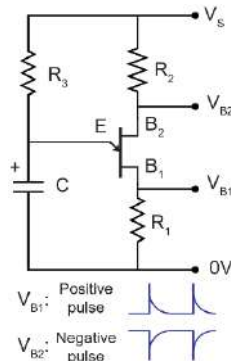


Figure 3. UJT-based relaxation oscillator

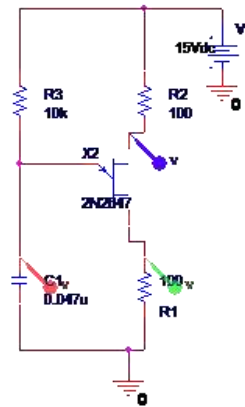


Figure 4. Neuron emulator circuit schematic drawn in OrCAD SPice

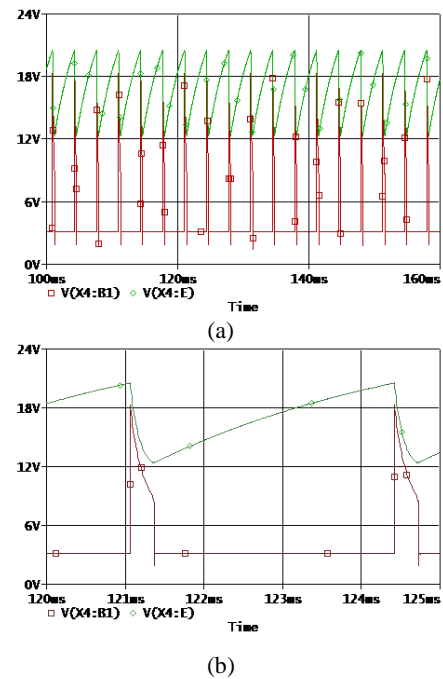


Figure 5. Neuron emulator waveforms. (a) The voltages of the capacitor and the resistor R1 vs. time (b) Zoomed the voltages of the capacitor and the resistor R1 vs. time

is used for making a neuron unit. The neurons are called U1 (the left one, also called a presynaptic neuron) and U2 (the right one, also called a postsynaptic neuron). The synaptic connection between two neurons is modeled with a resistor (R11) connecting the output of the first unit to the emitter of the next unit. A diode is used to ensure the connection is one-way. The Neuron Emulators are made of the components given in Table 1. The simulated waveforms are shown in Figure 7 (U1: red traces, U2: green traces). If the neuron circuits were in isolation, they would fire independently. However, here, they are connected through the resistor R11 which lets

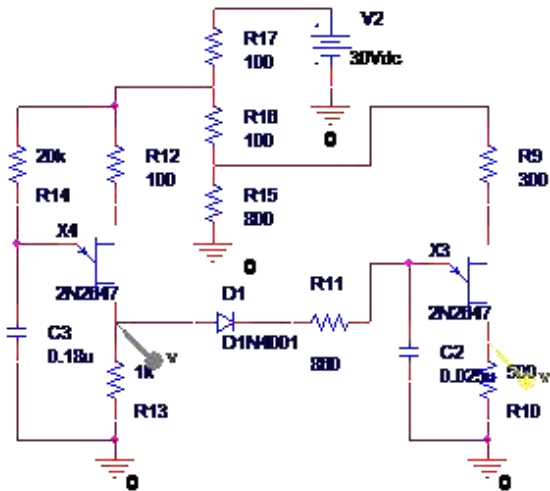


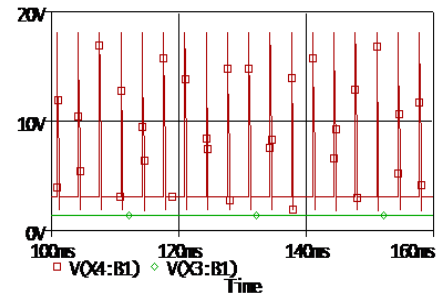
Figure 6. UJT-based two neurons with a synapse

TABLE 1. The Component Values of the Circuit Shown in Figure 6

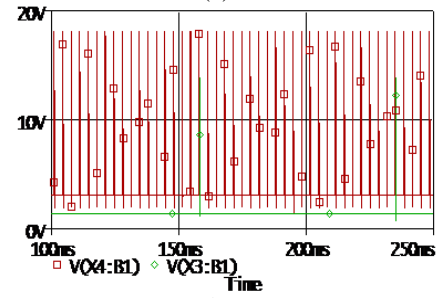
Components	
Resistors	R9=300 Ω, R10=500 Ω, R11=860 Ω, R12=100 Ω, R13=1 KΩ, R14=20 KΩ, R15=800 Ω, R16=100 Ω, and R17=100, Ω
Capacitors	C2=0.025 uF and C3=0.18 uF
Diode	1N4001
UJTs	2N2647
Source	V2=30 V

them interact. The first one’s frequency is not affected much although the second one U2 is also fed by the first one. The firing frequency of the second one is affected by the first one. Both of the neurons are fed by the same voltage source V_{cc} . The second one is fed by a lower voltage from the source V_{cc} using a voltage divider shown in Figure 7. The neuron circuit U1 is fed with a higher voltage than U2.

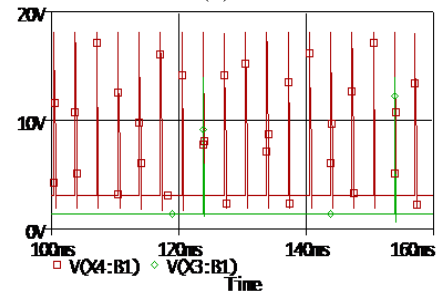
Figure 7a–e shows the results of the simulation for different synaptic weights between two neurons considering R11 as 100 MΩ, 5kΩ, 1.5kΩ, 100Ω, and 0 Ω, respectively. For modeling a very weak synaptic connection (e.g. U2 receives minimum synaptic input from U1), we had chosen a very high R11 (100 MΩ, i.e. almost open-circuit case) (Figure 7a). In this case, although U1 fired at its predefined rate, U2 didn’t generate any spikes. This is because C2 is charging through a very high R11 with a spike-like voltage input which prevents U2 to reach its threshold and generate a spike. As the synaptic strength increases (by decreasing R11), the firing rate of U2 increases while U1 continues to generate spikes at its predefined rate (Figure 7b-d). By decreasing R11, C2 is charging at a higher rate, and as a



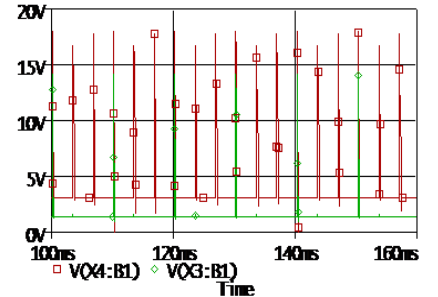
(a)



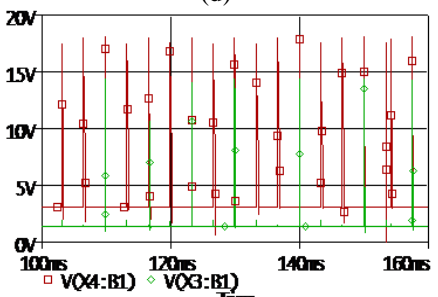
(b)



(c)



(d)



(e)

Figure 7. Effect of R11 which represents the synaptic coupling between U1 and U2. Synaptic connection increases from (a) to (e) (i.e. R11 decreases: 100MΩ, 5kΩ, 1.5kΩ, 100Ω and 0Ω). Red traces are for U1 and green traces are for U2

result, U2 is more likely to generate spikes. For example, if R11 is chosen $5k\Omega$, then U2 generates 1 spike for every 22 spikes of U1. In other words, after U1 fired 22 spikes, C2 charged to the threshold of U2 and made U2 fire a spike. If synaptic strength is increased by, for example, choosing R11 100Ω , then U2 fires at 1/3 rate of U1. In this case, C2 charged at a higher rate due to lower R11, so the firing rate of U2 increased. If R11 is chosen very small (i.e. it is shorted), which represents a very strong synaptic connection (i.e. saturated), then U2 generates spikes for every 2 or 3 spikes of U1 (Figure 7e). In this case, every spike generated by U1 directly charged C2 without R11, which is shorted. Therefore, higher firing rates were expected for U2 compared to the cases where R11 was not shorted. However, since the duration of spike pulses generated by U1 are so short that charging of C2 still takes some time (i.e. 2 or 3 spikes of U1) even when R11 was shorted. Therefore, this condition indicates a saturated synaptic coupling between two neurons. Overall, these results confirm our simplistic synapse model in UJT-based neurons.

The proposed UJT-based neuron and synaptic connection models are designed to be built with off-the-shelf components at a low cost. The models proposed by Tagluk [16] and Tagluk and Isik [17] consist of a voltage variable resistor (for synaptic connection), two capacitors, three resistors, one UJT, one BJT, and one DC source [17, 18]. The excitation of the neuron model was achieved with an AC source. Two units were coupled with a series of RLC circuits to mimic the axonal behavior of the neuron. In the current study, we used a simpler version of the neuron model which consisted of three resistors, one capacitor, one UJT, and one DC source. The synaptic coupling between two units was achieved with a diode and a resistor. Although the behavior of the former model is more realistic, it is harder to implement. The UJT-based neuron emulator and synaptic connection model proposed here can be used as an easy-to-demonstrate education material in low-budget laboratories. Furthermore, since the model had a minimum number of components, a more complex ensemble of neurons can be easily simulated on computers with low specifications or built on protoboards.

5. CONCLUSION

In this study, it is shown that a UJT-based neuron emulator circuit with a synaptic connection can be made using cheap off-the-shelf components easily. We demonstrated the firing rate of a UJT-neuron can be increased by utilizing spikes generated by another one with simulations made in OrCAD PSpice. This behavior represents excitatory connectivity between two neurons. Similarly, inhibitory connections can also be built using

UJT-neurons which would generate spikes with a negative voltage. If this neuron is connected to another unit as shown in Figure 6 (with an inversed diode direction), its negative spikes would discharge the capacitor of the postsynaptic neuron. As a result, the postsynaptic neurons firing period would elongate (i.e. firing rate would decrease). Due to space considerations, this is not shown in this paper. It is also possible to connect more than two UJT-neurons to a single postsynaptic unit via different resistors. The UJT-based neuron emulators would help teach neuroscience and biomedical engineering. They can also be improved by using VLSI circuits and used for neural studies.

6. REFERENCES

- Hodgkin, A.L. and Huxley, A.F., "A quantitative description of membrane current and its application to conduction and excitation in nerve", *The Journal of Physiology*, Vol. 117, No. 4, (1952), 500. doi: 10.1113/jphysiol.1952.sp004764
- FitzHugh, R., "Mathematical models of threshold phenomena in the nerve membrane", *The Bulletin of Mathematical Biophysics*, Vol. 17, No. 4, (1955), 257-278.
- Izhikevich, E.M., "Which model to use for cortical spiking neurons?", *IEEE Transactions on Neural Networks*, Vol. 15, No. 5, (2004), 1063-1070. doi: 10.1109/TNN.2004.832719
- Izhikevich, E.M. and Hoppensteadt, F., "Classification of bursting mappings", *International Journal of Bifurcation and Chaos*, Vol. 14, No. 11, (2004), 3847-3854. doi: 10.1142/S0218127404011739
- Nagumo, J., Arimoto, S. and Yoshizawa, S., "An active pulse transmission line simulating nerve axon", *Proceedings of the IRE*, Vol. 50, No. 10, (1962), 2061-2070. doi: 10.1109/JRPROC.1962.288235
- FitzHugh, R., "Impulses and physiological states in theoretical models of nerve membrane", *Biophysical Journal*, Vol. 1, No. 6, (1961), 445. doi: 10.1016/s0006-3495(61)86902-6
- Gonzales, O.A., Han, G., De Gyvez, J.P. and Sánchez-Sinencio, E., "Lorenz-based chaotic cryptosystem: A monolithic implementation", *IEEE Transactions on Circuits and Systems I: Fundamental Theory and Applications*, Vol. 47, No. 8, (2000), 1243-1247. doi: 10.1109/81.873879
- Linares-Barranco, B., Sánchez-Sinencio, E., Rodríguez-Vázquez, A. and Huertas, J.L., "A cmos implementation of fitzhugh-nagumo neuron model", *IEEE Journal of Solid-State Circuits*, Vol. 26, No. 7, (1991), 956-965. doi: 10.1109/4.92015
- Rajasekar, S., Murali, K. and Lakshmanan, M., "Control of chaos by nonfeedback methods in a simple electronic circuit system and the fitzhugh-nagumo equation", *Chaos, Solitons & Fractals*, Vol. 8, No. 9, (1997), 1545-1558. doi: 10.1016/S0960-0779(96)00154-3
- Tamaševičiūtė, E. and Mykolaitis, G., "Analogue modelling an array of the fitzhugh-nagumo oscillators", *Nonlinear Analysis: Modelling and Control*, Vol. 17, No. 1, (2012), 118-125. doi: 10.15388/NA.17.1.14082
- Zhao, J. and Kim, Y.-B., "Circuit implementation of fitzhugh-nagumo neuron model using field programmable analog arrays", in 2007 50th Midwest Symposium on Circuits and Systems, IEEE, (2007), 772-775. doi: 10.1109/MWSCAS.2007.4488691
- Petrovas, A., Lisauskas, S. and Slepikas, A., "Electronic model of fitzhugh-nagumo neuron", *Elektronika Ir Elektrotechnika*, Vol.

- 122, No. 6, (2012), 117-120. doi: 10.5755/j01.eee.122.6.1835
13. Tamaševičius, A., Bumelienė, S., Mykolaitis, G., Tamaševičiūtė, E. and Kirvaitis, R., "Desynchronization of mean-field coupled oscillators by remote virtual grounding", in 18th IEEE Workshop on Nonlinear Dynamics of Electronic Systems (NDES'2010).–Dresden, Germany. (2010), 30-33.
 14. Putzrath, F.L., *Processing apparatus utilizing simulated neurons*. 1965, Google Patents.
 15. Askew, W.J., *Unijunction transistor artificial neuron*. 1972, Google Patents.
 16. Tağluk, M.E., "A new dynamic electronic model of neuron's membrane", *Anatolian Science-Bilgisayar Bilimleri Dergisi*, Vol. 3, No. 1, (2018), 1-6.
 17. Tağluk, M.E. and Isik, I., "Communication in nano devices: Electronic based biophysical model of a neuron", *Nano Communication Networks*, Vol. 19, (2019), 134-147. doi: 10.1016/j.nancom.2019.01.006
 18. Chaturvedi, D., Malik, O. and Kalra, P., "Studies with a generalized neuron based pss on a multi-machine power system", (2004).
 19. Boylestad, R.L. and Nashelsky, L., "Electronic devices and circuit theory, Prentice Hall, (2012).
 20. Chitode, J., "Power electronics, Technical publications, (2009).

Persian Abstract

چکیده

از مدارهای شبیه ساز نوروں می توان برای آموزش و اثبات مفاهیم استفاده کرد. چنین شبیه سازهایی باید با اجزای ارزان و خارج از قفسه ساخته شوند. مدارهای شبیه ساز نوروں مبتنی بر ترانزیستور دو قطبی و MOSFET وجود دارد که به شدت در ادبیات استفاده می شود. از شبیه سازهای عصبی مبتنی بر Opamp نیز معمولاً استفاده می شود. در صورت استفاده از بسیاری از سلولهای عصبی در مطالعاتی مانند نمایش رزونانس شبانه روزی، از چنین مدارهایی به جای استفاده از شبیه سازهای عصبی مبتنی بر میکروکنترلر، راه حل ساده و ارزان ارائه می شود. ترانزیستور اتصال تک قطبی (UJT) معمولاً در کاربردهای الکترونیک صنعتی استفاده می شود. این یک مدار زمان بندی ارزان را فراهم می کند. اگرچه چند حق ثبت اختراع نوروں مصنوعی مبتنی بر UJT وجود دارد، ما قادر به یافتن مقالات تحقیقاتی در مورد نوروں های مصنوعی مبتنی بر UJT نبودیم. در این مطالعه، ما یک شبکه ساده از سلولهای عصبی مصنوعی مبتنی بر UJT را بررسی کردیم و رفتار جهشی و ترکیبگی آنها را با اتصالات سیناپسی بین سلولهای عصبی نشان دادیم. قابل ذکر است که می توان با استفاده از سنبله های تولید شده توسط دیگری با شبیه سازی، میزان شلیک یک نوروں UJT را افزایش داد. این رفتار نشان دهنده اتصال تحریکی بین دو نوروں است.



Digital Root-mean-square Signal Meter

O. V. Chernoyarov^{*a,b,c}, A. N. Glushkov^d, V. P. Lintvinenko^e, B. V. Matveev^e, A. N. Faulgaber^c

^a International Laboratory of Statistics of Stochastic Processes and Quantitative Finance, National Research Tomsk State University, Tomsk, Russia

^b Department of Mathematics, Physics and System Analysis, Faculty of Engineering, Maikop State Technological University, Maikop, Russia

^c Department of Electronics and Nanoelectronics, Faculty of Electrical Engineering, National Research University "MPEI", Moscow, Russia

^d Department of Infocommunication Systems and Technologies, Voronezh Institute of the Ministry of Internal Affairs of the Russian Federation, Voronezh, Russia

^e Department of Radio Engineering, Voronezh State Technical University, Voronezh, Russia

PAPER INFO

Paper history:

Received 19 July 2020

Received in revised form 31 August 2020

Accepted 03 September 2020

Keywords:

Alternating Signal

Root-mean-square Value

Meter

Fast Digital Processing

Simulation

ABSTRACT

This paper introduces a meter of the root-mean-square value of deterministic and stochastic signals of an arbitrary shape that are generated over the set time interval. Such a meter involves only the minimum number of simple arithmetic operations to obtain results, and it ensures a high degree of measurement accuracy. For this purpose, the direct calculation of the signal root-mean-square value is applied while the measurement of the half-period average straightened signal value is carried out by means of the traditional measurement devices. Implementation of this meter requires neither the knowledge of what the signal period is, nor the synchronization with the processed sampling. Simulation is then carried out demonstrating the high efficiency of the proposed measurement algorithm. We analyze the characteristics of the meter operating within a wide frequency range of the measurable signals. The recommendations concerning the hardware implementation of such a meter by means of the field programmable gate arrays are considered. The meter can be used when designing digital high-frequency AC voltmeters and ammeters and it can provide the readings that do not depend upon the signal waveform.

doi: 10.5829/ije.2020.33.11b.11

1. INTRODUCTION

Measuring the root-mean-square (RMS) values of alternating signals (currents and voltages) is a common task in various areas of electronic engineering [1-4]. There are various ways to perform such measurement [5, 6] that can be divided into several groups.

In the first group, the measuring principle is that the AC voltage is converted into the constant one using a rectifier, then the result is measured. On this basis, various high-precision measuring chips (RMS-to-DC converters) have been designed, for example, the ones provided by Analog Devices [7] and some other companies. In these devices, the half-period average

straightened value of a signal is measured and its scaling into the RMS value is carried out. A drawback of such devices is that their measurement results depend upon the waveform. Thus, for the common non-harmonic signals, it is necessary to recalculate the readings using a pre-calculated coefficient (Crest factor) specified for a particular waveform. If the waveform is unknown or if it changes during the operation, then the results of such measurements are invalid.

The second group of meters includes the devices with the direct reaction to the signal RMS value. First of all, these are thermal meters [5, 6] operable only when the input signal is powerful enough. Their drawback is their low accuracy.

*Corresponding Author Institutional Email: chernoyarovov@mpei.ru
(O. V. Chernoyarov)

The third group belongs to the analog RMS signal meters (True RMS-to-DC Converters) [7, 8]. They operate via generating the analog voltage RMS value by multiplying, integrating and extracting the square root from the result. They allow for a relatively simple technical implementation, but their accuracy is not very high, because performance of mathematical operations for signal processing is only approximately correct as it is influenced by the changes in environmental parameters.

A separate group is also formed by the digital meters of signal RMS values that use a digital signal processor (DSP) to process a particular sample of binary sampling codes by carrying out digital multiplication, integration (summation, accumulation) and square root operations [6]. Digital meters make it possible to apply the method of determining the signal RMS value by calculating its amplitude spectrum [7], but it presupposes significant computational costs for spectral analysis.

If the signal period is known or can be measured, a relatively small sample size can be chosen within this interval. Such an approach is implemented, for example, in digital oscilloscopes². At the same time, under the unknown signal period, a big sample size is required and that leads to a larger number of summations, which results in increasing the computational costs and decreasing the measurement operating speed. In addition, in common devices [6], the signal sampling frequency should be significantly greater than the signal bandwidth.

To implement the integration operation, a digital first-order low-pass infinite impulse response filter (IIR filter) is applied. However, in this case, the measurement accuracy depends on the measured signal frequency properties. This can only be acceptable in special cases, for example measuring either the voltage or the current in a power network.

The RMS value of a signal can be obtained more accurately by directly processing the recorded samples of the input signal as provided by the standard calculation algorithm [9]. However, in this case, the problem of real-time measurement implementation takes place. In this paper, in order to overcome this difficulty, it is proposed to use the fast processing algorithm in the procedures described in [10, 11]. The mathematical substantiation of the measuring procedure and the block diagram of the meter suitable for its software and hardware implementation are presented. The results of measuring deterministic signals and noise are analyzed by means of simulation. The problems of choosing the signal sampling frequency and the hardware implementation of the meter are also considered. It is shown that application of the proposed approach allows us to design high-precision devices that

can measure the signal RMS value that are invariant to the shape of the input signal.

The structure of the paper includes the following parts. In Section II, we present algorithms for calculating the signal RMS value for the cases when signal period is either known or unknown. We analyze the maximum errors in estimation of both the harmonic RMS values and the rectangular pulse sequences with different pulse ratios. It is noted that the brute force computation of the arbitrary signal RMS value requires a large number of addition operations. Section III presents the fast algorithm for measuring the arbitrary signal RMS value together with the block diagram of the corresponding meter. Analysis for the accuracy of the harmonic RMS value measurement is carried out by means of simulation. The artificial network voltage measurement accuracy is also tested using the same method. In Section IV, an example for measuring the band Gaussian process RMS value is provided, and it supports the operability and the efficiency of the introduced algorithm that are demonstrated during processing random signals. In Section V, a technique is described for choosing the sampling frequency for the analog-to-digital converter (ADC) of the measurement. It is shown that the proposed meter ensures high accuracy measurements within a wide range of signal frequencies. Finally, in Section VI, the hardware components required for the measurement implementation are specified.

2. CALCULATING THE ROOT-MEAN-SQUARE SIGNAL

The RMS value of a periodic signal with an arbitrary shape (current or voltage) $s(t)$ is determined by the expression [9, 12]:

$$S_{RMS} = \sqrt{\frac{1}{T_0} \int_{t_0}^{t_0+T_0} s^2(t) dt}, \quad (1)$$

where T_0 is the signal period, and t_0 is any arbitrary reference time of integration upon which the value of the integral (1) does not depend on. In order to calculate the value (1), it is necessary to know the signal period, but that is not always implementable, especially, when the signal frequency changes during measurements.

For an arbitrary integration interval T , firstly, one defines the value

$$S_{RMS} = \sqrt{\frac{1}{T} \int_{t_0}^{t_0+T} s^2(t) dt}. \quad (2)$$

It coincides with (1) when T is a multiple of T_0 and, in the general case, depends upon T and t_0 . The value

² www.rohde-schwarz.com

\tilde{S}_{RMS} can be considered as an estimation of the signal RMS value and its calculation does not require the knowledge of T_0 .

If the harmonic signal

$$s(t) = S \cos(\omega t + \varphi) \tag{3}$$

is processed, then, from (2), one gets

$$\tilde{S}_{RMS} = S_{RMS} \sqrt{1 + \frac{1}{\omega T} \cos(2\omega t_0 + 2\varphi + \omega T) \sin(\omega T)}, \tag{4}$$

where $S_{RMS} = S/\sqrt{2}$ is the exact RMS value of the periodic signal [5]. In (3), the notations are: S is the amplitude, $\omega = 2\pi/T_0$ is the frequency, φ is the initial phase of the signal. As the product of trigonometric functions in (4) is not greater than unity in absolute value, the relative error of estimating (4) from the integral (2) is determined by the inequality

$$\delta = \left| \frac{\tilde{S}_{RMS} - S_{RMS}}{S_{RMS}} \right| \leq \delta_{\max} = \frac{1}{4\pi K}, \tag{5}$$

where $K = \text{int}\{T/T_0\}$ is the number of signal periods within the integration interval, $\text{int}\{\cdot\}$ is an integer part.

Figure 1 shows the dependence of δ_{\max} (5) upon the normalized integration time T/T_0 . As it can be seen, this error is less than 0.8% under $K = 10$.

One of the most common models of inharmonic signals is the rectangular pulse. If, under the period T_0 and the duration τ (pulse ratio $Q = T_0/\tau$), the RMS value of positive rectangular pulses with the amplitude S is measured, then the maximum relative measurement error can be represented as [5], [6]

$$\delta_{\max} = \sqrt{\frac{Q(K+1)}{KQ+1}} - 1. \tag{6}$$

The values of δ_{\max} (6) with $Q = 2$ and $Q = 4$, are shown in Figure 2a and Figure 2b, respectively. It follows that, in these cases, the measurement error is high, but it becomes acceptable under $T/T_0 > 10 \dots 20$. Thus, the RMS estimation using (2) does not require knowledge of the signal period and provides a sufficiently high accuracy when $K > 10 \dots 20$.

If N samples are available from signal s_i , then the integral in (2) can be calculated by the method of rectangles as follows [13]:

$$\tilde{S}_{RMS_i} = \sqrt{\frac{1}{N} \sum_{k=0}^{N-1} s_{i-k}^2}. \tag{7}$$

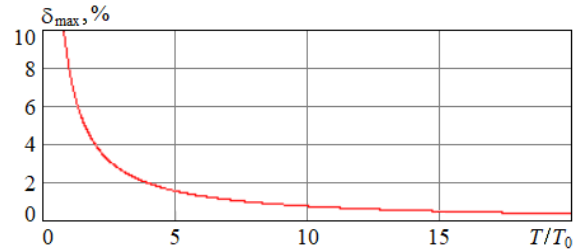


Figure 1. The maximum error of estimating the harmonic root-mean-square value

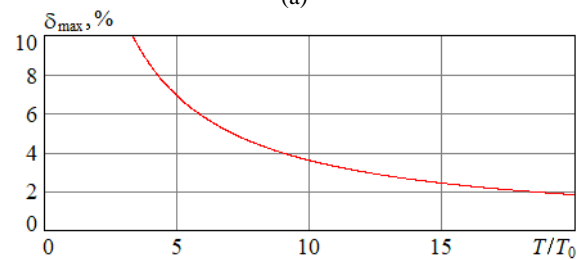
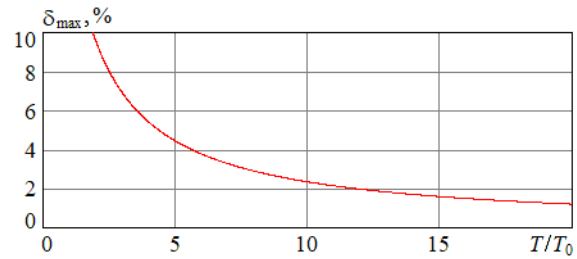


Figure 2. The maximum error of estimating the root-mean-square value of the rectangular pulse sequence with the different pulse ratios: a) $Q = 2$; b) $Q = 4$

It should be noted that numerical integration methods [19] require the generation of $K_0 = 50 \dots 200$ samples over the signal period. Thus, when measuring the signal RMS value, it is necessary to take $N = K_0 K \gg 1000$ samples from the ADC output, and the measurement accuracy will increase with N . Therefore, in order to effectively implement the estimation using (7), a fast computational procedure should be used with a minimum number of arithmetic operations. It is proposed to apply such a procedure that is based on the general approach of fast digital signal processing described in [10, 11].

3. THE ALGORITHM FOR MEASURING THE SIGNAL RMS VALUE

In Figure 3, the block diagram of measuring the signal RMS value is presented.

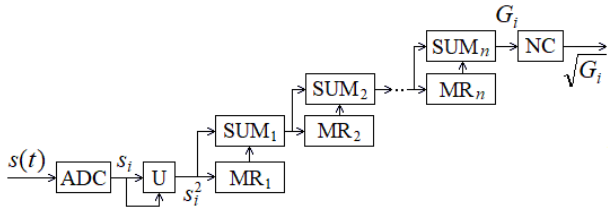


Figure 3. The block diagram of the meter of the signal RMS value

The input signal $s(t)$ arrives at the ADC input that generates the sequential samples s_i , where i is the number of the current sample, with the sampling frequency f_S . The samples s_i are passed to the square-law converter that can be implemented, for example, by means of the digital multiplier (U). In the first summator SUM_1 , the square of the sample s_i^2 produced at the output of the square-law converter is added to the preceding value s_{i-1}^2 that has been previously stored in the multi-bit one cell shifter MR_1 . Thus, at the output of the summator SUM_1 the value $s_i^2 + s_{i-1}^2$ appears. In the summator SUM_2 , this result is added to the value $s_{i-2}^2 + s_{i-3}^2$ that has been stored in the multi-bit two cell shifter MR_2 . After that, at the output of the summator SUM_2 , the sum $s_i^2 + s_{i-1}^2 + s_{i-2}^2 + s_{i-3}^2$ is formed. Further, similar calculations are carried out and at the output of the last summator SUM_n one gets:

$$G_i = \sum_{k=0}^{N-1} s_{i-k}^2, \tag{8}$$

where $n = \log_2 N$ is the number of summation stages and $N = 2^n$ is the sample size by which the signal RMS value is determined. It should be noted that the summation algorithm presented in Figure 3 requires a minimum number of operations. Therefore, the minimum hardware resources are used for its implementation by means of the field programmable gate arrays, for example.

The values G_i are moved to the non-linear converter (NC) that generates the value $\sqrt{G_i}$ at its output. The easiest way to calculate the square root is to use the storage device (SD), that is a hardware implementation. In this case, at the SD address input, the G_i binary code is received while the $\sqrt{G_i}$ binary code has been pre-recorded in the specified SD memory cell. For example, if the bus-widths of address and data are the same— $D=16$, then the SD capacity is 1 Mbit, and even when $D=24$, the SD capacity of only 384 Mbit is required

and that is technically feasible. Software implementation, on the other hand, requires that the square root should be calculated using the standard algorithms, i.e., the Heron formula [13] or the power series, for example.

The analysis of the accuracy of the harmonic RMS value measurement using Equation (7) is carried out by means of simulation. In Figure 4a, the dependence is plotted for the normalized RMS value \tilde{S}_{RMS_i}/S upon the current normalized time $i = t/\Delta$ (where $\Delta = 1/f_S$ is the sampling interval). It is assumed that the signal frequency is $f_0 = \omega/2\pi = 10$ kHz (the signal period is $T_0 = 1/f_0 = 100$ μ s), the sampling frequency is $f_S = 1$ MHz ($\Delta = 1$ μ s), the sample size is $N = 4096$, the number of samples within the period is $K_0 = 100$, and the number of periods within the averaging interval is $K \approx 41$. At the initial stage, the shifters are filled during 4.096 ms, and then the current measurements are performed, and they are, as one can see, fairly accurate. The right normalized result is equal to $1/\sqrt{2}$, and it is drawn by dashed line.

Figure 4b shows the precision errors of the measurements (hundredths of a percent). Their fluctuations are caused by sample shifting during the realization of the harmonic signal.

Of particular interest is the measurement of an artificial network with the voltage of 220 V and the frequency of 50 Hz. In Figure 5, the normalized response of the RMS value meter is presented for the case when the sample size is $N = 2^{13} = 8192$ and the sampling frequency is $f_S = 10$ kHz ($\Delta = 10^{-4}$ s).

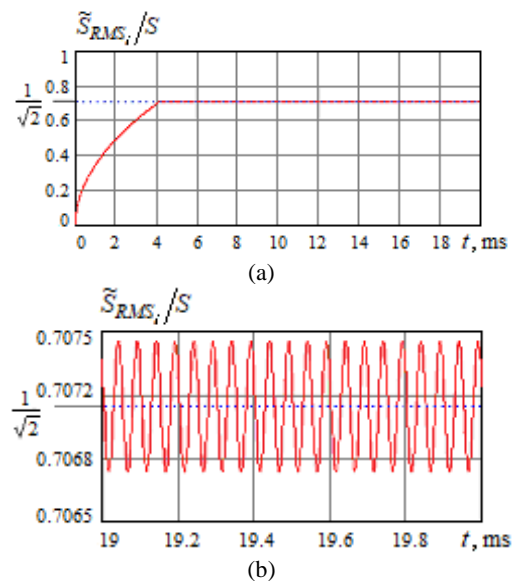


Figure 4. The results of measuring the normalized harmonic RMS value

However, the shape of the artificial network voltage and current may often differ from the sinusoidal one. Figures 6 and 7 show examples of distorted normalized signal and the result of its measurement by the introduced device. In the process, 40 periods are averaged approximately and 100 samples are generated within each period.

If the signal presented in Figure 6 is processed by a device that produces the half-period average voltage at its output while its scale is calibrated by the harmonic RMS values (such a measurement procedure is typical), then, as one can see from Figure 7, the measurement result is $\tilde{S}_{RMS}/S = 0.793$ (dashed line) while the theoretical RMS value is $\tilde{S}_{RMS}/S = 0.894$ (solid line after 0.82 s).

The analysis of the effect of m that is ADC bit-width indicates that the precision error in measuring the signal RMS value decreases significantly as m increases from

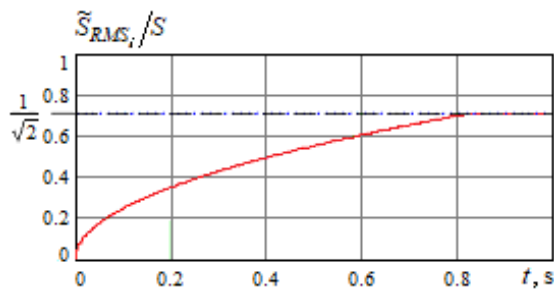


Figure 5. The results of measuring the normalized RMS value of an artificial network voltage

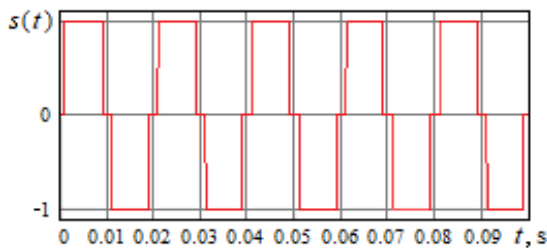


Figure 6. A distorted artificial network voltage

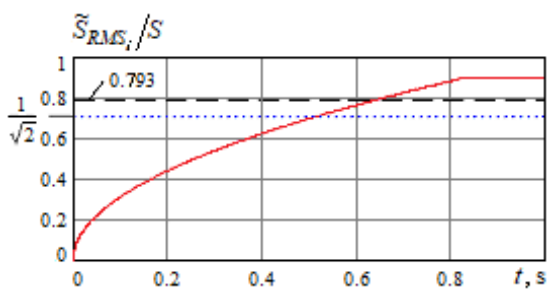


Figure 7. The results of measuring the normalized RMS value of a distorted artificial network voltage

3 to 6. However, if ADC bit-width increases further ($m \geq 8$), its precision error decreases only slightly. A significantly greater effect on decreasing the measurement precision error is produced by the increasing the sample size.

4. MEASURING THE NOISE RMS VALUE

The device presented in Figure 3 allows us to measure the RMS value of a random signal (noise).

Figure 8 shows the realization of the samples s_i of the band Gaussian random process with zero mathematical expectation and dispersion (mean power) S^2 .

Figure 9a draw dependence of the measured normalized value $\tilde{S}_{RMS,i}/S$ upon the number i of the processed sample, and in Figure 9b one can see the same dependence but for $i > N$. Under $N = 4096$ and ADC bit-width $m = 12$, the RMS relative measurement

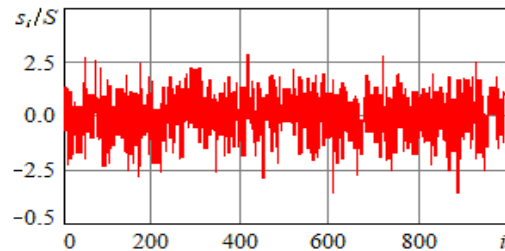
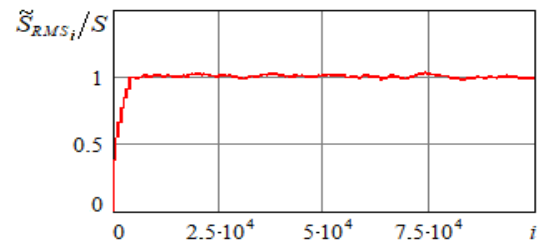
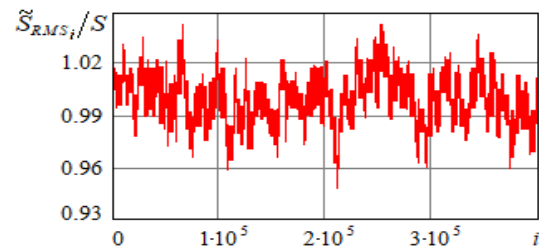


Figure 8. The realization of the centered band Gaussian random process



(a)



(b)

Figure 9. The results of measuring the normalized RMS value of the band Gaussian random process

error is equal to 1.4%. And if $N=1024$, then it increases up to 2.4%, while if $N=65536$, then it decreases down to 0.44%.

It can be noted that in order to determine the mean value and the dispersion of a random process [1], the fast-operation meter introduced in [14] can be used.

5. CHOOSING THE SAMPLING FREQUENCY

One should choose the sampling frequency f_S (sampling interval Δ) from the range $f_S=(50\dots200)f_0$ depending on the signal frequency f_0 . If the signal frequency varies within a wide limit, then it can be chosen so that, at the minimum frequency f_0 , a sufficiently large number of samples N occupies several periods $T_{0\max}=1/f_{0\min}$. This corresponds to the condition $T/T_{0\max}=Tf_{0\min}=(3\dots5)$. As

$T=N\Delta=N/f_S$, for the sampling frequency one gets:

$$f_S=N/T=Nf_{0\min}/(3\dots5). \quad (9)$$

For example, if $f_{0\min}=50$ Hz and $N=2^{10}=1024$, then, by applying (9), one can get $f_S=10$ kHz while with N increasing to $2^{16}=65536$ one gets $f_S=655$ kHz.

If, according to the rules of numerical integration [19], it is assumed that at least 20 samples are required to be generated within the signal period, then, for the maximum signal frequency, one would get the relation

$$f_{0\max}=f_S/20. \quad (10)$$

For example, if $f_S=655$ kHz and $N=2^{16}$, then one gets $f_{0\min}=50$ Hz and $f_{0\max}=32$ kHz. When implementing the meter, estimation of the signal frequency can be automatically generated and, in accordance with it, the desired sampling frequency can be chosen.

It should be noted that the measurement accuracy of the algorithm presented in Figure 3 significantly decreases, if the ratio f_S/f_0 lies in the $\pm(0.2\dots1)$ % vicinity of the values $n/2$, $n=1,2,\dots$. Figure 10 shows the results of simulating the meter operation when measuring the RMS value of the harmonic signals with the amplitude of 5 V and the different frequencies $f_{0\max}$. It is assumed that $N=4096$, $f_S=10$ kHz and the ADC is applied with the spread of ± 5 V and the bit-width $m=8$, while the sampling frequency differs for different signal frequencies. If the signal frequency is $f_0=f_S/2=5$ kHz and the initial phase φ in (3) is equal to $\pi/2$ (the samples at the ADC output

correspond to zero signal values), then the measured value of \tilde{S}_{RMS_i} is equal to zero. From Figures 10b, 10c, it follows that the precision error of measurement dramatically increases in $f_0=(f_S/2)\pm 10$ Hz vicinity.

In order to eliminate this effect, 1% random fluctuations can be introduced into the sampling frequency, for example.

In Figures 11, one can see the results of simulating the meter operation under the signal frequency $f_0=f_S/2=5$ kHz and when the random Gaussian oscillations of the sampling frequency of $f_S=10$ kHz are introduced with a standard deviation of 1 Hz.

From Figure 11, it follows that the measurement results become acceptable, and the precision error of measurement can be reduced as N increases.

The measurements of the signal RMS value can be carried out with a high accuracy at the signal frequencies that are much higher than the sampling frequency: $f_0 > f_S$. Thus, one sample takes place during several signal periods. Figure 12 shows the dependences similar to those drawn in Figure 11, if $f_S=10$ kHz and $f_0=53$ kHz (Figure 12a) or

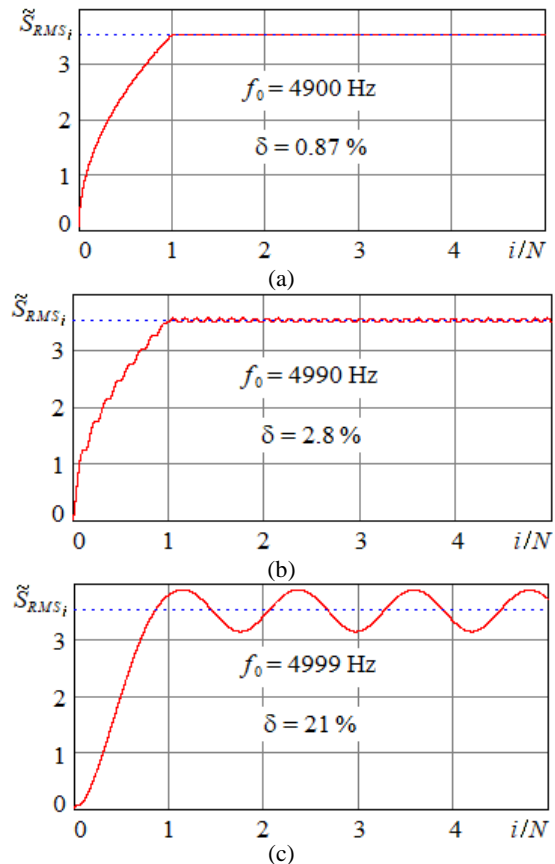


Figure 10. The influence of the ratio f_S/f_0 on the accuracy of measuring the harmonic RMS value

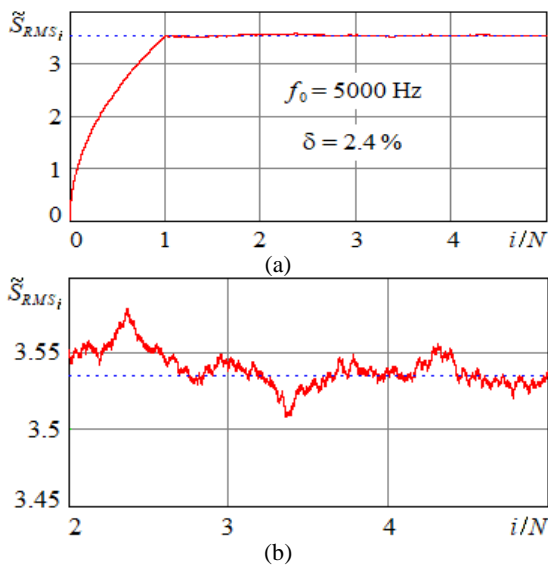


Figure 11. The results of measuring the harmonic RMS value when $f_0 = f_s / 2$

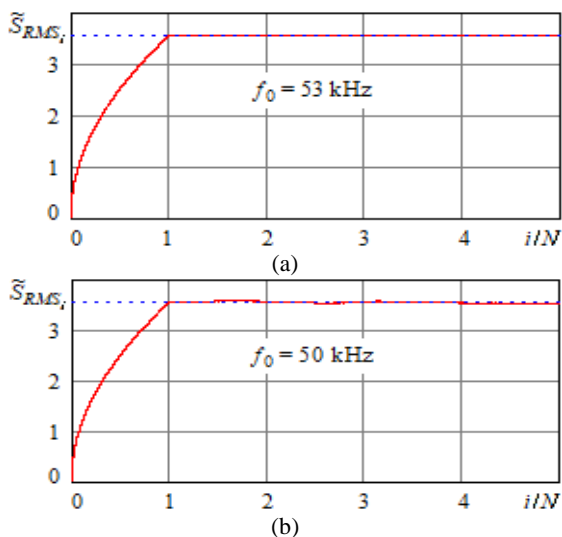


Figure 12. The results of measuring the harmonic RMS value when $f_0 > f_s$

$f_0 = 5f_s = 50$ kHz, while random oscillations of the sampling frequency are applied (Figure 12b). It is obvious that in the latter case the precision error of measurement will be greater.

Thus, the results demonstrate that the introduced signal RMS value meter provides high accuracy within a wide range of signal frequencies.

6. THE METER IMPLEMENTATION

It is recommended to implement the proposed signal RMS value meter by means of the FPGA [15]. As ADC,

for example, the integrated chips AD9211 or ADC1175 can be used. If the sample sizes $N = 2^{10} \dots 2^{14}$ are required to be processed, then relatively simple FPGA Cyclone III (produced by Altera) or Spartan-6 families (i.e., XC6SL25 produced by Xilinx, for example) can be applied.

7. CONCLUSION

The digital meter of the harmonic RMS value has been considered. It is shown that it provides the minimum number of arithmetic operations together with the high accuracy of direct measurement of the RMS value of both deterministic (harmonic and non-harmonic) signals and random processes. The precision error of measurement decreases significantly as the processed sample size increases. Based on the introduced meter, the digital high-frequency AC voltmeters and ammeters can be designed providing the readings that do not depend on the waveform and that can be implemented by means of field programmable gate arrays while utilizing minimal FPGA resources.

8. ACKNOWLEDGEMENT

This work was financially supported by the Ministry of Education and Science of the Russian Federation (research project No. FSWF-2020-0022).

9. REFERENCES

1. Maleki, M.R., Ghashghaei, R. and Amiri, A., "Simultaneous monitoring of multivariate process mean and variability in the presence of measurement error with linearly increasing variance under additive covariate model (research note)", *International Journal of Engineering, Transactions A: Basics*, Vol. 29, No. 4, (2016), 471-480, doi: 10.5829/idosi.ije.2016.29.04a.10.
2. Goudarzian, A. and Khosravi, A., "Voltage regulation of a negative output Luo converter using a pd-pi type sliding mode current controller", *International Journal of Engineering, Transactions B: Applications*, Vol. 32, No. 2, (2019), 184-191, doi: 10.5829/ije.2019.32.02b.13.
3. Gupta, P. and Pandey, R., "Voltage differencing buffered amplifier based voltage mode four quadrant analog multiplier and its applications", *International Journal of Engineering, Transactions A: Basics*, Vol. 32, No. 4, (2019), 528-535, doi: 10.5829/ije.2019.32.04a.10.
4. Aghabagheri, R., Miar-Naimi, H. and Javadi, M., "A phase noise reduction technique in IC cross-coupled oscillators with adjusting transistors operating regions", *International Journal of Engineering, Transactions A: Basics*, Vol. 33, No. 4, (2020), 560-566, doi: 10.5829/IJE.2020.33.04A.07.
5. Mazda, F.F., "Electronic instruments and measurement techniques, Cambridge University Press, (1987).
6. Webster, J.G., "Electrical measurement, signal processing, and displays, CRC Press, (2003).

7. AD, L.C., *Low power, true rms-to-dc converter, analog devices*. 2016.
8. Taha, S.M. And Abdul-Karim, M.A., "Direct digital rms measuring device", *International Journal of Electronics Theoretical and Experimental*, Vol. 59, No. 2, (1985), 199-210. doi: 10.1080/00207218508920693
9. Northrop, R.B., "Introduction to instrumentation and measurements, CRC press, (2005).
10. Chernoyarov, O., Faulgaber, A., Salnikova, A., Glushkov, A. and Litvinenko, V., "The hardware implementation of the multi-position signal digital demodulators", in 31st European Modeling and Simulation Symposium, EMSS 2019. Vol., No., (Year), 54-58.
11. Chernoyarov, O.V., Golpaiegani, L.A., Glushkov, A.N., Litvinenko, V. and Matveev, B.V., "Digital binary phase-shift keyed signal detector", *International Journal of Engineering, Transactions A: Basics*, Vol. 32, No. 4, (2019), 510-518, doi: 10.5829/ije.2019.32.04a.08.
12. Bird, J., "Engineering mathematics, Routledge, (2003).
13. Korn, G.A. and Korn, T.M., "Mathematical handbook for scientists and engineers: Definitions, theorems, and formulas for reference and review, Courier Corporation, (2000).
14. Salnikova, A.V., Litvinenko, V.P., Matveev, B.V., Glushkov, A.N., Litvinenko, Y.V. and Makarov, A.A., "The fast digital algorithm for measuring the parameters of the random processes", in 2019 International Seminar on Electron Devices Design and Production (SED), IEEE. (2019), 1-5.
15. Maxfield, C., "The design warrior's guide to fpgas: Devices, tools and flows, Elsevier, (2004).

Persian Abstract

در این مقاله یک مترینگ از مقدار میانگین مربع ریشه سیگنال های قطعی و تصادفی یک شکل دلخواه که در بازه زمانی تعیین شده تولید می شوند، معرفی می شود. برای دستیابی به نتیجه چنین سنجی فقط شامل حداقل تعداد عملیات ساده محاسباتی است و درجه بالایی از دقت اندازه گیری را تضمین می کند. برای این منظور، محاسبه مستقیم مقدار میانگین مربع ریشه سیگنال اعمال می شود در حالی که اندازه گیری میانگین سیگنال صاف شده نیمه دوره با استفاده از دستگاه های اندازه گیری سنتی انجام می شود. اجرای این کنتور نه به دانش دوره سیگنال و نه همگام سازی با نمونه گیری پردازش شده احتیاج دارد. سپس شبیه سازی برای نشان دادن کارایی بالای الگوریتم اندازه گیری پیشنهادی انجام می شود. ما مشخصات متر را در محدوده فرکانسی وسیعی از سیگنالهای قابل اندازه گیری کار می کنیم. توصیه های مربوط به اجرای سخت افزاری چنین کنتور با استفاده از آرایه های دروازه قابل برنامه ریزی میدانی در نظر گرفته شده است. از متر می توان هنگام طراحی ولت متر و آمپر متر AC با فرکانس بالا استفاده کرد و می تواند قرائت هایی را که به شکل موج سیگنال بستگی ندارند فراهم کند.



The Comparison of Neutron Beams through ${}^7\text{Li}(p,n)$ Reactions for the Design of a Thermal Neutron Radiography Facility using the MCNPX Code

J. G. Fantidis^{*a}, G. E. Nicolaou^b

^a Department of Electrical Engineering-Department of Physics, International Hellenic University, Kavala, Greece

^b Laboratory of Nuclear Technology, School of Engineering, 'Democritus' University of Thrace, Xanthi, Greece

PAPER INFO

Paper history:

Received 10 May 2020

Received in revised form 13 June 2020

Accepted 03 September 2020

Keywords:

${}^7\text{Li}(p,n)$ Reaction

MCNPX Monte Carlo Code

Non Destructive Testing

Thermal Neutron Radiography

ABSTRACT

In this work, a comparison of six neutron beams was carried out using the MCNPX Monte Carlo code for thermal neutron radiography purposes. The necessary neutrons produced via the ${}^7\text{Li}(p,n)$ reaction for 1 mA proton beam with energies 2.3, 2.5, 3, 4, 4.5, and 5 MeV. The design of the facility was governed from the purpose to achieve the maximum thermal neutron flux in the position of the investigated object. An extensive number of simulations were realized for every source under different conditions. The higher energy of proton beam provides higher intensity for the neutron source but at the same time, the produced spectrum shifted to the fast neutron area. Protons with energies from 2.3 to 3 MeV are more suitable when the thermal neutron content is the main issue of the facility design. Neutrons produced by proton beam in the energy range of 4–5 MeV provide higher thermal neutron fluxes at the cost of the thermal neutron content. The final choice is a compromise, between the thermal neutron content that can be tolerated, in combination with a workable thermal neutron flux.

doi: 10.5829/ije.2020.33.11b.12

1. INTRODUCTION

Radiography without a doubt is the most widespread non-destructive testing (NDT) in human history. Radiography today uses not only gamma or X-rays but also electrons, protons, and neutrons. Neutron radiography (NR) is maybe the most interesting case because neutron seems to be a complementary method compared to the powerful and most commonly used X-ray imaging. X-rays (and gamma rays) can penetrate effortlessly through light materials but cannot pass dense materials. Neutrons on the contrary direction easily penetrate even the dense metals, conversely attenuate strongly through some light elements such as hydrogen, boron, or lithium. The thermal neutrons range is the most interest for NR because in this range the neutrons have higher cross-sections and their detection is more efficient. Compared to the X-ray radiography thermal NR facilities are rather rare. The reason for this is the lack of high-intensity sources [1–3].

According to many previous works to increase not only the thermal NR units but also many other facilities, there is a need for non-reactor high-intensity neutron sources [3–6]. Accelerators although are not "low-priced" but have a considerably lower cost than nuclear reactors or spallation neutron sources, and seem like the most suitable solution. Proton, electrons, deuterium, and tritium accelerators on heavy or light materials target have been proposed; however, based on the results the ${}^7\text{Li}(p,n)$ reaction is the best solution both for thermal and epithermal neutrons beams because offer both soft spectrum and high-intensity neutron yield. Neutrons via ${}^7\text{Li}(p,n)$ reaction can be used for thermal NR, for Boron Neutron Capture Therapy, for medical isotope production, for physics cross-section experiments, and for the development of a quasi monoenergetic neutron beam [7–9].

However, the ${}^7\text{Li}(p,n)$ reaction requires special attention because the lithium metal has poor mechanical and chemical properties. In addition, based on the fact

*Corresponding Author Institutional Email: fantidis@teiemt.gr
(J. G. Fantidis)

that has a rather low melting temperature ($\approx 180^\circ\text{C}$) is necessary for the presence of an appropriate cooling system. Previous works from Bayanov et al. have indicated that is possible to cool a lithium target with water using up to 10mA proton beam [10, 11]. The energy of the protons determines the total neutron yield, the maximum and the minimum energy of the emitted neutrons. The increment of the energy in the protons beam increases the neutron flux but simultaneously provides a harder spectrum so a compromise is necessary.

A representative unit for thermal NR based on Deuterium-Tritium, Deuterium-Deuterium or Tritium-Tritium neutron generators, ^{252}Cf , $^{241}\text{Am/Be}$ isotopic neutron sources, and proton or electron accelerators usually on beryllium target [3, 7, 12–14]. The use of proton accelerators in a lithium target for NR facilities is rare. In this article, the proposed thermal NR facility improves the only previous similar proposed system [9] in four ways. Firstly, by using 6 different proton beam energy; secondly, to maximize the thermal neutron flux in the object the angle between the proton beam and the collimator was 0° ; thirdly, by using a smaller disk source with a lower proton beam current which reduces considerably the scattered neutrons and fourthly, optimizing the divergent collimator dimensions. Hence, this work aims to evaluate the performance of a thermal NR facility based on neutrons emitted when the lithium target bombarded by protons beams with 6 different energies 2.3, 2.5, 3, 4, 4.5, and 5 MeV. The facility firstly modified to maximize the flux of the thermal neutrons and secondly the quality of the beam enhanced using a sapphire filter. Both the design and the calculations have been simulated with the help of the MCNPX 2.5.0 Monte Carlo code [15, 16]. For this article, the results are based on the use of 1 mA protons beams as a result the presented facility does not require any special cooling system for the lithium target [7].

2. MATERIAL AND METHODS

2. 1. Neutron Source Although there are many articles that study and measure the neutron yield from lithium target for different energy of proton accelerator some discrepancies still exist [17, 18]. Theoretical the neutron yield emitted per second into solid angle $d\Omega$ when a thick lithium target bombarded by a proton beam can be calculated from the equation [19, 20]:

$$\frac{d^2N}{d\Omega dE_n} = i g D \left(\frac{d\sigma_{pn}}{d\Omega} \right)_{\text{CMS}} \frac{d\Omega_{\text{CMS}}}{d\Omega} \frac{dE_p}{dE_n} S^{-1}(E_p) \quad (1)$$

where i is the proton beam current in μA , g gives the number of protons per μA , D is the atomic density of ^7Li , $\left(\frac{d\sigma_{pn}}{d\Omega} \right)_{\text{CMS}}$ describes the differential cross-section for the $^7\text{Li}(p,n)$ reaction, E_p is the proton energy, E_n is the energy

of the emitted neutrons in the solid angle Ω and $S^{-1}(E_p)$ is the inverse stopping power in lithium.

In this article 6 protons beams with energies 2.3, 2.5, 3, 4, 4.5, and 5 MeV bombard thick lithium target. The lithium target is a disk with 4 cm diameter and $100\mu\text{m}$ thickness with the intention to minimize the unwanted flux of 478 keV γ -rays [15, 16]. The spectra of the emitted neutrons are shown in Figure 1 for proton current equal to 1 mA. The estimated total neutron yields are 5.78×10^{11} , 8.83×10^{11} , 1.56×10^{12} , 3.62×10^{12} , 4.96×10^{12} , and 6.48×10^{12} $\text{ncm}^{-2}\text{s}^{-1}$ for 2.3, 2.5, 3, 4, 4.5, and 5 MeV protons beams respectively. From the spectra is obvious that despite the relatively soft spectra more thermalization of the beams is necessary. According to many previous works, the best material for this purpose is the high-density polyethylene (HD-PE) so HD-PE was selected as a neutron moderator [3, 12].

2. 2. Collimator Design There are a number of parameters that govern the quality of the radiography produced by a thermal NR facility. The most important parameter is the L/D ratio, where L is the length of the collimator and D is the diameter of the inlet aperture. L/D ratio is used as an indicator of the efficacy of the neutron beam. A large L/D ratio value means better spatial resolution but in the same time decreases the thermal neutron flux (f_{th}) in the investigated object so is necessary a mutual compromise between high spatial resolution and high f_{th} . The part of neutrons lost due to collimation defining by the ratio [2]:

$$\varphi_i = 16 \cdot \varphi_o \left(\frac{L}{D} \right)^2 \quad (2)$$

where φ_i describes neutron intensity at the entrance to the collimator and φ_o is neutron flux at the exit of the collimator. The spatial resolution losses can be calculated by the geometric unsharpness u_g [2]:

$$u_g = L_f \cdot \left(\frac{D}{L_s} \right) \quad (3)$$

where L_s expresses the neutron source to investigated object distance and L_f is the image to object distance (usual equal to 0.5 cm). The divergence of the neutron beam is described by the equation [2]:

$$\theta = \tan^{-1} \left(\frac{I}{2L} \right) \quad (4)$$

where θ gives the half-angle of the beam divergence, I is the maximum dimension of the image plane and L is the length of the divergent collimator. Thermal neutron content (TNC) is the number of thermal neutrons within the neutron beam. Usually, this parameter has small values which can be improved using fast neutrons filters. The n/γ ratio, which is the ratio of neutron intensity of the beam versus the gamma components, is a factor that creates noise in the radiographic image and has suggested value $> 10^4$ $\text{ncm}^{-2}\text{mSv}^{-1}$ [1, 2].

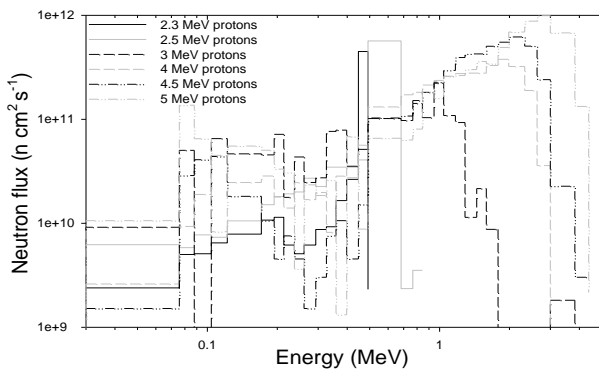


Figure 1. Neutron spectra for 1mA proton current

2. 3. Thermal Neutron Radiography Facility

The geometrical configuration of the proposed facility is shown in Figure 2. All the presented dimensions have been chosen with a criterion to provide the maximum f_{th} . Next to the neutron source, there is HD-PE moderator, the parameter a (distance between the source and convergent collimator) is equal to 1.4 cm for the 2.3 MeV proton beam and 1.7 cm for the others beams. The divergent collimator has a conical shape with radii 1.5 and 1 cm with the bigger one on the side of the source. The length b of the divergent collimator is 10 cm for the 2.3 and 2.5 MeV proton beams, 11 cm for 3, 4, 4.5 MeV proton beams, and 12 cm for the 5 MeV proton beam. The divergent collimator is void but to improve the TNC parameter can be filled with a single sapphire filter which is an excellent fast neutron filter [21].

Next to the convergent collimator, there is a divergent collimator with variable length ($L = 50-200$ cm) while the inlet aperture (D) is 1 cm. The divergent collimator has as lining material Boral with thickness 0.8 cm, while borated polyethylene (PE-B) and bismuth (bi) with thicknesses 3.2 and 1 cm were selected as filling materials. The aperture in the side of the investigated object (D_0) has a changeable dimension (14–18 cm). Boral and bi were also chosen as materials for the configuration of the aperture with dimensions 0.8 and 1.2 cm correspondingly; the first prevents the stray and scattered neutrons and the second minimizes the unwanted gamma-rays.

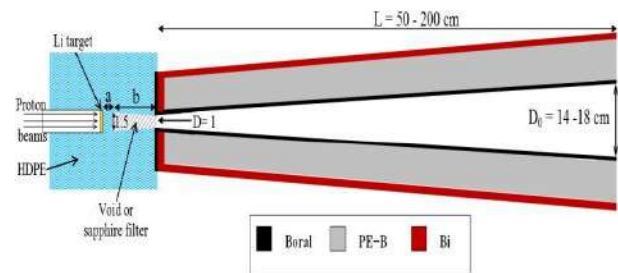


Figure 2. Geometric configuration of the simulated facility

3. RESULTS AND DISCUSSION

To evaluate and compare the 6 beams the presented facility was simulated for a wide range of the parameters which characterize a thermal NR unit. L/D ratio has values from 50 to 200, divergence angle (θ) varies from $1.29-4^\circ$ and the geometric unsharpness diversifies from 2.5×10^{-3} up to 1×10^{-2} . In this work, the n/γ ratio values are not presented because in each simulation has a value of at least two orders of magnitude higher than the recommended value (10^4 n·cm⁻²·mSv⁻¹). The f_{th} (with energy 0.01–0.3 eV) was calculated with the MCNPX code using the surface tally (F2). F2 tally calculates the averaged neutron flux in a surface in neutrons cm⁻² per starting neutron. In the presented facility this surface was placed 0.5 cm away from the divergent collimator and has a radius equal to the aperture beside the image detector [2].

f_{th} and TNC parameters for every source and for the different values of the basic parameters are shown in Table 1. From these results, it is evident that the 2.3 MeV proton beam offers the higher values for the TNC parameter but the minimum f_{th} in each simulation. In the opposite direction, the 5 MeV proton beam owing to the higher neutron yield provides the higher intensities for the f_{th} but with the smaller TNC values. For the same configurations, the f_{th} varies by a factor up to 5.43, in the same conditions the TNC fluctuates by a factor up to 2.27. However, in every simulation, the TNC has values less than 5.9%, which is not always practical. To overcome this drawback, the use of a fast neutron filter is necessary. Figures 3a-3c show the beam profile at the image plane with and without a single sapphire filter in

TABLE 1. Thermal NR calculated parameters for the 6 beams and for different L/D values

L/D	L (cm)	D0 (cm)	θ (deg)	U_g (cm)	2.3 MeV proton		2.5 MeV proton		3 MeV proton		4 MeV proton		4.5 MeV proton		5 MeV proton	
					f_{th} (ncm ⁻² s ⁻¹)	TNC (%)	f_{th} (ncm ⁻² s ⁻¹)	TNC (%)	f_{th} (ncm ⁻² s ⁻¹)	TNC (%)	f_{th} (ncm ⁻² s ⁻¹)	TNC (%)	f_{th} (ncm ⁻² s ⁻¹)	TNC (%)	f_{th} (ncm ⁻² s ⁻¹)	TNC (%)
50	50	14	4.00	1.00E-2	1.82E+5	5.85	2.29E+5	5.47	3.75E+5	5.25	5.98E+5	3.04	7.54E+5	2.77	9.69E+5	2.72
100	100	16	2.29	5.00E-3	4.67E+4	5.55	6.11E+4	5.40	9.95E+4	5.12	1.43E+5	2.69	1.86E+5	2.52	2.38E+5	2.45
150	150	18	1.71	3.33E-3	2.05E+4	5.37	2.66E+4	5.17	4.44E+4	5.02	6.54E+4	2.69	8.18E+4	2.43	1.08E+5	2.43
200	200	18	1.29	2.50 E-3	1.14E+4	5.29	1.47E+4	5.04	2.59E+4	5.01	3.75E+4	2.70	4.69E+4	2.44	6.08E+4	2.40

the convergent collimator for $L/D = 50$. The thermal neutrons (0.01–0.3 eV) are separated in 10 groups, the epithermal neutrons energy range (0.3 eV–0.1 MeV) are arranged in 26 groups and the fast neutrons are divided in 11 bands. The presence of the filter reduces significantly the fast neutrons in the cases of 2.3, 2.5, and 3 MeV protons beams, without important consequence on the thermal neutrons energy range.

Figures 4a-4c illustrate that for harder neutron spectra although there is a noticeable reduction in the fast neutrons band the quantity of them is still rather high. The thermal energy range presents again a small decrement. f_{th} and TNC parameters were also calculated for each source and each L/D ratio for 3 different thickness of the sapphire filter. For the 2.3 MeV proton beam, the results are listed in Table 2. The TNC parameter is nearly stable for the same thickness of the sapphire filter and practical independent of the L/D ratio. The TNC is about 18%, 37%, and 68% for 3, 6 and 10, cm thicknesses of the

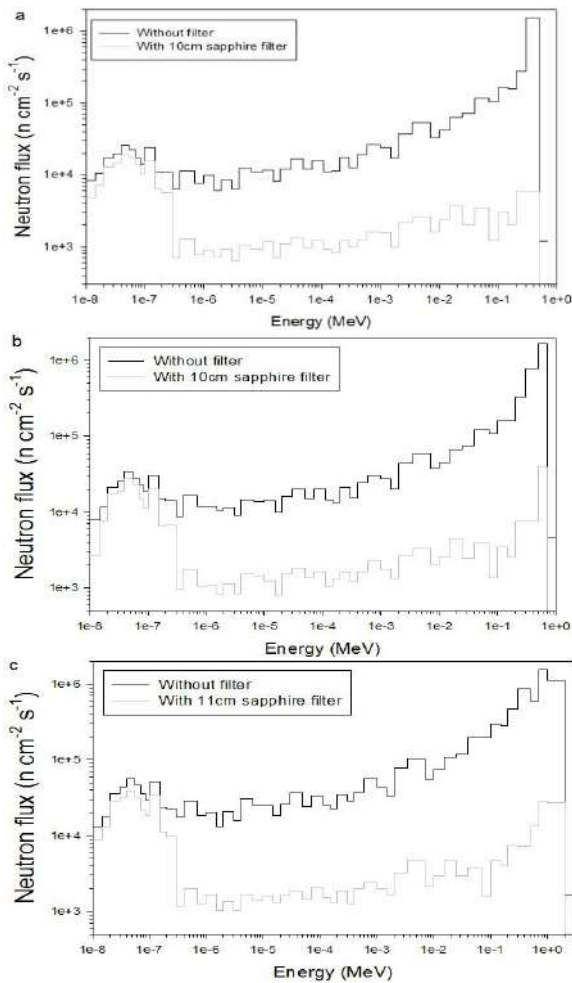


Figure 3. Neutron spectra at the image position for $L/D=50$, a) 2.3 MeV, b) 2.5 MeV, c) 3 MeV protons energy respectively

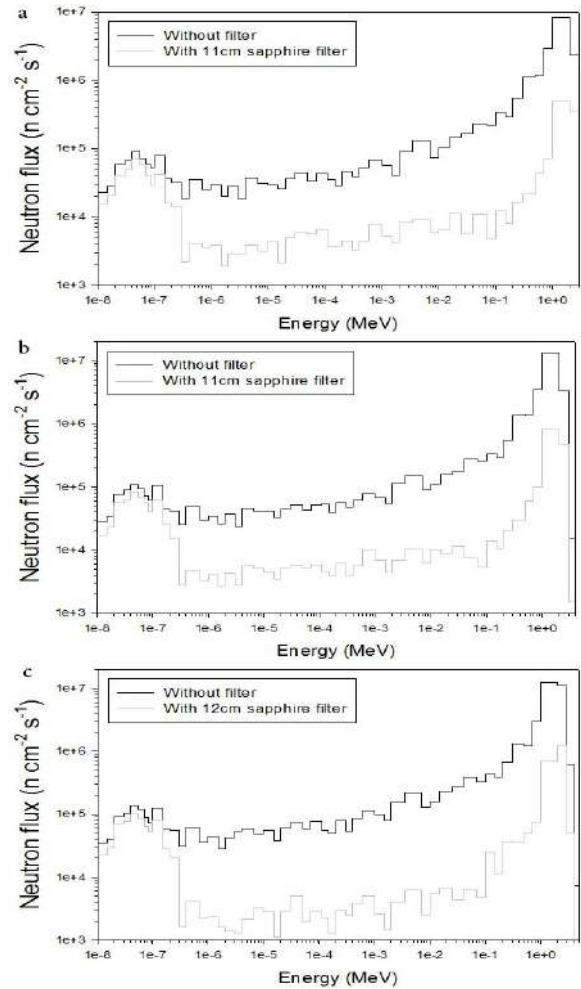


Figure 4. Neutron spectra at the image position for $L/D=50$, a) 4 MeV, b) 4.5 MeV, c) 5 MeV protons energy respectively

filter respectively. At the same time, the reduction of the f_{th} is about 11%, 21%, and 33%. The second beam gives lower TNC values for the same thicknesses of the filter with percentages in the region of 13%, 28%, and 57% and a similar tendency for the f_{th} (Table 3). Similar

TABLE 2. Thermal NR simulated parameters using a proton beam with energy 2.3 MeV

L/D	Sapphire filter (cm)					
	3		6		10	
	f_{th} ($ncm^{-2}s^{-1}$)	TNC (%)	f_{th} ($ncm^{-2}s^{-1}$)	TNC (%)	f_{th} ($ncm^{-2}s^{-1}$)	TNC (%)
50	2.49E+5	18.55	2.21E+5	37.85	1.93E+5	67.90
100	6.38E+4	18.34	5.67E+4	37.36	4.95E+4	68.27
150	2.80E+4	17.94	2.48E+4	37.17	2.17E+4	67.97
200	1.56E+4	17.80	1.39E+4	36.88	1.21E+4	67.62

TABLE 3. Thermal NR simulated parameters using a proton beam with energy 2.5 MeV

L/D	Sapphire filter (cm)					
	3		6		10	
	f_{th} ($ncm^{-2}s^{-1}$)	TNC (%)	f_{th} ($ncm^{-2}s^{-1}$)	TNC (%)	f_{th} ($ncm^{-2}s^{-1}$)	TNC (%)
50	2.05E+5	13.40	1.82E+5	28.90	1.59E+5	58.13
100	5.46E+4	13.43	4.86E+4	29.26	4.24E+4	58.35
150	2.38E+4	12.95	2.12E+4	28.55	1.85E+4	58.37
200	1.32E+4	12.70	1.17E+4	28.07	1.02E+4	57.95

behavior, both for the TNC and the f_{th} , presents and the 3 MeV proton beam. The filter with thickness 3, 6, and 11 cm reduces the f_{th} by a factor 1.12, 1.26, and 1.48 respectively, at the same time the TNC ratio is about 12%, 28%, and 64% (Table 4).

For proton energy > 3 MeV the neutron spectra are harder so the TNC parameter gives lower percentages while the f_{th} does not have significant alteration, with a decrement in the flux similar to the previous cases. Table 5 shows the results for the 4 MeV proton beam for 3, 6, and 11 cm of a sapphire filter; the TNC is approximately 5%, 11%, and 27% correspondingly. In the case of 4.5 MeV proton beam (Table 6) for the same thicknesses of the filter, the TNC values are lower compared with the 4

TABLE 4. Thermal NR simulated parameters using a proton beam with energy 3 MeV

L/D	Sapphire filter (cm)					
	3		6		11	
	f_{th} ($ncm^{-2}s^{-1}$)	TNC (%)	f_{th} ($ncm^{-2}s^{-1}$)	TNC (%)	f_{th} ($ncm^{-2}s^{-1}$)	TNC (%)
50	3.36E+5	13.06	2.99E+5	27.87	2.54E+5	61.77
100	8.90E+4	12.94	7.91E+4	28.03	6.73E+4	64.19
150	3.97E+4	12.81	3.53E+4	27.99	3.00E+4	64.17
200	2.32E+4	13.14	2.06E+4	28.80	1.75E+4	65.66

TABLE 5. Thermal NR simulated parameters using a proton beam with energy 4 MeV

L/D	Sapphire filter (cm)					
	3		6		11	
	f_{th} ($ncm^{-2}s^{-1}$)	TNC (%)	f_{th} ($ncm^{-2}s^{-1}$)	TNC (%)	f_{th} ($ncm^{-2}s^{-1}$)	TNC (%)
50	5.35E+5	6.37	4.75E+5	12.09	4.04E+5	25.76
100	1.28E+5	5.77	1.14E+5	11.48	9.65E+4	27.18
150	5.85E+4	5.00	5.20E+4	11.68	4.42E+4	28.83
200	3.36E+4	5.87	2.98E+4	11.91	2.54E+4	29.98

MeV proton beam (5%, 10%, and 25%). As expected the neutrons produced by 5 MeV proton beam provide the lower TNC values owing to the harder spectra so the TNC for 3, 6, and 12 cm of sapphire filter has values about 5%, 9%, and 21% respectively (Table 7).

TABLE 6. Thermal NR simulated parameters using a proton beam with energy 4.5 MeV

L/D	Sapphire filter (cm)					
	3		6		11	
	f_{th} ($ncm^{-2}s^{-1}$)	TNC (%)	f_{th} ($ncm^{-2}s^{-1}$)	TNC (%)	f_{th} ($ncm^{-2}s^{-1}$)	TNC (%)
50	6.74E+5	5.76	5.99E+5	10.90	5.10E+5	23.13
100	1.67E+5	5.34	1.48E+5	10.55	1.26E+5	24.92
150	7.31E+4	5.12	6.50E+4	10.16	5.53E+4	25.76
200	4.19E+4	5.20	3.72E+4	10.45	3.17E+4	26.73

TABLE 7. Thermal NR simulated parameters using a proton beam with energy 5 MeV

L/D	Sapphire filter (cm)					
	3		6		12	
	f_{th} ($ncm^{-2}s^{-1}$)	TNC (%)	f_{th} ($ncm^{-2}s^{-1}$)	TNC (%)	f_{th} ($ncm^{-2}s^{-1}$)	TNC (%)
50	8.67E+5	5.10	7.70E+5	9.09	6.33E+5	21.42
100	2.13E+5	4.69	1.89E+5	8.49	1.56E+5	21.49
150	9.68E+4	4.68	8.61E+4	8.52	7.07E+4	22.00
200	5.44E+4	4.63	4.84E+4	8.52	3.97E+4	22.62

4. CONCLUSION

The performance of six neutrons beams generated by ${}^7Li(p,n)$ reaction with proton energy in the range between 2.3 up to 5 MeV for a thermal neutron radiography facility was evaluated using the MCNPX Monte Carlo code. The geometrical configuration of the facility has been designed with the intention to maximize the f_{th} which reaches at the image position. For each source, the facility has been simulated for a wide range of the parameters which characterize every thermal radiography system. To reduce the intensity of the fast neutrons and enhance the quality of the beam a single sapphire was used as a fast neutron filter. The presence of the filter improves drastically the TNC without significant sacrifice in the f_{th} values. Neutrons which produced by proton energy from 2.3 to 3 MeV provide softer spectra and better TNC values but with lower f_{th} , on the contrary, neutrons generated by proton energy in the range 4 to 5 MeV offer higher f_{th} but the TNC, even though the use of a filter, has a relatively low percentage.

For this reason, is compulsory a mutual compromise between f_{th} and TNC.

5. REFERENCES

- Hawkesworth, M. R. "Neutron radiography. Equipment and methods." *Atomic Energy Review*, Vol. 15, No. 2, (1977), 169–220. Retrieved from http://inis.iaea.org/Search/search.aspx?orig_q=RN:8343576
- Hardt, P. von der, and Röttger, H. Neutron radiography handbook: nuclear science and technology. Springer Science & Business Media, 2012.
- Fantidis, J. G. "The use of electron linac for high quality thermal neutron radiography unit." *Nuclear Instruments and Methods in Physics Research, Section A: Accelerators, Spectrometers, Detectors and Associated Equipment*, Vol. 908, (2018), 361–366. <https://doi.org/10.1016/j.nima.2018.08.114>
- Pirouz, F., Najafpour, G., Jahanshahi, M., and Sharifzadeh Baei, M. "Plant-based calcium fructoborate as boron-carrying nanoparticles for neutron cancer therapy." *International Journal of Engineering, Transactions A: Basics*, Vol. 32, No. 4, (2019), 460–466. <https://doi.org/10.5829/ije.2019.32.04a.01>
- Chichester, D. L., Simpson, J. D., and Lemchak, M. "Advanced compact accelerator neutron generator technology for active neutron interrogation field work." *Journal of Radioanalytical and Nuclear Chemistry*, Vol. 271, No. 3, (2007), 629–637. <https://doi.org/10.1007/s10967-007-0318-7>
- Anderson, I. S., Andreani, C., Carpenter, J. M., Festa, G., Gorini, G., Loong, C. K., and Senesi, R. "Research opportunities with compact accelerator-driven neutron sources." *Physics Reports*. Elsevier B.V. <https://doi.org/10.1016/j.physrep.2016.07.007>
- Fantidis, J. G. "A study of a transportable thermal neutron radiography unit based on a compact RFI linac." *Journal of Radioanalytical and Nuclear Chemistry*, Vol. 293, No. 1, (2012), 95–101. <https://doi.org/10.1007/s10967-012-1736-8>
- Mashnik, S. G., Chadwick, M. B., Hughes, H. G., Little, R. C., MacFarlane, R. E., Waters, L. S., and Young, P. G. "7-Li(p,n) Nuclear Data Library for Incident Proton Energies to 150 MeV." In *Proceeding 2000 ANS/ENS International Meeting, Nuclear Applications of Accelerator Technology* (pp. 1–11). Retrieved from <http://arxiv.org/abs/nucl-th/0011066>
- Fantidis, J. G. "Beam shaping assembly study for BNCT facility based on a 2.5 MeV proton accelerator on Li target." *Journal of Theoretical and Applied Physics*, Vol. 12, No. 4, (2018), 249–256. <https://doi.org/10.1007/s40094-018-0312-1>
- Bayanov, B., Belov, V., Kindyuk, V., Oparin, E., and Taskaev, S. "Lithium neutron producing target for BINP accelerator-based neutron source." *Applied Radiation and Isotopes*, Vol. 61, No. 5, (2004), 817–821. <https://doi.org/10.1016/j.apradiso.2004.05.032>
- Bayanov, B., Kashaeva, E., Makarov, A., Malyshekin, G., Samarin, S., and Taskaev, S. "A neutron producing target for BINP accelerator-based neutron source." *Applied Radiation and Isotopes*, Vol. 67, No. 7-8 SUPPL., (2009), S282–S284. <https://doi.org/10.1016/j.apradiso.2009.03.076>
- Da Silva, A. X., and Crispim, V. R. "Study of a neutron radiography system using 252Cf neutron source." *Radiation Physics and Chemistry*, Vol. 61, No. 3, (2001), 515–517. [https://doi.org/10.1016/S0969-806X\(01\)00318-8](https://doi.org/10.1016/S0969-806X(01)00318-8)
- Fantidis, J. G., Nicolaou, G. E., and Tsagas, N. F. "A transportable neutron radiography system." *Journal of Radioanalytical and Nuclear Chemistry*, Vol. 284, No. 2, (2010), 479–484. <https://doi.org/10.1007/s10967-010-0502-z>
- Fantidis, J. G., Bandekas, D. V., Constantinou, P., and Vordos, N. "Fast and thermal neutron radiographies based on a compact neutron generator." *Journal of Theoretical and Applied Physics*, Vol. 6, No. 1, (2012), 1–8. <https://doi.org/10.1186/2251-7235-6-20>
- Hendricks, J. S., Mckinney, G. W., Waters, L. S., Roberts, T. L., Egdorf, H. W., Finch, J. P., Trelle, H. R., Pitcher, E. J., Mayo, D. R., Swinhoe, M. T., Lebenhaft, J. MCNPX extensions version 2.5. 0 (Report No. LA-UR-05-2675), 2005. Retrieved from https://mcnp.lanl.gov/pdf_files/la-ur-05-2675.pdf
- Miresghhi, M. "Simulation of a Neutron Detector for Real Time Imaging Applications." *International Journal of Engineering*, Vol. 11, No. 4, (1998), 207–212. Retrieved from http://www.ije.ir/article_71214.html
- Atanackovic, J., Matysiak, W., Witharana, S., Dubeau, J., and Waker, A. J. "Measurements of neutron energy spectra from ${}^7\text{Li}(p,n){}^7\text{Be}$ reaction with bonner sphere spectrometer, nested Neutron spectrometer and ROSPEC." *Radiation Protection Dosimetry*, Vol. 161, No. 1-4, (2014), 221–224. <https://doi.org/10.1093/rpd/nct314>
- Bakshi, A. K., Dawn, S., Suryanarayana, S. V., and Datta, D. "Spectrometry and dosimetry of neutron beams produced by ${}^7\text{Li}(p,n)$ reactions in the proton energy range of 3–5 MeV." *Nuclear Instruments and Methods in Physics Research, Section A: Accelerators, Spectrometers, Detectors and Associated Equipment*, Vol. 949, (2020), 162926. <https://doi.org/10.1016/j.nima.2019.162926>
- Allen, D. A., and Beynon, T. D. "A design study for an accelerator-based epithermal neutron beam for BNCT." *Physics in Medicine and Biology*, Vol. 40, No. 5, (1995), 807–821. <https://doi.org/10.1088/0031-9155/40/5/007>
- Matysiak, W., Prestwich, W. V., and Byun, S. H. "Precise measurements of the thick target neutron yields of the ${}^7\text{Li}(p,n)$ reaction." *Nuclear Instruments and Methods in Physics Research, Section A: Accelerators, Spectrometers, Detectors and Associated Equipment*, Vol. 643, No. 1, (2011), 47–52. <https://doi.org/10.1016/j.nima.2011.04.034>
- Mildner, D. F. R., and Lamaze, G. P. "Neutron Transmission of Single-Crystal Sapphire." *Journal of Applied Crystallography*, Vol. 31, No. 6, (1998), 835–840. <https://doi.org/10.1107/S0021889898005846>

Persian Abstract

چکیده

در این کار مقایسه شش پرتوی نوترونی با استفاده از کد MCNPX مونت کارلو با هدف رادیوگرافی نوترونی حرارتی انجام شده است. نوترون‌های لازم از طریق واکنش ${}^7\text{Li}(p,n)$ برای پرتو پروتون ۱ میلی‌آمپر با انرژی ۲/۳، ۲/۵، ۳، ۴، ۵/۱ و ۵ MeV تولید شده‌اند. طراحی امکانات برای دستیابی به حداکثر شار نوترون حرارتی در موقعیت هدف مورد بررسی انجام شد. تعداد زیادی از شبیه‌سازی‌ها برای هر منبع تحت شرایط مختلف انجام شد. انرژی بالاتر پرتو پروتون شدت بیشتری برای منبع نوترون فراهم می‌کند اما در عین حال طیف تولید شده به ناحیه نوترون سریع منتقل می‌شود. پروتون‌هایی با انرژی از ۲/۳ تا ۳ MeV مناسب‌ترند. وقتی محتوای نوترون حرارتی مسئله اصلی طراحی تسهیلات است. نوترون‌های تولید شده توسط پرتو پروتون در گستره انرژی ۵/۴ مگا الکترون ولت شار نوترون حرارتی بالاتری را با هزینه محتوای نوترون حرارتی فراهم می‌کنند. انتخاب نهایی یک سازش بین محتوای نوترون حرارتی که قابل تحمل است، در ترکیب با یک شار نوترون حرارتی قابل استفاده می‌باشد.



An Ultra-low-power Static Random-Access Memory Cell Using Tunneling Field Effect Transistor

N. Arunkumar^a, N. Senathipathi^a, S. Dhanasekar^{*b}, P. Malin Bruntha^c, C. Priya^d

^a Department of ECE, P.A College of Engineering and Technology, Pollachi, India

^b Department of ECE, Sri Eshwar College of Engineering, Coimbatore, India

^c Department of ECE, Karunya Institute of Technology and Sciences, Coimbatore, India

^d Department of ECE, Karpagam College of Engineering Coimbatore, India

PAPER INFO

Paper history:

Received 28 February 2020

Received in revised form 04 August 2020

Accepted 03 September 2020

Keywords:

Static Random-Access Memory

Homojunction

Heterojunction

Tunneling Field Effect Transistor

Complementary Metal Oxide Semiconductor

ABSTRACT

In this research article, an Ultra-low-power 1-bit SRAM cell is introduced using Tunneling Field Effect Transistor (TFET). This paper investigates feasible 6T SRAM configurations on improved N-type and P-type TFETs integrated on both InAs (Homojunction) and GaSb-InAs (Heterojunction) platforms. The voltage transfer characteristics and basic parameters of both Homo and Heterojunctions are examined and compared. The proposed TFET based SRAM enhances the stability in the hold, read, and write operations. This work evaluates the potential of TFET which can replace MOSFET due to the improved performance with low-power consumption, high speed, low sub-threshold slope, and supply voltage ($V_{DD} = 0.2$ V). The results are correlated with CMOS 32nm technology. The proposed SRAM TFET cell is implemented using 30nm technology and simulated using an H-SPIICE simulator with the help of Verilog-A models. The proposed SRAM TFET cell architecture achieves low power dissipation and attains high performance as compared to the CMOS and FINFET.

doi: 10.5829/ije.2020.33.11b.13

NOMENCLATURE

C_d	Depletion layer capacitance	Q	Elementary charge
C_{ox}	Gate oxide capacitance	Const	Device dimensions and materials parameter
T	Temperature	V_{gs}	Gate source voltage
k	Boltzmann constant		

1. INTRODUCTION

In the present scenario, several researchers are working towards reducing the size of the transistors to make miniature Integrated Chip (IC) [1]. The silicon CMOS technology has become an effective fabrication process for high performance and lucrative VLSI circuits. Most of the VLSI industries are using CMOS, which is having a high sub-threshold slope and high-off current at room temperature [5]. Due to this factor, the leakage current and heat of the system is also increased [7]. In SRAM cell, thick gate oxide present in the long channel device is used to reduce the leakage current. OFDM transceiver IC is

used to provide high-speed data transmission in wideband wireless communication [8]. TFET is a forthcoming transistor that is studied extensively on the way towards power-efficient integrated circuits as a replacement of CMOS in the supply voltage regime below $V_{DD} = 0.3$ V [3-5].

In this work, the TFET characteristics are briefly explained and TFET based SRAM cell is designed with two different types: Homojunction and Heterojunction [9-12]. These results are compared with the 32 nm CMOS SRAM design. The sub-threshold slope, power and supply voltages are reduced. The switching speed of the system can also be increased by using TFETs [10].

*Corresponding Author Email: dhanasekar.sm@gmail.com
(S. Dhanasekar)

This paper methodized the Tunneling Field Effect Transistor in Section 2. Homojunction and Heterojunction TFETs are presented in Section 3. Section 4 portrays the proposed TFET based SRAM design. The results of SRAM design are discussed in Section 5. The article concluded in Section 6.

2. TUNNELING FIELD EFFECT TRANSISTOR

For achieving low energy electrons, a new type of transistor TFET is proposed, which is used in the family of Field Effect Transistor (FET) under the division of MOSFET [2]. The MOSFET is working based on the thermionic emission principle but TFET operates based on the quantum tunneling mechanism, because of this sub-threshold slope of TFET is less than 60mV/dec at room temperature [6].

2. 1. Structure and Operation of TFET The TFET structure is analogous to the MOS transistor excluding the source and drain terminals shown in Figure 1. In TFET, the source terminal is doped with a p-type material and the drain terminal is doped with an n-type material. The TFET structure also named as P-I-N (P-type source terminal, intrinsic region, and N-type drain terminal) structure [3].

The tunneling process occurs at the sufficient gate bias where the electron moves from the lower band of the p-type source terminal to the upper band of drain terminal [5]. If the gate bias is reduced, the current cannot flow a long time because of band misalignment [13-14]. When the transistor attains off condition it is in the same mode and there are no electrons will move from p-type to n-type terminal [15-17].

The NTFET Tunneling process is shown in Figure 2. The operation of NTFET is the same as the operation of PTFET but the difference attains only the majority

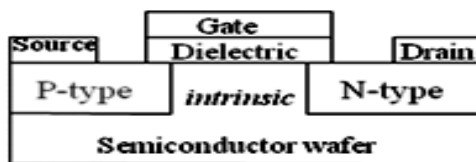


Figure 1. Basic Structure of TFET

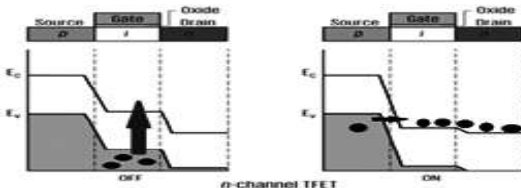


Figure 2. NTFET Tunneling Process

carriers. In NTFET, the majority carriers are electrons and holes are the majority carriers in PTFET. The gate voltage is a negative voltage for PTFET, it is same as the MOSFET but there is no body bias in TFET [11]. In the N-channel case, the Fermi level is very close to the valence band edge due to high density of states for holes. In the P-channel, the Fermi level degeneracy is quite high due to low density of states for electrons. This causes a high energy tail, which limits the sub-threshold slope and gives rise to a strong temperature dependence similar to that of a MOSFET [23].

2. 2. Sub-threshold Swing The sub-threshold swing is the reciprocal value of the sub-threshold slope. The sub-threshold slope is a slope of logarithmic drain current and gate voltage characteristic of MOSFET. The sub-threshold swing of MOSFET is given below:

$$SS_{\text{MOSFET}} = \ln(10) \left(\frac{kT}{q} \right) \left(1 + \frac{C_d}{C_{ox}} \right) \text{ [mV/dec]} \quad (1)$$

Based on Equation (1), the leakage current of the conventional device lies in the sub-threshold region. The above equation is used only for MOSFET. For calculating the sub-threshold swing of TFET, another equation is used as the mechanism depends on the tunneling barrier width [4] which is given by:

$$SS_{\text{TFET}} = \frac{V_{gs}^2}{5.75(V_{gs} + \text{Const})} \text{ [mV/dec]} \quad (2)$$

If the sub-threshold swing of a device is small, then the leakage current, power dissipation and the threshold voltage of a device will also occur quite low [18]. Field Programmable Gate Array (FPGA) provides more flexible, accurate in simulating, testing and gives end to end solutions for reprogramming the proposed designs in the hardware [19].

3. HOMOJUNCTION AND HETEROJUNCTION TUNNEL FIELD EFFECT TRANSISTORS

The sub-threshold slope, power consumption and delay of the TFET are reduced based on the band-gap of the materials which is used for TFET fabrication. TFET is divided into two categories based on semiconducting materials.

3. 1. InAs Homojunction A Homojunction is a semiconductor material that has equal band gaps in between two layers of similar semiconductors with different doping concentrations. InAs is used for high electron mobility and it is a direct band-gap material [12]. The values of basic parameters for InAs are energy gap=0.354 eV, Intrinsic carrier concentration=1.1015 cm⁻³, Intrinsic resistivity=0.16 Ω.cm, Effective conduction band density of states =8.7x10¹⁶ cm⁻³, Effective valence band density of states=6.6x10¹⁸ cm⁻³.

3. 2. GaSb-InAs Heterojunction A Heterojunction is a semiconductor material which is having unequal band gaps in between two layers of dissimilar semiconductors. The energy band diagram of Heterojunction types is shown in Figure 3. It works at high frequency and also used in High Electron Mobility Transistors (HEMT). TFET operates at minimum voltage when the band gaps of crystalline semiconductors are unequal [20]. The Heterojunction semiconductor alignment is divided into three types. Those are a Straddling gap, Staggered gap and Broken gap [12].

In this paper, the two types of TFETs, Homojunction and Heterojunction are simulated. these two TFETs are compared with its basic parameters based on the results. When it is in contact, GaSb and InAs have non-overlapping band-gap, which forms more interesting phenomena in heterostructure from those materials. In an intrinsic heterostructure, the carriers are generated by the migration of charges from GaSb to InAs layers. Here the sheet densities of mobile electrons and holes are the same [11].

For a large number of experiments, it is useful to control the electron-hole ratio. In the broken band-gap arrangement of GaSb-InAs heterostructure, InAs conduction band occurs lower in energy than the GaSb valence band, it causes charge. Mobilization from the GaSb to the InAs layers [21]. Due to this arrangement, intrinsic populations of mobile electrons and holes are generated in the absence of doping. For thin InAs wells, quantization of the confinement energy becomes significant at low temperature, leading to quasi-two-dimensional behavior as the carrier wave functions are restricted in growth to the direction for a number of states corresponding to discrete sub-band energies [22].

4. PROPOSED TUNNEL FIELD EFFECT TRANSISTOR BASED STATIC RANDOM-ACCESS MEMORY DESIGN

Static Random-Access Memory (SRAM) is a volatile semiconducting memory, which is used to store on condition without periodic data as long as the power supply is refreshed. SRAM is a high-speed memory cell in the RAM family. The 6T TFET SRAM circuit is shown in Figure 4.

4. 1. SRAM Cell Operation The SRAM cell contains six TFET transistors which are X1, X2, X3, X4,

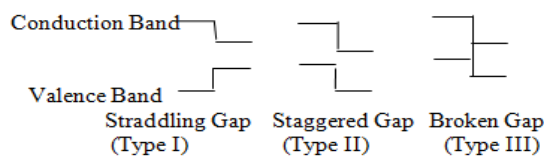


Figure 3. Heterojunction Types

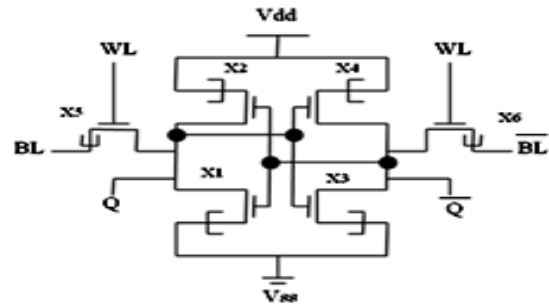


Figure 4. 6T TFET SRAM Circuit

X5, and X6. Here two TFET inverters (X1, X2, X3 and X4) are cross-coupled. During read and write operations the access is controlled by two additional TFET transistors X5 and X6. Because of this architecture, the supply voltage of a cell is less than 0.25 V, the power dissipation is also very low and it has high noise immunity. There are three stages present in SRAM named as read, write and hold mode operations. The working of these stages is given below.

4. 1. 1. Hold For the hold operation the word line should be 0 (WL = 0). So, the access transistors X5 and X6 are not able to connect with the bit lines because of this SRAM keeps the present data in the cross-coupled inverters (X1, X2, X3, and X4) as long as the supply voltage is ON.

4. 1. 2. Reading To read the data from SRAM cell Word Line (WL) is always in the ON condition and both the bit lines should be recharged. The sense amplifier is used to sense the data from the SRAM cell. The output of the SRAM cell is given as input of sense amplifier. The Q and \bar{Q} are the inputs of sense amplifier, if $Q < \bar{Q}$ then the output of sense amplifier is 0, and if $Q > \bar{Q}$ then the output is 1.

4. 1. 3. Writing To write a 1 into the SRAM cell, first WL and BL (Bit Line) should be 1 and \bar{BL} should be 0. If 0 is written to the SRAM cell, then the value of BL should be inverted.

5. RESULTS AND DISCUSSION

5. 1. SRAM Write Operation by using TFET In Homojunction TFET when the word line is ON (WL=1), the SRAM circuit allows the external input inside the cell to store the data. If WL=0, then SRAM circuit keeps the previous data which is shown in Figure 5. The power of the Homojunction SRAM is 17.8 nW.

In Heterojunction TFET, when the word line is ON (WL=1), the SRAM circuit allows the external input, inside to store the data. If WL=0, then the GaSb-InAs

SRAM circuit keeps the previous data which is shown in Figure 6. The power of the Heterojunction SRAM is 0.38nW.

5. 2. SRAM Read Operation by using TFET In 6T TFET SRAM Read Operation, the sense amplifier is connected to read the stored data from SRAM cell. For read operation, the word line should be 0 (WL=0). The output of the Homojunction TFET SRAM read operation result is shown in Figure 7. The power of the Homojunction SRAM cell is 208.2 nW.

For a read operation, the word line should be 0 (WL=0). The output of the Hetrojunction TFET SRAM read operation result is shown in Figure 8. The power of Heterojunction SRAM cell is 1.87 nW.

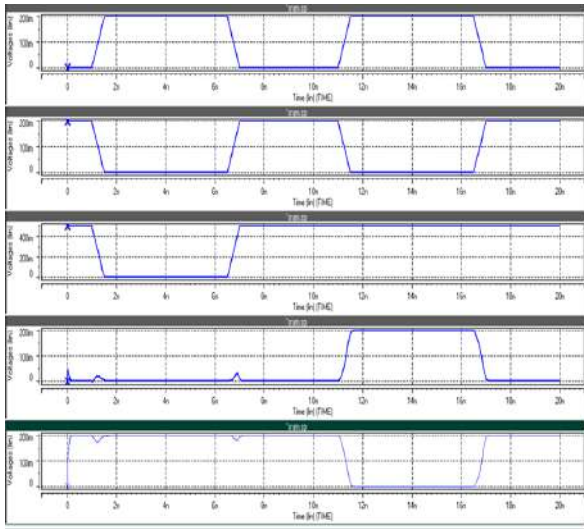


Figure 5. Homojunction 6T SRAM write operation result

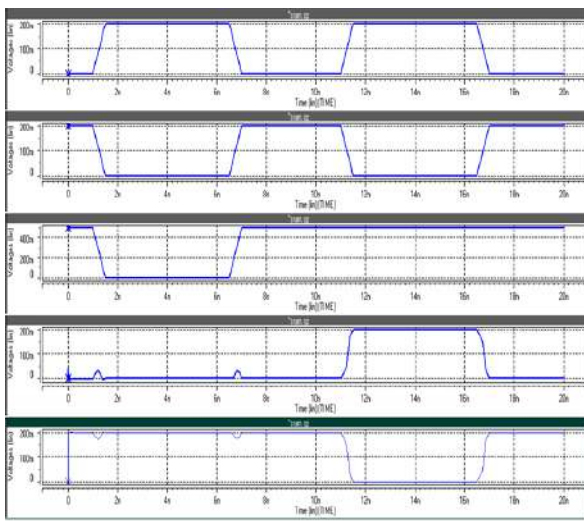


Figure 6. Heterojunction 6T SRAM write operation result

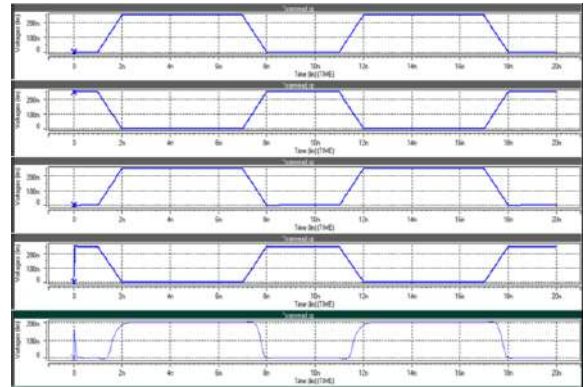


Figure 7. Homojunction TFET SRAM read operation result

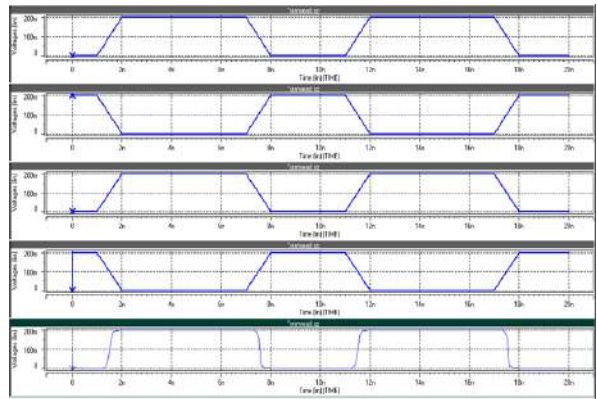


Figure 8. Heterojunction TFET SRAM read operation result

5. 3. Heterojunction vs Homojunction The sub-threshold slope of the device is very low if we use Heterojunction GaSb-InAs TFET. Heterojunction TFET has a small band-gap, when compared to the Homojunction TFET. Due to the small band-gap the charge carriers can move easily which enhances the speed of the transistor. Hence GaSb-InAs Heterojunction TFET is best for device fabrication because the power consumption and the propagation delay are very low is given in Table 1.

TABLE 1. Performance Comparison of Homojunction Vs Heterojunction

Circuit	Homo junction			Heterojunction		
	Power (nW)	tpLH (ns)	tpHL (ns)	Power (nW)	tpLH (ns)	tpHL (ns)
SRAM Write	17.8	10.1	15.1	0.38	10.1	9.9
SRAM Read	208.2	9.9	0.18	1.87	0.0007	0.0128

5. 4. SRAM Operation Using 32nm Technology

5. 4. 1. Write Operation In the CMOS 32 nm SRAM write operation circuit, when the word line is ON (WL=1), the SRAM circuit allows the external input, to store the data. If WL=0, then the SRAM circuit keeps the previous data which is shown in Figure 9. The power of the 32nm CMOS SRAM is 0.704 nW.

5. 4. 2. Read Operation The CMOS 32nm SRAM read operation is done by using a sense amplifier which is used for reading the stored data from the memory device. For read operation the word line should be 0 (WL=0). Then, the output of the SRAM cell is connected as an input to the sense amplifier. The power of 32nm CMOS SRAM cell is 14.1 nW. Q and \bar{Q} are the inputs of a sense amplifier and also the output of the SRAM cell. After writing the data into SRAM memory cell, the reading operation will take place. The simulation result of CMOS SRAM read operation is shown in Figure 10.

5. 4. 3. CMOS Vs TFET The heterojunction TFET SRAM and CMOS SRAM parameters are compared because it has already proved that Heterojunction is better than Homojunction. From Table 2, it is concluded that the TFET is better than the CMOS by comparing the parameters like power and propagation delay.

After comparison of CMOS, TFET and FINFET Technologies in Table 3, it is concluded that TFET is better than CMOS and FINFET. TFET gives very low sub-threshold swing at room temperature compared with CMOS and FINFET. TFET transistor shows higher performance than FINFET-based logic due to its lower parasitic capacitance. In addition, the leakage power of TFET is also reduced compared to FINFET and CMOS. Hence, TFET operates on high speed with low power, and low supply voltage.

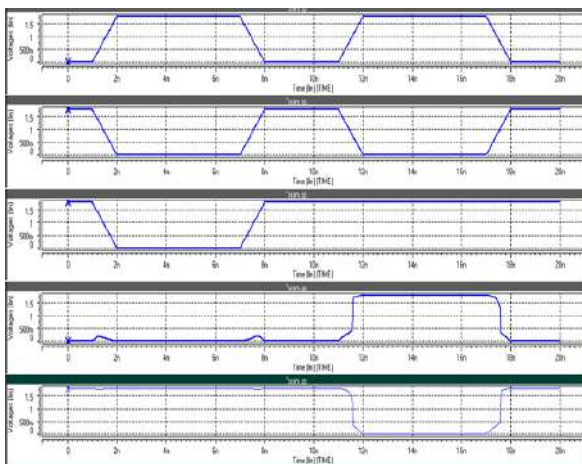


Figure 9. 6T CMOS SRAM write operation result

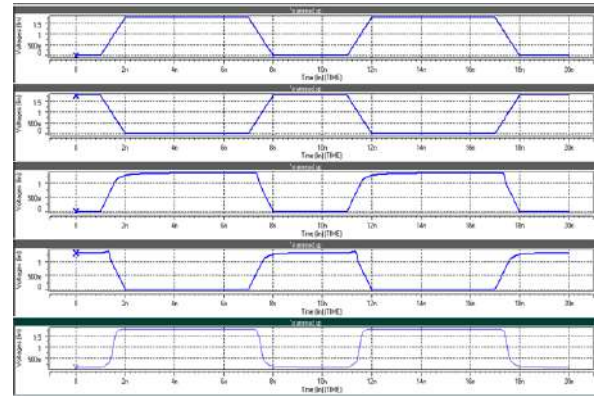


Figure 10. CMOS SRAM read operation result

TABLE 2. Performance Comparison of CMOS Vs TFET

Circuit	CMOS			TFET (Heterojunction)		
	Power (nW)	tpLH (ns)	tpHL (ns)	Power (nW)	tpLH (ns)	tpHL (ns)
SRAM Write	0.704	10.2	10	0.38	10.1	9.9
SRAM Read	14.1	0.00095	0.0024	1.87	0.0007	0.0128

TABLE 3. Basic parameters values for CMOS, TFET and FINFET

Parameters	CMOS	TFET	FINFET
Channel Length	32 nm	30nm	22nm
Supply Voltage	1.8V	0.25V	0.9V
Threshold Voltage	0.53V	0.05V	0.36
Sub-threshold Slope	60mV/dec	17mV/dec	>70mV/dec
Leakage Power	1.74pW	0.39pW	0.98pW
ION (uA/um)	HVT	LVT	
	90	380	400 850

6. CONCLUSIONS

In this paper Heterojunction and Homojunction 6T SRAM cell is designed and simulated using TFET and it is observed that the Heterojunction SRAM cell performs better than the Homojunction in terms of speed and power consumption. Also, the performance of 30 nm TFET is compared with the 32 nm CMOS technology based on the various parameters such as channel length, supply voltage, threshold voltage, power and sub-threshold slope. Hence the proposed 6T-TFET SRAM offers better results than 6T-CMOS SRAM.

7. REFERENCES

- Dhanasekar S, Ramesh J, "VLSI Implementation of Variable Bit Rate OFDM Transceiver System with Multi-Radix FFT/IFFT Processor for wireless applications", *Journal of Electrical Engineering*, Vol. 3, No. 1, (2018), 1-10.
- Emanuele Baravelli, Elena Gnani, Antonio Gnudi and Susanna Reggiani, "TFET Inverters with n-/p-devices on the same technology platform for low-voltage/low-power applications", *IEEE Transactions on Electron Devices*, Vol. 61, No. 2, (2014), 473-478, doi: 10.1109/TED.2013.2294792
- Anthony Villalon, Gilles Le Carval, Sebastien Martinie, Cyrille Le Royer, Marie-Anne Jaud and Sorin Cristoloveanu, "Further insights in TFET operation", *IEEE Transactions on Electron Devices*, Vol. 61, No. 8, (2014), 2893-73-2898, doi: 10.1109/TED.2014.2325600
- Yingxin Qiu, Runsheng Wang, Qianqian Huang and Ru Huang, "A comparative study on the impacts of interfece traps on tunneling FET and MOSFET", *IEEE Transactions on Electron Devices*, Vol. 61, No. 5, (2014),1284-1291, doi: 10.1109/TED.2014.2312330
- Siyuranga O. Koswatta, Mark S. Lundstrom and Dmitri E. Nikonov, "Performance comparison between p-i-n tunneling transistors and conventional MOSFETs", *IEEE Transactions on Electron Devices*, Vol. 56, No. 3, (2009), 456-465, doi: 10.1109/TED.2008.2011934
- Sung Hwan Kim, Sapan Agarwal, Zachery A Jacobson, Peter Matheu, Chenming Hu and Tsu-Jae King Liu, "Tunnel field effect transistor with raised germanium source", *IEEE Electron Device Letters*, Vol. 31, No. 10, (2010), 1107-1109, doi: 10.1109/LED.2010.2061214
- Ramanathan Gandhi, Zhixian Chen, Navab Singh, Kaustav Banerjee and Sungjoo Lee, "Vertical Si-Nanowire n-type tunneling FETs with low sub-threshold swing($\leq 50\text{mV/decade}$) at room temperature", *IEEE Electron Device Letters*, Vol. 32, No. 4, (2011), 437-439, doi: 10.1109/LED.2011.2106757
- Dhanasekar S, Ramesh J, "FPGA Implementation of Variable Bit Rate OFDM Transceiver System for Wireless Applications", Proceedings of IEEE International Conference on Innovations in Electrical, Electronics, Instrumentation and Media Technology, (2017), 343-346, doi: 10.1109/ICIEEIMT.2017.8116863
- Chun-Hsing and Nguyen Dang Chien, "Sub-10-nm tunnel field-effect transistor with graded Si/Ge heterojunction", *IEEE Electron Device Letters*, Vol. 32, No. 11,(2011), 1498-1500, doi: 10.1109/LED.2011.2164512
- Rui Li, Yeqing Lu, Guangle Zhou, Qingmin Liu, Soo Doo Chae, Tim Vasen, Wan Sik Hwang, Qin Zhang, Patrick Fay, Tom Kosel, Mark Wistey, Huili Xing and Alan Seabaugh, "AlGaSb/InAs tunnel field-effect transistor with on-current of $78\mu\text{A}/\mu\text{m}$ at 0.5V", *IEEE Electron Device Letters*, Vol. 33, No. 3, (2012), 363-365, doi: 10.1109/LED.2011.2179915
- Ram Asra, Mayank Shrinivastava, Kota V. R. M. Murali, Rajan K. Pandey, Harald Gossner and V. Ramgopal Rao, "A tunnel FET for Vdd Scaling Below 0.6V with a CMOS-comparable performance", *IEEE Transactions on Electron Devices*, Vol. 58, No. 7,(2011), 1855-1863, doi: 10.1109/TED.2011.2140322
- Lining Zhang and Mansun Chan, "SPICE modelling of double-gate tunnel-FETs including channel transports", *IEEE Transactions on Electron Devices*, Vol. 61, No. 2, (2014), 300-307, doi: 10.1109/TED.2013.2295237
- Yoonmyung Lee, Daeyeon Kim, Jin Cai and Isaac Lauer, "Low-power circuit analysis and design based on hetero- junction tunneling transistors (HETTs)", *IEEE Transactions Very Large Scale Integration Systems*, Vol. 21, No. 9, (2013), 1632-1643, doi: 10.1109/TVLSI.2012.2213103
- Y.-N. Chen, M.-L. Fan, V. P.-H. Hu, P. Su, and C.-T. Chuang, "Design and analysis of robust tunneling FET SRAM", *IEEE Trans. Electron Devices*, Vol. 60, No. 3, (2013), 1092-1098, doi: 10.1109/TED.2013.2239297
- N. Hossain, A. Iqbal, H. Shishupal, and M. H. Chowdhury, "Tunneling transistor based 6T SRAM bitcell circuit design in sub-10nm domain", Proc. Midwest Symp. Circuits Syst., (2017), doi: 10.1109/MWSCAS.2017.8053215.
- A. Sharma, A. G. Akkala, J. P. Kulkarni, and K. Roy, "Source-underlapped GaSb-InAs TFETs with applications to gain cell embedded DRAMs", *IEEE Transactions on Electron Devices*, Vol. 63, No. 6, (2016), 2563-2569, doi: 10.1109/TED.2016.2555627
- Ming-Hsien Tu, Jihi-Yu Lin, Ming-Chien Tsai and Chien-Yu Lu "A single-ended disturb-free 9T sub-threshold SRAM with cross-point data-aware write word-line structure, negative bit-line, and adaptive read operation timing tracing", *IEEE Journal of Solid-State Circuits*, Vol. 47, No. 6, (2012), 1469-1482, doi: 10.1109/JSSC.2012.2187474
- Sebastiano Strangio, Pierpaolo Palestri, David Esseni, Luca Selmi and Felice Crupi, "Impact of TFET unidirectionality and ambipolarity on the performance of 6T SRAM cells", *IEEE Journal of Electron Devices Society*, Vol. 3, No. 3, (2015), 223-232, doi: 10.1109/JEDS.2015.2392793
- Dhanasekar S, Malin Bruntha P, Martin Sagayam K, "An Improved Area Efficient 16-QAM Transceiver Design using Vedic Multiplier for Wireless Applications", *International Journal of Recent Technology and Engineering*, Vol.8, No. 3, (2019), 4419-4425, doi: 10.35940/ijrte.C5535.098319
- Alan C. Seabaugh and Qin Zhang, "Low-voltage tunnel transistors for beyond low-voltage tunnel transistors for beyond CMOS logic", Proc. IEEE, Vol. 98, No. 12, (2015), 2095-2110, doi: 10.1109/JPROC.2010.2070470
- Mahmood Uddin Mohammed and Masud H. Chowdhury, "Reliability and Energy Efficiency of the Tunneling Transistor-Based 6T SRAM Cell in Sub-10 nm Domain", *IEEE Transactions on Circuits and Systems-II*, Vol. 65, No. 12, (2018),1829-1833, doi: 10.1109/TCSII.2018.2874897
- Jheng-Sin Liu,, Michael B. Clavel and Mantu K. Hudait, "An Energy-Efficient Tensile-Strained Ge/InGaAs TFET 7T SRAM Cell Architecture for Ultralow-Voltage Applications", *IEEE Transactions On Electron Devices*, Vol. 64, No. 5, (2017), 2193-2200, doi: 10.1109/TED.2017.2675364
- Sayed Ahmad, Syed Afzal Ahmad, Mohd Muqeem, Naushad Alam and Mohd Hasan "TFET-Based Robust 7T SRAM Cell for Low Power Application", *IEEE Transactions on Electron Devices*, Vol. 66, No. 9, (2019), 3834-3840, doi: 10.1109/TED.2019.2931567

Persian Abstract

چکیده

در این مقاله تحقیقاتی، یک سلول ۱ بیتی SRAM بسیار کم مصرف با استفاده از ترانزیستور تاثیر Tunneling Field Effect (TFET) معرفی شده است. در این مقاله پیکربندی های ۶T SRAM امکان پذیر در TFET های نوع N و P از نوع یکپارچه شده در هر دو سیستم عامل InAs هم سازگاری (GaSb-InAs Heterojunction) بررسی شده است. مشخصات انتقال ولتاژ و پارامترهای اساسی هر دو همو و توابع هتروژن بررسی و مقایسه می شوند. SRAM مبتنی بر TFET پایداری در عملیات نگه داشتن، خواندن و نوشتن را افزایش می دهد. این کار پتانسیل TFET را ارزیابی می کند که می تواند به دلیل بهبود عملکرد با مصرف کم انرژی، سرعت زیاد، شیب زیر آستانه کم و ولتاژ تغذیه ($V_{DD} = 0.2$ ولت) جایگزین MOSFET شود. نتایج با فناوری CMOS 32nm در ارتباط است. سلول پیشنهادی SRAM TFET با استفاده از فناوری ۳۰nm پیاده سازی شده و با استفاده از شبیه ساز H-SPICE با کمک مدل های Verilog-A شبیه سازی شده است. معماری سلول پیشنهادی SRAM TFET باعث اتلاف انرژی کم و عملکرد بسیار بالاتر در مقایسه با CMOS و FINFET می شود.



A New Variable Frequency Zero Voltage Switching Control Method for Boost Converter Operating in Boundary Conduction Mode

S. Norouzi^a, H. Ghoreishy^{*a}, A. Ale Ahmad^a, F. Tahami^b

^a Department of Electrical and Computer Engineering, Babol Noshirvani University of Technology, Babol, Iran

^b Department of Electrical and Computer Engineering, Sharif University of Technology, Tehran, Iran

PAPER INFO

Paper history:

Received 03 August 2020

Received in revised form 15 September 2020

Accepted 21 September 2020

Keywords:

Boundary Conduction Mode

DC-DC Gan Boost Converter

Fully Zero Voltage Switching

High Frequency Switching

Valley Switching

Extended Switching

Zero Current Switching

ABSTRACT

This paper proposes a new variable frequency zero voltage switching (ZVS) control method for boost converter operating in boundary conduction mode (BCM). The intended method keeps the converter in BCM despite of the load and input voltage variations. This is done by changing switching frequency in a certain specified range. The proposed method can guarantee circuit performance in BCM via zero-crossing detection of the inductor current and changing the switching frequency. In addition, with a slight modification in control structure, it is possible to achieve a fully ZVS in all cases. This converter control is carried out in analog form without using microprocessors which, compared with the digital one, has less noise, cost and processing challenges in high frequency applications. Simulation results obtained from applying the proposed method on a GaN-based synchronous boost converter in two different switching frequency ranges (100KHz and 1MHz) are indicative of the proposed strategy advantages.

doi: 10.5829/ije.2020.33.11b.14

NOMENCLATURE

L	Inductor	Q_R	Charge for switch capacitor
D	Duty Cycle	I_L	Inductor current
V_i	Input Voltage	I_e	Extended current
V_{out}	Output Voltage	I_{em}	Negative maximum of inductor current
f_{sw}	Switching Frequency	T_R	Resonance time
C_{oss}	Switch capacitor		

1. INTRODUCTION

DC-DC boost converters are particularly significant due to their high voltage gain, input current continuity, and power factor correction. As it is known, different Pulse Width Modulation (PWM) methods are the well-known control strategies for these converters. Conventionally, in these methods, the voltage on the switch or its current is unexpectedly switched off and on, known as hard

switching. Switching losses, high stresses, limitations in higher frequencies, noise amplification, and electromagnetic interferences are among the important shortcomings of hard switching. In general, to minimize the size and volume of the power electronic converters, switching frequency should be increased which, in turn, increases switching losses and Electromagnetic Interferences (EMI). To solve these issues, soft switching methods are widely employed [1, 2].

*Corresponding Author Institutional Email: ghoreishy@nit.ac.ir (H. Ghoreishy)

Soft switching techniques include Zero Current Switching (ZCS) and Zero Voltage Switching (ZVS). Using soft switching causes switching losses reduction, high efficiency, better temperature control of switches in power electronic converters [3–7].

Resonant converters are the first category of the soft switching converters. Resonance circuits are used for creating soft switching conditions in these converters. One drawback of the resonant converters is the change in structure of the converter topology where the application of passive elements in the system leads to volume and cost increment [8]. One desirable method for the realization of soft switching in DC-DC converters is converter operation in Boundary Conduction Mode (BCM); so that, unlike resonant converters, this is conducted without the slightest change in the structure of the power electronic converter. Designing in BCM mode causes reduction of the input inductor size, loss reduction of switch turn-on time and reduction of some issues regarding reverse recovery compared with design in Continuous Conduction Mode (CCM). In addition, by slightly modifying the controller, the ZVS or near ZVS (also called valley switching) can be easily achieved. Boost Power Factor Correction (PFC) converters are widely used since the switching loss of the power switch can be minimized by ZVS or valley switching [9–11].

Over the past decades, due to space limitations and issues related to weight and cost reduction, the evolution of power electronic systems tended toward systems with high energy density, leading to an efficiency increase [12–15]. High frequency Silicon switch circuits have unacceptable switching loss. Therefore, in order to obtain the appropriate voltage and current ripples, large passive elements are required. The capacitors and inductors mainly comprise a large amount of volume and area. Due to the usage of large capacitors, problems such as reduced converter efficiency and inappropriate ripple have arisen. Nevertheless, designing the converter in BCM generates more current stress, which increases switch conductive losses and size of the input filter. Wide-bandgap (WBG) switches such as SiC (Silicon carbide) and GaN (Gallium nitride) are used to solve this problem due to the low gate charge and the input and output capacitors that operate at a higher switching frequency [16–19].

Regarding properties of GaN transistors, BCM with valley switching in a boost converter was exposed as an ideal application of newly emerged GaN products. This is because the parasitic elements of the devices can be best accommodated at high frequencies i.e. losses of the devices can be minimized [20].

One of the highly significant considerations in designing circuit operation in BCM is the zero-crossing detection of the inductor current. Various methods are proposed for zero-crossing detection of the inductor current and converter operation in BCM. An inductor

was used for current monitoring in [21]. Inverse current detection by a freewheeling switch was investigated and implemented in [22]. An RC filter for zero current detection was used in [23] by a series resistance in predictive online digital control method. Some sensors are employed for measuring inductor current, which are not appropriate in high frequency applications due to limitations in bandwidth, price and inaccurate current measurement. Therefore, current mirror technique, which is known as SenseFet in power electronic applications, are used for current monitoring. This technique is a simple and low-cost method with high efficiency [24, 25]. In this method, a GaN switch is used as SenseFet and the voltage drop of the sensor resistor is proportionate with switch current. Bandwidth is not limited in this method and measures current with high accuracy [26].

The BCM performance in DC-DC converters can be guaranteed by controlling the switching frequency. Regarding this matter, Variable on-time (VOT) control, which is a variable frequency technique, has been described in [27]. In this method, input voltage [28] or peak switch current [29] sampling is used to define the slope of the ramp signal, which is compared with the error amplifier output. Another method is the hysteresis control strategy in which the inductor current is limited between upper and lower bands. If the current crosses either bands, the switch control signal will be changed and the converter will remain in BCM [30].

A new method to implement ZVS in BCM with 5 MHz switching frequency is proposed in [31] which increases efficiency up to $\eta=98\%$. As presented in [32, 33], having a MHz switching frequency greatly reduces size of the inductor and converter input filter that significantly affects power density of the system. Nonetheless, conditions for a fully ZVS requires input and output voltages to be within a certain range. A ZVS extension method for BCM synchronous converter is presented in [34], such that synchronous rectifier ON-time is increased in bidirectional converter; therefore, a negative inductor current, capable of discharging capacitor of the main switch, is generated. A control method for achieving ZVS is implemented in [35] by eliminating dependency to input and output ratio in a MHz BCM boost based power factor correction circuit. To obtain the negative inductor current needed for achieving ZVS, sampling of the converter input and output voltages is required [36].

All the above methods were performed assuming that the circuit remains in BCM despite the changes in input and output parameters. However, any research that covers both BCM guarantee and circuit performance in fully ZVS has not been conducted yet.

A new high frequency method for controlling boost converter in BCM is proposed in this paper. The proposed method keeps boost converter in BCM despite of load and input voltage variations by changing

switching frequency in a certain specified range. After determining the desired frequency at which the converter returns to BCM, the controller keeps the switching frequency in a projected range. The applied converter is a synchronous boost converter using WBG devices. This method can guarantee circuit performance in BCM by zero-crossing detection of the inductor current and by changing switching frequency. In addition, with a slight change in control structure, it's possible to achieve a fully ZVS in all cases. This converter control is carried out in analog form without using microprocessors which, compared with digital one, has less noise, cost and processing challenges in high frequency applications.

The basic performance of the proposed control method is discussed in Section 2; presents the BCM operation both under valley and extended ZVS. The equations that define the converter operation under these modes are presented in Section 3. The proposed self-regulating control method for ZVS extension operation is proposed in Section 4. Simulation results are examined in Section 5 to ensure the accuracy of the proposed control algorithm method.

2. PROPOSED BOUNDARY CONDUCTION MODE CONTROL IN A BOOST CONVERTER MODEL

The proposed BCM control method is studied in this section. In order to show the desirable performance of this technique, it is applied to a synchronous boost converter in which the diode is replaced by a power electronic switch leading to conduction loss reduction and system efficiency increase [37].

It should be noted that the proposed control method is also applicable to the conventional boost converter. On the contrary, the realization of fully ZVS occurs only when the converter diode is replaced with a synchronous switch. In order to have an integrated control strategy, both BCM control and fully ZVS realization have been applied on the synchronous boost converter.

Synchronous boost converter along with the proposed BCM control technique is shown in Figure 1.

Firstly, the boost converter is designed in BCM. Then, applying the boundary condition, inductor size is obtained via Equation (1):

$$L_{BCM} = \frac{D(1-D)^2R}{2f_{sw}} \tag{1}$$

where D is the main switch duty cycle, R is the load and f_{sw} is the switching frequency. In this control method, the switching frequency varies in a pre-defined range. This range, by which the circuit can continue to operate in BCM, must first be calculated. To this end, the relationship between the input voltage, output power and output voltage variations are shown in Equation (2).

$$L_{BCM} \frac{2I_{Lave}}{(V_i - \frac{V_i^2}{V_{out}})} = L_{BCM} \frac{2P_{out}}{V_i^2(1 - \frac{V_i}{V_{out}})} = \frac{1}{f_{sw}} \tag{2}$$

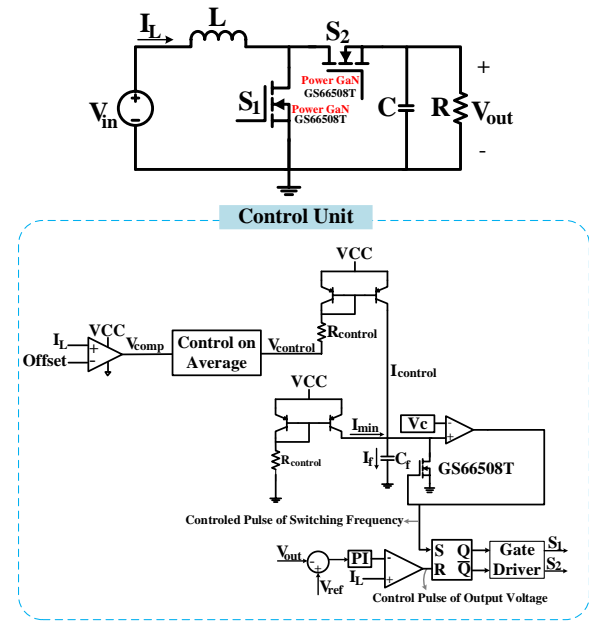


Figure 1. The boost converter and the proposed control block diagram

According to Equation (2), if load current increases at the presence of the constant input and output voltages, the converter performance mode will change from BCM to CCM. The frequency variation range in which the circuit can be maintained in BCM is dependent on the input voltage, output voltage and power variations.

Figure 2 shows the frequency variations versus the input voltage and output power according to Equation (2). As can be seen from the figure, by a proper control of the switching frequency, converter can always be kept in BCM despite of the load and input voltage variations. As the output current increases, the converter performance changes from BCM to CCM.

As shown in Figure 3, the inductor current has the same mean value in both BCM and CCM operation modes. If the converter is shifted to CCM, the control strategy can return it to BCM by reducing the frequency.

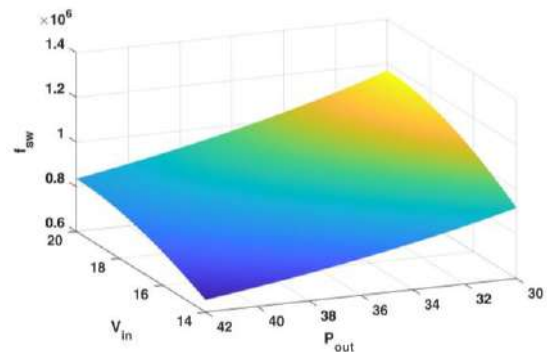


Figure 2. Frequency variation range versus input voltage and output power

In the proposed method, after inductor current sampling, an offset with a value close to zero is compared with this current. Comparator output is shown as V_{comp} in Equation (3). According to this equation, if inductor current is lower than offset value, the comparator output would be +5V.

$$V_{comp} = \begin{cases} +5 & I_L < \text{offset} \\ 0 & I_L > \text{offset} \end{cases} \quad (3)$$

where V_{comp} is a square wave. By applying this waveform to control on average block, V_{comp} average signal ($V_{control}$) is computed according to Equation (4). Then, according to Equation (5), $V_{control}$ is applied to regulate $I_{control}$. This current charges C_f and plays a crucial role in determining switching frequency of the converter.

$$V_{control} = V_{cc} - \frac{k_p \int_T V_{comp} dt}{T} \quad (4)$$

$$I_{control} = \frac{V_{cc} - V_{EB} - V_{control}}{R_{control}} \quad (5)$$

If $I_{control}$ is zero, there would be no charging source for C_f , and production of the switching frequency required for circuit performance would be disrupted. In this case, an auxiliary current source should be used to generate I_{min} for C_f charging and minimum required frequency. In general, required current for C_f charging is calculated according to Equation (6).

$$I_f = I_{control} + I_{min} \quad (6)$$

$$I_{min} = \frac{V_{cc} - V_{EB}}{R_{min}} \quad (7)$$

To discharge the capacitor, its voltage should be compared with V_c reference value. When the capacitor voltage reaches to V_c , the comparator output connected to the control switch gate is set to logic state 1. Therefore, the intended switch is turned on and the capacitor will be short-circuited. Hence, the capacitor begins to discharge. By continuous charging and discharging of the capacitor, a pulse is produced at the comparator output, the frequency of which is according to Equation (8).

$$f_{sw} = \frac{I_f}{C_f V_c} \quad (8)$$

Therefore, by applying the proposed control method, switching frequency could be regulated for circuit performance in BCM. Peak current mode method is used

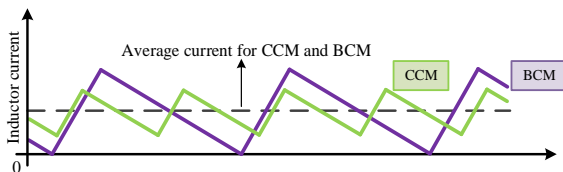


Figure 3. Inductor current in BCM and CCM modes with same mean value

to stabilize the output voltage in this converter. The output pulse generated by the capacitor charging and discharging (which determines switching frequency of the converter), is inserted into a RS flip-flop set port. On the other hand, reset pulse of the intended flip-flop is applied by PI controller responsible for setting the output voltage error to zero. The flip-flop output and its complement, generate commands for S_1 and S_2 switches, respectively. In this paper, by a slight change in control structure, the condition is provided for circuit performance in fully ZVS, as discussed in the following.

3. OPERATION ANALYSIS OF BOOST CONVERTER

Inductor current in a switching interval of synchronous boost converter working in BCM is shown in Figure 4 [38].

It should be noted that given the input and output ranges and converter control method, each of these three states in Figure 4 could occur in this converter. If complete control is not applied to the converter operating in BCM, depending on the input and output ratio, modes (a) and (b) can be possible; such that in the case of $V_{in} < V_{out} / 2$, (a) and for $V_{in} > V_{out} / 2$, (b) is possible. Likewise, by appropriate control, fully ZVS can be achieved according to (c). Each switching interval includes two major times (T_{ON} and T_{OFF}) and two resonant times in all three above-mentioned states. However, all three states are similar in the first two subintervals and different in third and fourth subintervals. In the following, the first two subintervals are examined first, then three states are explained, separately.

Primary current of the inductor (I_L) and primary voltage of the capacitor of the main switch (S_1) at the beginning of each circuit switching interval is assumed as Equation (9):

$$I_L(t_0) = 0, \quad V_{DS1}(t_0) = 0 \quad (9)$$

Each switching interval of this converter is divided into four subintervals, each of which is discussed below.

Subinterval 1 [$t_0 < t < t_1$]: S_1 is turned on during this interval and inductor current increases linearly with the slope of $\frac{di}{dt} = \frac{V_{in}}{L}$. This subinterval is called turn-on time (T_{ON}), the length of which is determined by control loop of the output voltage regulation. S_1 is turned off at t_1 .

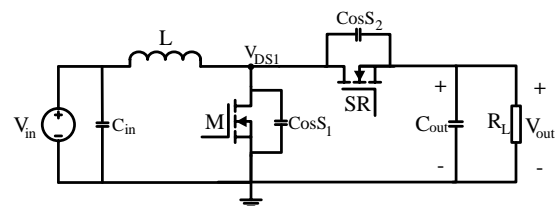


Figure 4. Synchronous boost converter

The ultimate value of I_L and V_{DS1} and length of this subinterval are as below:

$$T_{ON}=t_1-t_0, I_L(t_1)=I_p, V_{DS1}(t_1)=0 \quad (10)$$

Subinterval 2 [$t_1 < t < t_2$]: During this subinterval, both S_1 and S_2 are off, and a resonance occurs between the non-linear capacitors of S_1 and S_2 (C_{OSS1}, C_{OSS2}) and the inductor; therefore, C_{OSS1}, C_{OSS2} will be discharged. The length of this subinterval is short, and high inductor current is with the amount of I_p . Hence, this subinterval can be neglected for the following calculations.

The ultimate value of I_L and V_{DS1} and length of this subinterval are as below:

$$T_{R1}=t_2-t_1, I_L(t_2)=I_{pp} \gg I_p, V_{DS1}(t_2)=V_{out} \quad (11)$$

Subinterval 3 [$t_2 < t < t_3$]: When C_{OSS2} is fully discharged, diode of S_2 switch begins to flow inductor current. In fact, after a short delay (T_{R1}), S_2 switch is turned on at zero voltage. At this interval, voltage applied to the inductor is negative, thus I_L is reduced. Due to the fact that S_1 is off at this interval, this is the off-time (T_{off}).

The ultimate value of I_L and V_{DS1} and length of this subinterval are as below:

$$T_{off}=t_3-t_2, I_L(t_3)=0, V_{DS1}(t_2)=V_{out} \quad (12)$$

Subinterval 4 [$t_3 < t < t_4$]: When I_L reaches to zero, switch S_1 is turned off and the equivalent circuit is like Figure 6; therefore, a resonance occurs between the capacitor and inductor and an oscillation with the frequency of $\omega_0 = \frac{1}{\sqrt{L(C_{OSS1}+C_{OSS2})}}$ begins, the behavior of which depends

on the ratio of input and output voltage, i.e. $\frac{V_{in}}{V_{out}}$.

3. 1. Natural Switching Operation ($V_{in} < \frac{V_{out}}{2}$)

When input voltage is less than $V_{out}/2$, according to Figure 5(a), V_{DS1} will be zero, and S_1 is turned on at zero voltage and negative current.

3. 2. Valley Switching Operation ($V_{in} > \frac{V_{out}}{2}$)

When input voltage is greater than $V_{out}/2$, according to Figure 5(b), V_{DS1} will be zero at resonance interval of T_{R2} , because inductor does not have enough energy to discharge capacitor and S_2 turns on at a small voltage of V_{valley} . In this case, switching loss is reduced, but fully ZVS does not occur.

The ultimate value of I_L and V_{DS1} and length of this subinterval are as below:

$$T_{off}=t_4-t_3, I_L(t_3)=0, V_{DS1}(t_2)=2V_{in}-V_{out}=V_{valley} \quad (13)$$

To solve this issue and achieve ZVS, S_2 should be stayed on for a longer period of time. As it can be observed in Figure 5(c), during T_{R2} , inductor current should reach to an appropriate negative current so that C_{OSS1} is fully discharged and S_1 turned on both at zero voltage and current.

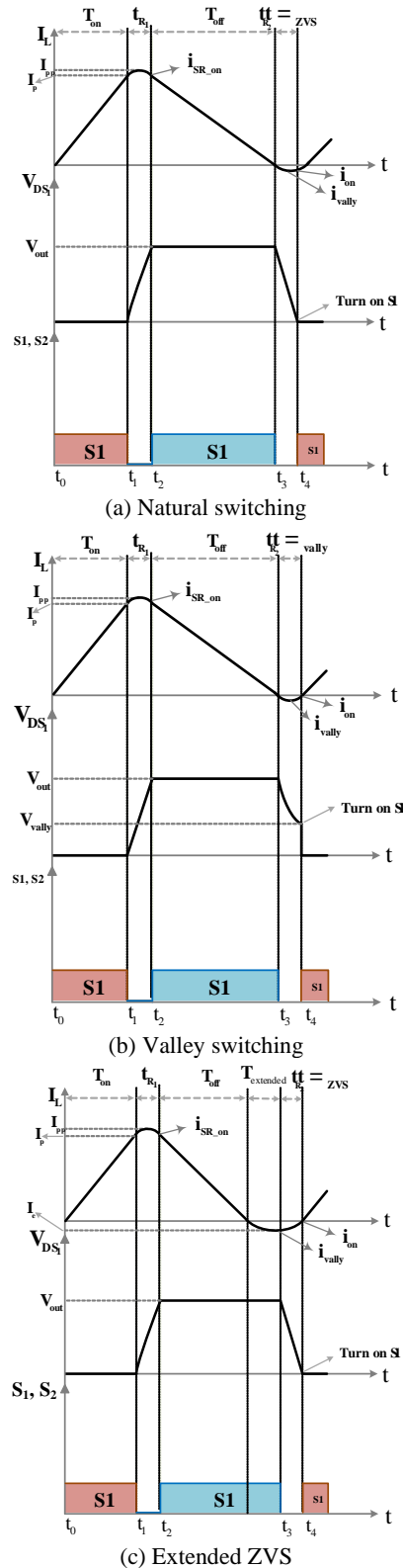


Figure 5. Current and voltage waveforms: (a) BCM natural switching operating waveforms when $V_{in} \leq 0.5V_{out}$, (b) BCM valley switching operating waveforms when $V_{in} > 0.5V_{out}$, (c) Operation waveforms based on the proposed extended ZVS control.

4. PROPOSED ANALOG ZVS CONTROL STRATEGY

In this section, the required current (I_e) to achieve fully ZVS is calculated. Since this current depends on C_{OSS} switch capacitor and this capacitor is non-linear, according to the datasheet [39], the equationship between C_{OSS} and V_{DS} in $[0-V_{OUT}]$ is estimated as Equation (14):

$$C_{OSS} = aV_{DS}^3 + bV_{DS}^2 + cV_{DS} + d \quad (14)$$

The coefficient of a, b, c, and d are calculated using cftool software.

To achieve fully ZVS, I_L should be reduced to I_e . After reaching to I_e according to Figure 5(c), S_1 is turned off and C_{OSS1} begins to charge and C_{OSS2} begins to discharge. In this case, according to Figure 4, C_{OSS1} and C_{OSS2} are in parallel ($C = C_{OSS1} || C_{OSS2}$), and the equivalent circuit is according to Figure 6. Capacitor C is assumed linear and its average value is estimated as Equation (15).

$$\begin{cases} Q_R = \int_0^{V_{out}} C_{OSS} dv_{DS} \\ C = C_{ave} = \frac{Q_R}{V_{out}} \end{cases} \quad (15)$$

According to Figure 7, inductor current will be as follows:

$$\begin{cases} I_L(t) = A \cos \omega_0 t + B \sin \omega_0 t + CV_{in} \\ A = I_e - CV_{in} \\ B = \sqrt{\frac{C}{L}} (V_{in} - V_{out}) \\ \omega_0 = \frac{1}{\sqrt{LC}} \end{cases} \quad (16)$$

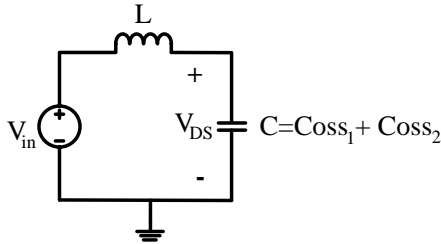


Figure 6. Equivalent resonant circuit

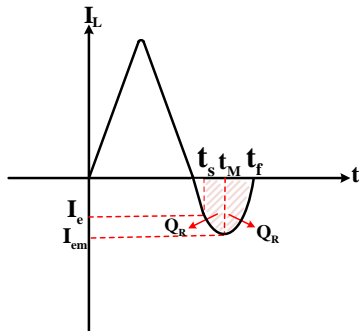


Figure 7. Detailed inductor current

To calculate I_e current, Equation (17) is used in diagram of Figure 7:

$$Q_R = \int_{t_s}^{t_m} I_L dt = \int_{t_1}^{t_2} I_L dt \quad (17)$$

In $[t_s - t_m]$, Q_R is shown as Equation (18):

$$Q_R = \frac{A}{\omega_0} \sin \omega_0 t_m - \frac{B}{\omega_0} \cos \omega_0 t_m + CV_{in} t_m + \frac{B}{\omega_0} \quad (18)$$

And in $[t_m - t_f]$:

$$Q_R = \frac{A}{\omega_0} (\sin \omega_0 t_f - \sin \omega_0 t_m) - \frac{B}{\omega_0} (\cos \omega_0 t_f - \cos \omega_0 t_m) + CV_{in} (t_f - t_m) \quad (19)$$

T_m and t_f values are calculated according to Equations (20) and (21):

$$t_m = L \frac{I_{em} - I_e}{V_{in} - V_{out}} \quad (20)$$

$$t_f = L \frac{I_{em} - I_e}{V_{in} - V_{out}} - \frac{LI_{em}}{V_{in}} \quad (21)$$

Using Equations (18)-(21) and Taylor extension, Q_R will be close to zero, I_e and I_{em} (I_{em} is the negative maximum of I_L) will be according to Equations (22) and (23):

$$\begin{cases} I_e = \sqrt{k_1^2 (1 - 2k_2 V_{out})^2 - 4(1 - k_1 (V_{out} - V_{in})) (k_1 k_2 (V_{out} + V_{in}))} \\ k_1 = \frac{Q}{L} (V_{in} - V_{out}) \\ k_2 = \frac{1}{2V_{in}} \end{cases} \quad (22)$$

$$I_{em} = \frac{k_1 + I_e^2}{I_e} \quad (23)$$

Since $T_{SW} = T_{on} + T_{off} + T_e + T_R$, each subinterval is obtained according to Equation (24):

$$\begin{cases} T_{on} = \frac{LI_{em}}{V_n} \\ T_{off} = \frac{LI_{em}}{V_o - V_n} \\ T_e = \frac{-LI_e}{V_o - V_n} \\ T_R = L \frac{I_e - I_{em}}{V_o - V_n} - \frac{LI_{em}}{V_n} \end{cases} \quad (24)$$

As stated in Section 2, the proposed closed-loop control system guarantees converter performance in BCM. Given the attained equations, fully ZVS can be obtained by a slight change in this control system. To this end, pulse commands going to S_1 and S_2 should be changed according to Figure 8. In addition, offset value computed by I_e should be replaced by Equation (22). Therefore, control loop of inductor current, in this section, determines I_e instead of zero-crossing detection. When I_L becomes equal with I_e , controlled pulse of the switching frequency goes to the R port of flip-flop2 and commands S_2 to turn off. Then, this pulse is delayed as long as T_R time span, calculated in Equation (24). C_{OSS1} is fully discharged during this time, then S_2 is commanded to be turned on. It should be noted that, as before, S_1 turn-off

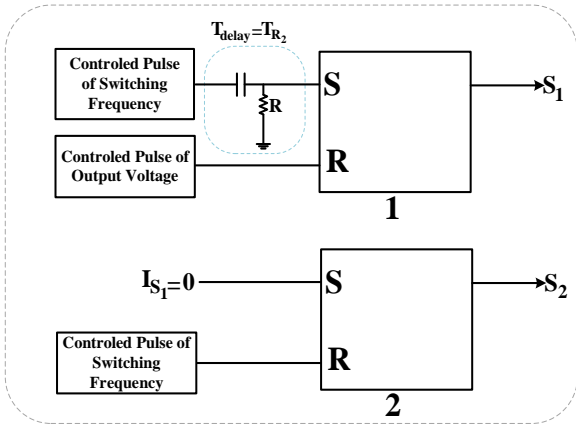


Figure 8. The simplified control diagram of the proposed system control strategy

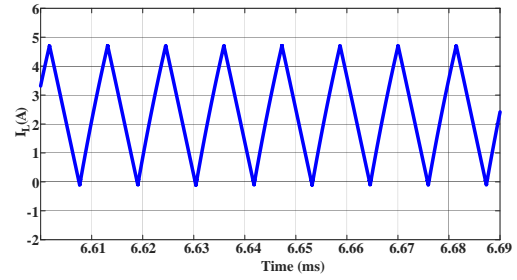
command is issued by control loop of voltage stabilizer. To reduce the loss more than ever, turn-on command of S_2 is issued after reaching S_1 current to zero. Given the above, it is clear that the proposed control method guarantees both ZVS and ZCS.

5. SIMULATION RESULTS

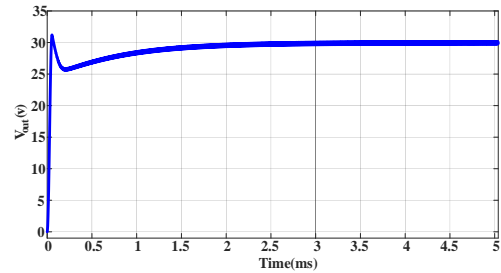
In order to validate the accuracy of the circuit performance, the proposed method is applied to a synchronous boost converter and implemented in the LTspice software. Also, the values of the circuit parameters are displayed in Table 1.

Boost converter simulation is conducted by the proposed control technique in two switching frequency ranges. At first, the intended converter is simulated at 100KHz to prove the accurate performance in BCM despite load changes; then, at 1MHz switching frequency to prove that control system can achieve fully ZVS.

The steady state inductor current in BCM is shown in Figure 9(a). As can be seen from the figure, under nominal frequency and rated load, the proposed control



(a)



(b)

Figure 9. Simulation results: (a) Inductor current, (b) Output voltage

algorithm maintains the inductor current in BCM. Figure 9(b) shows the output voltage. As is depicted in the figure, by using the peak current mode control method, the output voltage of the circuit conforms well to its reference value. This voltage reaches to its ultimate value after 1.5ms. In this case, the load resistance and the switching frequency values are equal to 25Ω and 100 kHz respectively.

Figure 10 shows the converter output voltage at the presence of increasing the load current up to 20%. As it can be seen in Figure 10, the output voltage reaches to its reference value after 0.5ms. Moreover, due to the increase in the load current, the converter mode has changed from BCM to CCM. However, the controller performs in such a manner that the inductor current returns to BCM shortly after the load changes. The load resistance and the switching frequency values are equal to 20Ω and 80KHz respectively. It means that the controller has decreased the switching frequency in order to yield the BCM condition.

TABLE 1. Simulation parameters

Parameters/Devices	Symbol	Value/Number
Inductor	L	17uH($f_{sw}=100KHz$) 1.7uH($f_{sw}=1MHz$)
Output Capacitor	C	17.2uF($f_{sw}=100KHz$) 17.2uF($f_{sw}=1MHz$)
Switch	S	GS66508T
Input Voltage	V_{in}	17V
Output Voltage	V_{out}	30V
Load	R_{Load}	25Ω
Output Power	P_{out}	36W

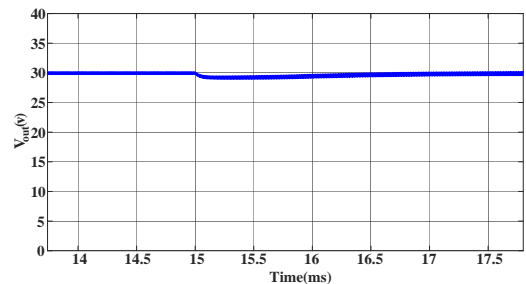


Figure 10. Output voltage at CCM and BCM regions

Figure 11 illustrates the output pulse from the comparator. According to this figure, inductor current returns from CCM to BCM after 0.5ms. As noted before, this pulse will then be entered to the averaged block.

Figure 12 shows inductor current during load current variations. As is depicted in the figure, inductor current is primarily in CCM mode. In this case, controller begins to operate and reduces the switching frequency.

Also, in Figure 13, by 20% reduction of load current, first inductor current flows from BCM to DCM; then in a short period of time (about 0.4ms), the controller

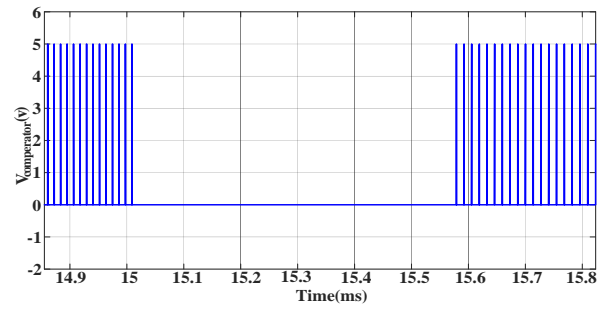


Figure 11. $V_{comparator}$ at different CCM and BCM regions

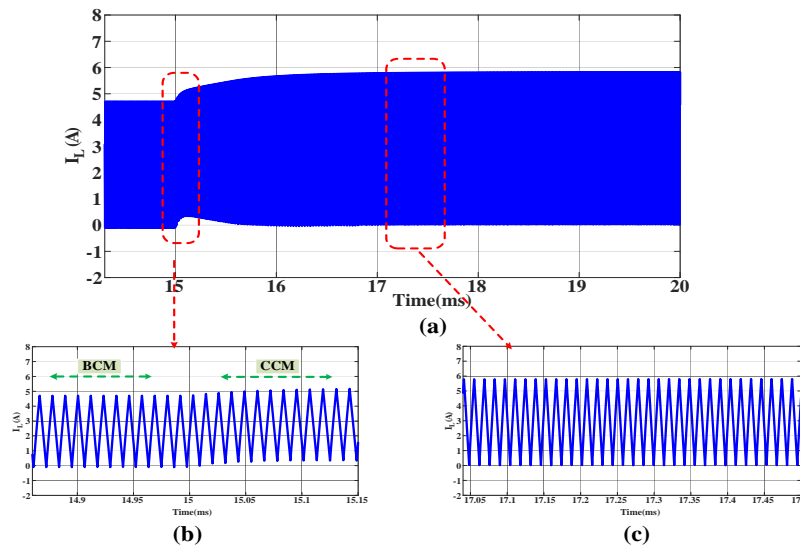


Figure 12. Inductor current at different CCM and BCM region: (a) converter operation at different CCM and BCM regions, (b) initial BCM conduction ($R=25\Omega$) and transient to CCM ($R=20\Omega$) (First area), (c) new BCM steady-state condition after performing the control scheme (Second area)

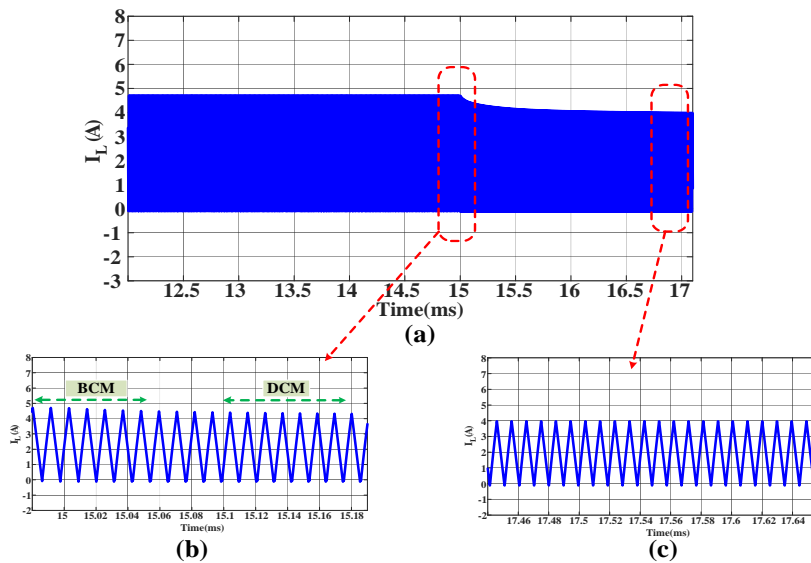


Figure 13. Inductor current at different DCM and BCM region: (a) converter operation at different DCM and BCM regions, (b) initial BCM conduction ($R=25\Omega$) and transient to DCM ($R=30\Omega$) (First area), (c) new BCM steady-state condition after performing the control scheme (Second area)

increases switching frequency with an accurate detection of the converter performance, and converter is returned to BCM. The output voltage, in these variations, has reached to reference value in less than 0.6ms, shown in Figure 14.

In the following, simulation results of the intended converter will be examined using the proposed control method to achieve fully ZVS in 1MHz switching frequency.

Extended closed-loop control with V_{IN} , V_{OUT} , V_{DS1} , and I_L in $V_{out}=30V, V_{in}=17V, f_s=1MHz$ to achieve fully ZVS is shown in Figure 15.

Pulse commands applied to S_1 and S_2 are shown in Figure 16. Turn-on command of S_1 is issued in ZVS and ZCS. S_1 state is “ON” during T_{on} . S_2 turn-on command will be issued when S_1 current reaches to zero. When I_L is equal to I_c (calculated in Section 4), S_2 will be turned off. Also seen in the related figure, S_1 turn-on command is delayed as much as T_R time. V_{DS1} and V_{DS2} (Figure 17) proves the accurate performance of the proposed control method.

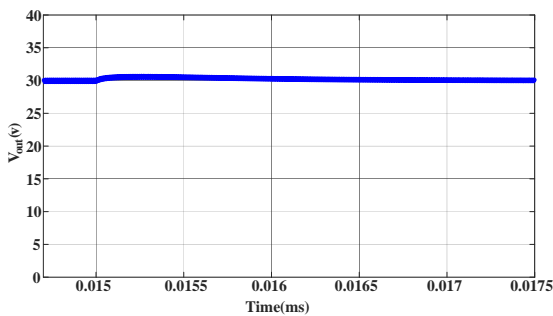


Figure 14. Output voltage at different DCM and BCM regions

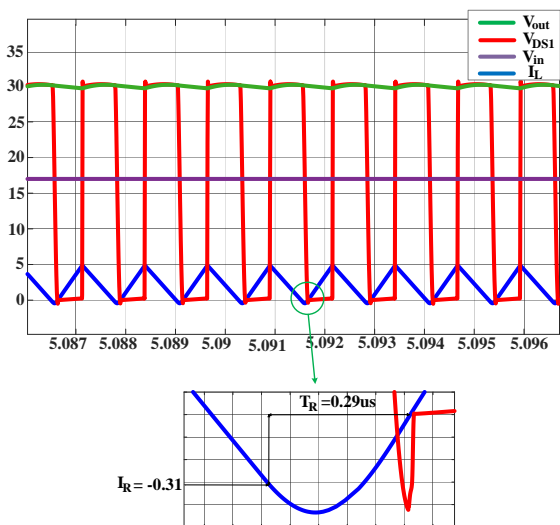


Figure 15. ZVS operation waveforms with the proposed ZVS control: $P_{out}=36W, V_{out}=30V, V_{in}=17V, f_s=1MHz$

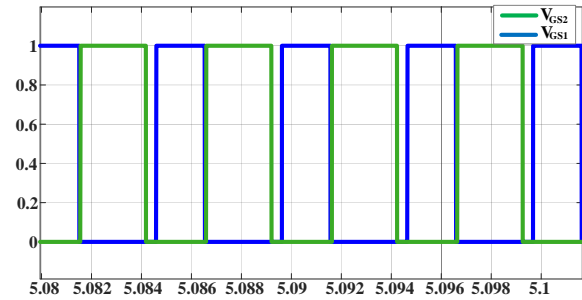


Figure 16. Pulse commands applied to S_1 and S_2

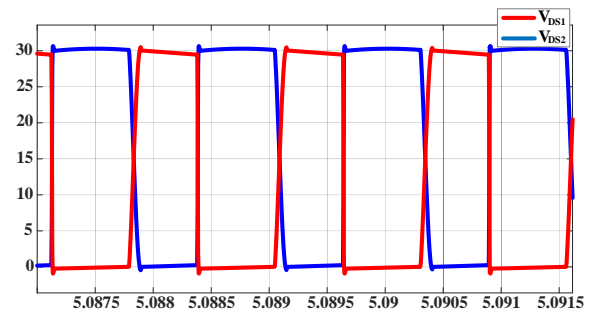


Figure 17. Zoomed in ZVS switching waveforms with improved ZVS time margin based on the proposed ZVS control

6. CONCLUSION

A new variable frequency ZVS control method for boost converter operating in BCM has been proposed in this paper. This technique is carried out in analog form without using microprocessor as analog controllers have less noise, less cost and processing problems in high frequency applications. The intended method keeps the converter in BCM in spite of load and input voltage variations by changing switching frequency in a certain specified range. In addition, with a slight change in control structure, it's possible to achieve a fully ZVS in both $V_{in} < V_{out}/2$ and $V_{in} > V_{out}/2$ cases. Simulation results obtained from applying the proposed method on a GaN-based synchronous boost converter in two different switching frequency ranges (100KHz and 1MHz) verify the proposed strategy advantages.

7. REFERENCES

- Hariya, A., Matsuura, K., Yanagi, H., Tomioka, S., Ishizuka, Y., and Ninomiya, T. "Five-Megahertz PWM-Controlled Current-Mode Resonant DC-DC Step-Down Converter Using GaN-HEMTs." *IEEE Transactions on Industry Applications*, Vol. 51, No. 4, (2015), 3263–3272. <https://doi.org/10.1109/TIA.2015.2391439>
- Sarvi, M., Derakhshan, M., and Sedighzadeh, M. "A New

- Intelligent Controller for Parallel DC/DC Converters.” *International Journal of Engineering, Transactions A: Basics*, Vol. 27, No. 1, (2014), 131–142. <https://doi.org/10.5829/idosi.ije.2014.27.01a.16>
3. Mohammadi, M. R., and Farzanehfard, H. “A New Family of Zero-Voltage-Transition Nonisolated Bidirectional Converters with Simple Auxiliary Circuit.” *IEEE Transactions on Industrial Electronics*, Vol. 63, No. 3, (2016), 1519–1527. <https://doi.org/10.1109/TIE.2015.2498907>
 4. Huang, W., and Moschopoulos, G. “A new family of zero-voltage-transition PWM converters with dual active auxiliary circuits.” *IEEE Transactions on Power Electronics*, Vol. 21, No. 2, (2006), 370–379. <https://doi.org/10.1109/TPEL.2005.869749>
 5. Zhang, Y., and Sen, P. C. “A new soft-switching technique for buck, boost, and buck-boost converters.” *IEEE Transactions on Industry Applications*, Vol. 39, No. 6, (2003), 1775–1782. <https://doi.org/10.1109/TIA.2003.818964>
 6. Subramanian, N., Prasanth, P., Srinivasan, R., Subhesh, R. R., and Seyezhai, R. “Analysis and Experimentation of Soft Switched Interleaved Boost Converter for Photovoltaic Applications.” *International Journal of Engineering, Transactions A: Basics*, Vol. 28, No. 10, (2015), 1469–1475. <https://doi.org/10.5829/idosi.ije.2015.28.10a.10>
 7. R, S., and Nair, M. “Simulation and Experimental Verification of Closed Loop Operation of Buck / Boost DC-DC Converter with Soft Switching.” *International Journal of Engineering, Transactions A: Basics*, Vol. 25, No. 4, (2012), 267–274. Retrieved from http://www.ije.ir/article_72033.html
 8. Liu, K. H., and Lee, F. C. “Zero-voltage switching technique in DC/DC converters.” In PESC Record - IEEE Annual Power Electronics Specialists Conference, (1986), 58–70. <https://doi.org/10.1109/pesc.1986.7415546>
 9. Huber, L., Irving, B. T., and Jovanović, M. M. “Review and stability analysis of PLL-based interleaving control of DCM/CCM boundary boost PFC converters.” *IEEE Transactions on Power Electronics*, Vol. 24, No. 8, (2009), 1992–1999. <https://doi.org/10.1109/TPEL.2009.2018560>
 10. Husev, O., Liivik, L., Blaabjerg, F., Chub, A., Vinnikov, D., and Roasto, I. “Galvanically Isolated Quasi-Z-Source DC-DC Converter With a Novel ZVS and ZCS Technique.” *IEEE Transactions on Industrial Electronics*, Vol. 62, No. 12, (2015), 7547–7556. <https://doi.org/10.1109/TIE.2015.2455522>
 11. Liu, Z., Huang, Z., Lee, F. C., and Li, Q. “Digital-Based Interleaving Control for GaN-Based MHz CRM Totem-Pole PFC.” *IEEE Journal of Emerging and Selected Topics in Power Electronics*, Vol. 4, No. 3, (2016), 808–814. <https://doi.org/10.1109/JESTPE.2016.2571302>
 12. Waffler, S., and Kolar, J. W. “Efficiency optimization of an automotive multi-phase bi-directional DC-DC converter.” In IEEE 6th International Power Electronics and Motion Control Conference, IPEMC '09, (2009), 566–572. <https://doi.org/10.1109/IPEMC.2009.5157451>
 13. Hartmann, M., Miniboeck, J., Ertl, H., and Kolar, J. W. “A three-phase delta switch rectifier for use in modern aircraft.” *IEEE Transactions on Industrial Electronics*, Vol. 59, No. 9, (2012), 3635–3647. <https://doi.org/10.1109/TIE.2011.2158770>
 14. Hartmann, M., and Kolar, J. W. “Analysis of the trade-off between input current quality and efficiency of high switching frequency PWM rectifiers.” In International Power Electronics Conference - ECCE Asia -, IPEC 2010, (2010), 534–541. <https://doi.org/10.1109/IPEC.2010.5543283>
 15. Badstuebner, U., Biela, J., Christen, D., and Kolar, J. W. “Optimization of a 5-kW telecom phase-shift dc-dc converter with magnetically integrated current doubler.” *IEEE Transactions on Industrial Electronics*, Vol. 58, No. 10, (2011), 4736–4745. <https://doi.org/10.1109/TIE.2010.2103536>
 16. Nussbaumer, T., Raggl, K., and Kolar, J. W. “Design guidelines for interleaved single-phase boost PFC circuits.” *IEEE Transactions on Industrial Electronics*, Vol. 56, No. 7, (2009), 2559–2573. <https://doi.org/10.1109/TIE.2009.2020073>
 17. Wang, Z., Wang, S., Kong, P., and Lee, F. C. “DM EMI noise prediction for constant on-time, critical mode power factor correction converters.” *IEEE Transactions on Power Electronics*, Vol. 27, No. 7, (2012), 3150–3157. <https://doi.org/10.1109/TPEL.2011.2182059>
 18. Hernandez, J. C., Mira, M. C., Petersen, L. P., Andersen, M. A. E., and Petersen, N. H. “Zero Voltage Switching Control Method for MHz Boundary Conduction Mode Converters.” *IEEE Transactions on Industrial Electronics*, Vol. 67, No. 2, (2020), 1544–1554. <https://doi.org/10.1109/TIE.2019.2926039>
 19. Zhang, Y., Yao, C., Zhang, X., Chen, H., Li, H., and Wang, J. “Power Loss Model for GaN-Based MHz Critical Conduction Mode Power Factor Correction Circuits.” *IEEE Journal of Emerging and Selected Topics in Power Electronics*, Vol. 8, No. 1, (2020), 141–151. <https://doi.org/10.1109/JESTPE.2019.2948148>
 20. Wang, W., Pansier, F., Popovic, J., and Ferreira, J. A. “Design and optimization of a GaN GIT based PFC boost converter.” *Chinese Journal of Electrical Engineering*, Vol. 3, No. 3, (2019), 34–43. <https://doi.org/10.23919/cjee.2017.8250422>
 21. Choi, H. “Interleaved boundary conduction mode (BCM) buck power factor correction (PFC) converter.” *IEEE Transactions on Power Electronics*, Vol. 28, No. 6, (2013), 2629–2634. <https://doi.org/10.1109/TPEL.2012.2222930>
 22. Gao, Y., Wang, S., Li, H., Chen, L., Fan, S., and Geng, L. “A novel zero-current-detector for DCM operation in synchronous converter.” In IEEE International Symposium on Industrial Electronics, (2012), 99–104. <https://doi.org/10.1109/ISIE.2012.6237066>
 23. Chang, Y. T., and Lai, Y. S. “Online parameter tuning technique for predictive current-mode control operating in boundary conduction mode.” *IEEE Transactions on Industrial Electronics*, Vol. 56, No. 8, (2009), 3214–3221. <https://doi.org/10.1109/TIE.2009.2024651>
 24. Liu, P., Zhang, L., Huang, A. Q., Guo, S., and Lei, Y. “High bandwidth current sensing of SiC MOSFET with a Si current mirror.” In WiPDA 2016 - 4th IEEE Workshop on Wide Bandgap Power Devices and Applications, (2016), 200–203. <https://doi.org/10.1109/WiPDA.2016.7799937>
 25. Wen, Y., Rose, M., Fernandes, R., Van Otten, R., Bergveld, H. J., and Trescases, O. “A Dual-Mode Driver IC with Monolithic Negative Drive-Voltage Capability and Digital Current-Mode Controller for Depletion-Mode GaN HEMT.” *IEEE Transactions on Power Electronics*, Vol. 32, No. 1, (2017), 423–432. <https://doi.org/10.1109/TPEL.2016.2537002>
 26. Biglarbegan, M., Kim, N., and Parkhideh, B. “Boundary Conduction Mode Control of a Boost Converter with Active Switch Current-Mirroring Sensing.” *IEEE Transactions on Power Electronics*, Vol. 33, No. 1, (2018), 32–36. <https://doi.org/10.1109/TPEL.2017.2716934>
 27. Ren, X., Zhou, Y., Guo, Z., Wu, Y., Zhang, Z., and Chen, Q. “Simple Analog-Based Accurate Variable On-time Control for Critical Conduction Mode Boost Power Factor Correction Converters.” *IEEE Journal of Emerging and Selected Topics in Power Electronics*, Vol. 8, No. 4, (2019), 4025–4036. <https://doi.org/10.1109/JESTPE.2019.2926794>
 28. Kim, J. W., Choi, S. M., and Kim, K. T. “Variable on-time control of the critical conduction mode boost power factor correction converter to improve zero-crossing distortion.” In Proceedings of the International Conference on Power Electronics and Drive Systems (Vol. 2), (2005), 1542–1546. <https://doi.org/10.1109/peds.2005.1619933>

29. Tsai, J. C., Chen, C. L., Chen, Y. T., Ni, C. L., Chen, C. Y., and Chen, K. H. "Perturbation on-time (POT) technique in power factor correction (PFC) controller for low total harmonic distortion and high power factor." *IEEE Transactions on Power Electronics*, Vol. 28, No. 1, (2013), 199–212. <https://doi.org/10.1109/TPEL.2012.2195333>
30. Hariharan, K., and Kapat, S. "Need for variable frequency control in DC-DC switching converters - Challenges and opportunities using digital implementation." *Proceedings of the Indian National Science Academy*, Vol. 84, No. 3, (2018), 657–668. <https://doi.org/10.16943/ptinsa/2018/49334>
31. Huang, X., Liu, Z., Lee, F. C., and Li, Q. "Characterization and enhancement of high-voltage cascode GaN devices." *IEEE Transactions on Electron Devices*, Vol. 62, No. 2, (2015), 270–277. <https://doi.org/10.1109/TED.2014.2358534>
32. Hernandez, J. C., Petersen, L. P., and Andersen, M. A. E. "Characterization and evaluation of 600 v range devices for active power factor correction in boundary and continuous conduction modes." In Conference Proceedings - IEEE Applied Power Electronics Conference and Exposition - APEC, (2015), 1911–1916. <https://doi.org/10.1109/APEC.2015.7104607>
33. Hernandez, J. C., Petersen, L. P., and Andersen, M. A. E. "A comparison between boundary and continuous conduction modes in single phase PFC using 600V range devices." In Proceedings of the International Conference on Power Electronics and Drive Systems, (2015), 1019–1023. <https://doi.org/10.1109/PEDS.2015.7203487>
34. Su, B., Zhang, J., and Lu, Z. "Totem-pole boost bridgeless PFC rectifier with simple zero-current detection and full-range ZVS operating at the boundary of DCM/CCM." *IEEE Transactions on Power Electronics*, Vol. 26, No. 2, (2011), 427–435. <https://doi.org/10.1109/TPEL.2010.2059046>
35. Liu, Z., Huang, X., Mu, M., Yang, Y., Lee, F. C., and Li, Q. "Design and evaluation of gan-based dual-phase interleaved MHz critical mode PFC converter." In IEEE Energy Conversion Congress and Exposition, ECCE, (2014), 611–616. <https://doi.org/10.1109/ECCE.2014.6953451>
36. Marxgut, C., Krismer, F., Bortis, D., and Kolar, J. W. "Ultraflat interleaved triangular current mode (TCM) single-phase PFC rectifier." *IEEE Transactions on Power Electronics*, Vol. 29, No. 2, (2014), 873–882. <https://doi.org/10.1109/TPEL.2013.2258941>
37. Chen, Y., Asadi, P., and Parto, P. "Comparative analysis of power stage losses for synchronous buck converter in diode emulation mode vs. continuous conduction mode at light load condition." In Conference Proceedings - IEEE Applied Power Electronics Conference and Exposition - APEC, (2010), 1578–1583. <https://doi.org/10.1109/APEC.2010.5433442>
38. Huber, L., Irving, B. T., and Jovanović, M. M. "Effect of valley switching and switching-frequency limitation on line-current distortions of DCM/CCM boundary boost PFC converters." *IEEE Transactions on Power Electronics*, Vol. 24, No. 2, (2009), 339–347. <https://doi.org/10.1109/TPEL.2008.2006053>
39. GaN Systems, "GS66508T, Top-side cooled 650 V E-mode GaN transistor datasheet", GaN-on silicon power transistor, (2009), 1-37.

Persian Abstract

چکیده

در این مقاله یک روش کنترلی فرکانس متغیر از کلیدزنی در ولتاژ صفر برای مبدل بوستی که در مد هدایت مرزی کار می‌کنند، پیشنهاد گردیده است. روش مذکور قادر است علیرغم تغییرات بار و ولتاژ ورودی، مبدل را از طریق تغییر فرکانس کلیدزنی در یک محدوده معین، همواره در مد هدایت مرزی نگاه دارد. تضمین باقی ماندن در این مد، با تشخیص لحظه گذر از صفر جریان سلف و تغییر فرکانس کلیدزنی امکان‌پذیر است. علاوه بر آن، با تغییر مختصری در ساختار کنترلی، دستیابی به کلیدزنی در ولتاژ صفر به طور کامل محقق می‌گردد. کنترل این مبدل به صورت آنالوگ و بدون استفاده از میکروپروسسور می‌باشد که در مقایسه با کنترل‌کننده‌های دیجیتال، دارای نویز کمتر، هزینه و چالش‌های پردازشی کمتری در کاربردهای فرکانس بالا است. نتایج شبیه‌سازی حاصل از اعمال روش پیشنهادی بر روی یک مبدل بوست سنکرون بر مبنای کلیدهای فرکانس بالای GaN، در دو محدوده متفاوت از فرکانس کلیدزنی (۱۰۰ کیلوهرتز و ۱ مگاهرتز) تاییدکننده مزایای استراتژی مذکور می‌باشد.



Evaluation and Ranking of Sustainable Third-party Logistics Providers using the D-Analytic Hierarchy Process

I. Dadashpour, A. Bozorgi-Amiri*

School of Industrial Engineering, College of Engineering, University of Tehran, Tehran, Iran

PAPER INFO

Paper history:

Received 02 July 2020
Received in revised form 23 July 2020
Accepted 03 September 2020

Keywords:

*D- Analytic Hierarchy Process
Dairy Industry
Multi-criteria Decision Making
Sustainable Logistics
Third-party Logistics*

ABSTRACT

Nowadays, the relative importance of logistics and sustainable supply chain cannot be denied and third-party logistics as one of the logistics management strategies can play an important role for many industry owners to consider their sustainability goals. The goal of this paper is to choose the best third-party logistics provider to achieve a sustainable logistics system, because third-party logistics service is mainly dependent on both transportation and workforces, managing them is one of the important issues of sustainability. Thus, third-party logistics providers need to be concerned about not only the economic criteria but also issues related to environmental and social sustainability in addition to two other dimensions namely technical and reputation. In this paper, a comprehensive classification of related criteria, sub-criteria, and sub-sub-criteria is proposed according to selecting the best third-party logistics provider. To evaluate and rank the proposed criteria, a D Number-Analytic Hierarchy Process method, as one of the proper and popular multi-criteria decision-making (MCDM) approaches, is utilized. Besides, a case study in dairy industry has been accomplished in the real-world to show the effectiveness and a better understanding of the proposed conceptual model. Finally, the best third-party logistics provider was identified among the alternatives for the proposed case study. The results showed that the proposed method could be a good alternative to conduct evaluations and the related sensitivity analysis, considering sustainability.

doi: 10.5829/ije.2020.33.11b.15

1. INTRODUCTION

Based on the definitions, a set of approaches that is utilized for efficient integration of the suppliers, manufacturers, and distributors is known as the Supply Chain Management (SCM). In such a way that, to minimize the system costs, the products are produced and distributed at the right quantities, to the right location and at the right time until the service level requirement is satisfied.

The operations flow includes material flow, financial resources, service and information that are extended in the supply chain from raw material through factories and warehouses to the end-users [1].

To enhance the operational performance, it is crucial for businesses to make the best advantage of their opportunities in the competitive global environment.

These days, given the business globalization, customer satisfaction and highly competitive global environment have made the firms collaborate closely with external partners [2]. Efficient cooperation with external partners in supply chain provides competitive advantage to the firms [3]. Outsourcing is known as one of these business practices which can make firms more competitive and profitable. One of the critical processes for achieving success in the business venture is logistics which helps firms to improve their competitiveness and also better responsiveness in customer service. Logistics management as one of the significant parts of the supply chain plays a vital role in increasing the efficiency of the supply chain [3]. Logistics is a part of the SCM which plans, uses, and controls the efficiency and effectiveness of the forward and backward flow as well as the inventory of products, services and information from the

*Corresponding Author Institutional Email: alibozorgi@ut.ac.ir
(A. Bozorgi-Amiri)

starting to the final point of the chain, to satisfy the consumers' demands. Accurate logistics management can positively affect the supply chain by creating less inventory lot, high productivity, more agility, short due dates, observing and tracking events and flows, enhancing consumers' service, etc. Some functions can be outsourced as well as some services which can be bought, in order to control logistics to operate effectively and efficiently in companies [4].

A concept called Third-Party Logistics (3PL) becomes immensely useful and a growing interest leading the industry owners to outsource the logistics activities to 3PLs. This concept is helpful for companies in order to decrease their logistics and inventory costs. The 3PL providers work as an independent company and their duties include the transferring of logistics services from a major manufacturer (Origin Company) to the vendor or user of the product or service under a specified contract. The concept of outsourcing is promoted by the advent of third-party logistics which made companies to rely on this concept. The increase of logistics activities outsourcing is mainly leading to benefits such as cost reduction, performance improvement, concentrating on main activities, etc.

Global focus in marketplace development convinced companies to reduce the supply chain management function of business. So, many companies tend to outsource their activities which it leads companies to focus on core business activities. The 3PL usually concentrate on main function such as improving the transportation system, customized services, market penetration, using advanced technologies and better logistic services [5]. Typically, the first party is a core company which provides products or services, the second party is the customer (or customers). Then, a firm which is hired to do either the first or second party's desires is a third party. Companies utilize 3PLs for outsourcing some parts or all of operations in their SCM.

Supply chain has become a complex and global concept that remaining resilient is a crucial factor for businesses for being successful in a fast-changing world [6]. Supply chain professionals have been focused on factors such as cost, quality, delivery and reliability, but over the recent years, the concept of sustainability has been added as one of the procurement criteria for many companies. In the past decade, much more attention has been paid to sustainable business development because of the government's, profit and non-profit organization's special attention to environmental, organization and social responsibility. Also, the emergence of changing economic order is the other think which convinces companies and industry owners to pay close attention to manufacturing and service sustainability [7]. Hence, in recent years, many companies made their activities and operations sustainable [8]. The sustainability concept has three major dimensions such as environmental, social and

economic, and companies consider these dimensions separately and simultaneously due to many studies in supply chain and logistics area. Sustainability can play an important role to reduce transportation costs and also environmental and social services constructive (SSC) factors, because of the outsourcing concept is relevant to transportation.

In order to develop SSC participation, it is crucial to evaluate and select the appropriate 3PL [9]. In some cases, risks such as losing control, long-term commitment, and some 3PL's performance failure are involved in the decision to outsource logistics [6]. Thus, it is important for any enterprise to select a suitable and compatible 3PL partner to be successful in competitive market place. In order to choose a well-rounded sustainable 3PL that can enhance the performance of supply chain, dimensions such as environmental, social and economic must be taking into account. The research gap is how to develop 3PLs in order to fulfill supply chain's needs to be sustainable.

In this paper, outsourcing logistics activities could be considered as a lever to achieve sustainability goals. The ability of 3PLs supply chain sustainability can play an important role in supply chain management concept [10]. It should be noted that the studies on this issue have been increased which indicates the importance of this topic. Therefore, it is better to pay more attention to these studies for companies that have internal or outsourced logistics and transportation activities.

Thus, the main purpose of this article is to select the best 3PL based on the concepts of sustainability. In this article, in addition to emphasizing the three main dimensions of sustainability, two other dimensions will be used along with economic, social and environmental dimensions. Selecting the 3PL providers that are famous in the logistics and 3PL area is important because origin companies can rely on 3PL easily. Another critical issue is the technical abilities of the 3PL companies because some products, like dairy products, need special conditions for maintenance and shipment. So, two dimensions including technical and reputation are regarded as criteria.

Regarding the aforementioned gap, among the significant contributions of previous studies on the literature of the sustainable 3PLs, most of them considered environmental as sustainable criteria and there were no studies addressing three main dimensions of sustainability, two other technical and reputation aspects and D-analytical hierarchy process (AHP) approach in 3PL simultaneously [11]. In order to cover the proposed research gap according to the investment as shown in Table 1, in this paper, an integrated MCDM method is provided for evaluating and selecting the best 3PL according to their sustainability performance view, reputation, and technical criteria.

The evaluation and clustering of the 3PLs which

contracts with the intended dairy factory is done by using MCDM approaches. The technique used in this article is AHP based on D numbers, named D-AHP. This method is the complete method in the fuzzy domain and also is based on the fuzzy priority relation. The D-AHP model in this paper evaluates the effects of sustainability on the fulfillment of 3PL service in supply chain [12]. This approach applies in different scenarios, such as the preference relation in the fuzzy environment that can be employed in case of uncertainty between experts' opinions when they have a clear view of the subject. But in some cases, the experts have the authority to not vote for a specific issue in which they do not have any idea. The steps of evaluation and ranking of the 3PL companies are shown in Figure 1.

The rest of this work is provided as follows: The literature of the issue is investigated in the section 2. Section 3 contains the description of the proposed method and material. In section 4, a case study in a famous dairy factory is provided and solved by the proposed method. Finally, conclusion is shown in section 5.

2. LITERATURE REVIEW

2. 1. Sustainable Third-party Logistics

To improve the effectiveness of substructure investments for sustainability, a comprehensive evaluation system is essential for supporting decision-making. One of the significant challenges for human society in the twenty-

first century is the growing of food demand, developing agriculture systems or enhancing the business and production activities, etc. without compromising the integrity of our environment [13].

Logistics service providers are able to align their current way of working with the sustainability measurement. Sustainable logistics is concerned with industry, city, and too many logistics activities which lead to greenhouse gas. Yang et al. [14] studied tax of carbon which limited the design model of city logistic network in China. Jiang et al. [15] measured the logistics and supply chain sustainability performance by adopting a multi-methodological approach. According to the results, for improving sustainable performance, performance indicators should be considered from different perspectives. Hernadewita and Saleh [16] worked on the sample of 3PL provider by using IT resources and analysis of route. The finding of the paper showed that concentrating on IT and customer centrisim is helpful for improving sustainable performance. In order to assist the decision makers in selecting the best 3PL in terms of environmental perspective, a two-phase model consist of analytic network process and data envelopment analysis has been used by Gardas et al. [17].

2. 2. Multi Criteria Decision Making Approach in 3pl Selection

There are many methods applied by researchers previously to meet the multi-criterion. It is entirely evident from the literature that 3PL selection consists of identical and mental parameters, but in the past few years, researchers have concentrated forcefully

TABLE 1. Categorizing the most related studies

S.no	Reference	Application area	Sustainability dimensions			Additional dimensions	Method
			Social	Environmental	Economical		
1	Yayla et al. [18]	A systematic decision support tool for 3PL provider evaluation, especially for 3PL transportation provider	✓	-	-	-	Buckley Fuzzy-AHP
2	Hwang et al. [19]	Third-party logistics (3PL)					AHP
3	Tajik et al. [20]	Sustainable Third-Party Reverse Logistics Provider Selection	✓	✓	✓	-	FAHP FTOPSIS
4	Datta et al. [21]	Selection of third-party reverse logistics provider	-	-	-	-	Fuzzy environmental
5	Prakash and Barua [22]	3PRL partner selection	-	-	-	Repetition	FAHP VIKOR
6	Govindan et al. [23]	Selection of third-party reverse logistics provider	-	-	-	-	ELECTRE I and SMAA
7	Deng et al. [24]	Supplier selection	-	-	-	-	D-AHP
8	Aslani et al. [25]	Sustainable supplier selection	✓	✓	✓	-	BWM
9	Raut et al. [26]	Third-party logistics (3PL) provider	-	✓	-	-	DEA & ANP
10	Jung [27]	A third-party logistics (3PL) provider	✓	-	-	-	FAHP
11	Choudhury et al. [28]	Evaluation and selection of third party logistics services providers	✓	✓	✓	-	DEA
12	Zarbakhshnia et al. [29]	Outsourcing sustainable reverse logistics	-	✓	✓	-	MOORA-G Fuzzy AHP
13	This work	Sustainable 3PI provider	✓	✓	✓	✓	D-AHP

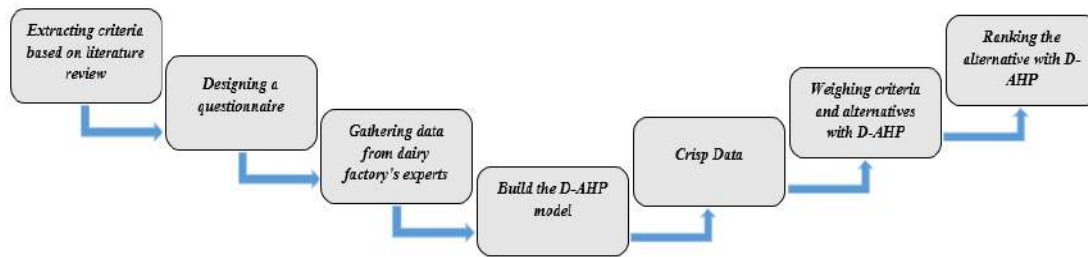


Figure 1. Steps of evaluation and ranking of the 3PL companies

on the analytical hierarchy process (AHP), DEA and fuzzy AHP, etc. [30, 31]. Table 2 indicates the studies which used MCDM approaches to select and evaluate the best 3PL providers by determining different criteria and sub-criteria. According to aforementioned statements in the introduction, AHP method based on D numbering is used in this study.

3. METHOD AND MATERIAL

3. 1. Construct D-Number by a Fuzzy Preference Relation

Dempster in his famous paper in last 60s provided a new opinion about the amount of probability in the Ω space [22]. Dempster with Shafer in their evidence theory extended the fuzzy theory and uncertainty which investigated in the real-world and their effect was tangible in it. But still, this opinion faults because it does not consider that the real-world and fuzzy space involves comments and the mind of people and possibilities in all of the aspects; for example, in this theory and a similar one in the past personal comments and opinions were not considered [32]. The D-number theory is used in this paper for selecting the best 3PL provider. The umpire on uncertainty in D-S theory is defined by the primary probability assignment (BPA) [33].

In the FPR, we can construct the decision matrices of pairwise comparison, according to the linguistic values of the expert's evaluation. The classic FPR R indicates on a set of alternatives $A = \{A_1, A_2, \dots, A_n\}$, the fuzzy set on set $A \times A$ and is specified by a membership function.

$$\mu_R: A \times A \rightarrow [0, 1] \tag{1}$$

When the cardinal of A is small, the FPR can simply be indicated by $n \times n$ matrix namely $R = [r_{ij}]_{n \times n}$ such that $r_{ij} = \mu_R(A_i, A_j), \forall i, j \in \{1, 2, \dots, n\}$.

$$R = \begin{matrix} & \begin{matrix} A_1 & A_2 & A_n \end{matrix} \\ \begin{matrix} A_1 \\ A_2 \\ A_n \end{matrix} & \begin{bmatrix} r_{11} & r_{12} & \dots & r_{1n} \\ r_{21} & r_{22} & \dots & r_{2n} \\ \vdots & \vdots & \ddots & \vdots \\ r_{n1} & r_{n2} & \dots & r_{nn} \end{bmatrix} \end{matrix} \tag{2}$$

where r_{ij} shows the preferred degree from an alternative A_j to alternative A_i .

$$r_{ij} = \mu_R(A_i, A_j) = \begin{cases} 0 & A_j \text{ is absolutely preferred to } A_i; \\ \in (0, 0.5) & A_j \text{ is preferred to } A_i \text{ to some degree;} \\ 0.5 & \text{Indifference between } A_i \text{ and } A_j; \\ \in (0.5, 1) & A_i \text{ is preferred to } A_j \text{ to some degree;} \\ 1 & A_i \text{ is absolutely preferred to } A_j. \end{cases} \tag{3}$$

For the one indicating the more uncertainty information, the D number preference relation should be created. To do this, we will represent the D number fuzzy preference relation by R_D for a group alternative A in set $A \times A$ and define the element as follows:

$$R_D: A \times A \rightarrow D \tag{4}$$

and the D number preference relation is shown as follows:

$$R_D = \begin{matrix} & \begin{matrix} A_1 & A_2 & A_n \end{matrix} \\ \begin{matrix} A_1 \\ A_2 \\ A_n \end{matrix} & \begin{bmatrix} D_{11} & D_{12} & \dots & D_{1n} \\ D_{21} & D_{22} & \dots & D_{2n} \\ \vdots & \vdots & \ddots & \vdots \\ D_{n1} & D_{n2} & \dots & D_{nn} \end{bmatrix} \end{matrix} \tag{5}$$

where $D_{ij} = \{(b_1^{ij}, v_1^{ij}), (b_2^{ij}, v_2^{ij}), \dots, (b_m^{ij}, v_m^{ij})\}, D_{ij} = \{(1 - b_1^{ij}, v_1^{ij}), (1 - b_2^{ij}, v_2^{ij}), \dots, (1 - b_m^{ij}, v_m^{ij})\}, \forall i, j \in \{1, 2, \dots, n\}$, and $b_k^{ij} \in [0, 1] \forall k \in \{1, 2, \dots, m\}$.

Accordingly, the classic FPR matrix Equation (2) is changed to the D numbers preference relation below:

$$R_D = \begin{matrix} & \begin{matrix} A_1 & A_2 & A_n \end{matrix} \\ \begin{matrix} A_1 \\ A_2 \\ A_n \end{matrix} & \begin{bmatrix} \{(r_{11} \cdot 1 \cdot 0)\} & \{(r_{12} \cdot 1 \cdot 0)\} \dots & \{(r_{1n} \cdot 1 \cdot 0)\} \\ \{(r_{21} \cdot 1 \cdot 0)\} & \{(r_{22} \cdot 1 \cdot 0)\} & \{(r_{2n} \cdot 1 \cdot 0)\} \\ \vdots & \vdots & \vdots \\ \{(r_{n1} \cdot 1 \cdot 0)\} & \{(r_{n2} \cdot 1 \cdot 0)\} \dots & \{(r_{nn} \cdot 1 \cdot 0)\} \end{bmatrix} \end{matrix} \tag{6}$$

Also, the matrix R has some properties: (1) $r_{ij} \gg 0$, (2) $r_{ij} + r_{ji} \equiv 1 \quad \forall i, j \in \{1, 2, \dots, n\}$, $r_{ii} = 0.5 \forall i \in \{1, 2, \dots, n\}$. R_D is transformed by Equation (9) to convert the D matrix to the crisp matrix by using the integer shown of the D number.

$$R_C = I(R_D) = \sum_{i=1}^n b_i^{ij} v_i^{ij} \tag{7}$$

In another step of the proposed method, the probability matrix should be constructed according to the crisp matrix to show the preference probability between

TABLE 2. Categorize of criteria in 3PL selection

Reference	Criteria	Sub-criteria
Yayla et al. [18]	Sustainable communication	Cost of transportation, Financial Health, Reputation of provider, SV-Similar Values
	Quality of service	On-Time Delivery, Emergency response, Reliability of deliverance, Dispatch Personnel Quality
	Continuous Improvement	Technological Improvement, Firm Infrastructure, Optimization Capability
Hwang et al. [19]	Performance	Accuracy of documents, Safety in transportation , Rate of shipment error, On-time delivery, Responsiveness
	Cost	Continuous cost decreasing, Cost control of value-added services Price
	Service	Problem-solving ability, Service of value-added, Service for customer support
	Quality assurance	Indicators key performance tracking, ISO compliance, Continuous improvement
	Intangible	Experience, Financial stability, Global scope, Profitability
Tajik et al. [20]	IT	Function coverage, Data security, System stability, System scalability
	Economic	Total cost, Quality, Technological abilities, Financial abilities, Delivery, Service, Relationship, Flexibility
	Environmental	Environmental management system, Environmental cost, management, Electrical and electronic equipment, Product recovery management
	Social	Employee interest and rights, Stakeholders rights, Work safety and labor health, Safety training, Respect for policy, Contractual stakeholders influence, Employment practices
	Finance performance	Logistics costs, Financial stability
Datta et al. [21]	Level of service	Being on time and reliable, Service quality, Responsiveness and flexibility
	Client communication	Long term relationship, Trust and information sharing, Benefit and risk-sharing
	Management	Performance management, Security and safety, Fame and experience
	Infrastructure	IT abilities, Logistics workforce
	Enterprise culture	Cultural fitness, Cultural innovation
Prakash and Barua [22]	Performance of firm	Time, Flexible capacity, Convenience
	Capacity of resources	Investment, Capacity, advanced components, equipment, warehousing, and storage
	Delivery of service	Level of service, Customized service, Ability of problem solving
	Reverse Logistics Operations	The collection, process, Sorting, Warehousing, Remanufacturing, Intermediate, Transportation, Recycle, Repair, Disposal
	IT and Communication System	Integrated System, Separate and Shared communication, RFID/EDI enabled the system, Information security system
	Geographical Location	Coverage, Destination and Market, Distribution, Shipment,
Govindan et al. [23]	Experience and fame	Image, Benefit and risk Sharing, Structure, Culture
	Cost Quality	Relationship, RL, Reduction cost, Service, Product/ service/people quality, Performance of product, Improvement in quality
	Capacity of RL	Financial, infrastructures, Skilled, Uncertainty factor
	Technology	Capacity of technology, Warehouse, Transportation, Inventory management, IT, Demand forecasting, Investment
	Relationship and communication	Mutual, Justices, useful, Flexibility, Trust, Quality of service
	Financial	Market share, Profitability, Wealth, popularity, loyalty of customer, Understanding business requirements
	Risk management	Monitoring, Communication, Policies of government, Complaint management, Transportation, order management
	Practices of RL	Redistribution, Feedback policy, packing, delivery
Environmental management system	Green level and Low carbon	recycle, remanufacturing, reuse, disposal, Environmental management, pollution, resource consumption, Oil consumption, carbon emissions
	Environmental management system	ISO 14000, environmental policies, Environmental activities
	Micro-social impact	Employee satisfaction, customer satisfaction, stakeholder satisfaction, overall working relations
	Macro-social impact	Health, local community, human factors

pairwise alternatives. The element of the probability matrix is indicated by R_p and calculated by equation (10) that the symbol “>” denotes the “prefer to” [25].

$$P_r(A_i > A_j) = 1 \text{ if } c_{ij} > 0.5 \text{ and } P_r(A_i > A_j) = 0 \text{ if } c_{ij} \leq 0.5 \tag{8}$$

After constructing the probability matrix, the triangulation method is used to rank the alternative. In this method, all of the elements above the main diagonal are nonzero and the process of triangulation is: first, calculating the sum of each row’s elements and also finding the largest number between them. Second, deleting the largest number of row and column of the matrix, in the next step, the first and second steps should be repeated until the R_p matrix becomes empty. Finally, a triangular matrix is constructed according to the principle matrix and rows deleting regularity. The triangular matrix is presented by R_p^t then through this matrix, alternatives can be ranked according to the rows deleting order which means that the first alternative is the largest number of the row at the first step of triangulation [32].

To determine the weight of alternative, at first the crisp matrix (R_C) should be triangularized and then, the number above the main diagonal should be used and after determining these using a number, one row above the main diagonal and after specific, Equation (9) is computed.

$$\begin{aligned} \lambda(W_i - W_j) &= X \\ \lambda(W_j - W_k) &= Y \\ W_i + W_j + W_k &= 1 \end{aligned} \tag{9}$$

λ represents the granular information, that shows the expert’s cognitive capability, the value of λ is related to the cognitive ability of an expert, as it sees the amount of weight depending on λ . Therefore, for calculating the λ , follow the below scheme:

$$\lambda = \begin{cases} \lfloor \frac{\lambda}{2} \rfloor & \text{Information includes the highly credible} \\ n & \text{Information includes the medium credible} \\ \frac{n^2}{2} & \text{Information includes the low credible} \end{cases} \tag{10}$$

n represents the number of alternatives and λ show the lower bound by λ , which $\lfloor \frac{\lambda}{2} \rfloor = \min\{k \in \mathbb{Z} \mid k \geq \lfloor \frac{\lambda}{2} \rfloor\}$.

After calculating the weight of each level, for determining the preference relation of the decision-making problem, the process of integration of each level’s weight is done as shown in Table 3 where m represents the number of criteria. Finally, the best alternative is selected and ranked [33, 34].

The classic AHP method will be condemned due to the inability to show and control the uncertainty in a variable for mental and linguistic data [35]. This factor is the main weakness of this method which is rooted in the scales used in this method. Therefore, for covering this main weakness, the fuzzy approach was created. Fuzzy logic which is against standard reasoning, is considered as a powerful tool for solving issues related to the complex systems including the problems linked to the argument, human inference, and decision [36]. But in this method, the expert could not or will not answer a question in some cases because of the gaps and the lack of sufficient information about an issue. Hence, for covering this defect, a novel method called D-AHP can be proposed which uses the D number, introduced by D-S theory that was described in the last section. As it is shown in Figure 2, the scale used in this method is based on the preference relation that was described in the last section considered the differs to the Saaty’s scale and all aspect [37]. The priorities of the alternatives can be reached by integrating each row’s weight. Generally, the D relation preference and method are illustrated in Figure 2 that this algorithm is applied to the D-AHP method [34].

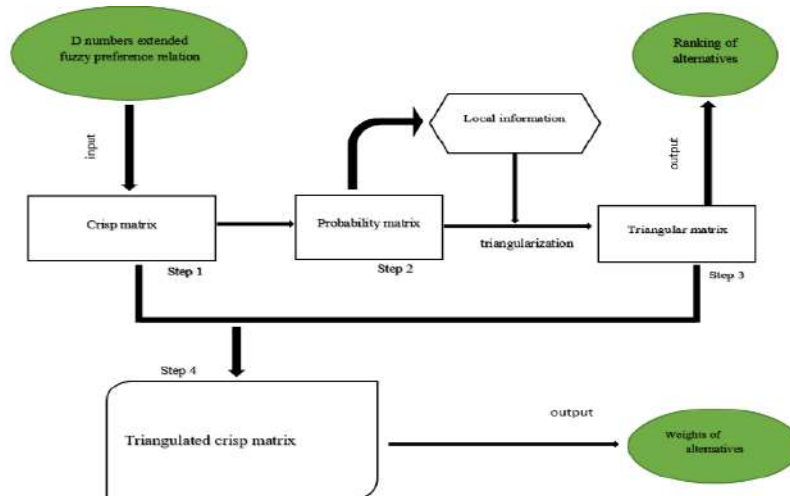


Figure 2. Illustration of the D number preference relation algorithm [25]

TABLE 3. Process the integration of each level’s weight

Criteria	C_1	C_2	C_m	Weight
Alternative	c_1	c_2	c_m	
A_1	a_{11}	a_{12}	a_{1m}	$W_1 = \sum_{i=1}^m c_i a_{1i}$
A_2	a_{21}	a_{22}	a_{2m}	$W_2 = \sum_{i=2}^m c_i a_{2i}$
⋮	⋮	⋮	⋮	⋮
A_n	a_{n1}	a_{n1}	a_{nm}	$W_n = \sum_{i=1}^m c_i a_{ni}$

4. MODEL TESTING

A case study illustrates the effectiveness and impact of outsourcing transportation activities in our proposed model. In this regard, the real data of a dairy factory operating in northern Iran was examined. The dairy factory has an extensive service network.

The case study is conducted in a famous dairy factory in the north of Iran. One of the affiliated providers of this factory performs the specific distribution process of the products. This factory includes 1200 trucks and 3000 workforces and will respond to 1 million orders each month, which these orders are more than 1250 tons of products monthly.

The proposed factory also contracted with five different 3PL providers out of the factory, named briefly A1, A2, A3, A4, and A5 in order to distribute its products. The aim of this paper is to evaluate and cluster these five 3PL providers, according to the experts' comments and experiences. Thirty experts including logistics manager and transportation experts commented on criteria, sub-criteria, and sub-sub-criteria which were investigated from literature review.

4. 1. Criteria Evaluation for Selecting the 3pl Provider

3PL selection is one of the multi-criteria decision-making problems. Also, it is a complicated process because of multiple criteria like price, quality, delivery, agility, technical, etc [38]. Along with creating a set of criteria, sub-criteria, and sub-sub-criteria, a corporation can be better to choose a 3PL provider. In this way, it chooses the best time and place and can meet its operations and logistics requirements the best, such as transportation [39]. In spite of the beliefs of the majority of people, who believe that the vital step in the problems of 3PLs is the selection of criteria and sub-criteria, in this study the focus is more on the goals of the company and government policies. Therefore, due to this policy, the goals refer to the sustainability aspect, such as social, economic, and environmental, with two additional, technical and reputation, dimensions. The criteria in the 3PL selection subject is impacted by many

attributes, such as availability to the international distribution networks [40] and the size of the company used for 3PL. Table 4 shows the criteria, sub-criteria, and sub-sub-criteria considered in this paper, which are categorized according to the articles in Table 2 and the previous studies.

As mentioned above, the main idea of selecting the best 3PL provider in the transportation subject has considered all dimensions of sustainability with two proposed additional dimensions. The technological sub-criteria have included agile, flexible, quality, IT, resource, location, and service. The sub-criteria play an essential role in the definition of criteria. These criteria have all of significant meanings for companies and manufacturers in the field of transportation. Another aspect added to sustainability is reputation, actually when the companies trust the 3PL provider that has an appropriate background and experience during the years of their activities. The extracted criteria, sub-criteria, and sub-sub-criteria were far more than a literary review, which after consulting with one of the experts in the transportation department of the proposed dairy factory, was reduced to the present. The structure of the proposed MCDM model is shown in Figure 3 under the framework of D-AHP that is extended by a D number in fuzzy relation preference and different credibility of scale.

5. RESULTS AND DISCUSSION

In this section, by using the numerical example, the proposed D-AHP method’s steps are used to solve the 3PL selection problem. As shown above, Figure 3 demonstrates the five levels of the hierarchical structure of our problem for 3PL selection derived from literature review in Tables 2 and 3. The goal of the study is choosing and ranking the best 3PL provider from the sustainability and two surplus dimensions, among five alternatives. The D number preference relation of criteria, sub-criteria, sub-sub-criteria, and alternatives in each level can be constructed according to this structure.

In this paper, we have utilized points of view of 30 expert’s working at the dairy factory. Table 4 shows the D number preference relation of criteria and their pairwise comparison matrix based on expert’s suggestion, which the weight of criteria, calculated by the proposed method and the evaluation of the criteria judge to the highly believable that is shown in Table 5. The priority relation of sub-criteria, sub-sub-criteria, and alternative are determined by acquiring the proposed method. The weight of each level is determined by integrating the previous level’s weight as shown in Table 3. In this case, experts at first assessed the question then answered it according to company’s policy. After evaluating their suggestion, calculated it by D number

algorithm. Hereby determines the weight of all levels separately. Finally integrated the weights of all levels based on D-AHP algorithm. The result of it is represented in Table 5.

As obtained results summarized in Table 6, the alternatives are sorted from A_5 to A_1 , respectively according to the expert suggestion. Due to the Equation

(20), the validity of information taken from experts depends on the experts' level of ability and their expertise and science. The value of λ will change in case of using the different expert with distinct judging. In this paper, ten experts' opinions with close knowledge and judgment about 3PL selection are used for evaluating the criteria and sub-criteria and sub-sub-criteria. So, the credibility

TABLE 4. Criteria, sub-criteria and sub-sub-criteria

Criteria	Sub-Criteria	Sub-Sub-criteria
Economically C_1	Overall Cost C_{11}	Reverse logistics cost (C_{111}), cost of relationship (C_{112}), Transportation cost (C_{113}), logistic cost (C_{114}), cost reduction (C_{115}), value-added services (C_{116}), price (C_{117})
	Economic C_{12}	Quality (C_{121}), Technology Capabilities (C_{122}), Financial Capabilities (C_{123}), Delivery (C_{124}), Service (C_{125}), Relationship (C_{126}), Flexibility (C_{127})
	Environmental C_2	Green level C_{21}
Sustainability C_3	Human resource Policies C_{31}	Satisfaction level (C_{311}), Qualified talents (C_{312}), Training (C_{313}), employee performance (C_{314})
	Macro Social C_{32}	Customer satisfaction (C_{321}), Health (C_{322}), safety (C_{323}), Voice of customer (C_{324}), Performance management (C_{325}), security (C_{326})
	Micro Social C_{33}	Transportation safety (C_{331}), employment stability (C_{332}), Financial health (C_{333}), Contractual stakeholders influence (C_{334}), Employment practices (C_{335}), The rights of stakeholders (C_{336}), Work safety (C_{337}), labor health (C_{338})
Two additional dimensions C_4	Agile C_{41}	Delivery Reliability (C_{411}), Response in an emergency (C_{412}), Delivery Performance (C_{413}), Responsiveness (C_{414}), On-time delivery (C_{415}), Timeless (C_{416})
	Flexible C_{42}	System stability (C_{421}), Flexible Capacity (C_{422})
	Quality C_{43}	Quality of Dispatch (C_{431}), Document accuracy (C_{432}), Quality of product (C_{433})
	IT C_{44}	Information technology capacity (C_{441}), Data security (C_{442})
	Resource C_{45}	Continuous improvement (C_{451}), Financial capability (C_{452}), Specialized infrastructures (C_{453}), Skilled manpower (C_{454}), Investment (C_{455}), capacity (C_{456}), advanced components (C_{457}), equipment (C_{458})
	Location C_{46}	The geographical range of services (C_{461}), Geographical location (C_{462}), Destination (C_{463}), Market (C_{464}), Coverage (C_{467}).
	Service C_{47}	Problem-solving capability (C_{471}), Value-added service (C_{472}), Customer support service (C_{473}), Global scope (C_{474})
Reputation C_5	Experience C_{51}	Image (C_{511}), Shared benefits and risks (C_{512}), structure (C_{513}), culture (C_{514})

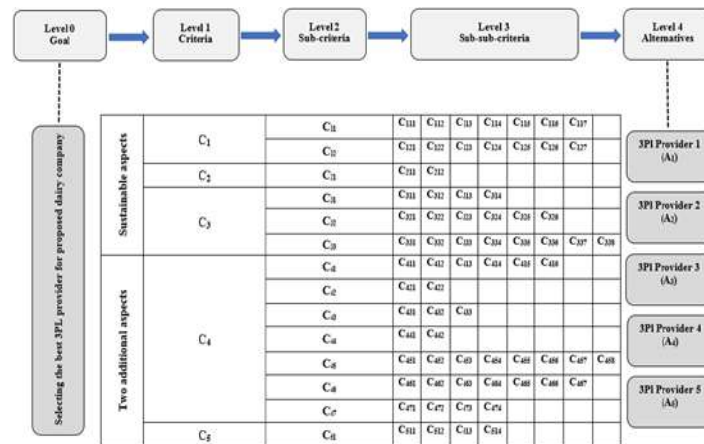


Figure 3. Structure of the proposed model

TABLE 5. D number preference relation of criteria and these weights

Criteria	Economical	Reputation	Social	Technical	Environmental	Weight ($\lambda = \left\lfloor \frac{\lambda}{\lambda} \right\rfloor$)
Economical	{(0.5,1.0)}	{(0.85,1.0)}	{(0.75,0.4), (0.85,0.6)}	{(0.75,1.0)}	{(0.58,1.0)}	0.1328
Reputation	{(0.15,1.0)}	{(0.5,1.0)}	{(0.62,1.0)}	{(0.55,1.0)}	{(0.75,1.0)}	0.2028
Social	{(0.25,0.4), (0.15,0.6)}	{(0.38,1.0)}	{(0.5,1.0)}	{(0.6,1.0)}	{(0.68,1.0)}	0.2268
Technical	{(0.25,1.0)}	{(0.45,1)}	{(0.4,1.0)}	{(0.5,1.0)}	{(0.62,1.0)}	0.2068
Environmental	{(0.42,1.0)}	{(0.25,1.0)}	{(0.32,1.0)}	{(0.38,1.0)}	{(0.5,1.0)}	0.2308

TABLE 6. The weight and ranking of alternative with criteria

Alternative / Criteria	Economically 0.1328	Environmental 0.2308	Social 0.2068	Technical 0.2268	Reputation 0.2028	Weight	Ranking
A1	0.0920	0.0656	0.0625	0.0962	0.0819	0.0787	5
A2	0.1431	0.1236	0.1153	0.1006	0.1430	0.1232	4
A3	0.1931	0.1791	0.1727	0.1806	0.1628	0.1767	3
A4	0.2434	0.3086	0.2539	0.2942	0.2765	0.2788	2
A5	0.3279	0.3231	0.3075	0.3662	0.3336	0.3324	1

Inconsistency Degree=0.0645

of our information is almost high that subsequently the number of λ is small and for this problem, consider the number of λ equal 1, which equals the minimum number of the column's number (k).

In this case, experts at first assessed the question then answered it according to company's policy. After evaluating their suggestion, calculated it by D number algorithm. Hereby determines the weight of all levels separately. Finally integrated the weights of all levels based on D-AHP algorithm. The results of the weight of alternatives are represented in Table 5.

As data summarized in Table 6, the alternatives are sorted from A_5 to A_1 respectively according to the expert suggestion. Due to Equation (20), the validity of information taken from experts depends on the experts' level of ability and their expertise and science. The value of λ will change in case of using the different expert with distinct judging. In this paper, ten experts' opinions with close knowledge and judgment about 3PL selection are used for evaluating the criteria and sub-criteria and sub-sub-criteria. So, the credibility of our information is almost high that subsequently the number of λ is small and for this problem, consider the number of λ equal 1, which equals the minimum number of the column's number (k).

The inconsistency degree of proposed D number preference relation is calculated as Equation (11) which is defined according to the triangular matrix. The inconsistency degree of this problem, according to the probability triangular matrix is equal to 0.0645.

$$I.D = \frac{\sum_{i=1}^n \sum_{j<i}^n R_p^T(i,j)}{n(n-1)/2} \tag{11}$$

This paper helps the manager and industry owners in reducing their transportation cost, frugality of time and entrust and outsourcing all or some of their transportation parts, as well as the protection of the environment and reducing the pollution in transportation, due to the considering sustainability dimensions along with technical and reputation.

In fact, the managers of the dairy industry can use the proposed concepts and solution methods of this study in order to understand the effect of proper 3PL company selection in reducing transportation cost and also enhancing customer satisfaction. Because outsourcing the transportation activities to a good and well-known 3PL company can play an important role reducing the purchase costs of transportation vehicles and labor costs. Considering good technical condition as mentioned in our study, in transferring goods lead to least damage which is a factor for increasing customer satisfaction.

The performance of supply chain is as one of most important competitive factors in many industries. As mentioned, selecting the proper third part logistics provider can help companies in transportations cost reduction and better flow of distribution processes, which it leads to better supply chain performance. This paper can be helpful for industry owners to evaluate the best 3PL providers, by considering different criteria such as quick access, security, high capacity and etc., in order to enhance their supply chain efficiency. In this paper, the fifth provider (A5) ranked the best among other considered providers. So, it's clear that the provider A5 is the best candidate if the proposed dairy factory wants to take advantages of 3PLs.

To validate the sensitive analysis of questions, the value of λ is compared with a different rating of credibility. As is shown in Table 7, the value of λ does not affect on clustering of available alternatives in this dairy factory. There are only a few differences in the amount of weight in different situations and it is clear that the alternatives' weights are more than any other cases when the value of λ adopts its highest rate. Also, these variations in the weights of different credibility are shown in Table 6.

Finally, the fuzzy logic and evidence theory assessment is used in many studies [41]. Selection of 3PL companies is done by considering the expert's comment evaluated in this article by using D-number theory based on fuzzy preference relation.

According to Zhou et al. [37] the result of the comparison between D-number theory with fuzzy logic and evidence theory is shown in Table 8. This comparison indicates that the method of D-numbers is more independent in evaluations than other used methods. This method is proper even in the case of experts' lack of knowledge. The reason for this advantage is rooted in linguistic variables and large scales of the method. Due to comparison with the available techniques, founding the D-number theory has Excel to other methods. The pianist's probability transformation process is needed for the evaluation of dependency when evidence theory and AHP are used. But in the proposed method, the dependence is evaluated without this transformation process [37].

TABLE 7. Weight and ranking of the attribute in three situations

3PL provider	High credibility		Medium credibility		Low credibility	
	Weight	ranking	Weight	ranking	Weight	ranking
A_1	0.078	5	0.035	5	0.028	5
A_2	0.123	4	0.111	4	0.092	4
A_3	0.176	3	0.132	3	0.115	3
A_4	0.278	2	0.241	2	0.226	2
A_5	0.332	1	0.315	1	0.298	1

TABLE 8. The superiority of D- number

Method	The linguistic scale of fuzziness	The evaluation of the expert's mental
D number theory	✓	✓
Fuzzy logic	✓	×
Evidence theory	×	✓

5. CONCLUSION

In this paper, the fifth provider (A_5) ranked the best among other considered providers with the D-AHP method. So, it's clear that the provider A_5 is the best candidate if the proposed dairy factory wants to take advantages of 3PLs. In some industrial companies like dairy companies, logistic activities play a significant role due to the sensitivity of products to decay. In these cases, 3PL companies can have a significant effect on the logistic systems' performance. Therefore, a proper decision making model for evaluating the 3PLs before making contract is helpful for managers to cooperate by third-party logistics with better view of their performance.

Transportation cost and decay reduction are two main reasons that leads dairy companies to collaborate with

third-party logistics. Therefore, exact and proper criteria definition is very important to select the best company for outsourcing logistic activities. So, the main aim of this paper is to evaluate the best 3PL providers by considering sustainable aspects, environmental, social and economic, and also two other additional aspects such as technical and reputation. The D-AHP method is used to evaluation of defined criteria, sub-criteria and sub-sub-criteria. Finally, it is found that the company A_5 is best one among all 3PL providers. In this regard, the proposed dairy factory can make the proper policy for sending the products to the retailers and customers by lower costs and higher efficiency. Further research in this field could be explored in future studies by considering the following topics; some criteria based

On renewable energy and using another method for evaluating and ranking the alternatives like rough AHP.

6. REFERENCES

- Fazlollahtabar, H. *Supply Chain Management Models: Forward, Reverse, Uncertain, and Intelligent Foundations with Case Studies*. CRC Press, 2018.
- Wang, G., Dou, W., Zhu, W., and Zhou, N. "The effects of firm capabilities on external collaboration and performance: The moderating role of market turbulence." *Journal of Business Research*, Vol. 68, No. 9, (2015), 1928–1936. <https://doi.org/10.1016/j.jbusres.2015.01.002>
- Ross, D. F. *Distribution Planning and Control*, Springer, 2015. <https://doi.org/10.1007/978-1-4419-8939-0>
- Beiki, H., Seyedhosseini, S. M., Ghezavati, V. R., and Seyedaliakbar, S. M. "Multi-objective optimization of multi-vehicle relief logistics considering satisfaction levels under uncertainty." *International Journal of Engineering, Transactions B: Applications*, Vol. 33, No. 5, (2020), 814–824. <https://doi.org/10.5829/IJE.2020.33.05B.13>
- Kannan, G., Pokharel, S., and Kumar, P. S. "A hybrid approach using ISM and fuzzy TOPSIS for the selection of reverse logistics provider." *Resources, Conservation and Recycling*, Vol. 54, No. 1, (2009), 28–36. <https://doi.org/10.1016/j.resconrec.2009.06.004>
- Gharaei, A., and Jolai, F. "A multi-agent approach to the integrated production scheduling and distribution problem in multi-factory supply chain." *Applied Soft Computing Journal*, Vol. 65, (2018), 577–589. <https://doi.org/10.1016/j.asoc.2018.02.002>
- Ageron, B., Gunasekaran, A., and Spalanzani, A. "Sustainable supply management: An empirical study." *International Journal of Production Economics*, Vol. 140, No. 1, (2012), 168–182. <https://doi.org/10.1016/j.ijpe.2011.04.007>
- Tideman, S. G., C. Arts, M., and Zandee, D. P. "Sustainable Leadership: Towards a Workable Definition." *Journal of Corporate Citizenship*, Vol. 49, (2013), 13–33. Retrieved from <https://www.jstor.org/stable/jcorpciti.49.17?seq=1>
- Baruffaldi, G., Accorsi, R., and Manzini, R. "Warehouse management system customization and information availability in 3pl companies: A decision-support tool." *Industrial Management and Data Systems*, Vol. 119, No. 2, (2019), 251–273. <https://doi.org/10.1108/IMDS-01-2018-0033>
- Zarbakhshnia, N., Soleimani, H., and Ghaderi, H. "Sustainable third-party reverse logistics provider evaluation and selection using fuzzy SWARA and developed fuzzy COPRAS in the presence of risk criteria." *Applied Soft Computing Journal*, Vol. 65, (2018), 307–319. <https://doi.org/10.1016/j.asoc.2018.01.023>
- Raut, R., Narkhede, B. E., Gardas, B. B., and Luong, H. T. "An ISM approach for the barrier analysis in implementing sustainable practices: The Indian oil and gas sector." *Benchmarking*, Vol. 25, No. 4, (2018), 1245–1271. <https://doi.org/10.1108/BIJ-05-2016-0073>
- Al-Aomar, R., and Hussain, M. "An assessment of green practices in a hotel supply chain: A study of UAE hotels." *Journal of Hospitality and Tourism Management*, Vol. 32, (2017), 71–81. <https://doi.org/10.1016/j.jhtm.2017.04.002>
- Teixeira, M. S., Maran, V., de Oliveira, J. P. M., Winter, M., and Machado, A. "Situation-aware model for multi-objective decision making in ambient intelligence." *Applied Soft Computing Journal*, Vol. 81, (2019), 105532. <https://doi.org/10.1016/j.asoc.2019.105532>
- Yang, Z., Yang, D., Dyer, C., He, X., Smola, A., and Hovy, E. "Hierarchical attention networks for document classification." In 2016 Conference of the North American Chapter of the Association for Computational Linguistics: Human Language Technologies, (2016), 1480–1489. <https://doi.org/10.18653/v1/n16-1174>
- Jiang, J., Wu, D., Chen, Y., and Li, K. "Complex network oriented artificial bee colony algorithm for global bi-objective optimization in three-echelon supply chain." *Applied Soft Computing Journal*, Vol. 76, (2019), 193–204. <https://doi.org/10.1016/j.asoc.2018.12.006>
- Hernadewita, H., and Saleh, B. I. "Identifying tools and methods for risk identification and assessment in construction supply chain." *International Journal of Engineering, Transactions A: Basics*, Vol. 33, No. 7, (2020), 1311–1320. <https://doi.org/10.5829/ije.2020.33.07a.18>
- Gardas, B. B., Raut, R. D., and Narkhede, B. "Modelling the challenges to sustainability in the textile and apparel (T&A) sector: A Delphi-DEMATEL approach." *Sustainable Production and Consumption*, Vol. 15, (2018), 96–108. <https://doi.org/10.1016/j.spc.2018.05.001>
- Yayla, A. Y., Oztekin, A., Gumus, A. T., and Gunasekaran, A. "A hybrid data analytic methodology for 3PL transportation provider evaluation using fuzzy multi-criteria decision making." *International Journal of Production Research*, Vol. 53, No. 20, (2015), 6097–6113. <https://doi.org/10.1080/00207543.2015.1022266>
- Hwang, B. N., Chen, T. T., and Lin, J. T. "3PL selection criteria in integrated circuit manufacturing industry in Taiwan." *Supply Chain Management*, Vol. 21, No. 1, (2016), 103–124. <https://doi.org/10.1108/SCM-03-2014-0089>
- Tajik, G., Azadnia, A. H., Ma'aram, A. B., and Hassan, S. A. H. S. "A hybrid fuzzy MCDM approach for sustainable third-party reverse logistics provider selection." In *Advanced Materials Research* (Vol. 845), (2014), 521–526. <https://doi.org/10.4028/www.scientific.net/AMR.845.521>
- Datta, S., Samantra, C., Mahapatra, S. S., Mandal, G., and Majumdar, G. "Appraisal and selection of third party logistics service providers in fuzzy environment." *Benchmarking*, Vol. 20, No. 4, (2013), 537–548. <https://doi.org/10.1108/BIJ-11-2011-0087>
- Prakash, C., and Barua, M. K. "A combined MCDM approach for evaluation and selection of third-party reverse logistics partner for Indian electronics industry." *Sustainable Production and Consumption*, Vol. 7, (2016), 66–78. <https://doi.org/10.1016/j.spc.2016.04.001>
- Govindan, K., Kadziński, M., Ehling, R., and Miebs, G. "Selection of a sustainable third-party reverse logistics provider based on the robustness analysis of an outranking graph kernel conducted with ELECTRE I and SMAA." *Omega (United Kingdom)*, Vol. 85, (2019), 1–15. <https://doi.org/10.1016/j.omega.2018.05.007>
- Deng, X., Hu, Y., Deng, Y., and Mahadevan, S. "Supplier selection using AHP methodology extended by D numbers." *Expert Systems with Applications*, Vol. 41, No. 1, (2014), 156–167. <https://doi.org/10.1016/j.eswa.2013.07.018>
- Aslani, B., Rabiee, M., and Tavana, M. "An integrated information fusion and grey multi-criteria decision-making framework for sustainable supplier selection." *International Journal of Systems Science: Operations and Logistics*, (2020). <https://doi.org/10.1080/23302674.2020.1776414>
- Raut, R., Kharat, M., Kamble, S., and Kumar, C. S. "Sustainable evaluation and selection of potential third-party logistics (3PL) providers: An integrated MCDM approach." *Benchmarking*, Vol. 25, No. 1, (2018), 76–97. <https://doi.org/10.1108/BIJ-05-2016-0065>
- Jung, H. "Evaluation of Third Party Logistics Providers Considering Social Sustainability." *Sustainability*, Vol. 9, No. 777, (2017), 1–18. <https://doi.org/10.3390/su9050777>
- Choudhury, N., Raut, R. D., Gardas, B. B., Kharat, M. G., and Ichake, S. "Evaluation and selection of third party logistics services providers using data envelopment analysis: a sustainable

- approach." *International Journal of Business Excellence*, Vol. 14, No. 4, (2018), 427–453. Retrieved from <https://ideas.repec.org/a/ids/ijbexc/v14y2018i4p427-453.html>
29. Zarbakhshnia, N., Wu, Y., Govindan, K., and Soleimani, H. "A novel hybrid multiple attribute decision-making approach for outsourcing sustainable reverse logistics." *Journal of Cleaner Production*, Vol. 242, (2020), 118461. <https://doi.org/10.1016/j.jclepro.2019.118461>
 30. Falsini, D., Fondi, F., and Schiraldi, M. M. "A logistics provider evaluation and selection methodology based on AHP, DEA and linear programming integration." *International Journal of Production Research*, Vol. 50, No. 17, (2012), 4822–4829. <https://doi.org/10.1080/00207543.2012.657969>
 31. Zhang, G., Shang, J., and Li, W. "An information granulation entropy-based model for third-party logistics providers evaluation." *International Journal of Production Research*, Vol. 50, No. 1, (2012), 177–190. <https://doi.org/10.1080/00207543.2011.571453>
 32. Xiao, F. "A Multiple-Criteria Decision-Making Method Based on D Numbers and Belief Entropy." *International Journal of Fuzzy Systems*, Vol. 21, No. 4, (2019), 1144–1153. <https://doi.org/10.1007/s40815-019-00620-2>
 33. Huang, X., Wang, N., and Wei, D. "Investment decision using D numbers." In Proceedings of the 28th Chinese Control and Decision Conference, (2016), 4164–4167. <https://doi.org/10.1109/CCDC.2016.7531712>
 34. Deng, X., and Deng, Y. "D-AHP method with different credibility of information." *Soft Computing*, Vol. 23, No. 2, (2019), 683–691. <https://doi.org/10.1007/s00500-017-2993-9>
 35. Ghayoomi, M., Abooei, M. H., Vahdatzad, M. A., and Ebrahimi, A. "Designing a model for creation of export consortiain business cluster." *International Journal of Engineering, Transactions C: Aspects*, Vol. 33, No. 3, (2020), 459–467. <https://doi.org/10.5829/ije.2020.33.03c.10>
 36. Deng, X., and Jiang, W. "Evaluating Green Supply Chain Management Practices Under Fuzzy Environment: A Novel Method Based on D Number Theory." *International Journal of Fuzzy Systems*, Vol. 21, No. 5, (2019), 1389–1402. <https://doi.org/10.1007/s40815-019-00639-5>
 37. Zhou, X., Deng, X., Deng, Y., and Mahadevan, S. "Dependence assessment in human reliability analysis based on D numbers and AHP." *Nuclear Engineering and Design*, Vol. 313, (2017), 243–252. <https://doi.org/10.1016/j.nucengdes.2016.12.001>
 38. Stopka, O. "Draft to implement a logistics information system for corporate management using multi-criteria decision making methods." *Transport Economics and Logistics*, Vol. 82, (2020), 43–56. <https://doi.org/10.26881/etil.2019.82.04>
 39. Gao, T. G., Huang, M., Wang, Q., and Wang, X. W. "Dynamic organization model of automated negotiation for 3PL providers selection." *Information Sciences*, Vol. 531, (2020), 139–158. <https://doi.org/10.1016/j.ins.2020.03.086>
 40. Bask, A. H. "Relationships among TPL providers and members of supply chains – a strategic perspective." *Journal of Business & Industrial Marketing*, Vol. 16, No. 6, (2001), 470–486. <https://doi.org/10.1108/EUM00000000006021>
 41. Su, X., Mahadevan, S., Xu, P., and Deng, Y. "Dependence Assessment in Human Reliability Analysis Using Evidence Theory and AHP." *Risk Analysis*, Vol. 35, No. 7, (2015), 1296–1316. <https://doi.org/10.1111/risa.12347>

Persian Abstract

چکیده

امروزه نمی‌توان اهمیت نسبی لجستیک و زنجیره تأمین پایدار را انکار کرد، همچنین لجستیک شخص ثالث به عنوان یکی از استراتژی‌های مدیریت لجستیک می‌تواند برای بسیاری از صاحبان صنایع نقش مهمی ایفا کند تا اهداف پایداری خود را در نظر بگیرند. هدف این مقاله انتخاب بهترین ارائه‌دهنده تدارکات شخص ثالث برای دستیابی به یک سیستم تدارکات پایدار است. زیرا خدمات تدارکات شخص ثالث عمدتاً به هر دو نیروی حمل و نقل و نیروی کار وابسته است. مدیریت آنها یکی از موضوعات مهم پایداری است. بنابراین، ارائه‌دهندگان تدارکات شخص ثالث باید علاوه بر ابعاد اصلی پایداری که اقتصادی، اجتماعی و زیست محیطی می‌باشند، در مورد دو بعد فنی و شهرت که به ابعاد اصلی اضافه شده‌اند نیز دغدغه داشته باشند. در این مقاله، با توجه به انتخاب بهترین ارائه‌دهنده تدارکات شخص ثالث، طبقه‌بندی جامعی از معیارها، زیرمعیارها و زیر-زیرمعیارهای مرتبط ارائه شده است. برای ارزیابی و رتبه‌بندی معیارهای پیشنهادی، از روش فرایند تحلیل سلسله مراتبی عددی D، به عنوان یکی از رویکردهای تصمیم‌گیری چند معیاره، استفاده شده است. علاوه بر این، یک مطالعه موردی در صنعت لبنیات برای نشان دادن اثربخشی و درک بهتر از مدل مفهومی پیشنهادی، در دنیای واقعی انجام شده است. سرانجام، بهترین ارائه‌دهنده تدارکات شخص ثالث در میان گزینه‌های مورد مطالعه موردی مشخص شد. نتایج نشان داد که روش پیشنهادی با توجه به پایداری می‌تواند جایگزین مناسبی برای انجام ارزیابی‌ها و تجزیه و تحلیل حساسیت مربوطه باشد.



Case Study in Increasing Overall Equipment Effectiveness on Progressive Press Machine Using Plan-do-check-act Cycle

C. Jaqin, A. Rozak*, H. Hardi Purba

Industrial Engineering Program, Mercu Buana University, Jakarta, Indonesia

PAPER INFO

Paper history:

Received 09 April 2020
Received in revised form 20 July 2020
Accepted 03 September 2020

Keywords:

Total Productive Maintenance
Availability
Overall Equipment Effectiveness
Plan-do-check-act Cycle

ABSTRACT

Press automotive components manufacturer in Indonesia with the Overall Equipment Effectiveness (OEE) achievement was 60.7%, it was below than world company level as mention in Japanese Institute of Plant Maintenance (JIPM)- Total Productive Maintenance (TPM) standard, the biggest OEE components problem was availability value that achieved 63.3%, then the biggest availability problem was dies preparation time. Using TPM method and Plan-Do-Check-Act (PDCA) cycle with Pareto chart and Fishbone diagram, we succeeded to improve dies setting time within one months. We could increase the availability value from 63.3% became 67.8% and finally OEE value increased from 60.7% became 65.3%.

doi: 10.5829/ije.2020.33.11b.16

1. INTRODUCTION

Automotive industry was grown year by year, tough competition by introducing new car model and new car brand entered to Indonesian market. Car sales amount in Indonesia from 2016 until 2018 has extensively increased [1]. The demand of cars in Indonesia has increased well, thus car manufacturers compete to win the competitive car market [2]. Increasing in the exchange rate of United State of America dollar against the Indonesian rupiah had an influence on the increasing of imported components, and also increasing of the regional minimum wages in Indonesia had impacted on the increasing of labor cost [3]. Increasing the costs of Indonesian automotive manufacture forced automotive industries must improve the cost of operation through increasing productivity, reducing quality defect, eliminating waste, etcetera.

There were many researches in automotive industry using Total Productive Maintenance (TPM) method, researching in automotive components manufacturing especially in Computer Numerical Control (CNC) machining line by improving on availability rate from 91.8 to 95.7% and it impacted to the Overall Equipment Effectiveness (OEE) value increased from 63.8% to

88.1% after implementing the Autonomous Maintenance [4]. Then there was research in the maintenance sector of company which supplies automotive air-conditioning tubes, the improvement could increase the availability from 75 to 85%, and there was a significant increase in OEE from 74 to 82% [5].

This research was done in Indonesian automotive press components manufacturer. In this press production process need many press dies to produce many press parts. Other researchers who observed the components manufacturers that used mold/dies as follows, improvement in stamping production line using Single Minute Exchange of Dies (SMED) method, by reducing non added value activities, it could increase the clamps production capacity of press machine from 60,000 to 105,000 pcs/day [6]. Improvement in injection molding machines using SMED method, the improvement result for setup time reduced from 43.24 to 21.00 minutes, by reducing set up time for non added value activities [7]. Improvement proposal to increase the availability value on the insulation line in a cable manufacturing unit [8].

Step by step improvement to solve process problems had been done by various method, there was research improved performance of equipment by enhancement of

*Corresponding Author Email: ahmadrozak66@yahoo.com (A. Rozak)

speed factor [9], other research in thermal power plant improved a coal handling unit using a probabilistic approach [10]. Define-Measure-Analyse-Improve-Control (DMAIC) cycle and Failure Mode and Effect Analysis (FMEA) method were used to increase the Availability value from 91 to 96% in automotive company [11]. DMAIC and Supply Chain Operations Reference (SCOR) method was used to improve supply chain performance in the textile dye case became 93% [12]. The research did improvement in automotive company using Quality Function Deployment (QFD) method, it improved the rate of quality from 96.4% became 97.9% that impacted to increase OEE value from 92 to 93% [13]. QFD approach was used to increase the quality of chocolate products [14]. Following researches did the improvement using Plan-Do-Check-Act (PDCA) cycle. PDCA cycle was done to improve quality problem in an electronic components company, it decreased the quality defect till 79% [15]. PDCA cycle was also used for reducing the Cans Loss Index (CLI) in a beverage company, the improvement reduced CLI from 0.97% to 0.78% [16].

The purpose of this study is to analyze the application of TPM in automotive components manufacturer, especially on progressive press 600T machine. This machine still has big room to improve the productivity problem in order to reduce the process cost. This research completed the TPM improvement application result based on case study on progressive press 600T machine using PDCA problem solving cycle.

2. LITERATURE REVIEW

2.1. Total Productive Maintenance Ahuja and Khamba [17] reported that Total Productive Maintenance (TPM) is a unique Japanese philosophy, it has been developed based on the Productive Maintenance concepts and methodologies. TPM was introduced by Nippon Denso Co. Ltd. of Japan, a supplier of Toyota Motor Company Co. Ltd, Japan in 1971. Nakajima [18] introduced the Total Productive Maintenance refers to the key words: Total, Productive, and Maintenance, as follows:

- Total means involvement of all employees and management then covers the total life cycle of the production process.
- Productive means increasing productivity through zero accidents, zero defects and zero damage, then minimize the problems in the production process.
- Maintenance means maintaining good production system.

2.2. Overall Equipment Effectiveness The Overall Equipment Effectiveness (OEE) is a value that being used to evaluate and measure the extension of the

successful TPM implementation, this measurement is very important in order to find out which areas need to be improved in machine productivity and product quality.

OEE is formulated as Equation (1).

$$OEE = AV \times PE \times RQ \times 1,000,000\% \quad (1)$$

where Availability (AV) is formulated as Equation (2):

$$AV = \frac{\text{Loading Time} - \text{Breakdown Time}}{\text{Loading Time}} \times 100\% \quad (2)$$

Performance Efficiency (PE) is formulated as Equation (3):

$$PE = \frac{\text{Process Amount} \times \text{Ideal Cycle Time}}{\text{Loading Time} - \text{Breakdown Time}} \times 100\% \quad (3)$$

Rate of Quality (RQ) is formulated as Equation (4):

$$RQ = \frac{\text{Process Amount} \times \text{Defect Amount}}{\text{Process Amount}} \times 100\% \quad (4)$$

World Class Manufacturing OEE's Standard and it's three OEE factors are shown in Table 1 below:

2.3. PDCA Cycle The PDCA cycle is step by step improvement, it has four steps that started by "Plan" step then it is continued by "Do", "Check" and finalized by "Act" step. This method is based on process improvement according to Deming cycle.

In "Plan" step, it started to define the problems from research area, then we choose the priority problems that need to be improved from all listed problems, researchers usually utilize Fishbone diagram to find out the root causes. Furthermore we develop possible solutions plan based on root causes. A useful tool which helps to show the problem can be used Graph, Pareto Diagram, Histogram and Control Chart. Quality management methods to solve a problem on the production line using several quality tools can bring more significant benefits and be more productive [19].

In "Do" step, we improve all selected solutions plan. In order to avoid big problem in current process, it will be better if we have pilot solutions in order to confirm the validity and accuracy of analytical step before, thus we have time to make any corrections before applying the solutions on a large scale in actual process.

In "Control" step, we control the improvement result and process. In this stage need confirmation of any changes at the "Do" step before. It also needs to control of the process in order to minimize deviation from the each objective and ensure that all corrections are

TABLE 1. World class manufacturing OEE's standard

Availability (AV)	90%
Performance Efficiency (PE)	95%
Rate of Quality (RQ)	99%
Overall Equipment Effectiveness (OEE)	85%

implemented before happening bad impact on the result and the process. A useful tool which helps to control the data can be used Control Chart in order to identify the process wether controllabile or not.

In “Act” step, after successfully achieving problem solving activities, we need to standardize all activities in order to avoid same root causes occurred and impacted to the same problem happen. PDCA cycle as continues improvement cycle, therefore we must continue to do the others improvement by choosing new theme of problems.

3. RESEARCH METHODOLOGY

This research used secondary data that collected from press production report, it consists the press machine loading time, machine breakdown time, machine stand-by, production amount and number of defect products. The objective of this research is to find out a solution to the availability problems on the 600T progressive press machine. Researchers used Total Productive Maintenance method with utilization of Pareto diagram and Fishbone diagram. All problem solving activities use Plan-Do-Check-Act (PDCA) cycle.

The framework of this research is illustrated in Figure 1. Starting from gap between Overall Equipment Effectiveness (OEE) achievement and OEE company target on the 600T progressive press machine, then analyze the components of OEE problems using Pareto diagram as a tool to analyze the root causes. We did focus group discussion session and observed 600T progressive press machine directly in order to define and choose the problems that will be improved, after that we analyzed the root causes, then we proposed variant solution plans. We involved related parties such as Production, Maintenance, Inspection and Engineering section in order to increase the analysis accuracy and to propose variant solution plans.

4. RESULTS AND DISCUSSION

This research did improvement by utilizing Plan-Do-

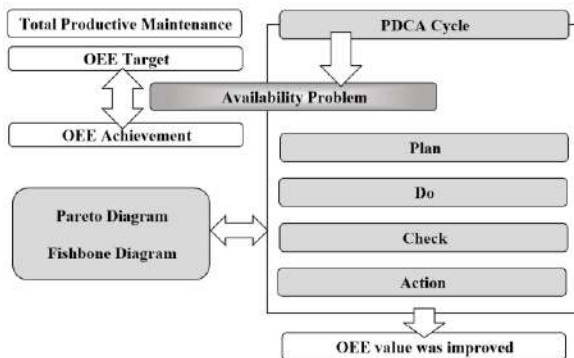


Figure 1. Research framework

Check-Act (PDCA) cycle based on previous research in wide area. The difference of this research and others are the improvement was held in automotive 600T progressive press machine using PDCA cycle with quality control tools. This 600T progressive press machine produced press components for car seat track adjuster and window regulator as shown in Figure 2.

4. 1. “Plan” Step

The first step is “Plan”, we started to observe the problems that found on the 600T progressive press machine. The comparison of OEE achievement and company target from October until December 2019 can be seen in Figure 3. The OEE company target was 75% while the OEE average achievement in three months was 60.7%, thus the OEE achievement was bellow than the world class company target as valued 85%. There was a gap that need to be improved the problem 14.3% to achieve company target and 24.3% to achieve world class company target.

We defined the OEE achievement problem based on three components such as Availability (AV), Performance Efficiency (PE) and Rate of Quality (RQ). The achievement of OEE components compared to world class company target as shown in Figure 4.



Figure 2. Press product image

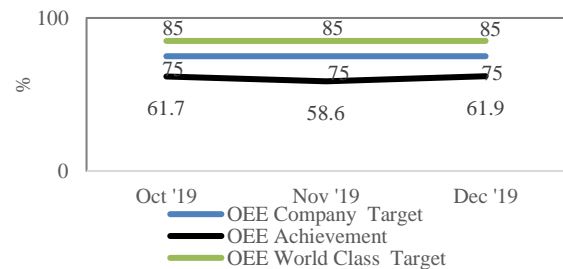


Figure 3. OEE achievement and company target

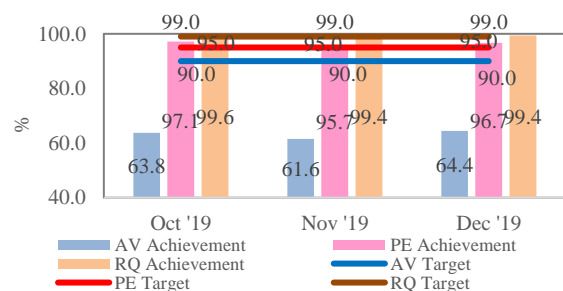


Figure 4. OEE components achievement and world class target

From Figure 4, we could see that the PE and RQ value achieved the world class target, just AV value did not achieve world class target. There was 26.7% gap between AV value achievement and world class target, thus we defined the 600T progressive press machine problem was availability achievement that need to be improved. We observed and measured the availability contribution problems in three months. We gathered related information for the availability problem in current process using Pareto chart, we found the biggest contribution time problem to the availability was Dies preparation than followed by Machine breakdown, Coil preparation, Quality Control check and Minor stoppages. All Availability problems contribution as shown in Figure 5.

Dies preparation flow process on 600T progressive press machine can be seen in Figure 6.

In this research we agreed to improve “End coil process problem” in dies preparation of 600T progressive press machine. We continued to measure the time of end coil preparation job as shown in Table 2.

From Table 2, we found that there were waste times in the End coil preparation job, such as Pulling end coil, Turning on switch and Checking pilot pin.

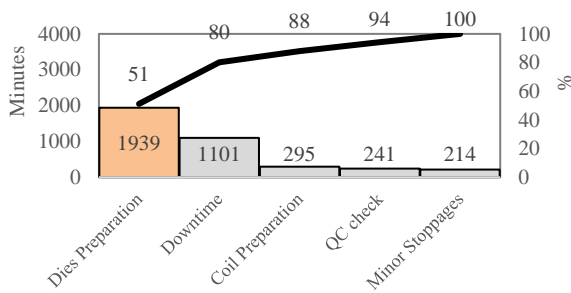


Figure 5. Availability problems contribution

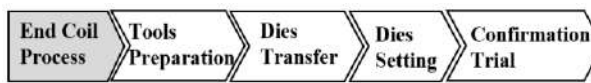


Figure 6. Dies preparation flow process

TABLE 2. End coil preparation detail job time

No.	Job	Actual Time (s)	Waste Time
1	Pulling end coil	71	Yes
2	Turning on switch	11	Yes
3	Moving dies before lower limit	28	No
4	Checking pilot pin	52	Yes
5	Moving dies until upper limit	28	No
TOTAL		190	

We analyzed the end coil process time was over than target. We involved all related parties in order to find out the causes of problem, we used Fishbone Diagram as shown in Figure 7. From Figure 7, we could inform that the effect of this problem was over time in the end coil process, it was written at head of fish. We started to find the root cause from problem finding in Table 2 as following activities: Pulling end coil, Turning on switch and Checking pilot pin. Using why-why question for pulling end coil over time was caused by weak clamping of end coil roller, it was caused by there was a gap between end coil roller and supporter. The overtime problem of turning on switch was caused by unstable of end coil position, it was caused by no stopper for end coil position. The overtime problem of checking pilot pin was caused by un clear seen of pilot pin hole, it was caused by not enough lighting in pin hole area. Thus the root causes of end coil preparation overtime were gap between end coil roller and supporter, no stopper for end coil position and not enough lighting in pin hole area.

For root cause of a gap between end coil roller and supporter, we proposed solutions plan: additional filler plate in coil adjuster and additional pressure spring in coil adjuster. For root cause of no stopper for end coil position, we proposed following solutions plan: additional stopper for end coil position and making end coil special sliding construction. For root cause of not enough lighting in pin hole area, we proposed following solutions plan: additional lamp for pin hole area and moving the current lamp position to pin hole area.

After discussion among researcher, we decided to choose the solutions plan as follow: for root cause of gap between end coil roller and supporter, we decided solutions plan was additional pressure spring in coil adjuster. For root cause of no end coil position stopper, we decided solution plan was additional stopper for end coil position. For root cause of not enough lighting in pin hole area, we decided solution plan was moving the current lamp position to the pin hole area.

4. 2. “Do” Step In the “Do” step, we improved all selected solutions plan within one month. In order to avoid big problem in current process, thus the improvements were done after working hours. First

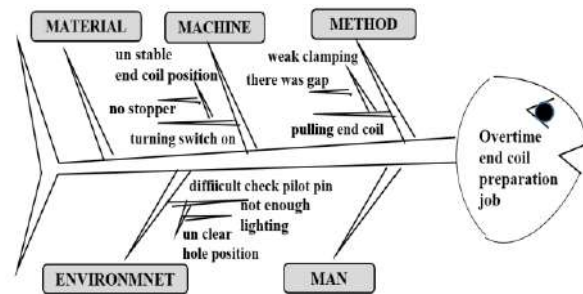


Figure 7. Fishbone Diagram

improvement was additional pressure spring on coil adjuster, first spring length was 30 mm, the coil movement was unsmooth, then it changed to 20 mm spring length, the coil movement was still unsmooth, then it change to 14 mm spring length, the coil movement was smooth in this condition. Second improvement was additional stopper for end coil position, after implementing this second solution, the end coil position have been fixed. Third improvement was moving the current lamp position to the pin hole area. Improvement activities as shown in Table 3.

4. 3. “Check” Step

In the “Check” step, we controlled the improvement result and process. First improvement was additional pressure spring on coil adjuster, in this improvement we could reduce time to pull the end coil from 71 seconds became 24 seconds. Second improvement was additional stopper for end coil position, in this improvement we could reduce time to fix the end coil position from 11 seconds became 1 second. Third improvement was moving the current lamp position to the pin hole area. After implementing this third solution, we could reduce time to check pilot pin from 52 to 28 seconds. Finally we could reduce end coil preparation time from 190 seconds became 109 seconds. Trend of time reduction for each improvement can be shown in Figure 8.

Based on reducing time of end coil preparation, we could calculate the Overall Equipment Effectiveness (OEE) components, it impacted to the increasing of Availability (AV) value. the result of three OEE components before and after improvement compare to the World class target can be shown in Figure 9.

TABLE 3. Improvement activities

No.	Improvement Activities	Spent Time (h)	Manpower (Person)	Cost (US \$)
1	Additional pressure spring	32	2	550
2	Additional stopper	16	2	170
3	Moving lamp position	8	2	120

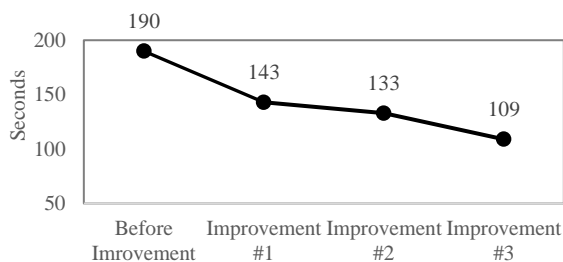


Figure 8. Trend of time reduction

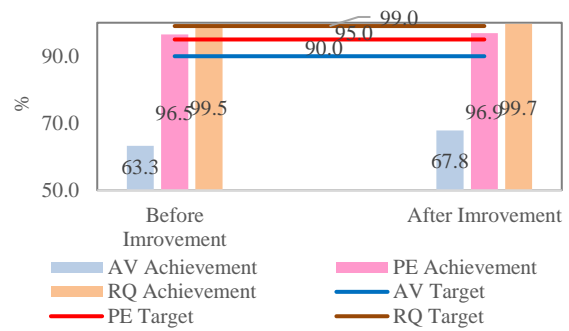


Figure 9. OEE components achievement comparison

Finally, this improvement could impact to OEE achievement from 61.9% in December 2019 became 65.5% in February 2020 as shown in Figure 10.

4. 4. “Act” Step

In the “Act” step, we standardized all activities in order to avoid same root causes occurred and impacted to the same problem happen. There were three root causes that needed to be controlled as follows: there was a gap between end coil roller then we standardized the function of pressure spring on coil adjuster, there was not stopper for end coil position then we standardized the function of additional stopper for end coil position and special sliding construction, lighting in pin hole area was not enough then we standardized the lamp position for pin hole area. Next action that will be improved is the problem in dies preparation especially in tools preparation job.

In order to avoid machine breakdown because of these improvements, we trained all related operators to do Autonomous Maintenance (AM) with following Autonomous Maintenance check sheet as shown in Figure 11.



Figure 10. OEE achievement after improvement

No.	ITEM	STANDARD	KEY POINT	IMAGE	INCHARGE	
					1st Shift	2nd Shift
1	Pressure spring on coil adjuster	Spring 14 mm	- Enough pressure - Adjustable bolt to add spring force			
2	Stopper for "end coil" position	On position	- It can stop "end coil" movement			
3	Lamp position for "pin hole" area	Lighting 300 Lux	- Enough lighting for pin hole area			

Figure 11. Autonomous Maintenance Check Sheet

5. CONCLUSION

Based on the previous average OEE value on the 600T progressive press machine was 60.7%, this achievement was lower than the World Class Manufacturing OEE's standard 85%. It was below than company's OEE target 70%. Thus there was gap 9.3% for improvement in order to achieve company target. From the data analysis, we found the biggest gap of OEE factors to the company target was AV as valued 63.3%, then we focused to increase the AV value. Based on Fishbone diagram, we found the root causes as follows: There was gap between end coil roller and supporter, There was not a stopper for end coil position, Lighting in pin hole area was not enough. Then improvement activities were done based on above root causes as follows: Improving coil table with pressure spring and stopper, and Moving lamp position to pin area. After implementing above improvements, we could increase AV value from 63.3 to 67.8% then impacted to OEE achievement from 60.7 to 65.3%.

We hope to others researcher can continue to do the research in TPM area in order to increase the OEE value based on improvement in utilization of Industrial Revolution 4.0.

6. REFERENCES

- Pawestri, V., Setiawan, A. and Linawati, L., "Pemodelan Data Penjualan Mobil Menggunakan Model Autoregressive Moving Average Berdasarkan Metode Bayesian", *Journal Sains Dan Edukasi Sains*, Vol. 2, No. 1, (2019), 26-35. <https://doi.org/10.24246/juses.v2i1p26-35>
- Kusuma, F.N. and Sharif, O. O., "Analisis Customer Value Index Dalam Memilih Mobil Hatchback Di Indonesia - Customer Value Index Analysis In Choosing Hatchback Car In Indonesia", *e-Proceeding of Management*, Vol. 6, No. 3, (2019), 5498-5509.
- Azhar, A. and Agung K, T., "Standarisasi Harga Pembangunan Kapal Perintis", *Journal Teknologi Maritim*, Vol. 2, No. 1, (2019), 1-6.
- Musa, M. A., Kasim, N. I., Razali, A. R., Mahadzir and Wan Saidin, W. A. N., "Improvement of Overall Equipment Effectiveness (OEE) through Implementation of Autonomous Maintenance in Crankcase Line", *Applied Mechanics and Materials*, Vol. 761, (2015), 165-169. doi:10.4028/www.scientific.net/AMM.761.180
- Guariente, P., Antonioli, I., Ferreira, L. P., Pereira, T. and Silva, F. J. G., "Implementing autonomous maintenance in an automotive components manufacturer", *Procedia Manufacturing*, Vol. 13, (2017), 1128-1134.
- Abraham, A., Ganapathi, K. N. and Motwani, K., "Setup Time Reduction through SMED Technique in a Stamping Production Line", *SAS Tech- Technical Journal RUAS*, Vol. 11, No. 2, (2012), 47-52.
- Low, S.-N., Chong, S.-H., Sim, H.-Y., Razalli, S. and Kamaruddin, S., "Measurement of Overall Performance Effectiveness in Setup Improvement", *Journal of Industrial Engineering*, Vol. 2014, (2014), 1-7. doi: 10.1155/2014/264980
- Nayak, D. M., Naidu, G. S., Shankar, V., Manager, A. and Manager, A., "Evaluation Of OEE In A Continuous Process Industry On An Insulation Line In A Cable Manufacturing Unit", *International Journal of Innovative Research in Science, Engineering and Technology*, Vol. 2, No. 5, (2013), 1629-1634.
- Mohammadi, M. and Rai, P., "Improving Performance of Mining Equipment Through Enhancement of Speed Factor: A Case Study" *International Journal of Engineering, Transactions C: Aspects*, Vol. 28, No. 9, (2015), 1392-1400. doi: 10.5829/idosi.ije.2015.28.09c.18
- Kumar, A. and Ram, M., "Reliability Measures Improvement and Sensitivity Analysis of a Coal Handling Unit for Thermal Power Plant", *International Journal of Engineering, Transactions C: Aspects*, Vol. 26, No. 9, (2013), 1059-1066. doi: 10.5829/idosi.ije.2013.26.09c.11
- Rozak, A., Jaqin, C. and Hasbullah, H., "Increasing overall equipment effectiveness in automotive company using DMAIC and FMEA method", *Journal Européen des Systèmes Automatisés*, Vol. 53, No. 1, (2020), 55-60. <https://doi.org/10.18280/jesa.530107>
- Hasibuan, S. and Dzikrillah, N., "Supply chain performance measurement and improvement for Indonesia chemical industry using SCOR and DMAIC method", *Saudi Journal of Engineering and Technology*, Vol. 3, (2018), 146-155. doi:10.21276/sjeat.2018.3.3.5
- Jaqin, C., Rozak, A. and Purba, H. H., "Quality Function Deployment for Quality Performance Analysis in Indonesian Automotive Company for Engine Manufacturing", *ComTech: Computer, Mathematics and Engineering Applications*, Vol. 11, No. 1, (2020), 11-18. doi: 10.21512/comtech.v11i1.6164
- Purba, H. H., Syamsul Maarif, M., Yuliasih, I. and Hermawan, A., "Product development of chocolate with quality function deployment approach: A case study in SMEs chocolate industry in Indonesia", *IOP Conference Series: Earth and Environmental Science* 209, (2018), 1-11. doi:10.1088/1755-1315/209/1/012011
- Realyvásquez-Vargas, A., Arredondo-Soto, K. C., Carrillo-Gutiérrez, T. and Ravelo, G., "Applying the Plan-Do-Check-Act (PDCA) cycle to reduce the defects in the manufacturing industry. A case study", *Applied Sciences*, Vol. 8, No. 11. (2018), 1-17. doi:10.3390/app8112181
- Silva, A. S., Medeiros, C. F. and Vieira, R. K., "Cleaner Production and PDCA cycle: Practical application for reducing the Cans Loss Index in a beverage company" *Journal of Cleaner Production*, Vol. 150, (2017), 324-338. <http://dx.doi.org/10.1016/j.jclepro.2017.03.033>
- Ahuja, I. P. S. and Khamba, J. S., "Total productive maintenance: Literature review and directions", *International Journal of Quality and Reliability Management*, Vol. 25, No. 7, (2008), 709-756. <https://doi.org/10.1108/02656710810890890>
- Nakajima, S. (1988), "Introduction to Total Productive Maintenance (TPM)", Productivity Press, Portland, OR.
- Wolniak, R., "Downtime in the Automotive Industry Production Process—Cause Analysis", *Quality Innovation Prosperity/ Kvalita Inovacia Prosperita*, Vol. 1745, (2019), 101-118. doi: 10.12776/QIP.V23I2.1259

Persian Abstract

چکیده

مطبوعات سازنده قطعات خودرو در اندونزی با موفقیت کلی تجهیزات (OEE) 60.7٪، آن را کمتر از سطح شرکت جهانی است، همانطور که در موسسه نگهداری کارخانه ژاپن (JIPM) ذکر شده است - استاندارد نگهداری تولیدی کل (TPM)، بزرگترین اجزای OEE مشکل مقدار در دسترس بودن بود که 63.3٪ بدست آورد، سپس بزرگترین مشکل در دسترس بودن زمان آماده سازی بود. با استفاده از روش TPM و چرخه (PDCA) Plan-Do-Check-Act با نمودار پارتو و نمودار Fishbone، ما موفق به بهبود زمان تنظیم قالب در طی یک ماه شدیم. ما می توانیم مقدار در دسترس بودن را از 63.3٪ به 67.8٪ و در نهایت مقدار OEE از 60.7٪ به 65.3٪ افزایش دهیم.



Designing a Sustainable Reverse Logistics Network Considering the Conditional Value at Risk and Uncertainty of Demand under Different Quality and Market Scenarios

S. Sajedi, A. H. Sarfaraz*, S. Bamdad, K. Khalili Damghani

Department of Industrial Engineering, South Tehran Branch, Islamic Azad University, Tehran, Iran

PAPER INFO

Paper history:

Received 06 June 2020
Received in revised form 17 July 2020
Accepted 05 September 2020

Keywords:

Closed-loop Supply Chain
Conditional Value at Risk
Fuzzy Inference System
Supply Chain Network Design
Sustainable

ABSTRACT

In recent years, regarding the issues such as lack of natural resources, government laws, environmental concerns and social responsibility reverse and closed-loop supply chains has been in the center of attention of researchers and decision-makers. Then, in this paper, a multi-objective multi-product multi-period mathematical model is presented in the sustainable closed-loop supply chain to locate distribution, collection, recycling, and disposal centers, considering the risk criterion. Conditional value at risk is used as the criterion of risk evaluation. The objectives of this research are to minimize the costs of the chain, reducing the adverse environmental effects and social responsibility in order to maximize job opportunities. Uncertainty in demand and demand-dependent parameters are modeled and determined by the fuzzy inference system. The proposed model has been solved using multi objective particle swarm optimization algorithm (MOPSO) approach and the results have been compared with Epsilon constraint method. Sensitivity analysis was performed on the problem parameters and the efficiency of the studied methods was investigated.

doi: 10.5829/ije.2020.33.11b.17

NOMENCLATURE

Indices			
		$C_{jk, sen}^s$	The cost / distance of transporting the product s from the production center j to the distribution center k in the scenario sen
I	Index of the set of fixed points for supply centers $i \in I$	$C_{kl, sen}^s$	The cost / distance of transporting the product s from the distribution center k to the customer center l in the scenario sen
J	Index of the set of fixed points for production centers $j \in J$	$C_{im, sen}^s$	The cost / distance of transporting each unit of the returned product s from the customer l to the collection and recovery center m in the scenario sen
K	Index of the set of potential points for distribution centers $k \in K$	$C_{mp, qs, sen}^s$	The cost / distance of transporting each unit of the returned product s with quality level qs from the collection and recovery center m to the recycling center p in the scenario sen
L	Index of the set of fixed points for customers $l \in L$	$C_{mn, qs, sen}^s$	The cost / distance of transporting each unit of the returned product s with quality level qs from the collection and recovery center m to the disposal center n in the scenario sen
M	Index of the set of potential points for collection and recovery centers $m \in M$	$C_{mj, qs, sen}^s$	The cost / distance of transporting each unit of the returned product s with quality level qs from the collection and recovery center m to the production center j in the scenario sen
P	Index of the set of potential points for recycling centers $p \in P$	$C_{pj, sen}^s$	The cost / distance of transporting each unit of the returned product s from the recycling center p to the production center j in the scenario sen
N	Index of the set of potential points for burial and disposal centers $n \in N$	$C_{jj, sen}^s$	The cost / distance of transporting each unit of the returned product s from the production center j to its own warehouse in the scenario sen

*Corresponding Author Email: dr.ahsarfaraz@yahoo.com (A. H. Sarfaraz)

Please cite this article as: S. Sajedi, A. H. Sarfaraz, S. Bamdad, K. Khalili Damghani, Designing a Sustainable Reverse Logistics Network Considering the Conditional Value at Risk and Uncertainty of Demand under Different Quality and Market Scenarios, International Journal of Engineering (IJE), IJE TRANSACTIONS B: Applications Vol. 33, No. 11, (November 2020) 2252-2271

S	Index of the set of products $s \in S$	$cq_{(jk, sen)}^s$	The cost / distance of transporting each unit of the returned product s from the warehouse of production center j to the distribution center k in the scenario sen
T	Index of the period $t \in T$	ca_i	Capacity of the supply center at location i
qs	Quality levels of returned products ($qs=qs_1, qs_2, \dots, QS$)	ca_j	Capacity of the production center at location j
sen	Set of scenarios ($sen=1, 2, \dots, scenario$)	ca_{jj}	Capacity of the warehouse of the production center at location j
Parameters		cr_j	Capacity to rebuild products at the production center at location j
O_k	The fixed amount of CO ₂ (in kilograms) released during the establishment of the distribution center k	ca_k	Capacity of the distribution center at location k
O'_m	The fixed amount of CO ₂ (in kilograms) released during the establishment of the collection center m	ca_m	Capacity of the collection and recovery center at location m
O''_p	The fixed amount of CO ₂ (in kilograms) released during the establishment of the recycling center p	ca_p	Capacity of the recycling center at location p
O'''_n	The fixed amount of CO ₂ (in kilograms) released during the establishment of the burial and disposal center n	ca_n	Capacity of the burial and disposal center at location n
w_{sen}	The probability of occurrence of the scenario sen	$h_{j, sen}^s$	The maintenance cost of each unit of the product s in the warehouse of the production center at location j in the scenario sen
CEM	The amount of CO ₂ (in kilograms) released from transportation of one unit of product in one kilometer	Variables	
$r_{l, qs, sen}^{st}$	Return rate of product s with quality level qs from customer l during period t in scenario sen	y_k	If the distribution center is established at location k , its value is 1, otherwise it is 0
$d_{l, sen}^{st}$	The amount of demand of product s by the customer l during period t in the scenario sen	y_m	If the collection center is established at location m , its value is 1, otherwise it is 0
$Price_{s, sen}$	The price of the product s delivered from the distributor to the customer in the scenario sen	y_p	If the recycling center is established at location p , its value is 1, otherwise it is 0
$fp_{s, qs}^{sen}$	The optimal price of a unit of returned product s with quality qs in the scenario sen	y_n	If the burial and disposal center is established at location n , its value is 1, otherwise it is 0
$cost_{s, sen}$	The cost of producing a unit of product s in the scenario sen	$x_{ij, sen}^{st}$	The amount of flow of the product s from the supply center i to the production center j during period t in the scenario sen
$costm_{s, sen}$	The cost of collecting a unit of product s in the scenario sen	$x_{jk, sen}^{st}$	The amount of flow of the product s from the production center j to the distribution center k during period t in the scenario sen
$costp_{s, sen}$	The cost of recycling a unit of product s in the scenario sen	$Q_{jj, sen}^{st}$	The amount of flow of the product s from the production center j to its own warehouse during period t in the scenario sen
$costn_{s, sen}$	The cost of disposing a unit of product s in the scenario sen	$x_{kl, sen}^{st}$	The amount of flow of the product s from the distribution center k to the customer l during period t in the scenario sen
$value_{s, sen}$	Value added to the system after recycling a unit of product s in the scenario sen	$Q_{jk, sen}^{st}$	The amount of flow of the product s from the warehouse of the production center j to the distribution center k during period t in the scenario sen
B_j^{st}	The return rate of the product s from the collection and recovery center to the production center during period t	$x_{im, qs, sen}^{st}$	The amount of flow of the returned product s with the quality level qs from the customer l to the collection center m during period t in the scenario sen
Bn^{st}	The return rate of the product s from the collection and recovery center to the burial and disposal center during period t	$x_{mp, qs, sen}^{st}$	The amount of flow of the returned product s with the quality level qs from the collection center m to the recycling center p during period t in the scenario sen
Bp^{st}	The return rate of the product s from the collection and recovery center to the recycling center during period t	$x_{mn, qs, sen}^{st}$	The amount of flow of the returned product s with the quality level qs from the collection center m to the burial and disposal center n during period t in the scenario sen
f_k	Fixed cost of establishing a distribution center at location k	$x_{mj, qs, sen}^{st}$	The amount of flow of the returned product s with the quality level qs from the collection center m to the production center j during period t in the scenario sen
f_m	Fixed cost of establishing a collection and recovery center at location m	$x_{pj, sen}^{st}$	The amount of flow of the reused product s from the recycling center p to the production center j during period t in the scenario sen
f_p	Fixed cost of establishing a recycling center at location p	$U_{j, sen}^{st}$	The amount of remaining inventory of the product s in the warehouse of the production center j during period t in the scenario sen
f_n	Fixed cost of establishing a burial and disposal center at location n	$\pi_{k, sen}$	The number of job opportunities created in the distribution center k in the scenario sen
$c_{ij, sen}^s$	The cost / distance of transporting the product s from the supply center i to the production center j in the scenario sen	$\pi_{inv, sen}$	The number of job opportunities created in reverse logistics centers in the scenario sen
		ψ_j	Average working days lost due to workplace injuries in the production center j per one unit of production

1. INTRODUCTION

Academically, the supply chain is defined as a system for converting raw materials, transporting products, and purchasing between different levels of supplier and customer [1]. In configuring logistics networks, we deal with two types of flows: 1. direct flow and 2. reverse flow. A reverse logistics network provides a flow between the used product supply market and the new product market. When the two markets overlap, a closed-loop or integrated network is created [2].

In the design of reverse logistics networks, the number of facilities required and the flow of materials between them are examined according to the structure of the supply chain [3]. Today, the main goals of customers are to receive the right goods and services in a short time, so this has changed the logistics approach of many companies. In most previous studies, the design of direct and reverse logistics networks has been studied separately; but, the configuration of the reverse logistics network has a significant impact on the direct logistics network. Design separation may lead to the production of non-optimal designs. Therefore, the design of direct and reverse logistics network should be integrated [4]. Pollution and emission of greenhouse gases have a great impact on the environment, and several recent studies on the mortality rate due to greenhouse gas emissions from production units showed the importance of this issue [5]. In recent years, regarding the issues such as lack of natural resources, government laws and environmental concerns, reverse and closed-loop supply chains have been in the center of attention of researchers and decision-makers [6]. Due to the laws that have been passed by the government recently, the issue of sustainability must be considered in all companies and organizations [7]. Sustainable supply chain means creating a coordinated supply chain by integrating economic, environmental and social considerations with the business systems within a supply chain. This integration is for the efficient and effective management of materials, information and flows related to the purchase, production and distribution of products or services, and its purpose is to meet the needs of stakeholders, increase profits, create competitive advantage and chain sustainability in the short and long term [8]. These types of chains seek to balance economic, environmental, and social objective function. In addition, at the request of customers to pay attention to the dimensions of sustainability in the production of products and services, international and governmental organizations have also passed and implemented laws in this field. An examination of the expansion of these laws shows that the number of these laws and their compulsoriness will increase in the future. To maintain their competitive advantage in the future, companies need to pay attention to these rules and move toward sustaining their processes [9]. In recent years, due

to increasing use of resources, increasing pollution, the current competitive market, as well as transportation costs, paying attention to the integration of reverse network problems with the forward network has created a special type of supply chain network, called sustainable closed loop supply chain [10].

Long-term and strategic decisions are effective in the design of the supply chain network, which means that changes in these decisions will lead to very high costs. Due to the constant changes in the business environment, considering the multi-product multi-period supply chains and assumptions that affect the model makes the supply chain problems more realistic and complicated [11]. Today, sustainable development and sustainability are the main issues of economic activities [1]. Sustainability dimensions for distribution and production systems include economic, environmental, and social aspects [7].

Environmental concerns have become more common recently, so one of the key issues in designing a supply chain is the effect of environmental effects created by carbon emissions, specifically known as CO₂ emissions. Considering the green supply chain can significantly address the concerns of customers and other stakeholders of the supply chain.

In addition to consider the design of the closed-loop for supply chains, it seems necessary to consider their contribution to environmental pollution. One of the main factors influencing environmental pollution is CO₂ emissions, which can be generated by continuous production of products, reproduction of returned products, transportation of products between different levels of supply chain and construction of facilities. This gas can also be produced through stored materials in warehouses, especially perishable materials that require special conditions, so considering this issue has been one of the topics of interest for researchers [4, 11–13].

Due to severe economic fluctuations and uncertainty in the amount of demand in different periods of production, organizations and managers of supply chains need to estimate the cost, revenue and conditions of production, distribution, sales, and establishment of facilities related to them and so on. They should also have a managerial view towards different situations so that they can make the best decision in the shortest possible time if the boom conditions turn into a recession or vice versa [14]. Therefore, in order to deal with the uncertainty, the scenarios of recession and boom of demand, which has been calculated as fuzzy, has been used which is considered as one of the contributions of this research.

Today, environmental studies are very important and should be considered in supply chain design. In today's competitive economy, many parameters such as cost and market demand can change, so in recent years the uncertainty of cost and demand has been considered in studies [15]. In addition to being a competitive

advantage, the green supply chain, which focuses specifically on environmentally friendly design, can also be a guarantor of sustainability. Green supply chain management can help reduce waste, cost, as well as improve communication with business partners and business conditions [16]. Uncertain factors cannot be ignored in order for a green supply chain to be effective enough. In many studies, this concept has been addressed as probabilistic [17]. However, it is very difficult to use probabilistic uncertainty in practice, and in many cases it is impossible to use and collect data due to time and systemic constraints. This issue causes many problems when using traditional supply [11]. For example, it is very difficult to find variable production prices in a situation where the price of raw materials fluctuates [18]. But The fuzzy logic can greatly help decision makers to deal with uncertainty [19].

Recently, environmental factors and commercial factors such as commitment have led to the consideration of risk in reverse logistics networks [20, 21]. Therefore, supply chain risks should be recognized in order for them to be managed [22, 23]. Risk sources may be environmental, organizational, or caused by the supply chain itself, so it will be very difficult to predict their impact under uncertainty. Since the sources of risk are so many and varied, it is impossible to completely eliminate them. There are also various internal and external factors and conditions that affect their intensity and weakness. Therefore, it is necessary to conduct studies that explain the various dimensions and components of this issue [24]. Understanding the risks of supply chain that decision makers face, allows managers to better detect and deal with unexpected events. Risk identification makes it possible to adapt to the uncertain conditions of a competitive environment and it will act as a strategic leverage in the process of competitiveness of organizations. The supply chain risk assessment process can help make strategic decisions and operational plans to help reduce the number of supply chain failures [24]. Conditional value at risk is one of the methods for calculating risk in financial engineering. Being linear and convex is one of the characteristics of conditional value at risk method which makes it a proper method for risk assessment [25]. Due to their complex nature, supply chains face a high degree of uncertainty that can adversely affect the quality of their performance [26]. Uncertainty in parameters can be divided into two systematic and environmental categories, which the latter are destructive factors that can affect the supply chain [14].

Therefore, in this study, uncertainty is used in relation to parameters (product quality and demand parameter). In recent years, some studies have been conducted on distribution and production systems to address the issue of sustainability [7]. But the simultaneous effect of risk and demand fuzzy uncertainty in the presence of different

market scenarios and quality has not been investigated in previous studies; therefore, in this research, we will simultaneously examine these issues.

The clear distinction between a traditional supply chain and a reverse supply chain is uncertainty in quality [27]. More specifically, the relevant literature on the supply chain considers the quality as deterministic [27–29]. Therefore, one of the prominent features of this research is the existence of quality uncertainty in the reverse route. Some topics in supply chain literature, such as supply chain risk management, sustainability, pricing, and revenue management, have been less studied [30]. Therefore, in this research, a new approach is presented that includes locating the sustainable closed loop supply chain with the presence of quality uncertainty and market scenarios considering the risk. Unlike traditional (forward) supply chains, there are various uncertainties in the reverse supply chain, such as price, quality, time, and rate of returned products [12].

This study is organized in five sections. In the second section, the related literature will be reviewed. In the third section, while stating the main problem of the research, modeling of the problem and also the approach used to estimate the uncertain demand will be presented. In the fourth section, numerical examples and results and sensitivity analysis of some model parameters will be presented. Finally, in the fifth section, conclusions and future research proposals will be expressed.

2. LITERATURE REVIEW

In this section, a review of previous literature on the design of a green closed-loop logistics network, risk modeling in the supply chain, and uncertainty modeling in the supply chain are examined, and at the end, the main innovations of this study are presented and analyzed.

2.1. Green Closed-loop Supply Chain

The study of Liu et al. [31] was one of the first studies that investigated the emission of greenhouse gases in marine units. In this study, traditional multi-criteria decision-making (MCDM) methods were developed using group fuzzy entropy and cloud technique [5]. In the last decade, the closed loop supply chain has attracted a lot of attention due to considering returned products, environmental factors, and customer rights. In this regard, it can be concluded that an effective closed loop supply chain covers environmental factors along with considering economic factors [32].

Karampour et al. [1] investigated an alternative method to reduce fuel consumption and emissions of pollutants in a supply chain, which can shift the Vendor Managed Inventory (VMI) to the Green VMI (GVMI). So they designed a two-echelon bi-objective green supply chain with a vendor and a number of retailers,

which aimed to increase chain profits and reduce carbon emissions through transportation. The proposed model was solved with Nondominated Sorting Genetic Algorithm (NSGA-II), Multi-Objective of Keshtel Algorithm (MOKA) and Multi-Objective of Red Deer Algorithm (MORDA), and finally a comparison between the three methods showed that the MORDA method performed better than the other two methods. Iqbal et al. [33] provided a mathematical model for minimizing energy consumption in a green chain. In their proposed supply chain, discarded materials were taken back from customers and returned to the collection centers to be recycled and reused as second-hand materials. Wang et al. [34] presented a mathematical model for pricing in a green supply chain. Their supply chain was considered to be reverse, including producers, distributors, customers and collection centers. The results indicated that the final price of the product was not affected by the collection method. Safaeian et al. [35] presented a 4-objective model to select the best supplier, and the order allocation operation was considered due to the incremental discount in a fuzzy environment in the presence of uncertainty. The fuzzy method used was Zimmermann, and to reduce the risk, demand was considered uncertain. The four objectives of this model were to reduce costs, increase service levels, increase product quality and reliability. Finally, the model was solved using the NSGAII method.

Wang and Li [36] presented an integer linear programming model for the design of reverse logistics networks, in which repair and reconstruction options were considered simultaneously. Considering risk as fuzzy was one of the innovations of their research. They considered minimizing risk and transportation costs simultaneously. Samuel et al [14] designed a deterministic mathematical model for a supply chain network under different carbon emission policies. They considered the quality of returned products in a closed-loop supply chain considering the different carbon emission policies. Finally, their proposed model was solved with a robust optimization approach.

Fathollahi-Fard et al. [37] provided a green home health care supply chain which started from the pharmacy and continued to the patient's home. In this supply chain, scheduling and routing were considered as a competitive advantage for organizations providing this type of service. Locating the nearest pharmacy and allocating it to the customer were two of the most important factors in this supply chain. Finally, the model was solved with the Simulated Annealing algorithm and the Epsilon constraint method was used to examine the solutions in small-scale. Baptista et al. [38] proposed a multi-period multi-stage stochastic mixed zero-one optimization model for establishment and expansion of reverse logistics processing networks to maximize profits. Among the innovations of their proposed model were simultaneous consideration of various uncertainties such

as demand, production cost, volume of returned products, and risk management.

Yun et al. [39] designed a sustainable closed loop supply chain with economic, environmental and social criteria. Their objectives included minimizing total costs, minimizing the amount of carbon dioxide emissions, and maximizing social impact. Three types of distribution channels were considered in this study, including normal delivery, direct delivery and direct shipment. Finally, the model was solved by a hybrid genetic algorithm. Rabbani et al. [40] presented a multi-objective, multi-period model for location and allocation in a sustainable supply chain. Considering the different technologies for vehicles that lead to different costs, including the cost of carbon dioxide emissions, was one of the contributions of this research. In order to deal with the uncertainty of the problem, Hybrid Robust Possibilistic Programming-II (HRPP-II) approach was used. Finally, a case study was solved with the Epsilon constraint approach. Roghanian and Cheraghalipour [41] presented a multi-objective mathematical model to reduce costs and reduce CO₂ emissions in the food supply chain. Among their research innovations were the consideration of all levels of decision-making, including the production of products, distribution, inventory, sustainability, the consideration of several vehicles in order to overcome shortages, as well as the location of facilities. Taleizadeh et al. [42] examined the supply chain design problem under uncertainty in demand and by integrating supply chain design and production planning for chain components. They adopted a robust optimization approach. To solve the model, they used a heuristic method to break down the main problem into two sub-problems. Uncertainty was considered as scenario-based, and considering the uncertainty of product quality was one of their research innovations.

Mehranfar et al. [7] designed a sustainable production-distribution system using mixed integer programming and used a hybrid metaheuristic method based on Whale optimization algorithm and simulated annealing to solve it. It was one of the first studies that used this approach to solve problems.

2. 2. Quantitative Modeling of Risk in Supply Chain

The most basic research that has examined sustainability in a closed-loop supply chain considering risk is for Rahimi and Ghezavati [43]. They offered a multi-period multi-objective linear programming model for a closed-loop supply chain considering risk and uncertainty. The objectives of this study included increasing profits and social effects as well as reducing environmental effects. Soleimani and Govindan [25] used a two-stage stochastic model to examine the effect of risk in a closed-loop supply chain using conditional value at risk. Khalili-Damghani and Ghasemi [44] provided a three-level supply chain based on conditional value at risk. In their model,

suppliers and producers sought to increase profits, and retailers sought to increase their profits by considering conditional value at risk.

2. 3. Modeling Uncertainty in Supply Chain

There are several ways to consider uncertainty, one of which involves fuzzy sets. Usually when the information available is ambiguous, fuzzy set theory can be used to consider uncertainty in the real world. Uncertainty is widely used in supply [12]. Chen et al. [45] conducted a study assuming uncertainty in demand.

Fathollahi-Fard et al. [19] modeled a multi-warehouse multi-period bi-objective home healthcare problem in a fuzzy environment. Jimenez fuzzy was used to control the uncertainty of travel time and patient satisfaction. Then, the model was solved by meta-heuristic methods and the results showed the proper performance of the model. Petrovic et al. [46] considered demand as uncertain in their study. El-Sayed et al. [47] used stochastic programming to determine the uncertainty of the problem parameters. Pishvaei et al. [48] used fuzzy mathematical programming for modeling. Ali et al. [49], while modeling a reverse supply chain, examined its application to air conditioning products. The uncertainty in the considered sustainable supply chain was fuzzy; in fact supply chain modeling (SCM) is extensively discussed in literature [50–65]. Locating collection and recycling centers was one of the most important objectives of this study. Abdi et al. [66]

modeled a two-objective closed loop supply chain using two-stage stochastic programming and applied robust method to control the uncertainties related to product production, customer demand, product price, and product return rate. Considering the objective function of cost and financial risk was among the contributions of this research. Finally, the model was solved using Whale Optimization Algorithm (WOA), Particle Swarm Optimization (PSO), Genetic Algorithm (GA) and Simulated Annealing (SA) methods and their results were compared.

Nezhadroshan et al. [50] studied a humanitarian logistics due to the need for emergency services in the case of disaster. Considering the robust uncertainty, resilience and various earthquake scenarios were among the contributions of this research. In their study, warehouses and distribution centers could be reopened and the inventory level of warehouses, distribution centers and the flow between facilities were determined by the model.

Table 1 categorizes and summarizes the literature review of the most relevant studies in the field of supply chain modeling in terms of the solution approach, the type of modeling, the type of objective functions, and attention to risk.

The research gap observed in the literature is as follows. The only study that examined the effect of risk as a part of the objective function on the closed-loop supply chain, considering environmental effects, is the

TABLE 1. Summary of literature review

Ref.	Approach				Risk	Model Type		Network Type			Objective		
	2stage	Stochastic	Fuzzy	Probabilistic		Deterministic	Non Deterministic	Direct	Reverse	Economic	Social	Environment	
[33]		*					*	*	*	*		*	
[49]			*				*		*	*			
[34]	*			*			*	*	*			*	
[66]	*		*		*			*	*	*			
[36]			*		*		*	*		*			
[24]						*		*	*	*	*	*	
[4]						*		*	*	*		*	
[51]		*			*		*	*	*	*			
[14]				*			*	*	*			*	
[42]				*			*	*	*			*	
[43]	*	*			*		*	*			*	*	
[52]		*					*	*	*			*	
[53]			*				*	*	*	*		*	
[15]		*					*	*	*			*	
[25]	*				*		*	*	*				

study of Rahimi and ghezavati [43]. Therefore, considering risk in the objective function with effective methods such as conditional value at risk is one of the issues that have received less attention. Therefore, in this paper, a multi-period multi-product multi-objective green closed-loop supply chain network design model is developed for locating distribution, collection, recycling, and burial centers by considering the conditional value at risk and scenario-based demand uncertainty; and it is estimated using fuzzy theory and fuzzy expert system alongside product quality scenarios.

3. DEFINITION OF THE PROBLEM

In this study, a green closed-loop supply chain is presented considering the quality of returned products, risk and fuzzy demand uncertainty under different scenarios. Figure 1 shows the conceptual model.

According to Figure 1, the demand is estimated using the fuzzy inference system and the method used is Mamdani inference system due to its successful use in many previous studies. Then the risk is added to the model as a part of the cost objective function using the conditional value at risk approach. In the supply chain considered in this study, the flow of returned products is determined based on their quality, then after solving the model, sensitivity analysis is performed on basic parameters such as alpha and lambda and by keeping the other parameters constant, its effects on the values of the objective function is investigated.

3. 1. Fuzzy Inference System In this section, Mamdani and Asilian's [60] inference system is used due

to its simple structure, acceptable results, simplicity of interpreting the results, and its success in previous studies [52-55]. In this study, a fuzzy inference engine has been designed to estimate the demand and its related scenarios. The fuzzy system used includes three operational stages, which are described in Figure 2.

3. 1. 1. Identifying Input Indicators To deal with the proposed uncertainty, the fuzzy inference system approach is used to estimate demand. Factors influencing demand uncertainty include price, quality, environmental effects, advertising, and availability. These factors are based on the studies of Prasad and Sounderpandian [64], Attaran and Attaran [65] and Bhardwaj and Palaparthi [52].

3. 1. 2. Fuzzification In this research, there are two scenarios of stagnation and boom for demand. In the proposed fuzzy system, the demand estimation criteria identified in the previous stage are the same for both the stagnation scenario and the boom scenario. They are considered as FIS inputs, and fuzzification operations are performed on them. In this stage, we consider membership functions for each input variable so that deterministic inputs become fuzzy and enter the fuzzy inference system.

3. 1. 3. Fuzzy Rules Rules are the main part of the FIS model. Fuzzy rules are determined as if-then based on expert opinions. A fuzzy rule can be as "if x_1 is a_1 AND x_2 is b_1 THEN y is c_1 " so x_1, x_2 are variables and y is the desired variable and a, b and c are linguistic variables, which are mentioned in Table 2.

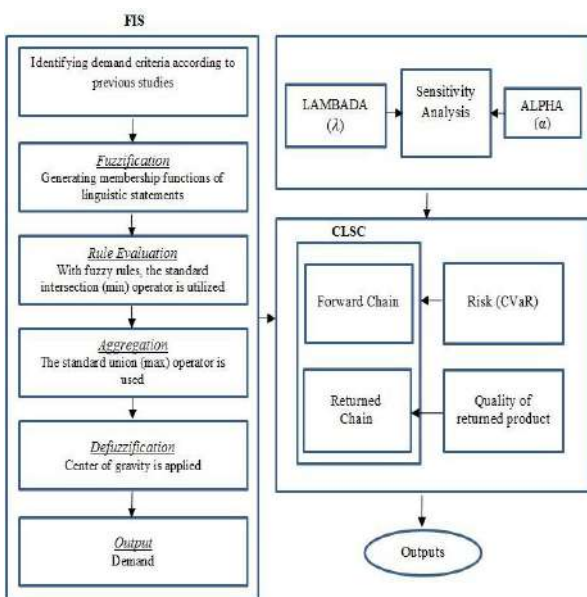


Figure 1. Conceptual model

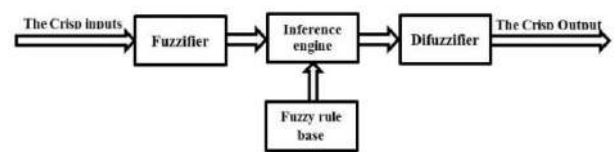


Figure 2. The Mamdani's FIS adapted from Amindoust et al. [58]

TABLE 2. FIS setting

Feature	Description
Fuzzy type	Mamdani
Number of experts	9
Complete rulebase	486
Input of each rule	5
Output	1
Linguistic features of inputs	3
Defuzzification method	COA(Center of area)

3. 1. 4. Inference Engine The main function of the fuzzy inference engine is adapting the rules to the inputs and to integrate the considered fuzzy sets according to the fuzzy rules.

3. 1. 5. Defuzzification It is converting fuzzy outputs to deterministic information. Among four parts of a fuzzy system, computing defuzzification has the most complexity in terms of computation, and it is Defuzzifier that finally determines the numerical value. Common defuzzification methods include: the center of area method (COA), bisector of area method (BOA), mean of maximum method (MOM), smallest of maximum method (SOM), and the largest of maximum method (LOM). In this research, the center of gravity method is used.

4. DETERMINING DEMAND WITH FUZZY MODEL

Some basic concepts should be defined to design a fuzzy demand estimation model, so these concepts are examined in the following sections.

4. 1. Determining the Membership Degree in the Proposed Model

The membership degrees used in the Fuzzy Inference System (FIS) of this research are in both trapezoidal and triangular forms. Trapezoidal fuzzy numbers are shown as $\tilde{w} = (a, b_1, b_2, c)$ according to Figure 3. Also, trapezoidal numbers are defined as relation. Based on relation, if $b_1 = b_2$, trapezoidal fuzzy numbers will become triangular fuzzy numbers.

$$\mu_{\tilde{w}}(x) = \begin{cases} 0 & x < a \\ \frac{x-a}{b_1-a} & a \leq x \leq b \\ \frac{x-c}{b_2-c} & b < x \leq c \\ 0 & x > c \end{cases} \quad (1)$$

4. 1. 1. Membership Function of Inputs and Outputs

At this stage, the membership function of inputs and outputs are used in the FIS system. The linguistic terms used in this study are "low", "average"

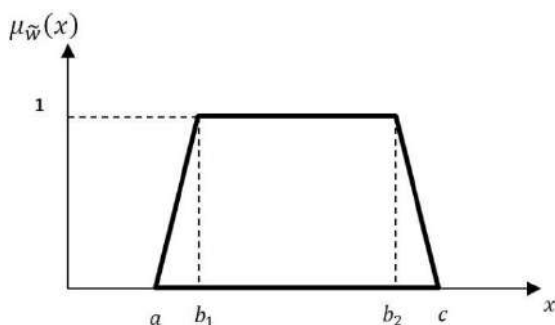


Figure 3. The trapezoidal fuzzy membership function

and "high" according to Figure 4. These variables are equivalent to fuzzy numbers in the range of 500-1500 for demand in the stagnation scenario and the range of 1500 to 3000 for demand in the boom scenario, which are shown in Table 2.

4. 1. 2. Membership Function for Criteria Weights

As mentioned in this study, there are 5 criteria for estimating demand and the linguistic terms to describe them are "low", "average" and "high". To determine the importance of weight of these variables, they are equated with trapezoidal fuzzy numbers in the range between zero and one. Figure 5 shows three fuzzy sets, and the weights of the linguistic variables are shown in Tables 3 and 4.

4. 2. Fuzzy Operators Mamdani and Larsen implication relations use the min and multiplier operators, respectively, to obtain the truth value of each

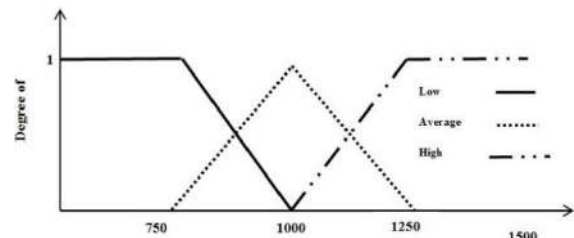


Figure 4. The triangular fuzzy membership function for stagnation scenario

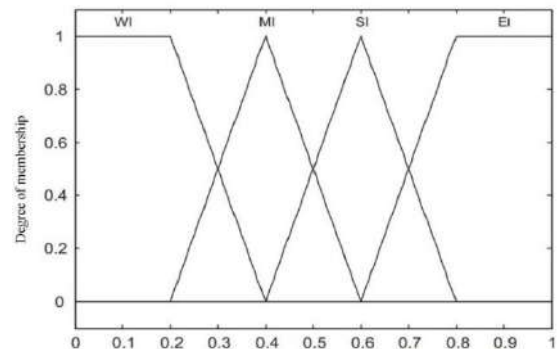


Figure 5. Membership functions for the weights of criteria

TABLE 3. The linguistic terms for demand evaluation

Scenario	Linguistic Terms	Fuzzy Set
Stagnation	Low	(500,750,1000)
	Average	(750,1000,1250)
	high	(1000,1250,1500)
Boom	Low	(1500,1750,2000)
	Average	(1750,2000,2500)
	high	(2000,2500,3000)

TABLE 4. The linguistic weighting terms for criteria

Linguistic Terms	Fuzzy Set
Weak importance (WI)	(0,0,0.2,0.4)
Moderate importance (MI)	(0.2,0.4,0.4,0.6)
Strong importance (SI)	(0.4, 0.6, 0.6,0.8)
Extreme importance (EI)	(0.6, 0.8, 1,1)

rule. Equations (1) and (2) show Mamdani and Larsen implication relations, respectively.

$$R(U, V) = \min[\mu_A(u), \mu_B(u)] \tag{2}$$

$$R(U, V) = \mu_A(u) \cdot \mu_B(u) \tag{3}$$

4. 3. Implementing the Fuzzy Rule-based System

As shown in Figure 5, the inputs of the fuzzy inference system include the criteria of price, quality, environmental effects, advertising, and availability, and the output of the system is the predicted amount of demand. Also, the rules for estimating demand in boom and stagnation scenarios are stated in Table 5.

In this study, the Mamdani implication relation has been used to obtain the truth value of each rule. As shown in Figure 5, the inputs to the fuzzy inference system include the criteria of price, quality, environmental effects, advertising, and availability, and the output of the system is the predicted amount of demand. Figure 6 shows mamdani FIS model.

Defuzzification is the process of converting a fuzzy set to a definite number. Therefore, the input of the defuzzification process is a fuzzy set (the result of the aggregation of output fuzzy sets) and its output is a number. There are various methods such as the center of gravity, bisector, mean of maximum, smallest of maximum, and the largest of maximum for defuzzification. However, the center of gravity method is the most commonly used method [56]. In this study, COA method was used for defuzzification. Equation (3) is the defuzzification relation based on the center of gravity.

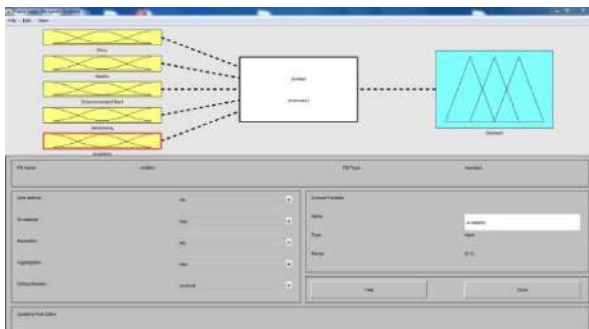


Figure 6. Mamdani FIS model

$$X_{COA} = \frac{\int_1^n \mu_i(x_i) x dx}{\int_1^n \mu_i(x_i) dx} \tag{4}$$

where x_i is a member of the set X , which is defined as $X = x_1, x_2, \dots, x_n$. The membership value (μ) indicates the degree of membership of each member of x_i in the fuzzy set X , which is shown as $X = x_1(\mu_1), x_2(\mu_2), \dots, x_n(\mu_n)$.

It is worthwhile to say that after multiplication of criteria and sub-criteria weights by customer’s demand in the boom and stagnation scenario, the range of demand ([500-1500] in stagnation scenario and [1500,3000] in boom scenario) is reduced. So, the obtained results do not satisfy the aims of designed rules and causes inadequate precision for the FIS outputs. To tackle this problem, the FIS inputs are normalized for remaining in the previous scale of inputs. This methodology must be repeated for each candidate scenario.

4. 5. Introducing the Research Problem

In this research, a four-level supply chain network includes suppliers, producers, distribution centers, and customers in direct route and includes collection, recycling, and disposal centers. This model is multi-product and multi-period. Distribution, collection, recycling and disposal centers can be reopened. Overproduction in factories is transported to the producer’s warehouse, and both the producer and the warehouse can send the products directly to the distribution centers. Suppliers, collection and recycling centers are responsible for providing components and raw materials to production equipment. New products are sent from factories to customers through distribution centers to meet their demand, and the reverse supply chain process begins with customer returned products. The decisive role in the flow of returned products is played by their quality, so that the returned products are disassembled according to their quality in the collection centers and high quality parts (qs_1) are sent to production centers, reproducible parts (qs_2) are sent to recycling centers, and non-usable parts (qs_3) are sent to the disposal centers. It should be noted that the demand parameter in the proposed model is considered as uncertain and to deal with the proposed uncertainty, the fuzzy inference system approach is used to estimate demand.

Therefore, the research steps are as follows. First, the values of uncertainty in demand are estimated using the fuzzy inference system approach and the identified factors. After mathematical modeling, the problem is solved using the multi-objective particle swarm meta-heuristic approach. Finally, sensitivity analysis are performed on the results. Figure 7 shows the research steps.

In the following, based on the definition of the problem, the mathematical model is designed and the components of the model are described. In this research,

TABLE 5. The fuzzy rule base matrix based on scenarios

Scenario	Criteria					
	Price	Quality	Environmental Effects	Advertising	Availability	Demand
Market boom	low	medium	low	medium	High	High
	low	High	medium	High	medium	High
	medium	medium	low	High	High	medium
	High	low	High	low	medium	low
Market stagnation	High	medium	medium	medium	low	low
	medium	low	High	low	medium	low

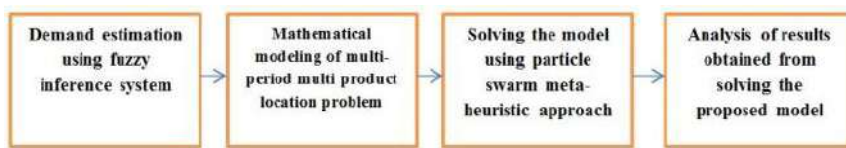


Figure 7. Research steps

the model determines the optimal amount of product delivery to the market based on the market situation and related scenarios. In this study, two modes are considered for different scenarios. The first scenario is boom and the second scenario is low boom of the market. Each of these scenarios will affect product demand and lead to a change in demand. And the probability of occurrence of both scenarios is equal.

In this study, two objective functions are considered. In the first objective function, we seek to reduce costs, and in the second objective function, we seek to minimize environmental effects and carbon dioxide emissions. Figure 8 shows the proposed supply chain structure.

4. 6. Model Assumptions

- Uncertainty in parameters such as demand is considered as scenario-based.
- The model is multi-product and multi-period and the shortage is not allowed in the model.
- Each seller can be served by all warehouses and each warehouse can be served by all distribution centers.
- Each product can be taken back in one period and each returned product can only be recycled, collected and disposed or sent to supply, production and distribution centers in that same period.
- Each unit of distance is considered equal to one unit of cost.

4. 7. The Main Structure of the Mathematical Model

Value at risk is a measure of financial risk, which is widely used in the financial industry [62]. For the decision variable x selected from the set X , for each $x \in X$, loss is $T = L(x, y)$ where x is the decision variable and y is the random variable, and in the significance level

$\alpha \in (0, 1)$ for the value at risk, loss of T is defined as follows [44].

$$VaR_\alpha(x) = \min\{\gamma | p\{y | L(x, y) \leq \gamma\} \geq \alpha\} \tag{5}$$

Due to not being convex and addable, the VaR criterion is not appropriate. Therefore, the conditional value at risk (CVaR) criterion is used, which is expressed as follows [30]:

$$CVaR_\alpha(x) = \varphi_\alpha(x) = E\{L(x, \varepsilon) | L(x, \varepsilon) \geq VaR_\alpha(x)\} = \frac{1}{1-\alpha} \int_{L(x, y) \geq VaR_\alpha(x)} L(x, y) f(y) dy \tag{6}$$

where $f(y)$ is density function of ε . Rockafellar and Uryasev [54] proved that to minimize CVaR, it is sufficient to minimize the following function:

$$CVaR_\alpha(x) = F_\alpha(x, y) = \gamma + \frac{1}{1-\alpha} E[[L(x, \varepsilon) - \gamma]^+] \tag{7}$$

In the above formula, the addition operator is as follows:

$$[t]^+ = \max\{0, t\} \tag{8}$$

The decision maker may consider a tolerance of previous loss (β), which this constraint is shown in Goh and Meng [55] as follows:

$$CVaR_\alpha(x) \leq \beta \tag{9}$$

4. 7. 1. Risk Modeling In general, the two indicators of cost minimization (profit maximization) and loss minimization are important for decision makers. To determine these two criteria simultaneously in a model, we use a risk aversion rate, $\lambda \in (0, 1)$, and the linear combination of this criterion and the cost criterion $f(x, y)$ in the objective function is expressed as follows ($h_1(x, y)$ represent the constraints of the problem):

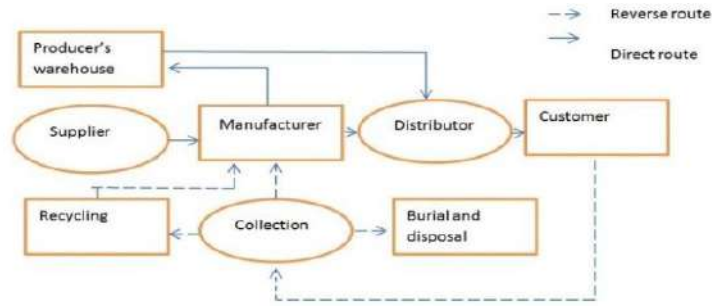


Figure 8. Proposed supply chain structure

$$\begin{aligned}
 & \text{Min}(1 - \lambda)E[f(x, y)] + \lambda \text{CVaR}\alpha(x) \\
 & E[h_l(x, y)] = 0 \quad l = 1, 2, \dots, \\
 & j E[h_l(x, y)] \leq 0 \quad l = j + 1, \dots, \\
 & k \text{CVaR}\alpha x \leq \beta x \in X
 \end{aligned} \tag{10}$$

By placing the formula of CVaR in the above model, we will have:

$$\begin{aligned}
 & \text{min}(1 - \lambda) E[f(x, y)] + \lambda(\gamma + \frac{1}{1-\alpha} E[[L(x, \varepsilon) - \gamma]^+]) \\
 & E[h_l(x, y)] = 0 \quad l = 1, 2, \dots, j \\
 & E[h_l(x, y)] \leq 0 \quad l = j + 1, \dots, k \\
 & \gamma + \frac{1}{1-\alpha} E[[L(x, \varepsilon) - \gamma]^+] \leq \beta \quad (x, \gamma) \in X * R
 \end{aligned} \tag{11}$$

Zhou et al. [48] rewrote the above function and made it linear:

$$F_\alpha(x, y) = \gamma + \theta \sum [L(x, y) - \gamma]^+ \quad \text{where } \theta = ((1 - \alpha) \text{sen})^{-1} \tag{12}$$

$$T_s = L(x, \varepsilon) - \gamma \tag{13}$$

and the final model, considering the risk and cost, is presented as follows:

$$\text{min}(1 - \lambda) E[f(x, y)] + \lambda(\gamma + \theta \sum_{s=1} T_s) \tag{14}$$

$$\begin{aligned}
 & \text{St:} \\
 & E[h_l(x, y)] = 0 \quad l = 1, 2, \dots, j \\
 & E[h_l(x, y)] \leq 0 \quad l = j + 1, \dots, k \\
 & T_s \geq L(x, \varepsilon) - \gamma \quad s = 1, 2, \dots, S \\
 & T_s \geq 0 \quad Z_s \in R \quad s = 1, 2, \dots, S \\
 & (\gamma + \theta \sum_{s=1} T_s) \leq \beta \quad (X, \gamma) \in X * R
 \end{aligned} \tag{15}$$

The objective function of cost minimization:

$$\begin{aligned}
 \text{min } z_1 = & (\sum_{k \in K} f_k y_k + \sum_{m \in M} f_m y_m + \\
 & \sum_{p \in P} f_p y_p + \sum_n f_n y_n) + w_{sen} \\
 & (\sum_t \sum_{sen} (\sum_{s \in S} \sum_{i \in I} \sum_{j \in J} c_{ij, sen}^s x_{ij, sen}^{st} + \\
 & \sum_{s \in S} \sum_{j \in J} c_{jj, sen}^s Q_{jj, sen}^{st} + \\
 & \sum_{s \in S} \sum_{j \in J} \sum_{k \in K} c_{jk, sen}^s x_{jk, sen}^{st} + \\
 & \sum_{s \in S} \sum_{ij \in J} \sum_{k \in K} c_{jk, sen}^s Q_{jk, sen}^{st} + \\
 & \sum_{s \in S} \sum_{k \in K} \sum_{l \in L} c_{kl, sen}^s x_{kl, sen}^{st} \\
 & + \sum_{sen \in Sen} (\sum_{s \in S} \sum_{l \in L} \sum_{m \in M} \\
 & c_{lm, sen}^s x_{lm, sen}^{st} + \\
 & \sum_{s \in S} \sum_{m \in M} \sum_{p \in P} c_{mp, sen}^s x_{mp, sen}^{st} \\
 & + \sum_{s \in S} \sum_{m \in M} \sum_{n \in N} c_{mn, sen}^s x_{mn, sen}^{st} +
 \end{aligned} \tag{16}$$

$$\begin{aligned}
 & \sum_{s \in S} \sum_{m \in M} \sum_{j \in J} c_{mj, sen}^s x_{mj, sen}^{st} + \\
 & \sum_{s \in S} \sum_{p \in P} \sum_{j \in J} c_{pj, sen}^s x_{pj, sen}^{st} + \\
 & \sum_{s \in S} \sum_{p \in P} \sum_{i \in I} c_{pi, sen}^s x_{pi, sen}^{st} + \\
 & \sum_{s \in S} \sum_{j \in J} h_{j, sen}^s U_{j, sen}^{st} \\
 & \sum_{t \in T} \sum_{sen \in Senario} \sum_{s \in S} \sum_{j \in J} \\
 & (\text{cos } t_{s, sen} (Q_{jj, sen}^{st} + \sum_{k \in K} x_{jk, sen}^{st}))
 \end{aligned}$$

The first objective function includes minimizing the cost of establishing facilities, the cost of transporting the flow of materials between centers, the cost of storing materials in the producer's warehouse, the cost of returning the product, the cost of collecting, the cost of recycling, the cost of burial and disposal, and the cost of production for each product. The second objective function:

$$\begin{aligned}
 \text{Min } z_2 = & TE + FE \quad FE = \sum_{k \in K} y_k \cdot o_k + \\
 & \sum_{m \in M} y_m \cdot o'_m + \sum_{p \in P} y_p \cdot o''_p + \\
 & \sum_{n \in N} y_n \cdot o'''_n \quad TE = \sum_{sen \in Sen} w_{sen} \cdot CEM
 \end{aligned}$$

$$\begin{aligned}
 & \sum_{s \in S} \sum_{i \in I} \sum_{j \in J} c_{ij, sen}^s x_{ij, sen}^{st} + \\
 & \sum_{s \in S} \sum_{j \in J} c_{jj, sen}^s Q_{jj, sen}^{st} \\
 & + \sum_{s \in S} \sum_{j \in J} \sum_{k \in K} c_{jk, sen}^s x_{jk, sen}^{st} + \\
 & \sum_{s \in S} \sum_{ij \in J} \sum_{k \in K} c_{jk, sen}^s Q_{jk, sen}^{st} + \\
 & \sum_{s \in S} \sum_{k \in K} \sum_{l \in L} c_{kl, sen}^s x_{kl, sen}^{st} \\
 & + \sum_{s \in S} \sum_{l \in L} \sum_{m \in M} c_{lm, sen}^s x_{lm, sen}^{st} + \\
 & \sum_{s \in S} \sum_{m \in M} \sum_{p \in P} c_{mp, sen}^s x_{mp, sen}^{st} \\
 & + \sum_{s \in S} \sum_{m \in M} \sum_{n \in N} c_{mn, sen}^s x_{mn, sen}^{st} + \\
 & \sum_{s \in S} \sum_{m \in M} \sum_{j \in J} c_{mj, sen}^s x_{mj, sen}^{st} + \\
 & \sum_{s \in S} \sum_{p \in P} \sum_{j \in J} c_{pj, sen}^s x_{pj, sen}^{st} + \\
 & \sum_{s \in S} \sum_{p \in P} \sum_{i \in I} c_{pi, sen}^s x_{pi, sen}^{st}
 \end{aligned} \tag{17}$$

The second objective function consists of two sections. The first section minimizes the adverse environmental effects (released carbon dioxide) caused by the establishment of potential centers. The second part of the objective function also minimizes the adverse environmental effects (released carbon dioxide) caused by the transportation and flow of products.

$$\begin{aligned}
 \text{max } z_3 = & \sum_{t \in T} \sum_{sen} (\sum_{k \in K} \pi_{k, sen} y_k + \\
 & \sum_{m \in M} \pi_{inv, sen} y_m + \sum_{p \in P} \pi_{inv, sen} y_p + \\
 & \sum_{n \in N} \pi_{inv, sen} y_n) - \\
 & \sum_{t \in T} \sum_{sen} (\sum_{j \in J} \sum_{s \in S} (\psi_j (Q_{jj, sen}^{st} + \\
 & \sum_{k \in K} x_{jk, sen}^{st})))
 \end{aligned}$$

The third objective function is expressed in the form of social responsibility as above. The first phrase of the objective function indicates the number of job opportunities created in the facilities with the ability to reopen, such as distribution, collection, recycling and burial and disposal centers. The second phrase indicates the workplace injuries in the above centers.

Constraints:

$$\sum_{k \in K} x_{kl, sen}^{st} = d_{l, sen}^{st} \forall l \in L, \forall s \in S, t \in T, sen \in \text{scenario} \quad (18)$$

$$\sum_{m \in M} x_{lm, qs, sen}^{st} = r_{l, qs, sen}^s (\sum_{s \in S} \sum_{l \in L} x_{kl, sen}^{st}) \forall l \in L, \forall s \in S, t \in T, qs, sen \in \text{scenario} \quad (19)$$

Constraints (18) and (19) ensure that the total demand of customers may not be met in the direct flow, and that all returned products will be collected from customer centers in the reverse flow.

$$\sum_{qs_1} \sum_{j \in J} x_{mj, qs, sen}^{st} = B_j^{st} \sum_{qs} (\sum_{l \in L} x_{lm, qs, sen}^{st}) \forall m \in M, \forall s \in S, t \in T, \forall sen \in \text{scenario} \quad (20)$$

$$\sum_{m \in M} x_{lm, qs, sen}^{st} = r_{l, qs, sen}^s (\sum_{s \in S} \sum_{l \in L} x_{kl, sen}^{st}) \forall l \in L, \forall s \in S, t \in T, qs, sen \in \text{scenario} \quad (21)$$

$$\sum_{qs_3} \sum_{n \in N} x_{mn, qs, sen}^{st} = B_n^{st} \sum_{qs} (\sum_{l \in L} x_{lm, qs, sen}^{st}) \forall m \in M, \forall s \in S, t \in T, \forall sen \in \text{scenario} \quad (22)$$

$$\sum_{j \in J} (x_{jk, sen}^{st} + Q_{jk, sen}^{st}) = \sum_{l \in L} x_{kl, sen}^{st} \forall k \in K, \forall s \in S, t \in T, \forall sen \in \text{scenario} \quad (23)$$

$$\sum_{qs_2} \sum_{m \in M} x_{mp, qs, sen}^{st} = \sum_{j \in J} x_{pj, sen}^{st} \forall p \in P, \forall s \in S, t \in T, \forall sen \in \text{scenario} \quad (24)$$

$$\sum_{i \in I} x_{ij, sen}^{st} + \sum_{qs_1} \sum_{m \in M} x_{mj, qs, sen}^{st} + \sum_{p \in P} x_{pj, sen}^{st} = \sum_{k \in K} x_{jk, sen}^{st} + Q_{jj, sen}^{st} \forall j \in J, \forall s \in S, t \in T, \forall sen \in \text{scenario} \quad (25)$$

$$\sum_{qs_1} \sum_{j \in J} x_{mj, qs, sen}^{st} + \sum_{qs_2} \sum_{p \in P} x_{mp, qs, sen}^{st} + \sum_{qs_3} \sum_{n \in N} x_{mn, qs, sen}^{st} = \sum_{qs} \sum_{l \in L} x_{lm, sen}^{st} \forall m \in M, \forall s \in S, t \in T, \forall sen \in \text{scenario} \quad (26)$$

$$U_{j, sen}^{st} = Q_{jj, sen}^{st} - \sum_{k \in K} Q_{jk, sen}^{st} \forall j \in J, \forall s \in S, t \in T, \forall sen \in \text{scenario} \quad (27)$$

Constraints (20) to (27) relate to flow balance constraints in the nodes.

$$\sum_{k \in K} Q_{jk, sen}^{st} \leq Q_{jj, sen}^{st} \forall j \in J, \forall s \in S, t \in T, \forall sen \in \text{scenario} \quad (28)$$

Constraint (28) ensures that the amount of outflow from the warehouse of the production center is less than the total inflow to the warehouse.

$$\sum_{s \in S} \sum_{j \in J} x_{ij, sen}^{st} \leq ca_i \forall i \in I, t \in T, \forall sen \in \text{scenario} \quad (29)$$

$$\sum_{s \in S} \sum_{k \in K} x_{jk, sen}^{st} + \sum_{s \in S} Q_{jj, sen}^{st} \leq ca_j \forall j \in J, t \in T, \forall sen \in \text{scenario} \quad (30)$$

$$\sum_{s \in S} \sum_{l \in L} x_{kl, sen}^{st} \leq ca_k y_k \forall k \in K, t \in T, \forall sen \in \text{scenario} \quad (31)$$

$$\sum_{qs_1} \sum_{s \in S} \sum_{j \in J} x_{mj, qs, sen}^{st} + \sum_{qs_3} \sum_{s \in S} \sum_{n \in N} x_{mn, qs, sen}^{st} + \sum_{qs_2} \sum_{s \in S} \sum_{p \in P} x_{mp, qs, sen}^{st} \leq ca_m y_m \forall m \in M, t \in T, \forall sen \in \text{scenario} \quad (32)$$

$$\sum_{s \in S} (\sum_{qs_1} \sum_{m \in M} x_{mj, qs, sen}^{st} + \sum_{p \in P} x_{pj, sen}^{st}) \leq cr_j \forall j \in J, t \in T, \forall sen \in \text{scenario} \quad (33)$$

$$\sum_{qs_3} \sum_{s \in S} \sum_{m \in M} x_{mn, qs, sen}^{st} \leq ca_n y_n \forall n \in N, t \in T, \forall sen \in \text{scenario} \quad (34)$$

$$\sum_{qs_2} \sum_{s \in S} \sum_{m \in M} x_{mp, qs, sen}^{st} \leq ca_p y_p \forall p \in P, t \in T, \forall sen \in \text{scenario} \quad (35)$$

$$\sum_{s \in S} U_{j, sen}^{st} \leq ca_j \forall j \in J, t \in T, \forall sen \in \text{scenario} \quad (36)$$

Relations (29) to (36) ensure that the flow is only between points in which a facility has been established and that the total flow in each facility does not exceed its capacity.

$$\sum_{k \in K} y_k \geq 1 \quad (37)$$

$$\sum_{m \in M} y_m \geq 1 \quad (38)$$

$$\sum_{p \in P} y_p \geq 1 \quad (39)$$

$$\sum_{n \in N} y_n \geq 1 \quad (40)$$

Relations (37) to (40) ensure that at least one of the potential centers is active.

$$B_j^{st} + B_p^{st} + B_n^{st} = 1 \forall s \in S, t \in T \quad (41)$$

Relation (41) ensures that the sum of the coefficients of the returned products is 1.

$$y_m, y_k, y_p, y_n \in \{0,1\} \forall m \in M, \forall k \in K, \forall p \in P, \forall n \in N, t \in T \quad (42)$$

$$x_{ij}^{st}, x_{jk}^{st}, Q_{jj}^{st}, U_j^{st}, x_{kl}^{st}, Q_{jk}^{st}, x_{lm}^{st}, x_{mj}^{st}, x_{mp}^{st}, x_{mn}^{st} \geq 0 \forall i \in I, \forall j \in J, \forall k \in K, \forall l \in L, \forall m \in M, \forall n \in N, \forall p \in P, t \in T \quad (43)$$

Constraints (42) and (43) are logical and obvious constraints related to problem decision variables.

5. SOLUTION METHOD

Solution method is as follow:

5. 1. Multi-objective Particle Swarm Solution Algorithm Figure 9 shows the structure of MOPSO optimization algorithm.

5. 2. Adjusting the Coefficients Managers look for better ways or solutions for improvement, which will help them manage the entire organization. Metaheuristic algorithms are easy, cost-effective, and important tools that allow researchers and managers to solve problems [56]. PSO method is one of the best problem solving techniques among swarm-based methods [56, 66].

In the MOPSO algorithm, the equations describing the behavior of the particles are as follows, in which Equations (44) and (45) determine the velocity and position of particle i at the moment t + 1.

$$V^i[t + 1] = wV^i[t] + c_1r_1(x^{i,best}[t] - x^i[t]) + c_2r_2(x^{g,best}[t] - x^i[t]) \tag{44}$$

$$x^i[t + 1] = x^i[t] + V^i[t + 1] \tag{45}$$

where $x^i[t]$ is the position of the particle i at time t, $V^i[t]$ is the velocity of the particle i at time t, $x^{i,best}[t]$ is the best position of the particle i at time t. Also, w is the inertia coefficient, r_1 and r_2 are random numbers between zero and one with uniform distribution, and c_1 and c_2 are the personal and global learning coefficients, respectively. The inertia coefficient w is an important parameter in particle swarm optimization algorithm, which has a direct effect on the convergence of the algorithm. In other words, it controls the effect of previous velocity on current velocity. A proper value for

w creates a balance between local search and global search and often reduces the number of iterations needed for convergence to a proper solution. Pishvae et al. [48] proposed the value of Equation (46) for the value of inertia.

$$w = w_{max} - \frac{w_{max}-w_{min}}{iter_{max}} \tag{46}$$

where w_{max} is the initial value of the inertia coefficient, w_{min} is the final value of the inertia coefficient, and $iter_{max}$ is the maximum number of iterations of the algorithm. Through this relation, the value of w is considered as large in initial stages to conduct a complete, global search of the search space. Then, during the implementation of the algorithm, the value of w is gradually reduced to bring the algorithm closer to the convergence boundary. According to Relation (46), the values of $iter_{max} = 500$, $w_{min} = 0.4$ and $w_{max} = 1.2$ are considered for each of the parameters. Also, 100 particles are used for searching the solution space.

5. 3. Displaying the Particles As can be seen in the Figure 10, in this study, the integer values are used to display the amount of remaining inventory of the product s in the warehouse of the production center j during period t in the scenario sen.

5. 4. Generation of Initial Solutions For the generation of initial particles, a quasi-random method is designed to use those particles between the two modes of minimum and maximum number of deliveries. The steps of this process for the generation of initial particles are as follows [57]:

All components of the first particle are considered equal to 1. This particle is the particle with the highest number of deliveries and always feasible. In other words, the first particle represents the mode in which we produce in all periods and send in all periods for all retailers.

We put the first and second particle as the first and second parent. Then, using the scattering crossover operator, we create the other required particles. To perform the scattered crossover operator, first a zero and one random array the same size as the particle is created.

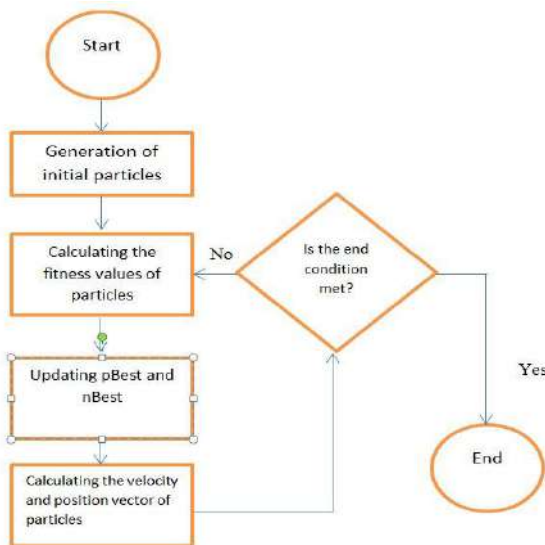


Figure 9. Structure of solution algorithm [48]

		t					
		Sen		Sen		Sen	
j	s	10	36	21	38	75	75
		9	56	68	26	62	48
s	s	26	97	54	71	40	57
		54	12	20	16	74	45
		60	10	15	82	76	60
		19	61	35	68	78	64

Figure 10. An example of displaying the particles

If the component i of the random array is 1, the component i of the child particle (new particle) will be equal to the component i of the parent 1 (the first particle), otherwise it will be equal to the component i of the parent 2 (the second particle). The operation of the scattered crossover operator is presented in Figure 11.

5. 5. Stop Criterion The maximum number of iterations for all problem modes is considered as 500.

5. 6. Computational Results Epsilon constraint method is one of the well-known approaches for dealing with multi-objective problems. It solves this type of problems by transferring all the objective functions except one of them to the constraints at each stage. The Pareto boundary can be created by the ϵ constraint method [50]. In this method, we always optimize one of the objectives, provided that we define the highest acceptable limit for other objectives in the form of constraints, so that [57]:

$$\begin{aligned} & \min f_1(x) \\ & x \in X \\ & f_2(x) \leq \epsilon_2 \\ & \vdots \\ & f_n(x) \leq \epsilon_n \end{aligned} \tag{47}$$

Table 6 shows the results of solving the model in small and medium scale. This table compares the results of the Epsilon constraint approach and particle swarm optimization. It should be noted that examples 1 to 4 are small scale and examples 5 to 8 are medium scale. The results of solving each of the two approaches are also listed in Table 6.

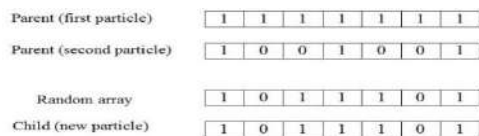


Figure 11. Performing the scattered crossover operator

According to Table 6, the mean error for all examples is below one percent. As it is obvious, the mean error percentage for objective function values is below one percent. Due to the small difference of error between the two algorithms, the accuracy of the performance and efficiency of the multi-objective particle swarm algorithm is proved, and the multi-objective particle swarm algorithm can be trusted to solve large scale problems. The results of the solution indicate that the growth rate of the solving time of the exact solution algorithm is much higher than that of the meta-heuristic algorithm. The mean solving time of the Epsilon constraint approach is 2047.25 seconds and the mean solving time of the particle swarm approach is 19 seconds. Therefore, according to the results of Table 6, we can trust the particle swarm algorithm to solve large scale problems as well as predict its good performance. Figure 12 shows the Pareto points obtained from numerical samples. The red points are the Pareto points for the particle swarm approach.

5. 7. Metrics to Evaluate Proposed Algorithm

To evaluate the accuracy of the proposed particle swarm algorithm, two metrics of MID and SM are presented.

Spacing: This metric calculates the standard deviation between the solutions and the Pareto points. This metric is defined as Equation (48):

$$SM = \frac{\sum_{i=1}^{n-1} |d_i - \bar{d}|}{(n-1)\bar{d}} \tag{48}$$

N is the number of Pareto points, d_i is the Euclidean distance between the two adjacent Pareto points, and \bar{d} is the average Euclidean distance of the solution points. The closer this value is to zero, the closer the Pareto points and the better the performance of the algorithm will be.

Mean ideal distance (MID): Calculates the convergence rate of Pareto points to the ideal point (0.0). This metric is defined as Equation (49):

TABLE 6. Comparative results of solution in small and medium scale

Epsilon Constraint				MOPSO				Error		
f_1	f_2	f_3	Time(s)	f_1	f_2	f_3	Time(s)	f_1	f_2	f_3
805	415	289	1	805	415	289	1	0	0	0
838	421	311	48	843	426.9	301	3	0.005967	0.01329	0.0332
952	429	314	53	956	432	304	7	0.004202	0.00582	0.0329
876	451	328	104	993	457	325	16	0.133562	0.01226	0.0092
1753	769	639	1799	1779	773	634	31	0.014832	0.00523	0.0079
1809	861	755	2131	1891	866	747	35	0.045329	0.00552	0.0107
1915	921	816	3313	1929	942	815	39	0.007311	0.02272	0.0012
2232	1151	996	8929	2234	1169	984	58	0.000896	0.01555	0.0122

$$MID = \frac{\sum_{i=1}^n \sqrt{\left(\frac{f_{1i} - f_1^{best}}{f_{1,total}^{max} - f_{1,total}^{min}}\right)^2 + \left(\frac{f_{2i} - f_2^{best}}{f_{2,total}^{max} - f_{2,total}^{min}}\right)^2 + \left(\frac{f_{3i} - f_3^{best}}{f_{3,total}^{max} - f_{3,total}^{min}}\right)^2}}{n} \quad (49)$$

f_{ji} is the value of j -th objective function for i -th Pareto front. $f_{j,total}^{max}$ and $f_{j,total}^{min}$ are respectively the highest and lowest values of the j -th objective function among the Pareto points. So the lower the MID value is, the better the performance of the algorithm will be.

Table 7 shows the metrics for small and medium scale problems. The results show that the mean of MID and SD metrics are 0.338 and 3.971 respectively. Therefore, the results of the solution can be trusted and the algorithm can be used to solve in large scale problems.

5. 8. Numerical Example

In this problem, the number of suppliers, producers and distributors is 5, the number of customer centers is 6, the number of collection, recycling and disposal centers is 5, the number of products is 2, the number of periods is 2, the number of scenarios is 2, and the number of quality levels is 3. Because it is a two-objective problem, the solutions are reported for 1 point of a specific Pareto point of a numerical example. The method of selecting a Pareto point is that due to the fact that the cost factor (first

objective function) is more important than social responsibility (second objective function), the Pareto point is selected for product number 1, which has the lowest cost. It should be noted that the amount of gamma calculated for the desired Pareto point is 66750. Some of the input parameters of the problem are in Table 8.

The results of solving the model in MATLAB 2018 software are as follows. Table 9 shows the Pareto points resulting from solving the proposed model. In this table, ten points (in large scale problem) are examined and the solving time indicates the appropriate performance of the proposed algorithm. Table 10 shows values of location of distribution, collection, recycling and disposal centers, Tables 11 and 12 show the amount of flow of the product from supply centers to production centers and the amount of flow of the product from the production centers to the distribution centers respectively.

5. 9. Sensitivity Analysis

In this section, we analyze the sensitivity of the important parameters of the

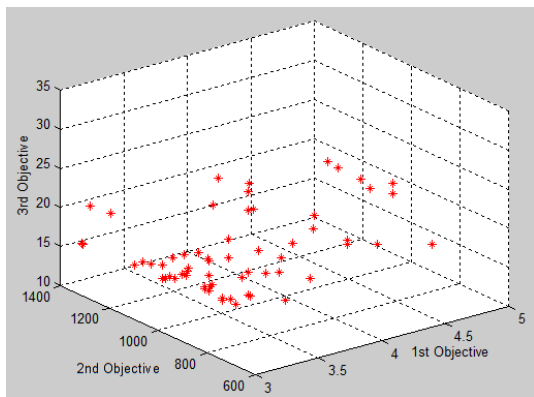


Figure 12. Pareto front

TABLE 7. Metrics for small and medium scale problems

MID	SD
0	0
0.217	2.584
0.244	2.845
0.257	3.168
0.27	3.621
0.441	5.11
0.468	5.138
0.475	5.335

TABLE 8. Problem parameters for $\alpha=0.95, \beta=1000000, \lambda=0.6$

Parameters	Uniform distribution function for each period
$d_{i,sen}^{st}$	500-3000
$cost_{s,sen}$	150-200
Bp^{st}	0.3-0.6
f_m	450-600
$C_{ij,sen}^s$	50-100
ca_i	400-500
Ca_p	400-500
O_k, O'_m, O''_p, O'''_n	200-300
CEM	0.2-0.4

TABLE 9. Pareto points obtained from solving the model

No	f_1	f_2	f_3	Time(s)	MID	SD
1	57313	2126	1825	2	0.358	2.649
2	57346	2135	1831	6	0.362	2.741
3	57167	2265	1832	7	0.389	3.002
4	56739	2283	1828	14	0.402	3.325
5	57627	2253	1827	19	0.415	3.778
6	57332	2260	1830	23	0.586	5.267
7	57316	2296	1831	26	0.613	5.295
8	57301	2835	1832	28	0.62	5.492
9	57321	2553	1829	32	0.649	5.681
10	57432	2568	1835	36	0.688	5.903

TABLE 10. Values of location of distribution, collection, recycling and disposal centers

Distribution Center	Collection Center	Recycling Center	Disposal Center	Center Number
1	1	0	1	1
1	1	1	0	2
1	1	0	1	3
1	1	0	1	4
1	0	1	0	5

TABLE 11. The amount of flow of the product from supply centers to production centers ($x_{ij,sen}^{st}$)

(I,j)/(sen,t)	(sen1,t1)	(sen1,t2)	(sen2,t1)	(sen2,t2)
(i1,j1)	265	523	662	650
(i1,j4)	534	634	1264	698
(i2,j3)	631	582	1482	1058
(i2,j2)	649	638	1560	750
(i3,j5)	635	602	716	1409
(i3,j4)	565	598	856	785
(i4,j1)	489	645	1078	716
(i4,j4)	649	552	941	705
(i5,j3)	573	586	798	1088
(i5,j4)	450	562	789	1390

TABLE 12. The amount of flow of the product from the production centers to the distribution centers ($x_{jk,sen}^{st}$)

(I,j)/(sen,t)	(sen1,t1)	(sen1,t2)	(sen2,t1)	(sen2,t2)
(k1,j2)	565	631	1438	895
(k1,j3)	675	504	875	1301
(k2,j1)	444	473	935	843
(k2,j2)	600	629	872	787
(k3,j5)	453	485	1384	1323
(k3,j4)	552	585	765	682
(k4,j4)	382	435	897	638
(k4,j3)	482	492	867	787
(k5,j1)	468	459	1256	956
(k5,j2)	453	510	796	861

model and examine the effects of changing them on the variables and objective functions. As shown in Figure 13 shows the amount of changes of the first objective function relative to the values of the alpha variables. As can be seen, higher amounts of alpha lead to higher costs. This increase is not linear and uniform, and the biggest

change occurs in the increase from 0.8 to 0.9, which is much greater than the previous period, indicating that the alpha level of more than 0.8 will lead to more costs.

Figure 14 shows changes in risk aversion rate (λ) relative to cost. As can be seen, the cost has a completely linear relationship with the decision-maker's risk aversion rate; so the more risk tolerant the decision maker, the lower the value of the objective function will be, and we need to spend more to avoid the risk as much as possible. So, decision-maker only seeks to reduce costs, and also, if λ is assumed to be 1, it means that the probable loss has much more importance for the decision-maker than cost reduction.

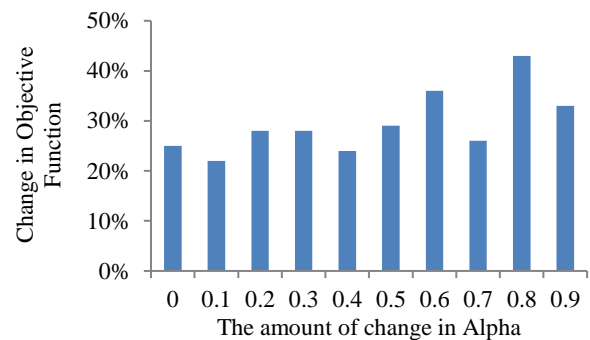


Figure 13. Sensitivity analysis of the objective function relative to alpha values

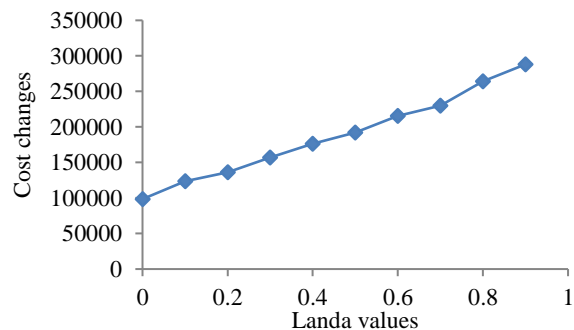


Figure 14. Cost changes relative to different λ values

6. CONCLUSION

In today's competitive world, reducing production costs and improving productivity are among the top priorities in the thoughts and production policies of industrial managers, and every company is trying to provide the best solutions to meet the above needs. Therefore, at each period, new approaches to inventory management and control, and distribution of products are proposed, including planning to reduce transportation costs and reduce risk in the supply chain. Therefore, managers must attach the same importance to the reverse supply chain as they do to the direct supply chain. Paying

attention to the social dimension in a supply chain, especially in the conditions of market instability and continuous market orientation towards recession and boom, can have many benefits for organizations and chain managers. For example, when the market is booming, with proper modeling and forecasting of the market conditions in times of recession, the unemployment rate, dismissal and even workplace injuries can be reduced greatly. This is the social responsibility of a company towards society, because such a forecast reduces crime, corruption and delinquency rates and so on and it can raise the level of hope and welfare in society. Therefore, in this study, a multi-objective mathematical model for locating and distributing products in a closed-loop supply chain has been presented considering risk and environmental factors. Considering the uncertainty of quality and uncertainty of demand along with minimizing risk and environmental impacts are among the main innovations of this research. Fuzzy inference system has been used to deal with uncertainty of demand, and this parameter has been estimated using 5 identified factors. The results of solving the model indicate that the mean of the Pareto points obtained from the first objective function is 57289.4, the mean of the Pareto points for the second objective function is 2357.4 and the third objective function is 1830. Finally, examining the error rate of the particle swarm approach and its much lower solving time than the Epsilon constraint method shows its high efficiency. The results of sensitivity analysis indicate that higher amounts of alpha lead to higher costs. This increase is not linear and uniform, and the biggest change occurs in the increase from 0.8 to 0.9, which is much greater than the previous period. The downward trend of the sensitivity analysis chart of the number of distribution centers relative to cost indicates that the increase in the capacity of centers will reduce costs. The reason is that with the increase in capacity, the need to establish new centers is greatly reduced. From a managerial point of view, it is recommended that managers should always have an estimate of demand in boom and recession periods. Also using the proposed model, they can have a very good view of the future of the supply chain by choosing the desired level of risk in CVaR through changing alpha values and its weighted parameter, i.e., lambda. So, the proposed model is very flexible for managers in order to improve the supply chain.

The following are recommended for future studies:

- Considering a competitive game between supply chain members (for example, distributor and producer) in the proposed model
- Considering other objectives in the model: for example, maximizing supply chain resilience or minimizing delivery time
- Problem solving with a two-level planning approach
- Considering multi-modal transport models, such as

considering trucks, containers, or rail and air transportation.

- Use of other uncertainty approaches, for example, robust optimization approach

7. REFERENCES

1. Karampour, M. M., Hajiaghahi-Keshteli, M., Fathollahi-Fard, A. M., and Tian, G. "Metaheuristics for a bi-objective green vendor managed inventory problem in a two-echelon supply chain network." *Scientia Iranica*, (2020). (In press) <https://doi.org/10.24200/sci.2020.53420.3228>
2. Zailani, S., Iranmanesh, M., Foroughi, B., Kim, K., and Hyun, S. S. "Effects of supply chain practices, integration and closed-loop supply chain activities on cost-containment of biodiesel." *Review of Managerial Science*, (2019), 1–21. <https://doi.org/10.1007/s11846-019-00332-9>
3. Fathollahi-Fard, A. M., Ranjbar-Bourani, M., Cheikhrouhou, N., and Hajiaghahi-Keshteli, M. "Novel modifications of social engineering optimizer to solve a truck scheduling problem in a cross-docking system." *Computers and Industrial Engineering*, Vol. 137, (2019), 106103. <https://doi.org/10.1016/j.cie.2019.106103>
4. Yavari, M., and Zaker, H. "Designing a resilient-green closed loop supply chain network for perishable products by considering disruption in both supply chain and power networks." *Computers and Chemical Engineering*, Vol. 134, (2020), 106680. <https://doi.org/10.1016/j.compchemeng.2019.106680>
5. Sahebjamnia, N., Goodarzi, F., and Hajiaghahi-Keshteli, M. "Optimization of multi-period three-echelon citrus supply chain problem." *Journal of Optimization in Industrial Engineering*, Vol. 13, No. 1, (2020), 39–53. <https://doi.org/10.22094/JOIE.2017.728.1463>
6. Ghasemi, P., and Talebi Brijani, E. "An Integrated FAHP-PROMETHEE Approach For Selecting The Best Flexible Manufacturing System | Ghasemi | European Online Journal of Natural and Social Sciences." *European Online Journal of Natural and Social Sciences*, Vol. 3, No. 4, (2014), 1137–1150. Retrieved from <http://european-science.com/eojnss/article/view/815>
7. Mehranfar, N., Hajiaghahi-Keshteli, M., and Fathollahi-Fard, A. M. "A Novel Hybrid Whale Optimization Algorithm to Solve a Production-Distribution Network Problem Considering Carbon Emissions." *International Journal of Engineering, Transactions C: Aspects*, Vol. 32, No. 12, (2019), 1781–1789. <https://doi.org/10.5829/ije.2019.32.12c.11>
8. Goodarzi, F., and Hosseini-Nasab, H. "Applying a fuzzy multi-objective model for a production–distribution network design problem by using a novel self-adoptive evolutionary algorithm." *International Journal of Systems Science: Operations and Logistics*, (2019). <https://doi.org/10.1080/23302674.2019.1607621>
9. Shirazi, H., Kia, R., and Ghasemi, P. "Ranking of hospitals in the case of COVID-19 outbreak: A new integrated approach using patient satisfaction criteria." *International Journal of Healthcare Management*, (2020), 1–13. <https://doi.org/10.1080/20479700.2020.1803622>
10. Babaeinesami, A., and Ghasemi, P. "Ranking of hospitals: A new approach comparing organizational learning criteria." *International Journal of Healthcare Management*, (2020). <https://doi.org/10.1080/20479700.2020.1728923>
11. Zhen, L., Huang, L., and Wang, W. "Green and sustainable closed-loop supply chain network design under uncertainty." *Journal of Cleaner Production*, Vol. 227, (2019), 1195–1209.

<https://doi.org/10.1016/j.jclepro.2019.04.098>

12. Soleimani, H., Govindan, K., Saghafi, H., and Jafari, H. "Fuzzy multi-objective sustainable and green closed-loop supply chain network design." *Computers and Industrial Engineering*, Vol. 109, (2017), 191–203. <https://doi.org/10.1016/j.cie.2017.04.038>
13. Giri, B. C., Mondal, C., and Maiti, T. "Analysing a closed-loop supply chain with selling price, warranty period and green sensitive consumer demand under revenue sharing contract." *Journal of Cleaner Production*, Vol. 190, (2018), 822–837. <https://doi.org/10.1016/j.jclepro.2018.04.092>
14. Samuel, C. N., Venkatadri, U., Diallo, C., and Khatab, A. "Robust closed-loop supply chain design with presorting, return quality and carbon emission considerations." *Journal of Cleaner Production*, Vol. 247, (2020), 119086. <https://doi.org/10.1016/j.jclepro.2019.119086>
15. Mohammed, A., and Wang, Q. "The fuzzy multi-objective distribution planner for a green meat supply chain." *International Journal of Production Economics*, Vol. 184, (2017), 47–58. <https://doi.org/10.1016/j.ijpe.2016.11.016>
16. Aziziankohan, A., Jolai, F., Khalilzadeh, M., Soltani, R., and Tavakkoli-Moghaddam, R. "Green supply chain management using the queuing theory to handle congestion and reduce energy consumption and emissions from supply chain transportation fleet." *Journal of Industrial Engineering and Management*, Vol. 10, No. 2Special Issue, (2017), 213–236. <https://doi.org/10.3926/jiem.2170>
17. Yang, D., and Xiao, T. "Pricing and green level decisions of a green supply chain with governmental interventions under fuzzy uncertainties." *Journal of Cleaner Production*, Vol. 149, (2017), 1174–1187. <https://doi.org/10.1016/j.jclepro.2017.02.138>
18. Mirmohammadi, S. H., and Sahraeian, R. "A novel sustainable closed-loop supply chain network design by considering routing and quality of products." *International Journal of Engineering, Transactions B: Applications*, Vol. 31, No. 11, (2018), 1918–1928. <https://doi.org/10.5829/ije.2018.31.11b.16>
19. Fathollahi-Fard, A. M., Ahmadi, A., Goodarzian, F., and Cheikhrouhou, N. "A bi-objective home healthcare routing and scheduling problem considering patients' satisfaction in a fuzzy environment." *Applied Soft Computing Journal*, Vol. 93, (2020), 106385. <https://doi.org/10.1016/j.asoc.2020.106385>
20. Baryannis, G., Validi, S., Dani, S., and Antoniou, G. "Supply chain risk management and artificial intelligence: state of the art and future research directions." *International Journal of Production Research*, Vol. 57, No. 7, (2019), 2179–2202. <https://doi.org/10.1080/00207543.2018.1530476>
21. Jiang, G., Wang, Q., Wang, K., Zhang, Q., and Zhou, J. "A Novel Closed-Loop Supply Chain Network Design Considering Enterprise Profit and Service Level." *Sustainability*, Vol. 12, No. 544, (2020), 1–21. <https://doi.org/10.3390/su12020544>
22. Ghasemi, P., Khalili-Damghani, K., Hafezolkotob, A., and Raissi, S. "Uncertain multi-objective multi-commodity multi-period multi-vehicle location-allocation model for earthquake evacuation planning." *Applied Mathematics and Computation*, Vol. 350, (2019), 105–132. <https://doi.org/10.1016/j.amc.2018.12.061>
23. He, R., Xiong, Y., and Lin, Z. "Carbon emissions in a dual channel closed loop supply chain: the impact of consumer free riding behavior." *Journal of Cleaner Production*, Vol. 134, No. Part A, (2016), 384–394. <https://doi.org/10.1016/j.jclepro.2016.02.142>
24. Ghasemi, P., Khalili-Damghani, K., Hafezolkotob, A., and Raissi, S. "Stochastic optimization model for distribution and evacuation planning (A case study of Tehran earthquake)." *Socio-Economic Planning Sciences*, Vol. 71, (2020), 100745. <https://doi.org/10.1016/j.seps.2019.100745>
25. Soleimani, H., and Govindan, K. "Reverse logistics network design and planning utilizing conditional value at risk." *European Journal of Operational Research*, Vol. 237, No. 2, (2014), 487–497. <https://doi.org/10.1016/j.ejor.2014.02.030>
26. Polo, A., Peña, N., Muñoz, D., Cañón, A., and Escobar, J. W. "Robust design of a closed-loop supply chain under uncertainty conditions integrating financial criteria." *Omega (United Kingdom)*, Vol. 88, (2019), 110–132. <https://doi.org/10.1016/j.omega.2018.09.003>
27. Jeihoonian, M., Kazemi Zanjani, M., and Gendreau, M. "Closed-loop supply chain network design under uncertain quality status: Case of durable products." *International Journal of Production Economics*, Vol. 183, (2017), 470–486. <https://doi.org/10.1016/j.ijpe.2016.07.023>
28. Aras, N., Aksen, D., and Gönül Tanuğur, A. "Locating collection centers for incentive-dependent returns under a pick-up policy with capacitated vehicles." *European Journal of Operational Research*, Vol. 191, No. 3, (2008), 1223–1240. <https://doi.org/10.1016/j.ejor.2007.08.002>
29. Das, K., and Chowdhury, A. H. "Designing a reverse logistics network for optimal collection, recovery and quality-based product-mix planning." *International Journal of Production Economics*, Vol. 135, No. 1, (2012), 209–221. <https://doi.org/10.1016/j.ijpe.2011.07.010>
30. Asgari, N., Nikbakhsh, E., Hill, A., and Farahani, R. Z. "Supply chain management 1982-2015: A review." *IMA Journal of Management Mathematics*, Vol. 27, No. 3, (2016), 353–379. <https://doi.org/10.1093/imaman/dpw004>
31. Liu, X., Tian, G., Fathollahi-Fard, A. M., and Mojtahedi, M. "Evaluation of ship's green degree using a novel hybrid approach combining group fuzzy entropy and cloud technique for the order of preference by similarity to the ideal solution theory." *Clean Technologies and Environmental Policy*, Vol. 22, No. 2, (2020), 493–512. <https://doi.org/10.1007/s10098-019-01798-7>
32. Garg, K., Kannan, D., Diabat, A., and Jha, P. C. "A multi-criteria optimization approach to manage environmental issues in closed loop supply chain network design." *Journal of Cleaner Production*, Vol. 100, (2015), 297–314. <https://doi.org/10.1016/j.jclepro.2015.02.075>
33. Iqbal, M. W., Kang, Y., and Jeon, H. W. "Zero waste strategy for green supply chain management with minimization of energy consumption." *Journal of Cleaner Production*, Vol. 245, (2020), 118827. <https://doi.org/10.1016/j.jclepro.2019.118827>
34. Wang, T., and Li, Q. "Endogenetic Risk Analysis of the Replenishment Supply Chain in Large Fresh Supermarket." *World Scientific Research Journal*, Vol. 6, No. 1, (2020), 165–172. [https://doi.org/10.6911/WSRJ.202001_6\(1\).0024](https://doi.org/10.6911/WSRJ.202001_6(1).0024)
35. Safaeian, M., Fathollahi-Fard, A. M., Tian, G., Li, Z., and Ke, H. "A multi-objective supplier selection and order allocation through incremental discount in a fuzzy environment." *Journal of Intelligent and Fuzzy Systems*, Vol. 37, No. 1, (2019), 1435–1455. <https://doi.org/10.3233/JIFS-182843>
36. Wang, J., Jiang, H., and Yu, M. "Pricing decisions in a dual-channel green supply chain with product customization." *Journal of Cleaner Production*, Vol. 247, (2020), 119101. <https://doi.org/10.1016/j.jclepro.2019.119101>
37. Fathollahi-Fard, A. M., Govindan, K., Hajiaghayi-Kesheli, M., and Ahmadi, A. "A green home health care supply chain: New modified simulated annealing algorithms." *Journal of Cleaner Production*, Vol. 240, (2019), 118200. <https://doi.org/10.1016/j.jclepro.2019.118200>
38. Baptista, S., Barbosa-Póvoa, A. P., Escudero, L. F., Gomes, M. I., and Pizarro, C. "On risk management of a two-stage stochastic mixed 0–1 model for the closed-loop supply chain design problem." *European Journal of Operational Research*, Vol. 274, No. 1, (2019), 91–107. <https://doi.org/10.1016/j.ejor.2018.09.041>
39. Yun, Y., Chuluunsukh, A., and Gen, M. "Sustainable Closed-

- Loop Supply Chain Design Problem: A Hybrid Genetic Algorithm Approach." *Mathematics*, Vol. 8, No. 84, (2020), 1–19. <https://doi.org/10.3390/math8010084>
40. Rabbani, M., Hosseini-Mokhallesun, S. A. A., Ordibazar, A. H., and Farrokhi-Asl, H. "A hybrid robust possibilistic approach for a sustainable supply chain location-allocation network design." *International Journal of Systems Science: Operations and Logistics*, Vol. 7, No. 1, (2020), 60–75. <https://doi.org/10.1080/23302674.2018.1506061>
 41. Roghanian, E., and Cheraghali-pour, A. "Addressing a set of meta-heuristics to solve a multi-objective model for closed-loop citrus supply chain considering CO2 emissions." *Journal of Cleaner Production*, Vol. 239, (2019), 118081. <https://doi.org/10.1016/j.jclepro.2019.118081>
 42. Taleizadeh, A. A., Alizadeh-Basban, N., and Niaki, S. T. A. "A closed-loop supply chain considering carbon reduction, quality improvement effort, and return policy under two remanufacturing scenarios." *Journal of Cleaner Production*, Vol. 232, (2019), 1230–1250. <https://doi.org/10.1016/j.jclepro.2019.05.372>
 43. Rahimi, M., and Ghezavati, V. "Sustainable multi-period reverse logistics network design and planning under uncertainty utilizing conditional value at risk (CVaR) for recycling construction and demolition waste." *Journal of Cleaner Production*, Vol. 172, (2018), 1567–1581. <https://doi.org/10.1016/j.jclepro.2017.10.240>
 44. Khalili-Damghani, K., and Ghasemi, P. "Uncertain Centralized/Decentralized Production-Distribution Planning Problem in Multi-Product Supply Chains:Fuzzy Mathematical Optimization Approaches." *Industrial Engineering & Management Systems*, Vol. 15, No. 2, (2016), 156–172. Retrieved from <https://www.dbpia.co.kr/Journal/articleDetail?nodeId=NODE06699601>
 45. Chen, C. L., Yuan, T. W., and Lee, W. C. "Multi-criteria fuzzy optimization for locating warehouses and distribution centers in a supply chain network." *Journal of the Chinese Institute of Chemical Engineers*, Vol. 38, No. 5–6, (2007), 393–407. <https://doi.org/10.1016/j.jcice.2007.08.001>
 46. Petrovic, D., Xie, Y., Burnham, K., and Petrovic, R. "Coordinated control of distribution supply chains in the presence of fuzzy customer demand." *European Journal of Operational Research*, Vol. 185, No. 1, (2008), 146–158. <https://doi.org/10.1016/j.ejor.2006.12.020>
 47. El-Sayed, M., Afia, N., and El-Kharbotly, A. "A stochastic model for forward-reverse logistics network design under risk." *Computers and Industrial Engineering*, Vol. 58, No. 3, (2010), 423–431. <https://doi.org/10.1016/j.cie.2008.09.040>
 48. Pishvae, M. S., Farahani, R. Z., and Dullaert, W. "A memetic algorithm for bi-objective integrated forward/reverse logistics network design." *Computers and Operations Research*, Vol. 37, No. 6, (2010), 1100–1112. <https://doi.org/10.1016/j.cor.2009.09.018>
 49. Ali, S. S., Paksoy, T., Torğul, B., and Kaur, R. "Reverse logistics optimization of an industrial air conditioner manufacturing company for designing sustainable supply chain: a fuzzy hybrid multi-criteria decision-making approach." *Wireless Networks*, Vol. 26, No. 8, (2020), 5759–5782. <https://doi.org/10.1007/s11276-019-02246-6>
 50. Nezhadroshan, A. M., Fathollahi-Fard, A. M., and Hajiaghaei-Keshteli, M. "A scenario-based possibilistic-stochastic programming approach to address resilient humanitarian logistics considering travel time and resilience levels of facilities." *International Journal of Systems Science: Operations and Logistics*, (2020), 1–27. <https://doi.org/10.1080/23302674.2020.1769766>
 51. Ma, L., Liu, Y., and Liu, Y. "Distributionally robust design for bicycle-sharing closed-loop supply chain network under risk-averse criterion." *Journal of Cleaner Production*, Vol. 246, (2020), 118967. <https://doi.org/10.1016/j.jclepro.2019.118967>
 52. Sunil, B., and Indrani, P. "ICFAI Journal of Supply Chain Management." *ICFAI Journal of Supply Chain Management*, Vol. 5, No. 3, (2008), 59–68. Retrieved from <https://biblioteca.sagrado.edu/eds/detail?db=bsu&an=35272238>
 53. Zhou, Y. ju, Chen, X. hong, and Wang, Z. run. "Optimal ordering quantities for multi-products with stochastic demand: Return-CVaR model." *International Journal of Production Economics*, Vol. 112, No. 2, (2008), 782–795. <https://doi.org/10.1016/j.ijpe.2007.04.014>
 54. Rockafellar, R. T., and Uryasev, S. "Conditional value-at-risk for general loss distributions." *Journal of Banking and Finance*, Vol. 26, No. 7, (2002), 1443–1471. [https://doi.org/10.1016/S0378-4266\(02\)00271-6](https://doi.org/10.1016/S0378-4266(02)00271-6)
 55. Goh, M., and Meng, F. "A stochastic model for supply chain risk management using conditional value at risk." In *Managing Supply Chain Risk and Vulnerability: Tools and Methods for Supply Chain Decision Makers* (pp. 141–157). Springer London., 2009. https://doi.org/10.1007/978-1-84882-634-2_8
 56. Fathollahi-Fard, A. M., Hajiaghaei-Keshteli, M., and Tavakkoli-Moghaddam, R. "Red deer algorithm (RDA): a new nature-inspired meta-heuristic." *Soft Computing*, Vol. 24, No. 19, (2020), 14637–14665. <https://doi.org/10.1007/s00500-020-04812-z>
 57. Xia, W., and Wu, Z. "An effective hybrid optimization approach for multi-objective flexible job-shop scheduling problems." *Computers and Industrial Engineering*, Vol. 48, No. 2, (2005), 409–425. <https://doi.org/10.1016/j.cie.2005.01.018>
 58. Mohammed, F., Selim, S. Z., Hassan, A., and Syed, M. N. "Multi-period planning of closed-loop supply chain with carbon policies under uncertainty." *Transportation Research Part D: Transport and Environment*, Vol. 51, (2017), 146–172. <https://doi.org/10.1016/j.trd.2016.10.033>
 59. Fazli-Khalaf, M., Mirzazadeh, A., and Pishvae, M. S. "A robust fuzzy stochastic programming model for the design of a reliable green closed-loop supply chain network." *Human and Ecological Risk Assessment*, Vol. 23, No. 8, (2017), 2119–2149. <https://doi.org/10.1080/10807039.2017.1367644>
 60. Fallah-Tafti, A., Vahdatzad, M. A., and Sadegheiyeh, A. "A comprehensive mathematical model for a location-routing-inventory problem under uncertain demand: A numerical illustration in cash-in-transit sector." *International Journal of Engineering, Transactions B: Applications*, Vol. 32, No. 11, (2019), 1634–1642. <https://doi.org/10.5829/ije.2019.32.11b.15>
 61. Ghasemi, P., Khalili-Damghani, K., Hafezolkotob, A., and Raissi, S. "A decentralized supply chain planning model: a case study of hardboard industry." *International Journal of Advanced Manufacturing Technology*, Vol. 93, No. 9–12, (2017), 3813–3836. <https://doi.org/10.1007/s00170-017-0802-3>
 62. Jung, H., and Jeong, S. J. "Managing demand uncertainty through fuzzy inference in supply chain planning." *International Journal of Production Research*, Vol. 50, No. 19, (2012), 5415–5429. <https://doi.org/10.1080/00207543.2011.631606>
 63. Amindoust, A., Ahmed, S., Saghafinia, A., and Bahreinejad, A. "Sustainable supplier selection: A ranking model based on fuzzy inference system." *Applied Soft Computing Journal*, Vol. 12, No. 6, (2012), 1668–1677. <https://doi.org/10.1016/j.asoc.2012.01.023>
 64. Prasad, S., and Sounderbandian, J. "Factors influencing global supply chain efficiency: Implications for information systems." *Supply Chain Management*, Vol. 8, No. 3, (2003), 241–250. <https://doi.org/10.1108/13598540310484636>
 65. Attaran, M., and Attaran, S. "Collaborative supply chain management: The most promising practice for building efficient and sustainable supply chains." *Business Process Management*

Journal, Vol. 13, No. 3, (2007), 390–404.
<https://doi.org/10.1108/14637150710752308>

66. Abdi, A., Abdi, A., Fathollahi-Fard, A. M., and Hajiaghayi-Keshteli, M. "A set of calibrated metaheuristics to address a

closed-loop supply chain network design problem under uncertainty." *International Journal of Systems Science: Operations and Logistics*, (2019).
<https://doi.org/10.1080/23302674.2019.1610197>

Persian Abstract

چکیده

در سال‌های اخیر با توجه به پیدایش مسائلی مانند کمبود منابع طبیعی، قوانین دولتی و نگرانی‌های زیست محیطی، زنجیره تامین‌های بازگشتی و حلقه بسته در مرکز توجه محققین و تصمیم‌گیرندگان این حوزه قرار گرفته است، بنابراین در این مقاله یک مدل ریاضی چندهدفه، چند کالایی و چنددوره‌ای در زنجیره تامین حلقه بسته پایدار جهت مکانیابی مراکز توزیع، جمع‌آوری، بازیافت و دفن با در نظر گرفتن معیار ریسک ارائه شده است. از ارزش در معرض خطر شرطی بعنوان معیار اندازه‌گیری ریسک استفاده شده است. اهداف این پژوهش عبارتند از کمینه کردن هزینه‌های زنجیره، به همراه کاهش اثرات نامطلوب زیست محیطی و در نظر گرفتن مسئولیت اجتماعی به منظور پیشینه کردن فرصت‌های شغلی می‌باشد. عدم قطعیت در تقاضا و پارامترهای وابسته به تقاضا، توسط سیستم استنتاج فازی مدلسازی و مشخص می‌گردد. مدل پیشنهادی با استفاده از رویکرد الگوریتم ذرات چند هدفه حل گردیده است و نتایج با روش اسپیلون محدودیت مقایسه شده‌اند. تحلیل حساسیت بر روی پارامترهای مساله انجام شده است و کارایی روش‌های مورد مطالعه بررسی شده‌اند.



A Green Hazardous Waste Location-routing Problem Considering the Risks Associated with Transportation and Population

F. Delfani^a, A. Kazemi^{i*a}, S. M. Seyedhosseini^b, S. T. A. Niaki^c

^a Faculty of Industrial and Mechanical Engineering, Qazvin Branch, Islamic Azad University, Qazvin, Iran

^b School of Industrial Engineering, Iran University of Science and Technology, Tehran, Iran

^c Department of Industrial Engineering, Sharif University of Technology, Tehran, Iran

PAPER INFO

Paper history:

Received August 08 2019

Received in revised form 18 October 2020

Accepted 20 October 2020

Keywords:

Hazardous Waste

Location-routing Problem

Green Emissions

Stochastic Constraint

Multi-objective Optimization

ABSTRACT

The researches on environmental and sustainability are an active topic, especially in the waste management. As such, the hazardous waste optimization is an active research topic in developing countries which may be integrated with carbon emissions and green subjects. This grand challenge motivates the current research to contribute a new multi-objective optimization model to address the green hazardous waste location-routing problem. The proposed multi-objective optimization model establishes four objectives simultaneously for the first time. In addition to the total cost and the greenhouse gas emissions of the transportation systems as the two main objectives, another objective function aims to minimize the risk of transportation of the hazardous waste alongside the waste residue associated with the people's exposure around transportation paths. Furthermore, the total risk linked with the population in a certain radius around the treatment and disposal centers is minimized. As the proposed model is complex with conflicting objectives, several multi-objective decision making (MODM) tools are employed and compared with each other based on different test problems associated with an industrial example. Based on the solution quality and the computational time, the technique for the order of preference by similarity to the ideal solution (TOPSIS) is selected as the strongest technique to assess the performances of all five MODM methodologies.

doi: 10.5829/ije.2020.33.11b.18

1. INTRODUCTION

Industrial hazardous waste and disposal are an active research topic in developing countries. The logistics of hazardous waste management is naturally complex regarding the transport network; increasing sensitivity to the costs of environmental impact; the practical limitations that often govern the location of processing facilities [1], the source of waste streams, recycling options, and the complexities of transportation management [2]. Regarding the challenge of transportation management [3], the largest source of pollution and environmental concerns in the logistics system is a significant optimization problem within itself.

As known, hazmat, i.e., the industrial hazardous substances resulted from many manufacturing processes,

is a dangerous and toxic posing risk to people most notably in developing countries [4]. Thus, the management of hazardous material substances including a series of actions such as systematically collecting, transporting, treating, recycling and disposing of hazardous substances, is very operational for governments and strategic for environmentalists [5]. The logistic activities of the hazmat motivated several studies to develop efficient optimization models and algorithms to be computationally manageable [6-8]. Although many studies have recently contributed to this research area, green hazardous waste optimization is still an open issue and scarce.

The current study has been motivated by the main needs and benefits of having an efficient green hazardous waste location-routing system that minimizes four

*Corresponding Author Email: abkaazemi@qiau.ac.ir (A. Kazemi)

objectives including the total cost, the total carbon emissions, as well as the risk associated with the transportation and the population in a certain radius around treatment and disposal centers. This study also considers a stochastic budget constraint estimated by a normal distribution to report more practical results for the first time. In addition, dealing with four conflicting objectives provides further practical results for the decision-makers of the hazardous waste management. Besides, based on the sustainable development paradigm which is of particular concern in developing countries, it is essential for managers to consider the risks of transportation and population to improve the reliability of the system as social factors in addition to the economic and environmental impacts of hazardous waste management. Hence, the present study can add some values to the literature.

As one of well-known studies in the area waste location-routing problem, with the supposition of the site and the flow of the hazardous waste between facilities as decision variables, a mathematical model was introduced by Cappanera et al. [9] to address the problems associated with the location and routing of the hazardous materials. In order to decompose the proposed model into location and routing sub-problems, they employed the Lagrangian relaxation approach and recommended a branch-and-bound solution method to reduce the gap existing among the lower and upper bounds by using an adaptive technique. Similarly, a multi-objective integer model was proposed by Nema and Gupta [10] for this problem. They took into consideration the location of the treatment centers as well as the disposal centers and the transportation routes whereby the hazardous wastes and the waste residues are transported from the origin nodes to the treatment and the disposal facilities as decision variables. This model was made by the purpose of reducing the overall transportation costs as well as reducing the risks associated with the transportation vehicles and facilities. Later in 2005, another multi-objective optimization approach for the hazardous waste location-routing problem was developed by Zhang et al. [11]. Their model aimed to reduce the total costs and the possible risks. They utilized a multi-objective optimization approach to help decision-makers in evaluating the location-routing decisions related to hazardous wastes. Furthermore, a mathematical model was proposed by Ahluwalia and Nema [12] to design an integrated computer waste management system by introducing a decision-support tool to select the optimal facility configurations related to the computer waste management. This included storing, treating, recycling, disposing and allocating the waste to the facilities. As an integer linear programming, their proposed model aimed to reduce environmental risks and the total costs. They used the Monte Carlo simulation technique to address the uncertainty of the amount of waste.

In a survey, Nagy and Salhi [13] conducted comprehensive research elaborating on the location-routing models and their exact and heuristic solution methods. A mathematical model was also developed by Emek and Kara [14] for the problems of the hazmat by considering variables such as disposal mode, the site of the disposal plants, as well as the routes whereby the hazmat was transported. Their research contributed to the body of knowledge by introducing a mathematical model that could select the disposal method to control air pollution and meet international standards. This was accomplished by using the Gaussian Plume equation to measure air pollution at the population centers.

As one of the earliest studies in the area of hazardous waste routing optimization with time windows, Berman et al. [15] proposed an optimization model that aimed at minimizing the network's overall costs. They solved the problem using a branch-and-price algorithm. In order to evade exposing a given population with hazmat or to impose a security measure, sometimes, the transportation company of the hazardous materials aims to find a set of routes with almost equal performance such that it will be able to switch among various routes. For this problem, Dadkar et al. [16] used a K-shortest path algorithm in which the performance of the highway facility was stochastic and could change over time considering each objective function separately. To obtain a proper trade-off between the geographic diversity and the performance, they offered a Mixed Integer Linear Programming (MILP) to determine a subset of paths.

As indicated recently in the literature, there is still a great deal of interest in developing optimization models and algorithms to address hazardous waste optimization problems. Since there are many reviews in the area of logistics of industrial hazardous waste [1, 4, 17, 18]; here, only recent advances and relevant works in this research area are collected and exposed as follows.

Recently, Xie et al. [19] proposed a multi-modal location and routing problem for the transportation of hazmat materials. They elaborated on a case study in the north of China to address a model that considers multi-commodity flow. Most notably, they only considered the total cost as the objective function to be minimized. Alongside dealing with greater complexity in terms of the problem description, the limitations of considering just a single optimization objective function have also been manifested. Vidović et al. [20] proposed an extended MILP model to optimize the economic benefits in a two-echelon logistics network that comprised the collection points, transfer stations, and end-users. Harijani et al. [21] applied a bi-objective MILP model to balance economic profit with qualitative, non-economic cost criteria. Another bi-objective MILP model was proposed by Asefi and Lim [22] to optimize transportation costs against time factors. Practical applications of bi-objective optimization have also been proposed to select the

optimal locations and allocations of waste facilities in Tehran, Iran [23]. Tehran was also the case study location for the research by Edalatpour et al. [17] which optimized an overall economic and environmental cost against various aspects of a comprehensive waste management network, including recycling and remanufacturing. At last but not least, another case study in Tehran was examined by Rabbani et al. [1] who proposed a location-routing problem for the case of hazardous materials. Their mathematical model dealt with different types of incompatible waste and took into account the aspects related to adaptation/compatibility with the treatment technologies. Another contribution of their work was related to the use of a heterogeneous transportation system to collect wastes compatible with their loads. In another study, Mahmoudsoltani et al. [4] tackled another realistic and practical issue in the field of management of hazardous materials. They considered several types of transportation routes such as roads or pipelines in which two objective functions including the total cost and risk were considered to be minimized. To solve the problem, they utilized three well-known multi-objective evolutionary algorithms. Moreover, Ebrahimi [24] proposed a multi-objective optimization model considering the sustainability aspects based on the triple line to assess the tire supply chain with discount supposition. An epsilon constraint method was applied in their work to solve a real case of the tire industry in Iran. Mohammadi et al. [18] provided a mixed-integer nonlinear programming model for the locating-routing problem of hazardous wastes. The components of their proposed logistic network were the manufacturers of hazardous waste and the disposal centers. Their model considered the risk of facility failure in addition to the consideration of the accidents due to the transport of hazardous wastes. To handle these uncertainties, they applied a chance-constrained and possibilistic programming approach. They employed a metaheuristic algorithm to find a near-optimal solution to their NP-hard problem. Their model was validated by a case study in Iran. However, despite Mahmoudsoltani et al., [4] and Rabbani et al. [1], this model did not consider the possibility of transport for the hazardous waste by pipelines and the transportation time and the reliability of the routes being selected. They did not assume different types of vehicles with different capacities either.

More recently, Hu et al. [25] proposed a multi-objective optimization model to seek out the optimal routes for hazardous wastes with traffic restrictions. This paper assumed multiple paths between every possible origin-destination pair. Another contribution was to develop an adaptive weight genetic algorithm. In another recent paper published by Rabbani et al. [26], a stochastic multi-period industrial hazardous waste location-routing-inventory problem considering the risk of transportation was proposed. To solve their NP-hard problem, a sim-

heuristic method by combining a non-dominated sorting genetic algorithm and Monte Carlo simulation was used. At last but not least, Pouriani et al. [27] developed a bi-level and robust optimization method to model the municipal solid waste management. Based on their proposed model, the establishment costs of solid waste collection centers were assumed at the lower level and the allocation of the waste to the various centers at the upper level. They validated their model in a case study in Babol, Iran. At last but not least, Delfani et al. [28] proposed a robust-possibilistic programming for a waste location-routing problem with the risk of transportation.

In order to have a conclusion, the aforementioned papers are classified based on the objective functions and the constraints utilized. This classification is given in the Electronic Supplementary Materials F1. The titles of the columns in this table are related to the type of the model, the objective functions, and the characteristics of the model. From the previous studies, there are six common objective functions including the total cost, carbon emissions, customer satisfaction, risk of transportation, risk of population, and the time of loading. The model's characteristics are related to the decisions obtained by the model based on the location, allocation, routing and inventory decisions. Some other suppositions are the use of uncertainty modeling such as stochastic or robust optimization, budget constraint, traffic restriction, technology selection for recycling, GIS model, multi-commodity and time windows. Based on these criteria, the following observations are identified:

- Fourteen studies considered multi-objective decision-making models.
- In addition to the total cost, the risk of transportation is well-studied as the second objective function in the literature.
- The location, allocation and routing decisions are considered in the majority of studies.
- Uncertainty modelling approaches are well-studied in many old and recent works.
- Carbon emissions are considered in three papers in addition to the current study.
- There is no study to consider the risk of transportation and population simultaneously.
- Only the present study considers the total cost, the risk of transportation and population in addition to the carbon emissions simultaneously.
- Inventory decisions, budget constraints, and traffic restrictions are still scarce in the literature.

Generally speaking, having increasing concerns about global warming, international rules urge the countries to minimize their total carbon emissions. Therefore, developing a green hazardous waste location-routing model seems worthy of investigation. To this end, this study establishes a multi-objective optimization model for the hazardous waste location-routing problem considering greenhouse gas emitted by the transportation

system as well as the risks associated with transportation and population. Briefly, the main highlights of this research article can be listed as follows:

- A new multi-objective optimization model for a green hazardous waste location-routing problem is developed.
- Four objectives based on the total cost, the carbon emissions, the risk associated with the transportation and population are contributed simultaneously.
- A stochastic budget constraint is applied to the proposed problem.
- Five well-established MODM techniques are employed to solve the model
- The MODM techniques are ranked using the TOPSIS method.

The structure of the rest of this paper is as follows. In section 2, the problem is explicitly defined and the mathematical formulation of the problem is given. Section 3 introduces some solution approaches, where some comparison measures are defined. Computational results are provided in section 4 in which the TOPSIS method is used to rank the solution approaches. Section 5 contains the results of some sensitivity analyses to determine the impacts of varying the main parameters of the model on the values of the objective functions. Finally, conclusions alongside some recommendations for future research are given in section 6.

2. PROBLEM DESCRIPTION AND MATHEMATICAL FORMULATION

The flow of the hazardous wastes in the network starts from their origin (generation) nodes. Then, making use of different transportation modes, the non-recyclable hazmat is sent to the treatment facilities with well-suited machinery whereas the recyclable hazardous wastes are transported to the recycling facilities. The treatment facilities send the recyclable waste residues to the recycling facilities; on the other hand, the non-recyclable ones are sent to the disposal facilities. Besides, the waste residues of the recycling facilities are sent to the disposal centers. An overview of the hazmat management network is exhibited in Figure 1.



Figure 1. An overview of the hazmat management network

As discussed earlier, this study follows a sustainable development paradigm for developing countries. Sustainability seeks to optimize the economic, environmental, and social impacts simultaneously. These goals conflict with each other in the majority of cases. As a result, a solution obtained by optimizing one objective does not cover all sustainability factors. Hence, multi-objective decision-making is needed. This study minimizes the total cost as the economic factor and carbon emissions as environmental impacts. To cover the social objectives, the current work focuses on the risks of transportation and population as two conflicting objectives.

Currently, up to our knowledge, there is no similar model to solve the location, routing, and transportation problems in a hazardous waste management network that simultaneously considers the greenhouse gas emissions in addition to the risks associated with transportation and population. As such, a multi-objective mathematical model is aimed for the green hazardous waste location-routing problem at hand to answer the following questions:

- ✓ Which technology could be established in which treatment centre?
- ✓ Which vehicle of a type and capacity could be used to route hazardous waste to treatment centres?
- ✓ Where to locate the disposal facilities?
- ✓ How to route waste residues to disposal facilities?
- ✓ Where to locate recycling facilities?
- ✓ Which vehicle type and capacity should be used to transport the produced hazardous waste from the generation nodes and the waste residues to the recycling centres?
- ✓ How many vehicles of different types are required in each hazardous waste generation node to transport hazardous waste to treatment centres?
- ✓ How many vehicles of different types are required in each hazardous waste generation node to transport hazardous waste to recycling centres?
- ✓ How many vehicles of different types are required in each treatment centre to transport hazardous waste to recycling centres?

The notations are given in Electronic Supplementary Materials F2. The developed mathematical model of the problem that simultaneously minimizes four objective functions Z1, Z2, Z3 and Z4 alongside proper constraints is presented as follows:

$$\begin{aligned}
 \text{Min } Z1 = & \sum_w \sum_g \sum_t \sum_v c_{grv} x_{wgrv} \\
 & + \sum_t \sum_d c_{ztd} z_{td} \\
 & + \sum_h \sum_d cv_{hd} v_{hd} \\
 & + \sum_g \sum_h \sum_v cr_{ghv} l_{ghv} \\
 & + \sum_t \sum_h \sum_v crr_{thv} k_{thv} \\
 & + \sum_q \sum_t fc_{q,t} f_{qt} \\
 & + \sum_d fd_d dz_d \\
 & + \sum_h fh_h bh_h
 \end{aligned} \tag{1}$$

$$Min Z2 = \sum_w \sum_g \sum_t \sum_v popgt_{gr} x_{wgrv} + \sum_t \sum_d popd_{td} z_{td} \quad (2)$$

$$n_{wgrv} \geq \frac{x_{wgrv}}{Cap_v} \quad \forall w, g, t, v \quad (20)$$

$$Min Z3 = \sum_w \sum_q \sum_t popa_{qt} y_{wqt} + \sum_d popb_d dis_d \quad (3)$$

$$n_{ghv} \geq \frac{l_{ghv}}{Cap_v} \quad \forall g, h, v \quad (21)$$

$$Min Z4 = \sum_w \sum_g \sum_t \sum_v n_{wgrv} dgt_{gt} cc_v + \sum_g \sum_h \sum_v n_{ghv} dhv_{gh} cc_v + \sum_t \sum_h \sum_v n_{thv} dth_{th} cc_v \quad (4)$$

$$n_{thv} \geq \frac{k_{thv}}{Cap_v} \quad \forall t, h, v \quad (22)$$

$$P \left\{ \sum_w \sum_g \sum_t \sum_v n_{wgrv} Cost_{gr} + \sum_g \sum_h \sum_v n_{ghv} Cost_{gh} + \sum_t \sum_h \sum_v n_{thv} Cost_{th} \leq Budget \right\} \geq \psi \quad (23)$$

s.t.

$$gen_{wg} = \alpha_{wg} gen_{wg} + \sum_t \sum_v x_{wgrv} \quad \forall g, w \quad (5)$$

$$x_{wgrv} \geq 0 \quad \forall w, g, t, v \quad (24)$$

$$\sum_w \alpha_{wg} gen_{wg} = \sum_h \sum_v l_{ghv} \quad \forall g \quad (6)$$

$$l_{ghv} \geq 0 \quad \forall g, h, v \quad (25)$$

$$\sum_g \sum_v x_{wgrv} = \sum_q y_{wqt} \quad \forall w, t \quad (7)$$

$$k_{thv} \geq 0 \quad \forall t, h, v \quad (26)$$

$$\sum_w \sum_q y_{wqt} (1 - r_{wq})(1 - \beta_{wq}) = \sum_d z_{td} \quad \forall t \quad (8)$$

$$y_{wqt} \geq 0 \quad \forall w, q, t \quad (27)$$

$$\sum_w \sum_q y_{wqt} (1 - r_{wq})(\beta_{wq}) = \sum_h \sum_v k_{thv} \quad \forall t \quad (9)$$

$$z_{td} \geq 0 \quad \forall t, d \quad (28)$$

$$\sum_t \sum_v k_{thv} + \sum_g \sum_v l_{ghv} = hr_h \quad \forall h \quad (10)$$

$$v_{hd} \geq 0 \quad \forall h, d \quad (29)$$

$$hr_h (1 - \gamma_h) = \sum_d v_{hd} \quad \forall h \quad (11)$$

$$dis_d \geq 0 \quad \forall d \quad (30)$$

$$\sum_h v_{hd} + \sum_t z_{td} = dis_d \quad \forall d \quad (12)$$

$$hr_h \geq 0 \quad \forall h \quad (31)$$

$$\sum_w y_{wqt} \leq tc_{qt} f_{qt} \quad \forall q, t \quad (13)$$

$$f_{qt} \in \{0, 1\} \quad \forall q, t \quad (32)$$

$$\sum_w y_{wqt} \geq tcm_{qt} f_{qt} \quad \forall q, t \quad (14)$$

$$b_h \in \{0, 1\} \quad \forall h \quad (33)$$

$$y_{wqt} \leq tc_{qt} Com_{wq} \quad \forall w, q, t \quad (15)$$

$$dz_d \in \{0, 1\} \quad \forall d \quad (34)$$

$$dis_d \leq dc_d dz_d \quad \forall d \quad (16)$$

$$n_{wgrv} \geq 0, \text{ int} \quad \forall w, g, t, v \quad (35)$$

$$dis_d \geq dcm_d dz_d \quad \forall d \quad (17)$$

$$n_{ghv} \geq 0, \text{ int} \quad \forall g, h, v \quad (36)$$

$$hr_h \leq rc_h b_h \quad \forall h \quad (18)$$

$$n_{thv} \geq 0, \text{ int} \quad \forall t, h, v \quad (37)$$

$$hr_h \geq rcm_h b_h \quad \forall h \quad (19)$$

As mentioned earlier, the first objective function Z1 is established to minimize the overall costs including the total transportation expenditures and the fixed establishment costs as imposed on the treatment, disposal, as well as recycling centers. The second objective function Z2 is meant to minimize the transportation risk of hazardous waste as well as waste residues associated with the people's exposure around transportation paths. The third objective function Z3 is

aimed to minimize the total risk related to the population living in a certain distance around treatment and disposal centers. Finally, the fourth objective function Z4 is defined to lessen the total carbon emission of the transportation system. Besides, Constraints (5-7) balance the flow of the hazardous waste from the generation nodes to the treatment and recycling facilities and waste residue from the treatment facilities to the recycling centers. Constraints (8-9) take into account the recycling proportion of the hazardous waste treated by treatment technologies and recycled hazardous waste proportion at the recycling centers. Constraint (10) ensures that the total amount of the waste recycled at each recycling center is equal to the flow arriving from the treatment facilities and the generation nodes to that recycling center. Constraint (11) determines the quantity of the waste residue sent from each recycling center to each disposal center. Constraints (12) guarantee that the sum of the waste sent to each disposal center is equal to the incoming flow from treatment centers and recycling nodes. Meanwhile, Constraints (13-19) present the capacity constraints of the treatment, the recycling, and the disposal nodes and the minimum required quantity of the hazardous waste and waste residue to establish or open the treatment, recycling and disposal facilities. Constraints (20-22) determine the number of each type of transportation vehicle in each center while considering the capacity of each type of vehicle. Constraint (23) presents the budget constraint which is assumed to limit the total fixed cost of the transportation system. As it is assumed in this research that the budget follows a normal distribution [25]. Constraint (23) can be written as follows:

$$\begin{aligned} & \sum_w \sum_g \sum_t \sum_v n_{wgrv} Cost_v \\ & + \sum_g \sum_h \sum_v n_{ghv} Cost_v + \sum_t \sum_h \sum_v n_{thv} Cost_v \\ & + Z_{\psi} \sigma_{Budget} \leq \mu_{Budget} \end{aligned} \tag{38}$$

3. SOLUTION METHODS

An ideal solution for the recommended multi-objective optimization model shown in expressions (1-37) is capable of simultaneously minimizing all the objective functions; nonetheless, as these functions are typically in conflict with each other in most of the cases, an ideal solution cannot be determined [28-30]. In these cases, the decision-maker tries to find solutions that make good trade-offs among the objective functions. Such solutions are known as Pareto or efficient solutions.

There are two general methodologies to obtain efficient solutions of a multi-objective optimization problem, namely the multi-objective decision making (MODM) and the multi-objective optimization methods

[29]. The first category of the solution methods aims to optimize the problem based on different approaches including minimization of the weighted deviation of the objective functions from the goals (the decision-maker specifies the best objective functions value) [30, 31]. In this method, the multi-objective optimization problem is changed to a single-objective optimization problem using some criteria. The second class of the solution methods provides numerous Pareto solutions to enable the decision-makers to choose a preferred one. As choosing a preferred solution among a certain set of Pareto solutions is cumbersome in many cases, in this research five MODM methods [30-32] have been selected to optimize the proposed multi-objective optimization problem. While in this paper an individual optimization method is first used to solve four single-objective optimization problems separately with the objective function values $Z_i^*; i=1,2,3,4$ representing their ideal solutions, these MODM methods are described as follows.

Due to page limitation, the details of the Lap-metric, goal attainment method (GA), Max-Min method, the goal programming method (GP) and the weighted sum method (WSM) are given in Electronic Supplementary Materials F3. The performances of the aforementioned five MODM methods are assessed in this paper in terms of the four averages they obtain for the four objective functions of the problem along with their required computational time (CPU-time) in seconds when they are used to solve some randomly-generated problems using the CPLEX solver provided in the GAMS software. Note that all experiments have been done on an INTEL Core 2 CPU with a 2.4 GHz processor and 2 GB of RAM.

4. COMPUTATIONAL RESULTS

Here, various test problems with diverse sizes are generated randomly. Table 1 tabulates the main parameters of the problems alongside the probability distributions used to generate random numbers. Note that the range of these parameters is taken from some case studies in Tehran as provided in the literature [1, 17, 23].

The generated problems are classified based on their sizes in terms of the indices (**g-t-w-d-h-q-v**) in Table 2. Besides, for every individual problem of small, medium and large sizes, three randomly-generated test problems are solved utilizing the aforementioned five MODM methods. As observed in Table 2, the average of each objective function value alongside the average CPU-time of each MODM method in solving these three randomly generated test problems in each size are reported. In addition, Figures 2-6 present a schematic view of the average values of the four objective functions as well as the CPU-time required by the five MODM methods in solving various test problems with different sizes.

The results in Table 3, as well as Figures 2-6, show that each solution method performs differently in terms of the five performance measures. That is why the TOPSIS method is utilized in the next section to choose an ideal solution algorithm.

TABLE 1. The main parameters of the problems

Parameters	Distribution	Parameters	Distribution
C_{grv}	~ Uniform (100,300)	β_{wq}	~ Uniform (0.2,0.7)
CZ_{id}	~ Uniform (200,500)	γ_h	~ Uniform (0.2,0.3)
Cv_{hd}	~ Uniform (50,200)	tc_{qt}	~ Uniform (1000,10000)
Cr_{ghv}	~ Uniform (100,500)	tcm_{qt}	~ Uniform (20,100)
Cr_{thv}	~ Uniform (50,500)	Com_{wq}	~ Uniform (0,1)

fd_d	~ Uniform (10000,30000)	dc_d	~ Uniform (1000,10000)
fh_h	~ Uniform (20000,40000)	dcm_d	~ Uniform (20,100)
$popgt_{gt}$	~ Uniform (100,300)	rc_h	~ Uniform (1000,10000)
$poptd_{id}$	~ Uniform (100,300)	rcm_h	~ Uniform (20,100)
$popa_{qt}$	~ Uniform (100,300)	Cap_v	~ Uniform (20,50)
$popb_d$	~ Uniform (100,300)	$Cost_v$	~ Uniform (100,500)
dgt_{gt}	~ Uniform (50,200)	Budget	~Normal (15000,2000)
CC_v	~ Uniform (50,100)	α_{wg}	~ Uniform (0.2,0.7)
dhv_{gh}	~ Uniform (50,200)	r_{wq}	~ Uniform (0.2,0.5)
gen_{wg}	~Uniform (100,500)		

TABLE 2. Results of solving various test problems

Problem Size ($g-t-w-d-h-q-v$)	Method	Average Z_1	Average Z_2	Average Z_3	Average Z_4	Average CPU-Time
5-5-3-5-5-3-2	LP-Metric	2673792.4	1493328.4	1484020.3	1304265.8	0.138
	GA	4520147.4	1927929.4	3855707.2	1090713.5	0.127
	Max-Min	4294688.5	2545882.8	2545882.8	3113495.1	0.112
	GP	3006386.2	1536061.1	1502934.9	1112638.2	0.139
	WSM	2895391.7	1720062.7	1490646.9	1084632.2	0.231
7-5-4-5-6-3-3	LP-Metric	3079834.1	1200036.5	1863539.3	1049942.6	0.250
	GA	4510677.3	2350515.4	3582271.6	5106643.2	0.128
	Max-Min	4181865.6	2776617.0	3036346.6	5028571.0	0.115
	GP	3233271.9	1163624.2	1821913.1	828606.4	0.212
	WSM	3149844.6	1224772.1	1819318.1	825386.2	0.137
10-7-4-7-8-5-3	LP-Metric	4755457.3	2814150.9	3510891.4	2372599.5	0.182
	GA	7066914.4	5209634.4	5209634.4	5287528.9	0.245
	Max-Min	8444197.8	5201881.0	5967626.7	7215629.0	0.290
	GP	4679416.3	2666911.5	3662147.6	3759724.7	0.250
	WSM	4734098.6	2789542.5	3498010.8	2367611.6	0.144
15-7-5-9-10-7-5	LP-Metric	8039154.6	4620117.0	4726292.5	2736342.5	0.366
	GA	12038899.2	8669810.7	8669810.7	9058031.2	0.355
	Max-Min	13704599.5	8642904.6	8642904.6	13079368.9	0.462
	GP	6853345.7	3805444.6	4824182.1	5388340.3	0.362
	WSM	7955229.1	4160111.4	4626702.7	2808197.6	0.475
20-8-5-10-10-10-5	LP-Metric	10318085.9	5760664.5	7166290.8	4428706.9	0.355
	GA	21618144.5	9862342.6	19724533.6	179219761.7	0.710
	Max-Min	18574876.9	14029805.3	14029805.3	20206683.4	0.494

	GP	10104969.2	5740334.0	6816704.1	6334490.5	1.500
	WSM	12426432.7	6482507.9	6976094.6	3252852.8	0.360
	LP-Metric	17445805.3	10243985.7	12901088.8	10005779.0	83.224
	GA	40148141.9	17057454.0	32696605.2	250919945.7	20.083
30-10-7-10-10-10-5	Max-Min	32611138.3	24407695.5	24407695.5	34621963.8	1.527
	GP	21306976.5	11173706.2	13076542.7	6949640.7	7.362
	WSM	20563552.7	12826761.5	12903291.1	6662785.9	79.152
	LP-Metric	33221311.5	18853507.7	26124301.1	13938957.4	6.412
	GA	107019894.3	34614866.6	69229581.6	173206953.7	88.327
40-15-10-15-15-10-10	Max-Min	78844422.2	50245262.6	51897268.8	58495892.6	37.030
	GP	36504031.0	19841243.0	26164440.5	11450607.3	29.490
	WSM	36251328.4	22087066.6	25887735.1	10995666.7	5.819
	LP-Metric	75186465.4	35187220.7	55151734.7	41337166.2	1384.650
	GA	174753873.7	102331023.6	110323366.4	949672115.8	7233.314
50-25-15-20-25-10-15	Max-Min	169836264.1	98540049.2	108687709.2	148843120.0	1100.457
	GP	70559920.7	34393191.6	52218221.1	323809940.1	821.461
	WSM	74837305.5	37235454.0	52278461.4	40406202.4	261.762

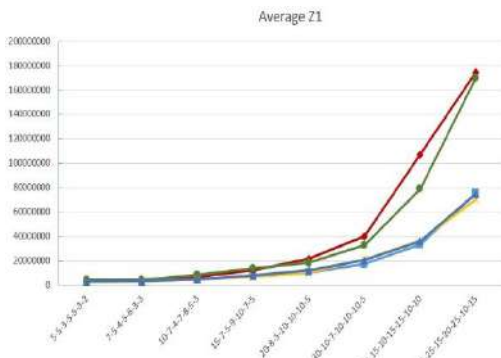


Figure 2. The average values of the first objective function

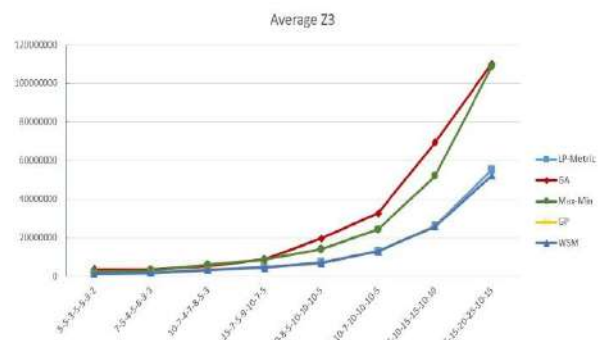


Figure 4. The average values of the third objective function

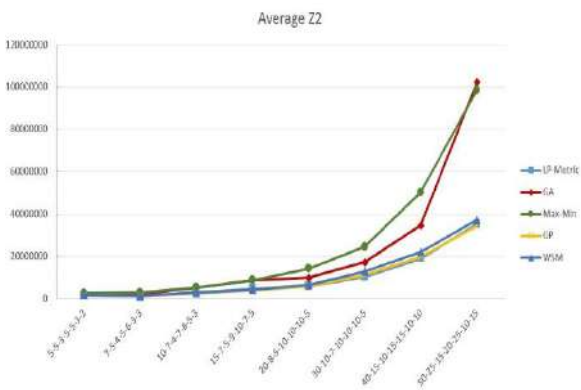


Figure 3. The average values of the second objective function

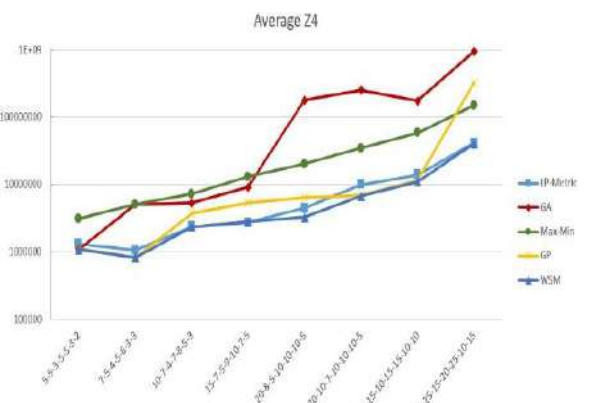


Figure 5. The average values of the fourth objective function

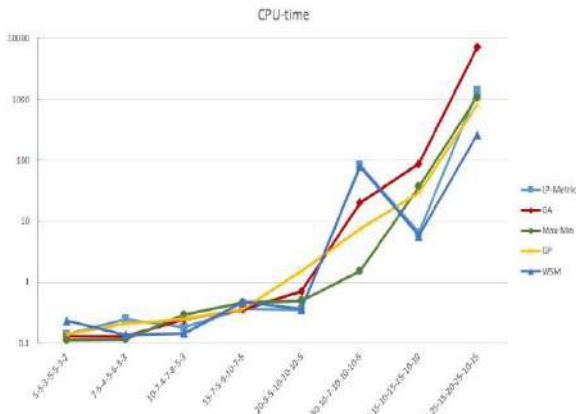


Figure 6. The average of the CPU Time

4. 1. TOPSIS Method

The TOPSIS has been introduced as a method to analyze multi-criterion decision making (MCDM) problems [31, 32]. Its main aim is to determine a substitute having the shortest (longliest) distance from the positive (negative) ideal solution. This study uses the TOPSIS method to provide a comparison between the performances of five multi-objective techniques and to rank them.

The first step involved in the TOPSIS method is to construct a decision matrix based on the MCDM methods (the aforementioned five solution methods) in the rows and the criteria (the aforementioned five performance measures) in the columns as shown in Table 3. Then, the other main steps shown in Figure 7 are taken in order to rank the methods in terms of all criteria simultaneously.

TABLE 3. The decision matrix

Method	Average Z ₁	Average Z ₂	Average Z ₃	Average Z ₄	Average CPU-Time
LP-Metric	19339988.3	10021626.4	14116019.9	9646719.99	184.447
GA	46459586.6	22752947.1	31661438.8	196695212	917.911
Max-Min	41311506.6	25798762.3	27401904.9	36325590.5	142.560
GP	19531039.7	10040064.5	13760885.8	44954248.5	107.597
WSM	20351647.9	11065784.8	13685032.6	8550416.93	43.510

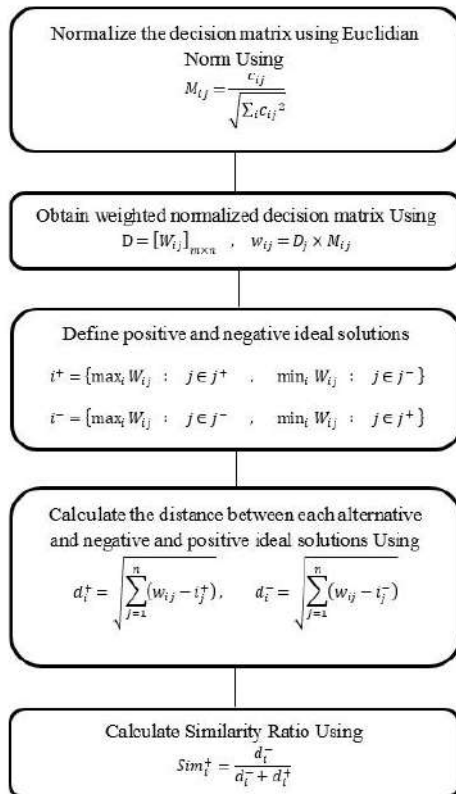


Figure 7. The main steps involved in the TOPSIS method [31]

In this regard, Table 4 summarizes the outcome of using the TOPSIS method to rank the solution methods.

As an MODM method with the largest similarity ratio is preferred by the TOPSIS approach, the results in Table 5 indicate that the LP-Metric with the similarity ratio of 0.5968 is the best solution method to solve the proposed MIP model of the problem at hand. Then, the GA, Max-Min, GP, and WSM are respectively the strongest methods.

5. SENSITIVITY ANALYSES

To investigate the impacts of the variations of the main parameters including *gen_{wg}* (produced hazardous waste at generation nodes), *tcm_{qt}* (Minimum required hazardous waste to open a treatment technology at a treatment center), Budget (total available budget), and *a_{wg}*

TABLE 4. The outcome of using the TOPSIS method

	Ranking	Similarity Ratio
LP-Metric	1	0.5968
GA	4	0.4532
Max-Min	5	0.4407
GP	3	0.5350
WSM	2	0.5501

(recycling hazardous waste proportion of a hazardous waste generated at a generation node) involved in the proposed model on the values of the four objective functions, some sensitivity analyses are carried out in this section. The variations are defined on the parameters at -50, -25, +25 and +50%. Table 5 tabularizes the results of these sensitivity analyses.

The results in Table 5 indicate that a raise to gen_{wg} significantly increases the values of all objective

functions. In addition, a raise in a_{wg} reduces such values, except the fourth objective function at +25%. Therefore, increasing a_{wg} in real-world situations can significantly reduce the risk and the total costs of the hazardous waste management chain. Figures 8-11 present the results of the sensitivity analysis graphically.

Based on these results, a comprehensive discussion is provided in Electronic Supplementary Materials F4.

TABLE 5. The results of some sensitivity analyses

Parameter	Change (%)	Z ₁	Z ₂	Z ₃	Z ₄
gen_{wg}	-0.50	3188728.083	1577780.467	2134800.210	811187.831
	-0.25	4679161.857	2365633.986	3202200.315	1159575.453
	+0.25	7328448.686	3942723.310	5337000.524	1810316.231
	+0.50	8620702.546	4731267.972	6404959.368	2137879.202
tcm_{qt}	-0.50	6036194.825	3154178.648	4269600.420	1470499.116
	-0.25	6036194.825	3154178.648	4269600.420	1470499.116
	+0.25	6047022.743	3154178.648	4269600.420	1470499.116
	+0.50	6223474.230	3154178.648	4269600.420	1490667.691
Budget	-0.50	6374325.825	3155835.203	4269600.420	1665141.275
	-0.25	6374325.825	3155835.203	4269600.420	1665141.275
	+0.25	5837475.464	3154178.648	4269600.420	1470499.116
α_{wg}	+0.50	6025591.583	3154178.648	4269600.420	1470499.116
	-0.50	6019803.386	4174292.853	4649144.417	1479600.475
	-0.25	5931821.639	3575031.875	4459372.418	1438653.828
	+0.25	5954363.759	2733518.653	4079828.421	1594639.432
	+0.50	5864064.226	2312582.902	3890056.422	1476272.281

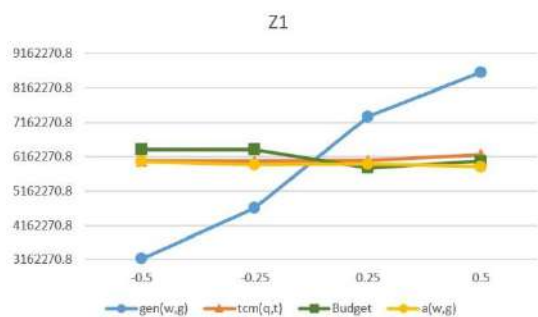


Figure 8. Variations of the first objective function value

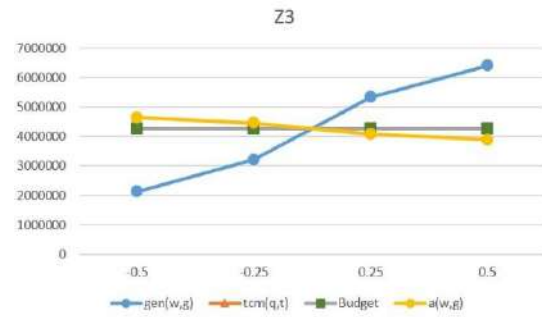


Figure 10. Variations of the third objective function value

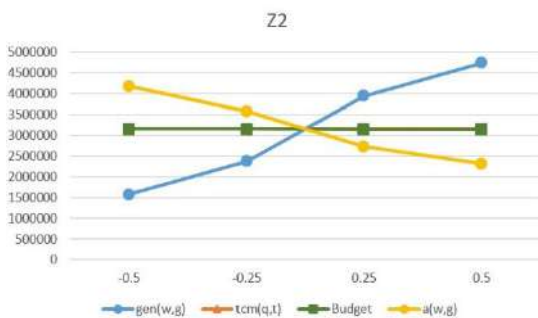


Figure 9. Variations of the second objective function value

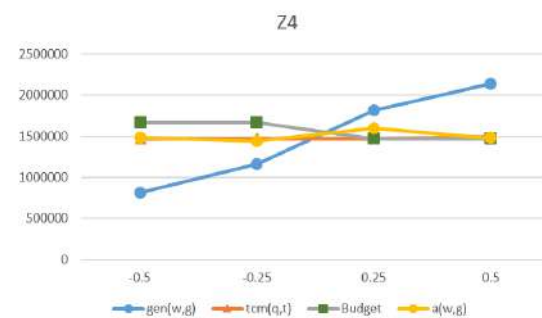


Figure 11. Variations of the fourth objective function value

6. CONCLUSION

In this research article, a multi-objective optimization model was introduced for a green hazardous waste location-routing problem. Four conflicting objective functions were taken into account to minimize the total costs, the risk of transportation of the hazmat and the waste residues associated with the residents' exposure around the transportation routes, the total risk related to the population in a certain radius around the treatment facilities and the disposal facilities along with the total carbon emission of the transportation system. Five MODM methods were utilized to solve the multi-objective optimization problem. Besides, various randomly generated test problems of different sizes were solved, based on which the performances of the solution methods were assessed in terms of four solution quality measures as well as their computational times. As the methods performed differently, the TOPSIS method was used to determine the superior MODM method considering equal weights for each comparison measure. Lastly, some sensitivity analyses were conducted to determine the most essential parameters affecting the values of the objective functions. The results confirmed that the amount of hazardous waste produced at generation nodes plays the most significant role in the proposed problem and the considered objective functions.

This study provides several new avenues for future studies. Using inventory decisions and policies is another topic that can increase the problem complexity. With regards to the formulation of the proposed problem, developing a robust optimization model would be of great importance as well. Regarding the solution algorithm, this study applied five well-established MODM techniques from the literature to analyze the objective functions. In this regard, using a new hybrid MODM technique can be considered in future works. In addition, as the proposed model is NP-hard, it is highly recommended to use efficient heuristics [33, 34] such as Lagrangian [35] or novel metaheuristics such as the social engineering optimizer and the red deer algorithm [33, 36-38] to solve the location-routing optimization problem at hand. Finally, several other sustainability dimensions such as job opportunities can be added [39].

7. APPENDIX

Electronic Supplementary Materials are available in the online version as an attachment.

8. REFERENCES

- Rabbani, M., Heidari, R., Farokhi-Asl, H. and Rahimi, N., "Using metaheuristic algorithms to solve a multi-objective industrial hazardous waste location-routing problem considering incompatible waste types", *Journal of Cleaner Production*, Vol. 170, (2018), 227-241. <https://doi.org/10.1016/j.jclepro.2017.09.029>
- Safaeian, M., Fathollahi-Fard, A.M., Tian, G., Li, Z. and Ke, H., "A multi-objective supplier selection and order allocation through incremental discount in a fuzzy environment", *Journal of Intelligent & Fuzzy Systems*, Vol. 37, No. 1, (2019), 1435-1455. DOI: 10.3233/JIFS-182843
- Fathollahi-Fard, A.M., Govindan, K., Hajiaghahi-Keshmeli, M. and Ahmadi, A., "A green home health care supply chain: New modified simulated annealing algorithms", *Journal of Cleaner Production*, Vol. 240, (2019), 118200. <https://doi.org/10.1016/j.jclepro.2019.118200>
- Mahmoudsoltani, F., Shahbandarzadeh, H. and Moghdani, R., "Using pareto-based multi-objective evolution algorithms in decision structure to transfer the hazardous materials to safety storage centre", *Journal of Cleaner Production*, Vol. 184, (2018), 893-911. <https://doi.org/10.1016/j.jclepro.2018.02.235>
- Samanlioglu, F., "A multi-objective mathematical model for the industrial hazardous waste location-routing problem", *European Journal of Operational Research*, Vol. 226, No. 2, (2013), 332-340. <https://doi.org/10.1016/j.ejor.2012.11.019>
- Beiki, H., Seyedhosseini, S., Ghezavati, V. and Seyedaliakbar, S., "A location-routing model for assessment of the injured people and relief distribution under uncertainty", *International Journal of Engineering*, Vol. 33, No. 7, (2020), 1274-1284. DOI: 10.5829/IJE.2020.33.07A.14
- Beiki, H., Seyedhosseini, S., Ghezavati, V. and Seyedaliakbar, S., "Multi-objective optimization of multi-vehicle relief logistics considering satisfaction levels under uncertainty", *International Journal of Engineering*, Vol. 33, No. 5, (2020), 814-824. DOI: 10.5829/IJE.2020.33.05B.13
- Bahadori-Chinibelagh, S., Fathollahi-Fard, A.M. and Hajiaghahi-Keshmeli, M., "Two constructive algorithms to address a multi-depot home healthcare routing problem", *IETE Journal of Research*, (2019), 1-7. <https://doi.org/10.1080/03772063.2019.1642802>
- Cappanera, P., Gallo, G. and Maffioli, F., "Discrete facility location and routing of obnoxious activities", *Discrete Applied Mathematics*, Vol. 133, No. 1-3, (2003), 3-28. [https://doi.org/10.1016/S0166-218X\(03\)00431-1](https://doi.org/10.1016/S0166-218X(03)00431-1)
- Nema, A. and Gupta, S., "Multiobjective risk analysis and optimization of regional hazardous waste management system", *Practice Periodical of Hazardous, Toxic, and Radioactive Waste Management*, Vol. 7, No. 2, (2003), 69-77. [https://doi.org/10.1061/\(ASCE\)1090-025X\(2003\)7:2\(69\)](https://doi.org/10.1061/(ASCE)1090-025X(2003)7:2(69))
- Zhang, M., Ma, Y. and Weng, K., "Location-routing model of hazardous materials distribution system based on risk bottleneck", in Proceedings of ICSSSM'05. 2005 International Conference on Services Systems and Services Management, (2005), IEEE. Vol. 1, 362-368. DOI: 10.1109/ICSSSM.2005.1499496
- Ahluwalia, P.K. and Nema, A.K., "Multi-objective reverse logistics model for integrated computer waste management", *Waste Management & Research*, Vol. 24, No. 6, (2006), 514-527. <https://doi.org/10.1177%2F0734242X06067252>
- Nagy, G. and Salhi, S., "Location-routing: Issues, models and methods", *European Journal of Operational Research*, Vol. 177, No. 2, (2007), 649-672. <https://doi.org/10.1016/j.ejor.2006.04.004>
- Emek, E. and Kara, B.Y., "Hazardous waste management problem: The case for incineration", *Computers & Operations Research*, Vol. 34, No. 5, (2007), 1424-1441. <https://doi.org/10.1016/j.cor.2005.06.011>
- Berman, O., Drezner, Z., Wang, Q. and Wesolowsky, G.O., "The route expropriation problem", *IIE Transactions*, Vol. 40, No. 4, (2008), 468-477. <https://doi.org/10.1080/07408170701592465>

16. Dadkar, Y., Jones, D. and Nozick, L., "Identifying geographically diverse routes for the transportation of hazardous materials", *Transportation Research Part E: Logistics and Transportation Review*, Vol. 44, No. 3, (2008), 333-349. <https://doi.org/10.1016/j.tre.2006.10.010>
17. Edalatpour, M., Mirzapour Al-e-hashem, S., Karimi, B. and Bahli, B., "Investigation on a novel sustainable model for waste management in megacities: A case study in tehran municipality", *Sustainable Cities and Society*, Vol. 36, (2018), 286-301. <https://doi.org/10.1016/j.scs.2017.09.019>
18. Mohammadi, M., Jula, P. and Tavakkoli-Moghaddam, R., "Design of a reliable multi-modal multi-commodity model for hazardous materials transportation under uncertainty", *European Journal of Operational Research*, Vol. 257, No. 3, (2017), 792-809. <https://doi.org/10.1016/j.ejor.2016.07.054>
19. Xie, Y., Lu, W., Wang, W. and Quadrifoglio, L., "A multimodal location and routing model for hazardous materials transportation", *Journal of Hazardous Materials*, Vol. 227, (2012), 135-141. <https://doi.org/10.1016/j.jhazmat.2012.05.028>
20. Vidović, M., Ratković, B., Bjelić, N. and Popović, D., "A two-echelon location-routing model for designing recycling logistics networks with profit: Milp and heuristic approach", *Expert Systems with Applications*, Vol. 51, (2016), 34-48. <https://doi.org/10.1016/j.eswa.2015.12.029>
21. Harijani, A.M., Mansour, S., Karimi, B. and Lee, C.-G., "Multi-period sustainable and integrated recycling network for municipal solid waste—a case study in tehran", *Journal of Cleaner Production*, Vol. 151, (2017), 96-108. <https://doi.org/10.1016/j.jclepro.2017.03.030>
22. Asefi, H. and Lim, S., "A novel multi-dimensional modeling approach to integrated municipal solid waste management", *Journal of Cleaner Production*, Vol. 166, (2017), 1131-1143. <https://doi.org/10.1016/j.jclepro.2017.08.061>
23. Habibi, F., Asadi, E., Sadjadi, S.J. and Barzinpour, F., "A multi-objective robust optimization model for site-selection and capacity allocation of municipal solid waste facilities: A case study in tehran", *Journal of Cleaner Production*, Vol. 166, (2017), 816-834. <https://doi.org/10.1016/j.jclepro.2017.08.063>
24. Ebrahimi, S.B., "A stochastic multi-objective location-allocation-routing problem for tire supply chain considering sustainability aspects and quantity discounts", *Journal of Cleaner Production*, Vol. 198, (2018), 704-720. <https://doi.org/10.1016/j.jclepro.2018.07.059>
25. Hu, H., Li, X., Zhang, Y., Shang, C. and Zhang, S., "Multi-objective location-routing model for hazardous material logistics with traffic restriction constraint in inter-city roads", *Computers & Industrial Engineering*, Vol. 128, (2019), 861-876. <https://doi.org/10.1016/j.cie.2018.10.044>
26. Rabbani, M., Heidari, R. and Yazdanparast, R., "A stochastic multi-period industrial hazardous waste location-routing problem: Integrating nsga-ii and monte carlo simulation", *European Journal of Operational Research*, Vol. 272, No. 3, (2019), 945-961. <https://doi.org/10.1016/j.ejor.2018.07.024>
27. Pouriani, S., Asadi-Gangraj, E. and Paydar, M.M., "A robust bi-level optimization modelling approach for municipal solid waste management; a real case study of iran", *Journal of Cleaner Production*, Vol. 240, (2019), 118125. <https://doi.org/10.1016/j.jclepro.2019.118125>
28. Delfani, F., Kazemi, A., SeyedHosseini, S.M. and Niaki, S.T.A., "A novel robust possibilistic programming approach for the hazardous waste location-routing problem considering the risks of transportation and population", *International Journal of Systems Science: Operations & Logistics*, Vol., No., (2020), 1-13. <https://doi.org/10.1080/23302674.2020.1781954>
29. Fathollahi-Fard, A.M., Ahmadi, A., Goodarzian, F. and Cheikhrouhou, N., "A bi-objective home healthcare routing and scheduling problem considering patients' satisfaction in a fuzzy environment", *Applied Soft Computing*, Vol. 93, No., (2020), 106385. <https://doi.org/10.1016/j.asoc.2020.106385>
30. Feng, Y., Zhang, Z., Tian, G., Fathollahi-Fard, A.M., Hao, N., Li, Z., Wang, W. and Tan, J., "A novel hybrid fuzzy grey topsis method: Supplier evaluation of a collaborative manufacturing enterprise", *Applied Sciences*, Vol. 9, No. 18, (2019), 3770. <https://doi.org/10.3390/app9183770>
31. Liu, X., Tian, G., Fathollahi-Fard, A.M. and Mojtahedi, M., "Evaluation of ship's green degree using a novel hybrid approach combining group fuzzy entropy and cloud technique for the order of preference by similarity to the ideal solution theory", *Clean Technologies and Environmental Policy*, Vol. 22, No. 2, (2020), 493-512. DOI: 10.1007/s10098-019-01798-7
32. Pasandideh, S.H.R., Niaki, S.T.A. and Asadi, K., "Optimizing a bi-objective multi-product multi-period three echelon supply chain network with warehouse reliability", *Expert Systems with Applications*, Vol. 42, No. 5, (2015), 2615-2623. <https://doi.org/10.1016/j.eswa.2014.11.018>
33. Fathollahi-Fard, A.M., Hajiaghahi-Keshteli, M. and Tavakkoli-Moghaddam, R., "The social engineering optimizer (SEO)", *Engineering Applications of Artificial Intelligence*, Vol. 72, No., (2018), 267-293. <https://doi.org/10.1016/j.engappai.2018.04.009>
34. Fathollahi-Fard, A.M., Ranjbar-Bourani, M., Cheikhrouhou, N. and Hajiaghahi-Keshteli, M., "Novel modifications of social engineering optimizer to solve a truck scheduling problem in a cross-docking system", *Computers & Industrial Engineering*, Vol. 137, (2019), 106103. <https://doi.org/10.1016/j.cie.2019.106103>
35. Fathollahi-Fard, A.M., Hajiaghahi-Keshteli, M., Tian, G. and Li, Z., "An adaptive lagrangian relaxation-based algorithm for a coordinated water supply and wastewater collection network design problem", *Information Sciences*, Vol. 512, (2020), 1335-1359. <https://doi.org/10.1016/j.ins.2019.10.062>
36. Fathollahi-Fard, A.M., Hajiaghahi-Keshteli, M. and Tavakkoli-Moghaddam, R., "Red deer algorithm (RDA): A new nature-inspired meta-heuristic", *Soft Computing*, Vol. 24, (2020), 1-29.
37. Safaeian, M., Etebari, F. and Vahdani, B., "An integrated quay crane assignment and scheduling problem with several contractors in container terminals", *Scientia Iranica*, (2019). <https://doi.org/10.24200/SCI.2019.53338.3191>
38. Safaeian, M., Etebari, F. and Vahdani, B., "A vehicle routing problem with two types of ships in container terminals", *Scientia Iranica*, (2020). <https://doi.org/10.24200/SCI.2020.55129.4090>
39. Fathollahi-Fard, A.M., Ahmadi, A. and Al-e-Hashem, S.M., "Sustainable closed-loop supply chain network for an integrated water supply and wastewater collection system under uncertainty", *Journal of Environmental Management*, Vol. 275, (2020), 111277. <https://doi.org/10.1016/j.jenvman.2020.111277>

Persian Abstract

چکیده

تحقیقات در مورد محیط زیست و پایداری یک موضوع فعال است، به ویژه در مدیریت پسماند. به همین ترتیب، بهینه سازی زباله های خطرناک یک موضوع تحقیقاتی فعال در کشورهای در حال توسعه است که ممکن است با انتشار کربن و افراد سبز ادغام شود. این چالش بزرگ انگیزه تحقیقات فعلی برای کمک به یک مدل جدید بهینه سازی چند هدفه برای رسیدگی به مسئله مسیریابی محل زباله های خطرناک سبز است. مدل بهینه سازی چند هدفه پیشنهادی برای اولین بار همزمان چهار هدف را تعیین می کند. علاوه بر هزینه کل و انتشار گازهای گلخانه ای سیستم های حمل و نقل به عنوان دو هدف اصلی، هدف دیگر این است که خطر حمل زباله های خطرناک در کنار پسماندهای زباله مرتبط با قرار گرفتن در معرض مردم در اطراف مسیرهای حمل و نقل را به حداقل برساند. علاوه بر این، کل خطر مرتبط با جمعیت در یک شعاع خاص در اطراف مراکز درمان و دفع به حداقل می رسد. از آنجا که مدل پیشنهادی پیچیده با اهداف متناقض است، چندین ابزار تصمیم گیری چند هدفه (MODM) استفاده شده و براساس مشکلات آزمون مختلف مرتبط با یک مثال صنعتی با یکدیگر مقایسه می شوند. بر اساس کیفیت راه حل و زمان محاسباتی، روش ترتیب ترجیح با شباهت به محلول ایده آل (TOPSIS) به عنوان قوی ترین تکنیک برای ارزیابی عملکرد هر پنج روش MODM انتخاب شده است.



A Hybrid Genetic Algorithm for Integrated Production and Distribution Scheduling Problem with Outsourcing Allowed

L. Izadi, F. Ahmadizar*, J. Arkat

Department of Industrial Engineering, University of Kurdistan, Sanandaj, Iran

PAPER INFO

Paper history:

Received 07 June 2020
Received in revised form 13 July 2020
Accepted 03 September 2020

Keywords:

Dominance Properties
Hybrid Genetic Algorithm
Inventory
Outsourcing
Production Scheduling
Vehicle Routing

ABSTRACT

In this paper, we studied a new integrated production scheduling, vehicle routing, inventory and outsourcing problem. The production phase considers parallel machine scheduling including setup times with outsourcing allowed and the distribution phase considered batch delivery by a fleet of homogenous vehicles with respect to holding cost of completed jobs. The objective of the Mixed Integer Linear Programming (MILP) formulated model is to minimize the total costs including production, outsourcing, holding, tardiness and distribution fixed and variable costs. Due to the nondeterministic polynomial time (Np)-hardness of the problem, we derive a number of dominance properties for the optimal solution and combine them with a Genetic Algorithm (GA) to solve the problem. To assess the efficiency and effectiveness of the proposed hybrid algorithm, we conduct the computational study on randomly generated instances. Sensitivity analyses showed the impacts of the parameters on the objective function were incorporated. In order to evaluate the significance of the differences among the results obtained by GA and GADP one-tailed paired t tests were performed and interval plots were depicted.

doi: 10.5829/ije.2020.33.11b.19

1. INTRODUCTION

Scheduling is a decision-making process in many manufacturing and service sectors, such as production, health, tourism, hospitality, and transportation [1]. Distribution is one of the elements of marketing which can be defined as the process of moving products from a manufacturer to the final consumer. In the other words, the most important duty of the distribution channel management is to send goods in the right place at the right time to the customers [2].

Recently, the global competition in the marketplace has forced the companies to minimize the amount of inventory required through the supply chain. However, the companies should be still responsive to the requirements of the customers. Minimized inventory can make an effective interaction between production and distribution processes leading to applicable effectiveness of integrated models [3, 4]. Outsourcing makes the manufacturers able to efficiently deal with fluctuations without keeping a high production or inventory capacity

[5]. Deciding whether to produce in-house or employ an external supplying source has always been a fundamental challenge in manufacturing industries [6, 7].

In recent years, researchers have attended the integrated production scheduling and vehicle routing problem (IPSVRP). As it will be discussed in detail in the literature review, in most of researches in the literature handling the demand fluctuations as well as overcoming the capacity limitation by outsourcing option to meet customers' requests were ignored. Inventory issue and holding costs have become very important in the current competitive world. However, inventory of completed jobs and related holding cost before departure of delivery vehicles are rarely considered in integrated scheduling production and vehicle routing problem studies. In this paper, integrated production scheduling, inventory and vehicle routing with outsourcing problem in the parallel machine environment is studied. There are customers that order special products from a company that have parallel identical production lines. The products are processed in one stage on the one of the in-house lines or outsourced

*Corresponding Author Institutional Email: f.ahmadizar@uok.ac.ir
(F. Ahmadizar)

to a subcontractor. After completing, the goods are delivered to the costumers by vehicles. In order to minimize the fixed costs and increase the percentage of vehicle use, the goods are batched and then delivered to the customers using vehicles in some tours. The objective is to minimize the total costs, including production, holding, outsourcing, transportation and tardiness penalty costs.

To the best of our knowledge, it is the first time that this problem is being investigated in the literature to reduce the research gap. Two well-known solution approaches were utilized in order to solve the problem, i.e. exact and heuristic methods (due to Np-hardness of the problem [8]). For the former, a Mixed Integer Linear Programming (MILP) is developed and for the latter, a hybrid meta-heuristic incorporating the dominance properties with a Genetic Algorithm (GA) is proposed. The numerical experiments are examined to validate the MILP. The computational study is conducted for evaluating the efficiency and effectiveness of the proposed hybrid algorithm. The performance of the proposed algorithm to find the optimality is verified by MILP for small and medium size instances. Afterward, the capability of the proposed algorithm for solving the considered problem for the large instances is provided comparing to MILP in computational time. After vast numerical experiments, it can be concluded that proposed algorithm is capable to find optimal or near-optimal solution in comparison to MILP with less computational time and more quality.

The main contributions of this study are specified as follow:

- In order to be more responsive to the customer requests, outsourcing option is addressed in the current problem.
- In order to handle inventory issues, the holding cost incurred to the system is considered in this research.
- To the best of our knowledge, it is the first time that both outsourcing option and inventory are integrated in the related literature.
- To solve the problem optimally, a MILP is developed and a new hybrid GA is proposed. Computational study is conducted to evaluate the performance of proposed algorithm.
- A hybrid algorithm is used in context of integrated production scheduling and vehicle routing problem. The derived dominance properties play a strong neighbour-hood search role for GA.

2. LITERATURE REVIEW

In this section, the related literature on IPSVRP is reviewed.

Van Buer et al. [9] introduced integrated production scheduling on single machine and vehicle routing

problem including the sufficient number of homogeneous vehicles with general order sizes.

In different researches, IPSVRP including batch delivery to multiple customers was investigated using adequate number of homogeneous vehicles with equal order sizes and single, parallel and bundling machine configuration [10, 11].

Several studies have been conducted on IPSVRP to multiple customers by batch delivery using limited number of homogeneous vehicles with single machine configuration [12–14].

Chen et al. [15] studied IPSVRP with time windows and stochastic demands at retailers for perishable food in order to maximize the expected total profit of the supplier. Besides, to deal with the problem, a combined algorithm of a constrained Nelder–Mead method and a heuristic was introduced.

Ullrich [16] investigated IPSVRP with multiple tours allowed for each vehicle to minimize the total tardiness. The integrated problem includes two sub-problems, parallel machines scheduling with ready times as well as the delivery of completed jobs with a fleet of heterogeneous vehicles. A genetic algorithm approach proposed to tackle the integrated problem indicates that the solutions of integrated problem are much more suitable than merged solutions of two sub-problems.

Amorim et al. [8] dealt with IPSVRP in parallel machine environment with set-up times comparing batching versus lot sizing for make-to-order production strategy in the cases with perishability of products. Results showed that lot sizing can lead to better solutions in comparison with batching.

Belho-Filho et al. [17] proposed an adaptive large neighborhood search (ALNS) framework to solve the problem of integrated lot sizing and scheduling and vehicle routing. Other characteristics of the problem are perishability nature of goods, parallel machine environment and sequence dependent setup times- are incurred because of reconfiguration of equipment for production different products. The objective is to minimize the sum of production costs, consist of setup and production cost, as well as distribution costs, including fixed cost of vehicle usage and distance proportional costs.

Kang et al. [18] studied IPSVRP with multiple vehicles and flow-shop machine configuration and outsourcing allowed in various stages in the manufacturing process. The objective is to minimize the total costs including production cost depending on various product types, factory setup cost and different outsourcing factories as well as transportation cost with multiple vehicles. To deal with the problem in large sizes, an efficient GA is proposed.

In order to minimize the total customer waiting time and the vehicle delivery cost, Li et al. tackled a multi-objective IPSVRP with a single machine and multiple

vehicles [19]. Applying the elite strategy, they solved the problem using non-dominated genetic algorithm.

To minimize required time to process and deliver all customer demands, Karaoglan and Kesen [20] investigated an integrated single machine scheduling and capacitated vehicle routing problem for single time-sensitive product. They developed a branch-and-cut (B&C) algorithm applying several valid inequalities in order to improve lower bounds besides using a simulated annealing approach based local search to enhance upper bounds to solve the problem [20].

Devapriya et al. [21] investigated the integrated production scheduling and vehicle routing problem for perishable products. The limited capacity vehicles can be utilized multiple times in planning horizon. The problem tackled by heuristics based on evolutionary algorithms is modelled to determine production schedule, fleet size, and vehicle's route at minimum cost [21].

Lacomme et al. [22] evaluated the IPSVRP including specific capacity constraints, limited lifespan of goods and special case of a single vehicle. A greedy randomized adaptive search procedure (GRASP) with an evolutionary local search (ELS) is developed to tackle the considered problem. Besides, a new set of instances with multiple vehicles is introduced for further research [22].

Tamannaeei and Rasti-Barzoki [23] investigated the IPSVRP to minimize the total weighted tardiness, fixed and variable transportation costs. A Branch-and-Bound (B&B) based exact procedure and a meta-heuristic genetic algorithm (GA) were proposed to solve the problem [23].

Tavares-Neto and Nagano [24] dealt with integrated scheduling production, inventory, and distribution problem aiming to integrate a scheduling of parallel machines considering sequence dependent setup time using a single vehicle with multiple routes for delivery. In order to solve the problem two new algorithms, i.e. an Iterated Greedy technique based improvement heuristic and a constructive heuristic, are proposed. Comparing the obtained results of the algorithms with a Mixed-Integer Programming model and an adapted Genetic Algorithm showed that the former can lead to better results [24].

Mohammadi et al. [25] studied an integrated flexible job-shop scheduling-vehicle routing problem with a time window. They modelled the problem as a novel bi-objective mixed integer, in which the first objective function tries to minimize a sum of the production and distribution scheduling costs, and the second objective function aims to minimize a weighted sum of delivery earliness and tardiness. They considered a furniture manufacturing company producing customized goods as a case study. In this study, an \mathcal{E} -constraint method is applied to solve small-sized real data and medium- and large-sized problems are solved by a Hybrid Particle Swarm Optimization algorithm [25].

Mousavi et al. [26] addressed production and air transportation scheduling problem with time windows for the due date aimed to minimize the total supply chain costs. They developed four algorithms (i.e., SA, GA, PSO and DPSO) and hybrid variable neighborhood search-simulated annealing to solve different size generated problems [26].

Literature studies have indicated that a few articles addressed inventory cost associated with integrated production and distribution system with batch delivery. In addition, the outsourcing option in manufacturing stage is often neglected, however the effective impact of outsourcing on reducing investment requirements and improving the response to customers' demands is shown in the relative literature. To the best of our knowledge, among the literature of integrated production scheduling and vehicle routing problem reviewed, only one paper has considered inventory and holding cost specially and only one paper has addressed outsourcing option while none of them regards both inventory and outsourcing simultaneously. In this paper, we consider holding cost and outsourcing option in IPSVRP for the first time. Meanwhile, the proposed hybrid meta-heuristic algorithm, i.e. dominance properties incorporated with genetic algorithm, is being newly used in the related literature.

3. PROBLEM DEFINITION

In this paper, we address coordination between production scheduling with outsourcing allowed and vehicle routing problem. There is a factory that receives orders containing P types of products from customers. Each type of products is processed in one production stage. Orders are processed on either in-house m identical parallel lines or single subcontractor's line. Sequence-dependent setup times satisfying the triangle inequality - between producing different products- are taken into account on in-house lines. Setup cost is calculated by multiplying setup times by the coefficient of setup cost. The jobs are outsourced with outsourcing cost oc_{ij} and lead time l_{ij} ; after processing, outsourced jobs are returned to the factory.

There are f customers in different geographic locations ordering a set of products. Customers' demand has to be delivered in strict due dates in some batches by routing with a fleet of homogeneous vehicles. Each vehicle starts the route from the depot of the factory and after visiting associated customers it returns to the depot of the factory. If customers' orders are delivered after associated due date, tardiness penalty will be incurred. Tardiness penalty is calculated by multiplying tardiness by penalty coefficient. Transportation cost is composed of two parts: fixed cost -usage cost of vehicle- and

variable cost-which is proportional to transportation time.

Because of batch delivery form, a completed job of a batch must be kept in the depot until other jobs in the same batch are completed. In the other words, the delivery is carried out when all the jobs in the batch are completed. The incurred holding cost can be calculated by multiplying holding time by holding cost rate for each job. The aim is to find a joint production and distribution schedule with minimum total cost of setup, holding, outsourcing, transportation and tardiness.

Assumptions of this problem are written as follows:

- Batch is a shipment containing one or more customers' order delivered by one vehicle.
- Each customer can order one or more products.
- Vehicles are available in time zero in factory.
- Capacity of each vehicle is greater than the total demand of each customer.
- Each customer is visited only once.

3. 1. Mathematical Formulation In this section, the problem is formulated in Mixed Integer Linear Programming (MILP). The parameters, variables, and constraints of model are provided as follow:

Parameters:

- j : Product indices.
- i : Customer indices ($i=0, n+1$ denoted production location).
- k : Production line indices.
- v : Vehicle indices.
- ij : Product j ordered by customer i .
- f : Number of customers.
- n_i : Number of jobs ordered by customer i .
- m : Number of production lines.
- N : Number of all jobs.
- P : Number of products.
- V : Number of vehicles.
- p_{ij} : Processing time of job ij .
- α_i : Tardiness penalty coefficient for customer i .
- β : Cost of per unit of setup time.
- $set_{jj'}$: Setup time between product j and j' .
- set_{0j} : Set up time for the first job j on each line.
- $t_{ii'}$: Travel time from the location of customer i to the location of customer i' . ($i=0, n+1$ denoted facility location).
- h_{ij} : Rate of holding cost for job ij (unit of cost in per unit of time).
- F_v : Fixed cost associated with each vehicle v .
- c^v : Cost per travelling unit time travelled by vehicle v .
- dem_{ij} : Demand of job ij .
- d_i : Due date of all jobs ordered by customer i .
- cap_v : Capacity of vehicle v .
- q : An enough large number.
- oc_{ij} : Outsourcing cost of job ij .
- l_{ij} : Lead time of outsourced job ij .

Variables:

- C_{ij} : Completion time of job ij .
- y_{kij} : A binary variable indicating whether job ij is processed first on machine k .
- $x_{ijj'}$: A binary variable indicating whether job ij is processed immediately before job $i'j'$ on the same machine.
- u_{ij} : A binary variable indicating whether job ij is processed last on a machine.
- H_{ij} : The time that job ij waits for completing other jobs belonging to its batch.
- w_i^v : Binary variable which takes the value 1 if customer order i is delivered by vehicle v ($i=0, i=f+1$ denote processing site).
- $z_{ii'}^v$: A binary variable which takes the value 1 if customer i is visited immediately before customer i' by vehicle $v \in V$ ($i=0, i=f+1$ denote processing site).
- z_{0i}^v : Binary variable which takes the value 1 if customer i is visited first by vehicle v .
- $z_{0,f+1}^v$: Binary variable which takes the value 1 if vehicle v remains in processing site without using.
- S_v : Start time of tour of vehicle v .
- T_i : Tardiness of jobs ordered by customer i .
- D_i : Delivery date of all jobs ordered by customer i .
- o_{ij} : A binary variable indicating whether job ij is outsourced.

$$\begin{aligned} \text{Min } & \sum_{i=1}^f \alpha_i T_i + \\ & \sum_{i=1}^f \sum_{j=1}^{n_i} \sum_{i'=1}^{n_{i'}} \sum_{j'=1}^{n_{i'}} \beta \text{ set}_{jj'} x_{ijj'} + \\ & \sum_{i=1}^f \sum_{j=1}^{n_i} \sum_{k=1}^m \beta \text{ set}_{0j} y_{kij} + \sum_{i=1}^f \sum_{j=1}^{n_i} H_{ij} h_{ij} + \quad (1) \\ & \sum_{v=1}^V F_v (1 - z_{0,f+1}^v) + \sum_{v=1}^V \sum_{i=0}^f \sum_{i'=1}^{f+1} c^v t_{ii'} z_{ii'}^v \\ & + \sum_{i=1}^f \sum_{j=1}^{n_i} oc_{ij} o_{ij} \end{aligned}$$

Objective (1) is to minimize the sum of production, distribution, outsourcing and holding costs. The total production cost is composed of sequence-dependent set-up costs. The distribution cost is composed of tardiness penalties and fixed vehicle usage costs as well as variable travel time proportional costs. The outsourcing cost is incurred by outsourcing the jobs. The holding cost is associated with holding finished goods in the factory depot.

Scheduling constraints:

$$\sum_{i=1}^f \sum_{j=1}^{n_i} y_{kij} \leq 1, k = 1, \dots, m \quad (2)$$

$$\sum_{k=1}^m y_{ki'j'} + \sum_{i=1}^f \sum_{j=1}^{n_i} x_{ijj'} + o_{i'j'} = 1, i' = 1, \dots, f, j' = 1, \dots, n_{i'}, ij \neq i'j' \quad (3)$$

$$\sum_{i'=1}^f \sum_{j'=1}^{n_{i'}} x_{ijj'} + u_{ij} + o_{ij} = 1, i = 1, \dots, f, j = 1, \dots, n_i \quad (4)$$

$$C_{ij} \geq p_{ij} y_{kij}, i = 1, \dots, f; j = 1, \dots, n_i; k = 1, \dots, m, ij \neq i'j' \quad (5)$$

$$C_{ij} \geq C_{i'j'} + p_{ij} + set_{j'} - q(1 - x_{i'j'ij}), i, i' = 1, \dots, f; j = 1, \dots, n_i; j' = 1, \dots, n_{i'}; ij \neq i'j' \quad (6)$$

$$C_{ij} \geq l_{ij}o_{ij}, i = 1, \dots, f, j = 1, \dots, n_i \quad (7)$$

Constraint (2) ensure there is at most one job which is the first to be processed on line k . Constraint (3) state each job is either processed after another one on a line or the first to be processed or outsourced. Constraint (4) state each job is either the last to be processed or precedes another job on a line or outsourced and Constraints (5), (6), (7) define the completion time of job ij .

Vehicle routing constraints:

$$\sum_{v=1}^V w_i^v = 1, i = 1, \dots, f \quad (8)$$

$$w_0^v \geq w_i^v, v = 1, \dots, V; i = 1, \dots, f \quad (9)$$

$$\sum_{i \neq i'}^f z_{ii'}^v = w_{i'}^v, v = 1, \dots, V, i' = 1, \dots, f \quad (10)$$

$$\sum_{i \neq i'}^{f+1} z_{ii'}^v = w_{i'}^v, v = 1, \dots, V; i' = 1, \dots, f \quad (11)$$

$$c_v \geq \sum_{i=1}^f \sum_{j=1}^{n_i} dem_{ij} w_i^v, v = 1, \dots, V \quad (12)$$

Constraint (8) assign each customer to exactly one vehicle and one tour. Constraint (9) guarantee a utilized vehicle that must start its trip from production facility. Constraints (10) and (11) explain the vehicle, that visits customer i' , travels either from another customer or from the processing site to the location of customer. Following the service, the vehicle can come-back to the processing site or deliver the other customer's order. Constraint (12) ensure that the number of jobs loaded in each vehicle does not exceed the capacity of vehicle.

Integration constraints:

$$S_v \geq C_{ij} - q(1 - w_i^v), i = 1, \dots, f, j = 1, \dots, n_i, v = 1, \dots, V \quad (13)$$

$$D_i \geq D_{i'} + t_{i'i} - q(1 - z_{ii'}^v), i, i' = 1, \dots, f, i \neq i', v = 1, \dots, V \quad (14)$$

$$D_i \geq S_v + t_{0i} - q(1 - w_i^v), i = 1, \dots, f, v = 1, \dots, V \quad (15)$$

$$T_i \geq D_i - d_i, i = 1, \dots, f \quad (16)$$

$$H_{ij} \geq S_v - C_{ij} - q(1 - w_i^v), i = 1, \dots, f, j = 1, \dots, n_i, v = 1, \dots, V \quad (17)$$

$$T_{ij}, S_v, C_{ij}, H_{ij}, D_i \geq 0, i = 1, \dots, f, j = 1, \dots, n_i, v = 1, \dots, V \quad (18)$$

$$x_{ij,i'j'}, y_{kij}, z_{ii'}^v, o_{ij} \in \{0,1\} \quad (19)$$

Constraint (13) guarantee that the starting time of vehicle v is greater than the completion time of the jobs delivered by this vehicle. Constraint (14) say that delivery date of

customer order i is greater than that of previous customer (production site) plus traveling time between two customer locations. Constraint (15) state that delivery date of jobs ordered by customer i is greater than the starting time of associated vehicle plus time distance between production site and location of customer i . Constraint (16) define the tardiness of orders of customer i . Constraint (17) explain the holding time of job ij in the factory and Constraints (18) and (19) define the variables.

4. DOMINANCE PROPERTIES

In this section, three lemmas, two corollaries, and five properties for the problem are introduced. Lemma 3 and property 2 that are derived from literature [27] and corollary 2 is derived from literature [28] are applied in production scheduling section in this research.

Lemma 1: The in-house jobs constructing a batch are not essentially processed on each line in a continuous way in the optimal solution.

Property 1: Given a solution in which a line after processing job ij belonging to batch v is idle for period time IT . If $S_v \geq C_{ij} + IT'$, where $0 < IT' \leq IT$, the processing of job ij must be postponed to complete at $C_{ij} + IT'$.

Corollary 1: In the optimal solution, each production line is not idle after processing the job, except the last job of a batch.

Lemma 2: The optimal solution is not essentially in non-delay form.

Proof: The objective function of the problem is composed of five parts including set-up cost, holding cost, outsourcing cost, tardiness cost and transportation cost. Tardiness cost is a regular performance measure that is non-decreasing in completion time. Set-up cost, outsourcing cost and transportation cost are not dependent on completion time however, holding cost is decreasing in completion time; if the completion time of a job (except the last job) belonging to a batch increases, then it becomes closer to departure time of the vehicle and consequently resulting in the shortened holding time. Therefore, the objective function of this article is not regular. Supposing a non-delay solution, any idle time inserted before processing a job that will lead to the increased completion time of the job as well as increased probable next jobs on the same line besides, the holding cost is decreased and consequently leading to decreased objective function. As a result, it can be concluded that this unnecessary idle time may improve the solution.

Property 2 Given a solution in which job ij belonging to batch v precedes immediately with job $i'j$ on the same line. If job ij is not the last job of the batch, $h_{i'j}p_{ij} < h_{ij}p_{i'j}$ and $S_v - C_{ij} \geq p_{i'j}$, the two jobs should be interchanged.

Proof: Suppose schedule I is the solution in which job $i'j$ belonging to batch v precedes immediately with job ij on the same line and the conditions mentioned above is satisfied. From corollary 1 there is no idle time between processing of these two jobs. Now, suppose schedule II in which jobs ij and $i'j$ are interchanged. Under solution II, the completion times of ij and $i'j$ are different from those in schedule I but, all the other jobs finish at the same time as in schedule I. The only difference between the two solutions lies in the holding cost of jobs ij and $i'j$.

Considering ST the time point at which job ij starts in schedule I and job $i'j$ starts in schedule II, the difference in cost of schedule I and II is as follow:

$$I: h_{i'j}(S_v - ST - p_{i'j}) + h_{ij}(S_v - ST - p_{i'j} - p_{ij})$$

$$II: h_{ij}(S_v - ST - p_{ij}) + h_{i'j}(S_v - ST - p_{ij} - p_{i'j})$$

After taking the differences of I and II, the following expression is obtained:

$$I - II: h_{i'j}p_{ij} - h_{ij}p_{i'j} > 0$$

Thus, the interchanging is cost effective and schedule II dominates schedule I and the proof is completed.

Property 3: Given a solution in which job $i'j'$ from batch v , that is not the last job of the batch, immediately precedes with job ij . If $S_v - C_{i'j'} \geq setup_{j'j} + p_{ij}$ and $h_{i'j'}(setup_{j'j} + p_{ij}) \geq h_{ij}(p_{i'j'})$, the two jobs should be interchanged.

Proof: Suppose a solution in which job $i'j'$ from batch v is not the last job of the batch and immediately precedes with job ij (schedule I). From corollary 1 there is no idle time between processing of these two jobs. Assume that $S_v - C_{i'j'} \geq setup_{j'j} + p_{ij}$ (without changing S_v after interchanging the two jobs), and $h_{i'j'}(setup_{j'j} + p_{ij}) \geq h_{ij}(p_{i'j'})$ as well as $setup_{j'j'} + setup_{j'j} \geq setup_{j''j}$ from triangular setup times assumption. Now, suppose schedule II in which jobs ij and $i'j'$ are interchanged. Under solution II, the completion times of ij and $i'j'$ are different from those as in schedule I but all the other jobs finish at the same time as in schedule I. Obviously, the differences between the two solutions are in the holding cost for jobs ij and $i'j'$ as well as setup cost; these differences are as follow:

$$I: \beta \cdot (setup_{j'j'} + setup_{j'j}) + h_{i'j'}(setup_{j'j} + p_{ij})$$

$$II: \beta \cdot setup_{j''j} + h_{ij}(p_{i'j'})$$

After taking the differences of I and II, based on assumptions, it is obtained that:

$$I - II: \beta \cdot (setup_{j'j'} + setup_{j'j} - setup_{j''j}) + h_{i'j'}(setup_{j'j} + p_{ij}) - h_{ij}(p_{i'j'}) \geq 0$$

Thus, the interchanging is cost effective; schedule II dominates schedule I and the proof is completed.

Property 4: Given a solution in which two jobs ij and $i'j'$ belong to batch v , job $i'j'$ is outsourced and job ij is processed in-house. If $p_{ij} \geq p_{i'j'}$, $l_{ij} \leq S_v$, $h_{i'j'}(C_{ij} - l_{i'j'} + p_{i'j'} - p_{ij}) + h_{ij}(l_{ij} - C_{ij}) > 0$ and $oc_{ij} < oc_{i'j'}$,

job $i'j'$ should be outsourced and job ij should be processed in-house.

Proof: Suppose schedule I is a solution in which two jobs ij and $i'j'$ belong to batch v , job $i'j'$ is outsourced and job ij is processed in-house. Assume that $p_{ij} \geq p_{i'j'}$, $l_{ij} \leq S_v$, $h_{i'j'}(C_{ij} - l_{i'j'} + p_{i'j'} - p_{ij}) + h_{ij}(l_{ij} - C_{ij}) > 0$ and $oc_{ij} < oc_{i'j'}$. Now, construct schedule II in which job ij is outsourced and job $i'j'$ is processed in-house replacing job ij . Schedule II must be constructed in the way that no change is occurred in S_v and completion times of the jobs after job $i'j'$. Since $p_{ij} \geq p_{i'j'}$, we insert an idle for time period $p_{ij} - p_{i'j'}$ after job $i'j'$. Afterwards, job $i'j'$ and the jobs before $i'j'$ belonging to the same line till the job which is the last job of its relative batch (called set A) are shifted to right for time period $p_{ij} - p_{i'j'}$; this reduces the holding time and cost of the jobs. The differences in the cost of the schedule I and II are in the holding cost of the jobs and outsourcing cost as follow:

$$I: OC_{i'j'} + h_{ij}(S_v - C_{ij}) + h_{i'j'}(S_v - l_{i'j'}) + \sum_{kl \in A} h_{kl}(p_{ij} - p_{i'j'})$$

$$II: OC_{ij} + h_{ij}(S_v - l_{ij}) + h_{i'j'}(S_v - C_{i'j'})$$

Since $C_{i'j'} = C_{ij} - p_{ij} + p_{i'j'}$ and based on assumptions, the difference of schedule I and II is obtained as follow:

$$I - II: (OC_{i'j'} - OC_{ij}) + h_{i'j'}(C_{ij} - l_{i'j'} + p_{i'j'} - p_{ij}) + h_{ij}(l_{ij} - C_{ij}) \geq 0$$

Thus, schedule II dominates schedule I and the proof is completed.

Property 5: Given a solution in which job $i'j'$ is outsourced and jobs ij and $i''j''$ are processed in the house in which job ij is produced immediately before (after) job $i''j''$. If $p_{i''j''} > p_{i'j'}$, $l_{i''j''} < S_v$, $oc_{i'j'} > oc_{i''j''}$ and $h_{i''j''}(l_{i''j''} - C_{i''j''}) + h_{i'j'}(C_{i''j''} - p_{i''j''} + p_{i'j'} - l_{i'j'}) > 0$, job $i''j''$ should be outsourced and job $i'j'$ should be processed in-house replacing job $i''j''$.

Proof: Suppose schedule I is a solution in which job $i'j'$ is outsourced and two jobs ij and $i''j''$ are processed in-house in which job ij is processed immediately before job $i''j''$. Assume that $p_{i''j''} > p_{i'j'}$, $l_{i''j''} < S_v$, $oc_{i'j'} > oc_{i''j''}$ and $h_{i''j''}(l_{i''j''} - C_{i''j''}) + h_{i'j'}(C_{i''j''} - p_{i''j''} + p_{i'j'} - l_{i'j'}) > 0$ as well as $setup_{j'j'} + setup_{j''j''} > setup_{j''j''}$ from triangular setup times assumption. Now, construct schedule II in which job $i''j''$ is outsourced and job $i'j'$ is processed in-house replacing job $i''j''$. Without changing the completion time of jobs except $i'j'$ in schedule II, insert an idle after $i'j'$ for time period $p_{i''j''} - p_{i'j'}$. Finally, to reduce holding time and consequently holding cost of the jobs, postpone job $i'j'$ and the jobs before $i'j'$ belonging to the same line until the job which is the last job of its relative batch (called set A). The differences in the cost of the schedule I and II are in the holding cost of the jobs, outsourcing cost and setup cost. The differences are as follow:

$$I: \beta(\text{setup}_{jj'} + \text{setup}_{j''j'}) + h_{i''j'}(S_v - C_{i''j'}) + h_{ij'}(S_v - l_{ij'}) + oc_{ij'} + \sum_{kl \in A} h_{kl}(p_{i''j'} - p_{ij'})$$

$$II: \beta(\text{setup}_{jj''}) + h_{i''j''}(S_v - l_{i''j''}) + h_{ij''}(S_v - C_{ij''}) + oc_{ij''}$$

Since $C_{ij'} = C_{i''j'} - p_{i''j'} + p_{ij'}$, the difference of schedules I and II are obtained as follow:

$$I - II: \beta(\text{setup}_{jj'} + \text{setup}_{j''j''} - \text{setup}_{jj''}) + h_{i''j''}(l_{i''j''} - C_{i''j''}) + h_{ij''}(C_{i''j''} - p_{i''j''} + p_{ij''} - l_{ij''}) + (oc_{ij'} - oc_{i''j''}) + \sum_{kl \in A} h_{kl}(p_{i''j'} - p_{ij'}) \geq 0$$

Thus, the changes are cost effective; schedule II dominates schedule I and the proof is completed. If job ij is processed immediately after job $i''j'$ and job $i''j''$ is processed before that, the proof is accomplished in the similar way.

5. SOLUTION APPROACH

To solve the problem efficiently, in this section a hybrid algorithm is proposed by incorporating a Genetic Algorithm (GA) with dominance properties, called GADP. The hybrid meta-heuristics with dominance properties are applied for solving some of previous scheduling or outsourcing problems; e.g. literatures [29, 30] proposed incorporating the dominance properties with genetic algorithm, literatures [5, 31] incorporated the dominance properties with ant colony algorithm.

Genetic algorithm [32–36] is one of the most well-known population based evolutionary meta-heuristics mimicking Darwinian principle of survival of the fittest, used for combinatorial problems. The initial population is generated by encoding the solutions of the considered problem to chromosomes. In the iterative steps, after selecting the parents, new generation is emerged by cross-over, mutation, and reproduction. The fitter individual has the higher probability to influence the latter generation of individuals. Therefore, by gradual improvement, the solutions move to the convergence toward the optimum. Finally, after reaching the termination criterion, the best found solution is reported.

No need for differentiability, convexity and continuity of the objective function is the major advantage of genetic algorithms. Furthermore, genetic algorithms can be relatively easily adjusted to almost every linear and non-linear problem. In order to reach the universal optimum, genetic algorithms with an elitist strategy have been verified, even in the case that the restrictions or objective function have non-smooth operators such as IF, MIN, MAX, and ABS functions. [37, 38].

The methodology of this paper is stated in main steps as follow:

1. Initialize a population of solutions randomly and
2. improve them by dominance properties (initialization).
3. Select parent chromosomes via the roulette wheel method (selection).

4. Do crossover process (crossover).
5. Implement mutation process (mutation).
6. Improve solutions by utilizing dominance properties (improvement).
7. Select survivors by using manner described in subsection 5-2 (select survivors)
8. Repeat steps 2 to 6 till the termination criterion is met (termination).

The details of the proposed method are expressed in the remainder.

5. 1. Initialization

5. 1. 1. Solution Representation

The solution

representation offered in the first step to design an algorithm for the problem. The solution representation is a string of symbols containing solution characteristics setting up a bridge that connects the original problem space and the solution space being searched by the algorithm. The algorithm performance can be affected significantly by definition of an appropriate solution representation strategy.

Each solution of the considered problem is characterized by two sections including scheduling section and vehicle routing section. Deciding which job must be processed in-house and which job must be outsourced and determining the scheduling of the in-house jobs are encoded in scheduling section. Whether each customer is serviced by which vehicle or the rout of each vehicle is encoded in the vehicle routing section. The solution representation must map characteristics of the problem into array of numbers.

The solution representation is a matrix containing two parts with $N+f$ entries of real numbers which N denotes the number of all jobs and f denotes the number of customers. The first part characterizing the scheduling problem contains N entries of real numbers from interval $[1, m+2)$ which m denotes the number of production lines. The second part characterizing the vehicle routing problem contains f entries of real numbers from interval $[1, V+1)$ which V denotes the number of vehicles. A representation for a solution with 2 lines, 6 jobs, 4 customers and 2 vehicles is shown in Figure 1.

5. 1. 2. Decoding Procedure

In this subsection,

we propose a decoding procedure for genetic algorithm of the problem. Decoding procedure plays an important role in algorithm efficiency.

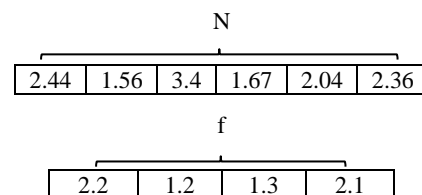


Figure 1. The solution representation

The jobs that should be produced with in-house lines and the jobs that should be outsourced as well as scheduling of the in-house jobs are indicated by decoding of the first part of the solution. The first part of the solution consists of real numbers having two integer and fractional parts. The integer part of each entry represents the number of the line producing the relative job, if the integer part is equal to $1, 2, \dots, m$ then the job will be produced in-house; otherwise, if the integer part is equal to $m+1$ then the job will be outsourced. The job sequence for each in-house line is indicated from increasing order of the fractional parts of the relative entries.

The routes and the vehicles assigning to each route are indicated from the second part of the solution. The integer part of entry representing the vehicle number delivering the request of relative customer and delivery route for each vehicle is obtained from increasing order of the fractional parts of the relative entries. The solution represented in Figure 1 is decoded as follow: from scheduling part, jobs 2 and 4 are processed on line 1, jobs 5, 6 and 1 are processed on line 2 consecutively, and job 3 is outsourced; and from vehicle routing part, customers 2 and 3 are serviced by vehicle 1 and customers 2 and 4 by vehicle 2 consecutively.

5. 1. 3. Generation of the Initial Population

The initial population is generated by producing a population of individuals randomly, matrices with $N+f$ entries of real numbers in determined intervals: N first entries from interval $[1, m+2)$ and f remained entries from interval $[1, V+1)$.

5. 2. Genetic Operators

In this section, the operators selection, reproduction, crossover, mutation as well as termination criteria used in proposed GA are presented as follow:

Selection: In GA search, selection strategy is considered as an important process leading to a proper performance direction. To select parents, one of the most effective selection strategies roulette wheel is used in this paper. The relative fitness can define whether an individual can be a parent according to fit_{ind}/Fit , where Fit determines the cumulated fitness of the current population. The fitness value of each individual is calculated from objective function of the problem in Equation (1).

Reproduction: Allowing the best organism(s) from the current generation to carry over to the next in the form of unchanged is regarded a practical variant of the general process of forming a new population. It supports the solution quality obtained by the GA and does not allow decreasing from one generation to the next.

Crossover: In order to produce offspring for the next generation, the chromosomes in the candidate population are subjected to crossover and mutation processes. In this article, the two-point crossover method is used with

crossover probability p_c . In two-point crossover, two random points are picked from parent chromosomes to produce offsprings, and the bits between the two points are chosen according to the bits between the parents organisms.

Mutation: In this paper, the uniform mutation method is used with mutation probability p_m . In uniform mutation, the value of a randomly chosen gene is replaced with a uniform random value selected between $[1, m+2)$ for production section of the chromosome and $[1, V+1)$ for VRP section of the chromosome.

Survivor selection: survivor selection of the proposed algorithm is described in the following. A percentage of the fittest individuals of the current population (p_r) is carried over to the next population unaltered. If offspring obtained from crossover is fitter than relative parent, the offspring is copied to the next generation and the parents are removed. Offspring obtained from mutation operator is being moved to the next population. The remainders of the next population are provided by the fittest individuals in the current population. This survivor selection strategy guarantees avoidance of premature convergence and divergence. In the search space of the proposed GA, diversification provided by mutation and intensification is supplied by copying the fittest solutions on the next generation and local search provided by dominance properties.

Termination criteria: According to the order of met criteria, two termination criteria are proposed for the GADP:

- no improvement is seen for defined number of generation
- the time limit 600 s is elapsed.

6. COMPUTATIONAL STUDY

In this section, the efficiency of proposed algorithm is investigated. In the following, data are generated and parameters are initialized systematically. Afterwards, instances in varied size are generated and solved by proposed algorithm. Finally, the results are compared with those of MILP to analyse the efficiency of the algorithm.

6. 1. Data Generation

Based on literatures [8, 17], the production lines are considered identical and production time of one unit of each type of product $p_j = 1, j = 1, 2, \dots, P$ is 1 in each line. The setup times are chosen in a way that the instances satisfy the triangle inequality. Setup times are randomly chosen out of the interval $[6, 10]$ with uniform distribution. In order to calculate setup cost, the amount of setup time is multiplied by value 25. There is no set-up time between producing jobs of the same type. All customers are randomly scattered in a square of locations from $(0, 0)$ to

(100, 100). The processing site is located at point (50, 50). Between all pairs of customers and the processing site, the Euclidean distance is calculated. The variable transportation cost between destinations is equal to the travel times. The number of vehicles is equal to that of customers. The fixed cost for utilizing each vehicle is set to 250. The capacity of the vehicle is obtained from $\frac{3 \sum_{ij} dem_{ij}}{f}$.

Based on literature [39], 70% of the demand of each job ij is randomly chosen out of the interval [40, 60] and the remaining is set to zero. The processing time of each job ij is computed through multiplying the demand by processing time of one unit of product j . The due dates are drawn from $[0.3 \sum_{ij} p_{ij}, 0.7 \sum_{ij} p_{ij}]$, the lead times from [100, 300] and the outsourcing cost from [100, 400] uniformly.

The rest of the parameters are chosen as follows. The rate of holding cost h_{ij} is randomly chosen out of the interval [1, 5]. The tardiness penalty cost is drawn randomly from interval [1, 10].

6. 2. Computational Results

Computational experiments are conducted to determine the performance of proposed mathematical model and GA hybridized with dominance properties (GADP). The results of proposed algorithm coded in C# are compared with those of MILP coded in GAMS and solved with CPLEX. All the computational experiments are performed using a computer with core i7 at 2.50GHz with 12GB Ram.

Through a preliminary experiment, the GA parameters must be set empirically and the different values for each parameter should be evaluated. In order to determine the best value of these parameters, parameter tuning must be performed. The population size is examined on $15(N+f)$, $20(N+f)$, $30(N+f)$ and $50(N+f)$, crossover rate p_c has been tested on 0.75, 0.8 and 0.85, mutation rate p_m has been tested on 0.2, 0.15 and 0.1 and reproduction rate p_r has been tested on 0.05, 0.1 and 0.15. Each combination of the parameter values is tested on 6 randomly chosen instances to ensure that the GADP performance is robust. The obtained experimental results indicate that the following values can lead to satisfactory outcomes, population size: $20(N+f)$, p_c : 0.75, p_m : 0.1 and p_r : 0.1.

To analyse sensitiveness of key parameters, 7 randomly instances are chosen. Four and three different values for the parameters population size and crossover rate are tested respectively and three and three different values for the parameters mutation rate and reproduction rate are tested. Each test is run 10 times. The average cost and average computational time are shown in Table 1. It is obviously that increasing the population size has good impact in quality of results due to increase the search space. From Table 1, it is perceived that increasing in population size more than $20(N+f)$ leads to increasing in

cost and computational time; it is occurred due to time limit (600 seconds).

In order to analyse the performance of proposed algorithm, generated instances are solved with some methods including:

- the MILP model implemented in GAMS in time limit 7200 seconds
- the proposed GA without the dominance properties
- the proposed GA hybridized with the dominance properties.

Now, the challenge in applying the proposed GA is that it may not perform better without the derived dominance properties; however, it may generate numerous additional solutions. Consequently, the performance comparison of the proposed GA with (GADP) and without (GA) the dominance properties can be used to prove their effectiveness and efficiency.

All instances including very small and small sizes as well as medium and large sizes are solved with the above stated methods and results are presented in Tables 2 and 3, respectively. As it is shown in the tables, the first column indicates the characteristics of the instances including number of the production lines (k), number of the products (P), number of the customers (f) as well as that of jobs (N). The values of k , P and f are imported as input data however number and configuration of the jobs (N) are randomly generated by the coded algorithm. In each row of the tables, minimum, average and maximum results obtained from each method for each instance are compared with the minimum solution achieved for that instance, besides, deviation percentage is mentioned as solution quality measure. In addition, the tables show the average CPU time, in seconds, for each problem instance spent by GAMS, GA, and GADP.

In Table 2, a value below MILP presented in boldface relates to a solution with optimality proven by GAMS, and an asterisk in Table 3 shows the failure of GAMS to identify even a possible solution within the imposed limited time. In Table 3, the times less than 7200 s spent by GAMS resulted in no optimal solution implies that GAMS has terminated due to memory limitations.

According to Tables 2 and 3, it can be concluded that obtaining optimal solutions for all of the instances with up to 2 production lines, 3 products, 5 customers and 14 jobs applying GAMS is possible. However, by increasing size of the instances, GAMS fails to find optimal solutions within a time limit of 7200 s; accordingly, for 2 instances with 56 and 57 jobs, it has failed to identify even a feasible solution within the imposed time limit.

In order to evaluate the significance of the differences among the results obtained by GA and GADP one-tailed paired t tests are performed. From Tables 2 and 3, a value below GADP presented in boldface relates to a solution with significant higher quality than solution obtained by GA. In 37 instances, results from GADP are significant better than those of GA.

TABLE 1. Sensitivity analyses of parameters

Population size (pop-size)		Reproduction rate (p_r)		Mutation rate (p_m)		Crossover rate (p_c)	
pop-size= 15($N+f$)		$p_r= 0.05$		$p_m= 0.05$		$p_c= 0.7$	
average cost	average time	average cost	average time	average cost	average time	average cost	average time
27398	40	25839	59	26215	120	25318	62
pop-size= 20($N+f$)		$p_r= 0.1$		$p_m= 0.1$		$p_c= 0.8$	
average cost	average time	average cost	average time	average cost	average time	average cost	average time
25318	70	25318	62	25318	62	26326	78
pop-size= 30($N+f$)		$p_r= 0.15$		$p_m= 0.2$		$p_c= 0.85$	
average cost	average time	average cost	average time	average cost	average time	average cost	average time
25728	101	25632	81	26892	87	26893	93
pop-size= 50($N+f$)							
average cost	average time						
26526	152						

TABLE 2. Very small and small instances

Instance (k,P,f)	N	MILP		GA			GADP				
		Quality	Time	Min	Ave	Max	Time	Min	Ave	Max	Time
(2,2,5)	6	0	5	0	0	0	4	0	0	0	5
	7	0	11	0	0	0	7	0	0	0	8
	8	0	80	0	0	0	9	0	0	0	6
	8	0	150	0	0	0	7	0	0	0	6
	9	0	162	0.01	0.01	0.01	11	0	0	0	14
Average		0	81.6	0	0	0	8	0	0	0	8
(2,2,7)	10	0	1276	0	0	0	10	0	0	0	12
	10	0	1250	0	0	0	6	0	0	0	4
	11	0	1327	0	0	0	6	0	0	0	4
	12	0	1537	0	0	0	27	0	0	0	19
	13	0	1522	0.03	0.03	0.03	18	0	0	0	16
Average		0	1443	0.01	0.01	0.01	13.4	0	0	0	11
(2,3,5)	10	0	3622	0	0	0	15	0	0	0	17
	11	0	5502	0.01	0.03	0.05	12	0	0	0	10
	11	0	2558	0	0	0	15	0	0	0	11
	12	0	2963	0	0	0	26	0	0	0	24
	12	0	1532	0.02	0.04	0.06	21	0	0.01	0.01	20
Average		0	3235.4	0.01	0.01	0.02	18	0	0	0	16
(2,3,7)	15	0.03	2304	0.03	0.03	0.05	30	0	0	0	26
	16	0.05	2250	0.02	0.02	0.04	26	0	0	0	24
	16	0.2	1902	0.03	0.06	0.12	29	0	0.03	0.04	13
	17	0.09	1509	0.01	0.03	0.06	21	0	0.01	0.02	14
	17	0.3	3264	0.01	0.04	0.08	30	0	0.02	0.05	42
Average		0.134	2242	0.02	0.04	0.07	27	0	0.01	0.02	24
(2,4,6)	16	0.2	1282	0.02	0.04	0.06	26	0	0	0	25
	17	0.16	1302	0.01	0.03	0.05	21	0	0	0	11
	17	0.19	1324	0.02	0.06	0.07	29	0	0	0	20
	18	0.4	2102	0.01	0.02	0.03	17	0	0	0.02	25
	18	0.39	2045	0.01	0.02	0.04	32	0	0.01	0.03	33

Average		0.268	1651	0.01	0.03	0.05	25	0	0	0.01	23
	18	0.2	1425	0	0.02	0.02	16	0	0	0	14
	18	0.24	1670	0.01	0.01	0.02	24	0	0	0	14
(2,5,5)	19	0.23	1710	0.04	0.04	0.04	25	0	0	0	15
	20	0.29	1754	0	0.01	0.02	16	0	0	0	18
	20	0.33	1826	0.01	0.01	0.02	18	0	0.01	0.02	16
Average		0.258	1677	0.01	0.02	0.03	20	0	0	0	15
Overall average		0.11	1721	0.01	0.02	0.03	22	0	0	0	16

TABLE 3. Medium and large instances

Instance		MILP		GA			GADP				
(k,P,f)	N	Quality	Time	Min	Ave	Max	Time	Min	Ave	Max	Time
	17	0.21	1357	0	0.01	0.02	25	0	0	0.01	15
	17	0.29	1331	0	0.01	0.03	16	0	0.01	0.03	18
(3,5,5)	18	0.22	1423	0	0.01	0.02	30	0	0.01	0.01	25
	18	0.25	1590	0	0	0.02	28	0	0	0.02	21
	20	0.2	1561	0	0.01	0.01	49	0	0.01	0.01	38
Average		0.23	1452	0	0.01	0.02	30	0	0.01	0.01	23
	24	0.31	1104	0	0.01	0.05	27	0	0	0.01	29
	24	0.35	1254	0.01	0.01	0.02	38	0	0	0	40
(3,5,7)	25	0.25	1038	0.01	0.01	0.03	37	0	0	0	28
	26	0.3	1361	0	0.02	0.04	61	0.02	0.03	0.04	33
	26	0.26	3995	0.02	0.03	0.03	43	0	0.01	0.01	40
Average		0.29	1750	0.01	0.02	0.03	41	0	0.01	0.01	34
	28	0.3	1602	0	0.02	0.08	72	0	0	0	80
	29	0.39	1632	0	0.01	0.03	65	0	0.01	0.01	93
(3,4,10)	30	0.2	1423	0	0.05	0.11	55	0	0.04	0.08	65
	30	0.35	1506	0	0.06	0.14	55	0	0.02	0.03	53
	31	0.37	1610	0	0.06	0.06	160	0	0.02	0.06	65
Average		0.23	1554	0	0.04	0.08	82	0	0.02	0.04	71
	38	0.23	2010	0	0.04	0.08	137	0	0.01	0.03	115
	39	0.28	7200	0	0.03	0.08	165	0	0.03	0.05	144
(3,5,11)	40	0.23	4251	0.04	0.05	0.08	155	0	0.01	0.01	133
	40	0.27	7200	0.02	0.07	0.11	140	0	0.01	0.03	146
	41	0.15	1568	0.02	0.08	0.12	150	0	0.02	0.04	142
Average		0.23	4390	0.02	0.05	0.1	150	0	0.02	0.09	136
	45	0.38	5487	0.05	0.09	0.12	224	0	0.02	0.03	223
	45	0.4	7200	0.08	0.13	0.16	189	0	0.08	0.12	196
(3,5,13)	45	0.1	3546	0.03	0.06	0.08	217	0	0.04	0.08	199
	47	0.27	6754	0	0.01	0.02	240	0	0.01	0.03	229
	48	0.3	6542	0.1	0.14	0.16	246	0	0.06	0.12	236
Average		0.29	5890	0.05	0.09	0.11	223	0	0.04	0.08	216
	54	0.35	7200	0.02	0.08	0.1	354	0	0.02	0.05	351
	55	0.14	6723	0.01	0.04	0.08	362	0	0.02	0.04	357
(4,7,10)	56	0.32	7200	0.05	0.09	0.11	384	0	0.02	0.03	374
	57	*	7200	0.02	0.04	0.06	402	0	0.03	0.04	396
	57	*	7200	0	0.03	0.06	431	0	0.04	0.07	420
Average		0.29	7104	0.02	0.06	0.08	387	0	0.03	0.05	380
Overall average		0.26	3690	0.02	0.05	0.07	153	0	0.02	0.05	143

GA can obtain optimal solutions for 10 small instances. On the very small and small instances and some of the medium instances, the results obtained from GA are comparable with those of MILP in the solution quality, although GA outperforms MILP in terms of CPU time; by increasing the size of the instances, GA outperforms in terms of solution quality as well.

Furthermore, GADP is able to achieve optimal solutions for all of the instances including up to 14 jobs that the optimality is verified by GAMS. GADP is successful in performance even for the instances with a large number of jobs; in addition, the worst and the best results obtained by GADP indicate insignificant differences.

Although GADP and GA both perform the same in terms of solution quality for the some instances with up to 2 production lines, 3 products, 5 customers and 12 jobs, by increasing the size of instances, GA fails to compete with GADP; even the worst results achieved by GADP are better in comparison with the best results obtained by GA.

Moreover, according to CPU time, except for four small instances, GA requires more computational effort than GA, due to lack of the dominance properties which play a significant role in the intensification of the search; by producing numerous additional solutions compared to GADP, GA converges to a final solution.

Two interval plots are depicted for final solution (cost) and computational time. Error ratio of these interval plots is set 0.05. The 95% confidence interval plots of the three algorithms have been depicted for the cost in Figure 2. The 95% confidence interval plots of these algorithms are shown for the computational time in Figure 3. From Figure 2, it is perceived that the two algorithms have significant differences in obtained final solution. Moreover, the considerable differences among the computational time of GA and GADP.

Therefore, applying the dominance properties to obtain better solutions in comparatively shorter computation times is recommended. Generally, based on

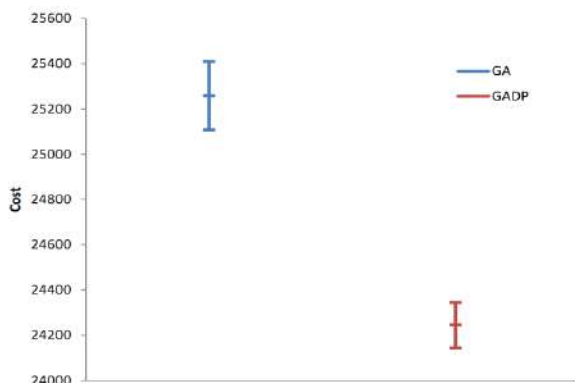


Figure 2. Confidence interval of GA and GADP for final solution

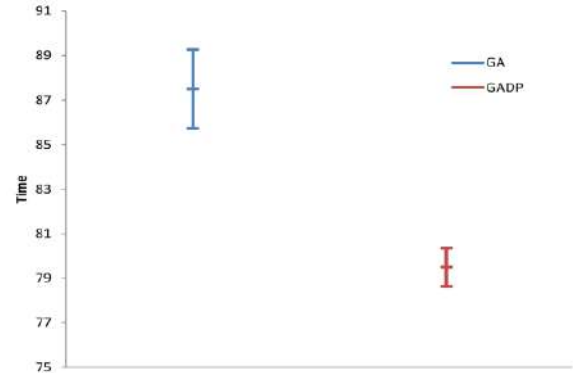


Figure 3. Confidence interval of GA and GADP for computational time

the computational results, GADP can be regarded as fast and robust as well as capable to provide an efficient approach to gain optimal or near- optimal solutions with small computational necessity.

7. CONCLUSION

The need to minimize the amount of inventory across the supply chain and to be responsive to customers' requests indicates the importance of using cooperated production and distribution models. To handle demand fluctuations without holding a high inventory forces manufacturer to outsource some jobs to a sub-contractor.

In this paper, a new integrated production scheduling, vehicle routing, inventory and outsourcing problem is modelled. Production phase considers parallel machine scheduling including setup times with outsourcing allowed and distribution phase investigates batch delivery by a fleet of homogenous vehicles with respect to holding cost of completed jobs. An example of this problem can be seen in dairy factory and paste factory. The aim of this paper is to find a schedule for joint in-house production and distribution as well as to determine the jobs that must be outsourced in the way that minimizes total cost of production, holding, outsourcing and distribution. The production cost consists of sequence-dependent set-up cost. The distribution cost consists of tardiness penalties and fixed vehicle usage cost and variable travel time proportional cost.

This paper presents a mathematical model for describing the problem and designs a hybrid algorithm using dominance properties combined with Genetic Algorithm (GA). Generating the initial population and improving the quality of solutions generated by the GA can be significantly affected by the dominance properties applied as a local search strategy. Finally, computational experiments are performed to evaluate the performance of solution approach. Therefore, applying the dominance properties to obtain better solutions in comparatively

shorter computation times is recommended. Generally, based on the computational results, GADP can be regarded as fast and robust as well as being capable to provide an efficient approach to gain optimal or near-optimal solutions with small computational necessity.

For future studies, we suggest utilizing a two-level distribution model including distribution centres in the first level and customers (i.e. retailers) in the second level. This type of distribution is able to cover more customer areas in scattered geographic location. Furthermore, outsourcing option is rarely considered in the literature. It is suggested to study the context of outsourcing option in the future works to fill this research gap.

8. REFERENCES

1. Taghizadehalvandi, M., and Kamisli Ozturk, Z. "Multi-objective Solution Approaches for Employee Shift Scheduling Problems in Service Sectors (RESEARCH NOTE)." *International Journal of Engineering, Transactions C: Aspects*, Vol. 32, No. 9, (2019), 1312–1319. <https://doi.org/10.5829/ije.2019.32.09c.12>
2. Amin-Tahmasb, H., and Hami, M. "Optimization of a Bi-objective Scheduling for Two Groups of Experienced and Inexperienced Distribution Staff Based on Capillary Marketing." *International Journal of Engineering, Transactions B: Applications*, Vol. 31, No. 11, (2018), 1943–1952. <https://doi.org/10.5829/ije.2018.31.11b.19>
3. Sarmiento, A. M., and Nagi, R. "A review of integrated analysis of production-distribution systems." *IIE Transactions (Institute of Industrial Engineers)*, Vol. 31, No. 11, (1999), 1061–1074. <https://doi.org/10.1080/07408179908969907>
4. Chang, Y. C., Li, V. C., and Chiang, C. J. "An ant colony optimization heuristic for an integrated production and distribution scheduling problem." *Engineering Optimization*, Vol. 46, No. 4, (2014), 503–520. <https://doi.org/10.1080/0305215X.2013.786062>
5. Ahmadizar, F., and Amiri, Z. "Outsourcing and scheduling for a two-machine flow shop with release times." *Engineering Optimization*, Vol. 50, No. 3, (2018), 483–498. <https://doi.org/10.1080/0305215X.2017.1325483>
6. McIvor, R. "The influence of capability considerations on the outsourcing decision: The case of a manufacturing company." *International Journal of Production Research*, Vol. 48, No. 17, (2010), 5031–5052. <https://doi.org/10.1080/00207540903049423>
7. Qi, X. "Outsourcing and production scheduling for a two-stage flow shop." *International Journal of Production Economics*, Vol. 129, No. 1, (2011), 43–50. <https://doi.org/10.1016/j.ijpe.2010.08.011>
8. Amorim, P., Belo-Filho, M. A. F., Toledo, F. M. B., Almeder, C., and Almada-Lobo, B. "Lot sizing versus batching in the production and distribution planning of perishable goods." *International Journal of Production Economics*, Vol. 146, No. 1, (2013), 208–218. <https://doi.org/10.1016/j.ijpe.2013.07.001>
9. Van Buer, M. G., Woodruff, D. L., and Olson, R. T. "Solving the medium newspaper production/distribution problem." *European Journal of Operational Research*, Vol. 115, No. 2, (1999), 237–253. [https://doi.org/10.1016/S0377-2217\(98\)00300-2](https://doi.org/10.1016/S0377-2217(98)00300-2)
10. Chen, Z. L., and Vairaktarakis, G. L. "Integrated scheduling of production and distribution operations." *Management Science*, Vol. 51, No. 4, (2005), 614–628. <https://doi.org/10.1287/mnsc.1040.0325>
11. Li, C. L., and Vairaktarakis, G. "Coordinating production and distribution of jobs with bundling operations." *IIE Transactions (Institute of Industrial Engineers)*, Vol. 39, No. 2, (2007), 203–215. <https://doi.org/10.1080/07408170600735561>
12. Chang, Y. C., and Lee, C. Y. "Machine scheduling with job delivery coordination." *European Journal of Operational Research*, Vol. 158, No. 2, (2004), 470–487. [https://doi.org/10.1016/S0377-2217\(03\)00364-3](https://doi.org/10.1016/S0377-2217(03)00364-3)
13. Li, C. L., Vairaktarakis, G., and Lee, C. Y. "Machine scheduling with deliveries to multiple customer locations." *European Journal of Operational Research*, Vol. 164, No. 1, (2005), 39–51. <https://doi.org/10.1016/j.ejor.2003.11.022>
14. Geismar, J. H. N., Laporte, G., Lei, L., and Sriskandarajah, C. "The integrated production and transportation scheduling problem for a product with a short lifespan." *INFORMS Journal on Computing*, Vol. 20, No. 1, (2008), 21–33. <https://doi.org/10.1287/ijoc.1060.0208>
15. Chen, H. K., Hsueh, C. F., and Chang, M. S. "Production scheduling and vehicle routing with time windows for perishable food products." *Computers and Operations Research*, Vol. 36, No. 7, (2009), 2311–2319. <https://doi.org/10.1016/j.cor.2008.09.010>
16. Ullrich, C. A. "Integrated machine scheduling and vehicle routing with time windows." *European Journal of Operational Research*, Vol. 227, No. 1, (2013), 152–165. <https://doi.org/10.1016/j.ejor.2012.11.049>
17. Belo-Filho, M. A. F., Amorim, P., and Almada-Lobo, B. "An adaptive large neighbourhood search for the operational integrated production and distribution problem of perishable products." *International Journal of Production Research*, Vol. 53, No. 20, (2015), 6040–6058. <https://doi.org/10.1080/00207543.2015.1010744>
18. Kang, H. Y., Pearn, W. L., Chung, I. P., and Lee, A. H. I. "An enhanced model for the integrated production and transportation problem in a multiple vehicles environment." *Soft Computing*, Vol. 20, No. 4, (2016), 1415–1435. <https://doi.org/10.1007/s00500-015-1595-7>
19. Li, K., Zhou, C., Leung, J. Y. T., and Ma, Y. "Integrated production and delivery with single machine and multiple vehicles." *Expert Systems with Applications*, Vol. 57, (2016), 12–20. <https://doi.org/10.1016/j.eswa.2016.02.033>
20. Karaođlan, İ., and Kesen, S. E. "The coordinated production and transportation scheduling problem with a time-sensitive product: a branch-and-cut algorithm." *International Journal of Production Research*, Vol. 55, No. 2, (2017), 536–557. <https://doi.org/10.1080/00207543.2016.1213916>
21. Devapriya, P., Ferrell, W., and Geismar, N. "Integrated production and distribution scheduling with a perishable product." *European Journal of Operational Research*, Vol. 259, No. 3, (2017), 906–916. <https://doi.org/10.1016/j.ejor.2016.09.019>
22. Lacomme, P., Moukrim, A., Quilliot, A., and Vinot, M. "Supply chain optimisation with both production and transportation integration: multiple vehicles for a single perishable product." *International Journal of Production Research*, Vol. 56, No. 12, (2018), 4313–4336. <https://doi.org/10.1080/00207543.2018.1431416>
23. Tamanna, M., and Rasti-Barzoki, M. "Mathematical programming and solution approaches for minimizing tardiness and transportation costs in the supply chain scheduling problem." *Computers and Industrial Engineering*, Vol. 127, (2019), 643–656. <https://doi.org/10.1016/j.cie.2018.11.003>
24. Tavares-Neto, R. F., and Nagano, M. S. "An Iterated Greedy approach to integrate production by multiple parallel machines and distribution by a single capacitated vehicle." *Swarm and Evolutionary Computation*, Vol. 44, (2019), 612–621. <https://doi.org/10.1016/j.swevo.2018.08.001>

25. Mohammadi, S., Al-e-Hashem, S. M. J. M., and Rekik, Y. "An integrated production scheduling and delivery route planning with multi-purpose machines: A case study from a furniture manufacturing company." *International Journal of Production Economics*, Vol. 219, (2020), 347–359. <https://doi.org/10.1016/j.ijpe.2019.05.017>
26. Mousavi, M., Hajiaghahi-Keshteli, M., and Tavakkoli-Moghaddam, R. "Two calibrated meta-heuristics to solve an integrated scheduling problem of production and air transportation with the interval due date." *Soft Computing*, Vol. 24, No. 21, (2020), 16383–16411. <https://doi.org/10.1007/s00500-020-04948-y>
27. L., I., F., A., and J., A. "A Hybrid Imperialist Competitive Algorithm for Integrated Scheduling of Production and Distribution with Vehicle Routing." *Journal of Industrial Engineering Research in Production Systems*, Vol. 6, No. 12, (2018), 63–81. Retrieved from <https://www.sid.ir/en/Journal/ViewPaper.aspx?ID=711650>
28. Ahmadizar, F., and Farhadi, S. "Single-machine batch delivery scheduling with job release dates, due windows and earliness, tardiness, holding and delivery costs." *Computers and Operations Research*, Vol. 53, (2015), 194–205. <https://doi.org/10.1016/j.cor.2014.08.012>
29. Chang, P. C., Chen, S. H., and Mani, V. "A hybrid genetic algorithm with dominance properties for single machine scheduling with dependent penalties." *Applied Mathematical Modelling*, Vol. 33, No. 1, (2009), 579–596. <https://doi.org/10.1016/j.apm.2008.01.006>
30. Chang, P. C., and Chen, S. H. "Integrating dominance properties with genetic algorithms for parallel machine scheduling problems with setup times." *Applied Soft Computing Journal*, Vol. 11, No. 1, (2011), 1263–1274. <https://doi.org/10.1016/j.asoc.2010.03.003>
31. Ahmadizar, F., and Hosseini, L. "Bi-criteria single machine scheduling with a time-dependent learning effect and release times." *Applied Mathematical Modelling*, Vol. 36, No. 12, (2012), 6203–6214. <https://doi.org/10.1016/j.apm.2012.02.002>
32. Holland, J. H. *Adaptation in natural and artificial systems: an introductory analysis with applications to biology, control and artificial intelligence*. MIT press, 1975. Retrieved from <https://ui.adsabs.harvard.edu/abs/1975anas.book....H/abstract>
33. Goldenberg, D. *Genetic algorithms in search, optimization and machine learning*. Addison-Wesley Publishing Company, 1989.
34. Davis, L. *Handbook of genetic algorithms*. Van Nostrand Reynold, 1991. Retrieved from <http://papers.cumincad.org/cgi-bin/works/paper/eaca>
35. Talbi, E. *Metaheuristics: from design to implementation*. John Wiley & Sons, 2009. Retrieved from https://books.google.com/books?hl=en&lr=&id=SIsa6zi5XV8C&oi=fnd&pg=PR7&ots=-bPJrReuCr&sig=kqHlxfQssPePngA0_zVafx3ljQs
36. Gendreau, M., and Potvin, J. *Handbook of metaheuristics*. Springer, 2010. Retrieved from <https://link.springer.com/content/pdf/10.1007/978-1-4419-1665-5.pdf>
37. Suzuki, J. "A Markov Chain Analysis on Simple Genetic Algorithms." *IEEE Transactions on Systems, Man, and Cybernetics*, Vol. 25, No. 4, (1995), 655–659. <https://doi.org/10.1109/21.370197>
38. Lozano, J. A., Larrañaga, P., Graña, M., and Albizuri, F. X. "Genetic algorithms: Bridging the convergence gap." *Theoretical Computer Science*, Vol. 229, No. 1–2, (1999), 11–22. [https://doi.org/10.1016/S0304-3975\(99\)00090-0](https://doi.org/10.1016/S0304-3975(99)00090-0)
39. Tavares Neto, R. F., Godinho Filho, M., and da Silva, F. M. "An ant colony optimization approach for the parallel machine scheduling problem with outsourcing allowed." *Journal of Intelligent Manufacturing*, Vol. 26, No. 3, (2015), 527–538. <https://doi.org/10.1007/s10845-013-0811-5>

Persian Abstract

چکیده

در این مقاله، یک مسأله جدید زمانبندی ادغامی تولید و مسیریابی وسایل نقلیه، با در نظر گرفتن برونسپاری و موجودی مورد مطالعه قرار گرفته است. بخش تولید، زمانبندی ماشین‌های موازی با در نظر گرفتن زمان‌های آماده‌سازی و مجاز بودن برونسپاری را بررسی می‌کند و بخش توزیع، تحویل دسته‌ای توسط یک ناوگان از وسایل حمل یکسان با در نظر گرفتن هزینه نگهداری کارهای تکمیل شده را بررسی می‌کند. مسأله به صورت برنامه‌ریزی خطی عدد صحیح فرموله شده و هدف، حداقل ساختن مجموع هزینه‌های تولید، برونسپاری، نگهداری، تأخیر و ثابت و متغیر حمل است. به دلیل **Np-hard** بودن، برای حل مسأله تعدادی قواعد غلبه استخراج شده و با یک الگوریتم ژنتیک ادغام شده است. برای ارزیابی کارایی و اثربخشی الگوریتم ترکیبی پیشنهادی، بر روی تعدادی نمونه مسائل تصادفی تولیدی مطالعه عددی انجام شده است. به منظور نشان دادن تأثیر پارامترهای کلیدی بر تابع هدف، آنالیز حساسیت انجام شده است. برای ارزیابی معناداری تفاوت جواب‌های به دست آمده از الگوریتم پیشنهادی با الگوریتم ژنتیک، آزمون آماری f انجام شده و نمودارهای بازه‌ای رسم شده است.



Application of Incomplete Analytic Hierarchy Process and Choquet Integral to Select the best Supplier and Order Allocation in Petroleum Industry

N. Maleki, M. Bagherifard, M. R. Gholamian*

School of Industrial Engineering, Iran University of Science and Technology (IUST), Tehran, Iran

PAPER INFO

Paper history:

Received 24 June 2020
Received in revised form 28 July 2020
Accepted 03 September 2020

Keywords:

Supplier Selection
Petroleum Industry
Multi-objective Linear Programming
Incomplete Analytic Hierarchy Process
Choquet Integral
 ϵ -constraint Method

ABSTRACT

In a powerful industry, supplier selection is one of the complex processes that can increase productivity and competitive advantages. Supplier selection includes different quantitative, qualitative, and also interactive criteria. In addition, the selection process has always faced with inadequate and incomplete data. Multi-criteria decision making (MCDM) is a useful approach that can be applied, for addressing the opting problems of a supplier considering mentioned issues. In this approach, the interaction between criteria can be considered with several methods, such as Choquet integral, which is a practical method for decision ranking. Also, incomplete data can be covered with incomplete analytic hierarchy process (AHP) method. Therefore, in this study, an application of Choquet integral along with incomplete AHP method is provided for supplier selection problem at the petroleum industry. After achieving the ranking rate of suppliers, requested orders are assigned to preferred suppliers by using multi-objective linear programming (MOLP) model and ϵ -constraint method to generate the Pareto optimal points. As a result, supplier 3 with weight 0.8274 was the most preferred supplier in which 50% of total orders was assigned to this supplier as the best selection.

doi: 10.5829/ije.2020.33.11b.20

1. INTRODUCTION

Reducing production costs in today's highly competitive organizations has always been a concern. Due to the large part of the total manufacturing cost, which is comprised of the cost of raw materials and components cost, selecting the most appropriate suppliers can significantly reduce the purchasing cost and increase the competitiveness of an organization. Companies endeavour to focus on their core business activities, and to outsource other activities. Subsequently, product quality, service delivery, and business performance are affected by the selection of supplier organizations. Increasing competition, market share, and business developments have altered the way of dealing with buyers and suppliers. Under these new circumstances, enhancing sustainable and collaborative relationships with suppliers can reduce costs and increase flexibility

against market changes. To increase profits, organizations should select appropriate suppliers, enhance strategic relations, and interact in an effective manner with them.

Selecting appropriate suppliers is necessary for oil and gas refineries and organizations. Supplier selection is a complex operation for engineering, procurement, and construction (EPC) contracts, which are large and critical. Decision-making operation in supplier selection requires multiple criteria [1]. Therefore, this investigation has been directed towards supplier selection that is devised as a Multi-criteria Decision Making (MCDM) method. Besides, organizations should select some of the given suppliers and allocate the best order in conformity with their performance due to considered criteria [2].

MCDM techniques assorted by Ho, et al. [3] and incorporated for selecting suppliers [4]. All these

*Corresponding Author Institutional Email: gholamian@iust.ac.ir
(M. R. Gholamian)

methods have the potential to cover different preferences of decision-makers. However, one of MCDM techniques called AHP is employed in many supplier selection researches. In other words, in reality, most criteria and sub-criteria have interaction with each other [5]; while the conventional methods of decision-making consider that the criteria are autonomous and independent from each other. This assumption puts limits on representing the best alternative [6]. As a solution, Choquet Integral has been applied for considering interaction among criteria and sub-criteria; although this method has been used in a few cases with actual applications [7].

Here, incomplete AHP with absolute deviation method and Choquet integral are applied for supplier selection and order allocation model, based on considered refinery experts' opinion. In other words, the purpose of this study is to select suppliers and allocate the best and optimal orders to them through unclear and ill-defined information *via* two complementary MCDM methods that deal with the problem.

The study is organized as follows: section 2, provides an exhaustive literature review on incomplete AHP and Choquet integral, then section 3 introduces preliminaries of these methods. After that, in section 4, some information about the considered case study is given. Additionally, for allocating, the usage of incomplete AHP and Choquet integral for supplier selection and Multi-Objective Linear Programming (MOLP) are presented. In section 5, relates to the model are given. Section 6 ends the study with the conclusion and future work recommendations.

2. LITERATURE REVIEW

Industries have used various methods for supplier selection process in recent years. Selecting the most authentic suppliers and preserving long-run cooperation with them is one of the most crucial decisions for all industries, especially those that relate to the petroleum and refinery plants. Practical methods in selection procedure should be implemented since choosing the right suppliers, which include qualitative and quantitative elements, is an important issue [8]. Some methods try to select the best supplier and some others are look for ranking the suppliers based on the gained rate.

Fuzzy TOPSIS method mixed with AHP method for oil project selection [9], and the combination of SCOR, AHP and TOPSIS approaches for supplier selection in the gas and oil industry are examples in this area [10].

With considering the type of companies and materials, different methods have been used in an integrated supplier selection problem, such as AHP for supplier performance rating in gas and oil exploration and production companies [11-12], SWOT and fuzzy

TOPSIS with linear programming for order allocations [13] and entropy weightings method with intuitionistic fuzzy TOPSIS to develop petroleum industry facilities [1].

Few studies in supplier selection through considering interaction between criteria exist. Fuzzy TOPSIS and generalized Choquet integral have been used separately to find a supplier selection problem [14]. In addition, to integrate criteria continuously, a method developed based on fuzzy integral was formulated [15]. Besides, AHP and fuzzy TOPSIS were used to identify the best suppliers, and a multi-period multi-objective optimization model was employed for allocating orders [16]. By taking subjective measures into account, fuzzy MULTIMOORA for selecting suppliers and fuzzy goal programming for deciding about the quantity of order allocation were used [17]. Meanwhile, by considering all-unit quantity discounts and two sets of criteria separately: traditional and green, fuzzy TOPSIS and AHP were implemented in supplier selection problem. Afterward, a single-product bi-objective integer linear programming model was used to allocate orders [18]. On the other hand, based on the mentioned studies, the application of incomplete AHP method was reviewed in this field. Pairwise comparison matrix (PCM) is an essential part of AHP. However, in many cases, it is hard to be completed and this makes incomplete information. Geometric mean, as a basic method, method was proposed by Harker [19]. Many subsequent studies were suggested by Harker's method as different methods to calculate the weights of criteria in incomplete AHP, as discussed in literature [20-21]. To this end, the least square method (LSM) is an effective one. Several studies deal with incomplete information by this method in order to estimate the comparative weight of alternatives [22]. In some of them, the logarithmic form of LSM (LLSM) has been used to solve nonlinear systems of LSM [23-25]. Additionally a homotopy procedure has been introduced [26]. In numerous studies, the LSM method was developed [27-28] in incomplete form by considering limitation on ordinal consistency. This opinion was approved by the equivalent multiplicative and additive form of LLSM. Other studies have been presented an explanation of multiplicative consistent by the LLSM method in an incomplete fuzzy preference relation [29]. By considering all of these applications, one can realize that LLSM is a simple, fine-tunable method for calculating the weight of incomplete AHP. To best of our knowledge and according to previous studies, with incomplete data, combination of incomplete AHP and Choquet integral has not been investigated. Whilst in many real-world case studies, there are always flaws in the received information from decision makers and in other hand, the criteria are not independent, and hence ignoring these facts will cause deviations from right decisions.

Therefore, in this study, we have tried to introduce a combination method of incomplete AHP and Choquet integral by minimizing the percentage error of decisions and considering the interactions between criteria. Then, a novel multi-objective model was introduced for allotting order to suppliers, with considering products guarantees.

3. PRELIMINARIES

3.1. Analytic Hierarchy Process (AHP) AHP has been applied in multi-criteria decision-making (MCDM) to identify priority of alternatives. The concept of this method is to illustrate the problem by using a hierarchy process that is, in fact, a presentation of the entire problem [30].

Based on this hierarchy process, the preference of alternatives can be obtained from the comparison operation by the decision-maker (DM) [31]. These preferences are presented as pairwise comparison matrix (PCM) by a 1 to 9 ratio scales as Table 1.

Definition 1. A matrix M is called pairwise comparison if it complies the condition $a_{ij} = \frac{1}{a_{ji}}$ for all i, j .

Definition 2. A matrix M is called consistent if it complies with the condition $a_{ij} \cdot a_{jk} = a_{ik}$ for all i, j, k . Preferences of decision-makers are declared subjectively; as a result, it is sensible for the existence of inconsistency in the decision matrix. To measure the degree of this inconsistency, the consistency index (CI) is presented by Saati [32].

If λ_{max} gives the eigenvalues of matrix M as follow:

$$M \cdot W = \lambda_{max} \cdot W \tag{1}$$

Then CI and consistency ratio (CR) is calculated in the following order:

$$CI = \frac{\lambda_{max} - n}{n - 1} \tag{2}$$

$$CR = \frac{CI}{RI} \tag{3}$$

TABLE 1. Saati's scales

Explanation	Definition	Score
Two criteria are of equal importance	equal importance	1
The importance of i is a little more than j	a little more importance	3
The importance of i is more than j	more important	5
The importance of i much more than j	much more importance	7
i is of absolute importance than j	absolute importance	9
When there are intermediate modes	intermediate modes	2,4,6,8

If $CR < 0.1$, the comparison matrix is accepted; otherwise, the preferences of the DMs are adjusted until $CR < 0.1$ [32].

Definition 3. Random index (RI) depends on the dimension of the comparison matrix that is given as Table 2 [32].

Definition 4. An incomplete pairwise comparisons matrix M is like as below, where the * mark indicates unknown elements:

$$M = \begin{bmatrix} 1 & * & a_{13} \\ * & 1 & a_{23} \\ a_{31} & a_{32} & 1 \end{bmatrix}$$

3.1.1. Least Square Method for Incomplete AHP

It is necessary to assess the incomplete information for determining the weights [33]. Therefore, LSM can be used in incomplete AHP to calculate the ratings as follows. The objective function is sum of the square of errors and the constraints represent the weighting conditions:

$$\begin{aligned} \min & \sum_{i=1}^n \sum_{j=1}^n \delta_{ij} (a_{ij} w_j - w_i)^2 \\ \text{s.t.} & \sum_{i=1}^n w_i = 1 \\ & w_i \geq 0, i = 1, 2, \dots, n \end{aligned} \tag{4}$$

$$\text{Where } \delta_{ij} = \begin{cases} 0 & a_{ij} \text{ is missing} \\ 1 & \text{otherwise} \end{cases}$$

3.2. Choquet Technique

By considering monotonous property, which can substitute additive property with a monotony property, and taking into account the potential interplay between criteria on computation, the importance of criterion and their coalitions are implied by fuzzy measurement theory method to the model [33].

Definition 5. Where $F(X)$ is power set for the finite set of criteria $x = \{x_1, x_2, \dots, x_n\}$. So, μ can be defined on $F(X)$ as non-additive fuzzy capacity with following properties [34].

- Boundary condition: $\mu(\varphi) = 0$ & $\mu(x) = 1$
- Monotonicity condition: If $A_1, A_2 \in F(x)$ & $A_1 \subseteq A_2$, then $\mu(A_1) \leq \mu(A_2)$

3.2.1. Calculating λ Fuzzy Measure

Definition 6. The λ fuzzy measure presents the interaction between each paired set like A_1 and A_2 , according to the following equation:

$$\mu(x) = \begin{cases} -\frac{1}{\lambda} [\prod_{i=1}^n (1 + \lambda \mu(x_i)) - 1] & \text{if } \lambda \neq 0 \\ \sum_{i=1}^n \mu(x_i) & \text{if } \lambda = 1 \end{cases} \tag{5}$$

TABLE 2. Random index

N	3	4	5	6	7	8	9	10
Ri	0.58	0.9	1.12	1.1	1.3	1.41	1.45	1.49

The λ parameter can be implied by boundary condition $\mu(x) = 1$, which is resulted by the following equation.

$$\lambda + 1 = \prod_{i=1}^n (1 + \lambda\mu(x_i)) \tag{6}$$

where μ is the fuzzy capacity on power set $F(X)$, and $A_1 \cap A_2 = \emptyset$. Thus, the following equation is demonstrated [33]:

$$\mu(A_1 \cup A_2) = \mu(A_1) + \mu(A_2) + \lambda\mu(A_1)\mu(A_2) \tag{7}$$

Of which $\lambda \in [-1, \infty] \forall A_1, A_2 \in F(x)$

3. 2. 2. Ranking Alternatives through the Choquet Fuzzy Integral

Definition 7. Let f be a measurable function on the set $x = \{x_1, x_2, \dots, x_n\}$, and μ be a fuzzy capacity on x then:

$$\int f d\mu = \sum_{i=1}^n \mu(x_i) [h(x_i) - h(x_{i-1})] \tag{8}$$

And also the following equation is considerable [3].

$$\int f d\mu = f(x_n) \cdot [\mu(H_n) - \mu(H_{n-1})] + f(x_{n-1}) \cdot [\mu(H_{n-1}) - \mu(H_{n-2})] + \dots + f(x_1) \cdot \mu(H_1) \tag{9}$$

Where $H_1 = \{x_1\}$, $H_2 = \{x_1, x_2\}$... $H_3 = \{x_1, x_2, \dots, x_n\}$
 Total weight of each supplier can be calculated with the fuzzy integral, which is determined in Equation (9) by addressing the Choquet integral. As mentioned, by using of the fuzzy integral, the interactions between criteria and sub-criteria have also been considered.

3. 3. Multi-objective Order Allocation Model

Assumption:

- i. Demand is constant
- ii. For any suppliers, shortage of the supplied product is not allowed
- iii. Transportation cost, holding cost and ordering cost is including in purchasing price
- iv. Single-Product is ordered from supplier with any quantity.

Index	
i	Index for suppliers = 1, 2... n .
Variable	
x_i	product order quantity from supplier i .
Parameters	
c_i	The product supply capacity of supplier i .
p_i	Purchasing price of products from supplier i .
Q	Maximum allowed defect value of the products.
q_i	Average defect percentage of the products from supplier i .
L	Maximum allowed late delivery value of products.
d_i	Percentage of products delivered late by supplier i .
D	Demand for the products
W_i	Overall weight of supplier i obtained by Choquet integral
g_i	Percentage of the products that use guarantees by the supplier i .

G Maximum allowed value of the products that need to be guaranteed

Objective Function:

$$\text{Min } Z_1 = \sum_{i=1}^n P_i x_i \tag{10}$$

$$\text{Max } Z_2 = \sum_{i=1}^n W_i x_i \tag{11}$$

Here, two objective functions are explained: cost and total efficiency.

Equation (10) minimizes the total cost, and Equation (11) represents the applicable aim to maximize the organizational efficiency by the received results from Choquet.

The constraints are presented as below:

$$\sum_{i=1}^n x_i = D \tag{12}$$

$$x_i \leq C_i \tag{13}$$

$$\sum_{i=1}^n q_i x_i \leq Q \tag{14}$$

$$\sum_{i=1}^n d_i x_i \leq L \tag{15}$$

$$\sum_{i=1}^n g_i x_i \leq G \tag{16}$$

$$x_i \geq 0 \tag{17}$$

They include demand satisfaction, the capacity of suppliers, banned admissible amount of quality rejection, the allowed value of late delivery quantities, allowed value of products that need to be guaranteed, and non-negativity constraint, respectively.

3. 3. 1. The Augmented ε -Constraint Method

The ε -constraint method is a well-known method for solving MOLP models to find a set of Pareto solutions. One of the ε -constraint methods that has been developed by Equation (18) is AUGMECON [35]. In this method, one objective function is optimized and the other objective functions act as constraints.

$$\text{Max}(z_1(x) + \varepsilon \times (s_2/r_2 + s_3/r_3 + \dots + (s_p/r_p))) \tag{18}$$

where ε is a sufficient slight number (generally between 10^{-3} and 10^{-6}), r_i is the variable range of i th objective function, and s_i is surplus or slack variable.

$$r_i = PIS_{fi} - NIS_{fi} \tag{19}$$

In Equation (19) PIS_{fi} and NIS_{fi} are ideal positive and negative solutions for i th objective function that are resulted from solving the model, only through this objective function.

Therefore, the linear programming model of order allocation problem, which includes two objectives and five sets of constraints, is calculated by the AUGMECON method with the help of GAMS (General Algebraic Modeling System) software.

4. CASE STUDY

In this section, application of the developed model based on a real-world case is explained to show its utility. The actual production demand data was provided by a case company for developing a new combination model of incomplete AHP, Choquet Integral, and MOLP to select suppliers and find an order plan.

4. 1. Explanation of the Subject and Recognition of Criteria

Heretofore, for supplier selection and order allocation problem, several MCDM techniques have been developed, however, the present combined model in this study was unnoticed. In addition, each main issue has been analyzed separately, and supplier selection and order allocation problems are discussed in two parts. An oil refinery is the case study, which plays a strategic role in the country's economy. Over the past few years, with the increase in foreign sanctions on Iran, oil companies were excluded from the oil and gas projects, and hence, the projects have been outsourced to domestic startups. Therefore, selecting appropriate suppliers and allocating the best orders is a vital issue for refinery's managers and has a significant and critical impact on the country's economy. In addition, if suppliers can encounter a refinery's requirements through right order allocation, the refinery can work in an efficient manner and raise benefits.

Through the numerous deliberation and discussions with refinery's experts, based on desired products,

reputation, history, competitive market advantage, and current strategies and by reviewing the pertinent studies, the criteria and sub-criteria for supplier selection problem were procured, so that 10 criteria were selected as shown in Table 3. Additionally, based on the supplier's product capacity, proposed price, location and delivery time, 5 potential alternatives (suppliers A1 to A5) were considered. Accordingly, the procedure of this study and the hierarchical process were developed and depicted in Figures 1 and 2, respectively.

TABLE 3. The criteria and sub-criteria for supplier selection

Criteria	Sub criteria	References
D ₁ Cost	c ₁₁ Material costs	[2] [10] [13] [36]
	c ₁₂ Transportation costs	[2] [10] [37]
	c ₂₁ On-time delivery	[11] [37]
D ₂ Delivery	c ₂₂ Delivery time	[11] [36]
	c ₂₃ Delivery capability	[37] [38]
	c ₃₁ Quality of product	[11] [17]
D ₃ Quality	c ₃₂ Quality control & standards	[2] [11] [13]
	c ₃₃ Quality certification	[1] [10] [11]
D ₄ Service	c ₄₁ after-sales services	[13] [37]
	c ₄₂ guarantees	[1] [37]

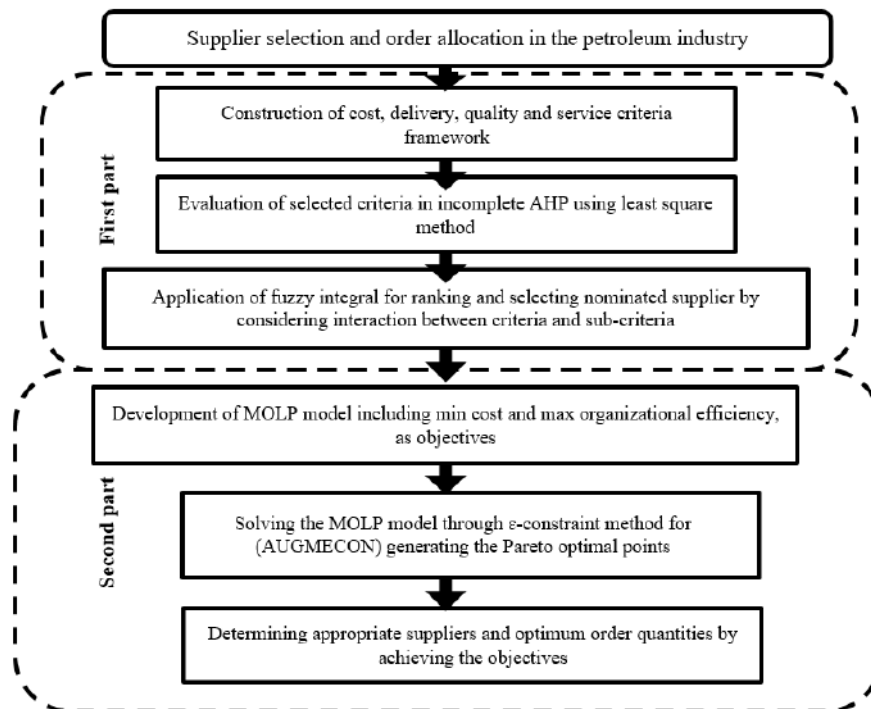


Figure 1. The procedure of this study

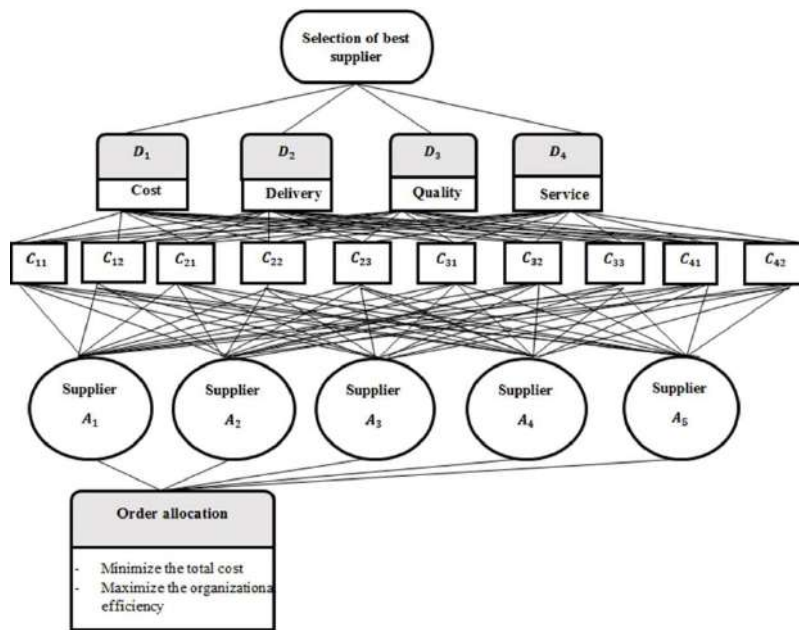


Figure 2. The hierarchical process of this study

4. 2. Matrix Collection and Processing

The mathematical computation in the AHP is simple, however, when dealing with incomplete information, this computation becomes more challenging. In this study, 16 primary *PCMs* were provided by 20 experts based on the criteria. Finally, several *PCMs*, as shown in Tables 4 (as an example) and 5 (as conclusion), were incomplete based on the following reasons:

- Lack of experts' knowledge
- Lack of experts' time

According to below incomplete *PCM(iPCM)*, for instance, regarding SC2 based on $M = (m_{ij})_{5 \times 5}$ ($i, j = 1, 2, \dots, 5$), m_{24} and m_{35} are two pairs of missing values.

$$\begin{bmatrix} 1 & 6.09 & 14.65 & 2.40 & 7.94 \\ 0.16 & 1 & 1.64 & * & 1.51 \\ 0.20 & 0.60 & 1 & 2.55 & * \\ 0.41 & * & 0.39 & 1 & 1.64 \\ 0.12 & 0.65 & * & 0.60 & 1 \end{bmatrix}$$

The issue is that what the method should be used in *iPCMs* for calculating the weight of criteria. In this section, the least square method (LSM) is applied by Equation (4) for calculating the weights (in both complete and incomplete *PCMs*) and the results are shown in Table 5, and local and global weights of alternative A_1 (as a sample) are summarized in Table 6. After calculating all the pairwise comparison matrices, the next step is to calculate the consistency of *PCMs* by Equation (3). Since *CR* is less than 10%, the *PCMs* can be considered consistent. Therefore, as a result of the Table 5, all *PCMs* and total hierarchical processes are consistent.

4. 3. Implementing Choquet Technique

Although the petroleum industry is a sensitive and tense industry and plays a very strategic role in the country's economy so, the right and accurate measurement can be very effective. However, surprisingly, the interaction between criteria and sub-criteria is often overlooked in its evaluations, analyses and decisions. Choquet Integral is able to consider certain types of interaction between criteria, and it makes Choquet Integral a powerful and necessary tool in petroleum industry decision making. In this section, the interaction among criteria is assessed by implementing the Choquet integral technique.

Mono and multi-members of fuzzy capacity sets, are extracted from the result of AHP as summarized in Table 7. To illustrate the calculations of Choquet integral, the calculation of D_2 for A_1 is presented as an example in Figure 3.

Finally, Table 8 represents the rate of each alternative, which is obtained from computing by Equation (9). The rank of each alternative is specified as $A_3 > A_1 > A_5 > A_4 > A_2$.

TABLE 4. Incomplete PCM for c_{12}

Transportati on costs	A ₁	A ₂	A ₃	A ₄	A ₅
A ₁	1	6.093	4.959	2.408	7.949
A ₂	0.164	1	1.643	*	1.515
A ₃	0.201	0.608	1	2.550	*
A ₄	0.415	*	0.392	1	1.643
A ₅	0.125	0.659	*	0.608	1

TABLE 5. λ_{max} and consistency rate (CR)

Pairwise Comparison Matrix	Complete	Incomplete	LSM	Weight	λ_{max}	CR	CR<0.1
PCMs for criteria		✓	✓		4.03	0.01	✓
PCMs for sub criteria	✓		✓		11.27	0.09	✓
PCMs for alternatives to SC1	✓		✓	0.32	5.44	0.09	✓
PCMs for alternatives to SC2		✓	✓	0.08	5.33	0.08	✓
PCMs for alternatives to SC3		✓	✓	0.17	5.29	0.03	✓
PCMs for alternatives to SC4	✓		✓	0.18	5.43	0.09	✓
PCMs for alternatives to SC5		✓	✓	0.06	5.40	0.08	✓
PCMs for alternatives to SC6	✓		✓	0.07	5.49	0.10	✓
PCMs for alternatives to SC7		✓	✓	0.05	5.45	0.10	✓
PCMs for alternatives to SC8	✓		✓	0.026	5.36	0.08	✓
PCMs for alternatives to SC9	✓		✓	0.004	5.41	0.09	✓
PCMs for alternatives to SC10		✓	✓	0.003	5.35	0.07	✓
PCMs for alternatives to C1	✓		✓	0.304	5.20	0.04	✓
PCMs for alternatives to C2	✓		✓	0.387	5.14	0.03	✓
PCMs for alternatives to C3	✓		✓	0.262	5.41	0.09	✓
PCMs for alternatives to C4	✓		✓	0.047	5.29	0.06	✓
Total hierarchical process						0.07	✓

TABLE 6. Local and global weights of alternative A₁

A ₁	Local	Global	D ₂	Local	Global	D ₃	Local	Global	D ₄	Local	Global
D ₁	0.119		D ₂	0.109		D ₃	0.368		D ₄	0.305	
c ₁₁	0.319	0.037	c ₂₁	0.28	0.03	c ₃₁	0.32	0.117	c ₄₁	0.297	0.09
c ₁₂	0.1	0.011	c ₂₂	0.227	0.024	c ₃₂	0.109	0.04	c ₄₂	0.103	0.031
			c ₂₃	0.216	0.023	c ₃₃	0.119	0.043			

TABLE 7. Criteria and sub criteria of fuzzy measures

Mono fuzzy measures		Multi fuzzy measures	
$\mu(D_1)$	0.301	$\mu(D_1, D_2)$	0.537
$\mu(D_2)$	0.278	$\mu(D_1, D_3)$	0.533
$\mu(D_3)$	0.273	$\mu(D_1, D_4)$	0.534
$\mu(D_4)$	0.146	$\mu(D_2, D_3)$	0.513
		$\mu(D_2, D_4)$	0.404
		$\mu(D_3, D_4)$	0.4
		$\mu(D_1, D_2, D_3, D_4)$	1
$\mu(C_{11})$	0.32	$\mu(C_{11}, C_{12})$	1
$\mu(C_{12})$	0.08		
$\mu(C_{21})$	0.17	$\mu(C_{21}, C_{22})$	0.389
$\mu(C_{22})$	0.18	$\mu(C_{21}, C_{23})$	0.34
$\mu(C_{23})$	0.06	$\mu(C_{22}, C_{23})$	0.349
$\mu(C_{31})$	0.07	$\mu(C_{31}, C_{32})$	0.395
$\mu(C_{32})$	0.05	$\mu(C_{31}, C_{33})$	0.216
$\mu(C_{34})$	0.026	$\mu(C_{32}, C_{33})$	0.147
$\mu(C_{41})$	0.004		
$\mu(C_{42})$	0.003	$\mu(C_{41}, C_{42})$	1

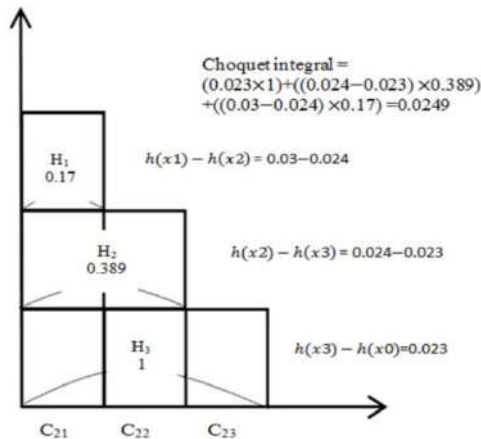


Figure 3. Choquet integral calculation for criteria D2

TABLE 8. The rate of alternatives

Suppliers	Rate	Rank
A ₁	0.1089	2
A ₂	0.0137	5
A ₃	0.8274	1
A ₄	0.0139	4
A ₅	0.0137	3

4. 4. Order Allocation Problem In this part, the order allocation problem for five potential suppliers is presented. The objective functions and constraints of the considered model were described in earlier sections. The extent of the best and optimal order for suppliers is calculated by Equations (10) to (17). Due to the suppliers' ability and capability, and refinery's demands, the following quantities are afforded: ($Q = 0.22\%$; $L = 0.39\%$; $G = 0.305\%$; $D=5000$ (Ton)), the capacity values and other information of each supplier are presented in Table 9.

In Table 9, capacity and purchasing price of each supplier are adapted by refinery's experts and average percentage of defect products (q_i), products delivered late (d_i), and products that use guarantees (g_i) are obtained from pairwise comparison matrices (PCM) in previous sections.

Objective function

$$\text{Min } Z_1 = 540x_1 + 570x_2 + 580x_3 + 570x_4 + 550x_5$$

$$\text{Max } Z_2 = 0.1089x_1 + 0.0137x_2 + 0.8274x_3 + 0.0139x_4 + 0.0362x_5$$

Subject to

$$x_1 + x_2 + x_3 + x_4 + x_5 = 5000$$

$$x_1 \leq 1500$$

$$x_2 \leq 1000$$

$$x_3 \leq 2500$$

$$x_4 \leq 2000$$

$$x_5 \leq 1500$$

$$\sum_{i=1}^n q_i x_i \leq 1100$$

$$\sum_{i=1}^n d_i x_i \leq 1950$$

$$\sum_{i=1}^n g_i x_i \leq 1525$$

$$x_i \geq 0, i=1 \dots 5$$

5. THE RESULT, SENSITIVITY ANALYSIS AND DISCUSSIONS

The augmented ϵ -constraint method produced 6 optimal Pareto solutions for order allocation calculation, as shown in Table 10. The augmented ϵ -constraint method determined the same number of interval solutions, by using grid points with equal distances. To get the preferable solution, each pair of optimal objective functions were depicted in Figure 4, which compares Pareto solution of objectives z_1 and z_2 ; and also product order quantity of each Pareto solution were shown in Figure 5. Finally, decision makers of the company selected solution number 6 as the most efficient solution. The optimal total cost, and the organizational efficiency based on this solution were $z_1=27535.98$, $z_2=1408.45$, and order allocation were $x_1=1500$, $x_2=340$, $x_3=2500$, $x_4=0$, $x_5=660$. Furthermore, in this solution, supplier A_3 gained the most weight and A_1 and A_5 were in the next, respectively; it is obvious that supplier A_3 was assigned 50%, supplier A_1 30% and supplier A_5 13.2% of total orders. It demonstrated that the weight of the criteria had relative importance, in the solution of objective functions.

The validation of proposed approach has been considered in two parts:

The first part relates to the assessment of pair-wise comparison matrices that has been done by calculating the amount of CR according to the Equation (3) and controlling of them ($CR < 0.1$).

In second part, at first, incomplete PCMs obtained were completed by Harker and LSM methods, and then global weights of criteria and total rank of alternatives have been obtained by TOPSIS and SAW as benchmark methods. The results of the comparison and ranking of suppliers were reported in Table 11.

TABLE 9. Capacity values of suppliers

Suppliers	A ₁	A ₂	A ₃	A ₄	A ₅
C _i (Ton)	1500	1000	2500	2000	1500
p _i (\$/Ton)	540	570	580	570	550
q _i (%)	0.368	0.04	0.444	0.077	0.071
d _i (%)	0.109	0.088	0.614	0.074	0.115
g _i (%)	0.305	0.057	0.421	0.042	0.176

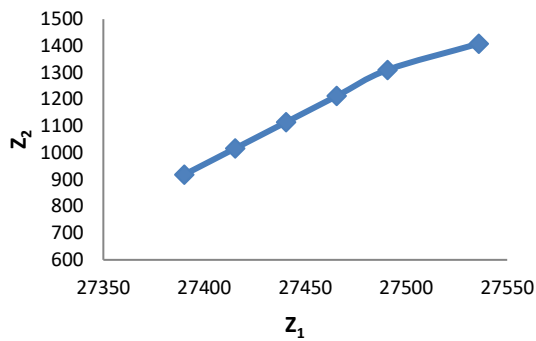


Figure 4. Pareto solution of objectives

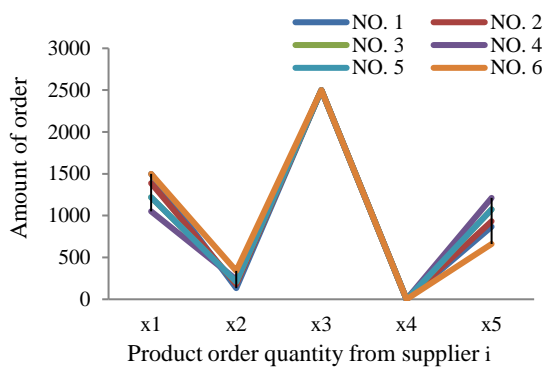


Figure 5. Optimal pareto solution of product order quantities

Clearly, the ranking of suppliers $A_3 > A_5 > A_1 > A_4 > A_2$ is approximately similar to the results of current study. The differences can be justified by interaction between criteria because of applying the Choquet technique, and the comparison confirms authentic results in the selected case.

TABLE 10. Optimal Pareto solution produced by the augmented ϵ -constraint method

NO	Z ₁	Z ₂	x ₁	x ₂	x ₃	x ₄	x ₅
1	27390.05	918.59	1500	133	2500	0	867
2	27415.24	1016.56	1387	180	2500	0	933
3	27440.43	1114.54	1219	208	2500	0	1073
4	27465.61	1212.51	1051	236	2500	0	1213
5	27490.8	1310.48	1219	208	2500	0	1073
6	27535.98	1408.45	1500	340	2500	0	660

In addition, the sensitivity analysis was conducted for the MOLP model. At first, by replacing the weights of alternatives obtained from the combination techniques with the coefficient of the second objective function that shown organizational efficiency, and then by assessing coefficient of parameters (q_i), (d_i) (g_i) obtained from LSM or Harker method, MOLP model have been solved with augmented ϵ -constraint method. It is noteworthy that in all benchmark methods, the same Pareto solutions were obtained. The optimum results were summarized in Table 12. The obtained weights from Choquet method had significantly effect on MOLP model and order allocation problem. Moreover, the results shown that, similar to the presented results of the first part supplier A3 gained the greatest order.

In a real case, the opinions' inconsistency of experts, lack of experts' time, interconnection between criteria, to name but a few, can lead to the incomplete data and incorrect results. As a result, managers should use specific and appropriate solution methods to deal with this incomplete and inaccurate information. The proposed solution method can help experts to make better decisions.

TABLE 11. Comparative results with different benchmark techniques

	Topsis & Harker	Rank	Topsis & LSM	Rank	Saw & LSM	Rank	Choquet & LSM	Rank
A ₁	0.1797	3	0.7989	3	0.1088	2	0.1089	2
A ₂	0.00032	5	0.2008	5	0.0137	5	0.0137	5
A ₃	0.8859	1	0.983	1	0.8271	1	0.8274	1
A ₄	0.0108	4	0.7978	4	0.0139	4	0.0139	4
A ₅	0.5323	2	0.8012	2	0.0362	3	0.0137	3

TABLE 12. Sensitivity analysis with different weights

	Z ₁	Z ₂	x ₁	x ₂	x ₃	x ₄	x ₅
Topsis & Harker	27575.53	2760.58	561	439	2500	0	1500
Topsis & LSM	27419.99	1810.54	780	453	2323	0	1414
Saw & LSM	27535.98	1407.62	1500	620	1449	0	1431
Choquet & LSM	27535.98	1408.45	1500	340	2500	0	660

Applying the presented method can provide appropriate orientation for achieving important decision goals. These results shows that this method can be a promising method to decide precisely in order to attain more organized performance in the state of incomplete and inaccurate data, especially in petroleum industry.

For future researches, this study can be extended by considering the role of some essential parameters such as quantity discount and lead time. Green supplier selection with sustainable criteria will be attended as another recommendation; additionally, uncertain parameters can be added to the robust or stochastic MOLP model.

6. CONCLUSION

In recent years, by handing over oil and gas projects to domestic startups, selecting appropriate suppliers and allocating suitable orders to them are basic problems for petroleum companies, which have significant and critical impacts on the country's economy.

This study discusses the supplier selection via two complementary MCDM methods; AHP with the least square method for unclear and incomplete information, and Choquet technique for considering the existing interaction between criteria. Furthermore, the order allocation problem was applied by developing the MOLP model to minimize the total cost and maximize the organizational efficiency by the Choquet technique, and then it was solved by the augmented ϵ -constraint method. At result, some optimal Pareto solutions were produced that one of them was selected from the reported solutions by the managers. The numerical results and sensitivity analysis were used to examine the weights resulted from the first part through the comparison with some benchmark methods. The results showed the similarity of the presented results with the gained previous results in benchmark methods.

Likewise, the sensitivity analysis of coefficient was preformed to check the effects of parameter and objective weights in the order allocation model (second part) through the same benchmark methods. It was obvious that second objective plays an important role and simultaneously, it confirms the impact of Choquet integral technique by considering interaction between criteria in order allocation problem.

7. REFERENCES

1. Wood. D.A, "Supplier selection for development of petroleum industry facilities, applying multi-criteria decision making techniques including fuzzy and intuitionistic fuzzy TOPSIS with flexible entropy weighting", *Journal of Natural Gas Science and Engineering*, Vol. 28, (2015), 594-612, doi: 10.1016/j.jngse.2015.12.021.
2. Li. S, and Zeng. W, "Risk analysis for the supplier selection problem using failure modes and effects analysis (FMEA)", *Journal of Intelligent Manufacturing*, Vol. 27, No. 6, (2016), 1309-1321, doi: 10.1007/s10845-014-0953-0.
3. Ho. W, Xu. X, and Dey. PK, "Multi-criteria decision making approaches for supplier evaluation and selection: A literature review", *European Journal of operational research*, Vol. 202, No. 1, (2010),16-24, doi: 10.1016/j.ejor.2009.05.009.
4. Tzeng. G-H, and Huang. J-J, "Multiple attribute decision making: methods and applications", CRC press, (2011).
5. Choquet. G, "Theory of capacities", in *Annales de l'institut Fourier*, Vol. 5, (1954), 131-295, doi: 10.5802/aif.53.
6. Grabisch. M, "The application of fuzzy integrals in multicriteria decision making", *European journal of operational research*, Vol. 89, No. 3, (1996), 445-456, doi: 10.1016/0377-2217(95)00176-X.
7. Bottero. M, Ferretti. V, Figueira. J.R, Greco. S, and Roy. B, "On the Choquet multiple criteria preference aggregation model: Theoretical and practical insights from a real-world application", *European Journal of Operational Research*, Vol. 271, No. 1, (2018),120-140, doi: 10.1016/j.ejor.2018.04.022.
8. Zegordi. S, Hosseinzadeh. A, Nahavandi. N, and Sadeghi Rad. R, "An integrated closed-loop supply chain configuration model and supplier selection based on offered discount policies", *International Journal of Engineering, Transactions C: Aspects*, Vol. 31, No. 3, (2018), 440-449, doi: 10.5829/ije.2018.31.03c.06.
9. Amiri. M.P, "Project selection for oil-fields development by using the AHP and fuzzy TOPSIS methods", *Expert Systems with Applications*, Vol. 37, No. 9, (2010), 6218-6224, doi: 10.1016/j.eswa.2010.02.103.
10. Wang. C-N, Huang. Y-F, Cheng. I, and Nguyen. V.T, "A multi-criteria decision-making (MCDM) approach using hybrid SCOR metrics, AHP, and TOPSIS for supplier evaluation and selection in the gas and oil industry", *Processes*, Vol. 6, No. 12, (2018), 252, doi: 10.3390/pr6120252.
11. Sivapornpunlerd. N, and Setamanit. S-o, "Supplier performance evaluation: a case study of thai offshore oil & gas exploration and production company", *ASBBS Proceedings*, Vol. 21, No. 1, (2014), 647.
12. Gholamian. K, Vakilifard. H, Talebnia. G, and Hejazi. R, "Conceptual Design of Sustainable Outsourcing with Balanced Scorecard Using Analytic Hierarchy Process: A Case Study for Fajr Jam Gas Refining Company", *International Journal of Engineering, Transactions A: Basics*, Vol. 33, No. 1, (2020),112-123, doi: 10.5829/ije.2020.33.01a.13.
13. Arabzad. S.M, Ghorbani. M, Razmi. J, and Shirouyehzad. H, "Employing fuzzy TOPSIS and SWOT for supplier selection and order allocation problem", *The International Journal of Advanced Manufacturing Technology*, Vol. 76, No. 5-8, (2015), 803-818, doi: /10.1007/s00170-014-6288-3.
14. Yildiz. A, and Yayla. A, "Application of fuzzy TOPSIS and generalized Choquet integral methods to select the best supplier", *Decision Science Letters*, Vol. 6, No. 2, (2017), 137-150, doi: 10.5267/j.dsl.2016.11.001.
15. Hernadewita. H, Saleh. B. I, "Identifying Tools and Methods for Risk Identification and Assessment in Construction Supply Chain", *International Journal of Engineering, Transactions A: Basics*, Vol. 33, No. 7, (2020), 1311-1320, doi: 10.5829/ije.2020.33.07a.18.
16. Hamdan. S, and Cheaitou. A, "Supplier selection and order allocation with green criteria: An MCDM and multi-objective optimization approach", *Computers & Operations Research*, Vol. 81, (2017), 282-304, doi: 10.1016/j.cor.2016.11.005.
17. Çebi. F, and Otay. İ, "A two-stage fuzzy approach for supplier evaluation and order allocation problem with quantity discounts

- and lead time”, *Information Sciences*, Vol. 339, (2016), 143-157, doi: 10.1016/j.ins.2015.12.032
18. Hamdan, S, and Cheaitou, A, “Dynamic green supplier selection and order allocation with quantity discounts and varying supplier availability”, *Computers & Industrial Engineering*, Vol. 110, (2017), 573-589, doi: 10.1016/j.cie.2017.03.028.
 19. Harker. P.T, “Incomplete pairwise comparisons in the analytic hierarchy process”, *Mathematical Modelling*, Vol. 9, No. 11, (1987), 837-848, doi: 10.1016/0270-0255(87)90503-3.
 20. Chen, K, Kou, G, Tam, J. M, and Song, Y, “Bridging the gap between missing and inconsistent values in eliciting preference from pairwise comparison matrices” *Annals of Operations Research*, Vol. 235, No. 1, (2015), 155-175, doi: 10.1007/s10479-016-2396-9.
 21. Ergu, D, Kou, G, Peng, Y, and Zhang, M, “Estimating the missing values for the incomplete decision matrix and consistency optimization in emergency management”, *Applied Mathematical Modelling*, Vol. 40, No. 1, (2016), 254-267, doi: 10.1016/j.apm.2015.04.047.
 22. Gao, S, Zhang, Z, and Cao, C, “Calculating Weights Methods in Complete Matrices and Incomplete Matrices”, *Journal of Software*, Vol. 5, No. 3, (2010), 304-311, doi: 10.4304/jsw.5.3.304-311.
 23. Kaoru, T, “A Logarithmic Least Squares Method for Incomplete Pairwise Comparisons in the Analytic Hierarchy Process”, *Institute for Policy Science Research Report*, Vol. 94, No. 2, (1993).
 24. Bozóki, S, Csató, L, and Temesi, J, “An application of incomplete pairwise comparison matrices for ranking top tennis players”, *European Journal of Operational Research*, Vol. 248, No. 1, (2016), 211-218, doi: 10.1016/j.ejor.2015.06.069.
 25. Bozóki, S, “A method for solving LSM problems of small size in the AHP”, *Central European Journal of Operations Research*, Vol. 11, No. 1, (2003), 17-33.
 26. Bozóki, S, “Solution of the least squares method problem of pairwise comparison matrices”, *Central European Journal of Operations Research*, Vol. 16, No. 4, (2008), 345, doi: 10.1007/s10100-008-0063-1.
 27. Faramondi, L, Oliva, G, and Bozóki, S, “Incomplete Analytic Hierarchy Process with Minimum Ordinal Violations”, *IEEE Transactions on Automatic Control*, (2020), doi: 10.1109/TAC.2020.3004788.
 28. Foroozesh, N, and Tavakkoli-Moghaddam, R, “Sustainable Supplier Selection by a New Hybrid Support Vector-model based on the Cuckoo Optimization Algorithm”, *International Journal of Engineering, Transactions C: Aspects*, Vol. 30, No. 6, (2017), 867-875, doi: 10.5829/ije.2017.30.06c.07.
 29. Xu, Y, Patnayakuni, R, and Wang, H, “Logarithmic least squares method to priority for group decision making with incomplete fuzzy preference relations”, *Applied Mathematical Modelling*, Vol. 37, No. 4, (2013), 2139-2152, doi: 10.1016/j.apm.2012.05.010.
 30. Gomez-Ruiz, J.A, Karanik, M, and Peláez, J.I, “Estimation of missing judgments in AHP pairwise matrices using a neural network-based model”, *Applied Mathematics and Computation*, Vol. 216, No. 10, (2010), 2959-2975, doi: 10.1016/j.amc.2010.04.009.
 31. Zhou, X, Hu, Y, Deng, Y, Chan, F.T, and Ishizaka, A, “A DEMATEL-based completion method for incomplete pairwise comparison matrix in AHP”, *Annals of Operations Research*, Vol. 271, No. 2, (2018), 1045-1066, doi: 10.1007/s10479-018-2769-3.
 32. Saaty, T.L, “Decision making—the analytic hierarchy and network processes (AHP/ANP)”, *Journal of Systems Science and Systems Engineering*, Vol. 13, No. 1, (2004), 1-35, doi: 10.1007/s11518-006-0151-5.
 33. Ghayoomi, M, Abooei, M. H, Vahdatzad, M. A, and Ebrahimi, A, “Designing a Model for Creation of Export Consortiain Business Cluster”, *International Journal of Engineering, Transactions C: Aspects*, Vol. 33, No. 3, (2020), 459-467, doi: 10.5829/ije.2020.33.03c.10.
 34. Sugeno, M, “Theory of fuzzy integrals and its applications”, *Doct. Thesis, Tokyo Institute of technology*, (1974).
 35. Mavrotas, G, “Effective implementation of the ϵ -constraint method in multi-objective mathematical programming problems”, *Applied Mathematics and Computation*, Vol. 213, No. 2, (2009), 455-465, doi: 10.1016/j.amc.2009.03.037.
 36. Rao, C, Xiao, X, Goh, M, Zheng, J, and Wen, J, “Compound mechanism design of supplier selection based on multi-attribute auction and risk management of supply chain”, *Computers & Industrial Engineering*, Vol. 105, (2017), 63-75, doi: 10.1016/j.cie.2016.12.042.
 37. Banaeian, N, Nielsen, I.E, Mobli, H, and Omid, M, “Green supplier selection in edible oil production by a hybrid model using Delphi method and Green Data Envelopment Analysis (GDEA)”, *Management and Production Engineering Review*, Vol. 5, No. 4, (2014), 3-8, doi: 10.2478/mp-2014-0030.
 38. Kaviani, M.A, Yazdi, A.K, Ocampo, L, and Kusi-Sarpong, S, “An integrated grey-based multi-criteria decision-making approach for supplier evaluation and selection in the oil and gas industry”, *Kybernetes*, (2019), doi: 10.1108/K-05-2018-0265.

Persian Abstract

چکیده

انتخاب تأمین کننده از فرآیندهای پیچیده ای است که می تواند بهره وری و مزیت رقابتی را در یک صنعت قدرتمند افزایش دهد. انتخاب تأمین کننده دارای معیارهای مختلف، از قبیل معیارهای کمی، کیفی و معیارهایی است که برهم کنش، بین آنها وجود دارد. به علاوه فرایند انتخاب، همواره با داده های ناکافی و ناکامل مواجه است. تصمیم گیری چند معیاره (MCDM) رویکرد مفیدی است که می تواند در مسئله انتخاب یک تأمین کننده با در نظر گیری چالشهای مورد اشاره بکار گرفته شود. در این رویکرد، برهم کنش بین معیارها را می توان با روش هایی مانند انتگرال چوکوت، که روشی کاربردی برای رتبه بندی در فرایند تصمیم گیری است، در نظر گرفت. همچنین ناکافی بودن داده ها توسط روش AHP ناقص می تواند پوشش داده می شود. بنابراین، در این مطالعه به منظور انتخاب تأمین کننده در صنعت نفت، از انتگرال چوکوت همراه با روش AHP ناقص استفاده شده است. تخصیص سفارشات درخواستی با استفاده از مدل برنامه ریزی خطی چند هدفه (MOLP) و روش اسپیلون محدودیت برای تولید نقاط بهینه پارتو، پس از دستیابی به رتبه بندی تأمین کنندگان انجام شده است. نتایج نشان می دهد که، تأمین کننده ی سوم با وزن ۰.۸۲۷۴ ارجح ترین تأمین کننده است که بر این اساس ۵۰٪ از کل سفارشات به این تأمین کننده به عنوان بهترین انتخاب، تخصیص داده شده است.



Modeling and Analyzing Supporting Systems for Smart Manufacturing Systems with Stochastic, Technical and Economic Dependences

M. A. Farsi*^a, E. Zio^b

^a Aerospace Research Institute, Ministry of Science, Research and Technology, Iran

^b Energy Engineering Department, Polytechnic di Milano, Italy

PAPER INFO

Paper history:

Received 27 June 2020

Received in revised form 25 July 2020

Accepted 03 September 2020

Keywords:

Smart Manufacturing System

Supporting System

Maintenance Policy

Spare Part Inventory

ABSTRACT

Smart manufacturing systems are triggering the next industrial revolution. They are intended to be collaborative manufacturing systems that respond in real time to meet the system's changing demands and conditions. Different types of dependencies among system components are introduced to enable this and to improve system performance, including structural, stochastic, technical and economic dependences. Supporting systems are also introduced to this aim, through specified interfaces. In this paper, the role of maintenance policy, spare part inventory and buffer size as supporting systems of smart systems is considered. Load-sharing dependence, adaptive control with feedback and economic dependence are specifically considered, and their effect is studied via Monte Carlo simulation. Results show that smart systems with properly designed supporting systems have undoubtedly increased system complexity and dependencies, but can indeed increase availability and production volume, and system efficiency overall, with total cost reduced.

doi: 10.5829/ije.2020.33.11b.21

NOMENCLATURE

A	System availability	Shc	Shut down cost
Alfa	The scale parameter of the weibull distribution	SL_i	the stress level during the i-th duration
C	Cost	t	time
CI_i	the production cost of the i th machine	T	Working time
CS_{ij}	the spare part cost	TC	the total cost
CR_{ij}	the replacement action cost	V	The production volume
m	Nuber of stopping times	Greek Symbols	
n	the number of spare parts for a machine	μ	The mean
$R(t)$	The reliability of component	σ	Standard division
STC	Store cost		

1. INTRODUCTION

Over the past decade, the topic of Smart Manufacturing (SM) has been more than a conversation among thought leaders, manufacturing experts and world-class companies: it has become a concrete initiative all over the world. Different definitions have been proposed for SM, such as the recent one from a leading organization like the National Institute of Standards and Technology (NIST) [1]: Smart Manufacturing systems are systems

that are “fully-integrated, collaborative manufacturing systems that respond in real time to meet changing demands and conditions in the factory, in the supply network, and in customer needs.” The shared view is that the smart manufacturing system covers all subjects from A to Z for component production and employs computer controls for high levels of adaptability. For this, different types of dependencies are introduced in the system to enable communication among manufacturing machines and improve production volume; but the complexity and

*Corresponding Author Institutional Email: Farsi@ari.ac.ir
(M. A. Farsi)

vulnerability of the systems are significantly increased, also.

Besides, supporting systems, such as maintenance and spare parts inventory, influence the effectiveness of the smart manufacturing system, and must be smart too. Maintenance costs can rise up to sixty percent of the production costs and up to a third of these costs may be due to unnecessary or poorly executed maintenance [2]. In a smart manufacturing system for enhancing performance and solving existing and future problems, all machines are monitored, data are collected and analyzed to predict and prevent performance degradation and potential failures. Big data, complicated dependencies among sub-systems and conflicting requirements pose challenges to this system; and render its management difficult. The different studies have been conducted in this field that in the rest of this section, some of these studies on maintenance and structure dependence, spare parts and maintenance, and buffer as a balancer in production lines are reviewed.

Maintenance policy: In recent years, several studies about maintenance policies and supply chain for smart and intelligent systems have been conducted. Cheng [3] used a Neural Network to predict the remaining useful life (RUL) of a multi-component system, in which economic dependence exists among the components. The proposed method included two-level failure probability thresholds, based on which Condition-based Maintenance (CBM) was applied. Zhou et al. [4] studied a system with economic dependence and high maintenance cost. Tian and Liao [5] applied a proportional hazards model to optimize system maintenance with monitoring and CBM. Bian and Gebraeel [6] investigated a multi-component system with degradation rate interactions and proposed a method for stochastic modeling and real-time prognostics. Opportunistic CBM strategies for systems with economic dependencies and redundancy was considered by Keizer et al. [7]. Zhang and Zeng [8] studied an identical multi-unit system to find the best periodic condition-based opportunistic preventive maintenance and safety policy for spare parts management. Minou et al. applied Markov Decision Processes to determine the optimal replacement time that minimizes the long-run average cost per time unit [9]. They investigated a load-sharing system with economic dependence and demonstrated that the load sharing effects among components could lead to a significantly more expensive maintenance policy. Other studies can be found in the literature on CBM modeling and optimization [10].

Spare parts inventory management: we know that maintenance effectiveness depends on spare parts inventory management. Spare parts inventory influences the maintenance cost and system availability. Thus, its relevant characteristics should be considered, such as ordering and replacement times, storage condition,

logistics problem. Some studies have been performed for joint optimization of spare parts and maintenance [11, 12]. Wang et al. [13] modeled the spare parts for a system monitored during operation. They found the optimal preventive maintenance threshold to satisfy the spare parts support requirements. Lin et al. showed that condition-based inventory policy increases about twenty percent of the system efficiency [14]. Auweraer and Boute proposed a method to forecast spare part demand based on service maintenance information [15]. Driessen et al. [16] proposed a framework for maintenance and spare parts planning and control; focused on demand and spare parts ordering to conduct the optimum maintenance.

Buffer influence: In industrial practice, production rates of machines may be changed, or machines may be preventively stopped for maintenance, but the production line stability and balance should be kept. In this situation, other machines continue their work to produce the products. For this, buffers are installed as intermediate storages to overcome the unbalancing and fluctuation. Buffer size and location optimization in a production line have been studied as an NP-hard optimization problem [17], from the production point of view. For example, Lutz et al. [18] applied scheduling policies and dispatching rules to determine buffer size and location. Weiss et al. [19] considered the buffer allocation problem, providing a review about this challenge and categorizing the previous studies, characteristics of flow line, objectives function and constraints, and solution method. Gan and Shi [20] studied a simple series system with respect to the spare part ordering problem of the upstream machine and buffer level, within the maintenance optimization of the downstream machine.

As mentioned in the literature, a production system performance and availability depends on system configuration, maintenance policy and spare parts inventory. The literature shows that these topics are deeply separately studied, but their simultaneously influences have been received less attention. Therefore, this dependence should be considered for adequate modelling and analysis. We investigate this topic in this paper, and present a method for modeling this relationship. In our study, smart manufacturing systems under Preventive Maintenance (PM) and CBM policies with load-sharing, series structure and economic dependencies are considered, and the influence of the important characteristics on the system performance is explored. Load-sharing structure is a complex dependence in the system behavior modelling, and the previous studies usually consider the simpler structures such as series or parallel configuration. Another contribution is the study on an adaptive control to decrease buffer influence, reduce total cost and improve system availability. Also, it can be said that the main contribution is considering different types of

dependencies (stochastic, technical and economic) in the system modelling.

In the next section, a manufacturing system is defined, and its structure and dependencies among components are illustrated. In Section 3, a method for system modeling is proposed and a simulation method to determine system availability and total cost is presented. In Section 4, the influence of the most important parameters on the system performance is investigated and the results of the simulation are presented. In Section 5, the results are discussed and the advantages and drawbacks of the proposed method are discussed, and directions of the future studies are suggested.

2. SYSTEM DEFINITION

Production systems layout is designed primarily based on the production processes which are necessary to make a product and their efficiency. Different structures and dependencies are used in industrial manufacturing systems. The series structure is often applied for sequential and multi-machine system installation in a production line. Each element of the series structure may consist of more than one machine. Buffers are used as intermediate storage spaces to increase production line stability. Indeed, the production rates of the machines are not equal and when a machine is stopped due to preventive maintenance or shortage of input materials, other machines work and their product should be stored. When the stopped machine operates again, the stored parts are consumed. Consider, for example, a smart manufacturing system (Figure 1) that consists of two stages: upstream and downstream. Four machines are used in upstream with series-parallel structure and load-sharing dependence. Load-sharing structure allows keeping the system performance at the desired level. For example, when M1 or M2 is stopped, this section is stopped, but another parallel-section (M3&M4) continues its operation, although under higher load than before. In this situation, the stress on the components may also be higher and the probability of failure of the active machines may be increased.

A machine is used in the downstream stage to adjust the production rate according to the output of the upstream stage. In the smart manufacturing system, when the amount of workpieces in the buffer is less than a specified value, a trigger signal is sent to reduce the downstream production rate, and another signal is created to increase production rate when the amount of workpieces in the buffer is more than the predefined threshold.

Also, in such smart manufacturing system, all machines are monitored, and data are collected to evaluate their state and predict the RUL of the critical

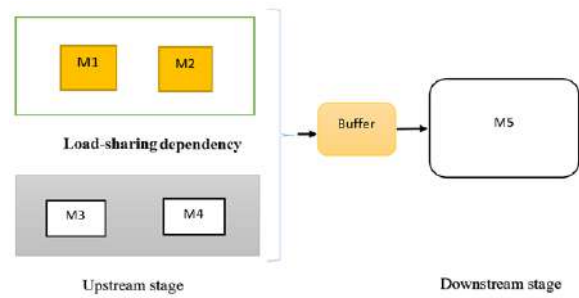


Figure 1. System structure

units that are most prone to failure. In this system, it is assumed that Weibull distributions describe their stochastic lifetimes. Depending on the reliability of the units, ordering and replacement times of spare parts are defined. Also, preventive maintenance is conducted based on a scheduled plan, as specified for each section of the system. Moreover, opportunistic maintenance is considered for cost reduction and increase of system availability.

3. SYSTEM MODELLING

In this section, the proposed framework for system modeling and performance determination is described. In this framework, the reliability is considered as a critical item for decision making in maintenance and spare parts management and decreases the system costs. Thus, reliability function and its variation according to the system structure are introduced, then the system logic is described and finally the proposed flowchart is presented in the next sections.

3.1. Component Reliability

In this paper, a complex structure is studied that can adapt production rate based on the system state. As a consequence, the stress on a machine may change and so does the expected lifetime; reliability is, then, calculated based on the conditional reliability formula (Equation (1)).

$$R(\tau|t) = \frac{R(t+\tau)}{R(t)} \quad (1)$$

where $R(\tau|t)$ is the component reliability of a component that has worked until t and should continue to work for a duration τ , $R(t)$ is the component reliability at the specified time t and $R(t + \tau)$ indicates the component reliability at the end of the stress duration time $(t + \tau)$. If the stress level has varied in q instances before this time, the reliability is calculated as follows:

$$R(t + \tau) = R(\tau|t) \times (\prod_{i=0}^q R(t_{i+1}|t_i)) \times R(t_0) \quad (2)$$

The time duration of each stress level i is defined as (t_i, t_{i+1}) , and $t_{q+1} = t$.

In this study, the RUL of a component is modeled by a Weibull distribution and when the modeled stress level is varied, its parameters are updated. The new Alfa can be calculated as follows:

$$Alfa_{i+1} = Alfa_i \times \frac{SL_{i+1}}{SL_i} \quad (3)$$

Notice that the stress level of a machine relates to its state and that of other machines, and the buffer. If buffer and load-sharing situation impress that a machine stress should be increased, then its stress grows up. Sometimes buffer can balance the production rate, thus the stress is not increased.

3. 2. System Logic Description System reliability is determined also by the relationship among the components in the system logic configuration. In the system considered in this case study, the upstream stage has a parallel structure and includes four machines where M1&M2 are in series, and M3&M4 are in series. These machines part of a load-sharing structure, and the upstream stage is in series with the buffer and the downstream machine (M5). It is assumed that when the system production outcome is zero, the system is down whereas in the other states, the system is active although at different production levels. Indeed, the production volume depends on the buffer size and downstream stage availability. Also, upstream and downstream machines influence the buffer size. This type of technical dependence is considered in the system modeling.

3. 3. Cost Modelling Different formulas have been proposed for maintenance cost modeling [21-23], and several parameters have been considered as direct and indirect costs. In this study, a new formula is proposed that covers new parameters considered for system modeling. In this formula, spare parts cost, replacement cost, preventive maintenance cost, shortage cost (shutdown time), storage room cost and the cost of idle state are considered, and the following equation is derived:

$$TC = \sum_{l=1}^m \sum_{j=1}^n CS_{ij} + \sum_{l=1}^m \sum_{j=1}^n CR_{lj} + \sum_{l=1}^m CPM_l + \sum_{l=1}^m \sum_{q=1}^{s_m} ShC_{l,q} + \sum_{k=1}^h STC_k + \sum_{l=1}^m CI_l \quad (4)$$

In practical industry, the total cost per one product is often used.

$$TCr = TC/V \quad (5)$$

3. 3. Availability Quantification Availability defines the ratio of the working time to the total time and is an important parameter to evaluate a manufacturing system, because the production rate depends on system availability. In this study, the Monte Carlo simulation

method is used for system modeling and availability quantification.

Figure 2 shows the framework proposed to determine system availability and cost. Component states, preventive maintenance tasks and RULs are considered to decide on the next ordering, replacement and repair times. In the first step of the method, these times are randomly computed by Monte Carlo simulation for all components and the closest/smallest time is selected. Since, the process that its time is closest should be early conducted.

Depending on the repair type, the repair duration is calculated. Uncertainty in the repair times is defined as a normal distribution and a random variable is sampled to determine the repair duration.

If the stopped machine is one of the upstream stage machines, the series machine is stopped too, whereas the parallel machines continue to work but under higher stress. Thus, the failure rate, RULs and repair times are updated by Equations (2) and (3).

In the repair duration, we deal with two states. In one state, all machines work without failure: this situation is ideal and the system is available. In the other state, one or more machines are stopped. The buffer in this situation is very important for production line stability because if the downstream stage is also stopped, the workpieces produced upstream should be stored in the buffer. In the second situation, the repair times are recomputed and the system state is investigated. If a machine fails, this duration is extended and calculations are repeated so that after the repair duration, all machines are ready to work and available.

After the repair, the new failure times of the components are randomly calculated and the working time is determined. If the desired duration (2000 hr) is greater than T, this cycle is repeated. Also, if the simulation iteration number is less than the number of repeated Monte Carlo runs considered (20000 in this study), the whole procedure is repeated. At the end of the framework, the total cost and system availability are determined. In a nutshell, this framework includes two loops, in the inner loop, C&A are calculated for the desired time (2000 hr) and in the outer cycle this procedure is repeated by 20000 iterations and finally, the average values for A&C are calculated.

In some types of manufacturing systems, since the production rate (at a reasonable cost) is more important than availability, the production volume is also considered. When new times are computed, the production state is checked and if the production rate is increased, stress on active machines is increased to balance the production line, and if production rate is reduced, stress on active machines is decreased. This variation is considered in the machines RULs and maintenance times updating.

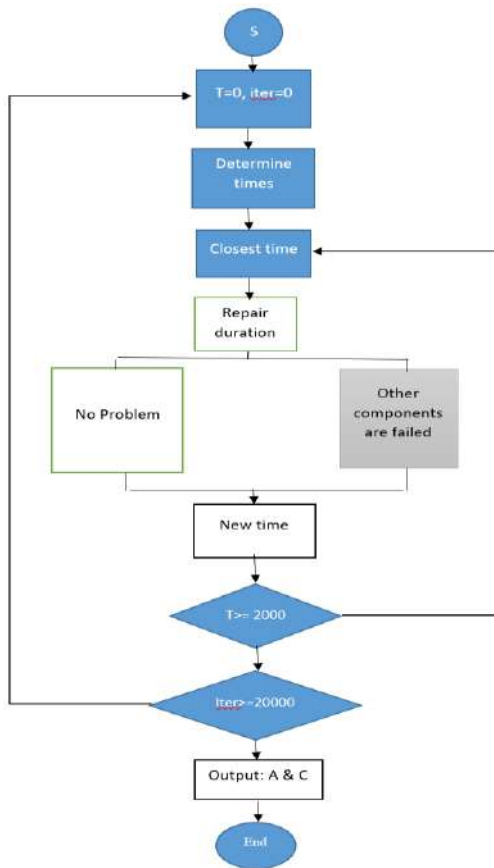


Figure 2. The proposed framework for the system modeling

Other assumptions made in the model include:

- A timetable defines preventive maintenance.
- Spare parts order is carried out when reliability decreases to a specified level.
- Spare parts replacement is performed when reliability is zero.
- Spare parts are provided by a supplier with predefined cost, delivery interval and quality level.
- Preventive maintenance and replacement tasks durations follow normal distributions with given (μ, σ) .
- When a spare part is replaced, preventive maintenance tasks about this machine is accomplished too.
- The buffer has fixed thresholds of minimum and maximum sizes.
- When M1 is repaired, M2 is stopped and its preventive maintenance tasks are performed too, and vice versa.
- When M3 is repaired, M4 is stopped and its preventive maintenance tasks are performed too, and vice versa.

4. SENSITIVITY ANALYSIS

In this paper, maintenance, spare parts inventory and production planning for smart manufacturing systems are

studied. Different parameters, such as spare parts cost and quality, ordering time, opportunistic maintenance, system logic and buffer size influence the system performance. In this section, these parameters are introduced and their influence is investigated.

4. 1. System Logic A manufacturing system layout design is difficult, since different parameters have to be considered. Series or parallel structure is usually utilized for layout planning. The system shown in Figure 1 has a series-parallel structure. Assume the production rate of M1 & M2 is eight components per hour, and M3 & M4 produce ten components per hour, and the production rate for M5 is 18 components per hour. In this situation, the availability of the upstream stage is 0.9038 for 2000 hr working time, and 24904 products are made. On the other hand, downstream availability is 0.8785, and it needs 31622 workpieces. Thus, the downstream has a problem of workpiece shortage, due to the system stop-pages for preventive maintenance. If the load-sharing structure is implemented, when a machine at upstream is stopped, other machines work under higher stress and the production line stability is improved, because the availability of the upstream is raised up to 0.9835 and the number of the total products is 35406. Then, the load-sharing structure helps in production planning and layout design of a manufacturing system, for system performance increase.

4. 2. Adaptive Production Control In the past section, the influence of the load-sharing structure on the system performance has been explained. The load-sharing structure increases the upstream production rate. However, the downstream machine cannot consume all workpieces produced, and its production rate needs to be increased. Therefore, another machine in the downstream may be added, which needs more production space and a new cost due to the installation of a new machine; also, the idle time of this stage is increased. As the second plan, we can use adaptive control with feedback to manage this disturbance. When the upstream output production is more than the ordinary capacity of the downstream stage and buffer size, the downstream machine is stressed to increase production; when the workpieces volume in the buffer is not enough, the downstream machine decreases its production rate. Table 1 shows the results of these schemes of implementation.

This Table shows that the system with feedback reduces the machine availability because of stress variation, but the production volume is increased and the system production stability is improved.

4. 3. Ordering Time Ordering time is an essential parameter for CBM and spare parts management. The ordering time must be correlated with failure or fault detection times. In industrial practice, spare parts are

TABLE 1. System performance with and without feedback

Upstream production volume	Downstream production volume (without feedback)	Downstream availability (without feedback)	Downstream production volume (with feedback)	Downstream availability (with feedback)
35406	31622	0.8785	35385	0.8760

usually ordered when the failure probability is greater than a specified threshold or the reliability is less than a desired value. In this paper, different thresholds are considered and their effect are studied on system availability and cost. Figure 3 shows the correlation between the downstream and upstream availability with different ordering time thresholds.

This figure shows that whenever the selected ordering time threshold is close to one, availability is decreased because of shutdowns increase and spare parts shortage. If after the part replacement, the next spare parts are ordered, or in other words, the threshold is close to zero, the availability and production volume are increased, since the probability of spare parts shortage is reduced.

When spare parts are ordered at an incorrect time, the cost is increased because of production stop-page or storage cost increase. Figure 4 shows the relationship between the cost and ordering threshold. The best ordering threshold (reliability value) for the mentioned system is 0.8, and when spare parts ordering is carried out sooner than this time, the cost is increased due to storage cost. If spare parts are ordered with a delay, the cost is increased due to spare parts shortage or system stoppage production.

4. 4. Spare Parts Storage Storage management is one of the most important parameters for spare parts provision and usually is considered as an indirect cost for maintenance management. A space within the factory is used as storage. This space increases the total cost and when the number of spare parts is increased, storage space needs to be increased too. In this study, the storage cost is considered in the total cost:

$$STC = \sum_{j=1}^m \sum_{i=1}^n time_{ji} \times constant\ cost \tag{6}$$

where $time_{ji}$ is storage duration for the spare part i of

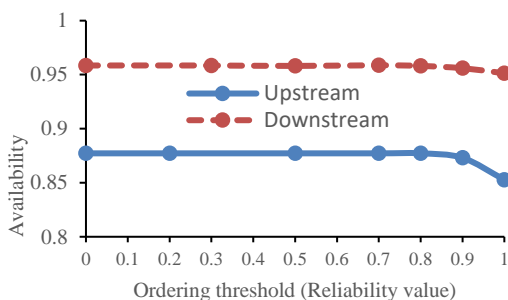


Figure 3. The influence of ordering time on the availability

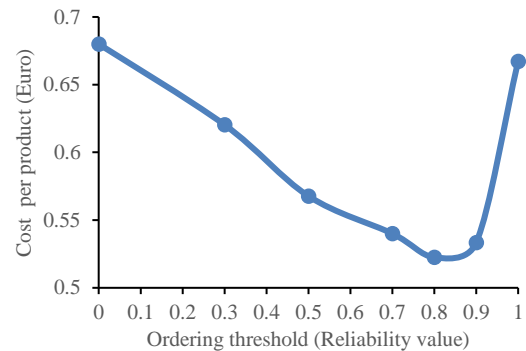


Figure 4. The influence of ordering time on the cost per component

machine j , and relates to the ordering time and replacement time.

4. 5. Opportunistic Maintenance Window

Opportunistic maintenance is defined as maintenance of an item that is deferred or advanced in time when an unplanned opportunity becomes available [24]. An opportunity arises if the failure of some other parts of a system allows the component in question to be maintained [25]. In this situation, the maintenance opportunity window determination is very important and its size can influence the system cost and availability. Opportunistic maintenance is considered when a machine is stopped for PM or spare parts replacement. In this situation, the desired maintenance is simultaneously accomplished if the opportunity window is greater than the time of the PM tasks. In this study, the opportunity window is selected as an interval between zero and 60 hr for a machine. Figure 5 shows that in the upstream stage, the influence of the opportunity window size on system performance is different from the downstream stage, because of the load-sharing dependence among the components. An opportunity window size increase results in a stress increase on the other components and a system cost increase, because failure probability is raised. In this situation, the load-sharing over-shadows the opportunistic maintenance effect. For the downstream machine, the opportunity window size is important.

Opportunistic maintenance in general decreases system cost, but the cost is increased if the opportunity window is large, because components may be replaced sooner than their expected lifetime.

4. 6. Buffer Size Buffer, as a storage between two stages of a production line, stabilizes production line, but it reduces valuable space in a factory and increases production cost. Therefore, in advanced manufacturing system buffer size is kept small. However, if the buffer is omitted, when a machine is out of service in the same production line, other machines should be stopped too. A buffer is usually determined by considering two thresholds of minimum and maximum sizes. Minimum size is significant for production line stability and downstream stop-page reduction due to the workpieces shortage, especially when the amount of the production rate of two stages are the same or the downstream capacity is more than the upstream capacity. Maximum buffer size relates to the production cost and space. In this study, the influence of these thresholds is investigated for two situations: traditional and adaptive control manufacturing.

In a traditional setting, machines work independently of each other, and a large buffer may be necessary. For instance, if the working time is 2000 hours, given the two stages availabilities and production rates (Table 1), the upstream stage produces 3784 workpieces more than the downstream machine capacity as follows.

Production volume of the upstream stage: 35406

Production volume of the downstream stage: 31622

Difference production volume between the two stages=35406-31622=3784

The production rate of the upstream stage= $35406/2000=17.703$ components per hour

The production rate of the downstream stage= $31622/2000=15.811$ components per hour

Thus, for 200 hrs, the production volume of the upstream stage is:

$$P_u = 200 \times 17.703 \cong 3541$$

And the production volume of the downstream stage is:

$$P_D = 200 \times 15.811 \cong 3162$$

Thus,

$$\Delta P = P_u - P_D = 3541 - 3162 = 379.$$

If the buffer size is 380, to reduce the workpieces into the initial state (the buffer is empty), the downstream machine needs more time as follows.: $time = \frac{379}{15.811} = 23.97 \approx 24 \text{ hr}$

In this duration time, the upstream stage is idle and stopped.

When the adaptive and smart manufacturing system is applied, this problem is reduced, because the downstream machine can increase or decrease its production rate to overcome instability at the upstream output. When the workpiece volume in the buffer is less than the predefined threshold, the downstream production rate is decreased to avoid the workpiece shortage, and when the buffer is filled, its production rate is increased. In the proposed technique, all outputs of the upstream stage are used by the downstream machine and production stop-page is decreased. Also, the required buffer size is reduced. In this state, given the buffer size, at the end of working time and in the worst case, the buffer is full.

In this study, different values for buffer thresholds are considered (Figure 6). To compare the effect of different buffer thresholds on the system, a threshold is used as a reference and the other results are normalized. Figure 6a shows the influence of the maximum buffer size on the system performance. System capability to absorb production line fluctuation is increased with larger buffer size. Then, stress on the machines is reduced; consequently, system availability is increased and the cost per part is reduced. For a large threshold, this influence can be neglected.

Figure 6 (b) illustrates the minimum buffer size influence on the system performance. When this threshold has small values, the stress on the downstream machine is decreased; and it is increased for large values. The threshold effect on the upstream machine is opposite. The influence of the maximum buffer size on the system performance is more significant than that of the minimum buffer size.

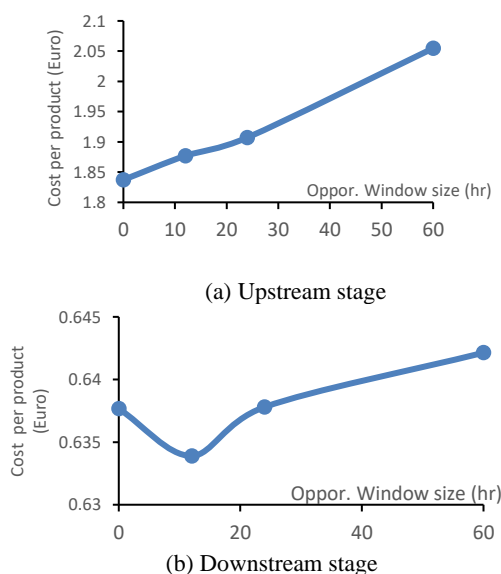
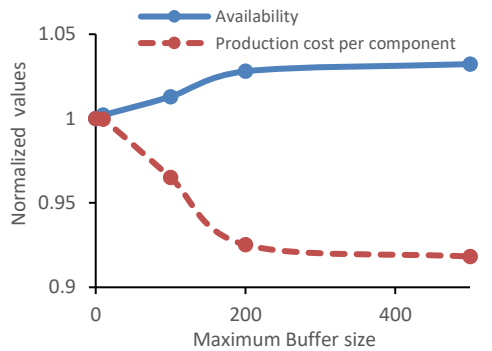


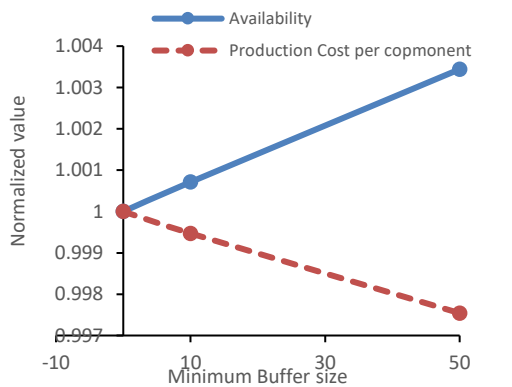
Figure 5. The influence of the opportunity window size on the cost

4. 7. Production Rate Ratio

The ratio of the production rate between machines is one of the main parameters considered for production line design. For design, the production rate for downstream and upstream is taken equal; but when maintenance and spare part inventory are jointly considered with production planning, the problem becomes complicated and it is necessary to find the optimal ratio between the downstream and upstream stages for production line balance.



(a) Maximum buffer size effect (minimum size=0)



(b) Minimum buffer size effect (maximum size=100)

Figure 6. Buffer size effect on the system

To study the influence of this parameter on the system performance, it is assumed that the downstream machine production rate can be varied from 0.83 to 1.22 times the upstream production rate. Figure 7 shows the production rate ratio effect on the cost per component and production volume for the system with adaptive control. These data are normalized and it is assumed that the upstream production volume is constant.

When the downstream production capacity is higher than the upstream capacity, the production volume of the downstream is greater than upstream, and sometimes it may be idle. Then, the downstream production rate should be decreased and the stress on its machines is also reduced. Consequently, the probability of failure and the cost per component is reduced. When the downstream capacity is less than the upstream, it works under higher stress; then, the probability of failure is increased and the total cost is increased too. Thanks to the adaptive control utilized in the system, the production volume is approximately constant and small variations in availability are generated by the delay in the adaptation process.

If the adaptive control is not utilized, in the extreme case that the downstream machine capacity is 1.11 times the upstream production, the production line stability is acceptable. In this state, in one percent of the working

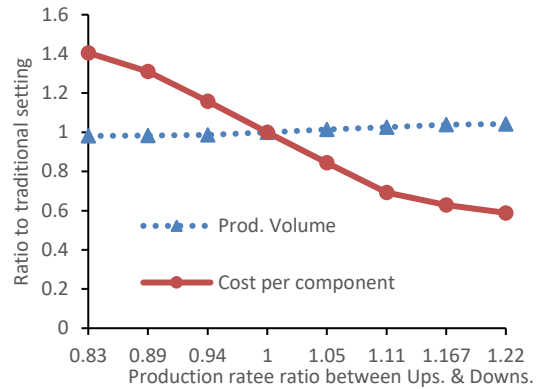


Figure 7. Production rate ratio effect

time, the downstream machine is idle due to the workpieces shortage, and in 2.5 percent of the working time, it faces an extra production from the upstream stage. These results show that if adaptive production control is not applied, the production line stability is decreased and the effectiveness of the buffer, maintenance and spare parts management is reduced.

5. CONCLUSION

Smart manufacturing systems are the next industrial revolution. For increased functionalities, benefits and efficiency, they involve complex structures with different dependencies, including structural, stochastic, economic and source dependencies. System complexity is increased due to the integration of supporting systems, such as maintenance, spare parts inventory, and buffer allocation.

In this paper, smart manufacturing systems with series-parallel structure which involve load-sharing, functional and economic dependencies are considered. Actually, smart systems with adaptive control and feedback are considered to improve system performance, production stability and the effectiveness of maintenance. The results show that the resilience and dynamic behavior of smart systems increases the systems adaptation to working conditions. The role of the buffer as a balancer in production lines to improve availability is very important and the optimum size of the buffer should be selected. Ordering time and replace time of spare parts depend on reliability and they can impress availability and the cost of the system. Opportunistic maintenance is a good idea, but its influence on availability depends on the machine's location on the production line. In the future studies, resource dependence, multi-state configuration, corrective maintenance policy, imperfect maintenance, customers' requirement variability, and spare parts quality variability will be considered.

6. REFERENCES

- Thompson, K., "Smart manufacturing operations planning and control program", Gaithersburg, MD: National Institute of Standards and Technology (NIST), (2014).
- Mobley, R.K., "An introduction to predictive maintenance, Elsevier, (2002).
- Chen, X., Xu, D. and XiAo, L., "Joint optimization of replacement and spare ordering for critical rotary component based on condition signal to date", *Eksploracja i Niezawodność*, Vol. 19, (2017), 76-85. DOI: 10.17531/ein.2017.1.11
- Zhu, Q., Peng, H. and van Houtum, G.-J., "A condition-based maintenance policy for multi-component systems with a high maintenance setup cost", *Or Spectrum*, Vol. 37, No. 4, (2015), 1007-1035.
- Tian, Z. and Liao, H., "Condition based maintenance optimization for multi-component systems using proportional hazards model", *Reliability Engineering & System Safety*, Vol. 96, No. 5, (2011), 581-589.
- Bian, L. and Gebraeel, N., "Stochastic modeling and real-time prognostics for multi-component systems with degradation rate interactions", *Iie Transactions*, Vol. 46, No. 5, (2014), 470-482.
- Keizer, M.C.O., Teunter, R.H. and Veldman, J., "Clustering condition-based maintenance for systems with redundancy and economic dependencies", *European Journal of Operational Research*, Vol. 251, No. 2, (2016), 531-540.
- Zhang, X. and Zeng, J., "Joint optimization of condition-based opportunistic maintenance and spare parts provisioning policy in multiunit systems", *European Journal of Operational Research*, Vol. 262, No. 2, (2017), 479-498. DOI: 10.1016/j.ejor.2017.03.019
- Keizer, M.C.O., Teunter, R.H., Veldman, J. and Babai, M.Z., "Condition-based maintenance for systems with economic dependence and load sharing", *International Journal of Production Economics*, Vol. 195, (2018), 319-327.
- Cheng, J., "Condition based maintenance optimization for multi-component systems based on neural network health prediction", Concordia University, (2010),
- Van Horenbeek, A., Buré, J., Cattrysse, D., Pintelon, L. and Vansteenwegen, P., "Joint maintenance and inventory optimization systems: A review", *International Journal of Production Economics*, Vol. 143, No. 2, (2013), 499-508. DOI:10.1016/j.ijpe.2012.04.001
- Lynch, P., Adendorff, K., Yadavalli, V. and Adetunji, O., "Optimal spares and preventive maintenance frequencies for constrained industrial systems", *Computers & Industrial Engineering*, Vol. 65, No. 3, (2013), 378-387. Doi:10.1016/j.cie.2013.03.005
- Wang, Y., Gu, H., Zhao, J. and Cheng, Z., "Modeling on spare parts inventory control under condition based maintenance strategy", *Journal of Shanghai Jiaotong University (Science)*, Vol. 21, No. 5, (2016), 600-604.
- Lin, X., Basten, R.J., Kranenburg, A. and van Houtum, G.-J., "Condition based spare parts supply", *Reliability Engineering & System Safety*, Vol. 168, (2017), 240-248.
- Van der Auweraer, S. and Boute, R., "Forecasting spare part demand using service maintenance information", *International Journal of Production Economics*, Vol. 213, (2019), 138-149.
- Driessen, M., Arts, J., van Houtum, G.-J., Rustenburg, J.W. and Huisman, B., "Maintenance spare parts planning and control: A framework for control and agenda for future research", *Production Planning & Control*, Vol. 26, No. 5, (2015), 407-426. DOI: 10.1080/09537287.2014.907586
- MacGregor Smith, J. and Cruz, F.R., "The buffer allocation problem for general finite buffer queueing networks", *IIE Transactions*, Vol. 37, No. 4, (2005), 343-365.
- Lutz, C.M., Davis, K.R. and Sun, M., "Determining buffer location and size in production lines using tabu search", *European Journal of Operational Research*, Vol. 106, No. 2-3, (1998), 301-316.
- Weiss, S., Schwarz, J.A. and Stolletz, R., "The buffer allocation problem in production lines: Formulations, solution methods, and instances", *IIE Transactions*, Vol. 51, No. 5, (2019), 456-485. DOI: 10.1080/24725854.2018.1442031
- Gan, S. and Shi, J., "Maintenance optimization for a production system with intermediate buffer and replacement part order considered", *Eksploracja i Niezawodność*, Vol. 16, No. 1, (2014), 140-149.
- Sharma, G., Kumar, A. and Jain, M., "Maintenance cost analysis for replacement model with perfect minimal repair", *International Journal of Engineering*, Vol. 15, No. 2, (2002), 161-168.
- Ghandali, R., Abooi, M. and Nezhad, F., "A pomdp framework to find optimal inspection and maintenance policies via availability and profit maximization for manufacturing systems", *International Journal of Engineering*, Vol. 31, No. 12, (2018), 2077-2084.
- Ram, M. and SINGH, V., "Modeling and availability analysis of internet data center with various maintenance policies", *International Journal of Engineering*, Vol. 27, No. 4, (2014), 599-608.
- TC, I., "Petroleum, petrochemical and natural gas industries—collection and exchange of reliability and maintenance data for equipment", Standard, (2007).
- Chang, Q., Ni, J., Bandyopadhyay, P., Biller, S. and Xiao, G., "Maintenance opportunity planning system", *Journal of Manufacturing Science and Engineering*, Vol. 129, (2007), 661-668.

Persian Abstract

چکیده

سیستم های هوشمند تولید بخشی از انقلاب صنعتی جدید هستند که نیازمند پاسخگویی برخط به نیازها و تغییرات ایجاد شده در سیستم هستند. در این سیستم ها انواع مختلف وابستگی برای بهبود راندمان استفاده می شود، وابستگی های از نوع ساختاری، استوکستیک، فنی و اقتصادی. سیستم های پشتیبان این نوع از خطوط تولید نیز دارای مرزهای مشترک و وابستگی هستند. در این مقاله نقش دیسیپلین تعمیر و نگهداری، تدارکات و پشتیبانی قطعات مصرفی و اندازه بافر در این خطوط تولید مورد بررسی قرار گرفته است. وظیفه مشترک و وابستگی ماشین ها در انجام ماموریت همراه با سیستم کنترل تطبیقی تولید و وابستگی اقتصادی بطور ویژه بررسی شده و اثر آنها بر میزان تولید و دسترس پذیری سیستم بوسیله روش مونت کارلو مدلسازی شده است. نتایج بیانگر این نکته است که هرچند طراحی این سیستم ها پیچیده بوده و وابستگی بین اجزای سیستم افزایش می یابد، اما میزان دسترس پذیری و حجم تولید نهایی افزایش یافته و با ارتقاء راندمان هزینه کل کاهش می یابد.



Optimization of Rubber Compound Design Process Using Artificial Neural Network and Genetic Algorithm

N. Ghaffarian*, M. Hamedi

Department of Industrial Engineering, Payame Noor University, Iran

PAPER INFO

Paper history:

Received 09 April 2020

Received in revised form 12 June 2020

Accepted 03 September 2020

Keywords:

Artificial Neural Network

Genetic Algorithm

Mechanical Properties

Optimization

Rubber Compound Design

ABSTRACT

In the rubber industry, the process of designing rubber compound is of great importance due to the impact on product specifications. The good performance of this process is a competitive advantage for manufacturers in this industry. The process of designing a rubber compound includes a set of activities related to selecting the best amount of raw materials to prepare a composition with the desired physical and mechanical properties. Currently, the most common method for designing a rubber compound is the experimental method based on trial and errors. This method is time consuming and expensive. In addition, the obtained combination is not necessarily the best combination. To improve the performance of the rubber compound we need to design the desired process, this research presented using a combination of artificial neural network and genetic algorithm, with an approach to reduce time and cost, while increasing accuracy. In this method, the behavior of the rubber compound was modeled with artificial neural network. Then, using Genetic Algorithm as a quick search technique. The optimal values of the four raw materials such as carbon, sulfur, oil and accelerator; in order to determine the specified value of the two characteristics .abrasion and rubber modulus at 300% elasticity at the lowest price. To evaluate the method, several samples of rubber compound designed with two method. The results showed that the artificial neural network model has the ability to predict the two characteristics of abrasion and modulus based on the four mentioned raw materials in the trained range with high accuracy. In addition, average results for genetic algorithm, is a price of 17% less and a design accuracy of 84.5% more than experimental method. The design speed with this method is 454 times higher than the experimental design speed. Based on the results, by designing the rubber compound with the integration of artificial intelligence and genetic algorithms has a better performance than the experimental method.

doi: 10.5829/ije.2020.33.11b.22

NOMENCLATURE

Notations	Definitions	Notations	Definitions
i	Index of raw materials in rubber compound	x_i^l	Minimum acceptable value for raw material i
k	Index of Target Functions	x_i^u	Maximum acceptable value for raw material i
C_i	Price per kg of raw material i	Y_k^l	Minimum acceptable value for target Functions k
Y_k^*	The value for the physical-mechanical property of K_m	Y_k^u	Maximum acceptable value for target Functions k
n	Number of rubber compound properties	x_i	Quantity of weight selected from raw material i
m	Number of raw materials	$Y_k(X)$	The K th properties value of the designated mixture

1. INTRODUCTION

Elastomers as a type of polymer material have special physical properties such as flexibility, extensibility, resiliency and durability. These unique properties in rubbers have made them widely used in a wide range of

applications. The required properties such as abrasion, toughness, hardness, tensile strength of rubber products require the mixing of rubber with different amounts of raw materials [1]. One of the important issues in the rubber industry is the choice of type and quantity of these raw materials under the design of rubber compound. If

*Corresponding Author Email: ni.ghaffarian@yahoo.com
(N. Ghaffarian)

the selection of raw materials is not in correct method, problems can arise such as inappropriate selection of raw materials or prolonging the selection process. Inappropriate selection of raw materials causes inefficiency in the product. When designing a rubber compound it is usually not difficult to obtain one of the properties stated in the required specifications alone, but when several properties are to be provided at the same time, due to differences in properties, problem arise. In the usual method, the designer, after receiving the blend specifications, combines his theoretical knowledge and practical experience with the blend selection. The steps for designing a rubber mixture based on the experimental method shown in Figure 1. According to the diagram, each repetition requires the construction of a rubber compound and laboratory tests. Obviously, this method is time consuming and expensive, and from an economic and competitive point of view, it is not an ideal method. On the other hand, in the experimental method, the designer chooses the first combination that has the desired properties, while this combination may not be the best combination in terms of price and properties. In addition, the experimental method depends on the designer's experience. Therefore, finding a precise, fast and inexpensive method to design a rubber compound that is not dependent on the individual is necessary for the rubber industry. The rubber compound designer faced with the problem of the effect of each material on each of the characteristics and choosing the best combination in terms of price and specifications. Of course, it is also important to consider the effect of the interaction of raw materials on properties, and the duration and cost of the design method.

Using statistical methods to design a rubber compound is one of the topics of research. Leu et al. [2] predicted the effects of changing material compositions on the physical and mechanical properties of composite material by statistical models. They drew behavior curves and according them determined the best combination of the raw materials to have the desired properties. Salvatori et al. [3] were used statistical experimental design for finding the best percentage of weight of three types of elastomer in a combination with the best final properties. In another research, Adamu et al. [4] were used statistical methods to determine the optimal composition for rubber rollers with best specifications. Research on the design of rubber compounds with statistical methods is not very different. However, it should be noted that the behavior of rubber compounds is highly nonlinear, and the use of the second-class model is not entirely reliable. In addition, statistical methods cannot predict the specification of the compound without laboratory testing and with the increase in the number of raw materials, the number of experimental tests increases, which is time consuming and expensive. Therefore, there is a need for a safe and less tested method.

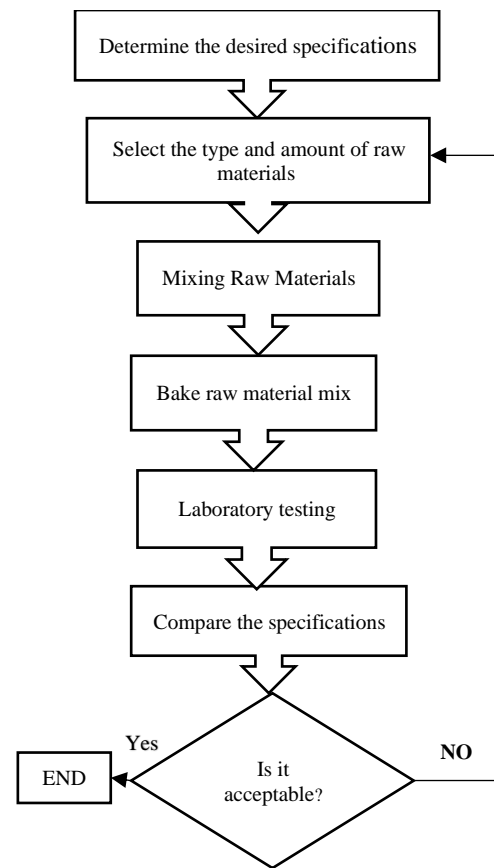


Figure 1. Rubber compound design process

Artificial intelligence modeling methods used to predict the behavior of dependent variables to reduce time and cost. Nateghi and Ahmadi [5] used artificial neural network (ANN) with statistical data to predict the properties of cement composite. They produced 36 different compounds, tested them, and developed the neural network. The design model was accurate enough. Zhang et al. [6] used artificial neural network modeling to predict the mechanical properties of a powder-plastic composite. They achieved optimal point from contour curves. In other work, Diaconescu et al. [7] used artificial neural network with statistical data to predict rubber properties. They generated the mixes with the lowest cost and maximum strength. Wang et al. and Xiang et al. [8, 9] in a separate research used artificial neural network to predict a characteristic value according to other characteristics of the rubber compound. Comparing the results showed that the accuracy of the network designed to predict a properties was better than experimental method. According to researches, the use of artificial neural network modeling is appropriate for predicting the nonlinear behavior of rubber compounds. However, as with the previous method, it requires a series of experimental tests as input data to the model. In previous researches, the optimal combination has been selected

using graphical methods. This method is complicated for examining the effect of several raw materials on several characteristics.

In other studies, has used of metaheuristics methods to select the optimal combination replaced graphical methods. Using these methods to solve optimization problems is an effective method that provides a set of answers in the shortest time. This method used in various engineering sciences. A study conducted by Mehranfar et al. [10] to optimize the supply chain by considering environmental issues and customer demands using a new hybrid metaheuristic based on whale optimization algorithm and simulated annealing as a successful optimizer method. In other study by Safaeian et al. [11], they solved a multi-objective problem by selecting a supplier and assigning an order, taking into account the different costs associated with the Non-dominated Sorting Genetic Algorithm. Fathollahi-Fard et al. [12] used an improved red deer algorithm to design a direct current electric motor. This method reduced design time. In several studies on home health care providers, has used new metaheuristics algorithms to optimize transportation and decision-making in resource allocation. These methods reduced the time, cost of transportation, and created a competitive advantage for the HHC in the supply chain [13-15]. Jalal et al. [16] used genetic algorithms to improve the design and construction of composite vessels. Patel and Suthar [17] used a genetic algorithm to determine the best variables in the design of a car engine. The engine efficiency designed in this way increased by 3.35%. Rahimi and Jafarnejad [18] for the design of automated cellular circuits, reduce the time of the designing by genetic algorithms. Correia et al. [19] optimized the values of three types of raw materials in a rubber mixture with EPDM base to achieve the minimum price. The results showed that it is possible quickly find a combination with the lowest price with metaheuristics methods.

In recent years, the use of a combination of artificial intelligence and metaheuristics methods has also found applications. In one work, Sebaaly et al. [20] used a combination of artificial neural network and genetic algorithm to optimize the asphalt mix. Their goal was to minimize the thickness of the bitumen, while not exceeding the allowable limit. Since some of the limitations of the problem were the complex functions of the physical properties of the raw materials, artificial neural network modeling used. The optimization problem solved with a genetic algorithm. Laboratory results confirmed this method. In other work, Pavia et al. [21] used the integration of neural network with genetic algorithm to optimize the properties of adhesives. They obtained complex relationships between independent and dependent variables from simulation and solved the problem by converting the objectives into a single goal with the genetic algorithm. The results showed that this method is a powerful tool to help shoe glue designers.

Review of the literature shows the use of a combination of statistical methods with artificial intelligence to model the behavior of rubber compound. However, there is no research to develop a model without multiple experiments. In addition, research does not show a combination of artificial intelligence and metaheuristics methods for designing rubber compounds in a multiple objective problem.

In this study, the aim is to provide a fast, accurate, low-cost method to design a rubber mixture with the desired characteristics and the lowest price. For this reason, artificial neural network used to model the behavior of rubber mixture. To reduce time and cost, the data needed to develop the network obtained from previous designs. Improper genetic algorithms used to select the optimal combination, which makes it possible to study several targets with high speed and ease.

2. RESEARCH METHODS

The present study is an applied research of industrial rubber parts manufacturing companies in which improvement of rubber design process is considered. The steps of the research shown in Figure 2.

2. 1. Mathematical Model of Rubber Compound Design Problem

In deciding whether to choose the right amount of raw materials in rubber blends, we articulate the mathematical design theme of rubber as Equation (1). Before describing the mathematical model, the components of the model introduced.

$$\left\{ \begin{array}{l} \min : Z = \{f_1(X), f_2(X), \dots, g(X)\} \quad k = 1, 2, \dots, n \end{array} \right. \quad (1)$$

$$\left\{ \begin{array}{l} f_k(X) = \left| \left(Y_k(X) - Y_k^* \right) \right| \quad k = 1, 2, \dots, n \end{array} \right. \quad (2)$$

$$\left\{ \begin{array}{l} g(X) = \sum_{i=1}^m C_i \cdot x_i \end{array} \right. \quad (3)$$

s.t.

$$x_i^l \leq x_i \leq x_i^u \quad (4)$$

$$Y_k^l \leq Y(X) \leq Y_k^u \quad X = (x_1, x_2, \dots, x_n) \quad n \in \mathbb{N} \quad (5)$$

Model Indexes:

i: Index of raw materials in rubber compound

k: Index of rubber properties in target function

Model Parameters:

C_i: Price per kg of raw material i

Y_k^{*}: The ideal value for K th properties

n: Number of rubber compound properties

m: Number of raw materials

x_i^l: Minimum acceptable value for raw material i

x_i^u: Maximum acceptable value for raw material i

Y_k^l: Minimum acceptable value for Y_k

Y_k^u: Maximum acceptable value for Y_k

Model Variables:

x_i: Quantity of weight selected from raw material i

Y_k(X): The design value for K th properties

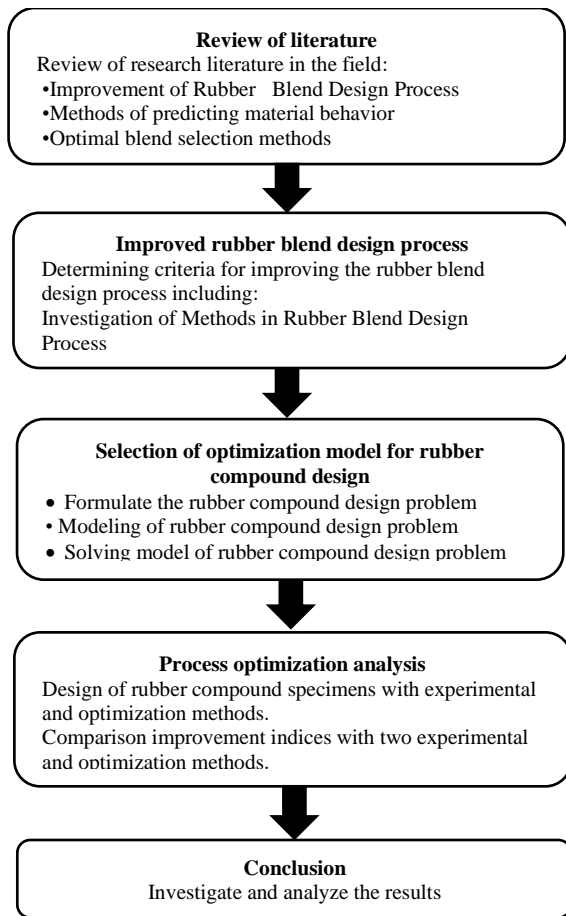


Figure 2. Steps of research

Mathematical Model:

where $f_k(X)$ is the error value for k th properties, with weight composition X of the raw material. In addition, $g(X)$ is the price of the rubber compound for the weight composition X of the raw material. The range of raw materials in rubber compound according to rubber technology given in Table 1.

2. 2. Predicting the Properties of Rubber Compound with Artificial Neural Network

Modeling with ANN used to determine the relationship between the amount of raw materials and the properties of rubber compound. The artificial neural network is a branch of artificial intelligence that be used to detect patterns and predict material behavior. Artificial neural network can simulate nonlinear functions with good accuracy [9]. Artificial neural networks such as the human brain are able to solve new problems using the Knowledge gained from previous experience [7]. In this model, the input is the amount of raw material and the output is the characteristic value of the rubber compound. Artificial neural network design performed in MATLAB software environment. For the modeling, the laboratory information available in the technical section of the rubber company is used. In this study, the ability of the

TABLE 1. Range of Raw Materials

NO	Material name	Minimum (kg)	Maximum (kg)
1	Zinc oxide	3	5
2	Stearic Acid	1	4
3	Antioxidant	0.5	5
4	Ozone	0.5	5
5	Paraffin	0.5	5
6	Carbon	15	85
7	Oil	2	30
8	Sulfur	0.25	5
9	Accelerator	0.25	5

network to predict the behavior of rubber compounds was determined by using the coefficient of determination (R^2) and mean square error (MSE).

2. 3. Finding the Optimal Combination of Raw Materials with Non-Dominated Sorting Genetic Algorithm

A proper search method needed to select the right amount of raw material. Genetic algorithm is the most popular technique in evolutionary computing. This method uses the rules of evolution to search for the best solution for multidimensional problems in finite time [9]. Non-Dominated Sorting Genetic Algorithm is suitable for solving multi-objective problems with conflicting goals. In this way, the best solution sought by forming an initial population of solutions and in an evolutionary manner. In this way, with an evolutionary algorithm searches for the best solutions from an initial population of solutions. In the genetic algorithm, each solution called a chromosome and the independent variables in that solution called genes. In this paper, each solution considered a weighted combination of raw materials. Each gene is the weight value of one of these raw materials. To begin the search, genetic algorithm parameters such as initial population, number of repeats, intersection and mutation ratio, and probability of mutation and range of raw materials specified. Then the genetic algorithm randomly generates a number of different weight combinations of the raw materials in the acceptable range. The artificial neural network model predicts the amount of properties of each compound. These values compared with the desired value. Finally, the best combination selected with the best properties and the lowest price. The design steps of the rubber compound by combining the artificial neural network and the genetic algorithm illustrated in Figure 3.

3. CASE STUDY

The rubber compound design is applicable to all industrial rubber parts companies and tire manufacturers.

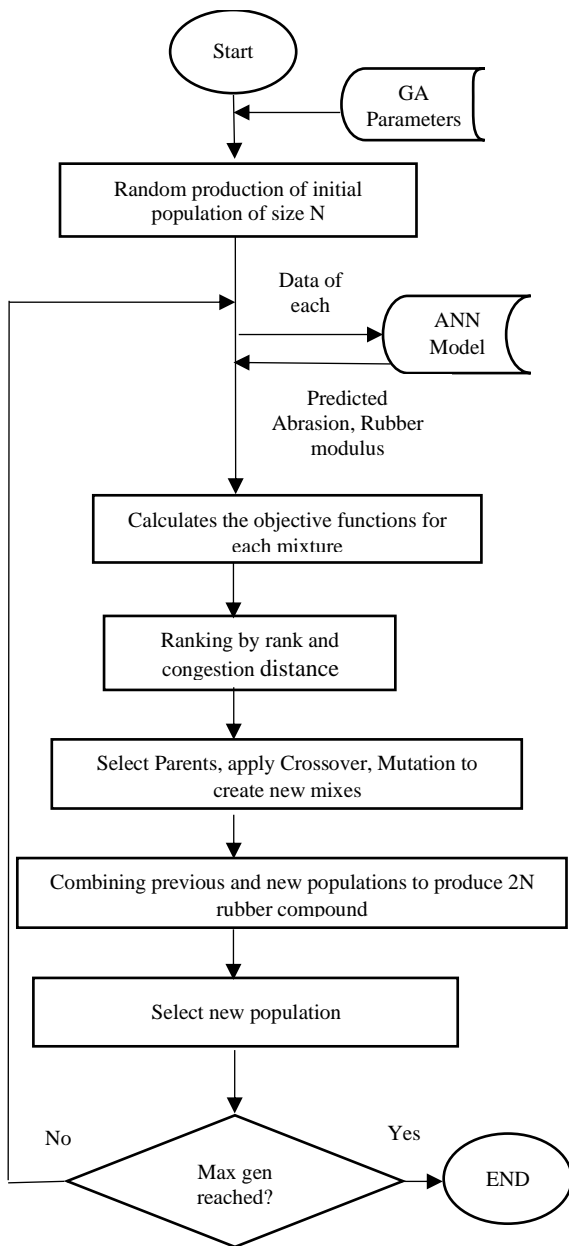


Figure 3. Flow chart for the ANN-GA approach

However, for manufacturers of industrial rubber parts due to product variety, the issue of rubber compound design is more important. In this study, to investigate the effectiveness of the proposed method, an industrial rubber parts company is considered Natural Rubber/ Styreen-Butadeen Rubber -based composites (NR/ SBR are the most widely used in rubber industry.

In addition, the two characteristics of abrasion and modulus are important for most industrial components. For this reason, a NR / SBR-based rubber compound designed, with a specific value for abrasion and modulus and at the lowest price. For the design of the blend, the amount of four raw materials of carbon, oil, sulfur and

accelerator is variable and the amount of other materials is constant. The specific values for modulus, abrasion, and their acceptable ranges given in Table 2.

To model the behavior of rubber blends, data on 47 rubber blends including the weight of the four raw materials and the two properties collected from the rubber company archive. Then this data used as input for training artificial neural network. For each of the two characteristics a multilayer perceptron neural network model developed in MATLAB software. The accuracy of the networks measured based on R^2 and MSE values. Then to search for the optimal combination, the genetic algorithm designed with the toolbox in MATLAB software. The algorithm parameters defined in accordance with Table 3.

The input data to the genetic algorithm is the desired values of modulus and abrasion and the acceptable range for it according to Table 2. Other input data is the acceptable value for the four raw materials according Table 1 and the raw material price. Genetic algorithms created 100 combinations of the four materials as the initial population. For each combination, the data sent to the ANN and the modulus and abrasion values were determined. Price was also determined for each combination with mathematical Equation (3).

The values of the objective functions calculated from Equations (2) and (3). After doing 400 repetitions, 35

TABLE 2. Desired Specification Value

Rubber Compound	Desired Specification Value	
	Abrasion(mm ³)	Modulus(MPa)
1	120±5	10±2
2	150±5	8±2
3	105±5	12±2

TABLE 3. Parameters of Genetic Algorithm

Parameter	Value
Initial population	100
The number of repetitions	400
Intersection ratio	0.7
Mutation ratio	0.1
Probability of mutation	0.02

TABLE 4. The select sample properties

Rubber compound	Abrasion(mm ³)		Modulus(MPa)	
	Ideal	Design	Ideal	Design
1	120	120.03	10	10.07
2	150	150	8	8.32
3	105	105	12	12.09

mixtures with the best target values presented. The amount of abrasion and rubber modulus for the selected sample from the 35 compounds given in Table 4.

This method evaluated by laboratory tests. For this purpose, a rubber compound designed experimentally for the desired specifications. The samples tested for abrasion and rubber modulus according to standard DIN 53516 and standard ASTM D 412 [22]. The results are presented in Table 5. A comparison of the values of objective functions in the optimization method with the experimental method given in Table 6.

4. RESULTS AND DISCUSSION

- According to the results obtained, it be said that more than 90% of the predicted values for abrasion and rubber modulus have a linear relationship with the results obtained from the laboratory test. Therefore, it is possible to predict the rubber modulus and abrasion of the rubber compound for the four raw materials of sulphur, accelerator, carbon and oil using an artificial neural network.
- The results show that this relationship is better for abrasion compared to modulus. Thus, we cannot use one model for all properties. In this method, the designed models has the necessary accuracy. Given that in this method the model is designed using data collected from previous mixtures, it should be said that this method is better in terms of time and cost than the methods presented in previous research.
- The results in Table 5 show that the accuracy of the model is higher in the trained range.
- The results collected in Tables 5 and 6 show that for different compounds designed by the optimization method, the abrasion values and the rubber module are closer to the ideal value. The average difference in the three compounds is 99% for abrasion and 80% for the rubber module. In addition, the design speed with the presented method is 454 times higher than the design speed with the experimental method. Therefore, by combining the genetic algorithm and the artificial neural network, it is possible to design a rubber compound with acceptable accuracy and speed.
- Using this method allows access to a set of answers and increases the designer's decision-making ability. In graphical methods, the problem solved as a single goal, which is long and time consuming and is complicated to examine the effect of several raw materials on several characteristics.
- The results show an improvement in process performance. This improvement was aimed at attracting customer satisfaction and gaining a competitive advantage for the organization. Other research on rubber blending has been done to improve

TABLE 5. The desired values of the properties and them by experimental and optimization methods

Rubber compound	Abrasion (mm ³)			Rubber modulus (MPa)		
	Des	Exp	Opti	Des	Exp	Opti
1	120	118.17	120.03	10	10.5	10.07
2	150	151	150	8	8.5	8.32
3	105	106	105	12	12.7	12.09

TABLE 6. Reduction of quality indicators in two method

Rubber compound	Reduction abrasion error (%)	Reduction modulus error (%)	Reduction price (%)	Reduction design time (%)
1	98	86	27	564
2	100	36	18	244
3	100	87	5	553
Average	99	70	17	454

the characteristics of a blend, and less research has been done on improving the rubber blending design process.

5. CONCLUSION

In this study, with the aim of reducing time and cost and increasing accuracy and ease in the process of designing rubber mixes, the issue of optimizing the process of designing rubber mixes has been investigated. The design of rubber blends has complexities such as nonlinear behavior of rubber mixtures, the effect of raw materials on each other and the effect on composition properties, large number of raw materials and characteristics, conflicting behavior of some characteristics, limitations in raw materials and characteristics. In addition to these issues, the price of the blend designed and the speed of the design is important. Given the complexities and the multiplicity of independent and dependent variables, this is a Non-deterministic Polynomial type (NP-hard) , and the Non-dominated Sorting. Genetic Algorithm used to select the optimal combination. In problem, the relationship between the amount of raw materials and the amount of properties modeled with an artificial neural network. This relationship is completely nonlinear. The behavior of different characteristics is quite different with constant raw materials, so a synthetic neural network model designed for each characteristic. In order for the method to be applicable in terms of product is designing for the customer, the available data in the organization were used to train the artificial neural network. The designed model had the necessary precision to predict the characteristics of the rubber compound. Of course, the model has a higher accuracy in the trained range. With a genetic algorithm designer, choose the final

answer based on the importance of each characteristic or price. The results showed that the process of designing rubber compound with this method has better results than the experimental method.

Finally, it was suggested to technical specialists of the rubber-producing units to apply this method in parallel with the experimental method and then replace it with confidence. It also suggested to researchers that use this method for other rubber compound characteristics such as hardness and tensile strength and for other rubber bases such as EPDM and chloroprene.

6. REFERENCES

- Silviya, E., Varma, S., Unnikrishnan, G. and Thomas, S., "4-compounding and mixing of polymers", *Advances in Polymer Processing: Woodhead Publishing*, Vol. 2, (2009), 71-105. ISBN:978-1-84569-1
- Leu, S.-Y., Yang, T.-H., Lo, S.-F. and Yang, T.-H., "Optimized material composition to improve the physical and mechanical properties of extruded wood-plastic composites (wpcs)", *Construction and Building Materials*, Vol. 29, (2012), 120-127. doi:10.1016/j.conbuildmat.2011.09.013
- Salvatori, P.E., Sánchez, G., Lombardi, A., Nicocia, E., Bortolato, S.A. and Boschetti, C.E., "Optimization of properties in a rubber compound containing a ternary polymer blend using response surface methodology", *Journal of Applied Polymer Science*, Vol. 135, No. 30, (2018), 46548. doi: 10.1002/APP.46548
- Adamu, M., Mohammed, B.S. and Liew, M.S., "Mechanical properties and performance of high volume fly ash roller compacted concrete containing crumb rubber and nano silica", *Construction and Building Materials*, Vol. 171, (2018), 521-538. https://doi.org/10.1016/j.conbuildmat.2018.03.138
- Nateghi-A, F. and Ahmadi, M.H., "Prediction of engineered cementitious composite material properties using artificial neural network", *International Journal of Engineering, Transactions B: Applications*, Vol. 32, (2019), 1534-1542, doi:10.5829/IJE.2019.32.11B.04
- Zhang, S.L., Zhang, Z.X., Xin, Z.X., Pal, K. and Kim, J.K., "Prediction of mechanical properties of polypropylene/waste ground rubber tire powder treated by bitumen composites via uniform design and artificial neural networks", *Materials & Design*, Vol. 31, No. 4, (2010), 1900-1905. doi:10.1016/j.matdes.2009.10.057
- Diaconescu, R.-M., Barbuta, M. and Harja, M., "Prediction of properties of polymer concrete composite with tire rubber using neural networks", *Materials Science and Engineering: B*, Vol. 178, No. 19, (2013), 1259-1267. doi:org/10.1016/j.mseb.2013.01.014
- Wang, B., Ma, J.H. and Wu, Y.P., "Application of artificial neural network in prediction of abrasion of rubber composites", *Materials & Design*, Vol. 49, (2013), 802-807. doi:org/10.1016/j.matdes.2013.01.047
- Xiang, K.-L., Xiang, P.-Y. and Wu, Y.-P., "Prediction of the fatigue life of natural rubber composites by artificial neural network approaches", *Materials & Design*, Vol. 57, (2014), 180-185. doi:org/10.1016/j.matdes.2013.12.044.
- Mehranfar, N., Hajiaghahi-Keshteli, M. and Fathollahi-Fard, A.M., "A novel hybrid whale optimization algorithm to solve a production-distribution network problem considering carbon emissions", *International Journal of Engineering, Transactions C: Aspects*, Vol. 32, No. 12, (2019), 1781-1789, doi:10.5829/IJE.2019.32.12C.11
- Safaeian, M., Fathollahi-Fard, A.M., Tian, G., Li, Z. and Ke, H., "A multi-objective supplier selection and order allocation through incremental discount in a fuzzy environment", *Journal of Intelligent & Fuzzy Systems*, Vol. 37, No. 1, (2019), 1435-1455. doi: 10.3233/JIFS-182843
- Fathollahi-Fard, A.M., Niaz Azari, M. and Hajiaghahi-Keshteli, M., "An improved red deer algorithm to address a direct current brushless motor design problem", *Scientia Iranica*, (2019). doi: 10.24200/SCI.2019.51909.2419
- Fathollahi-Fard, A.M., Govindan, K., Hajiaghahi-Keshteli, M. and Ahmadi, A., "A green home health care supply chain: New modified simulated annealing algorithms", *Journal of Cleaner Production*, Vol. 240, No., (2019), 118200. doi.org/10.1016/j.jclepro.2019.118200
- Fathollahi-Fard, A.M., Hajiaghahi-Keshteli, M. and Mirjalili, S., "A set of efficient heuristics for a home healthcare problem", *Neural Computing and Applications*, Vol. 32, No. 10, (2020), 6185-6205. doi: 10.1007/s00521-019-04126-8.
- Bahadori-Chinibelagh, S., Fathollahi-Fard, A.M. and Hajiaghahi-Keshteli, M., "Two constructive algorithms to address a multi-depot home healthcare routing problem", *IETE Journal of Research*, (2019), 1-7. doi.org/10.1080/03772063.2019.1642802
- Jalal, M., Mukhopadhyay, A.K. and Grasley, Z., "Design, manufacturing, and structural optimization of a composite float using particle swarm optimization and genetic algorithm", Proceedings of the Institution of Mechanical Engineers, Part L: *Journal of Materials: Design and Applications*, Vol. 233, No. 7, (2019), 1404-1418. doi: 10.5829/ije.2018.31.07a.07
- Suthar, B. and Patel, A., "Design optimization of axial flux surface mounted permanent magnet brushless dc motor for electrical vehicle based on genetic algorithm", *International Journal of Engineering, Transactions A Basics*, Vol. 31, No. 7, (2018), 1050-1056, doi: 10.5829/ije.2018.31.07a.07
- Parvane, M., Rahimi, E. and Jafarinejad, F., "Optimization of quantum cellular automata circuits by genetic algorithm", *International Journal of Engineering, Transactions B Applications*, Vol. 33, No. 2, (2020), 229-236, doi: 10.5829/IJE.2020.33.02B.07
- Correia, S.L., Palaoro, D. and Segadães, A.M., "Property optimisation of epdm rubber composites using mathematical and statistical strategies", *Advances in Materials Science and Engineering*, Vol. 2017, (2017). doi.org/10.1155/2017/2730830
- Sebaaly, H., Varma, S. and Maina, J.W., "Optimizing asphalt mix design process using artificial neural network and genetic algorithm", *Construction and Building Materials*, Vol. 168, (2018), 660-670. doi.org/10.1016/j.conbuildmat.2018.02.118
- Paiva, R.M., António, C.A. and da Silva, L.F., "Optimal design of adhesive composition in footwear industry based on creep rate minimization", *The International Journal of Advanced Manufacturing Technology*, Vol. 84, No. 9-12, (2016), 2097-2111. doi: 10.1007/s00170-015-7746-2.
- Committee, A., "Standard test methods for vulcanized rubber and thermoplastic rubbers and thermoplastic elastomers-tension [d412-98]", New York: American National Standards Institute, (1998).

Persian Abstract

چکیده

در صنعت لاستیک، فرآیند طراحی آمیزه لاستیکی به دلیل تاثیر بر خواص محصول از اهمیت بالایی برخوردار است. عملکرد خوب این فرآیند یک مزیت رقابتی برای تولید کنندگان این صنعت به شمار می آید. فرآیند طراحی آمیزه لاستیکی شامل فعالیت های مربوط به انتخاب بهترین مقدار از مواد اولیه برای تهیه ترکیبی با خواص فیزیکی مکانیکی مورد نظر است. در حال حاضر، روش معمول برای طراحی آمیزه لاستیکی، روش تجربی مبتنی بر حدس و خطا است. این روش زمان بر و پرهزینه است. علاوه بر این ترکیب بدست آمده الزاما بهترین ترکیب نیست. در این تحقیق، با هدف بهبود عملکرد فرآیند طراحی آمیزه لاستیکی، روشی تلفیقی از شبکه عصبی مصنوعی و الگو ریتم، با رویکرد کاهش زمان و هزینه و افزایش دقت طراحی ارائه شده است. در این روش، رفتار آمیزه لاستیکی با شبکه عصبی مصنوعی مدل سازی شد. سپس از الگو ریتم ژنتیک به عنوان یک تکنیک جستجوی سریع استفاده شد. مقدار بهینه از چهار ماده اولیه کربن، گوگرد، روغن و شتاب دهنده برای ساخت آمیزه لاستیکی با کمترین قیمت و مقدار مورد نظر از سایش و مدول لاستیکی در ۳۰۰٪ کشش تعیین شد. برای ارزیابی روش، چند نمونه آمیزه لاستیکی با دو روش طراحی شد. نتایج نشان داد، شبکه عصبی مصنوعی توانایی پیش بینی دو ویژگی را براساس چهار ماده اولیه ذکر شده در محدوده آموزش داده شده با دقت بالایی دارد. علاوه بر این با الگو ریتم ژنتیک به طور میانگین قیمت ۱۷٪ کمتر و دقت ۸۴.۵٪ بیشتر از روش تجربی بود. سرعت طراحی ۴۵۴ مرتبه بیشتر بود. براساس نتایج امکان طراحی آمیزه لاستیکی با ادغام هوش مصنوعی و الگو ریتم ژنتیک وجود دارد و عملکردی بهتر از روش تجربی دارد.



Modified Particle Swarm Optimization-Artificial Neural Network and Gene Expression Programming for Predicting High Temperature Oxidation Behavior of Ni-Cr-W-Mo Alloys

H. Hasibi^a, A. Mahmoudian^b, G. R. Khayati^{*a}

^a Department of Materials Science and Engineering, Shahid Bahonar University of Kerman, Kerman, Iran

^b Department of Metal, Institute of Science and High Technology and Environmental Sciences, Graduate University of Advanced Technology, Kerman, Iran

PAPER INFO

Paper history:

Received 24 May 2020
Received in revised form 28 July 2020
Accepted 02 August 2020

Keywords:

Artificial Neural Network
Gene Expression Programming
High-temperature Alloys
Modified Particle Swarm Optimization
Oxidation Behavior

ABSTRACT

This paper is an attempt to model the oxidation behavior of Ni-base alloys by considering the alloying elements, i.e., Cr, W, Mo, as variables. Modified particle swarm optimization-artificial neural network (MPSO-ANN) and gene expression programming (GEP) techniques were employed for modeling. Data set for construction of (MPSO-ANN) and GEP models selected from 66 cyclic oxidation performed in the temperature range of 400-1150 °C for 27 different Ni-based alloy samples at various amounts of Cr, W, and Mo. The weight percent of alloying elements selected as input variables and the changes of weight during the oxidation cycle considered as output. To analyze the performance of proposed models, various statistical indices, viz. root mean squared error (RMSE) and the correlation coefficient between two data sets (R^2) were utilized. The collected data of GEP randomly divided into 21 training sets and 6 testing sets. The results confirmed that the possibility of oxidation behavior modeling using GEP by $R^2 = 0.981$, RMSE = 0.0822. By consideration of oxidation resistance as criteria, Cr, Mo, and W enhanced the oxidation resistance of Ni-based alloys. The results showed that in the presence of Cr as alloying element, especially at Cr contents higher than 22 wt.%, the effect of W and Mo were negligible. However, the same trend was reversed at the sample with Cr content lower than 20 wt.%. In these cases, the effect of W and Mo on oxidation resistance were significantly enhanced.

doi: 10.5829/ije.2020.33.11b.23

1. INTRODUCTION

Ni-based alloys have extensive usages as high-temperature alloys due to relatively high resistance for the oxidation, e.g., structural materials for construction of the steam generator tubes and high-energy piping nozzles [1, 2]. Growing demand for new technologies enhanced the queries for advanced material with innovative properties, especially, high oxidation resistance, mechanical strength, and fabric ability. By consideration of these properties, alloys divided into the type with surface layer of Cr_2O_3 based scale for the oxidation behavior, and the type with Al_2O_3 -based scale

layer for protection against environmental agent [3–6]. Haynes alloy 230 is one of the most convenient Ni-based alloys with the surface layer of Cr_2O_3 based scale types. On the one hand, excellent high-temperature strength and on the other hand, acceptable environmental resistance has caused the evolution of Haynes 230 as a good candidate for application in high temperature components in aerospace as well as power industries [1]. According to literature, there would be endless queries for high-temperature structural alloys in the future, especially in power plants HR-120, HR-160 and Haynes 230 alloys are the most commercial chromium-forming alloys. The cycle oxidation

*Corresponding Author Email: khayatireza@gmail.com
(G. R. Khayati)

Please cite this article as: H. Hasibi, A. Mahmoudian, G. R. Khayati, Modified Particle Swarm Optimization-Artificial Neural Network and Gene Expression Programming for Predicting High Temperature Oxidation Behavior of Ni-Cr-W-Mo Alloys, International Journal of Engineering (IJE), IJE TRANSACTIONS B: Applications Vol. 33, No. 11, (November 2020) 2327-2338

resistance of these alloys is strongly dependent on the amount of alloying elements [7]. Specific characteristics of Haynes 230 alloys encourage the researchers to select as prime candidates for high-temperature usages. Accordingly, many studies have been designed for investigating the oxide scale formation as a function of operational temperature at different environmental conditions. For example, the presence of minor alloying elements in Haynes 230 significantly enhanced the oxidation resistance of alloys [4]. However, in some cases, some trend has been observed in binary alloys system at the presence of third alloying elements [4]. Investigating the literature revealed that the high-temperature resistance under thermal cycling condition of Cr_2O_3 -forming alloys is strongly affected by the amount of Si content [8]. Investigating the influence of Cr, W, and Mo on the oxidation resistance of Ni – Cr – W – Mo alloys is the main objective of this study. W and Mo constituents can enhance the high-temperature strength of high temperature alloys through solid solution hardening. While the oxidation resistance of Fe and Ni-base alloys are affected by W and Mo in various mechanisms. Typically, the presence of a higher contents of refractory metals, e.g., Mo, W, Ta, Re, is necessary for higher creep strength of Ni-based alloys [5, 9].

In their research, Yun et al. [1] proposed that accumulation of metallic Mo at the interface of oxide – metal and Mo^{6+} in Fe -24 wt.%, Cr -11 wt%. Mo-alloy has a high potential for the oxidation at 700 K and consequently enhanced the oxidation resistance. Similar observations have been reported about the positive effect of Cr and Al content in Ni-Co –Cr –Al –W –Mo – Ta –Re –Ru during the oxidation at 1100 °C and to the formation of a protective layer as NiAl_2O_4 [9]. In other researches, it has been shown that W and Mo cause volatile species as oxide phase to form and prevent the formation of fresh protective Cr_2O_3 layer after the spallation of oxide scale, and consequently there is not any linear relation between the amount of alloying elements and the oxidation behavior in the multi-component system [1]. Advances in computer hardware have made soft computing techniques more efficient. In addition, soft computing techniques may be used to model problems where the conventional approaches, such as regression analysis, fail or perform poorly [10]. Artificial neural networks, fuzzy logic, adaptive neuro-fuzzy interfaced, and GP are the most common soft computing techniques [11]. Use of AI techniques such as artificial neural networks (ANN) and gene expression programming (GEP) are popular in various fields of mathematics, engineering, medicine, economics, meteorology, and psychology are attracting interest in recent years [12]. ANN method provides a novel approach to predict the deformation behavior of materials under different conditions. ANN is an

artificial intelligence technology to simulate biological processes of the human brain [13, 14]. This system comprises operators interconnected via one-way signal flow channels. It collects the samples with a distributed coding which forms a trainable non-linear system. It is also self-adaptive to the environment to respond to the different inputs rationally [15]. Although ANNs typically build “black box” models, explicit formulas can be derived for a trained ANN model. A derivative-free optimization algorithm should be added to the training process of the ANN algorithm to avoid local minima, which leads to false convergence of the ANN model [10]. There are many papers on the applications of GEP in the literature for different engineering problems [11]. GEP is newer than the GP approach. GA by employment of genetic variation and operators selects the best individuals [12]. A combination of regression strategies and systematic design of the experiment is an efficient alternative approach for providing the experimental data in a new popularity model approach such as Gene expression programming. ANN and GEP can capture complex interactions among input/ output variables in a system without using prior knowledge about the nature of these interactions. To the best of our knowledge, there are some reports about the usage of two different AI applications: ANN and GEP together to compare prediction performance and explain experimental procedures [10, 11, 16–18].

This paper aims to evaluate the oxidation behavior of Ni-base alloys using PSO- ANN and GEP models [17]. In the current study, GEP (an advanced approach in artificial intelligent and modified PSO-artificial neural network strategy) has been utilized to construct a new model for the prediction and optimization of the oxidation resistance of Ni–Cr–W–Mo alloys as a function of main alloying element (i.e., Cr, W, Mo) using the reported data in the literature [1] as input. The samples produced by a combination of nominal composition in vacuum arc remelting furnace. XRD (X'pert MPD system of Philips instrument by $\text{Cu-K}\alpha$) and FESEM (MIRA3 model) were employed for phase analysis and morphological investigation, respectively. The motivation of this paper is to illustrate an appropriate model for the prediction of oxidation resistance of Ni–Cr–W–Mo alloys by artificial intelligence models as a function of the type and amount of alloying elements, (Cr, W, Mo) as well as determining the relative significance of input variable in output.

2. COLLECTION OF EXPERIMENTAL DATA

Determination of effective practical parameters as input has a key role in accurate modeling of specific output. Dae Won Yun et al. [1] have investigated the high-

temperature behavior of Ni–Cr–W–Mo alloys using Bayesian neural network. They used 66 experiments of oxidation cyclic on 27 samples of Ni–Cr–W–Mo alloys with various alloying elements. According to their experiments the oxidation cyclic behavior is mainly a function of alloying elements. Hence, various alloying content of Cr (18, 22, 26 wt.%), W (10, 14, 18 wt.%) and Mo (0, 2, 4 wt.%) were selected for the preparation of 27 different samples of Ni-base alloys. The alloying element content are selected as input and the weight changes after 66 cycles (mg/cm^2) are considered as output. Table 1 shows the chemical composition and corresponding weight changes for every sample [1].

TABLE 1. The details of experimental data for constructing of the GEP and modified PSO- ANN models [1]

Alloys name	Input			Output
	Cr (wt. %)	W (wt.%)	Mo (wt.%)	Weight changes after 66 cycles (mg/cm^2)
T01	18	10	0	-218.77
T02	18	10	2	-136.69
T03	18	10	4	-146.65
T04	18	14	0	-182.14
T05	18	14	2	-149.80
T06	18	14	4	-124.40
T07	18	18	0	-156.25
T08	18	18	2	-126.72
T09	18	18	4	-81.98
T10	22	10	0	-37.03
T11	22	10	2	-31.52
T12	22	10	4	-25.63
T13	22	14	0	-43.50
T14	22	14	2	-26.99
T15	22	14	4	-21.44
T16	22	18	0	-50.09
T17	22	18	2	-32.85
T18	22	18	4	-17.24
T19	26	10	0	-2.10
T20	26	10	2	-4.73
T21	26	10	4	-4.97
T22	26	14	0	-6.06
T23	26	14	2	-4.90
T24	26	14	4	-4.76
T25	26	18	0	-9.80
T26	26	18	2	-7.01
T27	26	18	4	-3.90

As shown in Figure 1(a), the effective formation of Ni-based alloying was confirmed in the typically XRD pattern of T13 sample. Minor segregation of W and Cr are the other events shown in Figure 1(b). the EDX point chemical analysis Figure 1(c) confirmed the presence of alloying elements in point A.

2. 1. Artificial Neural Network (ANN) ANN is a biologically inspired system developed to solve problems in the same way that the human brain would. Generally, the architecture of ANN consists of three different layers as follows i.e., input layer, hidden layer and output layer [19–23]. Back propagation is one of the most common methods for training ANN. The weight vector of network is also important since it is contributing to the better performance [24–26]. The meta-heuristic techniques have been getting attention to improve the parameters of ANN. Therefore, we apply PSO algorithm to optimize ANN'S weights [14, 27].

2. 2. Particle Swarm Optimization (PSO) Particle swarm optimization (PSO) is one of the most popular population-based stochastic optimization

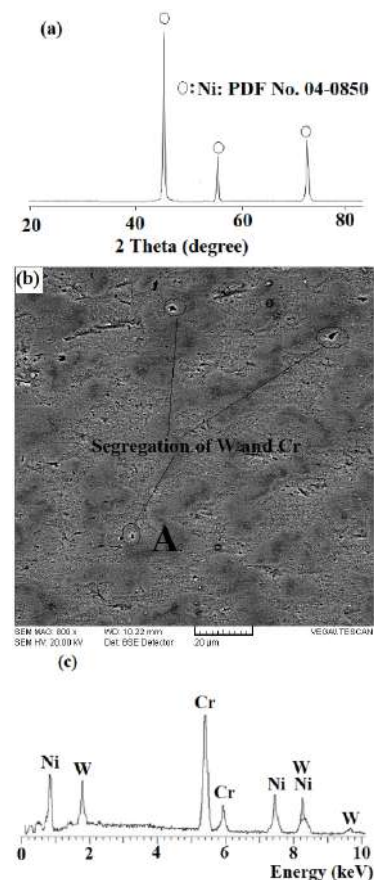


Figure 1. Typically illustration of (a) XRD pattern and (b) FESEM image and (c) EDX point chemical analysis of point A of as-cast T13 prepared alloy

algorithms [28]. PSO technique has received wide attention in recent years since it can converge to the optimization value quickly and has excellent robustness [29, 30]. The aim of the current study is to determine the most appropriate values for the weights and bias of NN (i.e., optimized NN) based on the PSO algorithm [31]. Then, we used optimized NN as the Fitness function of PSO to obtain the best values, of our futures.

2. 3. GEP Methodology

GEP is an advanced evolutionary approach with the ability to model the high complexity problems by the employment of a linear representation of a practical process with nonlinear behavior [32]. GEP provides a simple genetic operator, similar to the genetic algorithm, for the illustration of complex and expressive trees similar to the genetic programming [33, 34]. GEP, at first, dedicating a constant length of a chromosome to the initial population that is randomly generated [35]. At second step, the fitness of individuals of chromosomes is estimated and at the third step, by considering the higher fitness as criterion, the most appropriate individuals are selected to enhance the model accuracy. These stages are repeated until pre-defined generations number or until an appropriate model has been determined. Figure 2 illustrates the flowchart of Gene expression programming [36].

The input and output parameters for GEP modeling are the content of alloys elements, including Cr, Mo, W, and the weight changes after 66 cycles (mg/cm^2), respectively. To construct the GEP models, 21 set of experiments were employed for training and the remaining 6 sets were utilized for testing of the proposed models. GEP starts by random selection of 21 data set for training and 6 data set for testing the performance of proposed models. To model the oxidation behavior of Ni-base alloys, in the current study, GEP modeling was performed at the following steps:

1. Evaluation of the fitness of generated chromosomes by consideration of root relative squared error (RRSE) as fitness function;
2. Selection of the terminals and functions to construct the GEP chromosomes;
3. Determination of chromosomes architecture, i.e., a function of head size and gene number;
4. Definition of genetic operators and their related rates;
5. Finding of appropriate function for connecting the genes, i.e., “division”, “multiplication”, “subtraction”, and “addition” in GEP software [37].

Hence, GEP modeling is a time-consuming and complicated process [37]. By utilization of trial and error during the changing of GEP characteristics (as shown in Table 2) and monitoring the accuracy criteria until the acceptable models were obtained [38].

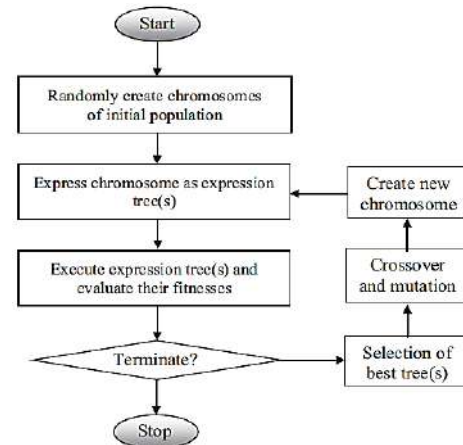


Figure 2. Providing the GEP flowchart [10]

TABLE 2. The characteristics of the training parameters of GEP models

GEP parameters definition	Choice
Function set	+, -, *, /, $\ln(x)$, x^2 , $\sqrt[3]{x}$, Tanh(x), Sech(x), Exp(x), atan(x), Max(x,y), Min(x,y), Not, Avg2, pow
Number of chromosomes	30
Head size	7,8 (GEP-10,GEP-11,GEP-12)
Number of genes	3
Linking function	Addition, multiplication
Fitness function error type	RRSE
Constant per gene	1
Mutation rate	0.00138, 0 (GEP-2, GEP-3, GEP-4, GEP-6, GEP-7, GEP-10, GEP-11)
Inversion rate	0(GEP-2, GEP-3, GEP-4, GEP-11), 0.00546 (GEP-1, GEP-5, GEP-8, GEP-9, GEP-12), 0.0082 (GEP-6, GEP-7, GEP-10)
One point recombination rate	0(GEP-2, GEP-3, GEP-4, GEP-11), 0.00277 (GEP-1, GEP-5, GEP-8, GEP-9, GEP-12), 0.0028 (GEP-6, GEP-7, GEP-10)
Two point recombination rate	0(GEP-2, GEP-3, GEP-4, GEP-11), 0.00277 (GEP-1, GEP-5, GEP-8, GEP-9, GEP-12), 0.0028 (GEP-6, GEP-7, GEP-10)

3. RESULTS AND DISCUSSIONS

Since GEP and MPSO-ANN are able to model specific output as a function of independent variables, the dependency of input variables must be checked at first. It was necessary to note that the presence of any dependency between input parameters, i.e., Cr (wt.%), W (wt.%), and Mo (wt.%) can evolve the problem and

exaggerate the strength of each input variable. This study used bivariate correlation analysis to determine the relationship between the practical parameters. Table 3 shows various correlation coefficients between practical parameters [39, 40]. As shown, there is not any interaction between the input parameters, and consequently, the collected experimental data set are appropriate for modeling by GEP and PSO-ANN.

3. 1. MPSO-ANN Model Results The evolution of 10 most appropriate MPSO-ANN models has been carried out by employment of two statistical indices, viz. root mean square error (RMSE) and the correlation coefficient between two data sets (R^2). It was necessary to note that the network with values of error indices closer to zero and value of R^2 closer to one shows better performance. Equations (1) and (2) show these indices.

$$RSME = \sqrt{\frac{1}{n} \sum_{i=1}^n (h_p - h_a)^2} \tag{1}$$

$$R^2 = 1 - \frac{\sum_{i=1}^n (h - h_p)^2}{\sum_{i=1}^n (h - h_a)^2} \tag{2}$$

in which, h_a , h_p , h_a^- and n are the experimental (target) value (actual weight changes after 66 cycles (mg/cm^2)), the predicted value of weight changes, the average of the actual value of weight changes during the two-run of measurements and the number of experimental samples, respectively.

Table 4 compares the 10 most appropriate MPSO-ANN models for the prediction of the oxidation resistance of Ni-based alloys in detail. As shown, various functions and neuron numbers caused the changes in the number of statistical indices. In addition, logsig and tansig are employed as activation functions during the optimization process.

Figure 3 compares the statistical indices for validation of proposed MPSO-ANN performances. In the case of RMSE (Figure 3(b)), the lower values of error belong to model 5 and consequently, this model shows higher performance with respect to the other. This situation belongs to model 9 for the case of R^2 as a threshold, because of its closer values to 1 (Figure 3(a)). If Fitness value, defined as the amount of both types of indices (error and R^2), the behavior of the proposed model as a function of network number can be monitored as shown in Figure 4. Accordingly, by

TABLE 3. Dearson’s correlation coefficients among all pairs of input variables

Parameters	Cr (wt.%)	W (wt.%)	Mo (wt.%)
Cr (wt.%)	1	0	0
W (wt.%)	0	1	0
Mo (wt.%)	0	0	1

TABLE 4. Details of trained MPSO-ANN models

Model	Neurons	Function	R^2	RMSE
PSO-ANN 1	8-7-1	logsig-purelin	0.8532	0.0086
PSO-ANN 2	8-4-1	tansig-purelin	0.9118	0.0003
PSO-ANN 3	8-8-1	tansig-purelin	0.8636	0.0005
PSO-ANN 4	8-3-1	logsig-purelin	0.7795	0.0008
PSO-ANN 5	8-14-1	logsig-purelin	0.8635	0.0002
PSO-ANN 6	8-12-1	tansig-purelin	0.8141	0.0048
PSO-ANN 7	8-17-1	logsig-purelin	0.8607	0.0006
PSO-ANN 8	8-28-1	logsig-purelin	0.8607	0.0006
PSO-ANN 9	8-25-1	tansig-purelin	0.9337	0.0014
PSO-ANN 10	8-16-1	logsig-purelin	0.9006	0.0030

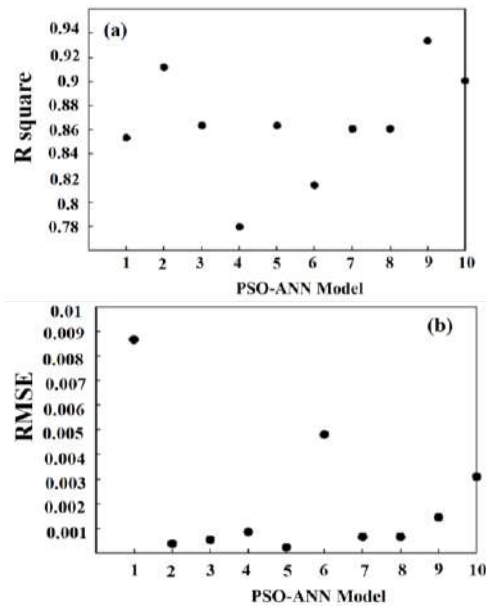


Figure 3. The statistical quality criteria of PSO-ANN networks (a) R^2 , (b) RMSE

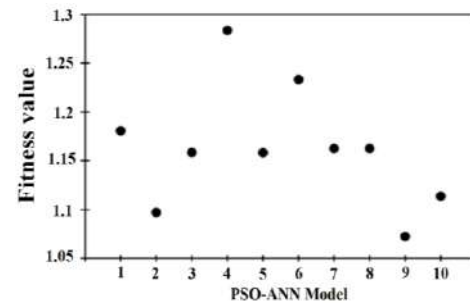


Figure 4. Fitness values of different ANN-PSO networks

consideration of both types of indices, including R^2 and RMSE, model 9 proposed as the most appropriate models in this study. Because of the best performance

was achieved when fitness value was closer to zero. Fitness value was proposed as Equation (3):

$$\text{Fitness value} = \text{RMSE} - \frac{1}{R^2} \quad (3)$$

In Figure 5, normalized data of weight loss as a function of various alloying elements have been reported and confirmed the acceptable performance of MPSO-ANN network. In addition, the accuracy of MPSO-ANN 9 network is higher for the estimation of the effect of Cr, W, and Mo.

3. 2. GEP Model Results

In current work, GEP, i.e., an advanced methodology in AI has been utilized to model the oxidation behavior of Ni-based alloys in the presence of Cr, W, and Mo as alloying elements. Hence, 12 different GEP models were proposed after evaluation of 100 models constructed with various GEP parameters including chromosome number, head size, gene number, linking function and function set [12].

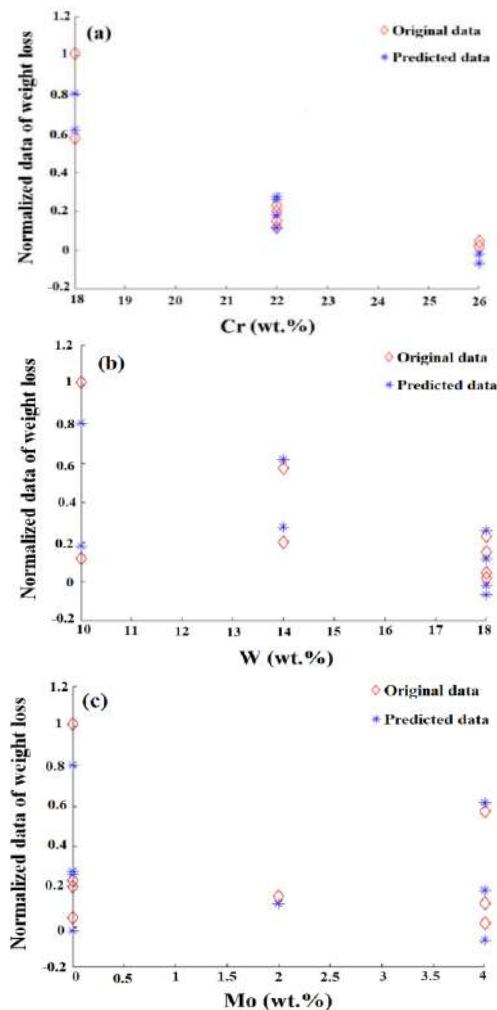


Figure 5. Predicted weight loss based on alloying elements Cr(a), W(b) and Mo(c) by hybrid ANN and MPSO algorithm

It was necessary to note that due to the possibility of various combination in GEP parameters, construction of GEP model for all these combinations need a huge amount of computational time. Table 5 indicates the training and test evaluation of GEP model after 66 oxidation cycles. In a similar approach for validation of PSO-ANN networks, the statistical indicator including root mean square error (RMSE) and an absolute fraction of variance (R^2) are utilized for validation of the accuracy GEP models [41]. As shown in Table 4, R^2 values changed in the range of 0.938-0.991 for the training step and 0.931-981 for the testing step. The minimum amount of RMSE is equal to 0.0572 in testing and 0.0279 for the training step, respectively. By consideration of the higher value of R^2 (close to 1) and lower value of RMSE (close to zero) as criteria, GEP-12, GEP-11, GEP-8 and GEP-9 were selected from 100 GEP investigated models. Figure 5 compares the changes of statistical indicators in training and testing of most appropriate GEP models. Analysis of Figure 6 reveals that GEP-11 shows higher accuracy with respect to the other GEP models in prediction of high-temperature oxidation behavior of Ni-Cr-W-Mo alloys.

Table 6 Summary of the most appropriate 12 GEP models.

Figure 7 shows the comparison of R^2 and MSE for GEP-8, GEP-9, GEP-11 and GEP-12 models in testing and training phases. In these Figures, the sample numbers shown in circles and hexagons, while the numbers in vertical axis belong to the weight changes after 66 cyclic oxidation tests. As can be seen, R^2 and RMSE training and testing of GEP-11 model confirmed the higher accuracy of GEP-11 respect to the other

TABLE 5. Statistics indicator values for the validation of proposed GEP models

Model	R^2		RMSE		Best Fitness	
	Train	Test	Train	Test	Train	Test
GEP-1	0.9380	0.9382	0.0770	0.0713	799.5	795.20
GEP-2	0.9706	0.9465	0.0529	0.0977	853.03	739.19
GEP-3	0.9903	0.9662	0.0302	0.0875	910.46	759.77
GEP-4	0.9445	0.9759	0.0731	0.0914	804.81	751.84
GEP-5	0.9913	0.9553	0.0290	0.1019	913.55	730.96
GEP-6	0.9738	0.9485	0.0528	0.0979	835.6	738.78
GEP-7	0.9867	0.9314	0.0354	0.0782	896.52	779.84
GEP-8	0.9824	0.9700	0.0412	0.0596	881.75	882.87
GEP-9	0.9887	0.9715	0.0325	0.0572	904.15	828.74
GEP-10	0.9823	0.9559	0.0408	0.0686	882.74	801.48
GEP-11	0.9919	0.9812	0.0279	0.0822	771.01	916.53
GEP-12	0.9637	0.9774	0.0604	0.063	835.62	813.66

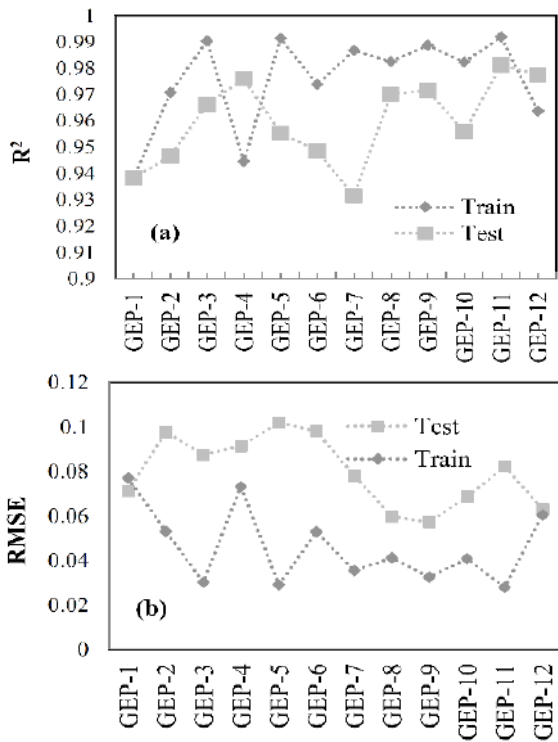


Figure 6. Different errors for training and testing data series in GEP models; (a) R² and (b) RMSE

models (Figures 7 (e) and 7 (f)). Accordingly, the empirical weight changes, after 66 cycles of oxidation of Ni-Cr-W-Mo alloys are in good agreement with the predicted weight variation with GEP-11.

Boxplot is a popular approach for the visual representation of data sets through their quartiles. Whisker, i.e., parallel lines extending from the boxes, is utilized to show the variability region at the upper and lower quartiles. Outliers are often shown as separate dots in the line with whiskers. Taking less space as well as its ability for comparing the distribution of any data set is the main advantage of boxplot [42]. Boxplot provides the possibility of determination of the outliers the symmetricity of data, the amount of data set tightly, direction, and amount of skewed diagrams as a visual representation.

To find the best model for the explanation of the oxidation behavior of Ni-Cr-W-Mo alloys, boxplot is utilized in this study. Accordingly, the residual error, defined as the difference between the predicted and experimental values, is plotted for various GEP models. Figure 8 compares the boxplot of the training and testing phase for various GEP models [42].

In boxplot, the rectangle displays the distance between the first and third quarters and the line within the rectangle determines the second quarter. The black lines outside the rectangle show the minimum and

maximum data values. Moreover, the outliers are illustrated in boxplot. As shown in Figure 8, GEP-11 and GEP-8 have shown the lowest amount of residual error. However, GEP-8 model illustrates higher outliers and caused a severe reduction of its performance. Moreover, exception the GEP-8 and GEP-12, the data tend toward the higher values and their distribution skewed to the top [42]. In Figure 8 b, all GEP models show at least one outlier data exceptional the GEP-12 with to outliers. In addition, GEP-8 and GEP-11 have lower values of residual errors.

TABLE 6. Summary of most appropriate GEP models in the prediction of the oxidation resistance

Model	Infering equation
GEP-1	$y = \min(\text{GEP3Rt}((\text{Cr} * \text{Mo}) + \text{GEP3Rt}((\text{W} + 0.492))), \text{Mo}) + ((1.0 - \text{Cr}) * (-0.640)) * (1.0 - \text{Cr}) * ((\text{Cr} + 0.640) ^ 2) + (((1.0 - \text{Mo}) - (-5.298 + \text{Mo})) + ((-5.298 + \text{Cr}) + \max(\text{Cr}, \text{Mo}) / 2.0) / 2.0)$
GEP-2	$y = (((1.0 - \text{Mo}) - (-7.388 + \text{Mo})) + \max(((\text{Cr} + \text{Cr}) / 2.0), (\text{Mo} + \text{W}) / 2.0)) / 2.0 + (((1.0 - \text{Cr}) * (-0.659)) * (1.0 + 0.659)) * ((\text{Cr} - 0.659) ^ 2) + \min((((1.35) - (\text{Cr} - 0.675)) + \text{GEP3Rt}(0.675)) / 2.0), \text{Mo})$
GEP-3	$y = ((\min(((\text{Cr} + \text{Cr}) + ((\text{W} + \text{Mo}) / 2.0)), \max(0.931, \text{Mo})) + \text{Cr}) / 2.0 + (1.0 / ((1.196 * (((\text{Cr} + \text{Cr}) + 1.196) + \exp(1.196)))) + (((0.281 * \text{W}) * \text{Mo} ^ 2) + ((\text{Cr} - 0.281) - (\text{Cr} ^ 2)) / 2.0)$
GEP-4	$y = \min((((((\text{Cr} + \text{Mo}) / 2.0) ^ 2 + \tanh((0.142 - \text{Mo})) / 2.0), \text{Mo}) + (((\min((\text{Cr} - 0.216), (\text{Mo} * 0.216)) + (\text{W} * 0.216)) / 2.0) + 0.216) + (\min((\text{Cr} + \text{Mo}), 0.759) + ((\text{Mo} * 0.759) - ((\text{Mo} + \text{Mo}) / 2.0)))$
GEP-5	$y = \tanh(((\text{GEP3Rt}(((1.940 + 2.486) / 2.0) + (\text{Cr} * \text{W})) ^ 2) ^ 2)) * \text{GEP3Rt}(\tanh((((((\text{W} + \text{Mo}) / 2.0) ^ 2) ^ 2 + \text{Cr})) * (((1.0 - \text{Mo}) + (\text{Cr} + \text{Mo}) - ((\text{Cr} ^ 2) + ((\text{W} + \text{Cr}) / 2.0)) / 2.0))$
GEP-6	$y = (((9.143 + (\text{Cr} + 9.143)) / 2.0) * ((9.143 - \text{Mo}) - (\text{Cr} ^ 2))) + ((\min(\text{Cr}, 0.139) - 0.278) + ((\text{W} * 0.139) * (\text{Cr} ^ 2))) + (((\text{Cr} + \text{W}) + (\text{Cr} + \text{Mo})) + ((1.0 - \text{W}) * (\text{Cr} + 0.45)) / 2.0)$
GEP-7	$y = \text{atan}(\exp(-0.707) * \text{GEP3Rt}(((\text{Cr} + \text{Mo}) / 2.0))) + \text{atan}(\text{atan}(\text{atan}(\text{GEP3Rt}(\max(\text{W} * 1.495, \text{Cr})))) + ((\text{GEP3Rt}(\text{Mo}) - \tanh(\text{Mo})) * (\max(0.804) - (1.0 - 0.402)))$
GEP-8	$y = ((\text{sech}(\text{Cr}) * (\text{Cr} + \text{Cr})) - \max(\max(0.113, \text{Cr}), (0.113 * \text{Cr}))) + (\text{atan}(\max(\text{Cr}, \text{W}) - (-0.612))) * ((0.374) - (\text{Mo} * \text{Cr})) + ((\min(\text{Mo}, \text{Cr}) + 0.321) * \max((\text{Cr} * \text{Cr}), \text{atan}(\text{Mo})))$
GEP-9	$y = \text{atan}(\text{atan}((-0.757 * \text{Cr})) + ((\tanh(\text{Cr}) + \text{atan}(\text{Cr})) / 2.0)) + \text{atan}(\text{atan}(((\text{atan}(\text{Mo}) + ((0.110 + \text{W}) / 2.0)) / 2.0) + (\text{Cr} + \text{Cr}))) + \max((((0.418 + \text{Cr}) - \text{W}) * (1.0 - \text{Cr})), \text{atan}(0))$
GEP-10	$y = \text{GEP3Rt}(\tanh((((0.840 - \text{Mo}) - \exp(\text{Cr})) * \exp(\exp(\text{Cr})))) * ((\tanh((\max(\text{W}, \text{Cr}) + (\text{Mo} + \text{Cr})) + \text{GEP3Rt}(\text{Cr}) / 2.0) * \min((-1.004), \text{GEP3Rt}(((\text{Cr} - 0.502) - \tanh(\text{Mo}))))$
GEP-11	$y = \max((1.0 - (1.0 - \tanh(\text{Cr}))), ((\min(\text{W}, \text{W}) + (0.127 * \text{Mo})) / 2.0) ^ 2) + (((\text{GEP3Rt}(\text{GEP3Rt}(\text{Cr})) + (\text{Mo} * 0.237)) / 2.0) / ((0.474) + (\text{Cr} + \text{Cr}))) + ((((-0.347 * \text{Cr}) - (-0.347)) + \tanh((\text{Cr} ^ 2)) / 2.0) * (-0.347))$
GEP-12	$y = (((((1.0 - \text{Cr}) - \text{Mo}) + (-0.427 * \text{W})) / 2.0) * (((\text{W} + \text{Cr}) / 2.0) + (\text{Cr} - 0.427)) / 2.0) + (\tanh(\text{Cr}) - \min(\text{Cr} - (\text{Cr} + \text{W}), (-0.869))) + ((1.0 / (\text{reallog}(((0.472) / 2.0)))) + (((\tanh(\text{Cr}) - \text{Cr}) + ((\text{Mo} + \text{Cr}) / 2.0)) / 2.0))$

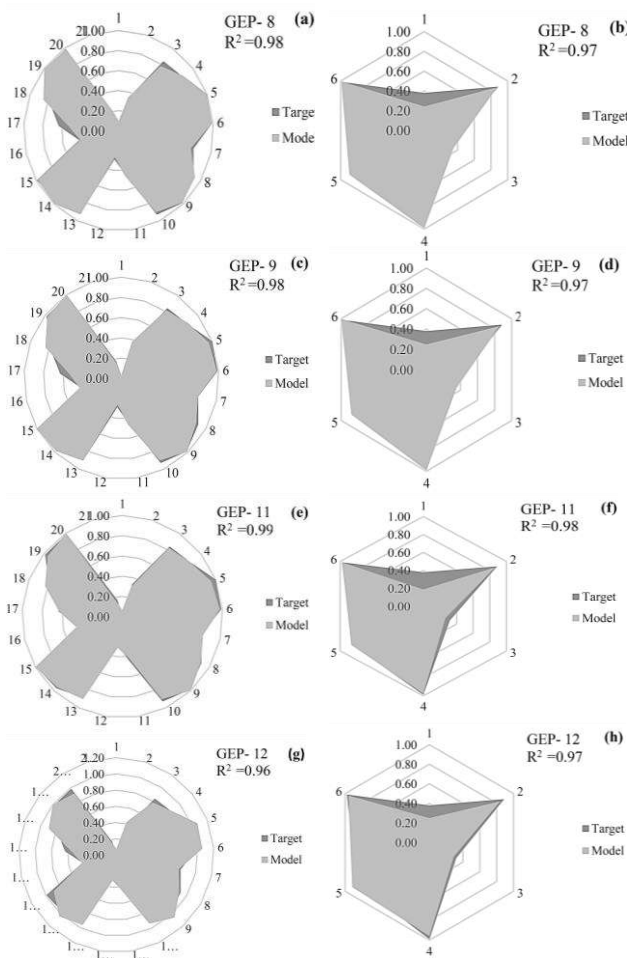


Figure 7. Comparison of R^2 and MSE for testing and training phases of the most appropriate model prepared by GEP; (a, b): training and testing of GEP-8; (c, d): training and testing of GEP-9; (e, f): training and testing of GEP-11; (g, h): training and testing related to GEP-12

Since, the aim of this study is to illustrate a model with the highest performances, the boxplot of 27 samples has been prepared by the most appropriate GEP models (Figure 9). Accordingly, in spite of the presence of an outlier in GEP-12, due to the wide distribution of residual error, this model was rejected. The other GEP models (GEP-8 and GEP-9) showed at least two outlier data, while GEP-11 has symmetrical distribution as well as one outlier data. Accordingly, GEP-11 has been proposed as the most appropriate model for prediction of the oxidation behavior of Ni-Cr-Mo-W alloys at high temperatures.

3. 3. Sensitivity Analysis Since, the proposed PSO- ANN network and GEP model have acceptable performance for the prediction of oxidation behavior, the sensitivity analysis was performed on both of them and the results were compared.

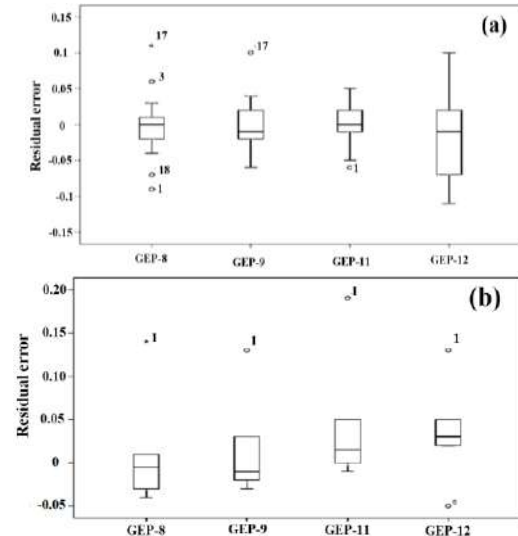


Figure 8. The values of residual error for GEP models in the form of boxplots for the (a) training and (b) testing datasets

3. 3. 1. Sensitivity Analysis using PSO- ANN Network

In this approach, the sensitivity analysis was performed by changing the values of each parameter in the range of lower and higher levels of practical values when the other parameters remained constant in their average values. In addition, to provide the possibility of illustration of all affected parameters with various values and their distribution, all inputs were standardized by definition of z- square [35].

$$Z = \frac{(h_i - \bar{h})}{\sigma} \tag{4}$$

where, h_i , \bar{h} , σ and Z are the i_{th} variable, the average, standard deviation of input parameters, and the standardized value of parameter, respectively. The display of weight changes versus the changes of any input parameters are shown in Figure 10. As shown, the change in the input parameter (Mo) versus the output parameter (weight changes after 66 cycles) is very small and it is as a straight line. Therefore, the weight percent of Mo has the least effect on the weight changes (oxidation resistance) while Cr and W have the most effect on oxidation resistance, respectively.

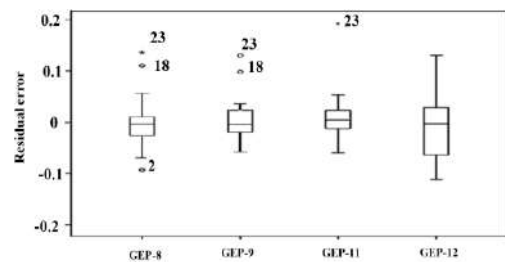


Figure 9. The values of residual error for GEP models in the form of box plots for all of 27 Ni-Cr-W-Mo alloys

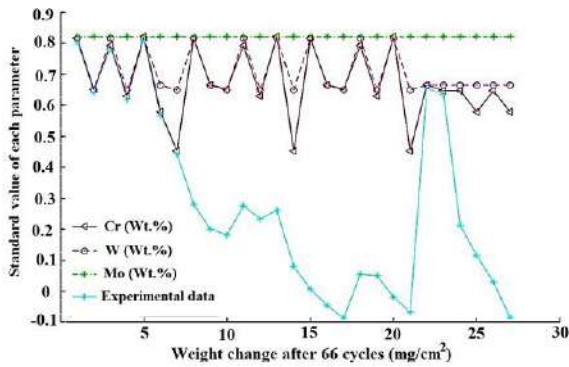


Figure 10. Sensitivity analysis of input parameters on the weight changes after 66 cycles [35]

3. 3. 2. Sensitivity Analysis using GEP Similar approach was used to determine the sensitivity analysis in current study. In this regard, various noises were created on the input data at 5 and 10 % and compared the amount of output error by actual values.

Figure 11 shows the sensitivity analysis to determine the relative significance of Cr content on the oxidation resistance of Ni-Cr-W-Mo alloys investigated in this study. According to this figure, the oxidation resistance of Ni-based alloys is proportional to their Cr content. Also, the positive effect of Cr amount on the oxidation resistance is more severe at higher Cr content, i.e., (T19-T27) alloys with 26 wt.% of Cr. However, the positive effect of Cr content in other samples with 22 and 18 wt.% of Cr is lower proportional to the amount

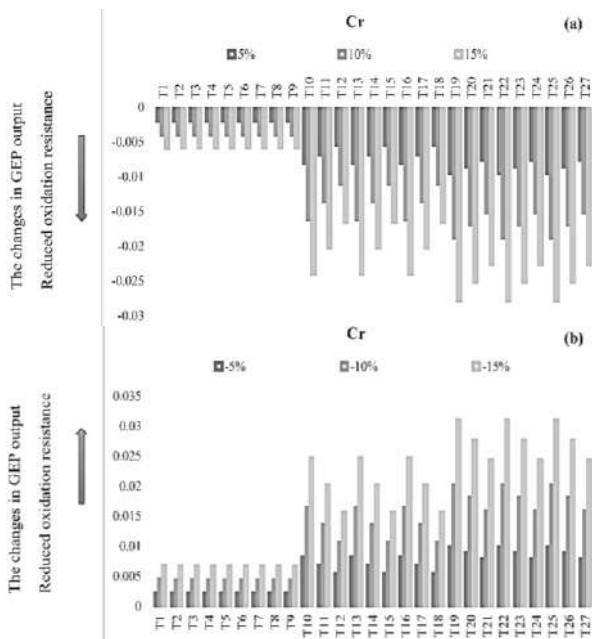


Figure 11. Sensitivity analysis for determination of the effect of Cr on the oxidation resistance of Ni-Cr-W-Mo alloys. (a) Increasing the Cr content, (b) Decreasing Cr content

of Cr in (T1, T2, T3, T4, T5, T6, T7, T8, T9), (T10, T11, T12, T13, T14, T15, T16, T17, T18) alloys. Moreover, the presence of Mo and W in the alloys with 22 wt.% and 26 wt.% of Cr decreased the positive effect of Cr in oxidation resistance. In this trend, W shows lower effect compared to Mo.

Figure 11 (b) reveals that the effect of reducing the Cr content on decreasing the oxidation resistance is higher in the sample with 26 wt.% of Cr with respect to the other. Also, the presence of Mo and W in alloys with 18 wt.% Cr compensates for the negative effect of lower Cr on the cyclic oxidation behavior. In this regard, Mo is more effective than the W.

The results of the sensitivity analysis on the effect of W content is shown in Figure 12. As shown in Figure 12 (a), similar to the effect of Cr, generally the addition of W amount enhances the oxidation resistance and this positive effect of W is more serious in alloys with the lower content of Cr. Also, by decreasing W content (Figure 12 (b)), oxidation resistance of low Cr content (18 wt.%) is decreased and this trend is intensified in the presence of Mo.

Analysis of Figure 13 (b) shows that similar trends to Cr and W have evolved in the presence of Mo on the oxidation resistance of Ni-Cr-Mo-W alloys. This effect is higher in low Cr content (18 wt.%) alloys. Moreover, decreasing Mo content decreased the oxidation resistance and this trend is more intensified in low Cr content alloys.

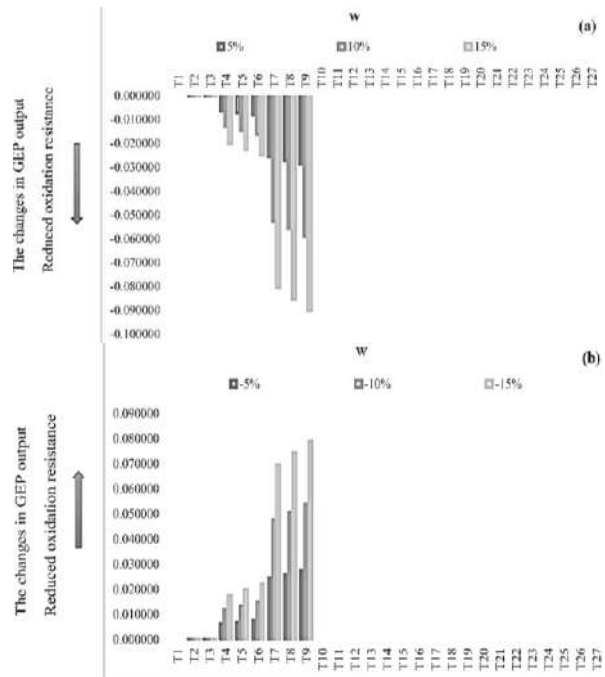


Figure 12. Sensitivity analysis for determination of the effect of W on the oxidation resistance of Ni-Cr-W-Mo alloys. (a) Increasing the W content, (b) Decreasing W content

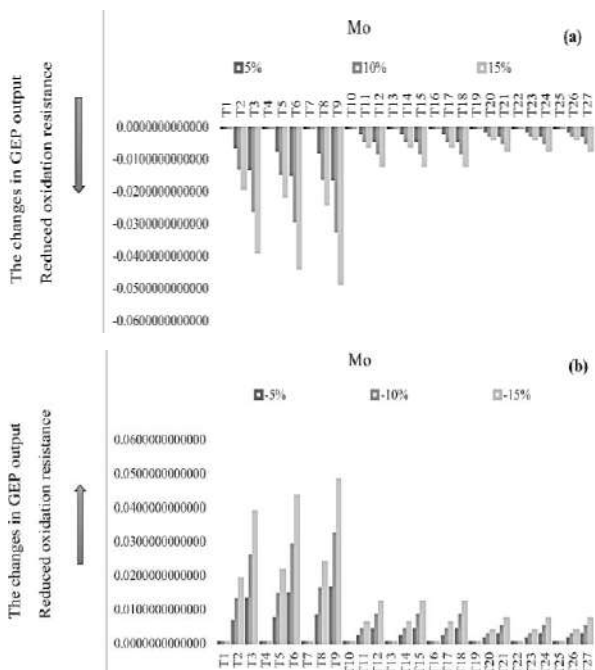


Figure 13. Sensitivity analysis for determination the effect of Mo on the oxidation resistance of Ni-Cr-W-Mo alloys. (a) Increasing the Mo content, (b) Decreasing Mo content

In conclusion, Cr, Mo and W enhanced the oxidation resistance of Ni-Cr-Mo-W alloys. However, in higher Cr containing alloys (alloys with 22 and 26 wt.% of Cr), the Cr content is administrated parameters on the oxidation behavior. The presence of Mo and W induced a positive effect on the oxidation behavior of 18 wt.% Cr. While this effect is reversed in high Cr content alloys (26 and 22 wt.% Cr).

In summary, the higher Cr contents facilitate the formation of adhesive Cr-rich oxide protective layer and induce higher temperature resistance. Typically in the alloys containing 26 wt.% Cr, the continuity and adhesivity of surface Cr_2O_3 layer disturbed in the presence of other alloying elements including W and Mo. It seems that these elements disturb the protective Cr_2O_3 surface films through the evaporation of W and Mo oxides [43]. While, in the case of alloys with Cr content lower than 22 wt.%, the effect of W and Mo were reversed. In this condition, such alloying oxides can provide robust surface protectivity of the oxide layer at high temperatures [44].

In Figure 14, the weight changes from experimental studies are compared with the predicted values using GEP- 11 and the MPSO-ANN 9 models. As can be seen, the values predicted by GEP- 11 model are more accurate than the MPSO model and are closer to real values and this means that the presented GEP model has achieved success in simulation of the high-temperature oxidation behavior of the Ni-based alloys.

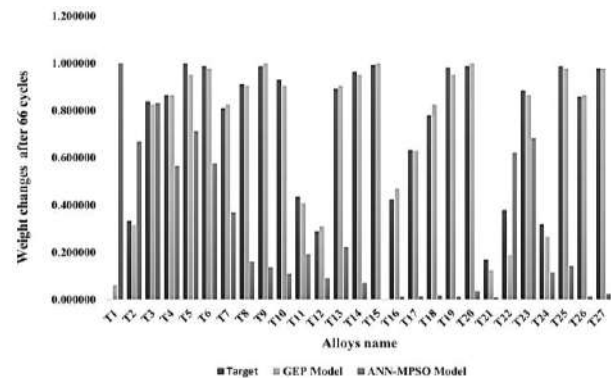


Figure 14. The comparison between the experimental weight changes (after 66 cycles) and the predicted weight changes by GEP and MPSO-ANN models

4. CONCLUSIONS

The prediction resistance of Ni-Cr-Mo-W alloys has a key role in the improvement and design of new high-temperature resistance materials. MPSO-ANN and GEP are increasingly being seen as a novel evolutionary algorithm, which enhanced many advantages of previously constructed models. Based on the results of the current study in which MPSO- ANN and GEP are utilized to model the oxidation behaviors of Ni-Cr-Mo-W alloys, confirmed that the GEP models have the higher performance for modeling of high-temperature resistance behavior. Accordingly, the GEP model and MPSO-ANN model with R^2 and RMSE values equal to 0.9919, 0.0279, 0.9337, and 0.0014, respectively proposed as appropriate models for prediction of the oxidation behavior of Ni-Cr-Mo-W alloys. Moreover, the sensitivity analysis revealed that at higher Cr content (i.e., 22 and 26 wt.%), Cr was administrated alloying elements on the high-temperature resistance, while, in the lower Cr content (i.e., 18 wt.%), the presence of Mo (with the higher effect), and W (with the lower effect) can compensate the lower content of Cr content.

5. REFERENCES

1. Yun, D. W., Seo, S. M., Jeong, H. W., Kim, I. S., and Yoo, Y. S. "Modelling high temperature oxidation behaviour of Ni-Cr-W-Mo alloys with Bayesian neural network." *Journal of Alloys and Compounds*, Vol. 587, (2014), 105–112. <https://doi.org/10.1016/j.jallcom.2013.10.138>
2. Smola, G., Gawel, R., Kyzioł, K., Miszczyk, M., and Grzesik, Z. "Influence of Nickel on the Oxidation Resistance at High Temperatures of Thin Chromium Coatings." *Oxidation of Metals*, Vol. 91, No. 5–6, (2019), 625–640. <https://doi.org/10.1007/s11085-019-09899-w>
3. Cho, S. H., Lee, S. K., Kim, D. Y., Lee, J. H., and Hur, J. M. "Effects of alloying elements of nickel-based alloys on the hot-corrosion behavior in an electrolytic reduction process." *Journal of Alloys and Compounds*, Vol. 695, (2017), 2878–2885.

- <https://doi.org/10.1016/j.jallcom.2016.11.394>
4. Tawancy, H. M. "On the behaviour of minor active elements during oxidation of selected Ni-base high-temperature alloys." *Materials at High Temperatures*, Vol. 34, No. 1, (2017), 22–32. <https://doi.org/10.1080/09603409.2016.1231861>
 5. Olivares, R. I., Young, D. J., Nguyen, T. D., and Marvig, P. "Resistance of High-Nickel, Heat-Resisting Alloys to Air and to Supercritical CO₂ at High Temperatures." *Oxidation of Metals*, Vol. 90, No. 1–2, (2018), 1–25. <https://doi.org/10.1007/s11085-017-9820-7>
 6. Kim, H. S., Park, S. J., Seo, S. M., Yoo, Y. S., Jeong, H. W., and Jang, H. J. "High temperature oxidation resistance of Ni-(5~13)Co-(10~16)Cr-(5~9)W-5Al-(1~1.5)Ti-(3~6)Ta alloys." *Metals and Materials International*, Vol. 22, No. 5, (2016), 789–796. <https://doi.org/10.1007/s12540-016-6305-1>
 7. Duan, R., Jalowicka, A., Unocic, K., Pint, B. A., Huczowski, P., Chyrkin, A., Grüner, D., Pillai, R., and Quadackers, W. J. "Predicting Oxidation-Limited Lifetime of Thin-Walled Components of NiCrW Alloy 230." *Oxidation of Metals*, Vol. 87, No. 1–2, (2017), 11–38. <https://doi.org/10.1007/s11085-016-9653-9>
 8. Sadeghimeresht, E., Reddy, L., Hussain, T., Huhtakangas, M., Markocsan, N., and Joshi, S. "Influence of KCl and HCl on high temperature corrosion of HVOF-sprayed NiCrAlY and NiCrMo coatings." *Materials and Design*, Vol. 148, (2018), 17–29. <https://doi.org/10.1016/j.matdes.2018.03.048>
 9. Yun, D. W., Seo, S. M., Jeong, H. W., and Yoo, Y. S. "Effect of refractory elements and Al on the high temperature oxidation of Ni-base superalloys and modelling of their oxidation resistance." *Journal of Alloys and Compounds*, Vol. 710, (2017), 8–19. <https://doi.org/10.1016/j.jallcom.2017.03.179>
 10. Gandomi, A. H., and Roke, D. A. "Assessment of artificial neural network and genetic programming as predictive tools." *Advances in Engineering Software*, Vol. 88, (2015), 63–72. <https://doi.org/10.1016/j.advengsoft.2015.05.007>
 11. Karahan, I. H., and Özdemir, R. "A comparison for grain size calculation of Cu-Zn alloys with genetic programming and neural networks." *Acta Physica Polonica A*, Vol. 128, No. 2, (2015), 427–431. <https://doi.org/10.12693/APhysPolA.128.B-427>
 12. Coşkun, M. İ., and Karahan, İ. H. "Modeling corrosion performance of the hydroxyapatite coated CoCrMo biomaterial alloys." *Journal of Alloys and Compounds*, Vol. 745, (2018), 840–848. <https://doi.org/10.1016/j.jallcom.2018.02.253>
 13. Ashtiani, H. R. R., and Shahsavari, P. "A comparative study on the phenomenological and artificial neural network models to predict hot deformation behavior of AlCuMgPb alloy." *Journal of Alloys and Compounds*, Vol. 687, (2016), 263–273. <https://doi.org/10.1016/j.jallcom.2016.04.300>
 14. Xu, D. S., Wang, H., Zhang, J. H., Bai, C. G., and Yang, R. "Titanium Alloys: From Properties Prediction to Performance Optimization." In *Handbook of Materials Modeling* (pp. 113–151), Springer International Publishing, 2020. https://doi.org/10.1007/978-3-319-44680-6_116
 15. Shakiba, M., Khayati, G. R., and Zeraati, M. "State-of-the-art predictive modeling of hydroxyapatite nanocrystallite size: a hybrid density functional theory and artificial neural networks." *Journal of Sol-Gel Science and Technology*, Vol. 92, No. 3, (2019), 641–651. <https://doi.org/10.1007/s10971-019-05113-0>
 16. Mahdavi Jafari, M., and Khayati, G. R. "Prediction of hydroxyapatite crystallite size prepared by sol–gel route: gene expression programming approach." *Journal of Sol-Gel Science and Technology*, Vol. 86, No. 1, (2018), 112–125. <https://doi.org/10.1007/s10971-018-4601-6>
 17. Jafari, M. M., Khayati, G. R., Hosseini, M., and Danesh-Manesh, H. "Modeling and Optimization of Roll-bonding Parameters for Bond Strength of Ti/Cu/Ti Clad Composites by Artificial Neural Networks and Genetic Algorithm." *International Journal of Engineering Transactions C: Aspects*, Vol. 30, No. 12, (2017), 1885–1893. <https://doi.org/10.5829/ije.2017.30.12c.10>
 18. Xu, C., Rangaiah, G. P., and Zhao, X. S. "Application of Artificial Neural Network and Genetic Programming in Modeling and Optimization of Ultraviolet Water Disinfection Reactors." *Chemical Engineering Communications*, Vol. 202, No. 11, (2015), 1415–1424. <https://doi.org/10.1080/00986445.2014.952813>
 19. Vakili, M., Khosrojerdi, S., Aghajannezhad, P., and Yahyaei, M. "A hybrid artificial neural network-genetic algorithm modeling approach for viscosity estimation of graphene nanoplatelets nanofluid using experimental data." *International Communications in Heat and Mass Transfer*, Vol. 82, (2017), 40–48. <https://doi.org/10.1016/j.icheatmasstransfer.2017.02.003>
 20. Raza, M. Q., and Khosravi, A. "A review on artificial intelligence based load demand forecasting techniques for smart grid and buildings." *Renewable and Sustainable Energy Reviews*, Vol. 50, (2015), 1352–1372. <https://doi.org/10.1016/j.rser.2015.04.065>
 21. khosrojerdi, S., Vakili, M., Yahyaei, M., and Kalhor, K. "Thermal conductivity modeling of graphene nanoplatelets/deionized water nanofluid by MLP neural network and theoretical modeling using experimental results." *International Communications in Heat and Mass Transfer*, Vol. 74, (2016), 11–17. <https://doi.org/10.1016/j.icheatmasstransfer.2016.03.010>
 22. Mahdavi, M., and Khayati, G. R. "Artificial Neural Network Based Prediction Hardness of Al2024-Multiwall Carbon Nanotube Composite Prepared by Mechanical Alloying." *International Journal of Engineering Transactions C: Aspects*, Vol. 29, No. 12, (2016), 1726–1733. <https://doi.org/10.5829/idosi.ije.2016.29.12c.11>
 23. Kalidass, S., and Mathavaraj Ravikumar, T. "Cutting Force Prediction in End Milling Process of AISI 304 Steel Using Solid Carbide Tools." *International Journal of Engineering, Transactions A: Basics*, Vol. 28, No. 7, (2015), 1074–1081. <https://doi.org/10.5829/idosi.ije.2015.28.07a.14>
 24. shafaei, A., and Khayati, G. R. "A predictive model on size of silver nanoparticles prepared by green synthesis method using hybrid artificial neural network-particle swarm optimization algorithm." *Measurement: Journal of the International Measurement Confederation*, Vol. 151, (2020), 107199. <https://doi.org/10.1016/j.measurement.2019.107199>
 25. da Silva, I. N., Hernane Spatti, D., Andrade Flauzino, R., Liboni, L. H. B., dos Reis Alves, S. F., da Silva, I. N., Hernane Spatti, D., Andrade Flauzino, R., Liboni, L. H. B., and dos Reis Alves, S. F. "Artificial Neural Network Architectures and Training Processes." In *Artificial Neural Networks* (pp. 21–28). Springer International Publishing, 2017. https://doi.org/10.1007/978-3-319-43162-8_2
 26. Maleki, E., and Kashyzadeh, K. R. "Effects of the hardened nickel coating on the fatigue behavior of CK45 steel: Experimental, finite element method, and artificial neural network modeling." *Iranian Journal of Materials Science and Engineering*, Vol. 14, No. 4, (2017), 81–99. <https://doi.org/10.22068/ijmse.14.4.81>
 27. Ansari, A., Heras, M., Nones, J., Mohammadpoor, M., and Torabi, F. "Predicting the performance of steam assisted gravity drainage (SAGD) method utilizing artificial neural network (ANN)." *Petroleum*, (2019). (In press) <https://doi.org/10.1016/j.petlm.2019.04.001>
 28. Gara, S., and Tsoumarev, O. "Optimization of cutting conditions in slotting of multidirectional CFRP laminate." *International Journal of Advanced Manufacturing Technology*, Vol. 95, No.

- 9–12, (2018), 3227–3242. <https://doi.org/10.1007/s00170-017-1451-2>
29. Gupta, I. K., Choubey, A., and Choubey, S. "Particle swarm optimization with selective multiple inertia weights." In 8th International Conference on Computing, Communications and Networking Technologies, (2017), 1-6. <https://doi.org/10.1109/ICCCNT.2017.8204132>
30. Kumar, N., and Kumar Sharma, S. "Inertia weight controlled pso for task scheduling in cloud computing." In 2018 International Conference on Computing, Power and Communication Technologies, (2018), 155–160. <https://doi.org/10.1109/GUCON.2018.8674994>
31. Nouri, M., Bekrar, A., Jemai, A., Niar, S., and Ammari, A. C. "An effective and distributed particle swarm optimization algorithm for flexible job-shop scheduling problem." *Journal of Intelligent Manufacturing*, Vol. 29, No. 3, (2018), 603–615. <https://doi.org/10.1007/s10845-015-1039-3>
32. Ebrahimzade, H., Khayati, G. R., and Schaffie, M. "A novel predictive model for estimation of cobalt leaching from waste Li-ion batteries: Application of genetic programming for design." *Journal of Environmental Chemical Engineering*, Vol. 6, No. 4, (2018), 3999–4007. <https://doi.org/10.1016/j.jece.2018.05.045>
33. Mansouri, I., Kisi, O., Sadeghian, P., Lee, C.-H., and Hu, J. "Prediction of Ultimate Strain and Strength of FRP-Confined Concrete Cylinders Using Soft Computing Methods." *Applied Sciences*, Vol. 7, No. 751, (2017), 1–14. <https://doi.org/10.3390/app7080751>
34. Ferreira, C. "Gene Expression Programming in Problem Solving." In *Soft Computing and Industry* (pp. 635–653). Springer London, 2002. https://doi.org/10.1007/978-1-4471-0123-9_54
35. Hoseinian, F. S., Faradonbeh, R. S., Abdollahzadeh, A., Rezai, B., and Soltani-Mohammadi, S. "Semi-autogenous mill power model development using gene expression programming." *Powder Technology*, Vol. 308, (2017), 61–69. <https://doi.org/10.1016/j.powtec.2016.11.045>
36. Mansouri, I., Chacón, R., and Hu, J. W. "Improved predictive model to the cross-sectional resistance of CFT." *Journal of Mechanical Science and Technology*, Vol. 31, No. 8, (2017), 3887–3895. <https://doi.org/10.1007/s12206-017-0733-9>
37. Mahdavi jafari, M., and Reza Khayati, G. "Adaptive neuro-fuzzy inference system and neural network in predicting the size of monodisperse silica and process optimization via simulated annealing algorithm." *Journal of Ultrafine Grained and Nanostructured Materials*, Vol. 51, No. 1, (2018), 43–52. <https://doi.org/10.22059/JUFGNSM.2018.01.06>
38. Al-Mosawe, A., Kalfat, R., and Al-Mahaidi, R. "Strength of Cfrp-steel double strap joints under impact loads using genetic programming." *Composite Structures*, Vol. 160, (2017), 1205–1211. <https://doi.org/10.1016/j.compstruct.2016.11.016>
39. Mansouri, I., Hu, J., and Kisi, O. "Novel Predictive Model of the Debonding Strength for Masonry Members Retrofitted with FRP." *Applied Sciences*, Vol. 6, No. 337, (2016), 1–13. <https://doi.org/10.3390/app6110337>
40. Gholampour, A., Gandomi, A. H., and Ozbakkaloglu, T. "New formulations for mechanical properties of recycled aggregate concrete using gene expression programming." *Construction and Building Materials*, Vol. 130, (2017), 122–145. <https://doi.org/10.1016/j.conbuildmat.2016.10.114>
41. Khandelwal, M., Armaghani, D. J., Faradonbeh, R. S., Ranjith, P. G., and Ghoraba, S. "A new model based on gene expression programming to estimate air flow in a single rock joint." *Environmental Earth Sciences*, Vol. 75, No. 9, (2016), 1–13. <https://doi.org/10.1007/s12665-016-5524-6>
42. Bakhsheshi-Rad, H. R., Abdollahi, M., Hamzah, E., Ismail, A. F., and Bahmanpour, M. "Modelling corrosion rate of biodegradable magnesium-based alloys: The case study of Mg-Zn-RE-xCa (x = 0, 0.5, 1.5, 3 and 6 wt%) alloys." *Journal of Alloys and Compounds*, Vol. 687, (2016), 630–642. <https://doi.org/10.1016/j.jallcom.2016.06.149>
43. Birks, N., Meier, G. H., and Pettit, F. S. *Introduction to the High Temperature Oxidation of Metals*. Cambridge University Press, 2006. Retrieved from <https://cds.cern.ch/record/1010949>
44. Park, S.-J., Seo, S.-M., Yoo, Y.-S., Jeong, H.-W., and Jang, H. "Statistical Study of the Effects of the Composition on the Oxidation Resistance of Ni-Based Superalloys" *Journal of Nanomaterials*, Vol. 2015, (2015), 1–11. <https://doi.org/10.1155/2015/929546>

Persian Abstract

چکیده

در این مقاله سعی شده تا با در نظر گرفتن عناصر آلیاژی W، Cr و Mo، به عنوان متغیر، رفتار اکسیداسیون آلیاژهای پایه نیکل مدل‌سازی شود. برای نیل به این هدف از شبکه‌های عصبی مصنوعی بهینه‌سازی ذرات اصلاح شده (MPSO-ANN) و تکنیک‌های برنامه‌نویسی بیان ژن (GEP) استفاده شدند. برای ساخت مدل‌های (MPSO-ANN) و (GEP) از نتایج ۶۶ نمونه اکسیداسیون سیکلی در محدوده دمای ۴۰۰–۱۱۵۰ درجه سانتی‌گراد روی ۲۷ نمونه آلیاژ پایه نیکل با مقادیر مختلف W، Cr و Mo استفاده شد. درصد عناصر آلیاژی به عنوان متغیرهای ورودی و تغییر وزن در چرخه اکسیداسیون به عنوان خروجی مدل در نظر گرفته شدند. برای تحلیل عملکرد مدل‌های پیشنهادی، شاخص‌های مختلف آماری، مانند جذر میانگین خطای مربعات (RMSE) و ضریب همبستگی بین دو مجموعه داده (R^2) استفاده شد. داده‌های جمع‌آوری شده برای مدل‌سازی GEP به طور تصادفی به ۲۱ مجموعه داده آموزشی و ۶ مجموعه داده آزمایشی تقسیم گردید. نتایج تأیید کرد که امکان مدل‌سازی رفتار اکسیداسیون با استفاده از GEP با مقادیر $RMSE = 0.8822$ ، $R^2 = 0.981$ وجود دارد. با در نظر گرفتن مقاومت در برابر اکسیداسیون به عنوان معیار، مشخص شد که W، Cr و Mo مقاومت به اکسیداسیون آلیاژهای پایه نیکل را افزایش می‌دهد. همچنین، حضور کروم به عنوان عنصر آلیاژی، به‌ویژه در مقادیر بالاتر از ۲۲ درصد وزنی، تأثیر W و Mo را به مقدار زیادی کاهش می‌دهد. در حالی که حضور W و Mo در نمونه با محتوای کروم کمتر از ۲۰ درصد باعث بهبود قابل ملاحظه مقاومت به اکسیداسیون می‌شود.



Effect of Water Absorption on the Tensile Characteristics of Natural/ Synthetic Fabrics Reinforced Hybrid Composites

R. A. Elsad^a, M. S. EL-Wazery^{*b}, A. M. EL-Kelity^b

^a Basic Science Department, Faculty of Engineering, Menoufia University, Shebin El-Kom, Egypt

^b Department of Production Engineering and Mechanical Design, Faculty of Engineering, Menoufia University, Shebin El-Kom, Egypt

PAPER INFO

Paper history:

Received 18 May 2020

Received in revised form 16 June 2020

Accepted 02 August 2020

Keywords:

Water Absorption

Swelling Thickness

Hybrid Composites

Tensile Strength

Interface

ABSTRACT

The effect of water absorption and swelling thickness on the tensile properties of flax/sisal/carbon/glass fabrics reinforced by unsaturated polyester-based hybrid composites was evaluated. Hybrid composites reinforced with different natural and synthetic fiber configurations have been processed using the Hand lay-up (HLU) technique. Water absorption test was carried out by immersing specimens in distilled water for different lengths of time, up to 1344 hours, and showed slight enhancement of water absorption for fibers configuration [C/C/C/C/C/C] up to 1.45%, but great enhancement of water absorption for fiber configuration [S/S/S/S/S/S] up to 14%. The tensile strength of samples before and after immersion in distilled water was evaluated. This result showed that the tensile strength of fibers configuration [C/C/F/F/C/C] is approaching fibers configuration [C/C/C/C/C/C] at dry condition. Fractured cross-section morphology of composites was investigated using scanning electron microscopy (SEM) to evaluate the fibers/matrix interface before and after hydro aging. The reduction in tensile strength due to water penetrating is slight for hybrid composite with synthetic fibers at the outer layer, but huge for hybrid composite with natural fibers at outer layer.

doi: 10.5829/ije.2020.33.11b.24

1. INTRODUCTION

Natural fiber strengthened polymer composites have raised great attention and interests among materials scientists due to the considerations of promoting an environmental friendly, high specific strength, low density, cheaply and biodegradable compared to the synthetic fiber-reinforced composites. The various types of natural fibers such as jute, hemp, sisal, bananas, flax, and bamboo can be very cost-effective material for applications such as automotive exterior, packing, building, construction industry, electric and electronic devices, and transportation [1-6]. One of the main major reasons for limitation using natural fibers is a high response of water absorption which distorts its mechanical properties. A lot of works used the combination of

synthetic fiber and natural fibers reinforced polymer to reduce the uptake water. Sanjay et al. [7] the water absorption of laminate [G/G/B/G/B/G/B/G/G] was slightly exceeded from that obtained for laminate configuration with glass only. Carbon-E-glass/polyester hybrid composites, prepared by hand lay-up at several stacking sequences, showed the maximum moisture ratio reached to 3% at immersion time 264 hour for the combination [G/G/G/G] [8]. Also, Jesthi et al. [9] used the same fibers (carbon and glass) reinforced polyester composites at various stacking sequences to evaluate the tensile strength after immersed into the seawater for 90 days. After seawater aging, the retention of tensile strength in both designations [C/ C/G/G/G] and [C/G/G/C/G] was greater than that of the glass laminate composite. Sivakumar et al. [10] the maximum percentage of water absorption of polymer composites

*Corresponding Author Email: eng_mahmoudsamir@yahoo.com
(M. S. EL-Wazery)

based on different weight fractions of the glass/nylon/jute obtained for the composition (glass 11% + Nylon 26% + jute 35%) and reached to 9.52%. The addition of jute fiber with glass fiber in polymer epoxy composite enhanced the tensile strength and impact energy but reduced the resistance for water absorption compared to pure glass composite [11]. The addition of the carbon layer to the flax fabrics reinforced epoxy composite improved the tensile strength and reached 288 MPa compared to the flax composite [12]. In addition, Gupta et al. [13] the highest water absorption ratio obtained for hybrid composite with sisal 20 wt% and glass 20 wt% and reached 6%, compared to other composites. In another study, Gupta and Deep et al. [14] the designation (G/S/G/S/G) provided maximum values of the tensile strength and flexural strength in both dry and wet conditions as compared to other stacking sequences. The hybridization using carbon fiber with natural fibers such as cross-ply flax-based polymer composite showed an enhancement in the tensile properties (284.8 MPa) and reduction in water absorption ratio (5.5%) compared to those without hybridization [15]. Girisha et al. [16] studied the effect of water absorption of composites reinforced by natural fibers such as sisal and coir at different weight fractions (20 %, 30 %, and 40%) on their tensile properties. The maximum tensile strength after hydro aging obtained for the hybrid composite reinforced by 40 wt% sisal-coir fiber reached 48 MPa. The water absorption of hybrid composite reinforced by jute/glass fiber in several environments such as seawater, distilled water, and acidic water has been investigated [17]. The samples immersed in distilled water gives maximum moisture content and higher value of the diffusion coefficient compared to other water conditions. Sathish et al. [18] hybrid composite reinforced 30% flax and 10 % bamboo exhibited maximum tensile strength (31.55 MPa) and minimum water absorption ratio (9.3%), compared with the natural bamboo composite. Gopal et al. [19] the composite sample (15% sisal: 15% jute: 5% flax) with comparison with various concentrations (20:10:5 and 25:5:5) gives a minimum ratio of water absorption (14.73%). The effect of carbon fiber hybridization on the water absorption of unidirectional and cross-ply flax specimens has been investigated [15]. Hybridization using synthetic fiber (carbon) with two types of natural fibers (UD and CP flax) gave maximum water absorption of the hybrid carbon/UD flax specimen and carbon/ CP specimens of approximately 2 and 8%, respectively. Calabrese et al. [20] used another synthetic fiber (glass fiber) with natural fiber (flax) reinforced epoxy composite to evaluate the water absorption capacity. This hybridization reduced the saturation in water absorption ratio to 6.9%. in addition, Saidane et al. [21] used the same hybridization [21], but at different layers configurations between the flax and carbon fibers, to study the effect of stacking sequence on tensile

strength after hydro aging effect. For the combination [G/F/F/F/F], the reduction in tensile strength was about 11%, while it reached to about 21% for the flax laminate.

In the present work, different fiber configurations of flax/sisal/glass/carbon reinforced unsaturated polyester hybrid composites have been prepared using Hand lay-up (HLU) route. The samples were immersed in distilled water to evaluate their resistance to water absorption and swelling thickness. The tensile strength test was carried out before and after hydro aging. In addition, fracture surfaces were examined using SEM to investigate bonding between layers before and after hydro aging.

2. MATERIALS AND EXPERIMENTAL PROCEDURE

2. 1. Materials and Manufacturing Composites with various accumulating sequences and proportional fibers content were manufactured using the hand lay-up technique. The unsaturated polyester and hardener with a proper proportion of 4:1 were mixed in the presence of a catalyst plus 1.5% resin using mechanical stirring for 5 min. The mixture was fed into the mold with dimension 250 x250 cm. Then, the fibers were laid according to the designated sequences. Finally, the roller was passed over the laid composite to remove bubbles formed during manufacturing. The prepared composites were kept at room temperature for two days to provide optimal stiffness and retraction. The fibers used to reinforce unsaturated polyester are flax, sisal, E-glass, carbon. Table 1 shows the physical and mechanical properties of the sisal, flax, E-glass, and carbon fabric reinforcements [23-26]. Non-hybrid and hybrid composite samples consist of six fabric layers. The combinations were named F, S, C, G, L1, L2, L3, L4, L5, L6, L7, and L8 according to the designation listed in Table. 2.

TABLE 1. Mechanical property of the used fabrics

Properties	Flax	Sisal	E-glass	Carbon
Density [g/cm ³]	1.40	1.46	2.55	1.78
Tensile strength (MPa)	1500	700	3400	4200-4800
Elastic modulus(GPa)	60-80	35	73	260
Shear modulus(Gpa)	28.2	18.2	33	110
Specific (E/d)	30	29	29	-
Poisson ratio	0.23	0.23	0.22	0.279
Elongation (%)	3.2	3-7	1.8-3.2	1.75-1.95
Moisture (%)	8-12	10-20	-	-
Fiber diameter(μm)	40-600	50-200	17	5-7
Lignin Content (%)	67/3	75 /12	-	-

2. 2. Water Absorption and Thickness Swelling Test

The water absorption and swelling thickness behavior of the non-hybrid and hybrid composite were evaluated. In order to study the effect of hydro aging, both weight and thickness of samples were measured before and after immersion for varies intervals time in distilled water. The weight of the sample was measured by using an electronic balance with an accuracy of 0.1mg. This procedure was repeated until the weight of the samples remained constant up to a 4-digit number with increasing time of immersion.

The estimated water absorption ratio and the swelling thickness percentage, is calculated using Equations (1) and (2) below:

$$WA(\%) = \frac{w_t - w_o}{w_o} \times 100 \quad (1)$$

where w_A , w_o , and w_t are the water absorption percentage, the weight of the initial and wet samples at a given time, respectively.

$$TS(\%) = \frac{t_t - t_o}{t_o} \times 100 \quad (2)$$

where TS, t_o and t_t are the thickness swelling percentage and the thickness of samples before and after immersion in distilled water respectively.

2. 3. Tensile Strength

Figure 1 show the setup and dimensions of the tensile test sample used to evaluate the tensile characteristics. The tensile strength of composites was measured before and after hydro aging with the universal testing machine (INSTRON 8801) at a crosshead speed of 5 mm/min. According to ASTM D638 standard, the average of five tensile strength measurements for each composite sample with dimension (165 mm x13 mm x4 mm) was recorded.

2. 4. Morphological Characterizations

The morphology of composites was investigated at fractured surface of samples using (SEM, Quanta FEJ20) at 20 kV.

TABLE 2. Designation of hybrid and non-hybrid composites and their relative fabric weight and volume fractions

Laminate	Fiber configurations	Wight fraction (wt. %)					Volume fraction (vt. %)				
		Matrix	Carbon	Glass	Flax	Sisal	Matrix	Carbon	Glass	Flax	Sisal
F	[F/F/F/F/F]	40	0	0	60	0	40.6	0	0	59.4	0
S	[S/S/S/S/S]	40	0	0	0	60	41.46	0	0	0	58.54
C	[C/C/C/C/C]	40	60	0	0	0	46.65	53.35	0	0	0
G	[G/G/G/G/G]	40	0	60	0	0	53.42	0	46.58	0	0
L1	[C/C/F/F/C]	40	40	0	20	0	44.46	33.88	0	21.66	0
L2	[F/F/C/C/F]	40	20	0	40	0	42.45	16.18	0	41.37	0
L3	[C/C/S/S/C]	40	40	0	0	20	44.78	34.14	0	0	21.08
L4	[S/S/C/C/S]	40	20	0	0	40	43.06	16.41	0	0	40.53
L5	[C/G/S/F/G/C]	40	20	20	10	10	47.24	18	12.12	11.52	11.12
L6	[G/C/S/F/C/G]	40	20	20	10	10	47.24	18	12.12	11.52	11.12
L7	[S/F/G/C/F/S]	40	10	10	20	20	43.92	8.37	5.63	21.41	20.67
L8	[F/S/C/G/S/F]	40	10	10	20	20	43.92	8.37	5.63	21.41	20.67

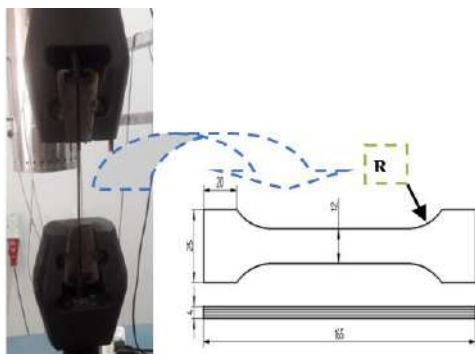


Figure 1. Set up and the dimensions of the tensile test sample

The cross-section of investigated samples is coated with 100 Å thick platinum in the JEOL sputter ion coater.

3. RESULTS AND DISCUSSIONS

3. 1. Water Absorption and Swelling Thickness Behavior

Figure 2 shows the dependency of water absorption ratio and swelling thickness on the immersion time for the hybrid and non-hybrid composites with various fiber configurations. Each data point was calculated from an average value of five samples for each laminate. These figures indicate that the

water absorption ratio for all laminates was increased with increasing immersion time until saturation point. These results coincide well with previous work for natural and synthetic fiber [1, 7]. From Figure 2 can be claimed that the non-hybrid composites with sisal or flax have the highest water absorption saturation up to 14% and 12%, and swelling thickness (20%), (18%), respectively. However, the minimum value of water absorption ratio was obtained for carbon composites with fiber configuration [C/C/C/C/C/C] and reached 1.45% as shown in Figure 2a. The small value of water absorption ratio, obtained for fiber configuration [C/C/C/C/C/C], can be attributed to low sensitivity of carbon to water absorption. Therefore, the swelling thickness diminished due to the smallest value of the water absorption ratio. It can be seen from Figure 2(b) that the trend of swelling thickness is similar to the water absorption behavior with immersion time until it reached the equilibrium conditions. In general, the constituents of flax and sisal fiber are cellulose and hemicellulose. The flow of water into the capillaries (pore absorption) and diffusion into amorphous body of cellulose and hemicellulose (fiber absorption) are the main sources for the uptake of water in natural fiber (flax and sisal). The probability of pores creation in natural fiber is high as compared to synthetic fiber. Therefore, the uptake of water in natural fiber is higher than that of synthetic fiber. Density and size of formed pores depended on the size, shape, and arrangement of natural fiber. The diffusion of water through an inter-molecular distance of chains leads to fiber swelling. The lower water uptake by flax fiber compared to sisal fiber reflects the fact that the number and size of pores in flax fiber are less than that in sisal fiber. High moisture susceptibility in natural fiber is considered one of the major issues in the usage of these fibers. Hence, we tend to use combination of natural and synthetic fibers. The water uptake ratio of hybrid composites laminate (L1) with fiber configuration [C/C/F/F/C/C] was around 37.6% of that obtained for non-hybrid composites with fiber configuration [F/F/F/F/F/F]. In addition, water uptake for laminate (L3) reached 50 % of that obtained for sample (S). The drop in water uptake for laminate (L1) as compared to laminate F can be attributed to the existence of carbon fibers layers at the top and the bottom of the stack which works as a barrier for contact between the water molecules and flax fibers. On the other hand, the water uptake percentage of laminates L2 and L4 reached 62.5% and 71.4% as compared to F and S laminates, respectively due to the existence of natural fabrics at outer layers. In comparison with hybrid-composites, the laminate L5 with fiber configuration [C/G/S/F/G/C] is in second place in resistance for water uptake after laminate L1 due to the hybridization by the hydrophobic carbon fibers and adhesion between resin matrix and fiber.

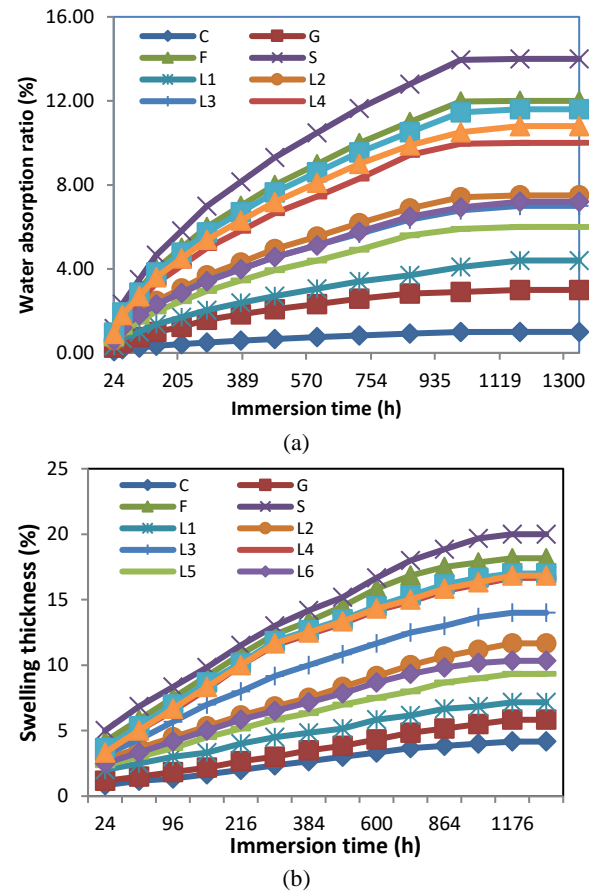


Figure 2. (a) Variation of the water absorption ratio and (b) Variation of the swelling thickness with the immersion time for the hybrid and non- hybrid composites at various fiber configurations

3. 2. Tensile Characteristics

Figures 3a and b show the load-displacement curves of the laminate (L1) with fiber configuration [C/C/F/F/C/C] before and after water absorption. These figures reflect the condition that the stress of a laminate (L1) sample before hydro aging gradually increased up to (73 MPa) at displacement 3.82 mm. However, the stress of this hybrid sample after the hydro aging enhanced up to 61 MPa at 4.1 mm displacement, and reduced abruptly down to 38 MPa at a maximum 4.40 mm displacement, and then, finally the sample was broken. The drop in the breaking stress for laminate (L1) sample after hydro aging can be attributed to the swelling of fibers which enhances the inter-molecular distance of chains as discussed in previous section. Both tensile strength and maximum strain of the hybrid and non-hybrid composites at different fiber configurations before and after hydro aging are listed in Table 3. Such a table reflects that the tensile strength of all samples before hydro aging is higher than those obtained after hydro aging.

Non-hybrid composites with flax laminate or sisal laminate have small tensile strength with considerable shifting to lower value after hydro aging. Additionally, it was found that the laminate (S) exhibited lower tensile strength compared to the laminate (F). In contrast, non-hybrid composite with carbon has the highest value of tensile strength with slight shifting to lower value after hydro aging effect. The hybrid-composites have moderate tensile strength. In general, mechanical properties of composites reinforced with fabric rely on the nature of each component in composites, distribution, and orientation of fiber through a matrix and of the interphase region between different components. The spread of water into pores as well as the inter-molecular distance of chains after hydro aging effect causes a reduction in the connection between the components of the sample as a whole. However, maximum strain of all

laminates was enhanced after hydro aging effect due to an increase in the plasticization effect.

The small value of tensile strength for laminates S and F can be attributed to the lower strength of sisal and flax fiber as well as poor interfacial adhesion between the matrix and fiber. The huge penetrating water through laminates S and F cause an adverse effect on the interfacial region, created between base matrix and fibers, and structural solidity. Therefore, the tensile strength of laminate S and F was extremely reduced after hydro aging while maximum strain was enhanced. When the flax fibers was placed at the core in the laminate (L1), the tensile strength before and after hydro aging was closest to the laminate (C). The response of water uptake for laminate L1 is weak because of the presence of carbon at outer layers. Hence, the change in tensile strength and maximum strain after hydro aging is slight. In contrast,

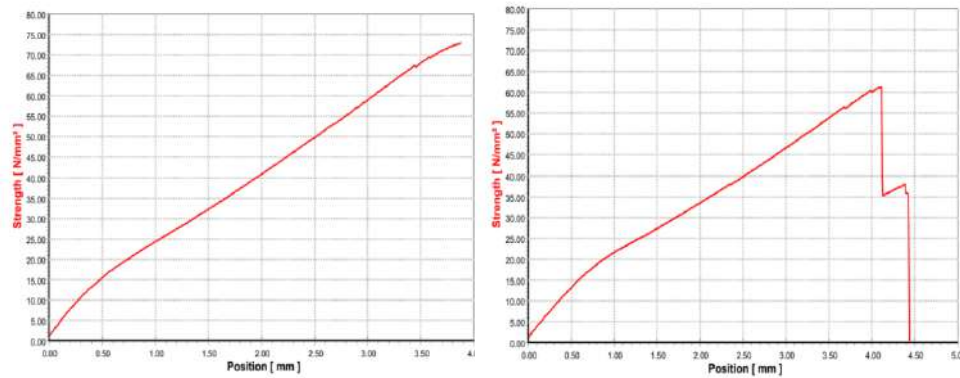


Figure 3. Load-displacement curves of hybrid composite samples with fiber configurations [C/C/F/F/C/C], a) Dry condition b) after hydro aging effect

TABLE 3. The tensile strength and maximum strain of the hybrid and non- hybrid composites at different fiber configurations before and after hydro ageing

Laminate	Fiber configurations	Dry samples		Immersed samples	
		Tensile strength (MPa)	Maximum strain (%)	Tensile strength (MPa)	Maximum strain (%)
F	[F/F/F/F/F]	14 ± 5.35	0.70	4.32 ± 5.45	1.30
S	[S/S/S/S/S]	10.25 ± 5.46	0.60	2.19 ± 5.22	1
C	[C/C/C/C/C]	86 ± 3.16	3.03	83 ± 3.22	3.12
G	[G/G/G/G/G]	25 ± 4.78	1.80	20 ± 4.80	2
L1	[C/C/F/F/C/C]	73 ± 3.16	2	61 ± 3.22	2.6
L2	[F/F/C/C/F/F]	31 ± 4.26	1.20	18 ± 4.37	1.80
L3	[C/C/S/S/C/C]	63 ± 3.35	2.5	51 ± 3.48	2.70
L4	[S/S/C/C/S/S]	21 ± 5.05	1.10	11 ± 5.20	1.60
L5	[C/G/S/F/G/C]	57 ± 3.57	2.30	48 ± 3.65	2.45
L6	[G/C/S/F/C/G]	40 ± 4.06	1.50	35 ± 4.11	1.70
L7	[S/F/G/C/F/S]	20 ± 4.56	1.35	9.43 ± 4.61	1.73
L8	[F/S/C/G/S/F]	27 ± 5.17	1.40	16 ± 5.23	1.80

the response of water uptake for laminate L2 is high because of the presence of flax at outer layers so the change in tensile strength and maximum strain after hydro aging is evident. The tensile strength of laminate L3 and L4 has low value as compared to laminate L1 and L2, respectively. This may be attributed to the difference in tensile strength between flax and sisal fibers. The tensile strength of laminate L5 reaches 66% of laminate (C). This is because of the arrangement between the natural and synthetic fibers, where the hybridization by an adding sisal and flax fabrics at the middle portion (core) gives lower modulus and toughness of the laminate. However, the enhancement in the tensile strength of laminate L8 reaches 93% and 163% as compared to laminate F and laminate S, respectively. This is due to the positioning of the carbon and glass fabrics in the core which gives high strength and stiffness of this laminate.

The non-hybrid composite with laminate (C) before hydro aging gives the maximum tensile strength as compared to all other samples. The enhancement in the tensile strength can be attributed to the good arrangement as well as bonding between the resin matrix and fiber at the interface which leads to an increase in the tensile strength. The response of water uptake for laminate C can be neglected because of the hydrophobic nature of carbon; so, the change in tensile strength and maximum strain do not exceed 3.5 and 6.5%, respectively. Nevertheless, the small decreasing in tensile strength can be attributed to the slight degradation at the interface between the resin matrix and fiber by the small water absorption effects, where confirms with the water absorption and swelling thickness results.

3.3. Microstructure Figures 4 to 6 illustrate the SEM images of the hybrid composites L1, L2, and L6, respectively before and after hydro aging. It can be clear from Figure 4a that the laminate L1 with fiber configuration (C/C/F/F/C/C) has good adhesion between the resin matrix and fiber for dry specimens. After hydro aging effect, the carbon fibers act a barrier between the water molecules and the flax fibers so the water molecules between them are very small causing lower interfacial deboning, breakdown and small swelling of fibers as shown in Figure 4b.

It is clearly seen in Figure 5a that the carbon fiber pull-outs and high voids content can be noticed for the dry specimens after the tensile test. As a result, the high void content in the hybrid composites with fiber configuration (F/F/C/C/F/F) causes the degradation in laminate and also gives poor interfacial adhesion bonding between the fiber and matrix. Therefore, the tensile strength of this laminate was reduced. In addition, loss contact between the resin matrix and fiber are detected after hydro aging as shown in Figure 5(b). As seen in

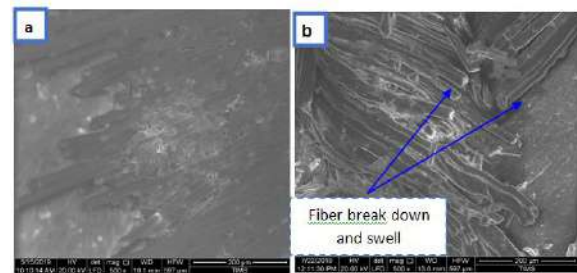


Figure 4. SEM image of hybrid composite with fiber configuration [C/C/F/F/C/C]: (a) dry specimen and (b) after hydro aging effect

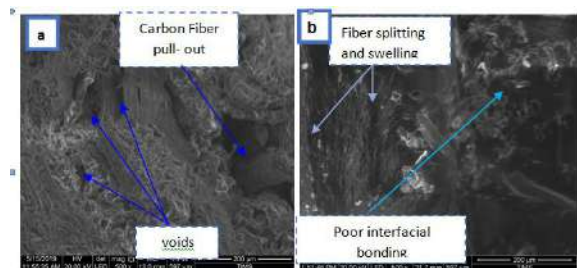


Figure 5. SEM image of hybrid composite with fiber configuration [F/F/C/C/F/F]: (a) dry specimen and (b) after hydro aging effect

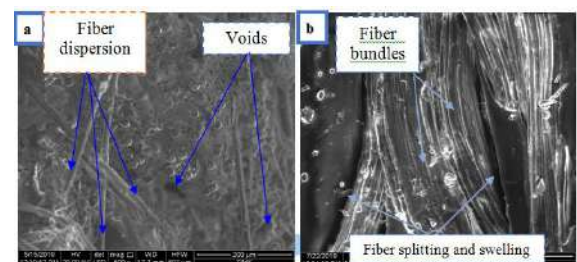


Figure 6. SEM image of hybrid composite with fiber configuration laminate L6 [G/C/F/S/C/G]: (a) dry specimen and (b) after hydro aging effect

Figure 6a, there are many voids at the interface between the matrix and fibers in laminate L6 with fiber configuration (G/C/F/S/C/G) for the dry specimens which cause a weak interfacial adhesion between the matrix resin and fibers. After hydro aging, the fiber was bundled and swelled as shown in Figure 6b due to the water absorption effects.

4. CONCLUSIONS

In this paper, the effect of various fiber configurations of sisal, flax, glass, and carbon fibers reinforced polyester resin hybrid composites on tensile properties before and after the hydro aging were investigated. From the current study, the following conclusions are summarized:

- Laminate (S) with fiber configuration [S/S/S/S/S/S] absorbs more amount of water up to 14 % while the laminate (C) with fiber configuration [C/C/C/C/C/C] absorbs minimum amount of water up to 1.45%.
- The laminate (C) with fiber configuration [C/C/C/C/C/C] exhibited maximum tensile strength (86 MPa) compared to all laminates and slight deterioration after hydro aging.
- The tensile strength of laminate L1 with fiber configuration [C/C/F/F/C/C] is closest to the obtained value for laminate (C).
- The deterioration in tensile strength after hydro aging is observed for hybrid-composites with natural fiber at outer layers, but slightly observed for hybrid-composites with synthetic fiber at outer layers.

5. REFERENCES

1. Boopalan, M., Niranjana, M. and Umopathy, M., "Study on the mechanical properties and thermal properties of jute and banana fiber reinforced epoxy hybrid composites", *Composites Part B: Engineering*, Vol. 51, (2013), 54-57. doi.org/10.1016/j.compositesb.2013.02.033
2. Prasad, A.R. and Rao, K.M., "Mechanical properties of natural fibre reinforced polyester composites: Jowar, sisal and bamboo", *Materials & Design*, Vol. 32, No. 8-9, (2011), 4658-4663. doi.org/10.1016/j.matdes.2011.03.015
3. Yan, L., Chou, N. and Jayaraman, K., "Flax fibre and its composites—a review", *Composites Part B: Engineering*, Vol. 56, (2014), 296-317. doi.org/10.1016/j.compositesb.2013.08.014
4. Venkateshwaran, N., Elayaperumal, A. and Sathiyaraj, G., "Prediction of tensile properties of hybrid-natural fiber composites", *Composites Part B: Engineering*, Vol. 43, No. 2, (2012), 793-796. doi.org/10.1016/j.compositesb.2011.08.023
5. Al-Maharma, A.Y. and Al-Huniti, N., "Critical review of the parameters affecting the effectiveness of moisture absorption treatments used for natural composites", *Journal of Composites Science*, Vol. 3, No. 1, (2019), 27. doi:10.3390/jcs3010027
6. Jawaid, M. and Khalil, H.A., "Cellulosic/synthetic fibre reinforced polymer hybrid composites: A review", *Carbohydrate polymers*, Vol. 86, No. 1, (2011), 1-18. doi.org/10.1016/j.carbpol.2011.04.043
7. Sanjay, M., Arpitha, G., Laxmana Naik, L., Gopalakrishna, K. and Yogesh, B., "Studies on mechanical properties of banana/e-glass fabrics reinforced polyester hybrid composites", *Journal of Material and Environmental Science*, Vol. 7, No. 9, (2016), 3179-3192.
8. El-Menshawey, O., El-Sissy, A., El-Wazery, M. and Elsad, R., "Electrical and mechanical performance of hybrid and non-hybrid composites", *International Journal of Engineering, Transactions A: Basics*, Vol. 32, No. 4, (2019), 580-586. doi: 10.5829/ije.2019.32.04a.16
9. Jesthi, D.K. and Nayak, R.K., "Evaluation of mechanical properties and morphology of seawater aged carbon and glass fiber reinforced polymer hybrid composites", *Composites Part B: Engineering*, Vol. 174, (2019), 106980. doi.org/10.1016/j.compositesb.2019.106980
10. Sivakumar, M., Ranjith, M., Sasikumar, S., Prabhu, D., Sabarish, C. and Sengottaiyan, P., "Mechanical properties and SEM analysis of glass/nylon/jute reinforced epoxy hybrid composites", *International Journal of Mechanical Engineering & Technology*, Vol. 7, (2016), 194-207.
11. Braga, R. and Magalhaes Jr, P., "Analysis of the mechanical and thermal properties of jute and glass fiber as reinforcement epoxy hybrid composites", *Materials science and Engineering: C*, Vol. 56, (2015), 269-273. doi.org/10.1016/j.msec.2015.06.031
12. Fiore, V., Valenza, A. and Di Bella, G., "Mechanical behavior of carbon/flax hybrid composites for structural applications", *Journal of Composite Materials*, Vol. 46, No. 17, (2012), 2089-2096. doi: 10.1177/0021998311429884
13. Gupta, M.K., Srivastava, R., Kumar, S., Gupta, S. and Nahak, B., "Mechanical and water absorption properties of hybrid sisal/glass fibre reinforced epoxy composite", *American Journal of Polymer Science & Engineering*, Vol. 3, No. 2, (2015), 208-219.
14. Gupta, M. and Deep, V., "Effect of water absorption and stacking sequences on the properties of hybrid sisal/glass fibre reinforced polyester composite", *Proceedings of the Institution of Mechanical Engineers, Part L: Journal of Materials: Design and Applications*, Vol. 233, No. 10, (2019), 2045-2056. doi: 10.1177/1464420718811867
15. Dhakal, H., Zhang, Z., Guthrie, R., MacMullen, J. and Bennett, N., "Development of flax/carbon fibre hybrid composites for enhanced properties", *Carbohydrate Polymers*, Vol. 96, No. 1, (2013), 1-8. doi:10.1016/j.carbpol.2013.03.074
16. Girisha, C., Sanjeevamurthy, G. and Srinivas, G., "Sisal/coconut coir natural fibers-epoxy composites: Water absorption and mechanical properties", *International Journal of Innovative Technology*, Vol. 2, (2012), 166-170.
17. Zamri, M.H., Akil, H.M., Bakar, A.A., Ishak, Z.A.M. and Cheng, L.W., "Effect of water absorption on pultruded jute/glass fiber-reinforced unsaturated polyester hybrid composites", *Journal of Composite Materials*, Vol. 46, No. 1, (2012), 51-61. doi.org/10.1177/0021998311410488
18. Sathish, S., Kumaresan, K., Prabhu, L. and Vigneshkumar, N., "Experimental investigation on volume fraction of mechanical and physical properties of flax and bamboo fibers reinforced hybrid epoxy composites", *Polymers and Polymer Composites*, Vol. 25, No. 3, (2017), 229-236. doi:10.1177/096739111702500309
19. Gopal, S., Aravindh, S., Dinesh, C., Gopinath, M. and Jagan, S., "Analysis of mechanical behaviour of sisal, jute, and flax fibre (hybrid) reinforced with epoxy resin composites", *International Journal of Innovation Research Science & Technology* Vol.3, (2017), 69-73.
20. Calabrese, L., Fiore, V., Scalici, T. and Valenza, A., "Experimental assessment of the improved properties during aging of flax/glass hybrid composite laminates for marine applications", *Journal of Applied Polymer Science*, Vol. 136, No. 14, (2019), 47203. doi.org/10.1002/app.47203
21. Saidane, E.H., Scida, D., Assarar, M., Sabhi, H. and Ayad, R., "Hybridisation effect on diffusion kinetic and tensile mechanical behaviour of epoxy based flax-glass composites", *Composites Part A: Applied Science and Manufacturing*, Vol. 87, (2016), 153-160. doi.org/10.1016/j.compositesa.2016.04.023

Persian Abstract

چکیده

تأثیر جذب آب و ضخامت تورمی بر خواص کششی پارچه های کتان / سیسیل / کربن / شیشه تقویت شده توسط کامپوزیت های ترکیبی مبتنی بر پلی استر غیر اشباع بررسی شد. کامپوزیت های ترکیبی تقویت شده با چیدمان های مختلف الیاف طبیعی و مصنوعی با استفاده از روش چیدن دستی تولید شده اند. آزمون جذب آب با غوطه وری آزمون ها در آب مقطر برای مدت زمان های مختلف تا ۱۳۴۴ ساعت انجام شد. نتایج آزمون ها پیشرفت اندکی در جذب آب برای پیکربندی الیاف [C / C / C / C / C / C] تا [C] ۱۴۵ درصد را نشان داد. اما، افزایش عالی جذب آب برای پیکربندی فیبر [S / S / S / S / S / S] تا ۱۴ درصد حاصل شد. استحکام کششی آزمون ها پیش و پس از غوطه وری شدن در آب مقطر بررسی شد. این نتیجه نشان داد که استحکام کششی پیکربندی الیاف [C / C / F / F / C / C] در شرایط خشک به پیکربندی الیاف [C / C / C / C / C / C] نزدیک می شود. مورفولوژی سطح مقطع شکسته کامپوزیت با استفاده از میکروسکوپ الکترونی روبشی (SEM) برای ارزیابی واسط فیبر / ماتریس پیش و پس از پیر شدن در آب بررسی شد. کاهش مقاومت کششی به دلیل نفوذ آب برای کامپوزیت هیبریدی با الیاف مصنوعی در لایه ی بیرونی اندک است، اما برای کامپوزیت ترکیبی با الیاف طبیعی در لایه ی بیرونی بسیار زیاد است.



Kinesiological Description of Hippotherapy as a Treatment Modality

M. A. Shahiri^{*a}, A. R. Arshi^a, A. Kazemi^a, V. Copper^b

^a Biomedical Engineering Faculty, Amirkabir University of Technology, Tehran, Iran

^b Chartered Physiotherapists in Therapeutic Riding and Hippotherapy, Riding for Disabled Association, United Kingdom

P A P E R I N F O

Paper history:

Received 28 April 2020

Received in revised form 19 June 2020

Accepted 23 September 2020

Keywords:

Dynamic Interaction

Event Identification

Hippotherapy

Musculoskeletal Modeling

Phase Plane

A B S T R A C T

Hippotherapy as a treatment modality relies on patient-equine dynamic interaction to enhance physical abilities in a range of neuromuscular diseases. The modality takes advantage of external stimulations in the form of kinetic and kinematic inputs to patient's upper body. Current practices and procedures could be greatly enhanced by an objective approach to session planning based on a predictive neuromuscular model. Individualization of the treatment program is both subject-specific and equine-specific. To this effect, kinesiological aspects of the three main upper body flexor-extensor muscles which are directly affected by this treatment modality are presented in a biomechanical model. Events and phases of this dynamic interaction are identified and described using a phase plane analysis. Physical interpretations of coefficients in the movement differential equation illustrates that the proposed approach and mathematical modeling have the potential to be tailored for various musculoskeletal or neuromuscular disorders. Validation results show that the model has the ability to simulate kinematic response and muscle forces of the patient upper body during a hippotherapy session. This predictive ability could provide the therapist with a tool to estimate the effects prior to therapy sessions and choose the most suitable combination of horse and exercises.

doi: 10.5829/ije.2020.33.11b.25

NOMENCLATURE

m	Total mass of UB	K_{RA} & K_{ES}	Linear spring coefficient of Hill muscle model for RA & ES respectively
l	Distance between UB center of mass and COR	K_{TP}	Torsion spring coefficient of Hill muscle model for Psoas
θ_g^*	Initial inclination of UB center of mass (as defined in Figure 1)	C_{RA} & C_{ES}	Linear dashpot coefficient of Hill muscle model for RA & ES respectively
F_{ES}	ES muscle force	C_{TP}	Rotary damper coefficient of Hill muscle model for Psoas
F_{RA}	RA muscle force	x_{RA}^* , x_{ES}^* & θ^*	Active initial length for RA, ES & Psoas muscles respectively
F_p	Psoas muscle force	b_1 , b_2 & r_p	Anthropometric measures as defined in Figure 2

1. INTRODUCTION

Hippotherapy (HT), as a treatment modality (TM) is performed by specifically trained physio/occupational therapists. The observation-based procedures in hippotherapy could be considered as a form of physical manipulation which take advantage of horse movements as well as exercises performed by the patient during horseback riding. The TM targets some of the

symptomatic problems faced by patients suffering from cerebral palsy (CP), multiple sclerosis (MS), motor control problems, neuromusculoskeletal (NMS) disorders and a wide range of other dysfunctions [1, 2].

The horse gait at walk exerts repetitive three-dimensional pseudo-sinusoidal mechanical stimuli on the patient, enhancing postural stability and maintenance of balance [3–6]. Spatiotemporal inputs affect the patient upper body (UB) through her/his hip. The UB is

*Corresponding Author Institutional Email: Shahiri@aut.ac.ir
(M. A. Shahiri)

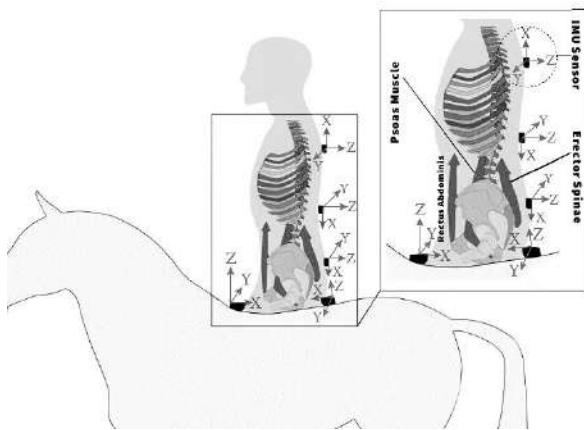


Figure 1. IMU sensors position and UB Flexor/Extensor muscles in sagittal plane

consequently experiencing a complex movement caused by a combination of posterior/anterior pelvic tilts (frontal-transversal plane), rotational pelvic movements (frontal-sagittal plane) and side-flexion (coronal-transversal plane) [7]. The complex motion is very similar in nature to hip movements during normal human walking gait [7, 8]. The modality hence provides a realistic dynamic simulation of hip movements for a patient who is otherwise incapable of autonomous normal gait, while simultaneously stimulating core and UB muscular structures [8, 9]. Here, even small changes in both the horse gait and patient riding position along with a myriad of possible exercises that can be performed during a therapy session, provide the therapist with tremendous opportunities in the manipulation of kinetic/kinematic inputs to patient hip [10].

That is why hippotherapy is used by specifically trained physiotherapists to improve posture, enhance body motion and maintain balance in both children and adult populations [11]. Other physiological effects of HT, such as cardiorespiratory responses and pelvic kinematics have also been addressed in studies on youth with and without cerebral palsy [12]. Although the study results indicated that HT did not effectively affect cardiorespiratory fitness, it is argued that it could facilitate improvement in functional outcomes such as gait, balance and posture. Other studies have investigated the sensorimotor, as well as psychomotor effects, where it is suggested that HT could save and normalize muscle tone for a longer period (up to three months), compared with traditional methods of physiotherapy [13]. Hippotherapy has also been shown to exhibit more beneficial effects, in certain circumstances, than traditional physiotherapy exercises in healthy older adults [14]. The modality has also been used to tackle issues faced by Autistic, Down's Syndrome and other NMS disorders [15–19].

Robotic HT and robotic physiotherapy has recently become a widespread clinical application to facilitate postural core stabilization [20–22]. The study results provide evidence of safety and efficacy of this treatment for postural instability control and sitting balance dysfunction that mitigates the risk of falls in CP. Long-term effects of a more intense robotic HT on a CP patient were also assessed in other studies [23]. Here, higher speeds of horse movement such as trot, canter and gallop as well as walk were simulated and the results showed significant improvement in postural muscle size in addition to improvements in static and dynamic stability.

While most studies provide clinical evidence of HT efficacy in addressing physical disabilities, the literature lacks suggestion of why and how these benefits occur; a point confirmed by the other studies [1]. It has also been shown that direct assessment of patient movements by physiotherapists (using a combined accelerometer-gyroscope device called an actimeter) is important for estimation of therapeutic efficacy [24]. Furthermore, like many other modalities, personalization of treatment is an issue increasingly addressed on the field. Individualization in hippotherapy requires recognition and identification of causal interactions between horse and the patient. The dynamic interactions take place through a series of phases and events, the summation of which, could be shown using state space trajectories for an intended landmark [25]. It, therefore, is essential to understand and be able to explain the events representing kinesiological and biomechanical characteristics of this external stimulus on patient's neuromuscular structures. Dynamic interaction is also significantly affected by characteristics such as equine gait which is in turn determined by the equine physical parameters. The effect of horse pace on spatiotemporal parameters of gait in children with CP and the effect of different types of saddles has also been studied [26, 27]. An extensive review on the subject has also suggested that more studies are required to identify all involved muscles and the degree of activation [1].

The literature on the subject has therefore not addressed a number of fundamental questions. The first issue is that an infrastructure in the shape of a combined musculoskeletal model for the interaction between the two systems is required so that the following questions could be addressed quantitatively and not qualitatively:

1. How does equine walking velocity, gait frequency, changing accelerations, physical parameters such as height, width and length, affect the dynamics of this interaction and how should such parameters be used in a patient specific and personalized approach?
2. How does alternative physical activities, such as sitting position, hand and/or body movements, reaching or throwing exercises, affect dynamic stability or core muscle activity of the patient and

what is the expected effect of each exercise on the patient muscular system?

3. How does the patient disability affect the dynamic interaction? (i.e. what happens when two patients with similar anthropometric parameters, but suffering from different disabilities, ride the same horse?)
4. Is it possible to quantitatively assess the positive or negative effects of this treatment modality during an HT session?

A detailed biomechanical description of the events taking place during this modality could contribute towards wider acceptance amongst mainstream medical professionals [1]. This study should hence attend to these concerns by suggesting a preliminary and expandable mathematical model capable of describing the fundamental biomechanical and dynamic interaction between the horse and patient. The current study intends to portray an image of both the structural and functional characteristics of kinetic/kinematic interactions between the horse and the patient starting from a suitable foundation for mathematical description of movement phases and events.

2.METHODS

2. 1. Musculoskeletal Model

The current study adopts a combination of inverse and forward dynamic approach towards musculoskeletal modeling to determine kinematic parameters as well as muscular forces. A quasi-quantitative study of the interaction between the main stabilizing muscles and the UB kinematic behavior during hippotherapy could provide a biomechanical description of this treatment modality. Due to unique situation of the problem, where neither the kinematics of UB nor any of the muscle forces are known, existing available software such as OpenSim cannot be used. The foundational model will include head and neck, arms and hands, the spine, rib cage and scapula as well as pelvic and femoral bone. However, in many hippotherapy sessions, side walkers could restrain the patient's legs to enhance stability. This diminishes the dynamic effect of legs on UB and thus allows for the exclusion of legs in the corresponding preliminary model. It is also assumed that the patient is discouraged from moving his/her upper extremity or head relative to the trunk. The UB could hence be represented by a single link connected through a joint to the pelvic link in this preliminary model.

Three force-bearing members representing the three primary muscle groups connect the upper body and pelvic links as shown in Figure 2. Two of these members represent Rectus Abdominis (RA) and Erector Spinae (ES) substituted by linear muscle models (linear spring-dashpot) and the third, represents Psoas muscle

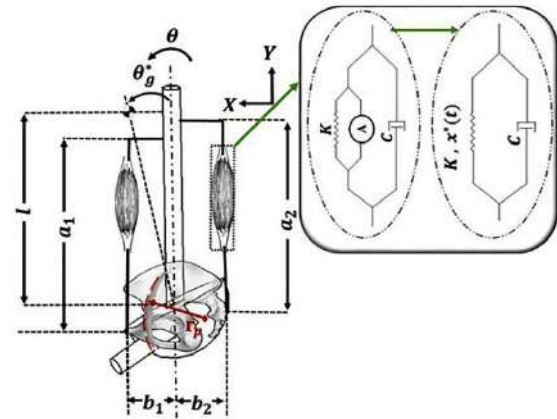


Figure 2. Two-dimensional dynamic model of the patient on sagittal plane

substituted by a rotational muscle model (rotational spring-dashpot).

The motion of the upper body during hippotherapy takes place in sagittal, transverse and frontal planes. The dynamic movements on the transverse plane are limited during hippotherapy and could be neglected at this stage. Linear and angular velocities are small and hence Coriolis acceleration effects could also be neglected. In the absence of Coriolis acceleration effects, it is possible to assume UB dynamics in two sagittal and frontal planes to be independent. To establish and understand the governing mechanisms, the preliminary model would focus on system dynamics in the sagittal plane.

Hill muscle model is used to substitute the three force-bearing members as shown in Figure 2.

The function of the active element $F_A(t)$ is not known at this stage. The effect of this active element is hence combined with spring passive force resulting in Equation (1):

$$F = K(x - x_0) + F_A(t) + C\dot{x} \tag{1}$$

$$\text{Assume: } F_A(t) = Kd^*(t) \tag{2}$$

$$\left. \begin{matrix} (1) \\ (2) \end{matrix} \right\} \rightarrow F = Kx - Kx_0 + Kd^*(t) + C\dot{x} \tag{3}$$

$$\text{Assume: } (x_0 - d^*(t)) = x^*(t) \tag{4}$$

$$\left. \begin{matrix} (3) \\ (4) \end{matrix} \right\} \rightarrow F = K(x - x^*(t)) + C\dot{x} \tag{5}$$

where $x^*(t)$ in Equations (4) and (5) is a substitute variable to cater to $F_A(t)$ which was removed from Equation (1). It should be noted that x^* could also be defined as "active initial length" of the muscle. Parameter $d^*(t)$ in Equations (2) to (4) (defined as $F_A(t)/k$) is a purely mathematical step in development of the model.

Solving forward dynamic equations for movement of UB center of mass by utilizing internal muscle forces based on Equation (5), leads to a second order nonlinear differential equation with variable coefficients for θ :

$$A(\theta)\ddot{\theta} + B(\theta)\dot{\theta} + C(\theta)\theta + D(\theta) = 0 \quad (6)$$

$$A(\theta) = \frac{4ml^2}{3} \quad (7)$$

$$B(\theta) = C_{TP} + C_{RA}b_1^2\cos^2\theta + C_{ES}b_2^2 \quad (8)$$

$$C(\theta) = K_{TP} + K_{ES}b_2^2 \quad (9)$$

$$D(\theta) = -K_{TP}\theta^* - ml(a_{oy}\sin(\theta - \theta_g^*)) - mla_{ox}\cos(\theta - \theta_g^*) - mlg\sin(\theta - \theta_g^*) - K_{ES}b_2x_{ES}^* + K_{RA}b_1(x_{RA}^* + b_1\sin\theta)\cos\theta \quad (10)$$

$$\theta^* = \frac{e_1K_{RA}b_1x_{RA}^*}{K_{TP}} \quad (11)$$

$$x_{ES}^* = \frac{K_{RA}x_{RA}^*b_{RA}(1+e_1)+mgl\sin\theta_g^*}{K_{ES}b_2} \quad (12)$$

$$F_{Rectus\ Abdominis} = F_{RA} = K_{RA}(x_{RA}^* + b_1\sin\theta) + C_{RA}b_1\dot{\theta}\cos\theta \quad (13)$$

$$F_{Erector\ Spinae} = F_{ES} = K_{ES}(x_{ES}^* - b_2\theta) - C_{ES}b_2\dot{\theta} \quad (14)$$

$$F_{Psoas} = F_p = \left(\frac{1}{T_p}\right) * \left(K_{TP}(\theta - \theta^*) + C_{TP}(\dot{\theta})\right) \quad (15)$$

Equation (6) is a nonlinear second order differential equation solved using numerical methods in MATLAB (R2017b).

2. 2.Validation

Model validation takes place through a single subject study to obtain upper body kinematic data as well as the horse gait characteristics. This is performed using a combination of inertial measurement units (IMU) and EMG sensors (Figure 3). Horse gait data along with rider personalized measurements were used as inputs to model simulation. Validation takes place through comparisons made between simulation and experimental results.

2. 3. Test Procedure

Tests were conducted on a healthy adult (25 years old, 174 cm height, 64kg weight, and BMI=21.14). The procedure was conducted in accordance with basic hippotherapy protocol. Informed consent was obtained and test procedure was approved by university ethics committee on human and animal tests. The experiment took advantage of a walking horse gait for a distance of 20 m in a shuttle test. Linear accelerations and angular velocities in three dimensions were recorded using five IMU sensors (Xsens-Netherlands). Three sensors were placed on bony landmarks of S1, T2, and T11 and the other two were

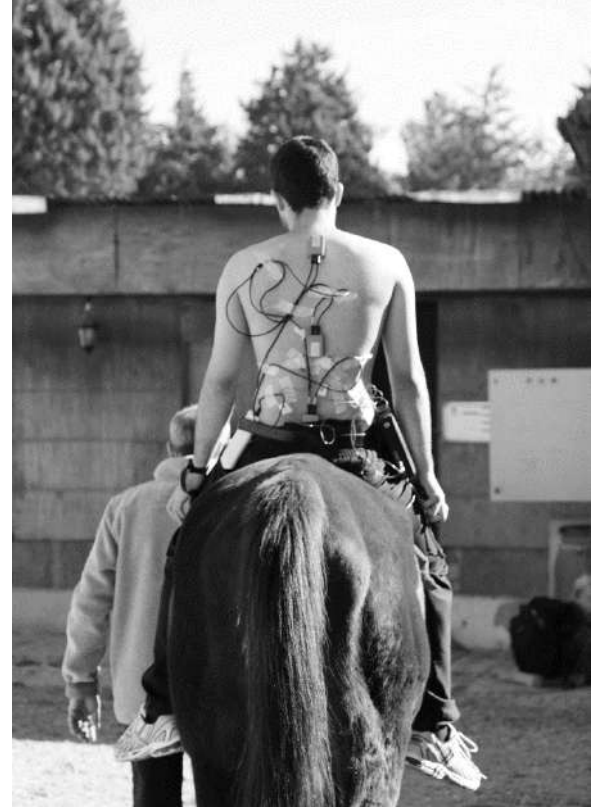


Figure 3. Test subject with IMU and EMG sensors attached

placed on the equine back region just before withers at points immediately in front and behind the rider hip area (Figure 1). Data acquisition was performed at 50 Hz for IMU sensors. The acquired data were transferred to the global coordinate frame using rotation matrices. Artifact elimination was achieved through the application of 4th order low pass filter with a cutoff frequency of 10 Hz [28, 29]

Activation signals associated with RA and ES were recorded at 1000 Hz using an 8-channel electromyography system (Biometrics Ltd). Electrode placement was based on a relevant reference [30]. Forth order low-pass filter was adopted at 20 Hz to eliminate the noise. An audio signal was used for manual synchronization and test initiation.

3. RESULTS

3. 1. Validation and Sensitivity Analysis

Results of the validation process for upper body kinematic simulation of the model is presented in Figure 4. Flexion/extension changes of UB center of mass predicted by the simulation as well as the corresponding data measured at T11 landmark (T11 is the closest bony landmark to the UB center of mass) are shown and compared in Figure 4.

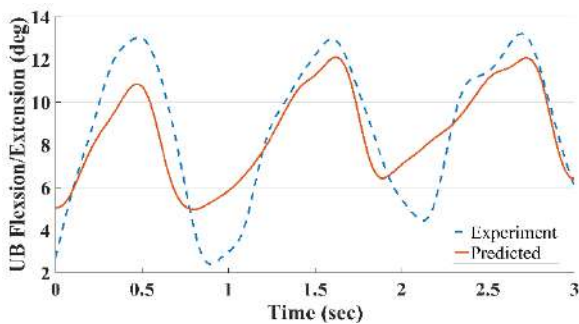


Figure 4. Predicted UB flexion/extension (dashed line) and measured flexion/extension (solid line) of UB center of mass

The sensitivity of the simulation results to uncertainties on the magnitude of muscle parameters is shown in Figure 5. The solid line in the middle shows the predicted normalized UB Flexion/Extension profile in two consecutive gait cycles (initially presumed muscle coefficients k and c). The dashed line shows the same parameter when muscle coefficients were decreased by %50 and the dotted line shows simulation results when muscle coefficients were increased by %50.

The sensitivity of simulation results to uncertainty in geometry (anthropometric measures) is also shown in Figure 6. A quasi-quantitative approach adopted in this study, investigates the profile of changes in kinematic and dynamic parameters, rather than their exact values. Therefore, normalized forms of the parameters are delineated. The normalized form is a dimensionless parameter calculated as: $\frac{\text{Flexion/Extension}}{\text{Max(Flexion/Extension)}}$. In both figures, normalized predicted UB Flexion/Extension changes in two consecutive gait cycles are illustrated. The solid line in the middle shows simulation results with rider's initial anthropometric data. Dashed line in Figure 6 shows simulation results when there was a 20% increase or decrease in b_1 value, while the dashed line shows the simulation results when there was a $\pm 20\%$ uncertainty in b_2 value.

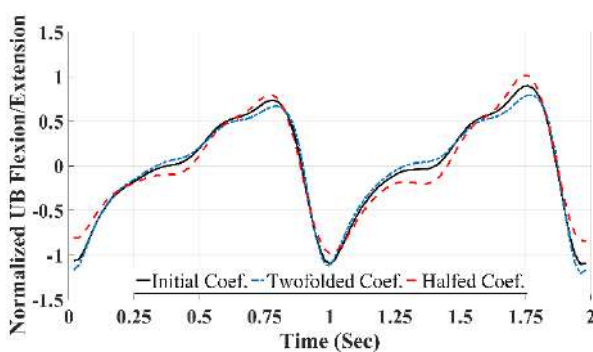


Figure 5. Sensitivity of simulation output to $\pm 50\%$ changes in muscle properties (k & c). Changes on dimensionless normalized UB Flexion/Extension against time.

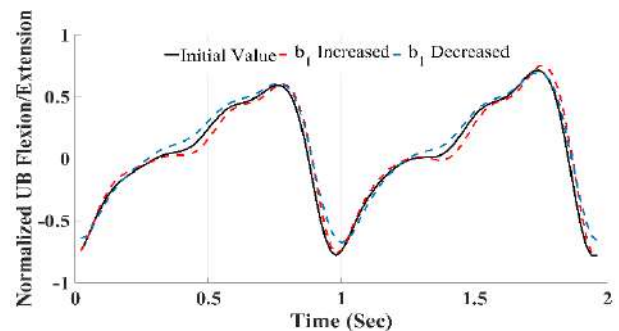


Figure 6. Simulation of the effect of uncertainty in anthropometric measures (b_1) upon output results. Changes on dimensionless normalized UB Flexion/Extension against time.

3. 2. Simulation Results

Equations (6) to (14) were solved using 4th order Runge-Kutta in MATLAB (R2017b). Input parameters (a_{ox} and a_{oy}) were obtained from the horse gait during the experimental test. Upper body kinematic behavior ($\theta(t)$) and three muscle group forces (F_{RA} , F_{ES} , F_p) in response to horse gait inputs were calculated/predicted. Figure 7 shows the normalized phase plane for rider UB kinematics ($\|\dot{\theta}\|$ Vs. $\|\theta\|$) for one gait cycle of the horse. The dimensionless normalized form is calculated by dividing the parameter's value by its maximum value in the cycle. Figure 8 illustrates the normalized force of the extensor muscle group (Erector Spinae) against one of the input signals, which is horse linear acceleration in forward direction (a_{ox}). A number of kinematic or kinetic significant points are marked in both Figures 7 and 8 simultaneously to describe and track various events in different movement phases.

4. DISCUSSION

4. 1. Modeling Concerns and Assumptions

Currently available software such as OpenSim are designed to solve either forward or inverse dynamic problems. The nature of input stimulation exerted to a single link, limits the adoption of such commercially/open source available software.

Instantaneous center of rotations of individual vertebrae and the associated three dimensional rotations of intervertebral fibrocartilage could be the subject of series of studies. Considering the narrow range of motion in this particular activity (during hippotherapy), where the range of Flexion/Extension of thorax in sagittal plane were less than ± 6 degrees (measured at T2, Figure 4), the assumption of fixed center of rotation can be acceptable.

4. 2. Validation and Sensitivity Analysis

Validation of simulated kinematic responses is shown in Figure 4. Comparison between predicted changes in UB

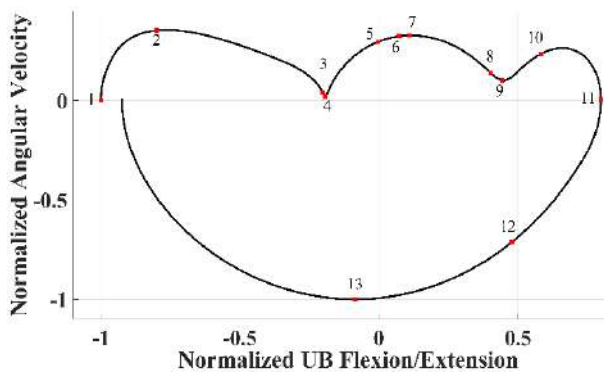


Figure 7. Normalized UB angular velocity Vs. normalized UB angle of the rider in sagittal plane. Both vertical and horizontal axes are dimensionless parameters.

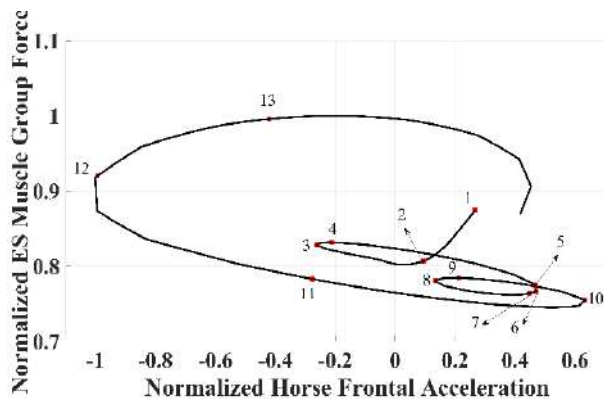


Figure 8. Normalized Erector Spinae force Vs. normalized acceleration of the horse in walking direction. Both vertical and horizontal axes are dimensionless parameters.

angle in the sagittal plane and the actual measured changes of this angle during the test indicates consistencies between predicted and experimental results. Accuracy of the predicted kinematics associated with the preliminary model is not of immediate concern due to deliberate model simplifications. However, similarities in dynamic profiling between the simulation result and empirical measurement shows that the adopted modeling approach provides a sound basis for demonstration of dynamic behavior of the patient's body during HT session. The horse kinematic parameters measured at locations mentioned in Figure 1 shows similar profiles to those presented in literature [7].

The sensitivity of the simulation results to changes in muscle model parameters is shown in Figure 5. Although the value of UB angle changes with the change of muscle model parameters, the trend of changes in the profile remains stable. The same phenomenon can be observed in Figure 6, where the sensitivity of the simulation results to uncertainties in anthropometric measures is illustrated. Figures 5 and 6 indicate that although the value of the simulation result is sensitive to model parameters,

normalized profile of the results does not alter significantly.

4. 3. Phase Identification

Phase planes shown in Figures 7 and 8 could be used to identify dynamic characteristics of individual phases or events. The following provides examples of phase and event descriptions;

From point 1 to 2, UB angle and angular velocity are increasing in the positive direction (Extension in the sagittal plane). The former diminishes the extensor muscle forces (Erector Spinae) due to muscular elastic properties and, the latter diminishes muscle forces due to viscous properties. Therefore, the overall erector spinae muscle force should show depletion in this period as confirmed by the graph in Figure 8.

From point 2 to 3, UB angle is increasing while the angular velocity is falling. The elastic component of muscle force is decreasing while its viscous component is increasing. This causes a functional conflict, resulting in an initial reduction followed by a rise in muscle force as shown in Figure 8.

When the horse is accelerating forward, patient's body inertia causes upper body center of mass to stay behind initially, resulting in an increase in angular velocity in the opposite direction. Forward acceleration of the horse starts to increase from point 3 (Figure 8) and the angular velocity rises with a slight delay from point 4 (Figure 7). The horse's forward acceleration begins to decrease from point 5 (Figure 8) which leads to a downturn of UB angular velocity from point 8 (Figure 7). Similar relations are also observed between horse acceleration and riders UB angular velocity in other phases of movement such as points 8, 10 and 12.

The characteristics outlined so far could portray repeatable and stable rules governing the relationship between UB kinematics and muscle forces. Extraction and identification of these rules could contribute towards estimation of changes in generated muscular forces through observation of upper body kinematics during the equine therapeutic session.

It could, therefore, be concluded that the relationship between patient's upper body kinematics and horse input acceleration is governed by relatively stable rules. It would hence be possible to predict patient's UB kinematics based on horse gait. This could then lead to a determination of muscular function from the predicted UB kinematics.

4. 4. Physical Interpretation of Coefficients

Coefficients of the differential equation describing θ , shown in Equation (6) could also provide information on system dynamics. The function $A(\theta)$ is associated with the characteristics of UB rotational inertia. This coefficient would change as the UB mass alters in circumstances where a separate weight is carried by the

patient or when there are morphological changes such as opening arms during prescribed neuromechanical exercises. Any alteration of this coefficient, assuming others remain unchanged, is an indication of increase or decrease of the amplitude of angular variations or changes in the amplitude of muscular forces.

Function $B(\theta)$ is associated with the viscous properties of muscles and it is dependent upon C_{RA} , C_{ES} and C_{TP} parameters. Variations on viscous characteristics of muscle tissue caused by disease, injury or disability, results in deviations in system dynamics through changes in this coefficient. Therefore, the pathological states could be simulated for an individual patient by adjusting parameters in $B(\theta)$.

The function $C(\theta)$ is related to elastic properties of the rotational spring. In other words, this coefficient is dependent upon the K_{TP} of the Psoas muscle and elastic coefficient and the moment arm of ES muscles. Any changes in this coefficient affects the relationship between muscle force and UB angle, thus influencing the range of forces and stability of the system. Rotational spring characteristics representing ES muscles ($K_{ES} b_2^2$) in $C(\theta)$, are influenced by the length of the moment arm, the radius of curvature of Sacrum as well as elastic characteristics of muscles. In a similar way, the characteristics of rotational spring representing Psoas muscles are affected by the modulus of elasticity as well as anatomic dimensions such as the angle or radius of curvature of the muscle (r_p).

$D(\theta)$ is a function of: a) linear acceleration inputs from the horse, b) elastic properties of RA and ES muscles, and c) active initial length of the muscles (x^*). Therefore any changes in any of these three parameters could lead to changes in system behavior by affecting $D(\theta)$. One interesting implication of this function is that linear acceleration inputs could be altered to assist personalized prescriptions leading to improved efficiency of Hippotherapy sessions. The inputs could, for example, change by changing the horse gait. The new gait could be the result of choosing a particular horse for a certain patient. Some diseases or impairments may have the ability to cause variation in the muscular elasticity and thus change $D(\theta)$. Changes in the initial muscle length could be voluntary by stiffening the muscle or could be caused by a disease or disorder like spasticity, muscular damage, or fatigue. All such causes, change function $D(\theta)$ in Equation (6) which in turn affects system behavior. Finally, any change in $\theta(t)$ results in variation of the system behavior and muscle forces as indicated by Equations (13), (14) and (15).

5. CONCLUSION

American Hippotherapy Association (AHA) defines hippotherapy as a purposeful manipulation of equine

movements to achieve functional outcomes. This study provides the basis for a musculoskeletal modeling approach, which has the capacity for both patient and equine specificity. Validation results show that the resulting simulation has the ability to predict kinematic response and muscle forces of the patient's upper body during a hippotherapy session. This predictive ability could provide the therapist with a tool to estimate the outcome, prior to therapy sessions and thus provide a choice of the most suitable combination of horse and exercises. Physical interpretations of coefficients in the movement differential equation (Equation (6)) illustrates that the proposed approach to mathematical modeling has the potential to adapt to various musculoskeletal or neuromuscular disorders.

The current study has a number of limitations requiring attention in the future efforts:

- The current simulation is based on a 2D model on sagittal plane, whereas the actual movement is in 3D plane and more muscles are involved.
- Changes in muscle activation due to stability control mechanisms such as muscle reflexes (stretch reflex, golgi tendon reflex and vestibulospinal reflex) are not simulated in this model.
- Upper extremities (arms and hands) and head and neck are assumed to not move relative to the trunk in this model. This assumption can only simulate the most basic form of hippotherapy practice.
- In the current model, the whole abdomen and thorax together is modelled as one rigid link with a fixed joint against pelvis. In wider ranges of trunk Flexion/Extension, this assumption can lead to unacceptable simulation errors.

This article has presented a kinesiology based mathematical model which describes the fundamental dynamic interaction between the horse and the patient during hippotherapy. The model could provide a sound basis for future studies of this highly complex treatment modality.

6. CONFLICT OF INTEREST STATEMENT

The authors certify that they have NO affiliations with or involvement in any organization or entity with any financial interest, or non-financial interest in the subject matter or materials discussed in this manuscript.

7. ACKNOWLEDGEMENT

The authors would like express gratitude to colleagues at Gait Laboratory in Shahid Beheshti University, Biorobotics laboratory at AUT, Mowafaghian Research Center and Zoljenah Riding Club. No funds were allocated to this study.

8. REFERENCES

- Rigby, B. R., and Grandjean, P. W. "The Efficacy of Equine-Assisted Activities and Therapies on Improving Physical Function." *The Journal of Alternative and Complementary Medicine*, Vol. 22, No. 1, (2016), 9–24. <https://doi.org/10.1089/acm.2015.0171>
- Uchiyama, H., Ohtani, N., and Ohta, M. "Three-dimensional analysis of horse and human gaits in therapeutic riding." *Applied Animal Behaviour Science*, Vol. 135, No. 4, (2011), 271–276. <https://doi.org/10.1016/j.applanim.2011.10.024>
- Champagne, D., Corriveau, H., and Dugas, C. "Effect of Hippotherapy on Motor Proficiency and Function in Children with Cerebral Palsy Who Walk." *Physical & Occupational Therapy In Pediatrics*, Vol. 37, No. 1, (2017), 51–63. <https://doi.org/10.3109/01942638.2015.1129386>
- Kwon, J.-Y., Chang, H. J., Yi, S.-H., Lee, J. Y., Shin, H.-Y., and Kim, Y.-H. "Effect of Hippotherapy on Gross Motor Function in Children with Cerebral Palsy: A Randomized Controlled Trial." *The Journal of Alternative and Complementary Medicine*, Vol. 21, No. 1, (2015), 15–21. <https://doi.org/10.1089/acm.2014.0021>
- Lee, C.-W., Kim, S. G., and Na, S. S. "The Effects of Hippotherapy and a Horse Riding Simulator on the Balance of Children with Cerebral Palsy." *Journal of Physical Therapy Science*, Vol. 26, No. 3, (2014), 423–425. <https://doi.org/10.1589/jpts.26.423>
- Moraes, A. G., Copetti, F., Angelo, V. R., Chiavoloni, L. L., and David, A. C. "The effects of hippotherapy on postural balance and functional ability in children with cerebral palsy." *Journal of Physical Therapy Science*, Vol. 28, No. 8, (2016), 2220–2226. <https://doi.org/10.1589/jpts.28.2220>
- Garner, B. A., and Rigby, B. R. "Human pelvis motions when walking and when riding a therapeutic horse." *Human Movement Science*, Vol. 39, (2015), 121–137. <https://doi.org/10.1016/j.humov.2014.06.011>
- Goldmann, T., and Vilimek, M. "Kinematics of human spine during hippotherapy." *Computer Methods in Biomechanics and Biomedical Engineering*, Vol. 15, No. sup1, (2012), 203–205. <https://doi.org/10.1080/10255842.2012.713619>
- Debusse, D., Chandler, C., and Gibb, C. "An exploration of German and British physiotherapists' views on the effects of hippotherapy and their measurement." *Physiotherapy Theory and Practice*, Vol. 21, No. 4, (2005), 219–242. <https://doi.org/10.1080/09593980500321143>
- Meregillano, G. "Hippotherapy." *Physical Medicine and Rehabilitation Clinics of North America*, Vol. 15, No. 4, (2004), 843–854. <https://doi.org/10.1016/j.pmr.2004.02.002>
- Heine, B. "Hippotherapy. A multisystem approach to the treatment of neuromuscular disorders." *Australian Journal of Physiotherapy*, Vol. 43, No. 2, (1997), 145–149. [https://doi.org/10.1016/S0004-9514\(14\)60407-5](https://doi.org/10.1016/S0004-9514(14)60407-5)
- Rigby, B. R., Gloeckner, A. R., Sessums, S., Lanning, B. A., and Grandjean, P. W. "Changes in Cardiorespiratory Responses and Kinematics With Hippotherapy in Youth With and Without Cerebral Palsy." *Research Quarterly for Exercise and Sport*, Vol. 88, No. 1, (2017), 26–35. <https://doi.org/10.1080/02701367.2016.1266458>
- Strashko, Y., Kapustianska, A. A., and Bobyrova, L. E. "Experience of using hippotherapy in complex effects on muscle spirals in children with spastic forms of cerebral palsy." *Wiadomosci Lekarskie*, Vol. 69, (2016), 527–529. <https://doi.org/27717938>
- Aranda-García, S., Iricibar, A., Planas, A., Prat-Subirana, J. A., and Angulo-Barroso, R. M. "Comparative Effects of Horse Exercise Versus Traditional Exercise Programs on Gait, Muscle Strength, and Body Balance in Healthy Older Adults." *Journal of Aging and Physical Activity*, Vol. 23, No. 1, (2015), 78–89. <https://doi.org/10.1123/JAPA.2012-0326>
- Borgi, M., Loliva, D., Cerino, S., Chiarotti, F., Venerosi, A., Bramini, M., Nonnis, E., Marcelli, M., Vinti, C., De Santis, C., ... Cirulli, F. "Effectiveness of a Standardized Equine-Assisted Therapy Program for Children with Autism Spectrum Disorder." *Journal of Autism and Developmental Disorders*, Vol. 46, No. 1, (2016), 1–9. <https://doi.org/10.1007/s10803-015-2530-6>
- Bronson, C., Brewerton, K., Ong, J., Palanca, C., and Sullivan, S. J. "Does hippotherapy improve balance in persons with multiple sclerosis: a systematic review." *European Journal of Physical and Rehabilitation Medicine*, Vol. 46, No. 3, (2010), 347–353. Retrieved from <https://www.minervamedica.it/en/journals/europa-medicophysica/article.php?cod=R33Y2010N03A0347>
- Champagne, D., and Dugas, C. "Improving gross motor function and postural control with hippotherapy in children with Down syndrome: Case reports." *Physiotherapy Theory and Practice*, Vol. 26, No. 8, (2010), 564–571. <https://doi.org/10.3109/09593981003623659>
- Steiner, H., and Kertesz, Z. "Effects of therapeutic horse riding on gait cycle parameters and some aspects of behavior of children with autism." *Acta Physiologica Hungarica*, Vol. 102, No. 3, (2015), 324–335. <https://doi.org/10.1556/036.102.2015.3.10>
- Hasan, C. Z., Jailani, R., Tahir, N. M., and Desa, H. M. "Vertical Ground Reaction Force Gait Patterns During Walking in Children with Autism Spectrum Disorders." *International Journal of Engineering - Transaction B: Applications*, Vol. 31, No. 5, (2018), 705–711. <https://doi.org/10.5829/ije.2018.31.05b.04>
- Cha, Y. J., Stanley, M., Shurtleff, T., and You, J. (Sung) H. "Long-term effects of robotic hippotherapy on dynamic postural stability in cerebral palsy." *Computer Assisted Surgery*, Vol. 21, No. sup1, (2016), 111–115. <https://doi.org/10.1080/24699322.2016.1240297>
- Zhang, K. "The Design and Realization of a Gait Rehabilitation Training Robot with Body Supporting Mechanism." *International Journal of Engineering - Transaction C: Aspects*, Vol. 29, No. 9, (2016), 1314–1318. <https://doi.org/10.5829/idosi.ije.2016.29.09c.18>
- Saadat, M., and Garmsiri, N. "A New Intelligent Approach to Patient-cooperative Control of Rehabilitation Robots." *International Journal of Engineering - Transaction C: Aspects*, Vol. 27, No. 3, (2014), 467–474. <https://doi.org/10.5829/idosi.ije.2014.27.03c.15>
- Park, J.-H., and You, J. S. H. "Innovative robotic hippotherapy improves postural muscle size and postural stability during the quiet stance and gait initiation in a child with cerebral palsy: A single case study." *NeuroRehabilitation*, Vol. 42, No. 2, (2018), 247–253. <https://doi.org/10.3233/NRE-172290>
- Ranciaro, M., Santos, E. L., Vara, M. F. F., Strasse, W. A. D., Franzo, D., Nogueira-Neto, G. N., Manffra, E. F., and Nohama, P. "Kinematic analysis of the evaluation of equine therapy patients with actimeter." In 2018 Global Medical Engineering Physics Exchanges/Pan American Health Care Exchanges (GMEPE/PAHCE), IEEE, 1–5. <https://doi.org/10.1109/GMEPE-PAHCE.2018.8400768>
- Navvab Motlagh, F., and Arshi, A. R. "Symmetry comparison between sacrum and center of mass during walking." *Proceedings of the Institution of Mechanical Engineers, Part H: Journal of Engineering in Medicine*, Vol. 230, No. 7, (2016), 682–689. <https://doi.org/10.1177/0954411916646402>
- Antunes, F. N., Pinho, A. S. do, Kleiner, A. F. R., Salazar, A. P., Eltz, G. D., de Oliveira Junior, A. A., Cechetti, F., Galli, M., and Pagnussat, A. S. "Different horse's paces during hippotherapy on spatio-temporal parameters of gait in children with bilateral spastic cerebral palsy: A feasibility study." *Research in*

- Developmental Disabilities*, Vol. 59, (2016), 65–72. <https://doi.org/10.1016/j.ridd.2016.07.015>
27. Ribeiro, M. F., Espindula, A. P., Bevilacqua Júnior, D. E., Tolentino, J. A., Silva, C. F. R. da, Araújo, M. F., Ferreira, A. A., and Teixeira, V. de P. A. "Activation of lower limb muscles with different types of mount in hippotherapy." *Journal of Bodywork and Movement Therapies*, Vol. 22, No. 1, (2018), 52–56. <https://doi.org/10.1016/j.jbmt.2017.03.020>
28. Esser, P., Dawes, H., Collett, J., and Howells, K. "IMU: Inertial sensing of vertical CoM movement." *Journal of Biomechanics*, Vol. 42, No. 10, (2009), 1578–1581. <https://doi.org/10.1016/j.jbiomech.2009.03.049>
29. Pfau, T., Ferrari, M., Parsons, K., and Wilson, A. "A hidden Markov model-based stride segmentation technique applied to equine inertial sensor trunk movement data." *Journal of Biomechanics*, Vol. 41, No. 1, (2008), 216–220. <https://doi.org/10.1016/j.jbiomech.2007.08.004>
30. Szpala, A., Rutkowska-Kucharska, A., Drapała, J., and Brzostowski, K. "Choosing the Right Body Position for Assessing Trunk Flexors and Extensors Torque Output." *Human Movement*, Vol. 12, No. 1, (2011), 57–64. <https://doi.org/10.2478/v10038-011-0005-y>

Persian Abstract

چکیده

هیپوتراپی (اسب درمانی) به عنوان یک روش درمانی، بر تعامل دینامیکی اسب-بیمار تکیه می‌کند، تا توانایی‌های جسمانی را در گستره‌ای از بیماری‌های عصبی-عضلانی ارتقاء بخشد. این روش درمانی از تحریک خارجی که به صورت ورودی سینتیک و سینماتیک بر بالاتنه‌ی فرد بیمار وارد می‌شوند بهره می‌برد. درمان‌ها و پروسه‌های درمانی که در حال حاضر انجام می‌شوند را می‌توان با یک رویکرد عینی برای برنامه‌ریزی جلسه‌درمانی بر مبنای مدل پیش‌بینی کننده‌ی عصبی-عضلانی، به مقدار زیادی ارتقاء بخشید. شخصی‌سازی برنامه‌ی درمانی برای هر بیمار خاص و بر اساس هر اسب خاص انجام می‌گردد. بدین منظور، ویژگی‌های کینزیولوژیکی سه عضله/گروه عضلانی اصلی بالاتنه (فلکسور-اکتوسور) که بصورت مستقیم در این روش درمانی دخیل بوده‌اند در مدل بیومکانیکی در نظر گرفته شده است. رویدادها و فازهای مختلف این تعامل دینامیکی مشخص شده و به کمک تحلیل نمودار صفحه فازی توصیف شده‌اند. تفسیر ضرایب معادلات دیفرانسیلی حرکت نشان می‌دهد که رویکرد پیشنهادی و مدل‌سازی ریاضی، پتانسیل آن را دارد که متناسب با طیف وسیعی از بیماری‌های اسکلتی-عصبی-عضلانی تنظیم گردد. نتایج اعتبارسنجی نشان می‌دهد که مدل ارائه شده توانایی شبیه‌سازی پاسخ سینماتیکی و نیروی عضلات بالاتنه بیمار را در طی یک جلسه اسب درمانی دارد. این توانایی پیش‌بینی، می‌تواند ابزاری را در اختیار درمانگر قرار دهد که به کمک آن اثرات درمان را قبل از اجرای جلسه‌ی درمانی تخمین بزند و به این ترتیب مناسب‌ترین ترکیب از اسب و تمرینات فیزیکی را انتخاب نماید.



Simulation of a GEF5 Gas Turbine Power Plant Using Fog Advanced Cycle and a Systematic Approach to Calculate Critical Relative Humidity

S. M. Arabi^a, H. Ghadamian^{*a}, M. Aminy^a, H. A. Ozgoli^b, B. Ahmadi^a, M. Khodsiani^a

^a Department of Energy, Materials & Energy Research Center (MERC), Tehran, Iran

^b Department of Mechanical Engineering, Iranian Research Organization for Science and Technology (IROST), Tehran, Iran

PAPER INFO

Paper history:

Received 06 July 2019

Received in revised form 08 August 2020

Accepted 03 September 2020

Keywords:

Gas Turbine

Simulation

Off-design Method

Inlet Air Cooling

Advanced Cycles

ABSTRACT

The ambient conditions have a significant effect on the generated power and efficiency of gas turbines [1]. These variations considerably affect power generation, fuel consumption, power plant emissions, and plant incomes. However, cooling the compressor inlet air has been widely used to reduce this deficiency [2]. In this paper, by simulating a specific gas unit in Thermoflow software, the effect of the FOG system on it was studied. Considering the error in determining the capacity of cooling systems based on the average values of dry and wet bulb temperatures, or even considering the worst possible temperature and humidity conditions, it is advisable to use ECDH or Evaporation cooling Degree Hours. Accordingly, by calculating ECDH under at ambient temperatures above 15 °C and changing the conditions of the model, the total production increase of the unit was estimated to be 4.7×10^6 kWh. In addition, the effect of relative humidity on payback time was examined, which illustrated the critical relative humidity for a gas unit would depend on the price of fuel, the purchase price of electricity, the design parameters of the unit and the expected payback time. For this gas unit, critical relative humidity was monitored based on expected payback time and electricity purchase price. Results showed that for a certain electricity price, at the shorter PBT, the critical RH is lower; therefore, the temperature drop and power enhancement will be greater. In addition, at a certain PBT, as the electricity price increases, the critical RH for the same PBT will be higher.

doi: 10.5829/ije.2020.33.11b.26

NOMENCLATURE

ECDH	Evaporation Cooling Degree Hours (°C.hr)	PBT	Payback Time (year)
EP	price of electricity	Q _{CL}	Designed capacity of cooling system
FP	price of fuel	RH	Relative Humidity (%)
GH	gross heat rate (kJ/kWh)	TD	Dry Bulb Temperature (°C)
H	Operating Hours (hr)	TW	Wet Bulb Temperature (°C)
Ki	initial investment cost	Greek Symbols	
LHV	Lower Heating Value (kJ/kg)	η_{gen}	generator efficiency

1. INTRODUCTION

Fossil fuels are non-renewable energy resources and demand for electricity is increasing. Therefore, it is essential to apply methods to generate electricity with higher efficiency in power plants with fossil fuels. One of the most used and popular power plants in recent years are gas turbines. Operation and design parameters have

notable effects on gas turbine performance. Many studies have been carried out in these subjects. However, finding the optimal parameters for the best performance such as the climate conditions which the gas turbine unit is placed in, is still a challenge.

In this regard, numerous types of research, and efforts have been carried out for the promotion of the Brayton cycle, the thermodynamic cycle of gas turbine power

*Corresponding Author Institutional Email: H.Ghadamian@merc.ac.ir
(H. Ghadamian)

plants. Pre-cooling of the compressor's inlet air is one of the most important and most used methods to increase both the thermal efficiency and the generated power of the gas-turbine cycles. The research of Ibrahim et al. [3] shows that a decrease of 10°C in the compressor inlet air temperature increases the gas turbine output power by 1%.

In higher intake air temperature, because the specific volume of the air increases, higher power will be consumed for the compression [4].

The rated capacity of the gas turbine is defined at ISO conditions (1bar, 15°C, 60% relative humidity). the gas turbine (GT) generated power decreases at the ambient temperature above 15°C, or when the plant is located in a warm/hot area, also cooling the inlet air below 15°C can lead to an enhancement of the gas turbine generated power compared to its rated power [5].

Sue and Chuang [6] reported that the location of the power station played an important role in its performance when the ambient temperature increases, the total power output decreases. Chakartegu et al [7] reported that when the intake temperature increases from 15 to 25°C, the gas turbine will lose approximately 7% of its power. The losses reach 15% of the power rating at 36°C of ambient temperature. Rising ambient temperature by 1°C reduces the output power and efficiency of the gas cycle by 0.6 and 0.18%, respectively [8]

The results of research by Najjar et al. [9] showed considerable positive effect of cooling the air before entering the compressor. This research also showed that at intense weather conditions (temperatures above 45°C and relative humidity more than 80%), applying their proposed inlet air cooling method will reduce the temperature of inlet air about 15°C which leads to an increase in net power generation and overall efficiency 35 and 50%, respectively.

Noroozian and Bidi [10] applied a turbo expander replacng pressure-reducing valve. The shaft of the turboexpander was coupled to the compressor shaft of a mechanical chiller, which was used for cooling the compressor inlet air. Ameri and Hejazi [11] evaluated the effect of applying an absorption chiller for precooling the compressor inlet air on a gas turbine capacity improvement.

Fogging method for inlet air cooling, because of its lower capital cost, is popular and more acceptable compared to other methods. In hot seasons, the demand for power increases. Therefore, it is important to enhance the gas turbine power generation unit for a higher power generation.

The fogging cooling method is used to compensate for the power drop due to high ambient temperature. Heavy mist of fine-water particles which is called "Fog", is sprayed out of some nozzles, typically installed close to the air filters for spraying enough water to allow the air to reach the saturation state [12]. This will reduce the

compressor power consumption due to the reduction of inlet air temperature. In addition, it causes greater power generation, higher efficiency and lower specific fuel consumption [13]. The effectiveness of these actions depends on the humidity of the air and the temperature; in general, not only the maximum increase in the dry and warm air, but also provides significant benefits in wet and tropical environments.

Ehyaei et al. [14] studied the effects of the inlet fog system on the performance of combined cycle power plants. Their results showed that the average output power increases by using inlet fogging method. Inlet fogging system has a positive effect on decreasing gas turbine exhaust air pollutions as well. The performance parameters such as compressor inlet temperature, compressor consumed power, gas turbine power output and cycle efficiency, with existing inlet fogging and wet compression process were investigated [15]. Ehyaei et al [16] studied the effect of a fogging cooling system on the performance of a combined cycle power plant by a comprehensive thermodynamic modeling method. They also specify the optimal design parameters. Their research results showed that by applying a fogging cooling system the efficiency will increase by 17.24, 3.6, and 3.5%, respectively, at three warm months of a year.

2. EVAPORATIVE COOLING SYSTEM

Using evaporative cooling methods is one of the easiest ways to increase the gas turbine's generating power. In the first method called the Media method, by increasing the relative humidity, or in other words, passing the air over wet layers, the dry temperature of the air will noticeably decrease due to the water evaporation.

"Relative Humidity" is the percent of moisture that exists in the air to the maximum amount of moisture that can exist in the air in that temperature, i.e. saturation humidity. In contrast, "Absolute Humidity" is the amount of moisture that exists in the air regardless of temperature.

Other evaporative cooling methods are spraying water into the air stream (fog) which is considered as an adiabatic cooling process and the process occurs in a line with stable wet bulb temperature on a psychrometric chart. Using fog system, especially in environments with low relative humidity in which the difference between wet & dry bulb temperature is high, is a good method.

Working principles of evaporative systems are the absorption of evaporation latent heat from the air by water, hence cooling the air. Accordingly, the evaporative cooling system's overall efficiency is defined based on the equation below, considering the temperature difference:

$$\eta = \frac{T_{1D} - T_{2D}}{T_{1D} - T_{2W}} \quad (1)$$

The w and D indexes refer to wet and dry bulb conditions, respectively.

In a fog system, the high-quality de-mineralized water is passed through stainless steel nozzles with ruby orifices. This process is performed by high-pressure pumps in the range of 70 to 160 bar (normally about 140 bar). The water is sprayed into the air stream in the form of little particles with a size of about 100 microns. The reason for spraying water in small particles is to increase the water contact surface with the air resulting in faster water evaporation rate.

Evaporative cooling systems, because of its low initial investment costs and simplicity of installation, are the most economical cooling methods in hot and dry regions [17-18]. De Lucia et al. [19] presented that evaporative inlet air cooling systems in different atmospheric conditions can promote the generated power by 2-4%. Chaker et al. [20] studied the maximum hours that an evaporative cooling system can operate in 122 different locations.

3. ANALYSIS OF CLIMATIC DATA AND ESTIMATION OF INLET COOLING POWER GAIN POTENTIAL

There are many problems and bugs during the analysis of climatic data. Averaging the data leads to some bugs. For example, Figure 1 shows the relation of dry bulb and wet bulb averages with different months at a specific location.

On the graph, linear behavior may lead to the conclusion that at a dry bulb temperature of 25°C the wet bulb is expected to be 20°C, which shows reducing the potential of about 5°C; or, in other words, the evaporative cooling potential. However, this result is completely wrong and erroneous. Since the curve is plotted by considering the mean WB temperature and the average DB temperature and does not show the matched conditions of the WB and DB temperature, it shows a very different cooling potential. These types of errors are usual in such studies. Some researchers also consider the "worst-case" of temperature and humidity in terms of evaporative cooling potential. This action is taken to ensure that the fog equipment will meet the required capacity in the worst-case conditions, but in practice, this situation never occurs, or rarely happens [20]. In addition, McNeilly [21] in his research mentions the necessity of avoiding this error. It should be mentioned that in this analysis the profile of ambient air temperature for a complete year or several consecutive years is considered. ECDH (evaporative cooling degree hour) values can be computed by these data. In this method, inlet fogging power enhancement potential at different periods can be analyzed accurately.

In Table 1 a sample calculation of ECDH for Zanbagh power plant is shown; This plant is located in Yazd

province, Iran at an altitude of 1285 meters from sea level. This table provides summary data for six months at ambient temperatures above-defined ISO temperature according to registered climatic data for the last 2 years of the operation of the power plant. The last row indicates the total ECDH (annual °C- hours of cooling potential) Which could be the basis for the evaluation of the use of the Fog and Media cooling system for this gas turbine at the mentioned site.

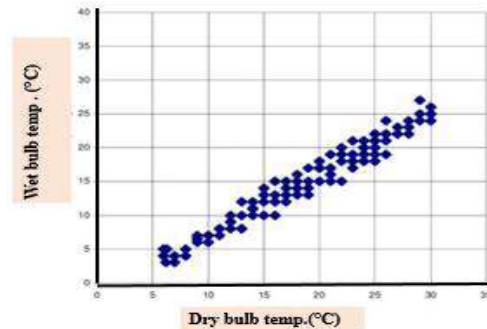


Figure 1. A typical pattern of Correlation of WB and DB temperatures averages in different months [20]

TABLE 1. A sample calculation that computes ECDH for Zanbagh power plant for six months at ambient temperatures above-defined ISO temperature

DB (°C)	Hrs	Avg coincident WB (°C)	Possible Temp. drop	ECDH (°C.Hrs)
52-60	0	27	25	0
50	9	24.8	25.2	226.8
48	20	23.55	24.45	489
46	42	22.55	23.45	984.9
44	96	21.65	22.35	2260.8
42	132	20.62	21.38	2822.16
40	148	19.47	20.53	3038.44
38	161	18.53	19.47	3134.67
36	162	17.43	18.57	3008.34
34	166	16.35	17.65	2929.9
32	164	15.22	16.78	2751.91
30	167	14.12	15.88	2651.96
28	241	13	15	3615
26	203	12	14	2842
24	122	11.65	12.35	1506.7
22	117	11.02	15.98	1284.66
20	96	10.88	9.12	875.52
18	87	10.65	7.35	639.45
16	81	9.6	6.4	518.4
Total ECDH				35550.61

Figure 2 also is a bar chart showing monthly ECDH from another site.

Figure 3 shows a general variation pattern of dry and wet bulb temperatures during a day. It is necessary to note that high relative humidity conditions do not match with high DB temperatures. According to this figure, between 14:00 and 15:30 (afternoon hours), the difference between DB and WB temperature is significant. In this widespread period, applying the FOG system is justifiable. As previously mentioned, the typical fault made by some researchers is designing cooling systems based on the highest relative humidity and the highest temperature which has been given for a month. The problem is that generally the highest RH and highest temperature do not occur simultaneously. It means that generally, the higher RH happens with the lower temperature and vice versa.

3. 1. Fog Inlet Air Cooling in High Humidity Areas

Even at the most humid climates in the warmest part of the day, a considerable decrease in air temperature using evaporative systems has been reported. The temperature of the air affects the amount of moisture that it can keep. The warmer air can hold more moisture relative to the cooler Air.

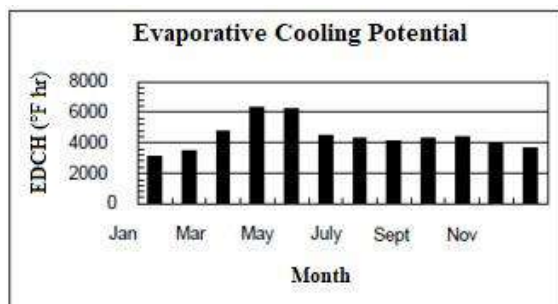


Figure 2. A typical pattern of ECDH in different months for an example site [20]

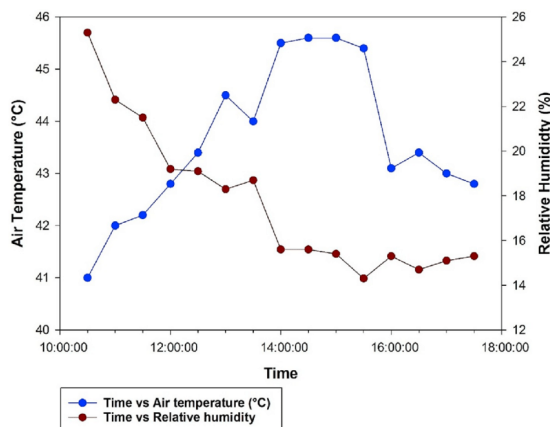


Figure 3. A typical pattern of daily variation of dry bulb and wet bulb temperatures [20]

RH is highest at low air temperature hours in a day (mornings and evenings) and lowest in the times with high air temperature (afternoons).

The fogging cooling systems are inexpensive and easy to install and make a small amount of pressure drop, and are used in humid climates in the summertime.

4. SIMULATION OF A SPECIFIED GAS TURBINE POWER PLANT

4. 1. Technical Details of the Simulated Unit

Gas turbine function matches the Bryton cycle; its main components are compressors, combustion chambers and turbines.

Gas turbine simulation and performance study in this research have been performed on a GEF5 gas unit in the Zanbagh power.

The technical specifications of the gas unit at standard conditions are given in Table 2. In addition, an overview of the unit is shown in Figure 4.

In this research, the GT unit operational data during one year was applied. Air is compressed in a seventeen stage axial compressor.

Ambient dry bulb temperature (Compressor inlet air temperature) of 36°C and an atmospheric pressure of

TABLE 2. Specification of Alstom GE-F5 gas turbines at standard conditions

Rotational Speed	5100	RPM
Inlet temperature	15	°C
Inlet relative humidity	60	%
Pressure ratio	9.7	
Inlet air pressure	101.325	kPa
Intake air flow rate	91.622	m ³ /s
Compressor pressure ratio	7.5	
Combustion efficiency	99	%
Specific heat capacity of the air	1.005	kJ/kg K
Specific heat capacity of flue gas	1.15	kJ/kg K
Lower heating value LHV	46670	kJ/kg
Isentropic efficiency of comp.	88.4	%
Isentropic efficiency of the turbine	89.6	%
Air mass flow rate	111.11	kg/s
The adiabatic efficiency of comp.	85	%
Fuel (natural gas) mass flow rate	1.69	kg/s
Mass of exhaust	112.8	kg/s
Flue gas temperature	521.2	(°C)
Flue gas specific heat (CP)	1.1339	
Output power	15.574	MW



Figure 4. Overview of the simulated unit

0.86 bar is considered for this simulation. According to the air temperature compared with the standard condition, the operating mass flow rate of the unit was computed.

4. 2. Simulation Software Thermoflow is thermal engineering software for modeling and simulation of the power and cogeneration units. It is a fully flexible software that allows modeling a broad range of mass and heat balances in power plants. Since 1987, Thermoflow has been one of the pioneers in the development of thermal engineering software for industrial plants. GT PRO, the first product of this company, is known worldwide as the most popular program for designing and simulating a gas turbine machine that can predict the performance of the plant as a function of its fixed equipment, control set-points, loads, and ambient conditions.

In this research GT, PRO 21.0 was used to model the gas turbine with and without a fogging system.

4. 3. Simulation Process A simulation in GTPRO software was carried on in order to get a general view of the situation. At first, a GE-F5 gas turbine unit with a simple cycle fueled with natural gas was selected. Then the properties of components were adjusted to fit the model on the real unit. It should be mentioned that the F5 model is not included in the software library, but according to the manufacturers operating manual, this type fits exactly with “General Electric GE 3411N”, which is available in the software library.

The simulation of the gas turbine unit with a fogging inlet air cooling systems contains the following assumptions:

- The ambient air contains 23.3% oxygen and 76.7% nitrogen by mass.
- The combination of gas fuel is considered methane.
- The pressure and temperature of natural gas in the feed line are 22.4 bars and 25°C respectively.
- The pressure loss of the combustion chamber is considered to be 3%.
- The mass flow rate of ambient air and its pressure and temperature are considered to be constant. The outputs of

the simulation of the investigated gas turbine at basic mode are shown in Figure 5.

- The effectiveness of the fogging system was considered 95%. This parameter represents a decrease in the air temperature to 95% of the difference between the dry and wet temperature of the inlet air.

4. 4. Verification of the Model In order to verify and ensure the modeling, by transferring calibrated measuring equipment to the site, some parameters of the operating unit in several positions accurately measured and compared with the values obtained from the model.

Table 3 shows the comparison of some measured values in the site with values obtained from the model at different hours of a day. Exhaust temperature, Compressor discharge temperature and Fuel consumption of the unit were considered for validation.

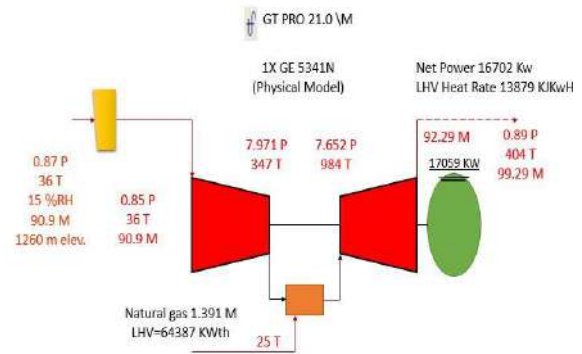


Figure 5. Simulation outputs of the investigated gas turbine at basic mode

TABLE 3. Comparison of some measured values with values obtained from the model

Deviation (%)	Model	Site	Time	
1.76	760.3	747.1	10:00	Exhaust temperature
1.30	757.8	748.1	12:00	
0.18	750.4	749.1	13:30	
1.50	737.9	749.1	15:00	
0.066	570.3	574.1	10:00	Comp. discharge temperature
0.29	576.5	578.1	12:00	
0.32	581.0	579.1	13:30	
0.39	578.9	581.1	15:00	
1.40	6510.7	6603.0	10:00	Fuel consumption
0.41	6481.2	6508.0	12:00	
1.09	6349.0	6419.0	13:30	
1.86	6205.9	6323.5	15:00	

According to these results, the model created in the software is highly consistent with the actual behavior of the unit. Therefore, the Fog system for cooling the incoming air according to calculated ECDH values was implemented on the model to evaluate its impact on unit performance.

Figure 7 shows the modeling of an investigated gas turbine by applying a fogging system at one of the ECDH value.

Several simulations for the different values of ECDH which are presented in Table 1 were done and the outputs of each stage are included in the final calculations.

4. 5. Results of Simulation The of the gas turbine performance simulation was done by GT PRO 21.0 software. Table 4 shows the output of the simulation. A sensitive analysis is required to show the influence of inlet temperature variations on the net power output, thermal efficiency, specific fuel consumption and heat-rate. This is done by using Thermoflow software.

Table 4 shows the results of simulations for comparison of the unit performance with and without the fogging system at a certain climate condition. According to the results, the gas turbine with a fogging system performs better than the gas turbine without a fogging system. The results show that by applying the fogging system, a drop occurs in the temperature system readings. the temperature drop in the exhaust is a confirmation for the cooling inside the system.

The results showed that by applying a fogging system, the thermal efficiency of the gas turbine system will increase as a result of a decrease in intake air temperature. The net power of the cycle also will increase because of decreasing the compressor consuming power and increasing the mass flow rate of gases that hit the turbine blades. According to the results of the model, applying fog system in the above-mentioned conditions will lead to increasing the power generation and cycle efficiency by 8 and 0.6%, respectively.

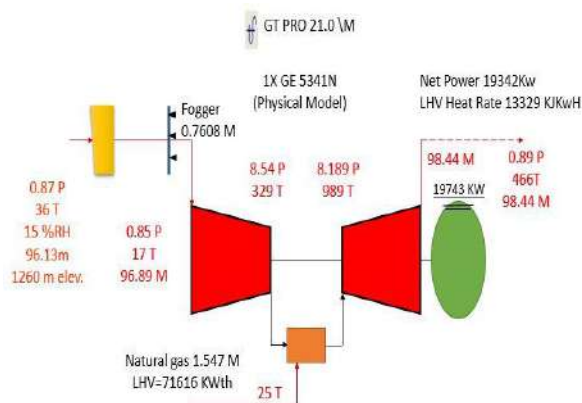


Figure 7. Output results of simulation with a fog system

The Specific fuel consumption of the cycle by using the fog system is lower than specific fuel consumption in the base cycle. Therefore, the use of the fog system, in addition to reducing energy consumption, will also reduce environmental pollutants. By examining the model in all of the ECDH values in Table 1, the overall increase in the power production of the gas turbine cycle using fog system will be about 35550.61 kilowatt-hours per year. This value is more accurate to be considered for designing, Economic analysis or to determine the cooling system capacity in comparison with considering average data or the worst scenario.

5. FINDING CRITICAL RELATIVE HUMIDITY

For finding critical relative humidity, the economic analysis and especially the payback period should be considered.

5. 1. Economic Analysis In economic considerations of fog system the capital costs, current costs, earnings due to using this system, interest rate, etc. should be considered .

a) Electricity production enhancement The net increase in net production is obtained from the following equation:

$$\Delta W = \Delta W_c + \Delta W_{gt} - \Delta W_i - \Delta W_f \tag{2}$$

By applying the fog cooling system, the changes in power output include:

- 1) the net power output of the cycle increases since by reducing compressor inlet air temperature its power consumption decreases (ΔW_c);
 - 2) the generated power of gas turbine increase since air density rises as $T_{i,c}$ declines (ΔW_{gt});
 - 3) because of installing cooling systems in the passage of inlet air, the pressure of inlet airdrops and as a result of the generated power decreases (ΔW_i);
 - 4) all kinds of evaporative cooling system have some subsidiary installations which have energy usage (W_f).
- The extra income which will be gained through applying the fog cooling system, is

$$I_{ext} = \Delta W \cdot \eta_{gen} \cdot EP \tag{3}$$

where EP is the price of electricity and η_{gen} is generator efficiency.

b) Extra fuel consumption By applying the fog system, the entering air mass flow increases, and as a result, the fuel consumption will be raised. This extra fuel consumptions of unit (ΔF , kg/s) can be calculated by:

$$\Delta F = (W_e \cdot GH_e - W_o \cdot GH_o) / (3.6LHV) \tag{4}$$

GH in this relation is the gross heat rate. Also, the Subscript e shows the values for the gas power plant with a fogging system and subscript 0 refers to the unit lacking a fogging system.

e) Initial investment cost The considered capacity for the evaporative cooling system has a major impact on the needed capital cost. The amount of initial investment can be calculated from the following equation.

$$I = k_i \cdot Q_{CL} \tag{5}$$

In the above equation, Q_{CL} refers to the evaporative cooling system considered capacity, and k_i shows the capital cost for a unit of cooling load.

5. 2. Finding Critical Relative Humidity for an Expected Payback Period

The annual net profit by applying the fog system includes the following items :
 - The obtained income from sales of extra generated power,
 - The yearly fee for maintenance and repair of the fogging system and additional fuel consumption.

$$S = (\Delta w \cdot \eta_{gen} \cdot EP - \Delta F \cdot FP) \cdot H - MC \tag{6}$$

which EP is the price of a Kilowatt-hour of generated power, H shows the number of working hours and FP is the price of a cubic meter of natural gas.

To gain a profit ($S > 0$), the Extra income should be greater than the sum of the mentioned cost. MC is the annual maintenance and operation costs of the system and η_{gen} is the generator efficiency.

$$PB = I/S \tag{7}$$

Several factors affect critical relative humidity, including: designed specifications of the power plant, ambient condition, power purchase price, Predicted PBT and the price of natural gas. Figure 8 shows the critical RH calculation steps for a Predicted PBT.

5. 3. Variation of Critical RH with Ambient Temperature, Electric Price, and PBT

If RH in the gas unit location is less than the critical RH, then the real payback time is shorter than Predicted PB and vice versa. In order to evaluate the installation of an evaporative cooling system on a gas unit, the mean values of critical RH are considered.

In Figure 9, the values of critical RH at several PBT and yearly mean temperature can be observed. To find the average annual temperature, we consider the average temperature of five warmest months of the year from May to September.

As is evident in a shorter time of PBT, the values of critical RH are also smaller. Obviously, this is if the annual average temperature is assumed to be constant. Because there is a higher difference between WB and DB temperature in a lower RH, considerable temperature

drops and more generated power is possible which leads to more yearly income and shorter PBT. In addition, for a longer payback period, the critical RH for different annual temperature gradually approach each other. The reason is that by increasing RH to a high level, the effect of cooling and temperature drop decreases and the

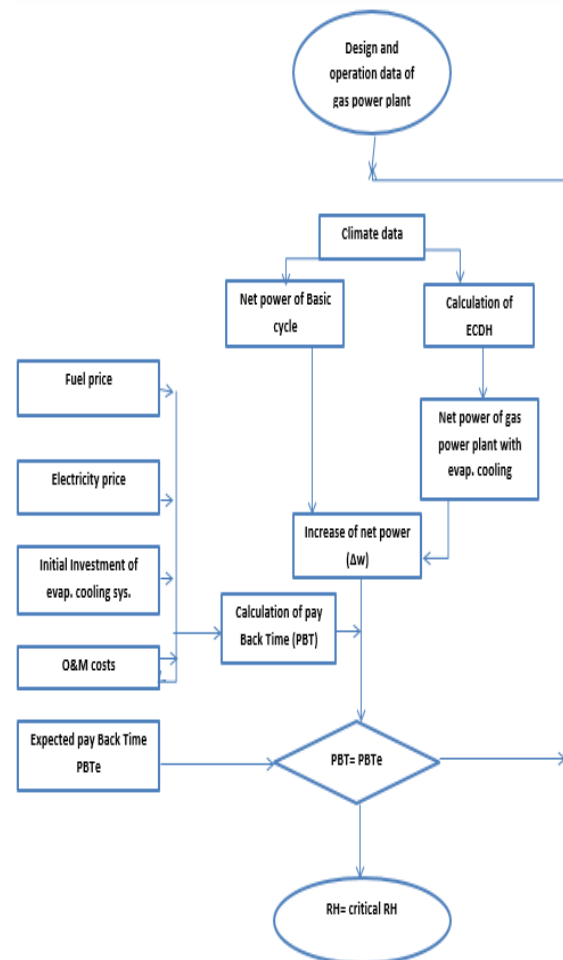


Figure 8. Flow chart for finding critical RH

behavior of the system at different net temperatures will be roughly the same.

The sensitivity analysis of critical RH shows that critical RH is affected by PBT and electricity price, which is shown in Figure 10.

According to the chart, for the specified PBT, at the lower electricity price, the critical RH should be lower in order to cause greater power enhancement. By greater power enhancement, the total increase in the income is equal to the case with higher electricity prices and higher critical RH. Also for a specified electricity price, at the shorter PBT, the critical RH is lower, and as a result, the reduction in temperature and power enhancement is greater. This result is also evident, when the values of

power price increase, the values of critical RH also increase for the same amount of payback time. Therefore, as the electricity price increases, the critical RH for the same PBT is higher. For example, for PBT of 3 years, the critical RH for electricity price of 0.07 \$/kWh is 21 and is 41% for electricity price of 0.12 \$/kWh.

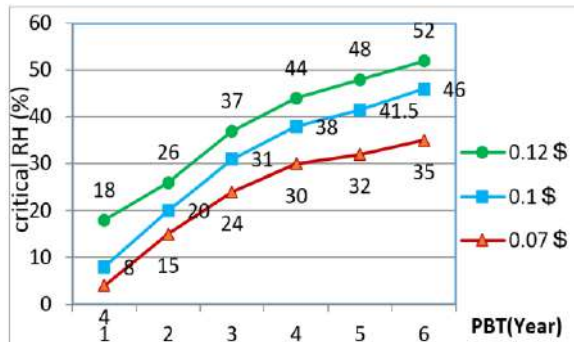


Figure 10. Critical RH variation with electricity price in Iran and PBT

6. CONCLUSION

Using the mean values of WB and DB for evaluation of the cooling capability of an evaporative system leads to incorrect estimation, because the Minimum and maximum values of WB and DB do not coincide simultaneously. In addition, we have considered the "worst-case" of temperature and humidity in terms of evaporative cooling potential. In practice, this never occurs or it rarely happens. In the analysis, the profile of ambient air temperature for a complete year or several consecutive years is considered. ECDH values can be generated employing these data and accordingly, accurate and detailed analysis of inlet fogging power gain potential at different periods can be done.

By examining the model in all of the ECDH values in Table 1, the overall increase in the power production of the GEF5 gas turbine by applying fog system will be about 35550 kilowatt-hours per year. This value is more accurate for designing economic analysis or for determining the cooling system capacity in comparison with average data or the worst-case scenario. In addition, the simulation of the GEF5 gas turbine showed that by using the fog system, at the same time, the efficiency increases, the compressor power consumption, and heat-rate decreases.

As mentioned earlier, several factors affect critical RH, such as designed specifications of the power plant, ambient condition, power purchase price, Predicted PBT and the price of natural gas. A review of critical RH under different climate conditions illustrated that for a shorter expected PBT the less value of critical RH will be obtained at a specific yearly average temperature.

According to the critical RH sensitivity analysis results, if the PBT is considered to be fixed for higher power purchase price higher value of critical RH will be achieved. That means the value of critical RH depends on the power purchase price and considered PBT.

7. ACKNOWLEDGMENT

The present study was supported by Materials and Energy Research Center (MERC) through PhD student grant No. 581394052 for the purpose of science development. We hereby acknowledge the supports.

8. REFERENCES

1. N. Shokati, F. Ranjbar, and F. Mohammadkhani, "Comparison of single-stage and two-stage tubular sofc-gt hybrid cycles: energy and exergy viewpoints", *International Journal of Engineering, Transactions A: Basics*, Vol. 28, No. 4, (2015), 618-626, doi: 10.5829/idosi.ije.2015.28.04a.17.
2. S. M. Arabi, M. Aminy, H. Ghadadian, H. A. Ozgoli, and B. Ahmadi, "Thermo-Economic Analysis of Applying Cooling System Using Fog on GE-F5 Gas Turbines (Case Study)", *Journal of Heat and Mass Transfer Research*, Vol. 4, No. 2, (2017), 73-81, doi: 10.22075/JHMTR.2017.1613.1106.
3. A. M. Al-Ibrahim, and A. Varnham, "A review of inlet air-cooling technologies for enhancing the performance of combustion turbines in Saudi Arabia", *Applied Thermal Engineering*, Vol. 30, No. 14-15, (2010), 1879-1888, doi: 10.1016/j.applthermaleng.2010.04.025.
4. A. P. Santos, and C. R. Andrade, "Analysis of gas turbine performance with inlet air cooling techniques applied to Brazilian sites", *Journal of Aerospace Technology and Management*, Volume 4, No. 3, (2012), 341-353, doi: 10.5028/jatm.2012.04032012.
5. S. Baakeem, J. Orfi, S. Alaqel, and H. Al-Ansary, "Impact of Ambient Conditions of Arab Gulf Countries on the Performance of Gas Turbines Using Energy and Exergy Analysis", *Entropy*, Vol. 19, No. 1, (2017), 32, doi: 10.3390/e19010032.
6. D. C. Sue, and C. C. Chuang, "Engineering design and exergy analyses for combustion gas turbine based power generation system", *Energy*, Vol. 29, No. 8, (2004), 1183-1205, doi: 10.1016/j.energy.2004.02.027.
7. R. Chacartegui, F. Jimenez-Espadafor, D. Sanchez, and T. Sanchez, "Analysis of combustion turbine inlet air cooling systems applied to an operating cogeneration power plant", *Energy Conversion and Management*, Vol. 49, No. 8, (2008), 2130-2141, doi: 10.1016/j.enconman.2008.02.023.
8. M. Farzaneh-Gord, and M. Deymi-Dashtebayaz, "Effect of various inlet air cooling methods on gas turbine performance", *Energy*, Vol. 36, No. 2, (2011), 1196-1205, doi: 10.1016/j.energy.2010.11.027.
9. Y. S. Najjar, A. M. Abubaker, and A. F. El-Khalil, "Novel inlet air cooling with gas turbine engines using cascaded waste-heat recovery for green sustainable energy", *Energy*, Vol. 93, No. 1, (2015), 770-785, doi: 10.1016/j.energy.2015.09.033.
10. A. Noroozian, and M. Bidi, "An applicable method for gas turbine efficiency improvement. Case study: Montazar Ghaem power plant, Iran", *Journal of Natural Gas Science and Engineering*, Vol. 28, No. 1, (2016), 95-105, doi: 10.1016/j.jngse.2015.11.032.

11. M. Ameri, and S. H. Hejazi, "The study of capacity enhancement of the Chabahar gas turbine installation using an absorption chiller". *Applied Thermal Engineering*, Vol. 24, No. 1, (2004), 59-68, doi: 10.1016/S1359-4311(03)00239-4.
12. X. Shi, B. Agnew, D. Che, and J. Gao, "Performance enhancement of conventional combined cycle power plant by inlet air cooling, inter-cooling and LNG cold energy utilization", *Applied Thermal Engineering*, Vol. 30, No. 14-15, (2010), 2003-2010, doi: 10.1016/j.applthermaleng.2010.05.005.
13. T. K. Ibrahim, M. M. Rahman, and A. N. Abdalla, "Improvement of gas turbine performance based on inlet air cooling systems: A technical review", *International Journal of Physical Sciences*, Vol. 6, No. 4, (2011), 620-627, doi: 10.5897/IJPS10.563.
14. M. A. Ehyaei, A. Mozafari, and M. H. Alibiglou, "Exergy, economic & environmental (3E) analysis of inlet fogging for gas turbine power plant", *Energy*, Vol. 36, No. 12, (2011), 6851-6861, doi: 10.1016/j.energy.2011.10.011.
15. S. Sanaye, and M. Tahani, "Analysis of gas turbine operating parameters with inlet fogging and wet compression processes", *Applied Thermal Engineering*, Vol. 30, No. 2-3, (2010), 234-244, doi: 10.1016/j.applthermaleng.2009.08.011.
16. M. A. Ehyaei, M. Tahani, P. Ahmadi, and M. Esfandiari, "Optimization of fog inlet air cooling system for combined cycle power plants using genetic algorithm", *Applied Thermal Engineering*, Vol. 76, No. 1, (2015), 449-461, doi: 10.1016/j.applthermaleng.2014.11.032.
17. R. Garetta, L. M. Romeo, and A. Gil, "Methodology for the economic evaluation of gas turbine air cooling systems in combined cycle applications", *Energy*, Vol. 29, No. 11, (2004), 1805-1818, doi: 10.1016/j.energy.2004.03.040.
18. H. H. Erdem, "Thermodynamic and economic assessments of gas turbine inlet air-cooling by evaporative technique", *International Journal of Exergy*, Vol. 6, No. 5, (2009), 605-619, doi: 10.1504/IJEX.2009.027492.
19. M. De Lucia, E. Carnevale, M. Falchetti, and A. Tessei, "Performance improvements of a natural gas injection station using gas turbine inlet air cooling". In ASME 1997 International Gas Turbine and Aeroengine Congress and Exhibition, American Society of Mechanical Engineers, (1997), V002T07A001-V002T07A001, doi: 10.1115/97-GT-508.
20. M. Chaker, and C. B. Meher-Homji, "Inlet fogging of gas turbine engines: climatic analysis of gas turbine evaporative cooling potential of international locations", In ASME Turbo Expo 2002: Power for Land, Sea, and Air, American Society of Mechanical Engineers, (2002), 371-386, doi: 10.1115/GT2002-30559.
21. J. D. McNeilly, "Application of Evaporative Coolers for Gas Turbine Power Plants", ASME Turbo Expo 2000: Power for Land, Sea, and Air, American Society of Mechanical Engineers, (2000), V003T03A005, doi: 10.1115/2000-GT-0303.

Persian Abstract

چکیده

میزان راندمان و توان خروجی توربین‌های گاز با تغییر شرایط محیط متغیر است. این تغییرات به شدت بر میزان تولید برق، مصرف سوخت، انتشار آلاینده‌ها و درآمد نیروگاه تاثیر می‌گذارد. با این حال، خنک کردن هوای ورودی کمپرسور توربین‌های گاز به طور گسترده‌ای برای جبران این معایب مورد استفاده واقع شده است. در این مقاله، با شبیه‌سازی یک واحد گازی مشخص در نرم‌افزار Thermoflow، اثر سیستم خنک‌کاری فاک بر روی آن مورد بررسی و تحلیل قرار گرفته است. با توجه این که در اکثر تحلیل‌های موجود، میانگین مقادیر دمای خشک و دمای مرطوب، یا در برخی موارد بدترین حالت از نظر دمایی و رطوبتی مبنای تعیین ظرفیت سیستم‌های خنک‌کن قرار می‌گیرد و این موضوع سبب خطا و انحراف در محاسبات می‌گردد، استفاده از ECDH با درجه-ساعت خنک‌کاری تبخیری به جای شرایط قبلی توصیه می‌گردد. با محاسبه‌ی ECDH در دماهای محیط بالاتر از ۱۵ درجه‌ی سانتیگراد و تغییر شرایط مدل، کل میزان افزایش تولید واحد با بکارگیری سیستم خنک‌کاری فاک معادل $4/7 \times 10^6$ کیلووات ساعت تخمین زده شد. همچنین تاثیر رطوبت نسبی بر مدت بازگشت سرمایه طرح‌های خنک‌کاری مورد بررسی قرار گرفته است که مشخص گردید رطوبت نسبی بحرانی برای یک واحد گازی به قیمت سوخت، قیمت خرید برق، پارامترهای طراحی واحد و مدت بازگشت سرمایه پیش‌بینی شده بستگی خواهد داشت. رطوبت نسبی بحرانی برای واحد گازی مورد مطالعه، بر اساس زمان بازگشت سرمایه پیش‌بینی شده و قیمت خرید برق فعلی مورد بررسی قرار گرفته است. نتایج نشان می‌دهد که برای یک قیمت خرید برق مشخص، با کاهش زمان بازگشت سرمایه مورد انتظار، رطوبت نسبی بحرانی، پایین‌تر است. بنابراین میزان کاهش دما و افزایش قدرت، در نتیجه به‌کارگیری سیستم‌های خنک‌کن بیشتر خواهد بود. همچنین در یک مدت بازگشت سرمایه مشخص، با افزایش قیمت برق، رطوبت نسبی بحرانی برای همان مدت بازگشت سرمایه بالاتر خواهد بود.



Combustion Behavior of Fuel Briquettes Made from Ulin Wood and Gelam Wood Residues

A. Amrullah*, A. Syarief, M. Saifudin

Department of Mechanical Engineering, Lambung Mangkurat University, Banjarmasin, South of Kalimantan, Indonesia

PAPER INFO

Paper history:

Received 18 May 2020

Received in revised form 16 June 2020

Accepted 02 August 2020

Keywords:

Compaction Pressure

Mixing Ratio

Combustion Rate

Bulk Density

ABSTRACT

Solid fuel from the briquetting of ulin wood and gelam wood residue was investigated in this work. The effect of compaction pressure (10, 12, and 15 MPa), and briquette formulation were investigated. The ulin wood and gelam wood were blended in the mixing ratios of 100:0, 70:30, 50:50, 30:70, and 0:100, respectively. The size of the particle was fixed of 50 μm . The ulin wood and gelam wood were carbonized under fixed temperature (500°C), and time (120 min). The gelatinized binder (cassava starch) was 20% of the total briquettes weight. The densification was carried out using the briquetting machine (piston-press type) laboratory scale. The compaction pressure briquette had a significant effect on some characteristics of briquette (ash content, moisture content, volatile matter, bulk density, and combustion rate). An increasing in compaction pressure briquettes resulted in low ash content, moisture content, and volatile matter but the reverse is the case for bulk density. However, the mixing ratio slightly affected. High combustion rate (3.18 g/min) achieved at low compaction pressure (10 MPa).

doi: 10.5829/ije.2020.33.11b.27

1. INTRODUCTION

The depletion of fossil-fuel reserves and increasing environmental pollution caused by the large-scale application of fossil fuel, the energy obtained from biomass and biomass waste has received much attention in recent years. This problem has driven researchers to develop possible methods of innovating new fuel resources. To handle the waste material, educating the citizen is contributive to careful strategies. Indonesia's biomass energy resources are abundant. 52% of the land was covered by forest, 13% of arable land, 12% of permanent crops, meadows, and pastures is about 6% and 17% of other lands [1]. Indonesia has huge biomass energy potential, not only an energy challenge but also potentially suitable bioenergy and can be distinguished between municipal [2], industrial waste [3], forest waste [4], and agriculture wastes [5,6]. However, only a small portion has been utilized. The biomass from forestry and

agriculture wastes is a plentiful feedstock for the production of solid fuels such as briquette. In the future, bioenergy conversion of biomass is also regarded to keep increasing. However, the characteristics of biomass such as moisture content, low energy density have required high cost for processing on direct combustion use [7]. There are several technologies for converting biomass into energy i.e., thermochemical conversion, biochemical conversion, and mechanical conversion. Among various thermochemical conversion technology carbonization is simple and promising. The biomass carbonization technique has benefits such as low raw material is needed, operational with the simple way, and low energy consumption [8–10].

In this context, Monedero et al. [11] examined the effect of hydrothermal carbonization on the properties, devolatilization, and combustion kinetics of Chilean biomass residues. They reported that carbon and heating value increased after HTC. Furthermore, Sun et al. [12] reported that the carbonization on raw biomass materials

*Corresponding Author Institutional Email: apip.amrullah@ulm.ac.id
(A. Amrullah)

could impact the natures of fuel and emission of PM_{2.5} significantly.

The briquetting technology is relatively well known. Many researchers studied the production of solid fuels briquette from rice husk and sawdust [13], coffee-pine [14], cow dung [14], corn cob [15], these and more studies remain few given the number of wastes generated from forestry and processing. Differences in hydro-geological conditions in different regions imply that the physical properties of forest wastes must be geo-specific [14,15]. Due to biomass variability, a continuous effort must be applied to the development and characterization of biomass briquettes for sustainable energy development.

Ulin wood and gelam wood are a key group of hardwood trees. A categorization that encompasses a wide range of species across varying ecological habitats [18]. The Borneo ulin wood, locally known as Belian, is a canopy tree found in the lowland dipterocarp rain forests of eastern, southern Kalimantan, and southern Sumatra (Indonesia). The residual of ulin wood and gelam wood can be converted into bioenergy resources. The carbon content of this wood is about 50%. According to reported data by Tumuluru et al. [19] biomass with high lignin, protein, or starch content possess better compaction than those with high cellulose content. As reported by Harahap et al. [20] the characteristics of nanocrystal from corn cob showed the atomic structure of cellulose nanocrystal quite regular so obtained a high crystallinity index. High crystallinity index indicated that the intact structure resulted in a porous and amorphous [21].

Recently, ulin wood materials have been introduced as building construction, bridge construction, and shipping or almost for the architecture field. Ulin wood and gelam wood in view decade decreased due to over-exploitation and this matter is causing some environmental problems. Therefore, briquetting technology is one of the promising technology to overcome this problem. To handling characteristics of feedstock and enhancing the volumetric calorific value of biomass, the densification process is a solution [22]. To make ulin wood and gelam wood treatment energetically efficient, not only the densification process is needed but also carbonization of the biomass before briquette production is another method to enhancing the properties of briquette such as removal volatile materials from the feedstock.

Because the different characteristics of the materials (ulin wood and gelam wood) in the context of volatile materials, studies into the combustion behavior of briquette fuels mixed ulin wood and gelam wood would be interest. Studies concerning the physical and combustion properties of agriculture residue bio-briquette were reported earlier [23]. However, to the best of author knowledge, no report into the effect of

compaction pressure and briquette mixed composition on the combustion behavior as well as combustion rate of forest residue (ulin wood and gelam wood) mixture have been published. Thus, we here aim to investigate the effect of compaction pressure and briquette mixed composition on the combustion behavior as well as combustion rate of fuel-briquettes made from ulin wood and gelam wood residues (a typical wood in South Kalimantan, Indonesia). This information must be important for the bioenergy sector to improve economic aspects and alternative uses for these natural materials.

2. MATERIALS AND METHODS

2.1. Preparation of raw materials The feedstock (ulin wood and gelam wood) used in this work was obtained from milling sites in Borneo, Southern Kalimantan. The whole feedstock was manually drying (sun dried) until achieving the lower moisture content (< 15 % dry basis). The characteristic of raw materials was obtained in our research group [19,20] as given in Table 1.

2.2. Carbonization and Preparation of Mixtures

The dried feedstock obtained was carbonized in the furnace at 500°C. The three factors considered are compaction pressure (10, 12, and 15 MPa), mixing ratio (0:100, 70:30, 50:50, 30:70, and 100:0). The particle was fixed of 50 µm. Binder concentration fixed of 20% (cassava starch) was the usual proportions for briquette production [26]. The cassava starch binder was prepared by mixing with the water and boiling them to obtain the good binder. 20% of the binder was mixed for each mixing ratio and was prepared for the compaction process.

2.3. Briquette Production

The compaction pressure of the briquette and mixing ratio were investigated. A manual hand briquetting press machine was used to compress the biomass in this study. The machine equipped with the cylinder briquetting die (id: 40 mm and length: 50 mm). The compaction pressure machine using the hydraulic press machine used in this study shown in Figure 1. To produced briquette, at first, the powdered raw materials mixed with the binder were placed in the die and pressed with the plunger by

TABEL 1. Characteristics of the raw materials

Raw Materials	Proximate analysis [wt%]			Ultimate analysis [wt%]			
	FC	VM	Ash	C	H	N	O
Ulin wood	22.8	74.3	2.8	49.2	5.6	0.3	44.7
Gelam wood	76.4	13.6	3.1	81.3	1.9	0.4	15.4



Figure 1. The compaction pressure machine using the hydraulic press machine

applying the pressure of 10, 12, and 15 MPa to get the briquettes at the desired shape. The holding time of each briquette was 100 s and the sample was produced in duplicate. Mass and weight were taken using a digital weighing immediately. Then sun-dried for 2-3 days to remove the moisture content and keep at room temperature.

3. ANALITICAL METHODS

3. 1. Moisture Content, Volatile Matter, and Ash Content

The calculation of moisture content, ash content and volatile matter in this study was conducted. The moisture content of the sample briquette is as follows:

$$MC(\text{wt}\%) = \frac{W_i - W_f}{W_i} \times 100\% \quad (1)$$

where W_i is the initial weight of the sample and W_f is the final weight of the sample after drying. The volatile matter (VM) for each sample was calculated based on the weight of the sample after drying in an oven and heated in the furnace, as indicated in Equation (2):

$$VM(\text{wt}\%) = \frac{W_{od} - W_{fd}}{W_{od}} \times 100\% \quad (2)$$

where W_{od} is the weight of the oven-dried sample and W_{fd} is the weight of the furnace-dried sample.

The ash content was calculated based on the procedure given in ASTM-D-317. The ash content (AC) determination method semblable with volatile matter (VM). However, the heating temperature was 550 °C for 5h and weight after cooling. The AC was determined using Equation (3) state as follows:

$$AC(\text{wt}\%) = \frac{SW_{(od)} - SW_{(fd)}}{SW_{(od)}} \times 100\% \quad (3)$$

where $SW_{(od)}$ is sample weight after drying in the oven and $SW_{(fd)}$ is sample weight after heated in the furnace and cooling in the desiccator.

3. 2. Bulk Density The density of the briquette was calculated after the pressing process was done. The density of the briquette initially as the ratio of mass to the volume of the briquette. This method agreed well with the previous study [27]. The bulk density was determined as:

$$\rho \left(g / cm^3 \right) = \frac{M}{V} \quad (4)$$

where ρ is the density of the briquette sample, the mass of the briquette sample (M), and volume of the briquette sample (V). the mass of briquette sample was weighed by using a digital weighing balance (KI-124-precision digital scale).

3. 3. Combustion Rate The combustion rate basically indicates the burning capability of the briquette. One of the briquette samples was weight before combustion, then the briquette sample was ignited and burned. The combustion time and the briquette sample weight were collected to determine the combustion ratio (Equation (5)).

$$\text{Combustion rate} (g / \text{min}) = \frac{W_{bb}}{\text{Combustion time}} \quad (5)$$

where W_{bb} is the weight of burned briquette sample (g) and combustion time (min).

4. RESULTS AND DISCUSSION

4. 1. Moisture Content, Ash Content, and Volatile Matter

Figures 2(a), 2(b), and 2(c) show the moisture content, ash content, and volatile matter of the briquette samples. The moisture content was decreased with higher compaction pressure. The briquette made from 0:100 mixing ratio of the ulin wood to gelam wood, 15 MPa compaction pressure exhibited the lower moisture content and higher moisture content of 3.0 (wt%) was observed for the briquette made from 100:0 (ulin wood and gelam wood) under compaction pressure of 10 MPa, it might be the hygroscopic character with the high porosity of the carbonized ulin wood and gelam wood materials. The results obtained good agreement with Mandra [28], who obtained the higher moisture content (6 - 8%) on high compacting pressure in case of the charcoal briquette from agricultural waste. Generally, low moisture content indicated high calorific value, and high moisture content represents the high energy consumption.

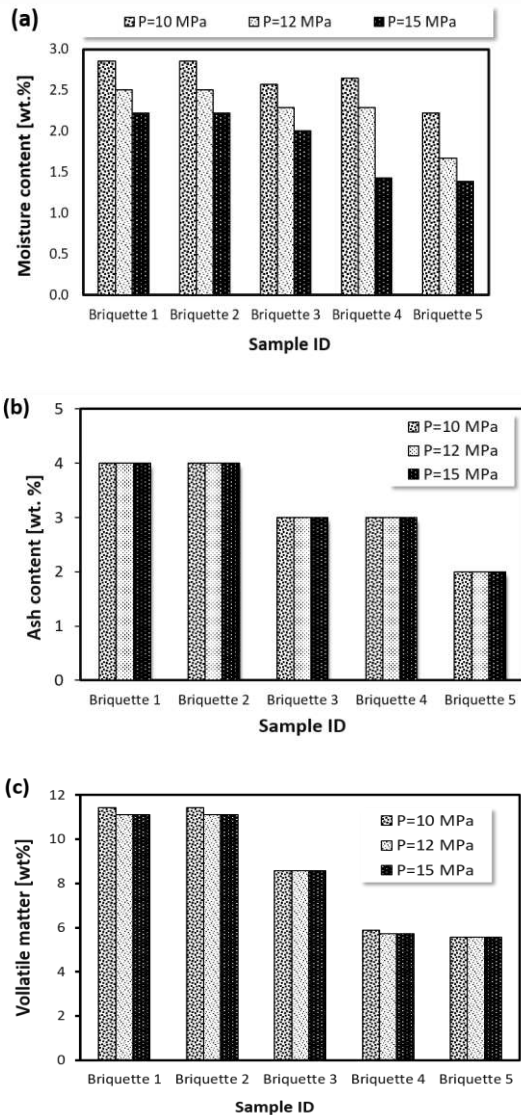


Figure 2. Effect of compaction pressure and mixing ratios on (a) moisture content, (b) ash content, and (c) volatile matter

From Figure 2, it is shown that the ash content, moisture content, and volatile matter were decreased with compaction pressure. It might be the high density of the briquette sample and some binder effect causes a reduction in ash, moisture content, and volatile matter. This result agrees well with a previous study [29] where ash content, moisture content, and volatile matter decreased when the resin was added into the briquettes.

4. 2. The Bulk Density of the Briquette Samples and it Comparison

The density of the briquette samples in this study ranged from 600-880 kg/m³ depending on the compaction pressure and mixing ratio of the briquettes. Figure 3(a) showed the density of the

briquette sample at different compaction die pressure. The same trend was observed for all briquette samples. Briquette density increased considerably as the compaction pressure. The value obtained was higher than the previous study, the comparison studies were demonstrated in Figure 3(b) in case of briquette made from corn stover [30], soda weed, and sawdust [31]. In case of corn stover the bulk density was obtained around 700 kg/m³, soda weed mixed sawdust was exceeded 700 kg/m³. The observations also consistent with the previous work conducted by Gong et al. [32] who observed that the briquette density decreased as moisture content increased in case of briquette made from mixture corn stover and peanut shells.

Adapa et al. [33] reported that the compact density could possibly be attributed to the moisture content for all raw materials (barley, canola, oat, and wheat straw). In contrast, Widyan et al. [34] showed that the briquette density increased with the moisture content for olive cake. Therefore, an optimal moisture content exists for each feedstock to produce briquettes with high density and strength. This study obtained that ulin wood and gelam wood mixed can be compacted into high-density briquettes (600-880 kg/m³) at a low moisture content range of 2-3%. The maximum density exceeded 880

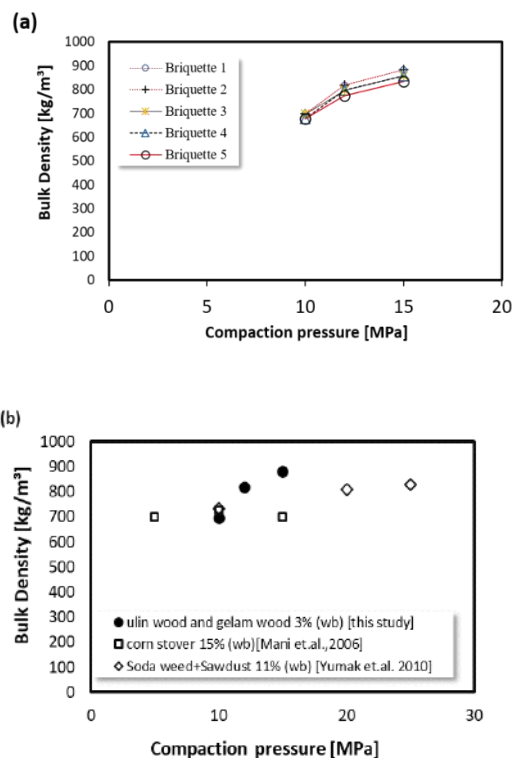


Figure 3. (a) Bulk density of the briquette sample in the different compaction die pressure (b) Bulk density comparison with other studies

kg/m³. These results agreed with previous study [35], who obtained the strong and crack-free briquette made from corn stover with lower moisture content.

4. 3. Determination of Combustion Behavior

In this study combustion characteristics (ash content, moisture content, and volatile matter), ignition time, and combustion rate were analyzed. Figure 4 present the combustion rate for all the briquettes sample with different mixing ratio and compaction pressure. The combustion rate of the briquette was in the range of 2-3 g/min. This result was agreed well with the previous results by Thabout et al. [36] who obtained 2-3 g/min of burning rate for the briquettes made from corn cob mixed with palm fiber. The results showed the combustion rate decreased with the increase of compaction pressure of the briquettes sample. This might be the increase of density for the higher compaction pressure briquette reduces the air within the product, this low porosity will restrict the mass and heat transfer during combustion. The same relationship was also reported by Pandey et al. [37] for pine needle briquettes and Chuangcharoen [38] for agriculture waste briquettes. They mentioned that different combustion rate has been caused by the distinct fixed carbon in the feedstock, briquette can be burn easily and quickly at lower fixed carbon and led to increasing the combustion rate.

The percentage of the initial mass per minute for the combustion rate can be expressed as the Normalized Burning Rate (NBR) as shown in Figure 5.

As shown in Figure 5, the steady-state flaming combustion phase or referred to as Normalized Burning Rate (NBR) expressed in percent of initial mass per minute. The briquette can sustain expressed by ignition phase. The combustion rate of the briquettes are associated with their morphological characteristics. The combustion temperature profile in the burning zone of the briquette are shown in Figures 6(a), 6(b), and 6(c). In

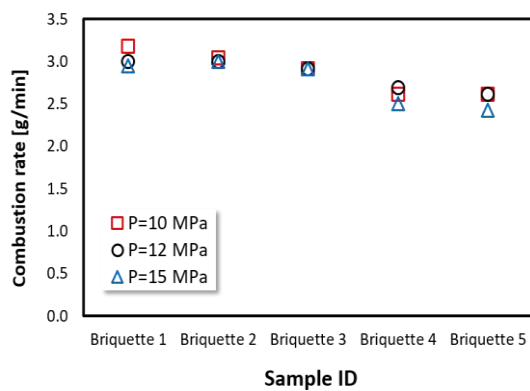


Figure 4. Combustion rate for all the briquettes sample with different mixing ratio and compaction pressure

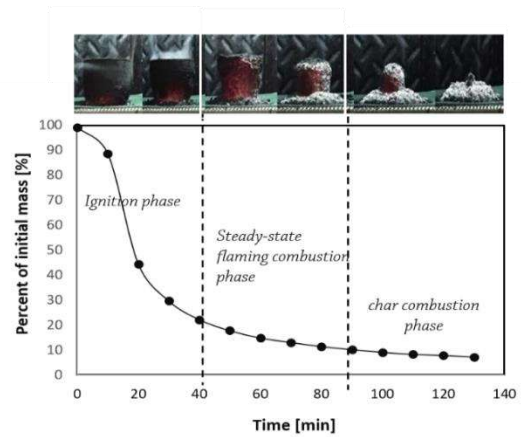


Figure 5. Normalized burning rate (NBR)

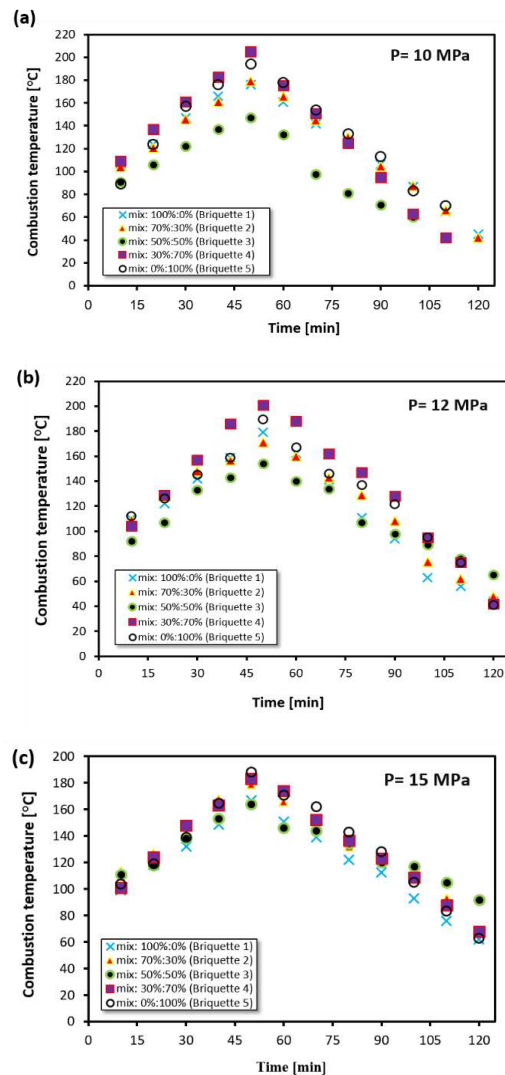


Figure 6. Combustion temperature profile at the different compaction pressure of (a) 10 MPa, (b) 12 MPa, and (c) 15 MPa

all curves of T (°C) versus t (min), typical temperatures and various of compaction pressure and mixing ratio of briquette were measured. All figures show the same trend which is some losses of mass appeared near 45°C, corresponding to the release of the moisture content and the rapid losses of mass reaching 10%/min.

5. CONCLUSION

We herein investigated and confirmed the effect varying compaction pressure and mixing ratios on the combustion behavior as well as the combustion rate of fuel-briquettes made from ulin wood and gelam wood respectively. Our results show the following:

1. The operating parameters (compaction pressure and mixing ratio) slightly affected the Ash content, MC, and VM.
2. Bulk density of all briquette samples increased with an increase in compaction pressure of up to 10 MPa.
3. Highest bulk density (880 kg/m³) can be obtained from the blend of carbonized ulin wood and gelam wood (70:30) mixing ratio and the lowest from briquette with the mixing ratio of 0:100 (exceeded 600 kg/m³).
4. The combustion rate decreased with an increase in compaction pressure. The slowest combustion rate obtained of 2.43 g/min briquette made from 0:100 of ulin wood and gelam wood and 15 MPa.

6. ACKNOWLEDGEMENT

The present study was supported by Department of Mechanical Engineering, Lambung Mangkurat University, South Kalimantan, Indonesia.

7. REFERENCES

1. T. Fungenzi, "Biomass as an opportunity to solve Indonesia's energy challenge" *Modul-Principles of Sustainability*, (2015).
2. A. Amrullah and Y. Matsumura, "Supercritical water gasification of sewage sludge in continuous reactor," *Bioresour. Technol.*, Vol. 249, (2017), 276-283, doi.org/10.1016/j.biortech.2017.10.002.
3. N. Kpai, I. Tankoano, M. Sawadogo, S. T. Tanoh, and S. Sidib, "Cleaner production in Burkina Faso: Case study of fuel briquettes made from cashew industry waste," *Journal of Cleaner Production*, Vol. 195, (2018), 1047-1056, doi.org/10.1016/j.jclepro.2018.05.261.
4. A. Gendek, M. Aniszewska, J. Mala, and J. Velebil, "Biomass and Bioenergy Evaluation of selected physical and mechanical properties of briquettes produced from cones of three coniferous tree species," *Biomass and Bioenergy*, Vol. 117, (2018), 173-179, doi.org/10.1016/j.biombioe.2018.07.025.
5. S. Mavaddati, "Rice classification and quality detection based on sparse coding technique," *International Journal of Engineering, Transactions B: Applications*, Vol. 31, No. 11, (2018), 1910-1917, doi: 10.5829/ije.2018.31.11b.15.
6. A. Azizifard, J. Arkat, and H. Farughi, "Sustainable surface water management and wastewater treatment plant location: A case study of Urmia lake," *International Journal of Engineering, Transactions A Basics*, Vol. 33, No. 4, (2020), 621-630, doi: 10.5829/ije.2020.33.04a.13.
7. M. Lubwama and V. A. Yiga, "Characteristics of briquettes developed from rice and coffee husks for domestic cooking applications in Uganda," *Renewable Energy*, Vol. 118, (2018), 43-55, DOI: 10.1016/j.renene.2017.11.003.
8. Y. Qiu, Z. Zheng, Z. Zhou, and G. D. Sheng, "Bioresource Technology Effectiveness and mechanisms of dye adsorption on a straw-based biochar," *Bioresour. Technol.*, Vol. 100, No. 21, (2009), 5348-5351, doi.org/10.1016/j.biortech.2009.05.054.
9. M. Abbasi, M. Sharafi Miyab, B. Tousi, and G. B. Gharehpetian, "Using dynamic thermal rating and energy storage systems technologies simultaneously for optimal integration and utilization of renewable energy sources," *International Journal of Engineering, Transactions A: Basics*, Vol. 33, No. 1, (2020), 92-104, doi: 10.5829/ije.2020.33.01a.11.
10. Du, Z., Li, Y., Wang, X., Wan, Y., Chen, Q., Wang, C., Lin, X., Liu, Y., Chen, P. and Ruan, R., "Microwave-assisted pyrolysis of microalgae for biofuel production," *Bioresour. Technol.*, Vol. 102, No. 7, (2011), 4890-4896, doi.org/10.1016/j.biortech.2011.01.055.
11. Monedero, E., Lapuerta, M., Pazo, A., Díaz-Robles, L.A., Pino-Cortés, E., Campos, V., Vallejo, F., Cubillos, F. and Gómez, J., "Effect of hydrothermal carbonization on the properties, devolatilization, and combustion kinetics of Chilean biomass residues," *Biomass and Bioenergy*, Vol. 130, (2019), 105387, doi.org/10.1016/j.biombioe.2019.105387.
12. Sun, J., Shen, Z., Zhang, Y., Zhang, Q., Lei, Y., Huang, Y., Niu, X., Xu, H., Cao, J., Ho, S.S.H. and Li, X., "Characterization of PM2.5 source profiles from typical biomass burning of maize straw, wheat straw, wood branch, and their processed products," *Atmospheric Environment*, Vol. 205, (2019), 36-45, doi.org/10.1016/j.atmosenv.2019.02.038.
13. A. Amaya, N. Medero, N. Tancredi, H. Silva, and C. Deiana, "Activated carbon briquettes from biomass materials," *Bioresour. Technol.*, Vol. 98, (2007), 1635-1641, doi.org/10.1016/j.biortech.2006.05.049.
14. Martínez, C.L.M., Sermiyagina, E., Carneiro, A.D.C.O., Vakkilainen, E. and Cardoso, M., "Production and characterization of coffee-pine wood residue briquettes as an alternative fuel for local firing systems in Brazil," *Biomass and Bioenergy*, Vol. 123, (2019), 70-77, DOI: 10.1016/j.biombioe.2019.02.013.
15. E. F. Aransiola, T. F. Oyewusi, J. A. Osunbitan, and L. A. O. Ogunjimi, "Effect of binder type, binder concentration and compacting pressure on some physical properties of carbonized corn cob briquette," *Energy Reports*, Vol. 5, (2019), 909-918, doi.org/10.1016/j.egy.2019.07.011.
16. R. I. Muazu and J. A. Stegemann, "Effects of operating variables on durability of fuel briquettes from rice husks and corn cobs," *Fuel Process Technology*, Vol. 133, (2015), 137-145, DOI: 10.1016/j.fuproc.2015.01.022.
17. S. V. Vassilev, D. Baxter, L. K. Andersen, and C. G. Vassileva, "An overview of the chemical composition of biomass," *Fuel*, Vol. 89, No. 5, (2010), 913-933, doi.org/10.1016/j.fuel.2009.10.022.
18. R. E. Williams, M. H. Gagen, R. P. D. Walsh, and K. Bidin, "On the development of a drill-borer for sampling tropical suprahardwoods: An example using the Borneo Ironwood *Eusideroxylon zwageri*," *Dendrochronologia*, Vol. 35, (2015), 99-104, DOI: 10.1016/j.dendro.2015.07.004.
19. J. S. Tumuluru, C. T. Wright, J. R. Hess, K. L. Kenney, and I. National, "A review of biomass densification systems to develop

- uniform feedstock commodities for bioenergy application,” *Biofuels Bioproducts & Biorefining*, (2011), 683-707, doi.org/10.1002/bbb.324.
20. H. Harahap, R. Nawansyah, and H. Nasution, “Isolation and Characterization of Nanocrystal from Corn cob Waste Using H₂SO₄ Hydrolysis Method,” *International Journal of Engineering, Transactions A: Basics* Vol. 31, No. 4, (2018), 533-537, doi: 10.5829/ije.2018.31.04a.03.
 21. L. Shao, H. Chen, Y. Li, J. Li, G. Chen, and G. Wang, “Pretreatment of corn stover via sodium hydroxide-urea solutions to improve the glucose yield,” *Bioresour Technol*, Vol. 307, (2020), 123191, DOI: 10.17485/ijst/2018/v11i23/123632.
 22. A. Journal, A. Sciences, and S. Publications, “Physical Characteristics of Maize Cob Briquette under Moderate Die Pressure,” *American Journal of Applied Sciences*, Vol. 4, No. 12, (2007), 995-998, DOI: 10.3844/ajassp.2007.995.998.
 23. M. Lubwama, V. Andrew, F. Muhairwe, and J. Kihedu, “Physical and combustion properties of agricultural residue bio-char bio-composite briquettes as sustainable domestic energy sources,” *Renewable Energy*, Vol. 148, (2020), 1002-1016, doi.org/10.1016/j.renene.2019.10.085.
 24. A. M. Widiyannita, R. B. Cahyono, and A. Budiman, “Study of pyrolysis of ulin wood residues Study of Pyrolysis of Ulin Wood Residues,” IAP Conference Proceeding, Vol.1755, 050004, (2017), 2016, doi.org/10.1063/1.4958487.
 25. Y. Xiao, Dong, H., Long, C., Zheng, M., Lei, B., Zhang, H. and Liu, Y., “Melaleuca bark based porous carbons for hydrogen storage,” *International Journal of Hydrogen Energy*, Vol. 39, No. 22, (2014), 11661-11667, doi.org/10.1016/j.ijhydene.2014.05.134.
 26. M. Lubwama and V. A. Yiga, “Development of groundnut shells and bagasse briquettes as sustainable fuel sources for domestic cooking applications in Uganda,” *Renewabl Energy*, Vol. 111, (2017), 532-542, DOI: 10.1016/j.renene.2017.04.041.
 27. F. Rabier, Temmerman, M., Böhm, T., Hartmann, H., Jensen, P.D., Rathbauer, J., Carrasco, J. and Fernández, M., “Particle density determination of pellets and briquettes,” *Biomass and Bioenergy*, Vol. 30, No. 11, (2006) 954-963, DOI: 10.1016/j.biombioe.2006.06.006.
 28. M. A. S. Mandra, “Characteristics of Charcoal Briquettes from Agricultural Waste with Compaction Pressure and Particle Size Variation as Alternative Fuel,” *International Energy Journal*, Vol. 19, (2019), 139-148.
 29. J. A. Kumar, K. V. Kumar, M. Petchimuthu, S. Iyahrja, and D. V. Kumar, “Comparative analysis of briquettes obtained from biomass and charcoal,” *Materials Today: Proceedings*, (2020), DOI: 10.1016/j.matpr.2020.02.918.
 30. S. Mani, L. G. Tabil, and S. Sokhansanj, “Specific energy requirement for compacting corn stover,” *Bioresour Technol* Vol. 97, (2006), 1420-1426, doi.org/10.1016/j.biortech.2005.06.019.
 31. H. Yumak, T. Ucar, and N. Seyidbekiroglu, “Briquetting soda weed (*Salsola tragus*) to be used as a rural fuel source,” *Biomass and Bioenergy*, Vol. 34, No. 5, (2010), 630-636, doi.org/10.1016/j.biombioe.2010.01.006.
 32. C. Characteristics, E. Requirement, and P. Shells, “Compression Characteristics and Energy Requirement of Briquettes Made from a Mixture of Corn Stover and Peanut Shells,” *BioResources*, Vol. 10, No. 3, (2015), 5515-5531, DOI: 10.15376/BIORES.10.3.5515-5531
 33. P. Adapa, L. Tabil, and G. Schoenau, “Compaction characteristics of barley, canola, oat and wheat straw,” *Biosystems Engineering*, Vol. 104, No. 3, (2009), 335-344, DOI: 10.1016/j.biosystemseng.2009.06.022.,
 34. M. I. Al-widyan, M. Abu-zreig, and N. H. Abu-hamdeh, “Physical durability and stability of olive cake briquettes,” *Canadian Biosystem Engineering*, Vol. 44, (2002), 3-41.
 35. P. D. Grover and S. K. Mishra, “Regional Wood Energy Development Programme In Asia Gcp / Ras / 154 / Net Biomass Briquetting : Technology and Practices,” Food and Agriculture Organization of the United Nations Bangkok, April 1996.
 36. M. Thabuot, T. Pagketanang, and K. Panyacharoen, “Effect of Applied Pressure and Binder Proportion on the Fuel Properties of Holey Bio-Briquettes”, *Energy Procedia*, Vol. 79, (2015), 890-895, doi.org/10.1016/j.egypro.2015.11.583.
 37. S. Pandey and R. P. Dhakal, “Pine Needle Briquettes : A Renewable Source of Energy,” *Environmental Science*, Vol. 3, No. 3, (2013), 254-260.
 38. T. Chungcharoen and N. Srisang, “Preparation and characterization of fuel briquettes made from dual agricultural waste : Cashew nut shells and areca nuts,” *Journal of Cleaner Production*, Vol. 256, (2020), 120434, doi.org/10.1016/j.jclepro.2020.120434.

Persian Abstract

چکیده

در این کار سوخت جامد حاصل از قالبگیری چوب اولین و باقی مانده چوب گلام مورد بررسی قرار گرفت. تأثیر فشار تراکم (۱۰، ۱۲ و ۱۵ مگاپاسکال) و فرمولاسیون بریکت مورد بررسی قرار گرفت. IW و GW به ترتیب در نسبتهای ۱:۱۰، ۰:۳۰، ۵۰:۵۰، ۷۰:۳۰ و ۱۰۰:۰ با هم مخلوط شدند. اندازه ذرات ۵۰ میکرومتر ثابت شد. IW و GW در دمای ثابت (۵۰۰ درجه سانتیگراد) و زمان (۱۲۰ دقیقه) کربن دار شدند. چسب ژلاتینیزه شده (نشاسته کاساوا) ۲۰٪ از کل وزن قالبها بود. تراکم با استفاده از مقیاس آزمایشگاهی دستگاه بریکتینگ (نوع پیستون - پرس) انجام شد. بریکت فشار تراکم بر برخی خصوصیات بریکت (میزان خاکستر، رطوبت، ماده فرار، چگالی فله و میزان احتراق) تأثیر معنی داری داشت. افزایش بریکتهای فشار تراکم منجر به پایین آمدن خاکستر، میزان رطوبت و مواد فرار شد اما برعکس آن برای چگالی فله است. با این حال، نسبت اختلاط کمی تحت تأثیر قرار گرفته است. سرعت احتراق بالاتر (۳/۱۸ گرم در دقیقه) در فشار تراکم کمتر (۱۰ مگاپاسکال) حاصل شد.



A Generalization for Model Reference Adaptive Control and Robust Model Reference Adaptive Control Adaptive Laws for a Class of Nonlinear Uncertain Systems with Application to Control of Wing Rock Phenomenon

J. Roshanian, E. Rahimzadeh*

Department of Aerospace Engineering, K.N. Toosi University of Technology, Tehran, Iran

PAPER INFO

Paper history:

Received 16 June 2020

Received in revised form 30 June 2020

Accepted 03 August 2020

Keywords:

Lyapunov's Direct Method

Model Reference Adaptive Control

Robust Model Reference Adaptive Control

General Adaptive Laws

Strictly Increasing Function

Wing Rock

ABSTRACT

Lyapunov's direct method is a primary tool for designing Model Reference Adaptive Control (MRAC) and robust MRAC schemes. In general, Lyapunov function candidates contain two categories of quadratic terms. The first category includes the system tracking error quadratic terms or, in some cases, consist of the system state quadratic terms. The second consists of the parameter estimation error quadratic terms. To design MRAC and Robust MRAC systems, researchers have used a limited variety for choosing quadratic terms. In this study, we consider a general form for the tracking error quadratic terms. We consider a strictly increasing function that belongs to the class of c^1 , which is a function of state tracking error quadratic terms. It yields a general structure for stable adaptive laws for updating controller parameters. For the MRAC scheme, the global asymptotic stability of the closed-loop system and stability and uniform bounded tracking of robust MRAC schemes are guaranteed. To evaluate the performance of the designed controllers, we consider the single DOF wing rock dynamics.

doi: 10.5829/ije.2020.33.11b.28

1. INTRODUCTION

Many combat aircraft may have to fly at a high angle of attack to obtain air superiority. In this situation, the flight occurs outside of the flight envelope in the nonlinear regime. In this situation, airflow separation may occur. In this situation, the boundary layer's speed relative to the wing is reduced to zero because the boundary layer moves against an adverse pressure gradient. When the aircraft moves through the air, cause the fluid flow to separate from the wing, and vortices are produced. The Wing Rock phenomenon is one of the undesirable motions which appears as limit cycle oscillations in the aircraft roll angle, leading to lateral directional instability and putting the flight in danger. Several experiments and investigations performed on a highly slender forebody and a highly swept delta wing. These studies confirmed that the interaction between the forebody and the wing vortices are the main cause of the wing rock motion [1-

10]. The exact analytical expression of the rolling moment coefficient is difficult to derive. Therefore, some researchers proposed several approximate models. A nonlinear aerodynamic model is proposed by Hsu and Lan [11] to drive the limit cycle amplitude and frequency of wing rock motion. based on the numerical simulation of the wing rock motion, an analytic expression for the roll moment coefficient is proposed by Nayfeh et al. [12]. The result was used to describe the phase plane analysis of the nonlinear motion, includes determining the type of equilibrium points and calculating domains of initial conditions that lead to oscillatory motion or divergence. A modified version of the wing rock model proposed by Hsu and Lan [11] is developed by Elzebeda et al. [13]. The numerical values of the coefficients, in the roll moment coefficient, are obtained by the curve fitting method. Data are collected from simulation results. The dynamical equations of motion of wing rock for aircraft,

*Corresponding Author Institutional Email: e.rahimzadeh@kntu.ac.ir
(E. Rahimzadeh)

which have single, two, and three rotational degrees of freedom, are proposed by Go [14].

The control of the wing rock is a significant research area and a series of studies based on the control methods presented in what follows. A neural-network identification based control (NNIAC) scheme using the L2 tracking technique is developed to reduce the effect of the approximation error on the tracking performance [15]. The proposed controller is applied to control a wing rock limit cycle to show its effectiveness. It has been reported in literature [16], a new reinforcement adaptive fuzzy control system for tracking control a wing rock motion in the presence of the uncertainty and unknown Elzebda is proposed. A fuzzy approximator is applied to identify the unknown nonlinear function. The reinforcement adaptive law derived from the Lyapunov stability theory. The proposed algorithm showed high tracking performance and robustness in the presence of uncertainty [17]. A simplified interval fuzzy sliding control scheme is proposed for suppressing and tracking the desired trajectories. The simulation results showed that the proposed algorithm could make the wing rock system reach the desired state without overshoots. A supervisory recurrent fuzzy neural network control (SRFNCC) system is proposed for the wing rock control system [18]. An adaptive feedback linearizing controller with the backstepping approach for the wing rock control is proposed in literature [19]. A new control law based on the variable structure model reference adaptive control is presented [20]. The wing rock problem with unstructured nonlinearity and disturbance input is considered. Simulation results showed good transient performance and disturbance rejection capability of the proposed controller.

The Lyapunov stability method, also known as the Lyapunov's direct method, is widely used in the design of adaptive algorithms for updating controller parameters or designing adaptive observers. An SM rotor flux observer has been developed to estimate rotor speed [21]. The stability of this observer is guaranteed by the Lyapunov's stability method. A new method for designing adaptive fuzzy dynamic sliding mode control for the nonlinear system is applied [22]. The process of deriving adaptive switching gain is performed by Lyapunov's direct method. A new adaptive control for direct-drive robot manipulators driven by PMSM in tracking application has been developed [23]. The control method has verified by the Lyapunov stability method. A robust adaptive controller is implemented to control a spacecraft simulator [24]. The proposed controller is designed based on nonlinear dynamics to overcome of model uncertainty. The stability of the robust adaptive controller is verified through Lyapunov's theorem. An observer-based robust controller with an adaptive mechanism designed by Lyapunov's method is proposed to control a robotic system [25]. A fuzzy adaptive sliding mode

controller was derived for a class of multi-agent systems [26]. The stability of the closed-loop system is verified by Lyapunov's method. Quadratic Lyapunov functions are widely applied in the analysis of linear and nonlinear systems and the design of adaptive systems. One of the methods of designing adaptive systems is based on Lyapunov's stability method, which is widely used in designing stable MRAC systems. By using a new non-quadratic Lyapunov function (NQLF), new adaptive Laws for the MRAC scheme presented in literature [27]. The author used e^4 instead of e^2 signal for the tracking error, in the Lyapunov function and the new stable adaptive laws which contain e^3 signal derived. By using the same Lyapunov function, new adaptive law which uses the cube of the same error signal for robust adaptive scheme, dead zone modification, is presented [28]. A control scheme for the robust adaptive tracking based on MRAC via a switching non-quadratic Lyapunov function is proposed [29]. In this study, we intend to design the MRAC and Robust MRAC controller by considering a general form for the Lyapunov function candidate. In section (2), we introduce the mathematical model of the wing rock proposed in literature [13]. In the section (3) we design MRAC with Matched parameter uncertainty with a general Lyapunov function candidate, In the section (4) we design MRAC modifications known as sigma modification and e-modification with the Lyapunov function introduced in section (3) and in the section (5) some simulations have done to evaluate the performance of the MRAC and Robust MRAC designed in the previous sections.

2. WING ROCK DYNAMICS AND PHASE PLANE ANALYSIS

The wing rock phenomenon happens in the six DOF space, but the dominant feature of this motion can be demonstrated by a one DOF oscillation along the longitudinal axis of aircraft. The mathematical models of the wing rock presented in the literature were obtained by the least-square fitting method in the data of the wind tunnel test. In this section, we introduce the one DOF roll moment coefficient, the modified Hsu and Lan model, studied by Elzebda et al. [13]:

$$C_L(\phi(t), \dot{\phi}(t)) = a_1\phi(t) + a_2\dot{\phi}(t) + a_3|\phi(t)|\dot{\phi}(t) + a_4|\dot{\phi}(t)|\dot{\phi}(t) + a_5\phi^3(t) \quad (1)$$

In Equation (1), $\phi(t)$ is the roll angle, $\dot{\phi}(t)$ is the roll rate, and a_i are the roll moment coefficients obtained by fitting this expression to the numerical simulation gathered from wind tunnel test using the least square criteria. The following equation of motion is considered in literature [12-13]:

$$\ddot{\phi}(t) = \frac{\rho U_\infty^2 S b}{2I_{xx}} C_L(\phi(t), \dot{\phi}(t)) + D\dot{\phi}(t) \quad (2)$$

In Equation (2), ρ is the air density, S is the plan form area, U_∞ is the freestream speed, b is the chord, and I_{xx} is the wing mass moment of inertia around the midspan axis. The effect of bearing viscous damping presented by the last term. Let:

$$E = \frac{\rho U_\infty^2 S b}{2I_{xx}} \tag{3}$$

Substituting Equation (2) into Equation (1) yields:

$$\ddot{\phi}(t) = Ea_1\phi(t) + (Ea_2 + D)\dot{\phi}(t) + Ea_3|\phi(t)|\dot{\phi}(t) + Ea_4|\dot{\phi}(t)|\dot{\phi}(t) + Ea_5\phi^3(t) \tag{4}$$

The values of E and the viscous damping coefficient, D is considered as [13]:

$$E = 0.354 \tag{5}$$

$$D = 0.001 \tag{6}$$

The values of the roll moment coefficients a_i , in the Equation (1) for different angles of attack are presented in Table 1.

Considering the initial condition $\phi(0) = 1$ (deg), $\dot{\phi}(0) = 0$ ($\frac{\text{deg}}{\text{sec}}$), and Angle of attack $\alpha = 22.5$ deg the uncontrolled motion of the wing rock phenomenon is presented in the Figures 1 to 4.

According to Figures 1 to 4, it is clear that although the initial condition is small, the roll angle develops into the limit cycle, which means that a small disturbance is sufficient to cause the wing rock oscillation. The mathematical control model for a single DOF wing rock phenomenon is considered as follows:

TABLE 1. Coefficients of Equation (1) [13]

$\alpha(\text{deg})$	a_1	a_2	a_3	a_4	a_5
15	-0.010259	-0.02143	0.05711	-0.0619	-0.146
21.5	-0.04177	0.01461	-0.06732	0.0841	0.046
22.5	-0.04569	0.02351	-0.09944	0.0689	0.0531
25	-0.05256	0.04568	-0.1765	0.0269	0.0606

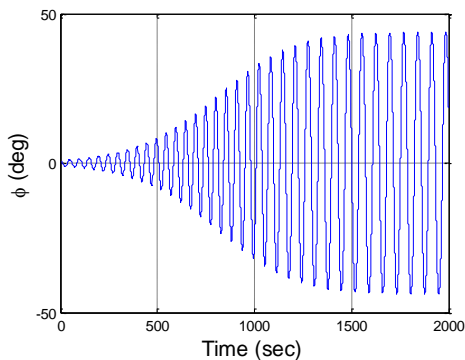


Figure 1. Roll Angle Limit Cycle build up $\alpha = 22.5$ deg

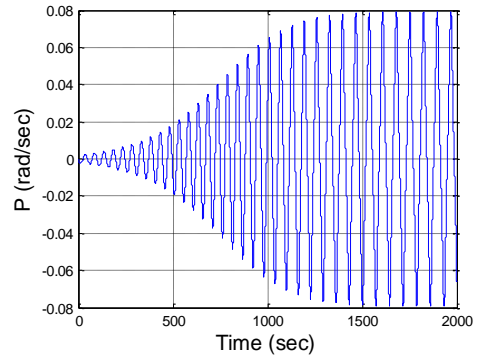


Figure 2. Roll Rate Limit Cycle build up $\alpha = 22.5$ deg

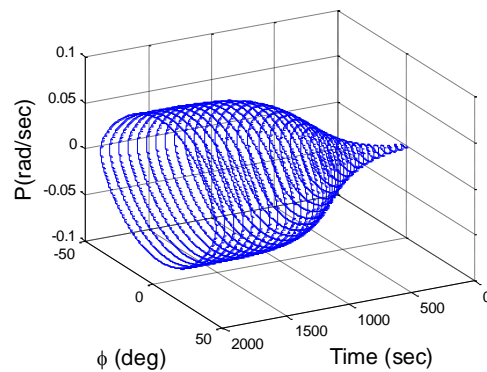


Figure 3. Wing Rock Limit Cycle $\alpha = 22.5$ deg

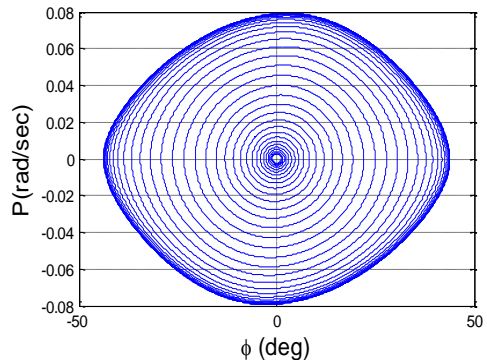


Figure 4. Wing Rock Phase Plane $\alpha = 22.5$ deg

$$\ddot{\phi} = EC_1 + D\dot{\phi} + d_0u \tag{7}$$

In Equation (7), d_0 is the control effectiveness, and u is the control signal. Let $x_1 = \phi$, $x_2 = \dot{\phi}$. The state-space representation of Equation (2) becomes:

$$\begin{aligned} \dot{x}_1 &= x_2 \\ \dot{x}_2 &= Ea_1x_1 + (Ea_2 + D)x_2 + Ea_3|x_1|x_2 + Ea_4|x_2|x_2 + Ea_5x_1^3 + d_0u \end{aligned} \tag{8}$$

Equation (8) can be written in the matrix form as follows:

$$\begin{bmatrix} \dot{x}_1(t) \\ \dot{x}_2(t) \end{bmatrix} = \begin{bmatrix} 0 & 1 \\ E a_1 & E a_2 + D \end{bmatrix} \begin{bmatrix} x_1(t) \\ x_2(t) \end{bmatrix} + \begin{bmatrix} 0 \\ 1 \end{bmatrix} d_0(u + \frac{E a_3}{d_0} |x_1| x_2 + \frac{E a_4}{d_0} |x_2| x_2 + \frac{E a_5}{d_0} x_1^3(t)) \quad (9)$$

3. MRAC DESIGN FOR MIMO SYSTEMS WITH MATCHED UNCERTAINTY

In this section, we design an MRAC controller with general stable adaptive laws for a class of nonlinear systems with parametric uncertainty. We consider a MIMO system in the form of Equation (10):

$$\dot{x}(t) = \mathbf{A}x(t) + \mathbf{B}\mathbf{A}(u(t) + \mathbf{M}(x(t))) \quad (10)$$

where in Equation (10), $x(t) \in \mathbf{R}^n$ is the system state vector, $\mathbf{A} \in \mathbf{R}^{n \times n}$ is supposed to be constant and unknown, $\mathbf{B} \in \mathbf{R}^{n \times m}$ is constant and known, $\mathbf{A} \in \mathbf{R}^{m \times m}$ is an unknown constant matrix, and it is supposed to be diagonal with strictly positive elements, $u(t) \in \mathbf{R}^m$ is the control input, we assume that the pair $(\mathbf{A}, \mathbf{B}\mathbf{A})$ is controllable. In general, $\mathbf{M}(x(t)): \mathbf{R}^n \rightarrow \mathbf{R}^m$ is an unknown vector function which its components are functions of $x(t)$, it is supposed that $\mathbf{M}(x(t))$ could be written in the form of Equation (11):

$$\mathbf{M}(x(t)) = \boldsymbol{\theta}^T(t)\boldsymbol{\mu}(x(t)) \quad (11)$$

In Equation (11), $\boldsymbol{\theta}(t) \in \mathbf{R}^{N \times m}$ is an unknown matrix with constant coefficients, and $\boldsymbol{\mu}(x(t)) \in \mathbf{R}^N$ is an N -dimensional regressor vector:

$$\boldsymbol{\mu}(x(t)) = (\boldsymbol{\mu}_1(x(t)), \boldsymbol{\mu}_2(x(t)), \boldsymbol{\mu}_3(x(t)), \dots, \boldsymbol{\mu}_N(x(t)))^T \quad (12)$$

Equation (11) represents the matched parametric uncertainty of the system. We consider the following reference model:

$$\dot{x}_m(t) = \mathbf{A}_m x_m(t) + \mathbf{B}_m r(t) \quad (13)$$

In Equation (13), \mathbf{A}_m is a model reference Hurwitz matrix, and $r(t)$ is a bounded reference command. We consider the following definition:

$$\tilde{x}(t) = x(t) - x_m(t) \quad (14)$$

Without having parametric uncertainty which means that \mathbf{A} and \mathbf{A} are known, we use the following ideal fixed gain control law:

$$u(t) = \mathbf{K}_x^T x(t) + \mathbf{K}_r^T r(t) - \boldsymbol{\theta}^T \boldsymbol{\mu}(x(t)) \quad (15)$$

Using Equations (15) and (10), yields:

$$\dot{x}(t) = \mathbf{A}x(t) + \mathbf{B}\mathbf{A}[\mathbf{K}_x^T x(t) + \mathbf{K}_r^T r(t)] = (\mathbf{A} + \mathbf{B}\mathbf{A}\mathbf{K}_x^T)x(t) + \mathbf{B}\mathbf{A}\mathbf{K}_r^T r(t) \quad (16)$$

Assumption: Given matrices \mathbf{A} and \mathbf{B} and an unknown matrix \mathbf{A} , there must exist unknown matrices \mathbf{K}_x and \mathbf{K}_r must satisfy Equation (17):

$$\mathbf{A}_m = \mathbf{A} + \mathbf{B}\mathbf{A}\mathbf{K}_x^T, \quad \mathbf{B}_m = \mathbf{B}\mathbf{A}\mathbf{K}_r^T \quad (17)$$

Now control input is chosen as follows:

$$u(t) = \hat{\mathbf{K}}_x^T(t)x(t) + \hat{\mathbf{K}}_r^T(t)r(t) - \hat{\boldsymbol{\theta}}^T(t)\boldsymbol{\mu}(x(t)) \quad (18)$$

Using Equations (18), (10), and (11) yields:

$$\dot{x}(t) = (\mathbf{A} + \mathbf{B}\mathbf{A}\hat{\mathbf{K}}_x^T(t))x(t) + \mathbf{B}\mathbf{A}(\hat{\mathbf{K}}_r^T(t)r(t) - (\hat{\boldsymbol{\theta}}(t) - \boldsymbol{\theta})^T \boldsymbol{\mu}(x(t))) \quad (19)$$

Subtracting Equation (13) from Equation (19), yields:

$$\dot{\tilde{x}} = (\mathbf{A} + \mathbf{B}\mathbf{A}\hat{\mathbf{K}}_x^T(t))\tilde{x}(t) + \mathbf{B}\mathbf{A}(\hat{\mathbf{K}}_r^T(t)r(t) - (\hat{\boldsymbol{\theta}}(t) - \boldsymbol{\theta})^T \boldsymbol{\mu}(x(t)) - \mathbf{A}_m x_m(t) - \mathbf{B}_m r(t)) \quad (20)$$

Using Equation (17), Equation (20) becomes:

$$\dot{\tilde{x}}(t) = \mathbf{A}_m \tilde{x}(t) + \mathbf{B}\mathbf{A}[(\hat{\mathbf{K}}_x(t) - \mathbf{K}_x)^T x(t) + (\hat{\mathbf{K}}_r(t) - \mathbf{K}_r)^T r(t) - (\hat{\boldsymbol{\theta}}(t) - \boldsymbol{\theta})^T \boldsymbol{\mu}(x(t))] \quad (21)$$

The parameter estimation errors are defined as follows:

$$\begin{cases} \tilde{\boldsymbol{\theta}}(t) = \hat{\boldsymbol{\theta}}(t) - \boldsymbol{\theta} \\ \tilde{\mathbf{K}}_x(t) = \hat{\mathbf{K}}_x(t) - \mathbf{K}_x \\ \tilde{\mathbf{K}}_r(t) = \hat{\mathbf{K}}_r(t) - \mathbf{K}_r \end{cases} \quad (22)$$

Substituting Equation (22) into Equation (21) yields the tracking error dynamics:

$$\dot{\tilde{x}}(t) = \mathbf{A}_m \tilde{x}(t) + \mathbf{B}\mathbf{A}[\tilde{\mathbf{K}}_x^T(t)x(t) + \tilde{\mathbf{K}}_r^T(t)r(t) - \tilde{\boldsymbol{\theta}}^T(t)\boldsymbol{\mu}(x(t))] \quad (23)$$

We consider a general quadratic Lyapunov function candidate in the form of Equation (24):

$$V = f(\tilde{x}^T(t)\mathbf{P}\tilde{x}(t)) + \text{tr}([\tilde{\mathbf{K}}_x^T(t)\Gamma_x^{-1}\tilde{\mathbf{K}}_x(t) + \tilde{\mathbf{K}}_r^T(t)\Gamma_r^{-1}\tilde{\mathbf{K}}_r(t) + \tilde{\boldsymbol{\theta}}^T(t)\Gamma_\theta^{-1}\tilde{\boldsymbol{\theta}}(t)]\Lambda) \quad (24)$$

In Equation (24), f is a scalar function, which is strictly increasing $f' > 0$ with $f(0)=0$, and it is supposed to be continuously differentiable ($f \in C^1$). Γ_x , Γ_r , and Γ_θ are symmetric positive definite matrices denote the rates of adaptation. \mathbf{P} is the symmetric positive definite matrix which is the unique solution of the algebraic Lyapunov equation with symmetric positive definite matrix \mathbf{Q} :

$$\mathbf{A}_m^T \mathbf{P} + \mathbf{P} \mathbf{A}_m = -\mathbf{Q} \quad (25)$$

The first time derivative of the Lyapunov function becomes:

$$\dot{V} = \frac{df(\tilde{x}^T(t)\mathbf{P}\tilde{x}(t))}{dt} + 2\text{tr}([\tilde{\mathbf{K}}_x^T(t)\Gamma_x^{-1}\dot{\tilde{\mathbf{K}}}_x(t) + \tilde{\mathbf{K}}_r^T(t)\Gamma_r^{-1}\dot{\tilde{\mathbf{K}}}_r(t) + \tilde{\boldsymbol{\theta}}^T(t)\Gamma_\theta^{-1}\dot{\tilde{\boldsymbol{\theta}}}(t)]\Lambda) \quad (26)$$

Using the chain rule for simplifying the time derivative yields:

$$\dot{V} = \frac{df(\tilde{x}^T(t)\mathbf{P}\tilde{x}(t))}{d(\tilde{x}^T(t)\mathbf{P}\tilde{x}(t))} \frac{d(\tilde{x}^T(t)\mathbf{P}\tilde{x}(t))}{dt} + 2\text{tr}([\tilde{\mathbf{K}}_x^T(t)\Gamma_x^{-1}\dot{\tilde{\mathbf{K}}}_x(t) + \tilde{\mathbf{K}}_r^T(t)\Gamma_r^{-1}\dot{\tilde{\mathbf{K}}}_r(t) + \tilde{\boldsymbol{\theta}}^T(t)\Gamma_\theta^{-1}\dot{\tilde{\boldsymbol{\theta}}}(t)]\Lambda) \quad (27)$$

The first term of Equation (27) can be written as follows:

$$\begin{aligned} \dot{V} = & (\dot{\tilde{\mathbf{x}}}^T(t)\mathbf{P}\tilde{\mathbf{x}}(t) + \tilde{\mathbf{x}}^T(t)\mathbf{P}\dot{\tilde{\mathbf{x}}}(t)) \frac{d(\tilde{\mathbf{x}}^T(t)\mathbf{P}\tilde{\mathbf{x}}(t))}{d(\tilde{\mathbf{x}}^T(t)\mathbf{P}\tilde{\mathbf{x}}(t))} + \\ & 2\text{tr}\left[\tilde{\mathbf{K}}_x^T(t)\Gamma_x^{-1}\dot{\tilde{\mathbf{K}}}_x(t) + \tilde{\mathbf{K}}_r^T(t)\Gamma_r^{-1}\dot{\tilde{\mathbf{K}}}_r(t) + \right. \\ & \left. \tilde{\boldsymbol{\theta}}^T(t)\Gamma_\theta^{-1}\dot{\tilde{\boldsymbol{\theta}}}(t)\right]\boldsymbol{\Lambda} \end{aligned} \quad (28)$$

Evaluating Equation (28) along the trajectory of the error dynamics Equation (23) yields:

$$\begin{aligned} \dot{V} = & -\left(\tilde{\mathbf{x}}^T(t)\mathbf{Q}\tilde{\mathbf{x}}(t)\right) \frac{d(\tilde{\mathbf{x}}^T(t)\mathbf{P}\tilde{\mathbf{x}}(t))}{d(\tilde{\mathbf{x}}^T(t)\mathbf{P}\tilde{\mathbf{x}}(t))} + \\ & 2\tilde{\mathbf{x}}^T(t)\mathbf{P}\mathbf{B}\boldsymbol{\Lambda}\tilde{\mathbf{K}}_x^T(t)\mathbf{x}(t) \frac{d(\tilde{\mathbf{x}}^T(t)\mathbf{P}\tilde{\mathbf{x}}(t))}{d(\tilde{\mathbf{x}}^T(t)\mathbf{P}\tilde{\mathbf{x}}(t))} + \\ & 2\tilde{\mathbf{x}}^T(t)\mathbf{P}\mathbf{B}\boldsymbol{\Lambda}\tilde{\mathbf{K}}_r^T(t)\mathbf{r}(t) \frac{d(\tilde{\mathbf{x}}^T(t)\mathbf{P}\tilde{\mathbf{x}}(t))}{d(\tilde{\mathbf{x}}^T(t)\mathbf{P}\tilde{\mathbf{x}}(t))} - \\ & 2\tilde{\mathbf{x}}^T(t)\mathbf{P}\mathbf{B}\boldsymbol{\Lambda}\tilde{\boldsymbol{\theta}}^T(t)\boldsymbol{\mu}(\mathbf{x}(t)) \frac{d(\tilde{\mathbf{x}}^T(t)\mathbf{P}\tilde{\mathbf{x}}(t))}{d(\tilde{\mathbf{x}}^T(t)\mathbf{P}\tilde{\mathbf{x}}(t))} + \\ & 2\text{tr}\left[\left[\tilde{\mathbf{K}}_x^T(t)\Gamma_x^{-1}\dot{\tilde{\mathbf{K}}}_x(t) + \tilde{\mathbf{K}}_r^T(t)\Gamma_r^{-1}\dot{\tilde{\mathbf{K}}}_r(t) + \right. \right. \\ & \left. \left. \tilde{\boldsymbol{\theta}}^T(t)\Gamma_\theta^{-1}\dot{\tilde{\boldsymbol{\theta}}}(t)\right]\boldsymbol{\Lambda} \right] \end{aligned} \quad (29)$$

Applying the vector-trace identity:

$$\mathbf{w}^T\mathbf{z} = \text{tr}(\mathbf{z}\mathbf{w}^T) \quad (30)$$

Yields:

$$\begin{aligned} \tilde{\mathbf{x}}^T(t)\mathbf{P}\mathbf{B}\boldsymbol{\Lambda}\tilde{\mathbf{K}}_x^T(t)\mathbf{x}(t) \frac{d(\tilde{\mathbf{x}}^T(t)\mathbf{P}\tilde{\mathbf{x}}(t))}{d(\tilde{\mathbf{x}}^T(t)\mathbf{P}\tilde{\mathbf{x}}(t))} = \\ \text{tr}\left(\tilde{\mathbf{K}}_x^T(t)\mathbf{x}(t)\tilde{\mathbf{x}}^T(t)\mathbf{P}\mathbf{B}\boldsymbol{\Lambda} \frac{d(\tilde{\mathbf{x}}^T(t)\mathbf{P}\tilde{\mathbf{x}}(t))}{d(\tilde{\mathbf{x}}^T(t)\mathbf{P}\tilde{\mathbf{x}}(t))}\right) \\ \tilde{\mathbf{x}}^T(t)\mathbf{P}\mathbf{B}\boldsymbol{\Lambda}\tilde{\mathbf{K}}_r^T(t)\mathbf{r}(t) \frac{d(\tilde{\mathbf{x}}^T(t)\mathbf{P}\tilde{\mathbf{x}}(t))}{d(\tilde{\mathbf{x}}^T(t)\mathbf{P}\tilde{\mathbf{x}}(t))} = \\ \text{tr}\left(\tilde{\mathbf{K}}_r^T(t)\mathbf{r}(t)\tilde{\mathbf{x}}^T(t)\mathbf{P}\mathbf{B}\boldsymbol{\Lambda} \frac{d(\tilde{\mathbf{x}}^T(t)\mathbf{P}\tilde{\mathbf{x}}(t))}{d(\tilde{\mathbf{x}}^T(t)\mathbf{P}\tilde{\mathbf{x}}(t))}\right) \\ \tilde{\mathbf{x}}^T(t)\mathbf{P}\mathbf{B}\boldsymbol{\Lambda}\tilde{\boldsymbol{\theta}}^T(t)\boldsymbol{\mu}(\mathbf{x}(t)) \frac{d(\tilde{\mathbf{x}}^T(t)\mathbf{P}\tilde{\mathbf{x}}(t))}{d(\tilde{\mathbf{x}}^T(t)\mathbf{P}\tilde{\mathbf{x}}(t))} = \\ \text{tr}\left(\tilde{\boldsymbol{\theta}}^T(t)\boldsymbol{\mu}(\mathbf{x}(t))\tilde{\mathbf{x}}^T(t)\mathbf{P}\mathbf{B}\boldsymbol{\Lambda} \frac{d(\tilde{\mathbf{x}}^T(t)\mathbf{P}\tilde{\mathbf{x}}(t))}{d(\tilde{\mathbf{x}}^T(t)\mathbf{P}\tilde{\mathbf{x}}(t))}\right) \end{aligned} \quad (31)$$

Using Equations (29) and (31) and Collecting similar terms gives:

$$\begin{aligned} \dot{V} = & -\tilde{\mathbf{x}}^T(t)\mathbf{Q}\tilde{\mathbf{x}}(t) \frac{d(\tilde{\mathbf{x}}^T(t)\mathbf{P}\tilde{\mathbf{x}}(t))}{d(\tilde{\mathbf{x}}^T(t)\mathbf{P}\tilde{\mathbf{x}}(t))} + \\ & 2\text{tr}\left(\tilde{\mathbf{K}}_x^T(t)\mathbf{x}(t)\tilde{\mathbf{x}}^T(t)\mathbf{P}\mathbf{B}\boldsymbol{\Lambda} \frac{d(\tilde{\mathbf{x}}^T(t)\mathbf{P}\tilde{\mathbf{x}}(t))}{d(\tilde{\mathbf{x}}^T(t)\mathbf{P}\tilde{\mathbf{x}}(t))} + \right. \\ & \left. \tilde{\mathbf{K}}_x^T(t)\Gamma_x^{-1}\dot{\tilde{\mathbf{K}}}_x(t)\boldsymbol{\Lambda}\right) + \\ & 2\text{tr}\left(\tilde{\mathbf{K}}_r^T(t)\mathbf{r}(t)\tilde{\mathbf{x}}^T(t)\mathbf{P}\mathbf{B}\boldsymbol{\Lambda} \frac{d(\tilde{\mathbf{x}}^T(t)\mathbf{P}\tilde{\mathbf{x}}(t))}{d(\tilde{\mathbf{x}}^T(t)\mathbf{P}\tilde{\mathbf{x}}(t))} + \right. \\ & \left. \tilde{\mathbf{K}}_r^T(t)\Gamma_r^{-1}\dot{\tilde{\mathbf{K}}}_r(t)\boldsymbol{\Lambda}\right) + \\ & 2\text{tr}\left(\tilde{\boldsymbol{\theta}}^T(t)\boldsymbol{\mu}(\mathbf{x}(t))\tilde{\mathbf{x}}^T(t)\mathbf{P}\mathbf{B}\boldsymbol{\Lambda} \frac{d(\tilde{\mathbf{x}}^T(t)\mathbf{P}\tilde{\mathbf{x}}(t))}{d(\tilde{\mathbf{x}}^T(t)\mathbf{P}\tilde{\mathbf{x}}(t))} - \right. \\ & \left. \tilde{\boldsymbol{\theta}}^T(t)\Gamma_\theta^{-1}\dot{\tilde{\boldsymbol{\theta}}}(t)\boldsymbol{\Lambda}\right) \end{aligned} \quad (32)$$

Choosing the following MRAC adaptive laws:

$$\begin{aligned} \dot{\tilde{\mathbf{K}}}_x(t) = & \dot{\hat{\mathbf{K}}}_x(t) - \dot{\mathbf{K}}_x = \dot{\hat{\mathbf{K}}}_x(t) = \\ & -\Gamma_x\mathbf{x}(t)\tilde{\mathbf{x}}^T(t)\mathbf{P}\mathbf{B} \frac{d(\tilde{\mathbf{x}}^T(t)\mathbf{P}\tilde{\mathbf{x}}(t))}{d(\tilde{\mathbf{x}}^T(t)\mathbf{P}\tilde{\mathbf{x}}(t))} \\ \dot{\tilde{\mathbf{K}}}_r(t) = & \dot{\hat{\mathbf{K}}}_r(t) - \dot{\mathbf{K}}_r = \dot{\hat{\mathbf{K}}}_r(t) = \\ & -\Gamma_r\mathbf{r}(t)\tilde{\mathbf{x}}^T(t)\mathbf{P}\mathbf{B} \frac{d(\tilde{\mathbf{x}}^T(t)\mathbf{P}\tilde{\mathbf{x}}(t))}{d(\tilde{\mathbf{x}}^T(t)\mathbf{P}\tilde{\mathbf{x}}(t))} \end{aligned} \quad (33)$$

$$\begin{aligned} \dot{\tilde{\boldsymbol{\theta}}}(t) = & \dot{\hat{\boldsymbol{\theta}}}(t) - \dot{\boldsymbol{\theta}} = \dot{\hat{\boldsymbol{\theta}}}(t) = \\ & \Gamma_\theta\boldsymbol{\mu}(\mathbf{x}(t))\tilde{\mathbf{x}}^T(t)\mathbf{P}\mathbf{B} \frac{d(\tilde{\mathbf{x}}^T(t)\mathbf{P}\tilde{\mathbf{x}}(t))}{d(\tilde{\mathbf{x}}^T(t)\mathbf{P}\tilde{\mathbf{x}}(t))} \end{aligned}$$

Yields:

$$\dot{V} = -\tilde{\mathbf{x}}^T(t)\mathbf{Q}\tilde{\mathbf{x}}(t) \frac{d(\tilde{\mathbf{x}}^T(t)\mathbf{P}\tilde{\mathbf{x}}(t))}{d(\tilde{\mathbf{x}}^T(t)\mathbf{P}\tilde{\mathbf{x}}(t))} \leq 0 \quad (34)$$

Equation (34) Proves uniform ultimate boundedness of $\tilde{\mathbf{x}}(t)$, $\tilde{\mathbf{K}}_x(t)$, $\tilde{\mathbf{K}}_r(t)$, $\tilde{\boldsymbol{\theta}}(t)$. Since \mathbf{r} is a bounded command and \mathbf{A}_m is a Hurwitz matrix, then \mathbf{x}_m , is bounded. Using Equation (14) $\mathbf{x} = \tilde{\mathbf{x}} + \mathbf{x}_m$, we can conclude that \mathbf{x} is a bounded signal. We know that the ideal control gains \mathbf{K}_x , \mathbf{K}_r , $\boldsymbol{\theta}$ are constant, therefore using the fact that $\tilde{\mathbf{K}}_x(t)$, $\tilde{\mathbf{K}}_r(t)$, $\tilde{\boldsymbol{\theta}}(t)$ are bounded, then using Equation (22) implies that $\hat{\mathbf{K}}_x(t)$, $\hat{\mathbf{K}}_r(t)$, $\hat{\boldsymbol{\theta}}(t)$ are bounded. Calculating the second time derivative of the Lyapunov function yields:

$$\begin{aligned} \ddot{V} = & -\left[\tilde{\mathbf{x}}^T(t)(\mathbf{A}_m^T\mathbf{Q} + \mathbf{Q}\mathbf{A}_m)\tilde{\mathbf{x}}(t) + \right. \\ & 2\tilde{\mathbf{x}}^T(t)\mathbf{P}\mathbf{B}\boldsymbol{\Lambda}\tilde{\mathbf{K}}_x^T(t)\mathbf{x}(t) + 2\tilde{\mathbf{x}}^T(t)\mathbf{P}\mathbf{B}\boldsymbol{\Lambda}\tilde{\mathbf{K}}_r^T(t)\mathbf{r}(t) - \\ & 2\tilde{\mathbf{x}}^T(t)\mathbf{P}\mathbf{B}\boldsymbol{\Lambda}\tilde{\boldsymbol{\theta}}^T(t)\boldsymbol{\mu}(\mathbf{x}(t))\left. \right] \frac{d(\tilde{\mathbf{x}}^T(t)\mathbf{P}\tilde{\mathbf{x}}(t))}{d(\tilde{\mathbf{x}}^T(t)\mathbf{P}\tilde{\mathbf{x}}(t))} - \\ & \tilde{\mathbf{x}}^T(t)\mathbf{Q}\tilde{\mathbf{x}}(t)\left[\tilde{\mathbf{x}}^T(t)(\mathbf{A}_m^T\mathbf{P} + \mathbf{P}\mathbf{A}_m)\tilde{\mathbf{x}}(t) + \right. \\ & 2\tilde{\mathbf{x}}^T(t)\mathbf{P}\mathbf{B}\boldsymbol{\Lambda}\tilde{\mathbf{K}}_x^T(t)\mathbf{x}(t) + 2\tilde{\mathbf{x}}^T(t)\mathbf{P}\mathbf{B}\boldsymbol{\Lambda}\tilde{\mathbf{K}}_r^T(t)\mathbf{r}(t) - \\ & \left. 2\tilde{\mathbf{x}}^T(t)\mathbf{P}\mathbf{B}\boldsymbol{\Lambda}\tilde{\boldsymbol{\theta}}^T(t)\boldsymbol{\mu}(\mathbf{x}(t))\right] \frac{d^2(\tilde{\mathbf{x}}^T(t)\mathbf{P}\tilde{\mathbf{x}}(t))}{(d(\tilde{\mathbf{x}}^T(t)\mathbf{P}\tilde{\mathbf{x}}(t)))^2} \end{aligned} \quad (35)$$

We know that every continuously differentiable function ($f \in C^1$) on a compact set is Lipschitz which has a bounded derivative (Appendix A). 1-Lipschitz condition yields 2-Lipschitz which guarantees the boundedness of the second time derivative (Appendix B). we can conclude that the second time derivative of the Lyapunov function is bounded:

$$\ddot{V} < \infty \quad (36)$$

Equations (34) and (36) indicate that \dot{V} is uniformly continuous of time. Since V is lower bounded and $\dot{V} \leq 0$ and \dot{V} is uniformly continuous then using Barbalat's lemma [30], yields:

$$\lim_{t \rightarrow \infty} \dot{V} = \lim_{t \rightarrow \infty} [-\tilde{\mathbf{x}}^T(t)\mathbf{Q}\tilde{\mathbf{x}}(t) \frac{d(\tilde{\mathbf{x}}^T(t)\mathbf{P}\tilde{\mathbf{x}}(t))}{d(\tilde{\mathbf{x}}^T(t)\mathbf{P}\tilde{\mathbf{x}}(t))}] = 0 \quad (37)$$

We know that $\frac{d(\tilde{\mathbf{x}}^T(t)\mathbf{P}\tilde{\mathbf{x}}(t))}{d(\tilde{\mathbf{x}}^T(t)\mathbf{P}\tilde{\mathbf{x}}(t))} > 0$, therefore:

$$\lim_{t \rightarrow \infty} -\tilde{\mathbf{x}}^T(t)\mathbf{Q}\tilde{\mathbf{x}}(t) = \mathbf{0} \rightarrow \lim_{t \rightarrow \infty} \|\mathbf{x}(t) - \mathbf{x}_m(t)\| = 0 \quad (38)$$

We prove that the tracking error globally uniformly asymptotically tends to zero. The general adaptive law Equation (33) can be considered as an simple adaptive law with variable adaptation gains, $\boldsymbol{\Gamma}' = \boldsymbol{\Gamma} \frac{d(\tilde{\mathbf{x}}^T(t)\mathbf{P}\tilde{\mathbf{x}}(t))}{d(\tilde{\mathbf{x}}^T(t)\mathbf{P}\tilde{\mathbf{x}}(t))}$ which yields:

$$\begin{aligned} \dot{\hat{\mathbf{K}}}_x(t) = & -\boldsymbol{\Gamma}'_x\mathbf{x}(t)\tilde{\mathbf{x}}^T(t)\mathbf{P}\mathbf{B} \\ \dot{\hat{\mathbf{K}}}_r(t) = & -\boldsymbol{\Gamma}'_r\mathbf{r}(t)\tilde{\mathbf{x}}^T(t)\mathbf{P}\mathbf{B} \\ \dot{\hat{\boldsymbol{\theta}}}(t) = & \boldsymbol{\Gamma}'_\theta\boldsymbol{\mu}(\mathbf{x}(t))\tilde{\mathbf{x}}^T(t)\mathbf{P}\mathbf{B} \end{aligned} \quad (39)$$

4. ROBUST MRAC SCHEMES

4.1. σ – Modification We consider a class of MIMO uncertain systems with matched parametric uncertainty subjected to a bounded external disturbance as follows:

$$\dot{\mathbf{x}}(t) = \mathbf{A}\mathbf{x}(t) + \mathbf{B}\mathbf{A}[\mathbf{u}(t) + \boldsymbol{\theta}^T\boldsymbol{\mu}(\mathbf{x})] + \boldsymbol{\zeta}(t) \quad (40)$$

In Equation (40), $\mathbf{x}(t) \in \mathbf{R}^n$ is the state vector of the system, $\mathbf{A} \in \mathbf{R}^{n \times n}$ is a known matrix, $\mathbf{B} \in \mathbf{R}^{n \times m}$ is a known control matrix we assume that the pair $(\mathbf{A}, \mathbf{B}\mathbf{A})$ is controllable, $\mathbf{u}(t) \in \mathbf{R}^m$ is the control signal, $\boldsymbol{\theta} \in \mathbf{R}^{p \times m}$ is a matrix of unknown parameters, $\boldsymbol{\mu}(\mathbf{x}) \in \mathbf{R}^p$ is the known regressor vector, which is a continuous Lipschitz function of $\mathbf{x}(t)$, and $\boldsymbol{\zeta}(t) \in \mathbf{R}^n$ is a bounded external disturbance. We consider the following reference model:

$$\dot{\mathbf{x}}_m(t) = \mathbf{A}_m\mathbf{x}_m(t) + \mathbf{B}_m\mathbf{r}(t) \quad (41)$$

In Equation (41), $\mathbf{A}_m \in \mathbf{R}^{n \times n}$ is a known Hurwitz matrix, $\mathbf{B}_m \in \mathbf{R}^{n \times r}$ is assumed to be known, and $\mathbf{r}(t) \in \mathbf{R}^r$ is a bounded time-varying reference command.

Assumption: given matrices \mathbf{A} and \mathbf{B} , there exist matrices \mathbf{K}_x and \mathbf{K}_r such that Equation (42) be satisfied.

$$\begin{aligned} \mathbf{A}_m &= \mathbf{A} + \mathbf{B}\mathbf{A}\mathbf{K}_x^T \\ \mathbf{B}_m &= \mathbf{B}\mathbf{A}\mathbf{K}_r^T \end{aligned} \quad (42)$$

We use the control input $\mathbf{u}(t)$ as follows:

$$\mathbf{u} = \mathbf{K}_x\mathbf{x} + \mathbf{K}_r\mathbf{r} - \tilde{\boldsymbol{\theta}}^T\boldsymbol{\mu}(\mathbf{x}) \quad (43)$$

Subtracting Equation (41) from Equation (40) yields:

$$\begin{aligned} \dot{\mathbf{x}}(t) - \dot{\mathbf{x}}_m(t) &= \mathbf{A}\mathbf{x}(t) + \mathbf{B}\mathbf{A}[\mathbf{u}(t) + \boldsymbol{\theta}^T\boldsymbol{\mu}(\mathbf{x})] + \\ &\boldsymbol{\zeta}(t) - \mathbf{A}_m\mathbf{x}_m(t) - \mathbf{B}_m\mathbf{r}(t) \end{aligned} \quad (44)$$

Substituting Equation (43) in Equation (44) and using Equation (42) gives:

$$\begin{aligned} \dot{\mathbf{x}}(t) - \dot{\mathbf{x}}_m(t) &= \mathbf{A}_m\mathbf{x}(t) - \mathbf{B}\mathbf{A}(\tilde{\boldsymbol{\theta}}^T - \boldsymbol{\theta}^T)\boldsymbol{\mu}(\mathbf{x}) + \\ &\boldsymbol{\zeta}(t) - \mathbf{A}_m\mathbf{x}_m(t) \end{aligned} \quad (45)$$

Simplifying Equation (45) yields the tracking error dynamics:

$$\dot{\tilde{\mathbf{x}}} = \mathbf{A}_m\tilde{\mathbf{x}} - \mathbf{B}\mathbf{A}\tilde{\boldsymbol{\theta}}^T\boldsymbol{\mu}(\mathbf{x}) + \boldsymbol{\zeta}(t) \quad (46)$$

The σ – Modification to the MRAC adaptive law is:

$$\dot{\tilde{\boldsymbol{\theta}}} = \Gamma(\boldsymbol{\mu}(\mathbf{x})\tilde{\mathbf{x}}^T\mathbf{P}\mathbf{B} \frac{df(\tilde{\mathbf{x}}^T(t)\mathbf{P}\tilde{\mathbf{x}}(t))}{d(\tilde{\mathbf{x}}^T(t)\mathbf{P}\tilde{\mathbf{x}}(t))} - \sigma\tilde{\boldsymbol{\theta}}) \quad (47)$$

In Equation (47), $\sigma > 0$ is the modification parameter. Now we consider the following radially unbounded Lyapunov function candidate:

$$V(\tilde{\mathbf{x}}, \tilde{\boldsymbol{\theta}}) = f(\tilde{\mathbf{x}}^T(t)\mathbf{P}\tilde{\mathbf{x}}(t)) + \text{tr}(\tilde{\boldsymbol{\theta}}^T\Gamma^{-1}\tilde{\boldsymbol{\theta}}\Lambda) \quad (48)$$

The first time derivative of the Lyapunov function candidates becomes:

$$\begin{aligned} \dot{V}(\tilde{\mathbf{x}}, \tilde{\boldsymbol{\theta}}) &= (\dot{\tilde{\mathbf{x}}}^T\mathbf{P}\tilde{\mathbf{x}} + \tilde{\mathbf{x}}^T\mathbf{P}\dot{\tilde{\mathbf{x}}}) \frac{df(\tilde{\mathbf{x}}^T(t)\mathbf{P}\tilde{\mathbf{x}}(t))}{d(\tilde{\mathbf{x}}^T(t)\mathbf{P}\tilde{\mathbf{x}}(t))} + \\ &2\text{tr}(\tilde{\boldsymbol{\theta}}^T\Gamma^{-1}\dot{\tilde{\boldsymbol{\theta}}}\Lambda) \end{aligned} \quad (49)$$

Using Equations (46) and (49) yields:

$$\begin{aligned} \dot{V}(\tilde{\mathbf{x}}, \tilde{\boldsymbol{\theta}}) &= [(\tilde{\mathbf{x}}^T\mathbf{A}_m^T - \boldsymbol{\mu}^T(\mathbf{x})\tilde{\boldsymbol{\theta}}\Lambda\mathbf{B}^T + \boldsymbol{\zeta}^T)\mathbf{P}\tilde{\mathbf{x}} + \\ &\tilde{\mathbf{x}}^T\mathbf{P}(\mathbf{A}_m\tilde{\mathbf{x}} - \mathbf{B}\mathbf{A}\tilde{\boldsymbol{\theta}}^T\boldsymbol{\mu}(\mathbf{x}) + \boldsymbol{\zeta})] \frac{df(\tilde{\mathbf{x}}^T(t)\mathbf{P}\tilde{\mathbf{x}}(t))}{d(\tilde{\mathbf{x}}^T(t)\mathbf{P}\tilde{\mathbf{x}}(t))} + \\ &2\text{tr}[\tilde{\boldsymbol{\theta}}^T\Gamma^{-1}(\Gamma[(\boldsymbol{\mu}(\mathbf{x})\tilde{\mathbf{x}}^T\mathbf{P}\mathbf{B} \frac{df(\tilde{\mathbf{x}}^T(t)\mathbf{P}\tilde{\mathbf{x}}(t))}{d(\tilde{\mathbf{x}}^T(t)\mathbf{P}\tilde{\mathbf{x}}(t))} - \sigma\tilde{\boldsymbol{\theta}})])\Lambda] \end{aligned} \quad (50)$$

Simplifying Equation (50) yields:

$$\begin{aligned} \dot{V}(\tilde{\mathbf{x}}, \tilde{\boldsymbol{\theta}}) &= \tilde{\mathbf{x}}^T[\mathbf{A}_m^T\mathbf{P} + \mathbf{P}\mathbf{A}_m]\tilde{\mathbf{x}} \frac{df(\tilde{\mathbf{x}}^T(t)\mathbf{P}\tilde{\mathbf{x}}(t))}{d(\tilde{\mathbf{x}}^T(t)\mathbf{P}\tilde{\mathbf{x}}(t))} + \\ &2\tilde{\mathbf{x}}^T\mathbf{P}\boldsymbol{\zeta} \frac{df(\tilde{\mathbf{x}}^T(t)\mathbf{P}\tilde{\mathbf{x}}(t))}{d(\tilde{\mathbf{x}}^T(t)\mathbf{P}\tilde{\mathbf{x}}(t))} \\ &- 2\tilde{\mathbf{x}}^T\mathbf{P}\mathbf{B}\mathbf{A}\tilde{\boldsymbol{\theta}}^T\boldsymbol{\mu}(\mathbf{x}) \frac{df(\tilde{\mathbf{x}}^T(t)\mathbf{P}\tilde{\mathbf{x}}(t))}{d(\tilde{\mathbf{x}}^T(t)\mathbf{P}\tilde{\mathbf{x}}(t))} + \\ &2\text{tr}[\tilde{\boldsymbol{\theta}}^T\boldsymbol{\mu}(\mathbf{x})\tilde{\mathbf{x}}^T\mathbf{P}\mathbf{B}\mathbf{A} \frac{df(\tilde{\mathbf{x}}^T(t)\mathbf{P}\tilde{\mathbf{x}}(t))}{d(\tilde{\mathbf{x}}^T(t)\mathbf{P}\tilde{\mathbf{x}}(t))} - \sigma\tilde{\boldsymbol{\theta}}^T\tilde{\boldsymbol{\theta}}\Lambda] \end{aligned} \quad (51)$$

Using the vector- trace identity Equation (30) and the algebraic Lyapunov equation:

$$\mathbf{A}_m^T\mathbf{P} + \mathbf{P}\mathbf{A}_m = -\mathbf{Q} \quad (52)$$

Equation (51) becomes:

$$\begin{aligned} \dot{V}(\tilde{\mathbf{x}}, \tilde{\boldsymbol{\theta}}) &= (-\tilde{\mathbf{x}}^T\mathbf{Q}\tilde{\mathbf{x}} + 2\tilde{\mathbf{x}}^T\mathbf{P}\boldsymbol{\zeta}) \frac{df(\tilde{\mathbf{x}}^T(t)\mathbf{P}\tilde{\mathbf{x}}(t))}{d(\tilde{\mathbf{x}}^T(t)\mathbf{P}\tilde{\mathbf{x}}(t))} - \\ &2\sigma\text{tr}[\tilde{\boldsymbol{\theta}}^T\tilde{\boldsymbol{\theta}}\Lambda] \end{aligned} \quad (53)$$

Using:

$$\tilde{\boldsymbol{\theta}} = \tilde{\boldsymbol{\theta}} + \boldsymbol{\theta} \quad (54)$$

Yields:

$$\begin{aligned} \dot{V}(\tilde{\mathbf{x}}, \tilde{\boldsymbol{\theta}}) &= (-\tilde{\mathbf{x}}^T\mathbf{Q}\tilde{\mathbf{x}} + 2\tilde{\mathbf{x}}^T\mathbf{P}\boldsymbol{\zeta}) \frac{df(\tilde{\mathbf{x}}^T(t)\mathbf{P}\tilde{\mathbf{x}}(t))}{d(\tilde{\mathbf{x}}^T(t)\mathbf{P}\tilde{\mathbf{x}}(t))} - \\ &2\sigma\text{tr}[\tilde{\boldsymbol{\theta}}^T\tilde{\boldsymbol{\theta}}\Lambda] - 2\sigma\text{tr}[\tilde{\boldsymbol{\theta}}^T\boldsymbol{\theta}\Lambda] \end{aligned} \quad (55)$$

We use the Frobenius norm definition, and the Cauchy Schwarz inequality (51) presented as follows:

$$\text{tr}[\tilde{\boldsymbol{\theta}}^T\tilde{\boldsymbol{\theta}}\Lambda] = \sum_{i=1}^n \sum_{j=1}^m \tilde{\theta}_{ij}^2 \Lambda_{ii} \geq \|\tilde{\boldsymbol{\theta}}\|_F^2 \Lambda_{\min} \quad (56)$$

$$|\text{tr}(\tilde{\boldsymbol{\theta}}^T\boldsymbol{\theta}\Lambda)| \leq \|\tilde{\boldsymbol{\theta}}^T\boldsymbol{\theta}\|_F \|\Lambda\|_F \leq \|\tilde{\boldsymbol{\theta}}\|_F \|\boldsymbol{\theta}\|_F \|\Lambda\|_F$$

The upper bound of the external disturbance and unknown parameters are considered as follows:

$$\zeta_0 = \max\|\boldsymbol{\zeta}\|_\infty \quad (57)$$

$$\theta_0 = \|\boldsymbol{\theta}\|_F$$

Using Equations (56), and (57), Equation (55) can be written as follows:

$$\begin{aligned} \dot{V}(\tilde{\mathbf{x}}, \tilde{\boldsymbol{\theta}}) &\leq [-\lambda_{\min}(\mathbf{Q})\|\tilde{\mathbf{x}}\|^2 + \\ &2\|\tilde{\mathbf{x}}\|\lambda_{\max}(\mathbf{P})\zeta_0] \frac{df(\tilde{\mathbf{x}}^T(t)\mathbf{P}\tilde{\mathbf{x}}(t))}{d(\tilde{\mathbf{x}}^T(t)\mathbf{P}\tilde{\mathbf{x}}(t))} - 2\sigma\|\tilde{\boldsymbol{\theta}}\|_F^2 \Lambda_{\min} + \\ &2\sigma\|\tilde{\boldsymbol{\theta}}\|_F \|\boldsymbol{\theta}\|_F \|\Lambda\|_F \end{aligned} \quad (58)$$

We use the following inequality:

$$2ab \leq a^2 + b^2 \quad (59)$$

Equation (58) becomes:

$$\begin{aligned}
\dot{V}(\tilde{\mathbf{x}}, \tilde{\boldsymbol{\theta}}) &\leq (-\lambda_{\min}(\mathbf{Q})\|\tilde{\mathbf{x}}\|^2 + \\
&2\|\tilde{\mathbf{x}}\|\lambda_{\max}(\mathbf{P})\zeta_0) \frac{df(\tilde{\mathbf{x}}^T(t)\mathbf{P}\tilde{\mathbf{x}}(t))}{d(\tilde{\mathbf{x}}^T(t)\mathbf{P}\tilde{\mathbf{x}}(t))} - 2\sigma\|\tilde{\boldsymbol{\theta}}\|_F^2\Lambda_{\min} + \\
&\sigma(\|\tilde{\boldsymbol{\theta}}\|_F^2 + \|\boldsymbol{\theta}\|_F^2)\|\Lambda\|_F \\
&= (-\lambda_{\min}(\mathbf{Q})\|\tilde{\mathbf{x}}\|^2 + \\
&2\|\tilde{\mathbf{x}}\|\lambda_{\max}(\mathbf{P})\zeta_0) \frac{df(\tilde{\mathbf{x}}^T(t)\mathbf{P}\tilde{\mathbf{x}}(t))}{d(\tilde{\mathbf{x}}^T(t)\mathbf{P}\tilde{\mathbf{x}}(t))} - \sigma\|\tilde{\boldsymbol{\theta}}\|_F^2(2\Lambda_{\min} + \\
&\|\Lambda\|_F) + \sigma\|\boldsymbol{\theta}\|_F^2\|\Lambda\|_F
\end{aligned} \quad (60)$$

If we choose:

$$\begin{aligned}
-\lambda_{\min}(\mathbf{Q})\|\tilde{\mathbf{x}}\|^2 + 2\|\tilde{\mathbf{x}}\|\lambda_{\max}(\mathbf{P})\zeta_0 &\leq 0 \\
-\sigma\|\tilde{\boldsymbol{\theta}}\|_F^2(2\Lambda_{\min} + \|\Lambda\|_F) + \sigma\|\boldsymbol{\theta}\|_F^2\|\Lambda\|_F &\leq 0
\end{aligned} \quad (61)$$

Or:

$$\begin{aligned}
\Omega = \{(\tilde{\mathbf{x}}, \tilde{\boldsymbol{\theta}}): \|\tilde{\mathbf{x}}\| < \frac{2\lambda_{\max}(\mathbf{P})\zeta_0}{\lambda_{\min}(\mathbf{Q})} \wedge \|\tilde{\boldsymbol{\theta}}\|_F \leq \\
\sqrt{\frac{\|\boldsymbol{\theta}\|_F^2\|\Lambda\|_F}{2\Lambda_{\min} + \|\Lambda\|_F}}\}
\end{aligned} \quad (62)$$

Then we have $\dot{V} \leq 0$ outside of the compact set Ω , and $\dot{V} > 0$ inside it. We prove that all signals in the closed-loop system are uniformly, ultimately bounded.

4. 2. e-Modification By definition, the e-Modification to the MRAC adaptive law that estimates $\tilde{\boldsymbol{\theta}}(t)$ is:

$$\dot{\tilde{\boldsymbol{\theta}}} = \Gamma \frac{df(\tilde{\mathbf{x}}^T(t)\mathbf{P}\tilde{\mathbf{x}}(t))}{d(\tilde{\mathbf{x}}^T(t)\mathbf{P}\tilde{\mathbf{x}}(t))} (\boldsymbol{\mu}(\mathbf{x})\tilde{\mathbf{x}}^T\mathbf{P}\mathbf{B} - \alpha\|\tilde{\mathbf{x}}^T\mathbf{P}\mathbf{B}\|\tilde{\boldsymbol{\theta}}) \quad (63)$$

In Equation (63), $\alpha > 0$ is the modification parameter. We consider the following radially unbounded Lyapunov function:

$$V(\tilde{\mathbf{x}}, \tilde{\boldsymbol{\theta}}) = f(\tilde{\mathbf{x}}^T(t)\mathbf{P}\tilde{\mathbf{x}}(t)) + \text{tr}(\tilde{\boldsymbol{\theta}}^T\Gamma^{-1}\tilde{\boldsymbol{\theta}}\Lambda) \quad (64)$$

The first time derivative of the Equation (64) becomes:

$$\begin{aligned}
\dot{V}(\tilde{\mathbf{x}}, \tilde{\boldsymbol{\theta}}) &= (\dot{\tilde{\mathbf{x}}}^T\mathbf{P}\tilde{\mathbf{x}} + \tilde{\mathbf{x}}^T\mathbf{P}\dot{\tilde{\mathbf{x}}}) \frac{df(\tilde{\mathbf{x}}^T(t)\mathbf{P}\tilde{\mathbf{x}}(t))}{d(\tilde{\mathbf{x}}^T(t)\mathbf{P}\tilde{\mathbf{x}}(t))} + \\
&2\text{tr}(\tilde{\boldsymbol{\theta}}^T\Gamma^{-1}\dot{\tilde{\boldsymbol{\theta}}}\Lambda)
\end{aligned} \quad (65)$$

Using the tracking error dynamics Equation (46) yields:

$$\begin{aligned}
\dot{V}(\tilde{\mathbf{x}}, \tilde{\boldsymbol{\theta}}) &= [(\tilde{\mathbf{x}}^T\mathbf{A}_m^T - \boldsymbol{\mu}^T(\mathbf{x})\tilde{\boldsymbol{\theta}}\Lambda\mathbf{B}^T + \boldsymbol{\zeta}^T)\mathbf{P}\tilde{\mathbf{x}} + \\
&\tilde{\mathbf{x}}^T\mathbf{P}(\mathbf{A}_m\tilde{\mathbf{x}} - \mathbf{B}\Lambda\tilde{\boldsymbol{\theta}}^T\boldsymbol{\mu}(\mathbf{x}) + \boldsymbol{\zeta})] \frac{df(\tilde{\mathbf{x}}^T(t)\mathbf{P}\tilde{\mathbf{x}}(t))}{d(\tilde{\mathbf{x}}^T(t)\mathbf{P}\tilde{\mathbf{x}}(t))} + \\
&2\text{tr}(\tilde{\boldsymbol{\theta}}^T\Gamma^{-1} \left(\Gamma \frac{df(\tilde{\mathbf{x}}^T(t)\mathbf{P}\tilde{\mathbf{x}}(t))}{d(\tilde{\mathbf{x}}^T(t)\mathbf{P}\tilde{\mathbf{x}}(t))} (\boldsymbol{\mu}(\mathbf{x})\tilde{\mathbf{x}}^T\mathbf{P}\mathbf{B} - \right. \\
&\left. \alpha\|\tilde{\mathbf{x}}^T\mathbf{P}\mathbf{B}\|\tilde{\boldsymbol{\theta}}\Lambda) \right)
\end{aligned} \quad (66)$$

Simplifying Equation (66) gives:

$$\begin{aligned}
\dot{V}(\tilde{\mathbf{x}}, \tilde{\boldsymbol{\theta}}) &= \tilde{\mathbf{x}}^T[\mathbf{A}_m^T\mathbf{P} + \mathbf{P}\mathbf{A}_m]\tilde{\mathbf{x}} \frac{df(\tilde{\mathbf{x}}^T(t)\mathbf{P}\tilde{\mathbf{x}}(t))}{d(\tilde{\mathbf{x}}^T(t)\mathbf{P}\tilde{\mathbf{x}}(t))} + \\
&2\tilde{\mathbf{x}}^T\mathbf{P}\boldsymbol{\zeta} \frac{df(\tilde{\mathbf{x}}^T(t)\mathbf{P}\tilde{\mathbf{x}}(t))}{d(\tilde{\mathbf{x}}^T(t)\mathbf{P}\tilde{\mathbf{x}}(t))} - \\
&2\tilde{\mathbf{x}}^T\mathbf{P}\mathbf{B}\Lambda\tilde{\boldsymbol{\theta}}^T\boldsymbol{\mu}(\mathbf{x}) \frac{df(\tilde{\mathbf{x}}^T(t)\mathbf{P}\tilde{\mathbf{x}}(t))}{d(\tilde{\mathbf{x}}^T(t)\mathbf{P}\tilde{\mathbf{x}}(t))} + \\
&2 \frac{df(\tilde{\mathbf{x}}^T(t)\mathbf{P}\tilde{\mathbf{x}}(t))}{d(\tilde{\mathbf{x}}^T(t)\mathbf{P}\tilde{\mathbf{x}}(t))} \text{tr}[(\tilde{\boldsymbol{\theta}}^T\boldsymbol{\mu}(\mathbf{x})\tilde{\mathbf{x}}^T\mathbf{P}\mathbf{B} - \alpha\|\tilde{\mathbf{x}}^T\mathbf{P}\mathbf{B}\|\tilde{\boldsymbol{\theta}})\Lambda]
\end{aligned} \quad (67)$$

Same as the previous section using the vector-trace identity Equation (30) and the algebraic Lyapunov Equation (52) yields:

$$\begin{aligned}
\dot{V}(\tilde{\mathbf{x}}, \tilde{\boldsymbol{\theta}}) &= (-\tilde{\mathbf{x}}^T\mathbf{Q}\tilde{\mathbf{x}} + 2\tilde{\mathbf{x}}^T\mathbf{P}\boldsymbol{\zeta}) \frac{df(\tilde{\mathbf{x}}^T(t)\mathbf{P}\tilde{\mathbf{x}}(t))}{d(\tilde{\mathbf{x}}^T(t)\mathbf{P}\tilde{\mathbf{x}}(t))} - \\
&2\alpha\|\tilde{\mathbf{x}}^T\mathbf{P}\mathbf{B}\|\text{tr}[\tilde{\boldsymbol{\theta}}^T\tilde{\boldsymbol{\theta}}\Lambda]
\end{aligned} \quad (68)$$

Using $\tilde{\boldsymbol{\theta}} = \tilde{\boldsymbol{\theta}} + \boldsymbol{\theta}$:

$$\begin{aligned}
\dot{V}(\tilde{\mathbf{x}}, \tilde{\boldsymbol{\theta}}) &= (-\tilde{\mathbf{x}}^T\mathbf{Q}\tilde{\mathbf{x}} + 2\tilde{\mathbf{x}}^T\mathbf{P}\boldsymbol{\zeta}) \frac{df(\tilde{\mathbf{x}}^T(t)\mathbf{P}\tilde{\mathbf{x}}(t))}{d(\tilde{\mathbf{x}}^T(t)\mathbf{P}\tilde{\mathbf{x}}(t))} - \\
&2\alpha\|\tilde{\mathbf{x}}^T\mathbf{P}\mathbf{B}\|\text{tr}[\tilde{\boldsymbol{\theta}}^T\tilde{\boldsymbol{\theta}}\Lambda] - 2\alpha\|\tilde{\mathbf{x}}^T\mathbf{P}\mathbf{B}\|\text{tr}[\tilde{\boldsymbol{\theta}}^T\boldsymbol{\theta}\Lambda]
\end{aligned} \quad (69)$$

Using the Frobenius norm and the Cauchy Schwartz inequality (56) and the upper bound of the external disturbance and unknown parameters Equation (57), we have the following inequality:

$$\begin{aligned}
\dot{V}(\tilde{\mathbf{x}}, \tilde{\boldsymbol{\theta}}) &\leq \\
&[-\lambda_{\min}(\mathbf{Q})\|\tilde{\mathbf{x}}\|^2 + 2\|\tilde{\mathbf{x}}\|\lambda_{\max}(\mathbf{P})\zeta_0] \frac{df(\tilde{\mathbf{x}}^T(t)\mathbf{P}\tilde{\mathbf{x}}(t))}{d(\tilde{\mathbf{x}}^T(t)\mathbf{P}\tilde{\mathbf{x}}(t))} - \\
&2\alpha\|\tilde{\mathbf{x}}^T\mathbf{P}\mathbf{B}\|\|\tilde{\boldsymbol{\theta}}\|_F^2\Lambda_{\min} + 2\alpha\|\tilde{\mathbf{x}}^T\mathbf{P}\mathbf{B}\|\|\tilde{\boldsymbol{\theta}}\|_F\|\boldsymbol{\theta}\|_F\|\Lambda\|_F
\end{aligned} \quad (70)$$

Using Equation (59) gives:

$$\begin{aligned}
\dot{V}(\tilde{\mathbf{x}}, \tilde{\boldsymbol{\theta}}) &\leq (-\lambda_{\min}(\mathbf{Q})\|\tilde{\mathbf{x}}\|^2 + \\
&2\|\tilde{\mathbf{x}}\|\lambda_{\max}(\mathbf{P})\zeta_0) \frac{df(\tilde{\mathbf{x}}^T(t)\mathbf{P}\tilde{\mathbf{x}}(t))}{d(\tilde{\mathbf{x}}^T(t)\mathbf{P}\tilde{\mathbf{x}}(t))} - \\
&2\alpha\|\tilde{\mathbf{x}}^T\mathbf{P}\mathbf{B}\|\|\tilde{\boldsymbol{\theta}}\|_F^2\Lambda_{\min} + \alpha\|\tilde{\mathbf{x}}^T\mathbf{P}\mathbf{B}\|(\|\tilde{\boldsymbol{\theta}}\|_F^2 + \\
&\|\boldsymbol{\theta}\|_F^2)\|\Lambda\|_F = (-\lambda_{\min}(\mathbf{Q})\|\tilde{\mathbf{x}}\|^2 + \\
&2\|\tilde{\mathbf{x}}\|\lambda_{\max}(\mathbf{P})\zeta_0) \frac{df(\tilde{\mathbf{x}}^T(t)\mathbf{P}\tilde{\mathbf{x}}(t))}{d(\tilde{\mathbf{x}}^T(t)\mathbf{P}\tilde{\mathbf{x}}(t))} - \\
&\alpha\|\tilde{\mathbf{x}}^T\mathbf{P}\mathbf{B}\|\|\tilde{\boldsymbol{\theta}}\|_F^2(2\Lambda_{\min} + \|\Lambda\|_F) + \\
&\alpha\|\tilde{\mathbf{x}}^T\mathbf{P}\mathbf{B}\|\|\boldsymbol{\theta}\|_F^2\|\Lambda\|_F
\end{aligned} \quad (71)$$

If we choose:

$$\begin{aligned}
-\lambda_{\min}(\mathbf{Q})\|\tilde{\mathbf{x}}\|^2 + 2\|\tilde{\mathbf{x}}\|\lambda_{\max}(\mathbf{P})\zeta_0 &\leq 0 \\
-\alpha\|\tilde{\mathbf{x}}^T\mathbf{P}\mathbf{B}\|\|\tilde{\boldsymbol{\theta}}\|_F^2(2\Lambda_{\min} + \|\Lambda\|_F) + \\
\alpha\|\tilde{\mathbf{x}}^T\mathbf{P}\mathbf{B}\|\|\boldsymbol{\theta}\|_F^2\|\Lambda\|_F &\leq 0
\end{aligned} \quad (72)$$

Or:

$$\begin{aligned}
\Omega = \{(\tilde{\mathbf{x}}, \tilde{\boldsymbol{\theta}}): \|\tilde{\mathbf{x}}\| < \frac{2\lambda_{\max}(\mathbf{P})\zeta_0}{\lambda_{\min}(\mathbf{Q})} \wedge \|\tilde{\boldsymbol{\theta}}\|_F \leq \\
\sqrt{\frac{\|\boldsymbol{\theta}\|_F^2\|\Lambda\|_F}{2\Lambda_{\min} + \|\Lambda\|_F}}\}
\end{aligned} \quad (73)$$

Same as the previous section, we have $\dot{V} \leq 0$ outside of the compact set Ω , and $\dot{V} > 0$ inside it, and all signals in the closed-loop system are uniformly ultimately bounded.

5. SIMULATIONS

5. 1. MRAC Scheme In this section, the validity of the proposed general MRAC adaptive law is verified by considering an arbitrary Lyapunov function candidate. The value of the control effectiveness (uncertainty) is chosen as:

$$d_0 = 1 \tag{74}$$

Considering The following initial conditions for the system states:

$$\begin{aligned} \phi_0 = 5 \text{ deg} \cdot P_0 = 0 \left(\frac{\text{deg}}{s}\right); \phi_0 = 3.75 \text{ deg} \cdot P_0 = \\ 0 \left(\frac{\text{deg}}{s}\right); \phi_0 = -3.75 \text{ deg} \cdot P_0 = 0 \left(\frac{\text{deg}}{s}\right); \phi_0 = \\ -5 \text{ deg} \cdot P_0 = 0 \left(\frac{\text{deg}}{s}\right) \end{aligned} \tag{75}$$

The reference roll dynamics can be considered in the state-space form:

$$\begin{bmatrix} \dot{\Phi}_m \\ \dot{P}_m \end{bmatrix} = \begin{bmatrix} 0 & 1 \\ -\omega_n^2 & -2\beta\omega_n \end{bmatrix} \begin{bmatrix} \Phi_m \\ P_m \end{bmatrix} + \begin{bmatrix} 0 \\ \omega_n^2 \end{bmatrix} r(t) \tag{76}$$

We use the following parameters for damping and natural frequency and adaptation gains:

$$\begin{aligned} \omega_n = -1. \quad \beta = 0.7 \\ \Gamma_r = 1. \quad \Gamma_x = \begin{bmatrix} 1 & 0 \\ 0 & 1 \end{bmatrix}. \quad \Gamma_\theta = \begin{bmatrix} 1 & 0 & 0 \\ 0 & 1 & 0 \\ 0 & 0 & 1 \end{bmatrix} \end{aligned} \tag{77}$$

Considering the scalar function:

$$f(u) = (1 + u)^{(1+u)^2} - 1 \quad u \geq 0 \tag{78}$$

The first derivative of this function becomes:

$$f'(u) = (1 + u)^{(1+u)^2} [(u + 1) + 2(u + 1)\text{Ln}(u + 1)] \tag{79}$$

It is clear that:

$$f(0) = 0 \text{ and } \forall u \geq 0. f'(u) > 0 \tag{80}$$

Given the fact that every quadratic term is equal or greater than zero, we use the following Lyapunov function candidate:

$$\begin{aligned} V = (1 + \tilde{x}^T(t)P\tilde{x}(t))^{(1+\tilde{x}^T(t)P\tilde{x}(t))^2} - 1 + \\ \text{tr}([\tilde{K}_x^T(t)\Gamma_x^{-1}\tilde{K}_x(t) + \tilde{K}_r^T(t)\Gamma_r^{-1}\tilde{K}_r(t) + \\ \tilde{\theta}^T(t)\Gamma_\theta^{-1}\tilde{\theta}(t)]\Lambda) \end{aligned} \tag{81}$$

According to Equation (33), we have the following adaptive laws:

$$\begin{aligned} \dot{\tilde{K}}_x(t) = -\Gamma_x \tilde{x}(t) \tilde{x}^T(t) P B [(1 + \\ \tilde{x}^T(t)P\tilde{x}(t))^{(1+\tilde{x}^T(t)P\tilde{x}(t))^2} \times (1 + \\ \tilde{x}^T(t)P\tilde{x}(t)) (1 + 2\text{Ln}(1 + \tilde{x}^T(t)P\tilde{x}(t)))] \\ \dot{\tilde{K}}_r(t) = -\Gamma_r r(t) \tilde{x}^T(t) P B [(1 + \\ \tilde{x}^T(t)P\tilde{x}(t))^{(1+\tilde{x}^T(t)P\tilde{x}(t))^2} \times (1 + \\ \tilde{x}^T(t)P\tilde{x}(t)) (1 + 2\text{Ln}(1 + \tilde{x}^T(t)P\tilde{x}(t)))] \end{aligned} \tag{82}$$

$$\begin{aligned} \dot{\tilde{\theta}}(t) = \Gamma_\theta \mu(\tilde{x}(t)) \tilde{x}^T(t) P B [(1 + \\ \tilde{x}^T(t)P\tilde{x}(t))^{(1+\tilde{x}^T(t)P\tilde{x}(t))^2} \times (1 + \\ \tilde{x}^T(t)P\tilde{x}(t)) (1 + 2\text{Ln}(1 + \tilde{x}^T(t)P\tilde{x}(t)))] \end{aligned}$$

Simulation results presented in Figures 5 to 8:

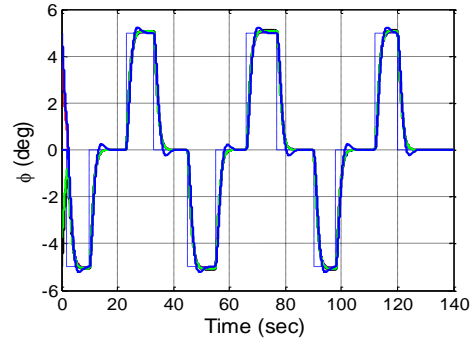


Figure 5. Roll Angle Tracking Performance

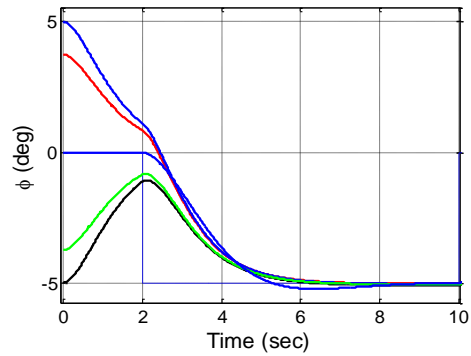


Figure 6. Zoomed Plot from Fig.1 (different initial conditions)

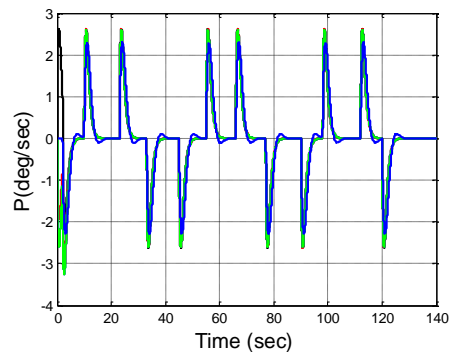


Figure 7. Roll Rate Tracking Performance

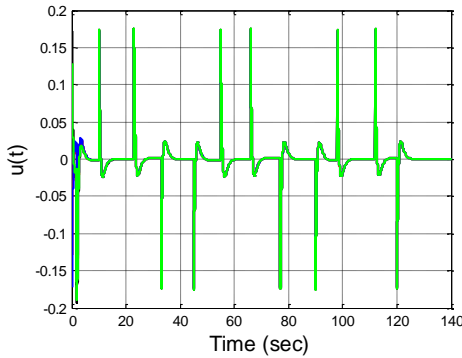


Figure 8. Control Signal (Maximum deflection (20 deg))

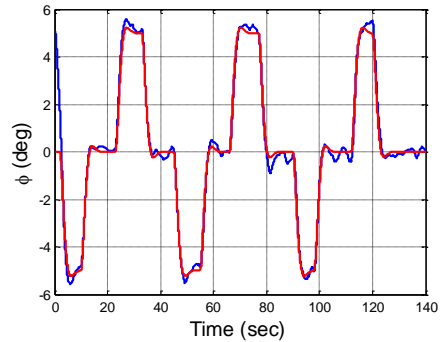


Figure 9. Roll Rate Tracking (σ -modification)

5. 2. Robust Mrac Schemes In this section, the performance of the robust MRAC controllers with general adaptive law by considering an arbitrary Lyapunov function is evaluated. We use the values of the parameters corresponding to $\alpha = 22.5$ deg (Table 1) and considering the following matrices \mathbf{Q} , $\mathbf{\Gamma}$ and modification parameter as follows:

$$\mathbf{Q} = \begin{bmatrix} 1 & 0 \\ 0 & 1 \end{bmatrix}, \mathbf{\Gamma} = \begin{bmatrix} 100 & 0 & 0 \\ 0 & 100 & 0 \\ 0 & 0 & 100 \end{bmatrix} \quad (83)$$

$$\sigma = 0.01, \alpha = 0.01$$

The external disturbance $\zeta(t)$ is modeled as a random process noise, uniformly distributed on the interval $\frac{\pi}{180}[-2 \ 2]$. We consider the following radially unbounded Lyapunov function as follows:

$$V(\tilde{\mathbf{x}}, \tilde{\boldsymbol{\theta}}) = (1 + \tilde{\mathbf{x}}^T(t)\mathbf{P}\tilde{\mathbf{x}}(t))^{(1+\tilde{\mathbf{x}}^T(t)\mathbf{P}\tilde{\mathbf{x}}(t))^2} - 1 + \text{tr}(\tilde{\boldsymbol{\theta}}^T\mathbf{\Gamma}^{-1}\tilde{\boldsymbol{\theta}}\boldsymbol{\Lambda}) \quad (84)$$

Consequently, from Equation (47), we have the following adaptation law for σ – modification scheme:

$$\begin{aligned} \dot{\tilde{\boldsymbol{\theta}}} = & \mathbf{\Gamma}(\boldsymbol{\mu}(\mathbf{x})\tilde{\mathbf{x}}^T\mathbf{P}\mathbf{B}\left(1 + \right. \\ & \left. \tilde{\mathbf{x}}^T(t)\mathbf{P}\tilde{\mathbf{x}}(t)\right)^{(1+\tilde{\mathbf{x}}^T(t)\mathbf{P}\tilde{\mathbf{x}}(t))^2} \left(1 + \tilde{\mathbf{x}}^T(t)\mathbf{P}\tilde{\mathbf{x}}(t)\right) \left(1 + \right. \\ & \left. 2\text{Ln}\left(1 + \tilde{\mathbf{x}}^T(t)\mathbf{P}\tilde{\mathbf{x}}(t)\right)\right) - \sigma\tilde{\boldsymbol{\theta}}) \end{aligned} \quad (85)$$

According to Equation (63), we have the following adaptation law for e – modification:

$$\begin{aligned} \dot{\tilde{\boldsymbol{\theta}}} = & \mathbf{\Gamma} \left(1 + \tilde{\mathbf{x}}^T(t)\mathbf{P}\tilde{\mathbf{x}}(t)\right)^{(1+\tilde{\mathbf{x}}^T(t)\mathbf{P}\tilde{\mathbf{x}}(t))^2} \left(1 + \right. \\ & \left. \tilde{\mathbf{x}}^T(t)\mathbf{P}\tilde{\mathbf{x}}(t)\right) \left(1 + 2\text{Ln}\left(1 + \right. \right. \\ & \left. \left. \tilde{\mathbf{x}}^T(t)\mathbf{P}\tilde{\mathbf{x}}(t)\right)\right) (\boldsymbol{\mu}(\mathbf{x})\tilde{\mathbf{x}}^T\mathbf{P}\mathbf{B} - \alpha\|\tilde{\mathbf{x}}^T\mathbf{P}\mathbf{B}\|\tilde{\boldsymbol{\theta}}) \end{aligned} \quad (86)$$

Simulation results presented in Figures 9 to 16:

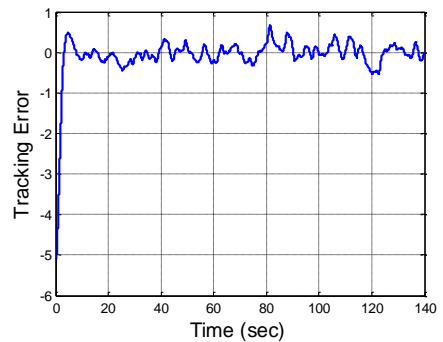


Figure 10. Roll Angle Tracking error

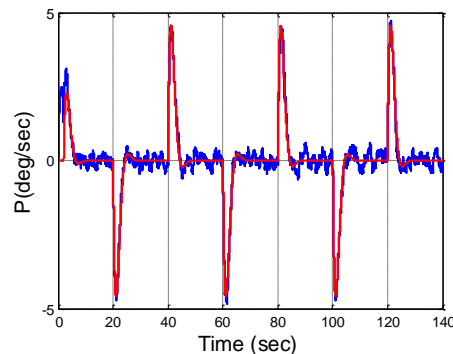


Figure 11. Roll Rate Tracking Performance (σ -modification)

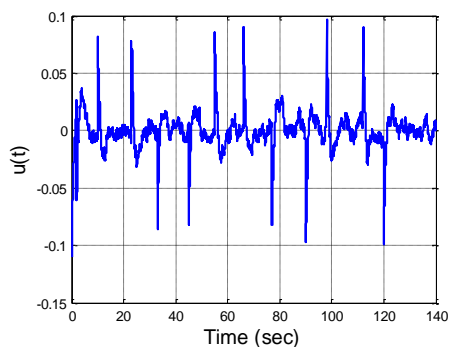


Figure 12. Control Signal

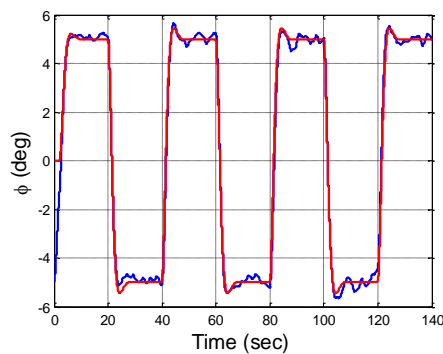


Figure 13. Roll Angle Tracking (e-modification)

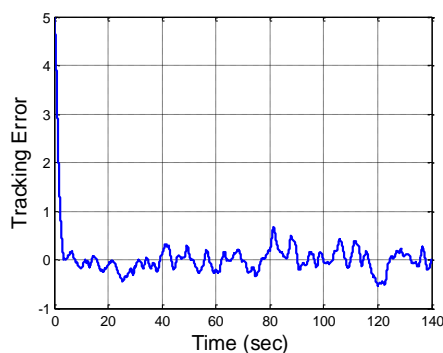


Figure 14. Roll Angle Tracking error

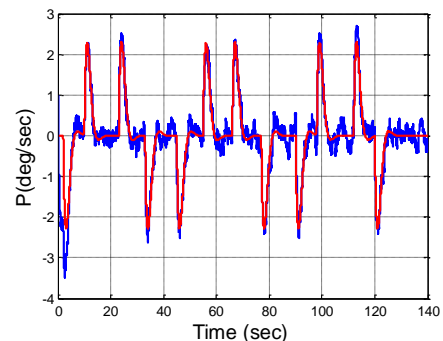


Figure 15. Roll Rate Tracking Performance (e-modification)

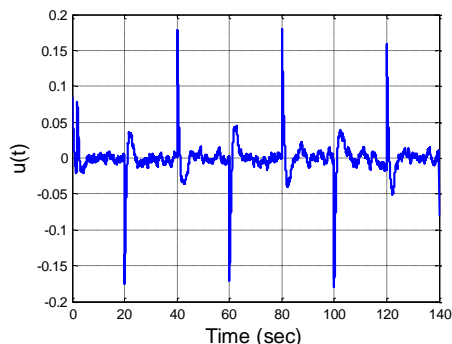


Figure 16. Control Signal

6. CONCLUSION

In this study, we proposed a general adaptive laws for MRAC and Robust MRAC schemes. In the simple MRAC structure, the adaptive laws derived from these type of Lyapunov function could be considered as an adaptive law which derived from common quadratic Lyapunov function with variable adaptation gains. This method can be applied to design Dead-zone modification and projection-based MRAC systems. The proposed Lyapunov function can be applied to design adaptive controllers designed by the Lyapunov's direct method.

7. REFERENCES

- Gursul, I., Wang, Z., "Flow control of tip/edge vortices", *AIAA Journal*, Vol. 56, No. 5, (2018), 1731-1749, doi: 10.2514/1.J056586.
- Chen, K., Dong, Y., Shi, Z., Tong, S. X., & Sha, J., "Experimental Study of the Suppression of Wing-Body Rock by Spanwise Blowing" In 2019 IEEE 10th International Conference on Mechanical and Aerospace Engineering (2019), 142-146. Doi: 10.1109/ICMAE.2019.8880951.
- Katz, J., "Wing/vortex interactions and wing rock", *Progress in Aerospace Sciences*, Vol. 35, No. 7, (1999), 727-750, doi: 10.1016/S0376-0421(99)00004-4.
- Ma, B. F., Wang, Z., Gursul, I. "Symmetry breaking and instabilities of conical vortex pairs over slender delta wings", *Journal of Fluid Mechanics*, Vol. 832, (2017), 41-72, doi: 10.1017/jfm.2017.648.
- Ma, B., Deng, X., Wang, B., "Effects of wing locations on wing rock induced by forebody vortices", *Chinese Journal of Aeronautics*, Vol. 29, No. 5, (2016), 1226-1236, doi: 10.1016/j.cja.2016.08.004.
- Gursul, I., Xie, W., "Origin of vortex wandering over delta wings", *Journal of Aircraft*, Vol. 37, No. 2, (2000), 348-350, doi: 10.2514/2.2603.
- Ericsson, L. E., "Various sources of wing rock", *Journal of Aircraft*, Vol.27, No. 6, (1990), 488-494, Doi: 10.2514/3.25309.
- Jun, Y.W., Nelson, R.C., "Leading-edge vortex dynamics on a slender oscillating wing", *Journal of Aircraft*, Vol. 25, No. 9, (1988), 815-819, doi: 10.2514/3.45664.
- Nguyen, L., Yip, L., Chambers, J., "Self-induced wing rock of slender delta wings", In *7th Atmospheric Flight Mechanics Conference*, (1981), 1883, doi: 10.2514/6.1981-1883.
- Ma, B. F., Wang, B., Deng, X. Y., "Effects of Reynolds numbers on wing rock induced by forebody vortices", *AIAA Journal*, Vol. 55, No. 9, (2017), 2980-2991, doi: 10.2514/1.J055461.
- Hsu, C. H., Lan, C. E., "Theory of wing rock", *Journal of Aircraft*, Vol. 22, No. 10, (1985), 920-924, doi: 10.2514/3.45225.
- Nayfeh, A. H., Elzebda, J. M., Mook, D. T., "Analytical study of the subsonic wing-rock phenomenon for slender delta wings", *Journal of Aircraft*, Vol. 26, No. 9, (1989), 805-808, doi: 10.2514/3.45844.
- Elzebda, J. M., Nayfeh, A. H., Mook, D. T., "Development of an analytical model of wing rock for slender delta wings", *Journal of Aircraft*, Vol. 26, No. 8, (1989), 737-743, doi: 10.2514/3.45833.
- Go, T. H., "Aircraft wing rock dynamics and control", Doctoral Dissertation, Massachusetts Institute of Technology, (1999).

15. Hsu, C. F., Lin, C. M., Chen, T. Y., "Neural-network-identification-based adaptive control of wing rock motions", *IEEE Proceedings-Control Theory and Applications*, Vol. 152, No.1, (2005), 65-71, doi: 10.1049/ip-cta:20050904.
16. Liu, Z. L., "Reinforcement adaptive fuzzy control of wing rock phenomena", *IEEE Proceedings-Control Theory and Applications*, Vol. 152, No. 6, (2005), 615-620, doi: 10.1049/ip-cta:20045072.
17. Tao, C. W., Taur, J. S., Chang, C. W., Chang, Y. H., "Simplified type-2 fuzzy sliding controller for wing rock system", *Fuzzy Sets and Systems*, Vol. 207, (2012), 111-129, doi: 10.1016/j.fss.2012.02.015.
18. Lin, C. M., Hsu, C. F., "Supervisory recurrent fuzzy neural network control of wing rock for slender delta wings", *IEEE Transactions on Fuzzy Systems*, Vol. 12, No. 5, (2004), 733-742, doi: 10.1109/TFUZZ.2004.834803.
19. Monahemi, M., Barlow, J., Krstic, M., "Control of wing rock motion of slender delta wings using adaptive feedback linearization", In Guidance, Navigation, and Control Conference, (1995), 3344, doi: 10.2514/6.1995-3344.
20. Araujo, A. D., Singh, S. N., "Variable structure adaptive control of wing-rock motion of slender delta wings", *Journal of Guidance, Control, and Dynamics*, Vol. 21, No. 2, (1998), 251-256, doi: 10.2514/2.4250.
21. Arab Markadeh, G. R., Soltani, J., "A Current-Based Output Feedback Sliding Mode Control for Speed Sensorless Induction Machine Drive Using Adaptive Sliding Mode Flux Observer", *International Journal of Engineering, Transactions A: Basics*, Vol. 19, No. 1, (2006), 21-34.
22. Karami-Mollae, A., "Adaptive Fuzzy Dynamic Sliding Mode Control of Nonlinear Systems", *International Journal of Engineering, Transactions B: Applications*, Vol. 29, No. 8, (2016) 1075-1086, doi: 10.5829/idosi.ije.2016.29.08b.07.
23. Sadeghijaleh, M., Fateh, M.M., "Adaptive Voltage-based Control of Direct-drive Robots Driven by Permanent Magnet Synchronous Motors", *International Journal of Engineering, Transactions A: Basics*, Vol. 30, No. 4, (2017), 507-515, doi: 10.5829/idosi.ije.2017.30.04a.08.
24. Malekzadeh, M., Shahbazi, B., "Robust Attitude Control of Spacecraft Simulator with External Disturbances", *International Journal of Engineering, Transactions A: Basics*, Vol. 30, No. 4, (2017), 567-574, doi: 10.5829/idosi.ije.2017.30.04a.15.
25. Gholipour, R., Fateh, M. M., "Designing a Robust Control Scheme for Robotic Systems with an Adaptive Observer", *International Journal of Engineering, Transactions B: Applications*, Vol. 32, No. 2, (2019), 284-291, doi: 10.5829/ije.2019.32.02b.12.
26. Manouchehri, P., Ghasemi, R., Toloee, A., "Distributed Fuzzy Adaptive Sliding Mode Formation for Nonlinear Multi-quadrotor Systems", *International Journal of Engineering, Transactions B: Applications*, Vol. 33, No. 5, (2020), 798-804, doi: 10.5829/IJE.2020.33.05B.11.
27. Rao, M. P. R. V., "Non-quadratic Lyapunov function and adaptive laws for model reference adaptive control", *Electronics Letters*, Vol. 34, No. 23, (1998), 2278-2280, doi: 10.1049/el:19981503.
28. Hassan, H. A., Rao, M. P. R. V., "Novel Robust Adaptive Control Scheme Using Non-Quadratic Lyapunov Functions For Higher Order Systems", In EUROCON The International Conference on Computer as a Tool IEEE (2005), Vol. 1, 286-289, doi: 10.1109/EURCON.2005.1629917.
29. Hosseinzadeh, M., Yazdanpanah, M. J., "Performance enhanced model reference adaptive control through switching non-quadratic Lyapunov functions", *Systems & Control Letters*, Vol. 76, (2015), 47-55, doi: 10.1016/j.sysconle.2014.12.001.
30. Lavretsky, E., Wise, K.A., "Robust and adaptive control", Springer, London, (2013), doi: 10.1007/978-1-4471-4396-3.

8. APPENDIX

8.1. Appendix A Let $\phi \neq M \subset \mathbb{R}^n$ be an open set, Let $\phi \neq N \subset M$ be a compact and convex set and let $f \in C^1(M, \mathbb{R})$ be a function. We prove that f is Lipschitz on N , in other words there exists $\alpha > 0$ such that

$$|f(x) - f(y)| \leq \alpha \|x - y\| \quad \forall x, y \in N \quad (\text{A.1})$$

By definition:

$$\rho(t): [0,1] \rightarrow N \quad (\text{A.2})$$

ρ is the line segment between x, y . so we have:

$$\rho(0) = x \quad (\text{A.3})$$

$$\rho(1) = y \quad (\text{A.4})$$

$$\rho'(t) = (y - x) \quad (\text{A.5})$$

Since N is convex so $\rho(t)$ lies entirely in N , hence in M . For $x, y \in N$ we have:

$$\|f(y) - f(x)\| = \left\| \int_0^1 \frac{df(\rho(t))}{dt} dt \right\| \cdot \left\| \int_0^1 \nabla f(\rho(t)) \rho'(t) dt \right\| \leq \int_0^1 \|\nabla f(\rho(t)) \rho'(t)\| dt \leq \int_0^1 \|\nabla f(\rho(t))\| \|\rho'(t)\| dt \quad (\text{A.6})$$

Since N is compact and $\nabla f \in C^0(M, \mathbb{R})$ so $\nabla f \in C^0(N, \mathbb{R})$, $\|\nabla f\|$ is bounded by some α on N so:

$$\int_0^1 \|\nabla f(\rho(t))\| \|\rho'(t)\| dt \leq \int_0^1 \alpha \|\rho'(t)\| dt \quad (\text{A.7})$$

Using (A.5) yields:

$$\int_0^1 \alpha \|\rho'(t)\| dt = \int_0^1 \alpha \|y - x\| dt = \alpha \|y - x\| \quad (\text{A.8})$$

Using (A.6), (A.7), and (A.8) yields:

$$\|f(y) - f(x)\| \leq \alpha \|y - x\| \quad (\text{A.9})$$

8.2. Appendix B

By definition:

$$[a, b] = \frac{f(a) - f(b)}{a - b} \quad (\text{B.1})$$

Using mean-value theorem yields:

$$\tau \in (a, b) \rightarrow f'(\tau) = [a, b] \quad (\text{B.2})$$

For $a < b < c$ we have:

$$|[a, b] - [b, c]| = |f'(\tau_1) - f'(\tau_2)| \leq L|a - c| \quad (\text{B.3})$$

Which proves boundedness of second-time derivative or 2-Lipschitz continuity of the function f .

Persian Abstract

چکیده

روش مستقیم لیاپانف یک از ابزارهای مهم طراحی سیستم های تطبیقی مدل مرجع و تطبیقی مقاوم می باشد. در حالت کلی تابع لیاپانف کاندید شامل ۲ دسته از عبارت های مربعی می باشد. اولین دسته شامل خطای تعقیب حالت و یا در حالت های خاص شامل حالت سیستم می باشد. دسته دوم شامل عبارت های مربعی خطای تخمین پارامترهای کنترلر می باشد. برای طراحی سیستم های تطبیقی مدل مرجع و تطبیقی مقاوم پژوهشگران تنوع محدودی در انتخاب توابع مربعی به کار برده اند. در این پژوهش، یک حالت کلی برای عبارت مربعی شامل متغیر خطای حالت تعقیب در نظر می گیریم. یک تابع دلخواه اکیدا صعودی که متعلق به توابع کلاس C^1 بوده و تابعی از چند جمله ای های مربعی خطای تعقیب حالت بوده در نظر گرفته می شود. با این انتخاب یک ساختار کلی برای قوانین تطبیق پارامترهای کنترلر بدست آورده می شود. برای سیستم مدل مرجع اثبات پایداری مجانبی فراگیر سیستم حلقه بسته و برای الگوریتم های تطبیقی مقاوم اثبات پایداری و ردیابی یکنواخت کراندار تضمین می گردد. در نهایت با هدف ارزیابی عملکرد کنترلرهای طراحی شده سیستم یک درجه آزادی پدیده وینگ راک در نظر گرفته شده است.



Regression Modeling and Process Analysis of Plug and Spot Welds Used in Automotive Body Panel Assembly

T. Saeheaw*

Department of Teacher Training in Mechanical Engineering, Faculty of Technical Education, King Mongkut's University of Technology North Bangkok, Bangkok, Thailand

PAPER INFO

Paper history:

Received 30 May 2020

Received in revised form 06 August 2020

Accepted 03 September 2020

Keywords:

Automotive Body Panel

Genetic Algorithm

Plug Weld

Spot Weld

Tensile Strength

ABSTRACT

Resistance spot welding is the primary welding process used in automotive body panel assembly. However, plug welding is widely used in automotive body repair due to its technical simplicity and cost benefits. In this paper, spot welding and plug welding using Tungsten Inert Gas (TIG) welding of an automotive body panel are compared. TIG welding is selected for plug welding because it offers the greatest flexibility to weld the widest range of materials, thicknesses, and types. The base material used in this study is JIS G3141 SPCC. Full factorial experimental design coupled with statistical and graphical analysis of the results using analysis of variance was applied to determine the significance of process parameters. Parameter interactions were investigated using regression analysis, model adequacy checks, and determination of optimum conditions. A genetic algorithm is used to predict the optimum combination of the process parameters to realize the highest strength level. For tensile-shear strength, the experimental results demonstrate that plug welding has a higher maximum load than spot welding. The optimum plug welding joints were obtained at a hole diameter of 9 mm and a welding current of 136 kA, with a maximum load of 8.2 kN. The maximum load of the spot weld joint, 7.4 kN, was found at a welding current of 70 kA, an electrode force of 0.25 MPa, and 10 cycles of welding time.

doi: 10.5829/ije.2020.33.11b.29

1. INTRODUCTION

Joining is a pivotal characteristic in automobile design. Generally, joints represent the weakest areas in an automobile's structure and often represent the initiation location for failures in service. Strength of the joints often determines the reliability and quality of a manufactured product. The development and application of new materials, compounded with welding optimization and structural optimization design, has allowed automobile body manufacturing technology to secure sufficient rigidity and safety performance. Nonetheless, in cases in where damage is caused by collisions, body damage restoration technology sees itself exceeded by the manufacturer's body manufacturing technology. The efficiency of body damage restoration technology is highly dependent on

an expert's skill and cannot be accessed quantitatively and objectively [1].

We can distinguish between the following processes in body repair work: (1) damage analysis and diagnosis, (2) measurement and correction of the vehicle system, (3) panel replacement and correction, (4) painting and rust prevention, and (5) technical analysis. Appropriate equipment is used in all processes. Body repair work highly relies on the method and type of welding. In order to guarantee the safety of a vehicle in operation, an optimized repair technique should take into consideration both welding and structural characteristics [2].

Spot welding is viable for short-time welds. Spot welding allows a small area to be heated, making heat deformation a negligible part of the process. Moreover, reproducibility of the weld's quality is excellent. Nonetheless, the welded material and its thickness must be taken into consideration. In order to join metals together, it is important to apply pressure at both sides

*Corresponding Author Institutional Email:
teerapun.s@fte.kmutnb.ac.th (T. Saeheaw)

of the joint, thus causing localized heating at the interface [3]. The safety design and durability of a vehicle are significantly affected by the failure performance and characteristics of spot welds. Even though spot welding is not extensively used, plug welding is commonly used as well. Plug welding uses a weld metal to fill a hole in the middle of a panel. The first step is to make a round hole in the outer sheet. Next, the hole is filled with a weld metal and panels are joined using arc spot welding, also called argon gas (Ar) welding. With plug welding, joining through one side of the panel becomes possible, thus making the usable range wider than the one achieved through spot welding [4]. Nonetheless, both spot and plug welding can be done regardless of the workpiece's position. While the load caused by a motor vehicle accident damages the vehicle body panel, weld seam damages are often generated by the action of shear loading.

2. LITERATURE REVIEW

RSW (Resistance spot welding) is the dominant process used to join thin sheet steel metal components by fusing discrete spots at the interface of a workpiece utilized for low-carbon steel body construction in crash repair and automotive production. A reliable, cost-effective, rapid, and automated process, RSW does not require noticeable operator skills. Nonetheless, RSW has a major flaw, i.e., inconsistency of quality from weld to weld. The complexity generated by numerous sources of variability increases production costs, complicates automation, and reduces weld quality [5]. Consequently, the parameters that affect weld quality must be determined and controlled.

When using RSW, electric current passes through two electrodes. Sheets are locally joined by their liquid phases produced due to Joule heating (I^2R), a process that generates melting and the production of a nugget. During the welding operation, the sheets are held together by the pressure from the electrode tips, creating fusion bonding at the atomic level between the materials. The joint forms when the fusion-bonded liquid phase cools under pressure. A typical fusion weld consists of the heat-affected zone and the fusion zone. RSW involves various parameters that can influence the mechanical performance and weldability of weldments. The weld nugget and the nugget's strength are controlled by weld parameters that significantly affect the weld quality. These parameters include electrode force, weld current, and welding time [6]. The Precision Metalforming Association provides not only valuable information about these dimensions but also straightforward guidance on the material types for spot welds. The nugget is also influenced by the electron tip design and the surface conditions set between the sheets. The diameter of the weld nugget is usually less

than the diameter of the impressions electrodes create on the material. Nonetheless, standards vary in regard to the range of parameters that are usually applied for specific materials. When a new RSW process is set up, it is necessary to set optimum parameters using a standard as a guideline. It is also necessary to verify the weld quality by destructive testing. The strength of a single spot-welded lap joint depends on properties of the base material and welding parameters. These factors influence the welds' mechanical behavior [7-9].

If certain conditions are met, using plug welds can be more advantageous than other types of welds [10]. The use of plug-welded joints is very popular in steel structures. An alternative to spot welding, plug welding is used by vehicle manufacturers if there is not sufficient access for a spot welder (i.e. double-sheeting structures, constructions with a profile stiffener, and complex structures). When plug welding is used, the connection is produced by the weld in the contact surface of adjoining parts and on the walls of circular openings. If done properly, plug welds can be stronger than the initial spot welds. In DIY (do it yourself) car restoration, plug welding is used instead of spot welding. It is usually done on panel flanges that have been initially spot-welded. This weld type is notably suitable in difficult maintenance conditions of welded constructions. Usually, plug welds are applied at the centre of doubler plates for lap joints. One of the doubler plates has round holes. Typically, welds start around the perimeter of the hole and spiral to the centre, using either another member behind the hole or backing. This type of welds avoids the buckling of lapped parts and transfers load by shear. In this type of welding, uniform fusion to the roots of the joints is required. To form the joint, weld metal is placed in the holes, penetrating and fusing with the base metal of the members. In order for the adjacent weld to easily melt the slag, the weld must be done quickly. Nonetheless, slag inclusions are commonplace. Weld shrinkage during cooling and solidification is one of the biggest problems with plug welds. This shrinkage produces significant residual stresses at the centre of the plug, which solidifies last. This causes micro-cracks in the original weld, alongside near-yield point residual stresses that could trigger cracking as a consequence of the applied stresses on the structure. The applied stresses are considerably less than the anticipated fatigue limit.

Rolls-Royce Motors² highly recommends the use of RSW, TIG welding, and metal inert gas (MIG) in the replacement of underframe and body panels. In MIG welding, a reel of filler wire is fed continuously by means of a welding torch under a shield of inert gas.

² <http://heritage.bentleymotors.com/en/technical-library/download/TSD4600.pdf>. Accessed 19 October 2019

The weld is protected from the atmosphere by the gas that surrounds the weld pool and the arc. When used for body repair work, MIG welding provides an important advantage: it generates a limited heated weld area. As a consequence, the distortion and contraction stresses are minimal. MIG welding equipment is suitable for intermittent, continuous, and plug welds. In order to achieve an adequate weld, it is necessary to clean to bare metal the areas of the panels that need to be welded. Additionally, any trace of sealing materials, grease, or paint needs to be removed. In the case of TIG welding, a tungsten electrode is attached to the welding torch. The torch supplies the inert gas to the weld area, while the filler wire is fed manually. The weld is protected from the atmosphere by the gas that surrounds the weld pool and the arc. Among all the welding processes, TIG welding is the most flexible. It produces the best-penetrating and cleanest welds, can be used on any type of material, and enables more control over the way the weld lays down. In the case of stick welding or MIG welding, the filler material functions as the electrode, i.e., it continuously feeds filler material inside the puddle. As opposed to other welding processes, the use of TIG welding allows welders to slow down, use filler, and work the puddle until they achieve the size and the look of weld they need. Apart from controlling the amount of added filler, welders can also control how much heat is put into the workpiece. This could turn into a significant advantage in those situations in which welders need to bridge a large gap and must add a considerable amount of filler material. In this context, the weld moves along gradually and begins to overheat. This allows welders to back off the pedal while still maintaining the arc and gas coverage, cool down the puddle, and continue welding. As a result, TIG welding is particularly suitable for filling holes, doing build-ups, and plug welding. Additionally, TIG welds are usually softer than stick welds or MIG welds. It can be concluded that TIG welds can be hammered, ground, and formed more easily. If a welder is working with sheet metal and needs to hammer around a welded area, this area is significantly less likely to crack. Since the weld nugget is more malleable, it is easier to manage. TIG welding is preferable because it grants increased control over the weld and the possibility to input less heat. Many experiments frequently use TIG welding process parameters such as welding speed, welding current, and filler diameter [11-14].

The plug welding schedule was provided by previous studies [15] and the American Welding Society [16]. According to AASHTO/AWS D1.5M/D1.5: 2002, the plug weld hole diameter must be $8 + t$ (mm) to achieve weld quality, where t represents thickness of the joined plate (mm). Finding valuable weld schedules for equal-thickness welding is extremely useful. Plug weld quality is significantly

affected by important factors such as the area of weld penetration, depth, and strength [17]. Nonetheless, the studies that have focused on plug welding are not abundant [2, 10, 18, 19]. In order to establish plug weld quality, the welds must be loaded in shear while the parts undergo tension loading. In particular cases, the welds can be loaded in tension, with the direction of loading being normal to the joint's plane, or a combination of shear and tension [20].

Strength testing plays an important role within a weldability study and represents an evaluation method as regards automobile body assembly. Among all the tests used to establish weld strength, static tensile-shear testing is by far the most frequent laboratory test. This happens because of its simplicity in specimen testing and fabrication [21]. The tensile-shear testing of a single lap joint workpiece distinguishes from standard homogeneous material testing. According to Zhang and Senkara [3], the results of the tensile test of the weld specimens are not shown in terms of tensile strength (MPa) but as tensile load at break (kN). It was found that specimen width is the most important factor that influences tensile-shear testing. It suffices with an overlap equal to the specimen width [21]. Even though the specimen length plays a less important role, the specimen must be long enough to enable clamping during testing. It was determined that a length of 150 mm is sufficient for all feasible widths [21]. Generally, in the steel and automotive industries, the diameter of a minimum acceptable nugget should range between $4t/2$ and $5t/2$, where t represents the nominal thickness of the sheet in mm [1].

More than often, the experimental optimization of a welding process proves to be a time-consuming and costly task. To solve this problem, the response optimizer method is widely used to determine the group of input variable settings that mutually optimize a set of responses. A full factorial design can trigger optimum process parameters without the need to derive a model for the welding process. Nonetheless, the increase in the number of input parameters leads to an exponential increase in the number of experiments, thus causing the full factorial method to become unrealistic [22]. Recent studies have attempted to address these problems by bringing forth a new approach to experimental optimization [22-24].

The aim of this study is to highlight the importance of the employed welding methods in restoring a damaged vehicle body. Research led into automobile body panel welding focuses chiefly on spot welding and its application in the production process. Plug welding is consistently used to repair damaged automobile body panels. Consequently, this study investigates the degree to which weld quality is influenced by welding parameters on weld quality.

3. METHODOLOGY

3. 1. Experimental Setup Generally, automobile parts use steel sheets of 0.6–2.0 mm thick. The present study focuses on the tensile test of a 1.2 mm thick steel sheet using JIS G3141 SPCC as a base material. JIS G3141 SPCC is a commercial cold-rolled low-carbon steel. SPCC steel is characterized by high weldability and formability. This type of steel is widely used in general applications, frequently in vehicle structures and panels, and significantly in the production of automobile parts (e.g. hoods, roofs, fenders, quarter panels, spring housings, oil pans). See Tables 1 and 2 for the chemical composition of the base material and its mechanical properties.

Test sheets (30 mm wide, 100 mm long) were prepared to comply with the JIS Z3136-1999 standard. Two sheets, with lap joints at the center of the sheets, were stacked and fabricated. As shown in Figure 1, the overall length of the joint part measured 170 mm and the overlap length was 30 mm. In order to determine their failure mode and strength, the welded joints underwent static tensile-shear tests.

3. 2. Spot Weld Procedure Spot welding was done using a TATASU spot welding machine (TOASEIKI SLP-50A5) and a truncated copper electrode with a face diameter of 6.5 mm. The welds were done at room temperature, in open air. Prior to welding, the surfaces of the steel sheets have been

TABLE 1. Chemical composition of JIS G3141 SPCC

C	Mn	P	S
0.04	0.20	0.015	0.006

TABLE 2. Mechanical properties of JIS G3141 SPCC

0.2YS (MPa)	UTS (MPa)	Elongation (%)
164	316	46

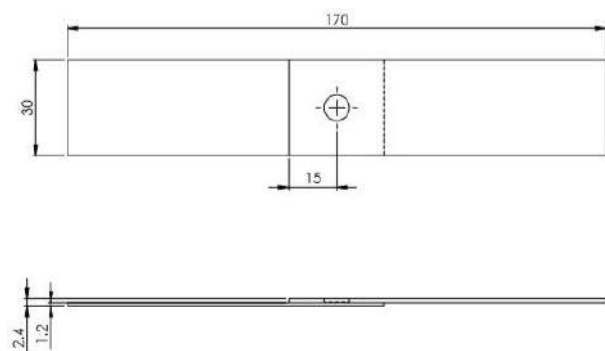


Figure 1. Dimensions of tensile test specimens (mm)

cleaned to remove dust, oxides, and grease. This was done to facilitate consistent spot weld quality.

3. 2. 1. Factorial Designs A brainstorming session with personnel from maintenance, quality, design, shop floor, and production was run to identify the process parameters. See Table 3 for the used parameters and their levels.

Therefore, in compliance with the design-of-experiments approach according to which the number of experiments is determined by a full factorial design, various “n = 3” parameters generated eight experiments structured into two levels. To enhance the reliability of the results, we made three replicates that resulted in 24 experiments. The process involved varying the welding time between 8 and 10 cycles, the electrode force between 0.20 and 0.25 Mpa, and the welding current between 70 and 75 kA. For static tensile-shear strength testing, both control factors (i.e. the hold time and the squeeze time) were kept constant at 20 cycles. Figure 2 shows the spot weld specimens of weld-bonded joints before the tensile-shear test.

3. 3. Plug Weld Procedure Prior to welding, the plug-welded joints had to be centered on a 30 mm overlap region. To facilitate TIG plug welding, the outer sheet in all specimens was drilled to obtain round holes. The sheet was afterwards clamped to the back sheet. Binder filling into the hole was used to form the joint. Two low-carbon steel sheets (1.2 mm thick, JIS G3141 SPCC) were plug-welded employing a Panasonic TIG welding machine with argon gas (TIG MINI 150). Due to its extensive industrial application, ER70S-6 filler metal was selected. In compliance with the AWS Specification for Carbon Steel Electrodes and Rods for Gas Shielded Arc Welding (A5.18-2005), ER70S-6 is utilized with thin to medium plate joints. Table 4 lists the standard mechanical properties of the weld metal in the as-welded condition and the standard chemical composition of the solid wire in accordance with AWS requirements.

3. 3. 1. Factorial Designs A brainstorming session with personnel from maintenance, quality, design, shop floor, and production was run to identify the process parameters. The aim of the experiment was to determine the key factors and their possible interactions that affect maximum load. Studying each

TABLE 3. Control factors and their levels used in spot weld

Symbol	Factor (unit)	Level 1	Level 2
A	Welding Current (kA)	70	75
B	Electrode Force (Mpa)	0.2	0.25
C	Welding Time (cycle)	8	10

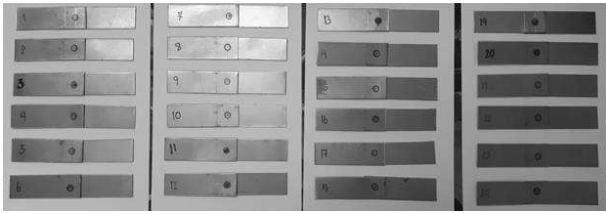


Figure 2. Prepared spot weld specimens before tensile-shear test

parameter involved three levels of control: high, medium, and low. In order to obtain a precise assessment of experimental error (or error variance), each trial condition was repeated three times.

The 3² full factorial designs with 3 replications were constituted by twenty-seven weld experiments. The hole diameter varied in a 7-9 mm range and weld current varied in a 100-140 kA range (see Table 5). The diameter of the welding wire and the gas flow rate were kept constant at 1.2 mm and 6 l/s, respectively, during all static tensile-shear strength tests. Figure 3 shows the plug weld specimens of weld-bonded joints prior to tensile-shear test.

3. 4. Tensile-shear Test As Figure 4 shows, in the tensile-shear test, specimens were clamped to a 50 kN Instron universal test machine (Model 5569). The crosshead velocity of 30 mm/min was kept constant, until the final failure of the joint. Maximum load is the most monitored variable in tensile-shear testing [21]. The specimens' failure modes were determined by analyzing the fractured samples.

TABLE 4. Typical chemical and mechanical properties of ER70S-6 in accordance with AWS requirements

C%	0.06-0.15
Si%	0.80-1.15
Mn%	1.40-1.85
P%	0.025 max.
S%	0.035 max.
Cu%	0.50 max.
0.2% OS (MPa)	400 min.
TS (MPa)	480 min.
EI (%)	22 min.
IV (J)	27 min.

TABLE 5. Plug welding control factors and levels

Symbol	Factor (unit)	Level 1	Level 2	Level 3
X	Hole Diameter (mm)	7	8	9
Y	Welding Current (kA)	100	120	140



Figure 3. Prepared plug weld specimens before tensile-shear test



Figure 4. Tensile test machine

3. 5. Regression Analysis A regression model corresponding to the subsequent second-order response function was used to perform a multiple regression analysis [25]:

$$y = \beta_0 + \sum_{i=1}^k \beta_i x_i + \sum_{i=1}^k \beta_{ii} x_i^2 + \sum_{j < i} \beta_{ij} x_i x_j + \varepsilon \tag{1}$$

where β_{ij} , β_{ii} , β_i and β_0 are the coefficients of interaction, quadratic, linear, and intercept variables respectively; y is the response or the dependent variable; x_j and x_i are the independent variables in the coded unit; and ε is the error term that justifies the effects of excluded parameters. The following equation was used for coding [25]:

$$x = \frac{X - (X_{high} + X_{low})/2}{(X_{high} - X_{low})/2} \tag{2}$$

where X is the natural variable, X_{low} and X_{high} are the low and high values of the natural variables, and x is the coded variable. During the analysis, the coefficients that triggered Equation (1) to fit better a set of recollected response variable data acquired from the optimization experiments were established using regression analysis in Minitab. This, effectively generated a regression model that describes the statistical relationship between the response variable and the predictors, and eliminating those predictors

whose statistical relationship with the response variables is not significant. Nonetheless, since the unimportant factor is part of a higher-order term, it was also included.

The model adequacy assessment aims at determining the extent to which all the test data and models agree. The model adequacy was analyzed using a standard probability plot of standardized residuals. Additionally, the global fit of the model was tested through the evaluation of the coefficient of determination (R^2).

3. 6. Optimum Welding Parameters

The Minitab optimization feature was employed to establish the optimum welding parameters. Despite the investigations and analyses that were conducted on the response optimizer, estimating the optimized combination of process parameters that allows for the highest possible strength level of the weld strength can be a demanding task. The present study has adopted a GA approach to achieve the optimum combination of process parameters under specific constraints and obtain the highest strength level. GA-based optimization is structured as follows.

Step 1: Create an initial chromosome population arbitrarily.

Step 2: Decode all the chromosomes' genes. For plug welding: (1) welding current, (2) hole diameter. For spot welding: (1) welding time, (2) electrode force, and (3) welding current.

Step 3: Use regression models to determine the weld strength's predicted value.

Step 4: Establish the fitness of all chromosomes; achieve the maximum (fitmax).

Step 5: Conduct the following genetic operations if $\text{fit max} \leq \text{required fitness}$ (fit required):

(a) Selection based upon the expected number control method,

(b) Crossover,

(c) Mutation, to create a new chromosome population. Then go to step 2. Otherwise, stop.

Maximizing the weld strength was the objective function. Consequently, the reciprocal of the objective functions was employed as the fitness functions. The potential solutions for an optimization problem are represented by the initial population (individual). Table 6 shows the GA parameters that were used to optimize the parameters of the welding process.

In the present study, the GA is set using the GA toolbox and it is optimized through the MATLAB programming fitness function. GA variables are identified, and the lower and upper bounds of the variables are the following.

As shown below, the spot weld process window for every variable was employed as the boundary constraints.

TABLE 6. Parameters for GA computations

Population size	50
Number of generations allowed	1%
Type of mutation	Adaptive feasible
Crossover rate	80%
Type of crossover	Scattered
Type of selection	Roulette wheel

$$70 \leq \text{welding current} \leq 75 \quad (3)$$

$$0.20 \leq \text{electrode force} \leq 0.25 \quad (4)$$

$$8 \leq \text{welding time} \leq 10 \quad (5)$$

As shown below, the plug weld process window for every variable was employed as the boundary constraints.

$$7 \leq \text{hole diameter} \leq 9 \quad (6)$$

$$100 \leq \text{welding current} \leq 140 \quad (7)$$

4. RESULTS AND DISCUSSION

4. 1. Spot Weld Procedure

4. 1. 1. Factorial Design of Welding Parameters

Table 7 shows the uncoded design matrix with the corresponding real factor settings and the respective maximum load for the spot weld experiment. In order to create adequate degrees of freedom for the error term, every trial condition was recreated three times. To minimize the effect of undesirable external influences

TABLE 7. Spot weld experimental layout with response values

Run/Trial	A	B	C	Maximum load (N)		
				1	2	3
1	70	0.2	8	6,383	6,511	6,411
2	75	0.2	8	6,958	6,621	6,701
3	70	0.25	8	7,064	7,046	7,107
4	75	0.25	8	7,099	7,213	7,250
5	70	0.2	10	6,894	6,699	6,701
6	75	0.2	10	6,570	6,438	6,536
7	70	0.25	10	7,418	7,379	7,456
8	75	0.25	10	7,355	7,500	7,190

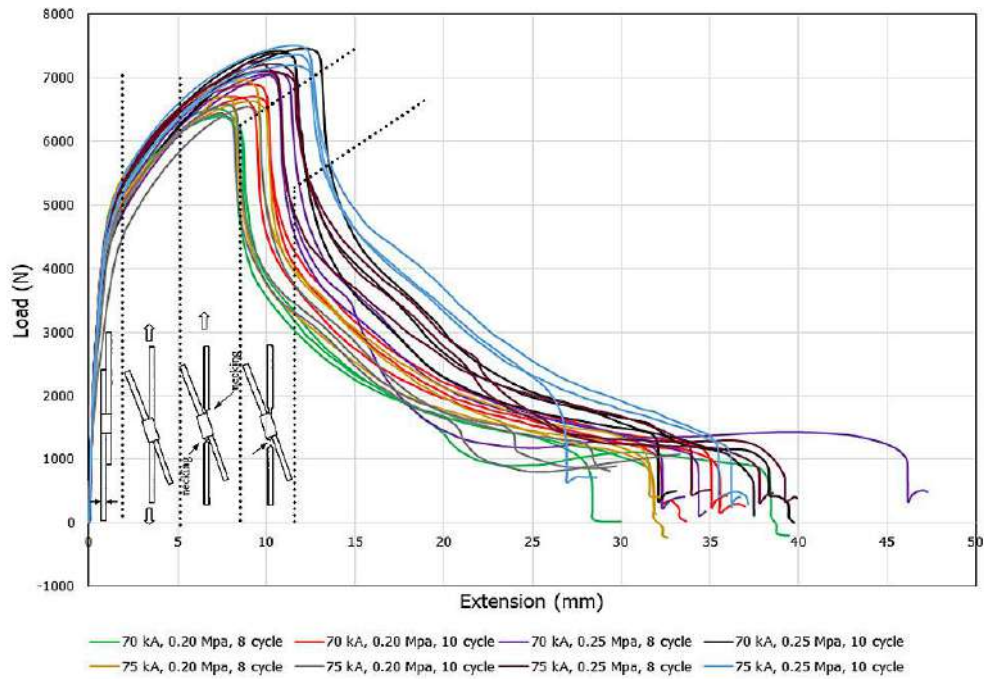


Figure 5. Load vs. extension curves of the spot weld joint

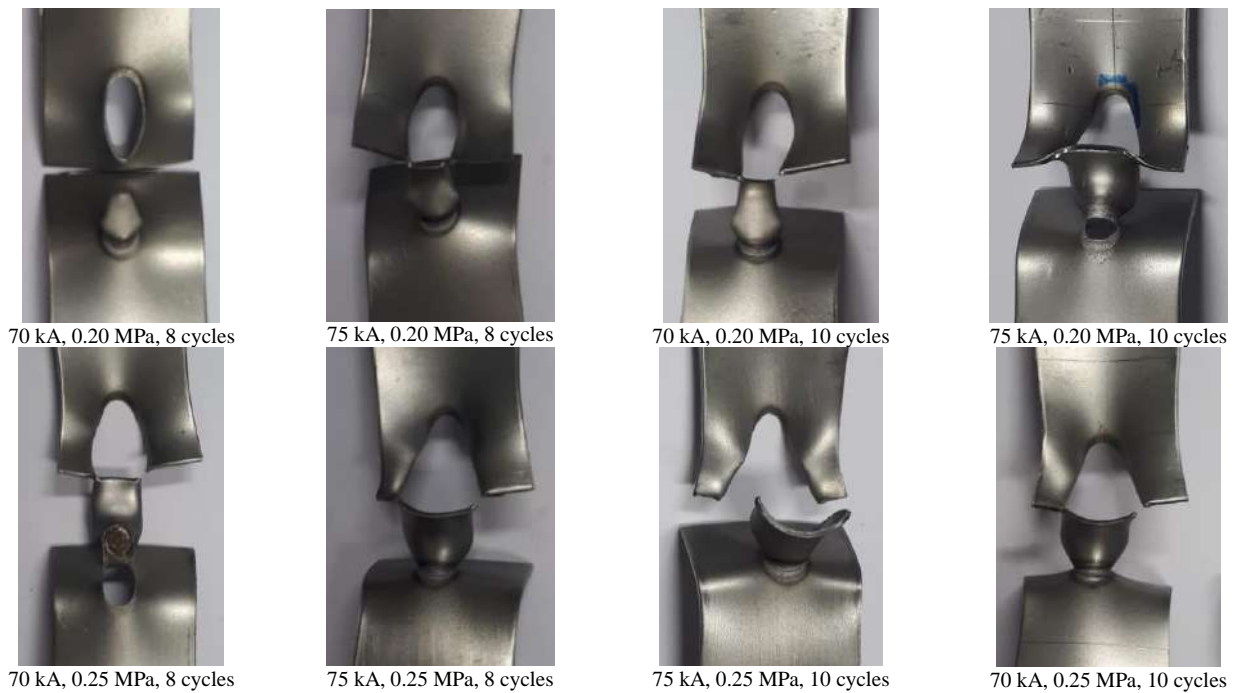


Figure 6. Failure mode of spot-welded samples

and lurking variables induced into the experiment, a randomization strategy was used. The use of the Minitab software allowed to determine which effects influence process variability the most.

Figures 5 and 6, respectively, show the load vs. extension curves and the failure mode of the spot weld

joint that were generated in the experiments. In the lap-shear test, as shown in Figure 5, the load vs. extension curve illustrates a nonlinear region before the maximum load is reached. Initially, the welded joint is pulled parallel to the force direction. The nugget rotates in order to align with the applied force direction. As the

load increases, localized necking of the sheet metal occurs at locations near the boundary of the base metal and the nugget. Once the maximum load is reached, the load begins to drop when the crack initiates and gradually decreases as the base metal tears around the weld nugget. Figure 6 displays the gradual changing trend in the growing order of the maximum loads. Higher forces and shorter times should be used conjointly. Higher welding current is necessary at shorter welding times. The necessary current depends on the size of the used electrode tip, the other parameters set, and the material type. If the current is low, the strength of the weld joint will be insufficient due to the brittleness of the created nugget. Since the welding current was continuously increased, the nugget diameter reached a maximum increase initially and then decreased progressively due to excessive splashing and melting. An adequate welding time setting would provide a good welding contact without generating burn marks on the workpiece surface and significant deformation. The transformation was complemented by a hardness decrease in the heat-affected zones of the welds and the nugget. As far as the welding force setup is concerned, improper welding force can cause a weak connection between the welding surfaces, thus generating metal splash and poor weld results. The higher the welding force of the electrode is, the greater the deformation on the workpieces will be. Due to this transformation, the current flows along different paths instead of a small spot generating a wide array of temperature distributions in the workpieces.

Regarding the failure modes, as presented in the ISO standards [26], in weld quality testing, all specimens coincide with the tearing of the base metal because the quantitative measurement of weld strength is attainable. Additionally, failure modes show if the size of the specimen is appropriate [21].

4. 1. 2. Regression Model Regression analysis sees the effect of a factor defined as the change in response caused by a change in the factor's level. Since it refers to the main factors of interest in the experiment, it is commonly called a main effect. Equation (8) gives the mathematical model for factorial design 2^3 , where N represents the mean of the maximum load, while A , B , and C indicate welding current, electrode force, welding time, respectively. Since the experimental results model ensures a good correlation ($R^2 = 92.61\%$), all the coefficients for the subsequent mathematical model were evaluated in the coded format. If the statistical model (R^2 (adj) = 90.55%) is adjusted, these values denote the percentage of data detected in the response and that can be explained by the mathematical model.

$$N = -17536 + 347.8A - 6247B + 2352C - 37.97A * C + 2111B * C \tag{8}$$

4. 1. 3. Model Adequacy Checking Figure 7 shows the ANOVA for the complete 2^3 factorial designs with three replicates. The obtained data shows that the main effects of welding time and electrode force are relevant for the maximum load. However, the welding current is not relevant, as it displays values over the significance level of (5%). The relationship between electrode force*welding time and welding current*welding time are relevant as the p-value is inferior to the significance level used at the 5% probability level ($p < 0.05$).

The analysis of a 2^k factorial design presumes that the observations are assigned normally and independently. Producing a normal probability plot of residuals is the most appropriate way to verify the normality assumption. As shown in Figure 8, the residual plot for the maximum load response is characterized as a significant procedure to guarantee that the developed mathematical models continually illustrate the responses of interest.

Factorial Regression: Max Load (N) versus Welding Current , Electrode Force , Welding Time

Backward Elimination of Terms

α to remove = 0.05

Analysis of Variance

Source	DF	Adj SS	Adj MS	F-Value	P-Value
Model	5	2362053	472410.6	45.09	0.000
Linear	3	2377162	792387.3	87.71	0.000
Welding Current (kA)	1	5494	5494	0.43	0.519
Electrode Force (Mpa)	1	2440816	2440816	192.39	0.000
Welding Time	1	130852	130852	10.31	0.005
2-Way Interactions	2	283131	141565.5	11.16	0.001
Welding Current (kA)*Welding Time	1	216260	216260	17.05	0.001
Electrode Force (Mpa)*Welding Time	1	66871	66871	5.27	0.034
Error	18	228359	12687		
Lack-of-Fit	2	57370	28685	2.68	0.099
Pure Error	16	170989	10687		
Total	23	3088651			

Model Summary

S	R-sq	R-sq(adj)	R-sq(pred)
112.635	92.61%	90.55%	86.86%

Figure 7. ANOVA results for the full factorial experiments with Table 7

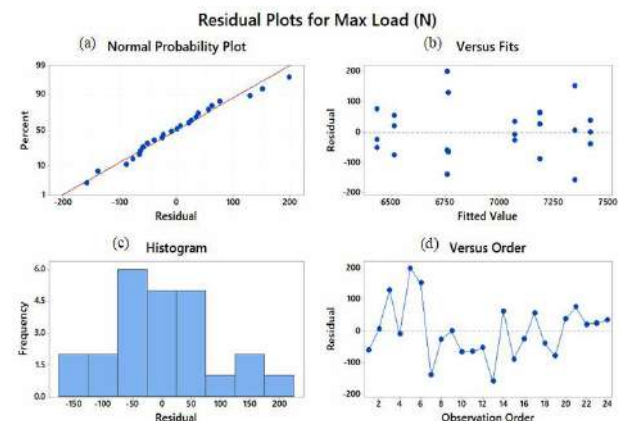


Figure 8. Residual plot for the spot weld experiment, (a) normal probability plots of residuals, (b) residuals versus fits plots, (c) histogram of residuals, and (d) residuals versus observation order

Typically, ANOVA assumptions are checked using four main diagnostic plots: (a) residuals versus the order, (b) histogram of standardized residuals, (c) versus fits for standardized residuals, and (d) normal probability plot for standardized residuals. Should these assumptions be satisfied, then standard least-squares regression will generate objective coefficient estimates with minimum variance. Figure 8a shows that residuals relatively fall along a straight line. Consequently, the normal distribution assumption is considered as satisfied. As shown in Figure 8b, all residual points are dispersed within lower and upper bounds, showing no pattern. This plot denotes that the independence assumption is also satisfied. The histogram shown in Figure 8c apparently forms a normal curve equally distributed around zero, showing that the normality assumption is more than likely true. Since Figure 8d shows that all residual points are spread irregularly over the graph within the lower and upper bounds showing no evident patterns, the assumption according to which residuals have a regular variance is confirmed. As a result, all diagnostic plots denote that all the necessary ANOVA assumptions are satisfied.

As shown in Figure 9, a Pareto plot can illustrate statistically significant effects. The interactions or factors on the outside of the dotted line at 2.12 are relevant in decreasing order: electrode force, welding time, welding current*welding time interaction electrode force*welding time interaction, and lastly, welding current*electrode force*welding time interaction. Put differently, these effects have significant impact on the mean maximum load, even if the welding current has no relevant impact on the mean maximum load. This result can be further supported by taking into consideration the main effects plot and interaction plot (as shown in Figures 10 and 11, respectively).

Figure 10 shows a graphic representation of the primary effects of the spot weld examined factors in regard to maximum load. According to the graph, it can be concluded that a factor is directly linked to the slope and length of the line in the graphic. The greater the

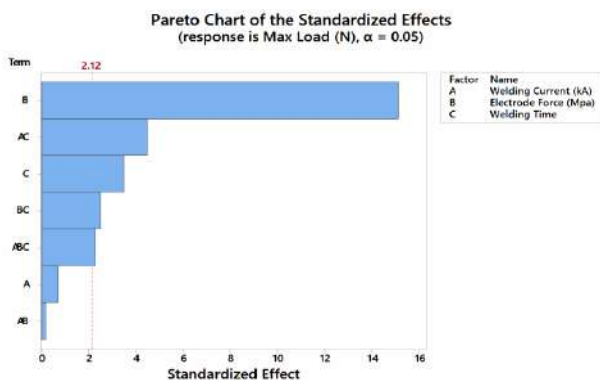


Figure 9. Pareto plot of effects on maximum load variability

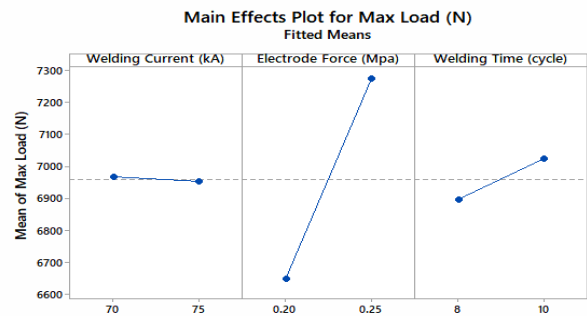


Figure 10. Main effects plot for spot weld experiment

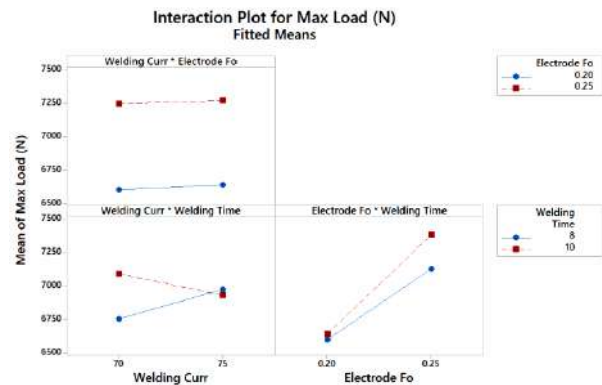


Figure 11. Interaction plot for the spot weld experiment

slope is, the higher the influence on the average maximum load increase will be when varying levels from low to high. Therefore, when these primary effects result from a 90.55% statistical adjustment, with a p-value inferior to 5% significance (representing a 95% confidence level), these results are valid for this spot procedure.

According to Figure 10, the electrode force has a significant impact on maximum load, while welding current has absolutely no impact due to the lower slope. Nonetheless, it should be noted that welding time is less sensitive to variability in maximum load if compared to electrode force.

As shown in Figure 11, the three two-factor interaction graphics denote a powerful interaction between “electrode force*welding time.” Maximum load reaches its highest when welding time and electrode force are kept at a high level, i.e. 10 cycles and 0.25 MPa, respectively. Likewise, maximum load reaches its minimum when welding time and electrode force both maintain a low level, i.e. 8 cycles and 0.20 MPa, respectively.

4. 1. 4. Determination of Optimum Parameters Regression Model

To establish the optimal conditions of maximum load, an optimization study is necessary. As soon as the model has been developed

and verified for adequacy, the optimization criteria must be set to determine the optimum conditions. In order to establish the combination of input variable settings that conjointly optimize a response, a response optimizer was employed. Consequently, 7,463 N was the predicted maximum load value.

As Figure 12 shows, the optimum parameters detected in uncoded units were weld time of 10 cycles, electrode force of 0.25 MPa, and weld current at 70 kA. As a final step, the confirmation test experiment must be conducted. To assess the accurateness of the value predicted by the suggested GA (see Figure 13), an experiment was conducted based upon the optimized process parameters.

The experiments carried out under the optimum conditions were replicated three times. The average value for maximum load turned out to be 7,348 N. The results in Table 8 clearly show that the GA predicted

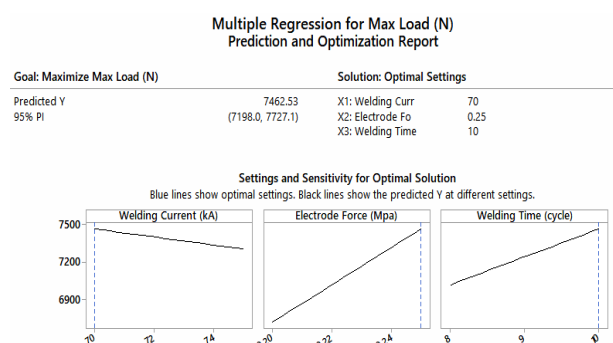


Figure 12. Response optimizer for the spot weld experiment

TABLE 8. Predicted maximum load of spot weld under optimum process parameters and experiment value

Predicted value by Response optimizer	7.463
Predicted value by GA	7.467
Experiment value	7.348

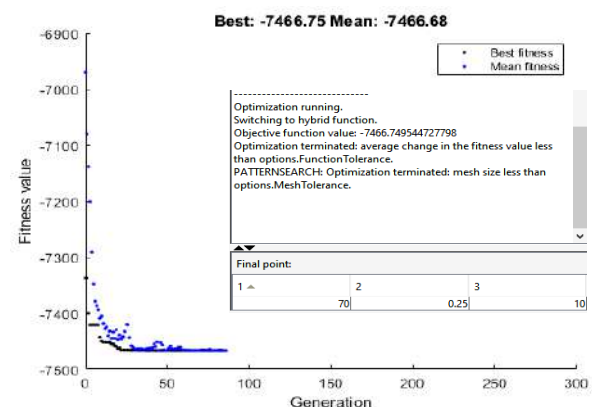


Figure 13. GA convergence plot for the optimal load of the spot weld

value is suitably close to the practical value that was obtained experimentally.

4. 2. Plug Weld Procedure

4. 2. 1. Factorial Design of Welding Parameters

An experimental layout that included all combinations of plug weld parameters and their respective levels was constructed to identify the significant interaction and main effects. Table 9 displays the real settings of the process parameters and the response values that were registered at each trial condition. As showed in Run/Trail 6, achieving weld accuracy and deeper penetration in plug welding of thin sheet metal demands experienced welders. The degree of experience and skill of the welder may affect the weld quality.

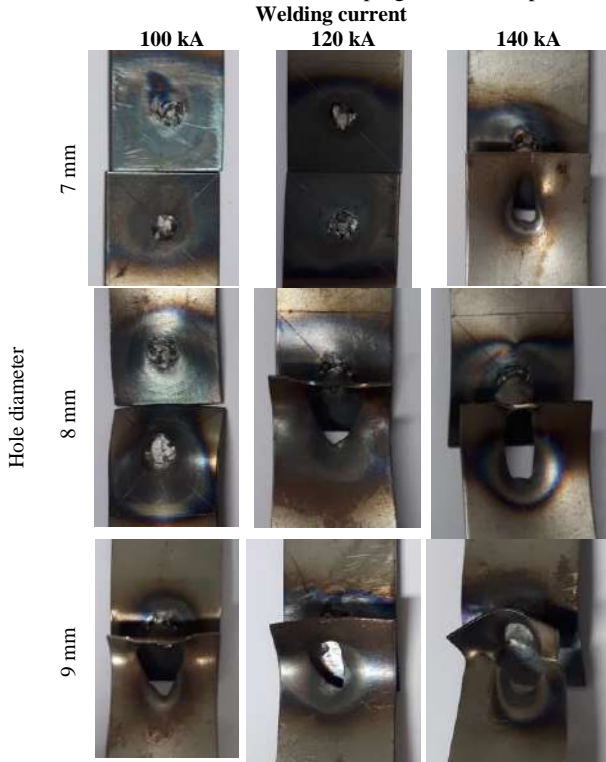
The failure mode of welded samples and load vs. extension curves derived from the plug weld joint tests can be found in Table 10 and Figure 14, respectively. The original crack formed after maximum load, whereas the rear sheet started to fold. In the configuration after the full separation, a button spawned from the thin sheet. The thin sheet behind the button was pulled away from the remaining thin sheet. As the welding current and hole diameter increased, tensile-shear load also increased. The shape of the curve’s “tail” relies on the post-failure mode. A long tail correlates with an interfacial failure, usually one-half button pullout and consequential tearing of the base metal alongside the loading direction. A short tail corresponds to a full button pullout [27]. Immediately after failure, the load drops to zero. The failure mode is usually a complete and clean button pullout.

The failure of the plug-welded sample, as shown in Figure 14, Failure Modes A, B and C correspond to pull-out failure, tearing of the base metal and interfacial failure. In Failure Mode A, the nugget rotates and the tensile load is increased, and then the localized necking occurs outside the nugget, resulting in crack

TABLE 9. Plug weld experimental layout with response values

Run/Trial	X	Y	Maximum load (N)		
			1	2	3
1	7	100	3.019	3.327	3.066
2	8	100	5.501	5.773	5.587
3	9	100	5.745	5.694	6.918
4	7	120	4.834	4.497	4.970
5	8	120	5.711	6.484	5.876
6	9	120	7.817	9.201	7.671
7	7	140	5.220	5.946	5.862
8	8	140	5.757	5.483	6.468
9	9	140	8.607	8.737	7.887

TABLE 10. Failure mode of plug-welded samples



initiations around the nugget’s periphery, while in Failure Mode C, failure occurs by crack propagation through the nugget. In the case of Failure Mode B, failure occurs by weld nugget being partially pulled out from the base metal. Plug-welded material with a 7 mm

hole diameter had low tensile-shear strength because of the low penetration size, leading to interfacial failure. The increment in tensile-shear load with increasing hole diameter was mainly attributed to the growth of penetration size. Assumedly, tensile-shear load increased when the hole diameter was increased to 8 mm.

4. 2. 2. Regression Model

Equation (9) gives the mathematical model for factorial design 3^2 terms of uncoded factors, where N represents the mean of the maximum load, and Y and X are the welding current and mean hole diameter, respectively. For the subsequent mathematical model, all coefficients have been estimated in their coded format, as derived from the experimental results. Additionally, the model ensures a good correlation ($R^2 = 93.71\%$). Adjusting the statistical model ($R^2(\text{adj}) = 90.92\%$) allows for these values to explain the variability to 90.92%.

$$N = -30058 + 1530X + 360Y - 1.323Y^2 \tag{9}$$

4. 2. 3. Model Adequacy Checking

Figure 15 provides the ANOVA results for the complete 3^2 factorial designs with three replicates. The data shows that the main effects of welding current and hole diameter are relevant for the maximum load. Since the p-value is inferior to the significance level established at 5% probability level ($p < 0.05$), the interaction between hole diameter*welding current can be considered significant. For compelling statistical conclusions, the ANOVA assumptions should be verified and tested using model diagnostic plots. A normal probability plot was used to test the normality of the data.

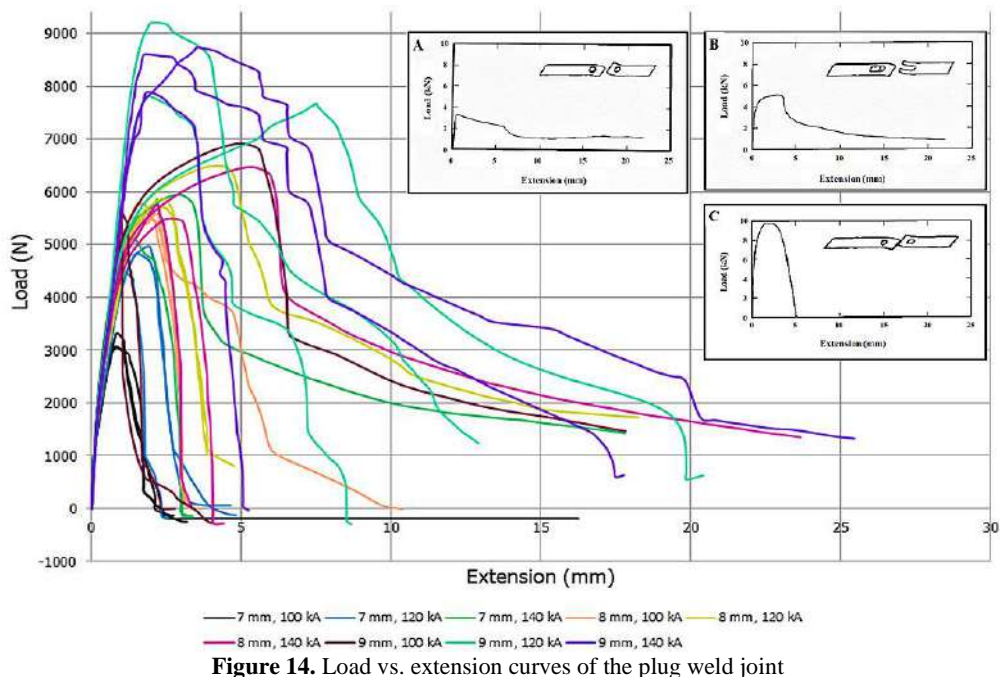


Figure 14. Load vs. extension curves of the plug weld joint

In Figure 16a, a normal probability plot is shown, revealing that the residuals fall on a straight line, indicating normal distribution. Figure 16b shows predicted plot versus residuals. Figure 16b displays the fitted response values versus the variation of the residuals. It is obvious that the data points distribution is random (patternless), indicating that error independency and variance constancy are valid. The plot of residuals versus order was used to verify lurking variables that could have influenced the response throughout the experiment. Apparently, the histogram shown in Figure 16c forms a normal curve equally distributed around zero, indicating that the normality assumption is more than likely true. Additionally, a variation of the residuals versus the run order was plotted to test data independence (Figure 16d). As expected for normally distributed data, it clearly indicated a random scatter. Considering the above discussion, it is obvious that the

General Factorial Regression: Max Load (N) versus Diameter (mm), Welding Current (kA)

Factor Information

Factor	Levels	Values
Diameter (mm)	3	7, 8, 9
Welding Current (kA)	3	100, 120, 140

Backward Elimination of Terms

α to remove = 0.05

Analysis of Variance

Source	DF	Adj SS	Adj MS	F-Value	P-Value
Model	8	62308829	7788604	33.54	0.000
Linear	4	57136493	14284123	61.52	0.000
Diameter (mm)	2	42388974	21194487	91.28	0.000
Welding Current (kA)	2	14747519	7373760	31.76	0.000
2-Way Interactions	4	5172336	1293084	5.57	0.004
Diameter (mm)*Welding Current (kA)	4	5172336	1293084	5.57	0.004
Error	18	4179648	232203		
Total	26	66488477			

Model Summary

S	R-sq	R-sq(adj)	R-sq(pred)
481.874	93.71%	90.92%	85.86%

Figure 15. ANOVA results for the full factorial experiments with Table 9

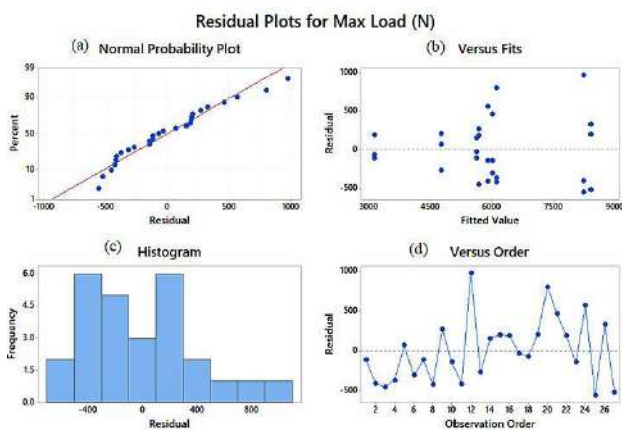


Figure 16. Residual plot for the plug weld experiment, (a) normal probability plots of residuals, (b) residuals versus fits plots, (c) histogram of residuals, and (d) residuals versus observation order

ANOVA assumptions, namely variance constancy, error independency, and error normality are validated. The normal plot for standardized effects can only be applied to 2^k designs and not to general factorial designs. Generally, factorial designs should be used to choose interaction terms and vital main effects rather than standardized effects (also called normalized effects). Figure 17 shows one of the effects of welding parameters on tensile-shear test samples. As shown, modifying the hole diameter from 7 mm to 9 mm caused a greater main effect than welding current.

Figure 18 reveals a strong interaction between welding current and hole diameter. It is obvious that the effect of the hole diameter at varying levels of welding current is different. Yield is maximum if welding current and hole diameter are maintained high levels, i.e., 140 kA and 9 mm, respectively.

4. 2. 4. Determination of Optimum Parameters

Figure 19 displays the optimal process conditions necessary to produce maximum load under specific conditions. The optimum conditions for maximum load yield as estimated by the response optimizer were welding current 140 kA and hole diameter 9 mm. at optimal conditions, the maximum value for tensile-shear strength was calculated at 8,213 N.

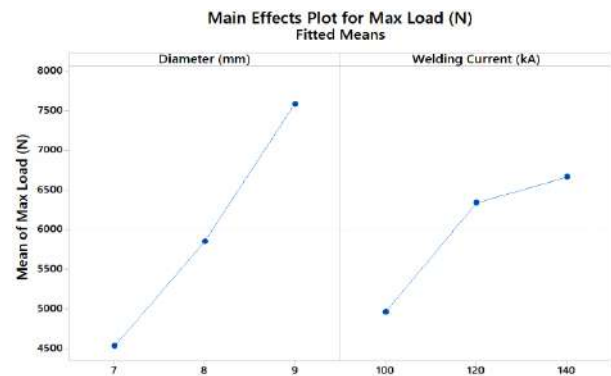


Figure 17. Main effects plot for the plug weld experiment

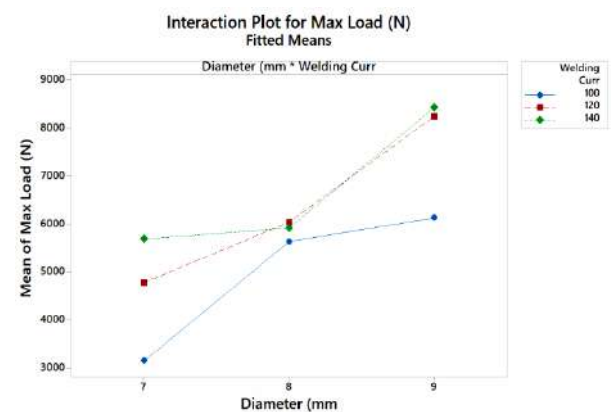


Figure 18. Interaction plot for the plug weld experiment

As Figure 20 shows, if the optimization problem is solved, the GA supplies optimum combinations of parameters to achieve maximum weld strength compared to the original set of welding parameters.

In order to confirm the accuracy of the established response optimizer function, three replicates of batch experiments have been conducted at optimal conditions. With nonlinear functions, optimum values may take place at the boundaries or in-between them. In the experiment conducted under optimal conditions, 8,262 N was the average value for maximum load.

Table 11 shows optimum welding conditions that lead to the maximum weld strength. The optimization results have been verified against factual experimental data, revealing that they are satisfactory.

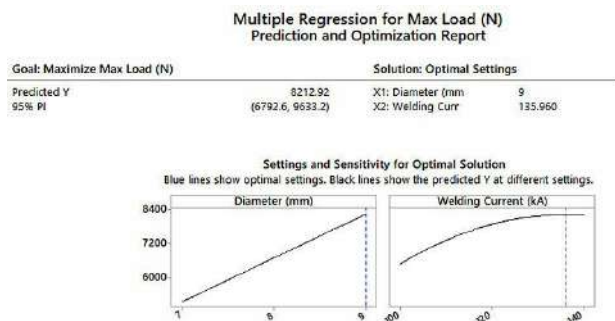


Figure 19. Response optimizer for the plug weld experiment

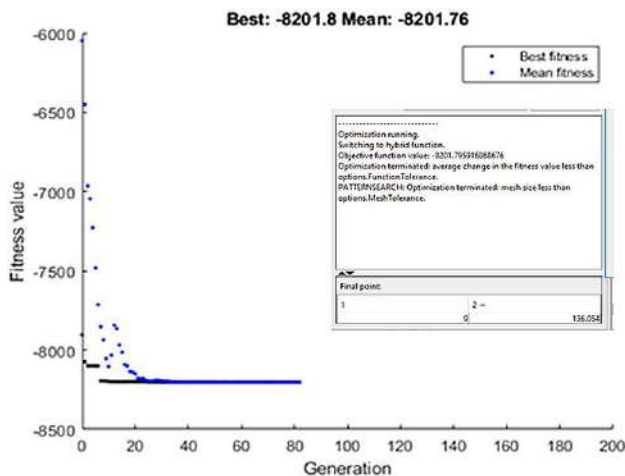


Figure 20. GA convergence plot for the optimal load of plug weld

TABLE 11. Predicted maximum load of plug weld under optimum process parameters and experiment value

	Hole diameter (mm)	Welding current (kA)	Maximum load (N)
RSM	9	135.960	8,213
GA	9	136.054	8,202
Experiment	9	136	8,262

5. CONCLUSIONS

The aim of this study was to evaluate the characteristics of plug welding and spot welding used in the vehicle body panel restoration process. The shear tension of welds was analyzed experimentally. Based on the statistical analysis and experimental results, the conclusions derived from the current investigation are summarized thusly.

The optimal spot welding parameters necessary to produce a maximum load of 7.4 kN were an electrode force of 0.25 MPa, a welding current of 70 kA, and a welding time of 10 cycles. The failure modes detected during tensile-shear testing caused full button failure tearing of the base metal in all tests. The JIS G3141 SPCC resistance factor is higher. Consequently, the current requirements are slightly lower. Because of the additional compressive strength that is inherent in JIS G3141 SPCC, electrode force is usually higher with this type of materials. Since metallurgical changes are greater with this type of materials, welding time is more critical. When welding this type of materials, it is advisable to employ longer welding times to permit more ductile welds and reduce the cooling rate.

The optimal plug welding parameters necessary to produce an 8.2 kN maximum load were a welding current of 136 kA and a hole diameter of 9 mm. The failure of the plug-welded sample happens in three modes: interfacial failure, tearing of the base metal, and button pullout. Plug welds are exceptionally tough and will not fail unexpectedly. Small diameter plug welds may be difficult. Full fusion achievement requires adequately trained and skilled welders. According to the recommendations provided by AWS, the minimum hole diameter necessary to guarantee the reliability of plug-welded materials based on 1 mm thin joined materials is 9 mm. Based on the 2 mm average joined material thickness, the minimum hole diameter must be 10 mm. The results show that the formula for plug weld proposed by AWS can be used for similar plug-welded metals with equal-thickness welding. Strengths were proportional to the amount of current. In order to ensure complete fusion and achieve the shear strength of the weld metal, the highest practical welding current for the used electrodes should be used for plug welds. This strength increase with welding current confirms the theory according to which ultimate shear strength relies on the amount of penetration.

In the case of spot welding, the test numbers that exceeded an upper limit caused burnt workpieces. In the case of values below the lower limit, the finished workpieces were non-adjacent. This experiment used thin sheets as plug welding specimens. A hole diameter above 9 mm would burn the joints. However, penetration does not occur if the hole diameter is less than 7 mm. Additionally, a welding current above 140

kA may burn the workpiece. Consequently, the optimum welding parameters in the present study are fit for joining similar SPCC steel sheet (1.2 mm thick) to attain the higher load value that complies with the actual engineering conditions.

The aim of this pilot study was to estimate the main parameters for the welding process of automotive body panels. The results can help manufacturers understand which parameters require less attention, narrower ranges, or tighter control. Lastly, this study will distinctly separate non-key from key parameters. If a process parameter that has been tested over this range presents no relevant effect on process performance, it is safe to consider it a non-key parameter. Nonetheless, even if digressions from these process parameters present no weldability impact, it is advisable to monitor them to guarantee consistent process control. Parameters with a measurable, significant effect are considered key parameters that must be tested in future sets of characterization experiments. The results of this study are expected to be applied to upcoming studies on practical optimization for repair and maintenance of automotive body panels.

6. ACKNOWLEDGMENT

This present research is funded by Faculty of Technical Education, King Mongkut's University of Technology North Bangkok, (contract No. FTE-2563-04).

7. REFERENCES

- Mallick, P., *Joining for lightweight vehicles*, in *Materials, design and manufacturing for lightweight vehicles*. 2010, Elsevier.275-308. doi: 10.1533/9781845697822.2.275
- Kwon, J., Kim, J. and Lee, Y., "Experimental study on spot weld and plug weld of automotive body panel", *Transactions of the Korean Society of Automotive Engineers*, Vol. 24, No. 6, (2016), 709-715. doi: 10.7467/KSAE.2016.24.6.709
- Zhang, H. and Senkara, J., "Resistance welding: Fundamentals and applications, CRC press, (2011).
- Duffy, J.E., "Auto body repair technology, Cengage Learning, (2014).
- Jou, M., "Real time monitoring weld quality of resistance spot welding for the fabrication of sheet metal assemblies", *Journal of Materials Processing Technology*, Vol. 132, No. 1-3, (2003), 102-113. doi: 10.1016/S0924-0136(02)00409-0
- Farrahi, G.H., Kashyzadeh, K.R., Minaei, M., Sharifpour, A. and Riazi, S., "Analysis of resistance spot welding process parameters effect on the weld quality of three-steel sheets used in automotive industry: Experimental and finite element simulation", *International Journal of Engineering, Transactions A: Basics*, Vol. 33, No. 1, (2020), 148-157. doi: 10.5829/ije.2020.33.01a.17
- Özyürek, D., "An effect of weld current and weld atmosphere on the resistance spot weldability of 304L austenitic stainless steel", *Materials & Design*, Vol. 29, No. 3, (2008), 597-603. doi: 10.1016/j.matdes.2007.03.008
- Darwish, S. and Al-Dekhial, S., "Micro-hardness of spot welded (bs 1050) commercial aluminium as correlated with welding variables and strength attributes", *Journal of Materials Processing Technology*, Vol. 91, No. 1-3, (1999), 43-51. doi: 10.1016/S0924-0136(98)00414-2
- Jamaludin, S.B., Hisyam, M., Shamsudin, S.R., Darus, M. and Wahid, M.F.M., "Study of spot welding of austenitic stainless steel type 304", *Journal of Applied Sciences Research*, Vol. 3, No. 11, (2007), 1494-1499.
- Gibson, G.J., "An investigation of plug and slot welds", M. S. Thesis, Lehigh University, (1937).
- Gopinath, V., Manojkumar, T., Sirajudeen, I., Yogeshwaran, S. and Chandran, V., "Optimization of process parameters in tig welding of aisi 202 stainless steel using response surface methodology", *International Journal of Applied Science and Engineering Research*, Vol. 10, No. 13, (2015), 11053-11057.
- Srirangan, A.K. and Paulraj, S., "Multi-response optimization of process parameters for tig welding of incoloy 800ht by taguchi grey relational analysis", *Engineering Science and Technology, an International Journal*, Vol. 19, No. 2, (2016), 811-817. doi: 10.1016/j.jestch.2015.10.003
- Simhachalam, D., Rao, M. and Raju, B.N., "Evaluation of mechanical properties of stainless steel (ss 304) by tig welding at heat affected zone", *International Journal of Engineering and Management Research*, Vol. 5, No. 4, (2015), 214-221.
- Duhan, R., "Effect of activated flux on properties of ss 304 using tig welding", *International Journal of Engineering, Transactions B: Applications*, Vol. 28, No. 2, (2015), 290-295. doi: 10.5829/idosi.ije.2015.28.02b.16
- Tsuruta, A., Arai, Y. and Tanaka, R., "On the strength of plug welding of thin steel sheets", *Journal of The Japan Welding Society*, Vol. 21, No. 5-7, (1952), 144-149. doi: 10.2207/qjwjs1943.21.144. doi: 10.2207/qjwjs1943.21.144.
- Committee, A.W.S.S.W., Society, A.W. and Institute, A.N.S., "Structural welding code--steel, Amer Welding Society, (1994).
- O'Brien, A. and Guzman, C., "Welding handbook: Welding processes, American Welding Society, (2007).
- Ilman, M.N. and Soekrisno, R., "Static and fatigue behavior of plug-welded dissimilar metal welds between carbon steel and austenitic stainless steel with different thicknesses", *International Journal of Mechanical and Materials Engineering*, Vol. 9, No. 1, (2014), 17. doi: 10.1186/s40712-014-0017-4
- Hadyś, D., "Mechanical properties of plug welds after micro-jet cooling", *Archives of Metallurgy and Materials*, Vol. 61, No. 4, (2016), 1771-1776. doi: 10.1515/amm-2016-0286
- Hasanbaşoğlu, A. and Kaçar, R., "Resistance spot weldability of dissimilar materials (aisi 316L-din en 10130-99 steels)", *Materials & design*, Vol. 28, No. 6, (2007), 1794-1800. doi: 10.1016/j.matdes.2006.05.013
- Zhou, M., Hu, S. and Zhang, H., "Critical specimen sizes for tensile-shear testing of steel sheets", *Welding Journal-New York-*, Vol. 78, (1999), 305-s.
- Kim, D. and Rhee, S., "Optimization of arc welding process parameters using a genetic algorithm", *Welding Journal (Miami, Fla)*, Vol. 80, No. 7, (2001), 184s-189s.
- Correia, D., Gonçalves, C., Junior, S.S. and Ferraresi, V., "Gmaw welding optimization using genetic algorithms", *Journal of the Brazilian society of Mechanical Sciences and Engineering*, Vol. 26, No. 1, (2004), 28-32. doi: 10.1590/S1678-58782004000100005
- Perez Pozo, L., Olivares Z, F. and Durán A, O., "Optimization of welding parameters using a genetic algorithm: A robotic arm-assisted implementation for recovery of pelton turbine blades", *Advances in Mechanical Engineering*, Vol. 7, No. 11, (2015), 1687814015617669. doi: 10.1177/1687814015617669

25. Myers, R.H., Montgomery, D.C. and Anderson-Cook, C.M., "Response surface methodology: Process and product optimization using designed experiments, John Wiley & Sons, (2016).
26. Association, J.S., "Specimens dimensions and procedure for shear testing resistance spot and embossed projection welded joints", Japanese Standards Association. Japan, JIS, 3136, (1999).
27. Chao, Y.J., "Ultimate strength and failure mechanism of resistance spot weld subjected to tensile, shear, or combined tensile/shear loads", *Journal of Engineering Materials and Technology*, Vol. 125, No. 2, (2003), 125-132. doi: 10.1115/1.1555648.

Persian Abstract

چکیده

جوش کاری نقطه‌ای مقاومتی یک فرایند اساسی جوش کاری است که در مونتاژ بدنه‌ی خودرو استفاده می‌شود. البته، جوش کاری دکمه‌ای به دلیل سادگی فنی و مزایای آن در تعمیر بدنه‌ی خودرو کاربردهای زیادی دارد. در این مقاله، جوش کاری نقطه‌ای و دکمه‌ای با استفاده از جوش کاری تنگستن-گاز بی‌اثر (TIG) برای پانل بدنه‌ی خودرو مقایسه شده است. جوش کاری TIG برای جوش کاری دکمه‌ای انتخاب می‌شود زیرا بیشترین انعطاف‌پذیری را برای جوش کاری گسترده‌ترین طیف مواد، ضخامت و انواع آن فراهم می‌کند. ماده‌ی پایه‌ی مورد استفاده در این مطالعه JIS G3141 SPCC است. برای تعیین اهمیت پارامترهای فرایند، از طرح آزمایشی فاکتوریل کامل همراه با تحلیل آماری و گرافیکی نتایج با استفاده از تحلیل واریانس استفاده شد. اندرکنش پارامترها با استفاده از تحلیل رگرسیون، بررسی کفایت مدل و تعیین شرایط بهینه بررسی شد. از الگوریتم ژنتیک برای پیش‌بینی ترکیب بهینه‌ی پارامترهای فرایند برای تحقق بالاترین سطح مقاومت استفاده می‌شود. برای مقاومت در برابر کشش، نتایج آزمایش نشان می‌دهد که بیشینه‌ی بار جوش کاری دکمه‌ای بالاتر از جوش کاری نقطه‌ای است. اتصالات بهینه‌ی جوش کاری دکمه‌ای در قطر سوراخ ۹ میلی‌متر و جریان ۱۳۶ کیلو آمپر، با حداکثر بار ۸.۲ کیلو نیوتن به دست آمد. بیشترین بار اتصال جوش نقطه‌ای ۷.۴ کیلو نیوتن، در جریان ۷۰ کیلو آمپر، نیروی الکتروود ۰.۲۵ مگا پاسکال و ۱۰ چرخه زمان جوش کاری مشاهده شد.



Prediction of Tool Force in Two Point Incremental Forming by Slab Analysis

M. Esmailian, K. Khalili*

Department of Mechanical Engineering, University of Birjand, Birjand, Iran

PAPER INFO

Paper history:

Received 30 June 2020

Received in revised form 26 August 2020

Accepted 03 September 2020

Keywords:

Two Point Incremental Forming

Tool Force

Slab Analysis

CNC Machine

ABSTRACT

Two-Point Incremental Forming (TPIF) method is a novel technique for producing free form shell parts. The main purpose of this study is to analyze the TPIF process, and, by approximate calculation, to find the force applied to the tool. One of the limitations of an incremental forming process is that during this process force applied to the tool is born by the machine. In this research, an equation for approximate prediction of the force applied to the tool is presented using the values of the yield stress of the sheet, friction coefficient, tool radius and thickness of the sheet; hence, the applied force can be calculated. By increasing the forming angle, the amount of the created local strain increases and the change in thickness and the force applied to the tool is enhanced. However, by increasing the angle of punch wall, less compressive stress is applied to the metal sheet due to the reduction in contact between the surface of the tool and punch wall. Analytical equations presented are validated by the results from experimental tests.

doi: 10.5829/ije.2020.33.11b.30

1. INTRODUCTION

Producing parts from metal sheets by using molds and special tools is not economical in research and development or in some industries, such as aerospace, where production circulation is low. Hence, using the incremental forming method is one of the best choices. To form parts, in addition to axial symmetric forms, some incremental forming methods, such as Single Point Incremental Forming (SPIF), in which the motion of the tool is guided by a Computer Numerical Control (CNC) machine, have been developed.

According to Figure 1, in this process, a small spherical-head tool that has a single-point contact with the sheet moves in a specific direction by the user and creates the final form on the sheet [1]. This process was first presented by Edward [2]. However, the main development of this method happened with the advent of CNC in the end of 1970s. In this period, Mason and Appleton [3] introduced the asymmetric incremental forming for the first time and indicated that, using CNC, the formability of a metal sheet is possible as a spherical-head tool moves on it. The main advantages of

incremental forming method are: 1) the low cost of this method compared to other conventional forming methods [4]; 2) high formability due to the possibility of changing the form of the final part by changing the CNC program [5]; 3) higher formability of the sheet compared to other methods because of applying force to points; and 4) high flexibility/simple set up in rapid prototyping, or when mass production is not an aim and ease of selecting the proper machine with less limitations due to the demand for lower forces [6].

Another type of incremental forming method is Two Point Incremental Forming (TPIF), in which a constant punch is placed at the bottom of the sheet, and a spherical-head tool incrementally places the sheet on the punch and the sheet is formed to the form of the bottom punch (Figure 2) [7]. The main difference between the two methods is the higher formability of the sheet.

Different parameters of the incremental forming process are investigated and analyzed by researchers. For instance, by using theories and simulations, different efficient parameters such as temperature [8-10], the maximum angle of the wall [11-13], the vertical pitch of tools [14-16], tool size [15-17] and the direction of the

*Corresponding Author Institutional Email: kkhalili@birjand.ac.ir (K. Khalili)

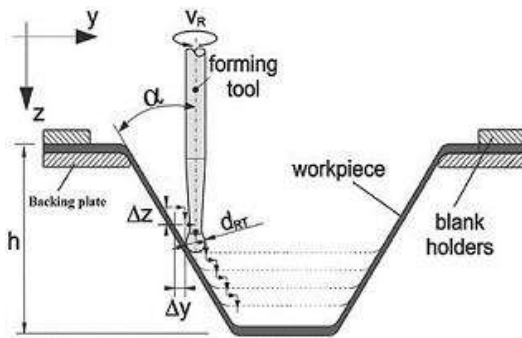


Figure 1. Basic principles of Single Point Incremental Forming [6]

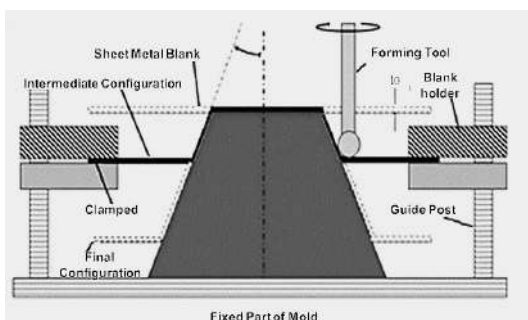


Figure 2. Basic principles of Two Point Incremental Forming [7]

tool [18-19] on the formability of the sheet are investigated. For example, by increasing temperature, decreasing vertical pitch and tool radius, the formability of sheet increases. Other studies have investigated failure and tearing modes of the sheet and parameters effective in the incremental forming process by using experimental methods, theories and simulations.

By investigating the formability of an annealed aluminum sheet in SPIF, Shim and Park [20] declared that the obtained forming limit graph is different from other conventional methods and it is similar to a direct line or a line with negative inclination. Kim and Park [21] studied the effect of process parameters on the formability of an annealed aluminum sheet in SPIF and indicated that, in this process, the formability of sheets is higher than other forming methods. In addition, by using experimental analysis and finite element analysis, they investigated the effect of process parameters, such as size and type of tool, processing rate and friction on the contact surface between the tool and sheet on incremental forming. Moreover, they figured out that by increasing processing rate and decreasing friction, the formability of the sheet is enhanced. Hirt et al. [22] studied two main limitations of the incremental forming process including the available maximum wall angle and the creation of geometrical deviation. They suggested several forming strategies and finite element modeling for incremental forming of the sheet for eliminating the limitations of this

process. Fan et al. [9] presented a method for examining the thinning limit of aluminum sheet by using a truncated cone with the variable angle of the wall. They used a circular arc for modeling a cone wall with variable angles. Silva et al. [23] experimentally studied the fracture mechanism in SPIF for an AA1050-H111 aluminum sheet. In this investigation, the truncated pyramid and cone parts, both with variable angle of the wall, were presented by using different tool diameters. Their results revealed that, by using tools with diameters less than 10 mm, local necking does not occur before fracture. By simulating finite element of incremental forming of a truncated pyramid and extracting forming limit graphs based on stress, Seong et al. [24] proved that the main minimum and maximum stresses are changed along sheet thickness causing the elimination of necking phenomena in SPIF process and, consequently, the enhancement of formability. Kura et al. [25] numerically and experimentally investigated the formability of an extra-tensile steel sheet in SPIF. In the above-mentioned research, a cone with variable wall angles consisting of circular, parabolic and oval was used. The average value of the maximum angle of the wall in the mentioned research was 75.27° .

Oraon and Sharma [26] used an artificial neural network to predict the minimum force required for single point incremental forming (SPIF) of thin sheets of Aluminium AA3003-O and calamine brass Cu67Zn33 alloy. Accordingly, the parameters for processing, i.e., step depth, the feed rate of the tool, spindle speed, wall angle, thickness of metal sheets and type of material were selected as input and the minimum vertical force component was selected as the model output.

Silva et al. [27] provided a new theoretical model for rotational symmetric SPIF that was developed under membrane analysis with bi-directional in-plane contact friction forces. As shown in Figure 3, they divided the formed parts surface into three areas: smooth surface area under surficial and tensile strain (A), rotational symmetric surface under surficial and tensile strain (B) and the angle under the condition of equal tension with two axes (C). Then, they presented a series of analytical

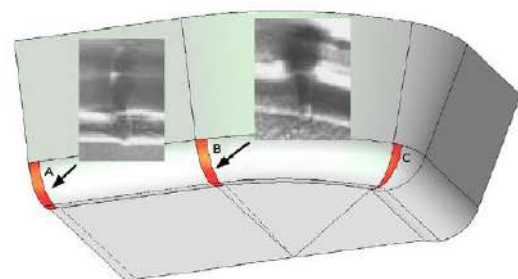


Figure 3. Instantaneous deformation zone and contact between forming tool and workpiece during SPIF [27]

equations for stress and strain values in SPIF. The analytical solutions had some simplifications (they considered the material as rigid, completely plastic and isotropic).

In another work, Silva and Martins [28] proposed a new level of understanding of two-point incremental forming (TPIF) with a partial die using a combined theoretical and experimental investigation. The theoretical developments include an innovative extension of the analytical model for rotational symmetric single point incremental forming (SPIF), originally developed by the authors, to address the influence of the major operating parameters on TPIF and to successfully explain the differences between SPIF and TPIF in formability.

By reviewing previous studies, it can be understood that most of the studies have investigated different aspects of SPIF, and the effect of efficient parameters of TPIF has not been theoretically considered in simulations [29-31]. In the incremental forming process of metal sheets, plastic deformation is considered in a small region of the sheet. Hence, to investigate the theoretical principles governing this process, stress values in this small region should be calculated. Moreover, to analyze this process, the incremental forming process and small deformation area should be considered. Due to the small forming area, the type of punch used at the bottom of the sheet is not important in analytical calculations. The form of punch is determined based on the final form of the product.

The main purpose of this study is an analytical solution for TPIF, and three important objectives are considered in this regard. After approximate calculation of the stress domain, the force applied to the tool can be determined. Approximate calculation of the force on the tool and its prediction before the process are highly important. The force applied to the spindle of CNC has special limitations; therefore, calculation of the force applied to the tool is an appropriate criterion for selecting the type of CNC. In addition, to select the material and size of the tool, the calculated force in this analysis can be used. Moreover, by investigating the force applied during the process, the critical points of TPIF and related conditions are determined. By analyzing this process through the slab method, some parameters such as tool radius, sheet thickness, friction coefficient and punch angle are calculated. Therefore, by calculating the stress domain based on these parameters, the effects of these parameters are investigated. The extracted analytical equations in this study are validated with the results obtained from experimental researches.

2. SLAB METHOD ANALYSIS

In TPIF, when the flat surface of a strained sheet is placed on the punch, the required deformation is created in the

metal sheet; hence, by moving on a specific profile (according to the punch form), a forming tool should perform straining operation on the flat sheet and place it on the punch. This process happens in a very short time by moving the tool on a specific point, and after crossing the tool, similar operations happens in other points of the sheet.

In the forming process, by using conical and multi-dimensional punches (Figure 4), the inclination of the punch wall remains constant and all the points on the sheet surface are strained to the angle α . Therefore, the sheet forming mechanism in different points is theoretically similar, and the values of the created stress and forces in the process remain unchanged.

Theoretical analysis of TPIF is carried on in a region where plastic deformation occurs. In this small region, a part of the spherical-head tool is in contact with the metal sheet. The contact of the tool with the metal sheet and consequently, the amount of applied force from tool to the sheet has a direct relationship with the angle of the punch wall. According to Figure 5, the spherical-head tool is tangent to the sheet surface from point A to point B. Hence, only this part of the tool (AB arc) performs the forming operation. The angle corresponding to this arc equals the angle of the punch wall to horizon (α). The distance of point A equals the vertical axis of the tool ($R_{\text{tool}}\sin\alpha$).

To analyze the incremental forming process, the slab method is used to select an element from the metal sheet on which the forming process is completely concentrated.

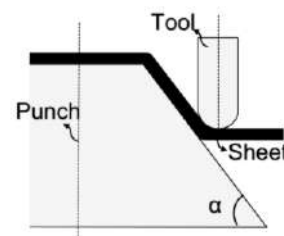


Figure 4. Forming process using conical punch

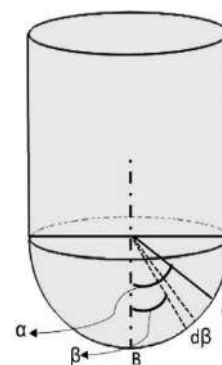


Figure 5. The range of contact of tool and sheet

As shown in Figure 5, this element is a part of the metal sheet placed along AB (contact area between the tool and sheet) at a distance of r from the horizontal axis of the tool. If β is the selected angle element with the vertical axis, the value of r changes from 0 to $R_{tool}\sin\alpha$. Moreover, the relationship between β and r is defined by Equation (1):

$$r = R_{tool}\sin\beta \tag{1}$$

In the calculations presented in this section, the sheet surface is inclined by the angle α and is placed on the punch. These equations are independent of the form of the punch and are usable for all TPIF processes.

In Figure 6, the applied loadings on an element of material are illustrated. This element is a small part of the metal sheet placed on AB arc at a distance of r from the vertical axis of the tool. The thickness of the top face of the element equals $t+dt$ and that of its bottom face equals t . Therefore, the change of sheet thickness in this small region is considered in calculations. As seen in Figure 6, three stress parameters in three orthogonal directions cause the application of force to different faces of the element. Along peripheral direction, the stress σ_θ is applied to two lateral faces of the element. In vertical direction (tangential direction on the tool surface), the stress parameter σ_γ , in addition to straining the smooth surface of the sheet and placing the sheet on the punch, cause the stretching of the sheet along this direction. In addition, the vertical stress applied by the tool to the sheet is denoted by σ_n . To extract balance equations, TPIF process is considered as a quasi-static process. Therefore,

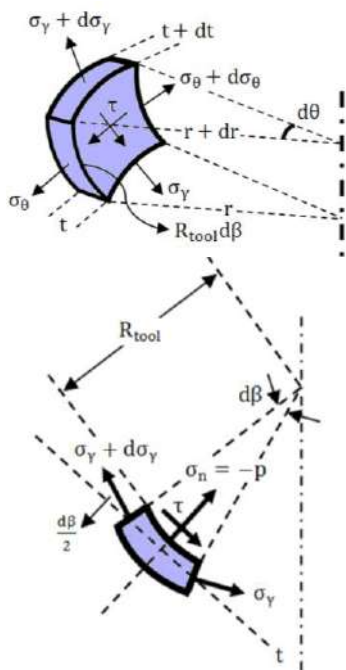


Figure 6. Stress components on the element

by using this method, an initial estimation of the created stress in the material and the required forces during the process are calculated.

In order to use Slab Method analysis, some assumptions are considered for simplifying the extraction of final equations. In these assumptions, the sheet used in forming process is considered an isotropic material, and the changes of yield stress during forming process and creation of rigidity in plastic area are neglected. Therefore, yield stress is considered a constant coefficient (Y).

As mentioned before, friction between the tool and sheet and contact between the sheet and punch create a shear stress on the sheet, which is considered in equations. However, because of its small value, the tensile and compressive stresses applied to the element are considered as the principal stresses. Therefore, to use equations in the plastic region, shear stress is ignored, and its effect is only considered in balance equations. In the presented slab method analysis, the extraction of exact equations is not considered; however, approximate calculation of the values of the stress and forces created during the process is important as an appropriate criterion for the tools and equipment required for the user. According to Figure (6), the balance equation along γ is defined as follows:

$$(\sigma_\gamma + d\sigma_\gamma)(r + dr)(t + dt)d\theta - \sigma_\gamma r d\theta - \tau R_{tool} d\beta r d\theta = 0 \tag{2}$$

In this analysis, the amount of normal stress (the compressive stress applied to the element) is equal to σ_n . Since the numerical value of this parameter is negative, positive P ($P = -\sigma_n$) is used. Therefore, by considering slip friction, shear stress among surfaces is obtained using Equation (3):

$$\tau = \mu p \tag{3}$$

Due to the small value of μp compared to shear yield stress ($Y/\sqrt{3}$), using this assumption is logical. It should be noted that the friction coefficient among surfaces (μ) is selected so that the effect of friction between the tool and sheet, and friction between the sheet and punch are simultaneously considered in calculations. Therefore, Equation (2) is presented as follows:

$$(\sigma_\gamma + d\sigma_\gamma)(r + dr)(t + dt)d\theta - \sigma_\gamma r d\theta - \mu p R_{tool} d\beta r d\theta = 0 \tag{4}$$

By ignoring the second-order differential terms, Equation (4) is simplified as follows:

$$d\sigma_\gamma r t + \sigma_\gamma r dt + \sigma_\gamma t dr - \mu p R_{tool} r d\beta = 0 \tag{5}$$

By using Equation (1) and substituting r in Equation (5), the following equation is obtained:

$$d\sigma_\gamma R_{tool} t \sin\beta + \sigma_\gamma R_{tool} \sin\beta dt + \sigma_\gamma R_{tool} t \cos\beta d\beta - \mu p R_{tool}^2 \sin\beta d\beta = 0 \tag{6}$$

Two sides of Equation (6) are distributed on this term; therefore,

$$\frac{d\sigma_Y}{dt} + \frac{\sigma_Y}{t} + \sigma_Y \cot\beta \frac{d\beta}{dt} - \frac{\mu p R_{tool}}{t} \frac{d\beta}{dt} = 0 \quad (7)$$

Now, to simplify Equation (7), one of the variables of this differential equation should be removed. Therefore, by using trigonometric rules, an acceptable estimation of changes in sheet thickness during the forming process can be obtained

$$t = t_0 \sin\left(\frac{\pi}{2} - \beta\right) = t_0 \cos\beta \quad (8)$$

By taking the derivative of two sides of Equation (8), $\left(\frac{d\beta}{dt}\right)$ is calculated as follows:

$$dt = -t_0 \sin\beta d\beta \Rightarrow \frac{d\beta}{dt} = -\frac{1}{t_0 \sin\beta} \quad (9)$$

In Equation (9), the negative sign indicates that the sheet thickness is reduced from point B to point A, by increasing the angle β . By using Equations (8) and (9), differential Equation (7) can be simplified as follows:

$$\frac{d\sigma_Y}{-t_0 \sin\beta d\beta} + \frac{\sigma_Y}{t_0 \cos\beta} + \sigma_Y \cot\beta \left(-\frac{1}{t_0 \sin\beta}\right) - \frac{\mu p R_{tool}}{t_0 \cos\beta} \left(-\frac{1}{t_0 \sin\beta}\right) = 0 \quad (10)$$

Hence:

$$\frac{d\sigma_Y}{d\beta} - \sigma_Y \tan\beta + \sigma_Y \cot\beta - \frac{\mu p R_{tool}}{t_0 \cos\beta} = 0 \quad (11)$$

By considering the incremental forming process as a straining process and by using constant volume law in the plastic area, the main strain equation is obtained as follows:

$$d\varepsilon_\theta = 0, d\varepsilon_Y + d\varepsilon_\theta + d\varepsilon_n = 0 \Rightarrow d\varepsilon_Y = -d\varepsilon_n \quad (12)$$

By using flow law, a relationship between stress and strain values in the plastic region can be found. Thus, one of the stress parameters can be calculated as the function of the two other parameters:

$$\frac{d\varepsilon_Y - d\varepsilon_\theta}{\sigma_Y - \sigma_\theta} = \frac{d\varepsilon_\theta - d\varepsilon_n}{\sigma_\theta - \sigma_n} \Rightarrow \frac{d\varepsilon_Y}{\sigma_Y - \sigma_\theta} = \frac{d\varepsilon_Y}{\sigma_\theta - \sigma_n} \Rightarrow \sigma_\theta = \frac{1}{2}(\sigma_Y + \sigma_n) \quad (13)$$

According to von Mises equation, the relationship between the main stress and yield stress is defined as follows:

$$Y = \frac{1}{\sqrt{2}} \sqrt{\left(\sigma_Y - \frac{1}{2}(\sigma_Y + \sigma_n)\right)^2 + \left(\frac{1}{2}(\sigma_Y + \sigma_n) - \sigma_n\right)^2 + (\sigma_n - \sigma_Y)^2} \quad (14)$$

By using Equation (13) and substituting σ_θ in von Mises equation, the following equation is obtained:

$$Y = \frac{\sqrt{3}}{2} |\sigma_Y - \sigma_n| \Rightarrow Y = \frac{\sqrt{3}}{2} |\sigma_Y + p| \Rightarrow \boxed{p = \frac{2\sqrt{3}}{3} Y - \sigma_Y} \quad (15)$$

By using the above equation, Equation (11) is simplified as follows:

$$\frac{d\sigma_Y}{d\beta} - \sigma_Y \tan\beta + \sigma_Y \cot\beta - \frac{\mu \left(\frac{2\sqrt{3}}{3} Y - \sigma_Y\right) R_{tool}}{t_0 \cos\beta} = 0 \quad (16)$$

The above differential equation can be presented as follows:

$$\frac{d\sigma_Y}{d\beta} + \sigma_Y \left(\cot\beta - \tan\beta - \frac{\mu R_{tool}}{t_0 \cos\beta}\right) - \frac{2\sqrt{3}}{3} \frac{\mu Y R_{tool}}{t_0 \cos\beta} = 0 \quad (17)$$

Two sides of Equation (17) are multiplied by the integrator factor $\left(K(\beta) = \left(\frac{\cos\beta}{1+\sin\beta}\right)^{\frac{\mu R_{tool}}{t_0}} \sin\beta \cos\beta\right)$; therefore,

$$d\left(\sigma_Y K(\beta)\right) = \frac{2\sqrt{3}}{3} \frac{\mu Y R_{tool}}{t_0 \cos\beta} K(\beta) d\beta \quad (18)$$

By integrating two sides of the above equation in $(0 \leq \beta \leq \alpha)$, the value of σ_Y is calculated as a function of α as follows:

$$\sigma_Y(\alpha) = \frac{2\sqrt{3}}{3} \frac{\mu Y R_{tool}}{t_0 K(\alpha)} \int_0^\alpha \frac{K(\beta)}{\cos\beta} d\beta \quad (19)$$

If the two terms M and $f(\alpha)$ are defined as follows:

$$M = \frac{\mu R_{tool}}{t_0} \quad (20)$$

$$f(\alpha) = \frac{1}{K(\alpha)} \int_0^\alpha \frac{K(\beta)}{\cos\beta} d\beta \quad (21)$$

then,

$$\sigma_Y = Y \left(\frac{2\sqrt{3}}{3} \frac{\mu R_{tool}}{t_0}\right) f(\alpha) \quad (22)$$

As shown, in Equation (20), the value of M depends on μ , R_{tool} and t_0 , which are the known parameters in experiments. However, due to the complexity of the function $k(\beta)$, the above integral is indeterminate and determining the value of stress along γ as a clear equation is not possible. When the value of M is as a coefficient of 0.5, a clear solution of this integral is available. In other cases, the largest approximation can be used or the value of integral can be obtained numerically. Additionally, in experimental tests, the radius of the forming tool is usually between 2.5 and 8 mm, the thickness of the metal sheet is almost 0.8 to 3 mm, and if the friction coefficient between surfaces is almost 0.1 to 0.25, the amount of M is between 0.5 and 2. It should be noted that by slightly changing these three parameters, the above-mentioned assumption is valid. These equations were solved for $M=1$ by Saberi et al. [32], and in this research, the equations are derived for other values of M.

The purpose of this research is to obtain a simple analytical equation for estimating the values of stress and force in this process, while, after integrating, these equations become more complex; hence, an equation with the function $f(\alpha) = \frac{A}{\cos^2 \alpha} + C$ is fitted in equations for different values of M. The values of A and C corresponding to the values of M are presented in Table 1. According to the values of R², the accuracy of the coincidence of fitted equations is acceptable.

By using Equation (23), stress along γ is calculated.

$$\sigma_\gamma = \frac{2\sqrt{3}}{3} Y \left(\frac{\mu R_{tool}}{t_0} \right) \left(\frac{A}{\cos^2 \alpha} + C \right) \quad (23)$$

After calculating stress along γ , the value of normal stress is determined by Equation (15). By neglecting small values of tangential and normal stress, the vertical force applied by the tool to the metal sheet is obtained by Equation (24):

$$(dF_{tool})_n = prd\theta R_{tool} d\beta \quad (24)$$

Using Equations (1) and (15) and integrating the two sides of the above equation, the following equation is obtained:

$$(F_{tool})_n = R_{tool} \int_0^\pi \left(\int_0^\alpha prd\beta \right) d\theta = \frac{\pi R_{tool}}{2} \int_0^\alpha \left(\frac{2\sqrt{3}}{3} Y - \sigma_\gamma(\beta) \right) (R_{tool} \sin\beta) d\beta \quad (25)$$

In Equation (25), the contact of the tool with the sheet along peripheral direction equals $\frac{\pi}{2}$, in radians. Now, the value of vertical force applied to the spherical-head tool can be calculated based on Equation (26):

$$(F_{tool})_n = \frac{\pi}{2} Y R_{tool}^2 \times \int_0^\alpha \left(\frac{2\sqrt{3}}{3} - \frac{2\sqrt{3}}{3} (M) \left(\frac{A}{\cos^2 \beta} + C \right) \right) \sin\beta d\beta \quad (26)$$

In most studies, the applied vertical force along the vertical direction to the tool is obtained. To calculate this force, Equation (27) is used:

$$(F_{tool})_{ny} = (F_{tool})_n \cos\alpha = \frac{\sqrt{3}}{3} \pi Y R_{tool}^2 \cos\alpha \times \left((1 - \cos\alpha) + M \left(A + C \cos\alpha - \frac{A}{\cos\alpha} - C \right) \right) \quad (27)$$

TABLE 1. Values of A and C corresponding to the values of M

M	A	C	R ²
0.5	0.2135	0.5012	0.9903
1	0.1204	0.3126	0.9965
1.5	0.0913	0.1005	0.9903
2	0.3122	-0.6980	0.9917

3. EXPERIMENTAL TESTS

The required equipment and their arrangement in TPIF are shown in Figure 7. By using this equipment and a CNC, the forming process can be performed.

The mold has two separate parts. The first part, on which the guides are placed, is fixed on the milling machine table. In this part, the punch is located and stabilized at the bottom of the sheet between the guides of mold (the fixed part), and the punch is set on it with some bolts. The second part of the mold (the movable part) is placed inside the guides and cannot be displaced along the vertical direction. This part of the mold, where the sheet and the clamp are placed and the two sheets are locked between them, can be detached from guides and separated from the fixed part. In this research, the tools are spherical-head cylinders with different diameters made by MO40 steel as shown in Figure 8.

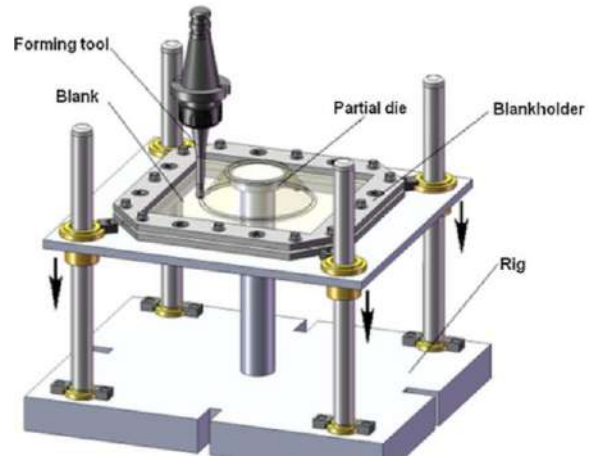


Figure 7. Experimental setup for two-point incremental forming [28]



Figure 8. Cylindrical tools with diameters of 5, 8, 12 and 16 mm

In Figure 9, the equipment used for the TPIF process of the present research is shown.

In the TPIF process, the punch creates a three-dimensional geometry for guiding the sheet and being a constant support for placing the sheet, and finally creating the form of punch on the sheet. Since in the TPIF method, compared to conventional forming techniques, forming forces are weak, there is no need for manufacturing the punch from solid materials. Since it is possible in the present study to cast pure blocks and proper machining, the punch is made of aluminum.

In the present research, a dynamometer is used to measure forces in incremental forming of the sheet on a CNC. The dynamometer is a KISTLER 9257B installed at the bottom of a mold supporting the metal sheet on the CNC table as shown in Figure 9. The direction of the z-axis of the dynamometer is along the axis of the incremental forming tool. Furthermore, the X and Y axes of the dynamometer are along X and Y directions of the CNC machine. In Figure 10, the incomplete pyramid formed by the TPIF process is shown.

4. RESULTS AND DISCUSSION

To investigate the validity of equations and to calculate the direction of the tool force in TPIF, a series of



Figure 9. Equipment used in TPIF process



Figure 10. Incomplete pyramid formed by TPIF process

experimental tests are carried out, and important parameters of these tests are presented in Table 2. Using numerical simulation, the coefficient of friction between tool and sheet is determined [33].

First, the conditions in Table 2 and Equation (27) are used to plot the force graphs for different values of M (Figure 11). Experimental tests are performed at an angle of 55° ; hence, in Figure 11, the intersection of force graphs for different values of M at an angle of 55° is specified with a vertical line.

In experimental tests, the values of force are measured using a dynamometer for the conditions mentioned in Table 2 and a pyramid with an angle of 55° and two tools with diameters of 8 and 16 mm. The curves of the forces applied to the corresponding tools are shown in Figure 12. These curves have been plotted using the Dynoware software, which is specific to the employed dynamometer.

The values of M proportional to each tool and the values obtained for tool force from Equation (27) are presented in Figure 11, and the average values of force obtained from experimental tests are depicted in Figure 12 and presented in Table 3. In the experimental tests, the values of force are obtained by the dynamometer and the average is calculated with the accompanying software.

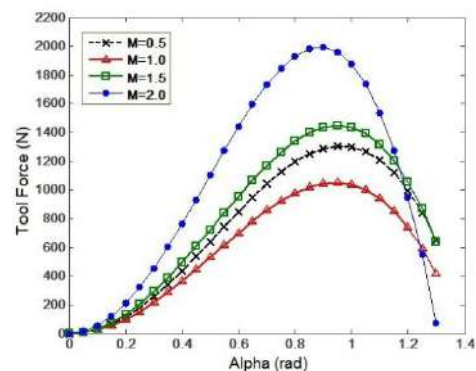


Figure 11. Force curves based on equation (27) for different values of M

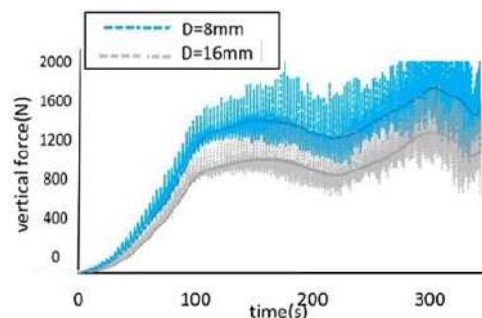


Figure 12. Vertical forces applied to tools with diameters of 8 and 16 mm for a pyramid angle of 55°

TABLE 2. Important parameters in experimental tests

Coefficient of friction between tool and sheet	Initial dimensions of sheet	Tool diameter	Sheet thickness	Sheet material	Yield stress of sheet
0.15	1800×1800 mm ²	8, 16 mm	1.2 mm	Aluminum 5053	210 MPa

TABLE 3. M values proportional to each tool and corresponding forces

Tool diameter (mm)	Friction coefficient	Sheet thickness	M value	Force (Equation (27))	Average force (experimental tests)
8	0.15	1.2	0.5	1300	1360
16	0.15	1.2	1	1050	1080

According to the values presented in Table 3 and the comparison of the forces calculated from Equation (27) and experimental tests, it can be seen that the maximum calculated error is 5%; that is, the results are in good agreement and the accuracy of equations is confirmed.

5. CONCLUSION

According to Figure 11, by increasing the angle α , the force applied to the tool enhances and the local strain created toward down side increases; based on $t=t_0\cos\alpha$, the change in the sheet thickness also increases. Hence, the enhancement of force with an increase in α is logical. The other point observed in Figure 11 is that at larger angles, the tool force is reduced. By increasing the angle of the punch wall, due to the reduction in contact between the surface of the tool, less compressive stress is applied to the metal sheet, and this is confirmed in Equations (15) and (23). Therefore, the force applied to tool with the enhancement of α increases, and at large angles, this force is reduced.

As shown in Equation (23), by decreasing the tool radius and increasing the sheet thickness, the stress created along γ is reduced. Therefore, due to the reduction in vertical stress, the sheet formability enhances. Ham and Jeswiet [34] confirmed the dependency of formability to tool radius and sheet thickness by using experimental tests.

One of the limitations of the incremental forming method is bearing the applied force by the machine during the process. In this research, an equation is presented for the prediction of the approximate value of the force applied to the tool. In this equation, with known values of the sheet yield stress, friction coefficient, tool radius and sheet thickness, the approximate value of the force applied to the tool can be calculated.

5. REFERENCES

- Naganathan, A., Penter, L., Sheet metal forming processes and applications, Hot stamping, ASM International, (2012).
- Edward, L., "Apparatus and process for incremental die less forming", Google Patents, (1967).
- Mason, B., Appleton, E., "Sheet metal forming for small batches using sacrificial tooling", Proceedings of the 3rd International Conference on Rotary Metalworking Processes, (1984), 495-512. doi : 10.1049/tpe.1984.0213 .
- Micari, F., Ambrogio, G., Filice, L., "Shape and dimensional accuracy in single point incremental forming: state of the art and future trends", *Journal of Materials Processing Technology*, Vol. 191, No. 1-3, (2007), 390-395. doi: 10.1016/j.jmatprotec.2007.03.066 .
- Filice, L., Ambrogio, G., Gaudio, M., "Optimized tool-path design to reduce thinning in incremental sheet forming process", *International Journal of Material Forming*, Vol. 6, No. 1, (2013), 173-178. doi: 10.1007/s12289-011-1065-4 .
- Tisza, M., "General overview of sheet incremental forming", *Journal of Achievements in Materials and Manufacturing Engineering*, Vol. 55, No. 1, (2012), 113-120.
- Attanasio, A., Ceretti, E., Giardini, C., Mazzoni, "Asymmetric two points incremental forming: improving surface quality and geometric accuracy by tool path optimization", *Journal of Materials Processing Technology*, Vol. 197, No. 1-3, (2008), 59-67. doi : 10.1016/j.jmatprotec.2007.05.053_.
- Duou, J., Callebaut, B., Verbert, J., De Baerdemaeker, "Laser assisted incremental forming: formability and accuracy improvement", *CIRP Annals-Manufacturing Technology*, Vol. 56, No. 1, (2007), 273-276. doi: 10.1016/j.cirp.2007.05.063 .
- Fan, G., Gao, L., Hussain, G., Wu, Z., "Electric hot incremental forming: a novel technique", *International Journal of Machine Tools and Manufacture*, Vol. 48, No. 15, (2008), 1688-1692. doi : 10.1016/j.ijmachtools.2008.07.010 .
- Ji, Y., Park, J., "Formability of magnesium AZ31 sheet in the incremental forming at warm temperature", *Journal of Materials Processing Technology*, Vol. 201, No. 1-3, (2008), 354-358. doi: 10.1016/j.jmatprotec.2007.11.206 .
- M. Ham and J. Jeswiet, "Single point incremental forming and forming criteria for AA3003", *CIRP Annals - Manufacturing Technology*, Vol. 55, No. 1, (2006), 241-244. doi : 10.1016/s0007-8506(07)60407-7 .
- Minutolo, FC., Durante, M., Formisano, A., Langella, A., "Evaluation of the maximum slope angle of simple geometries carried out by incremental forming process", *Journal of Materials Processing Technology*, Vol. 194, No. 1-3, (2007), 145-150. doi: 10.1016/j.jmatprotec.2007.04.109 .
- A. Bhattacharya, K. Maneesh, N. Venkata and J. Cao, "Formability and surface finish studies in single point incremental forming", *Journal of Manufacturing Science and Engineering*, Vol. 133, No. 6, (2011). doi: 10.1115/1.4005458 .

14. Ambrogio, G., Filice, L., Fratini, L., Micari, F., "Process mechanics analysis in single point incremental forming", *AIP Conference Proceedings*, Vol. 712, No. 1, (2004), 922-927. doi: 10.1063/1.1766645 .
15. Hussain, G., Gao, L. and Zhang, Z., "Formability evaluation of a pure titanium sheet in the cold incremental forming process", *The International Journal of Advanced Manufacturing Technology*, Vol. 37, No. 9, (2008), 920-926. doi: 10.1007/s00170-007-1043-7.
16. Nguyen, D., Park, J., Lee, H., Kim, Y., "Finite element method study of incremental sheet forming for complex shape and its improvement", *Proceedings of the Institution of Mechanical Engineers, Part B: Journal of Engineering Manufacture*, Vol. 224, No. 6, (2010), 913-924. doi: 10.1243/09544054jem1825 .
17. Han, F., Mo, J-h., "Numerical simulation and experimental investigation of incremental sheet forming process", *Journal of Central South University of Technology*, Vol. 15, No. 5, (2008), 581-587. doi: 10.1007/s11771-008-0109-5 .
18. Yamashita, M., Gotoh, M., Atsumi, S-Y., "Numerical simulation of incremental forming of sheet metal", *Journal of Materials Processing Technology*, Vol. 199, No. 1-3, (2008), 163-172. doi: 10.1016/j.jmatprotec.2007.07.037.
19. Zhou, LR., "Study on mechanism of NC sheet metal incremental forming", *Advanced Materials Research*, Vol. 239, (2011), 940-943. doi: 10.4028/www.scientific.net/amr.239-242.940 .
20. Shim, M.-S. and Park, J.-J., "The formability of aluminum sheet in incremental forming", *Journal of Materials Processing Technology*, Vol. 113, No. 1, (2001), 654-658. doi: 10.1016/s0924-0136(01)00679-3 .
21. Kim, Y. and Park, J., "Effect of process parameters on formability in incremental forming of sheet metal", *Journal of Materials Processing Technology*, Vol. 130, (2002), 42-46. doi: 10.1016/s0924-0136(02)00788-4.
22. Hirt, G., Ames, J., Bambach, M., Kopp, R., Forming strategies and process modelling for CNC incremental sheet forming. *CIRP Annals-Manufacturing Technology*, Vol. 53, No. 1, (2004), 203-206. doi: 10.1016/s0007-8506(07)60679-9 .
23. Silva, M., Nielsen, P., Bay, N., Martins, P., (2011). Failure mechanisms in single-point incremental forming of metals. *International Journal of Advanced Manufacturing Technology*, Vol. 56, No. 9, (2011), 893-903. doi: 10.1007/s00170-011-3254-1.
24. Seong, D.Y., Haque, M.Z., Kim, J.B., Stoughton, T.B. and Yoon, J. W., "Suppression of necking in incremental sheet forming", *International Journal of Solids and Structures*, Vol. 51, No. 15-16, (2014), 2840-2849. doi: 10.1016/j.ijsolstr.2014.04.007 .
25. Kurra, S. and Regalla, S. P., "Experimental and numerical studies on formability of extra-deep drawing steel in incremental sheet metal forming", *Journal of Materials Research and Technology*, Vol. 3, No. 2, (2014), 158-171. doi: 10.1016/j.jmrt.2014.03.009 .
26. Oraon, M., Sharma, V., Predicting Force in Single Point Incremental Forming by Using Artificial Neural Network. *International Journal of Engineering, Transaction A: Applications*, Vol. 31, No. 1, (2018), 88-95. doi: 10.5829/ije.2018.31.01a.13.
27. Silva, M., Skjoedt, M., Martins, P., Bay, N., (2008). Theory of single point incremental forming. *CIRP Annals Manufacturing Technology*, Vol. 57, No. 1, (2008), 247-252.
28. Emmens, W.C., Sebastiani, G. and van den Boogaard, A. H., "The technology of incremental sheet forming-a brief review of the history", *Journal of Materials Processing Technology*, Vol. 210, No. 8, (2010), 981-997. doi: 10.1016/j.jmatprotec.2010.02.014.
29. Perez-Santiago, R., Fiorentino, A., Marzi, R., Rodriguez, C., (2011). Advances in simulation of two point incremental forming. *AIP Conference Proceedings*, Vol. 1353, No. 1, (2011), 183-188. doi: 10.1063/1.3589512 .
30. Wang, QC., Hu, HH., Wu, JH., Cao, J., (2014). Research on Forming Accuracy of Two Point Incremental Forming for Aluminum 1060. *Advanced Materials Research*, Vol. 936, (2014), 1725-1729. doi: 10.4028/www.scientific.net/amr.936.1725 .
31. Saberi, A., Safavi, M., Kadkhodaei, M., Rabiei, F., Two-point incremental forming analysis using slab method and experimental data. *Modares Mechanical Engineering*, Vol. 13, No. 1, (2013), 61-69.
32. Silva, M. B., and Martins, P. A. F., "Two-Point Incremental Forming with Partial Die: Theory and Experimentation", *Journal of Materials Engineering and Performance*, Vol. 22, No. 4, (2013), 1018-1027. doi: 10.1007/s11665-012-0400-3 .
33. Esmailian, M., Khalili, Kh., "Finite element simulation of two-point incremental forming of free-form parts". *Iranian Journal of Materials Forming*, Vol. 5, No. 2, (2018), 26-35.
34. Ham, M., Jeswiet, J., "Forming Limit Curves in Single point incremental forming and the forming criteria for AA3003", *CIRP Annals-Manufacturing Technology*, Vol. 56, No. 1, (2010), 277-280. doi: 10.1016/j.cirp.2007.05.064.

Persian Abstract

چکیده

شکل‌دهی افزایشی مرحله‌ای دو نقطه‌ای یک روش جدید برای تولید قطعات پوسته‌ای با هندسه‌ی آزاد است. هدف اصلی این تحقیق به‌دست آوردن نیروی وارد به ابزار در فرایند شکل‌دهی افزایشی دو نقطه‌ای است. یکی از محدودیت‌های این فرایند، مقدار نیروی وارد بر ابزار است که دستگاه در حین فرایند می‌تواند تحمل کند. در این تحقیق یک معادله به‌منظور پیش‌بینی این مقدار نیرو ارائه می‌شود، که با در اختیار داشتن مقادیر تنش تسلیم ورق، ضریب اصطکاک، شعاع ابزار و ضخامت ورق، می‌توان این نیرو را محاسبه کرد. با افزایش زاویه‌ی شکل‌دهی، مقادیر کرنش موضعی ایجاد شده و نیروی وارد بر ابزار افزایش می‌یابد، اما با افزایش زاویه‌ی دیواره‌ی پانچ به دلیل کاهش سطح تکیه‌ی ابزار، تنش فشاری کمتری روی ورق فلزی وارد می‌شود. معادلات تحلیلی ارائه شده در این تحقیق با نتایج به‌دست آمده از آزمون‌های تجربی تایید شده است.



Experimental and Numerical Analysis of Permeability in Porous Media

Z. Sarparast^a, R. Abdoli^b, A. Rahbari^a, M. Varmazyar^{a,c}, K. Reza Kashyzadeh^{*d}

^a Department of Mechanical Engineering, Shahid Rajaee Teacher Training University, Tehran, Iran

^b Department of Mechanical Engineering, Islamic Azad University, Damavand Branch, Damavand, Iran

^c Wood Science and Technology Department, Faculty of Civil Engineering, Shahid Rajaee Teacher Training University, Tehran, Iran

^d Department of Mechanical and Instrumental Engineering, Academy of Engineering, Peoples' Friendship University of Russia (RUDN University), 6 Miklukho-Maklaya Street, Moscow, 117198, Russian Federation

PAPER INFO

Paper history:

Received 05 July 2020

Received in revised form 08 August 2020

Accepted 03 September 2020

Keywords:

Tissue Engineering

Porosity

Scaffold

Permeability

ABSTRACT

Using scaffold microstructure for bone tissue graft has been widely considered. Among the several properties of a scaffold, permeability plays a prominent role in the transport of nutrients, oxygen, and minerals. It is a key parameter which comprises various geometrical features such as pore shape, pore size and interconnectivity, porosity, and specific surface area. The main aim of this research is to characterize the permeability of the scaffold microstructure in terms of different pore sizes and porosity. To this end, cylindrical geometries for pores were modeled and the permeability coefficient was calculated using velocity and pressure drop and employing Darcy's law. The validation process of the numerical results was done by comparing with experimental data. In this regard, a simple experiment setup was presented based on the constant head method. Additionally, the scaffolds were built using Solid Freeform Fabrication (SFF) techniques. The results showed that increasing porosity leads to an increase in permeability. Moreover, the permeability increases as the pore size increases. Eventually, the reducing pore diameters have a significant effect on the flow and hence permeability (e.g., a 20% decrease in diameter yields a 76% decrease in permeability).

doi: 10.5829/ije.2020.33.11b.31

NOMENCLATURE

K	Intrinsic permeability (m^2)	μ	Dynamic fluid viscosity (Pa.s)
L	Specimen thickness (m)	ρ	Density (kg/m^3)
A	Cross-section area (m^2)	V	Velocity (m/s)
Q	Flow rate (m^3/s)	$2r$	Diameter of the pore (m)
ΔP	Pressure drop (Pa)	κ	Hydraulic conductivity (m/s)

1. INTRODUCTION

In recent years, significant findings in Bone Tissue Engineering (BTE) have been presented as a result of technological advances. The main purpose of bone graft is to increase the efficiency of the damaged bone. In addition, the bone graft substitutes by incorporating bone progenitor cells are used for specific purposes in different cases (e.g., the healing of bone fractures or between two bones across a diseased joint, to replace and regenerate

lost bone due to trauma, infection, or diseases) [1]. Therefore, the use of bone grafts to stimulate the new bone formation is widespread around the world. In this regard, there are three main types of bone grafts called autografts, allografts, and bone graft substitutes. Both autografts and allografts are widely used. However, their limitations lead to use of alternative methods such as bone graft substitutes. A prominent achievement has been made in BTE, in which a highly porous scaffold plays a fundamental role in guiding bone, vascular tissue

*Corresponding Author's Email: reza-kashi-zade-ka@rudn.ru (K. Reza Kashyzadeh)

growth, and regeneration in three dimensions [2]. In this case, porous scaffolds act as a temporary 3D structure that provides mechanical support for cell migration, cell adhesion, cell proliferation, and finally tissue regeneration [3-8].

Some of the most important features of a suitable scaffold are biocompatibility, biodegradability, and ability to diffuse cell nutrient and oxygen [9-14]. In addition, different architectural factors, including pore size, pore shape, porosity, and pore interconnectivity affect the efficiency of scaffold [15-18]. In this regard, increasing the pore size (diameter) leads to improve bone formation [19-23]. This result is based on the fact that the enhanced vascularization was observed in larger diameter which provides scaffold with higher oxygen tension and supply of nutrients, conditions that favored direct osteogenesis. Moreover, porosity plays an important role on the osteoconductive properties of the scaffold and the resultant bone tissue ingrowth and vascularization. In this regard, Karageorgiou and Kaplan have stated that higher values of porosity leads to enhance bone ingrowth [21]. In addition, Hollister et al. have investigated the effect of different values of porosity (30, 50, and 70%) in Polypropylene Fumarate/Tri-Calcium Phosphate (PPF/TCP) porous scaffolds [24]. The results of their research showed no significant differences in regenerated bone volume. To response to these conflicting results, a number of scholars have discussed on the permeability as a key parameter to determine scaffold's ability for mass transmission [25-29]. Furthermore, the dependency of permeability on structural parameters including porosity and pore size has been studied by Yang et al. [30]. Besides, Li et al. have proved that the permeability is a specific property of porous materials, which is independent of sample size and the fluid used to measure it [31].

The focus of the present research is on the biomimetic scaffolds and design criteria for their application in bone regeneration. To this end, permeability of the scaffolds was evaluated using simulation of fluid flow within interconnected pores by employing Darcy's law [3, 8, 17-18] in Computational Fluid dynamic (CFD) Analysis. Afterwards, to validate the proposed numerical model, the numerical results were compared with the experiment data obtained by authors. Eventually, by reviewing the literature reported in this paper, the effects of different structural parameters (porosity and pore size) on permeability was investigated using simulations and experiments as an innovation. It is examined quantitatively (not qualitatively) for the first time.

2. MATERIAL AND SPECIMENS

In the present research, the porous scaffolds were designed based on the repetition of a unit cell. A

schematic of the designed unit cell in detail is shown in Figure 1. A 3D printer using Solid Free Form (SFF) techniques was used to fabricate the specimens. Six types of scaffolds with different values of structural parameters were provided (Table 1). Figure 2 presents the built specimens of group I.

3. EXPERIMENTAL PROCEDURE

Permeability tests were performed based on Darcy's law which describes the flow of a fluid through a porous media [18].

$$K = \frac{\mu L Q}{A \Delta P} \quad (1)$$

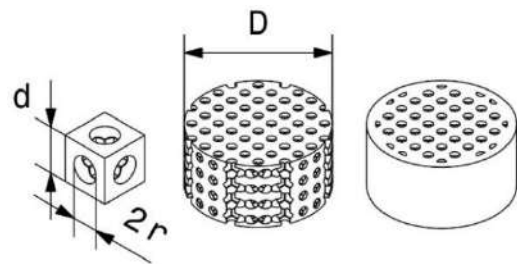


Figure 1. Schematic of the designed unit cell in detail

TABLE 1. Geometric specifications of the scaffolds manufactured by 3D printing

Parameter	Group I			Group II		
Unit cell (mm)	1.8			2		
Hole diameter (mm)	0.8	1	1.3	0.9	1.1	1.5
Porosity (%)	34	48	70	35	48	72

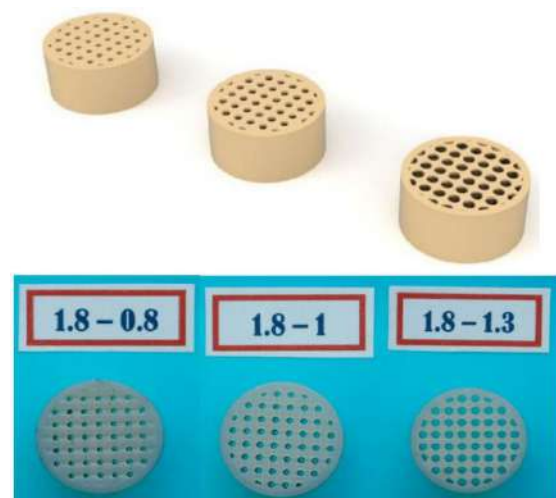


Figure 2. The built specimens of group I by 3D printing

Darcy's law is valid at the low value of Reynolds number, where the flow is laminar and viscous forces are predominant. In practice, Darcy's law is valid for the Reynolds number in the range of 1-10 [32]. In this regard, the Reynolds number is calculated as follows:

$$Re = \frac{\rho V(2r)_{pore}}{\mu} \quad (2)$$

In this study, the geometric parameters of scaffolds including diameter and length are 14 and 8 mm, respectively. Since the permeability is a parameter that is independent of fluid used to measure it and is related to the state of pores interconnectivity [30], water-glycerol at three different values of density and dynamic viscosity (Table 2) was used to fulfill Reynolds number range in Darcy's law.

The permeability measuring device was used to measure the intrinsic permeability as shown in Figure 3. The constant head (gravity-based) permeability test device is composed of an upper reservoir which maintains constant fluid level using fluid flow in and overflow out through separate pipes. Also, a pump has been used to return the overflow fluid from the overflow fluid tank to the fluid storage tank. To perform this test, a fixture with a flexible seating was designed. The most important feature of the designed fixture is that it is able to perform test settings with different scaffolds and various dimensions. The fluid which passes through the scaffold reaches the lower reservoir that is filled with enough amount of fluid to provide constant fluid level. Therefore, as soon as the fluid reaches the lower reservoir overflows to a collector seated on an electronic scale

(EK-300i AND weighing), the mass flow rates of the fluid are recorded consecutively by having the weight of the fluid in any particular time points. Afterwards, the data are sent to Win CT program for computer analyzing. As a result, the average mass flow rate is calculable through a period of time. Finally, the average mass flow rate is substituted in Equation (3) to calculate permeability coefficient of the porous scaffold. Three measurements for each scaffold specimen were conducted to ensure the repeatability of test results.

$$K = \kappa \frac{\mu}{\rho g} \quad (3)$$

4. NUMERICAL SIMULATION

In the present research, SolidWorks as one of the well-known Computed Aided Design (CAD) software was used to prepare the geometric model. In this regard, six different 3D models were designed according to Table 1.

TABLE 2. Values of density and dynamic viscosity of water-glycerol

Water-glycerol Properties	
μ (pa-s)	ρ (kg/m ³)
0.01	1158.7
0.0183	1179.5
0.047	1207

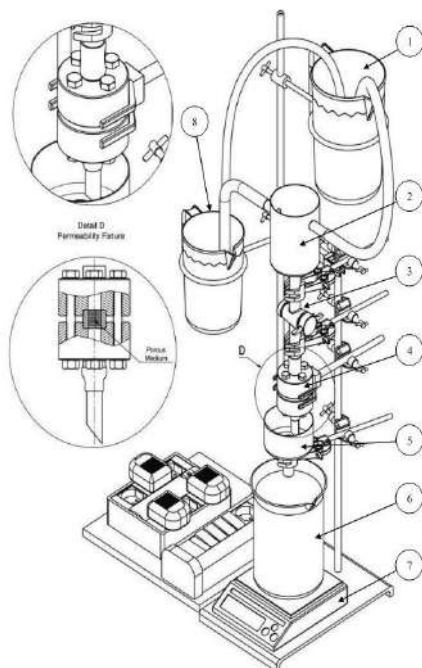


Figure 3. The 3D model of designed constant head permeability test setup, (1) Fluid storage tank, (2) Upper reservoir, (3) Valve, (4) Fixture, (5) Lower reservoir, (6) Collector, (7) Electronic scale, (8) Overflow fluid tank.

Furthermore, various modules of ANSYS 16.0 (i.e., ANSYS ICEM CFD, CFD packages, and ANSYS Fluent) were used to mesh the model, create Finite Volume Method (FVM), apply boundary conditions, and solve the problem.

The tetrahedral adaptation scheme (code 3D_TAG) was used based on the Biswas and Strawn statement [33]. In addition, mesh refinement was done by the first setting because the repeated refinement can lead to poor quality of mesh and affect the accuracy of the response. Moreover, mesh response sensitivity analysis was also performed to reduce computational costs and to determine the best parameters in the first setting such as element size [34-36]. Eventually, 100,000-600,000 tetrahedral meshes were generated on the designed scaffolds (the number of meshes depends on the scaffold sizes). Figure 4 illustrates the mesh model of one of the designed scaffolds as a representative.

The flow was simulated to study the mass flow rate, flow velocity, and flow pressure in scaffolds. To this end, a pressure-based solver and laminar, Newtonian, constant temperature, incompressible and homogeneous flow, inlet velocity between 0.03 m/s and 0.15 m/s, and outlet pressure of zero Pascal were assumed as boundary conditions. The schematic of inlet and outlet of fluid flow within the scaffolds is demonstrated in Figure 5. The equations of conservation of mass and momentum (Equation (4)) and continuity (Equation (5)) were used in this simulation. Finally, the permeability of scaffolds was computed based on Darcy’s law.

$$\rho(V \cdot \nabla V) = -\nabla P + \mu \nabla^2 V + \rho g \tag{4}$$

$$\varphi \frac{\partial \rho}{\partial t} + \nabla \cdot (\rho V) = 0 \tag{5}$$

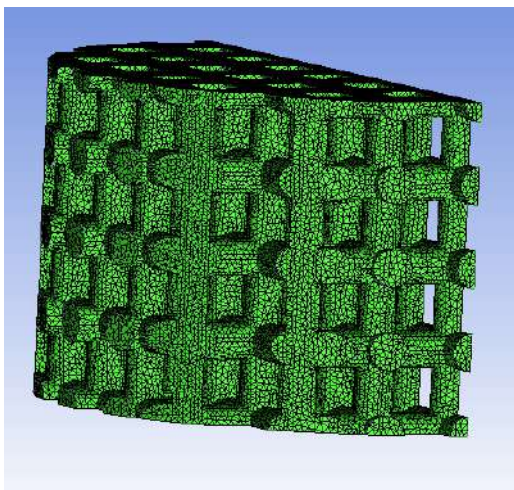


Figure 4. The mesh model of one of the designed scaffolds as a representative

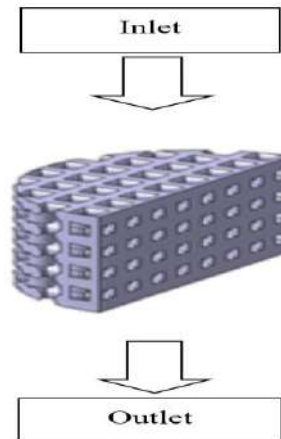


Figure 5. The schematic of inlet and outlet of fluid flow within the scaffolds used in ANSYS Fluent.

5. RESULTS AND DISCUSSION

5. 1. Numerical Results Numerical permeability coefficient values in terms of various porosity as a result of CFD analysis within an interval of (5.009-41.826) $\times 10^{-9}$ are presented in Figure 6. The contour maps in Figure 7 illustrate the range of velocities across the scaffold with unit cell size of 2mm and porosity of 70% and 35% for the longitudinal plane with the greatest flow rate at the center of the cylindrical pore.

The reliability of CFD calculations for predicting permeability of tissue engineering scaffolds were assessed with regards to computational data presented by Dias et al. [3]. Figure 8 presents the comparison of the numerical results obtained in this research and the Dias model.

5. 2. Experimental Results Figure 9 presents a comparison between the numerical results obtained in

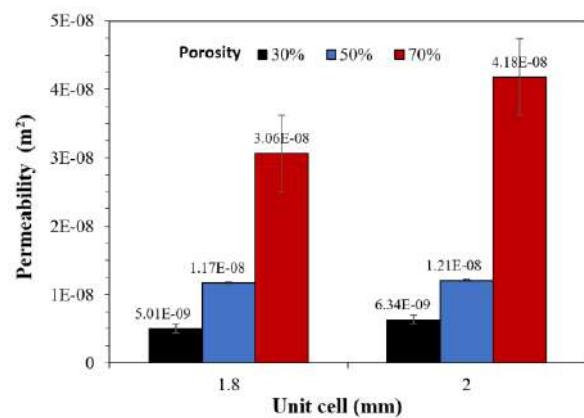


Figure 6. Numerical permeability coefficient values in terms of various porosity for different size of unit cell

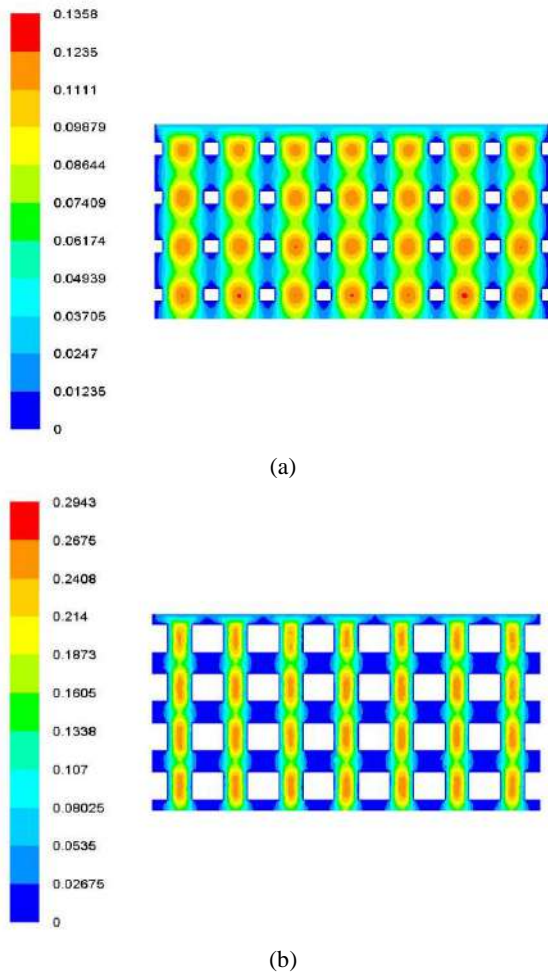


Figure 7. Velocity contour of the scaffold with unit cell size 2mm and different porosity including a) 70% and b) 30%

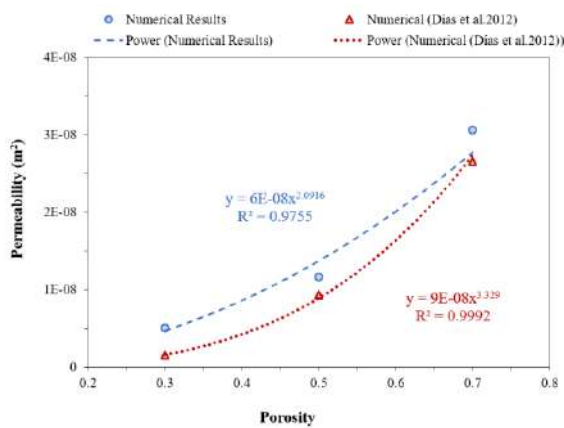


Figure 8. Comparison of permeability values versus porosity for scaffold with unit cell 1.8mm between present numerical model and Dias et al. model

this study and the experimental results for different cases of designed scaffolds. Both experiment and numerical

methods show the same trend for permeability versus porosity; increasing porosity leads to an increase in permeability. Moreover, the proposed numerical model also predicts the permeability values more than the real values (experimental data). The results indicated that the accuracy of presented numerical model decreases by raising porosity. In other words, the difference between the numerical and test results in porosity of 70 and 30% is the highest and lowest value, respectively.

5. 3. Effect of Pore Size The experimental data obtained in the previous section were used to examine the geometric effect of the design. Therefore, the influence of the pore size on the permeability is depicted in Figure 10. It is clear that the permeability increases as the pore size increases. Moreover, reducing pore diameters have a significant effect on the flow and hence permeability (e.g., 20% decrease in diameter yields a 76% decrease in permeability).

Next, the numerical results were compared with the experimental values (Figure 11). A linear relationship is obtained using regression method with $R^2=0.9605$, which indicates a good correlation between the numerical and the experimental data.

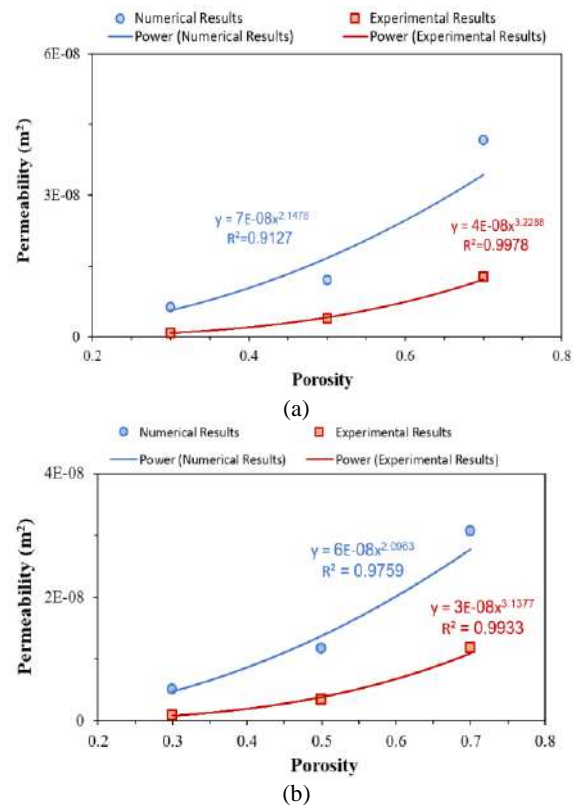


Figure 9. The relationship between permeability and porosity of designed scaffolds with a comparison of numerical and experimental results for different unit cell sizes: a) 2 mm and b) 1.8 mm

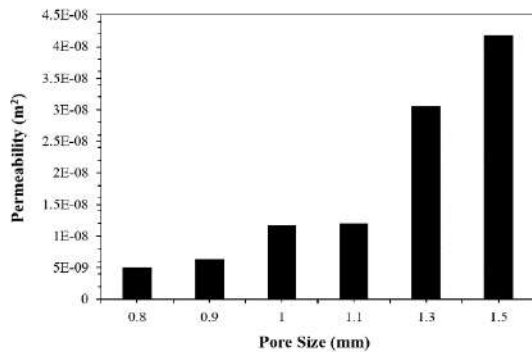


Figure 10. The impact of pore size on the permeability of designed scaffolds

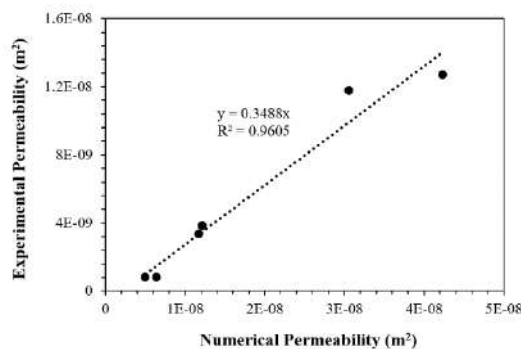


Figure 11. Relationship of experimental vs. numerical results

For a single hole, Hagen-Poiseuille equation described the pressure drop (Δp) through a cylindrical pipe as:

$$\Delta p = \frac{8Q\mu L}{\pi r^4} \quad (6)$$

By replacing Hagen-Poiseuille equation in Darcy's law it is possible to infer that permeability is proportional to the square of pore radius. Therefore, in this study, we can assume that:

$$K = \alpha \frac{r^2}{8} \quad (7)$$

By depicting experimental values versus numerical ones a linear relationship between data can be observed, according to Figure 11, this relation leads to a coefficient $\alpha = 0.3488$. In this regard, other researchers have similarly extracted the alpha coefficient [3, 29, 37-38]. In this respect, an adjustment should be proposed to the numerical values with the α coefficient. Permeability results after this fitting are demonstrated in Figure 12.

Given the fact that experimental results are smaller than numerical ones probably due to ignorance of reverse flow and surface effects such as wettability and roughness. Although, we considered laminar flow in the experimental procedure by utilizing water-glycerol to maintain Reynolds number between one and 10.

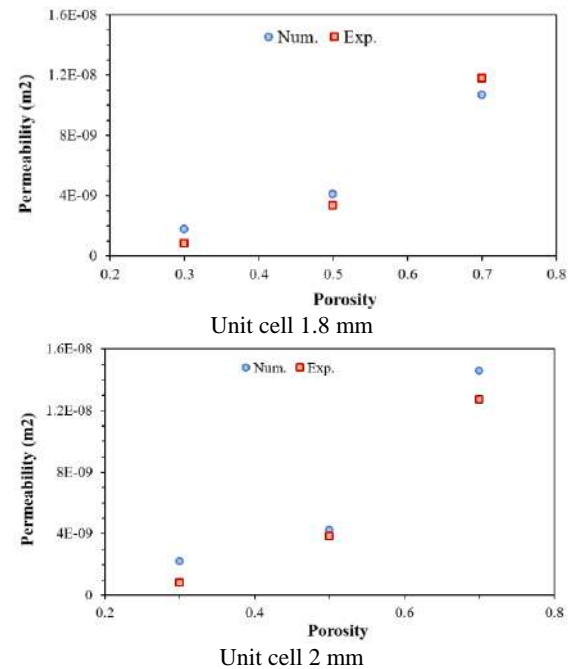


Figure 12. The relationship between permeability and porosity in the field of numerical and experimental results with consideration of the α coefficient

6. CONCLUSION

This study presents a design tool to investigate the effect of differences between design specifications and actual manufactured geometries on permeability to make it possible to predict permeability values numerically for porous materials with a certain design. Furthermore, it provides a criterion to predict permeability of scaffolds in terms of porosity for specific geometries to reduce the number of experimental studies necessary to validate design performance. In addition, it can be observed that permeability is a function of porosity and pore size. The main achievement of this research reveals that with the same porosity, higher permeability value can be achieved by only increasing pore size provided that mechanical properties were maintained in a bigger unit cell size.

7. ACKNOWLEDGMENTS

The publication has been prepared with the support of the "RUDN University Program 5-100".

8. REFERENCES

1. Polo-Corrales, L., Latorre-Esteves, M., and Ramirez-Vick, J. E., "Scaffold design for bone regeneration", *Journal of Nanoscience and Nanotechnology*, Vol. 14, No. 1, (2014), 15-56, DOI: 10.1166/jnn.2014.9127

2. Thavorniyutikarn. B, Chantarapanich. N, Sittthiseripratip. K, Thouas. G. A, and Chen. Q, "Bone tissue engineering scaffolding: computer-aided scaffolding techniques", *Progress in Biomaterials.*, Vol. 3, (2014), 61-102, DOI: 10.1007/s40204-014-0026-7
3. Dias. M. R, Fernandes. P. R, Guedes. J. M, and Hollister. S. J, "Permeability analysis of scaffolds for bone tissue engineering", *Journal of Biomechanics.*, Vol. 45, No. 6, (2012), 938-944, DOI: 10.1016/j.jbiomech.2012.01.019
4. Chan. G, and Mooney. D. J, "New materials for tissue engineering: towards greater control over the biological response", *Trends in Biotechnology.*, Vol. 26, No. 7, (2008), 382-392, DOI: 10.1016/j.tibtech.2008.03.011
5. Lemon. G, Reinwald. Y, White. L. J, Howdle. S. M, Shakesheff. K. M, and King. J. R, "Interconnectivity analysis of supercritical CO₂-foamed scaffolds", *Computer Methods and Programs in Biomedicine.*, Vol. 106, No. 3, (2012), 139-149, DOI: 10.1016/j.cmpb.2010.08.010
6. Ochoa. I, Sanz-Herrera. J. A, García-Aznar. J. M, Doblaré. M, Yunos. D. M, and Boccaccini. A. R, "Permeability evaluation of 45S5 Bioglass®-based scaffolds for bone tissue engineering", *Journal of Biomechanics.*, Vol. 42, No. 3, (2009), 257-260, DOI: 10.1016/j.jbiomech.2008.10.030
7. Reinwald. Y, Johal. R. K, Ghaemmghami. A. M, Rose. F. R. A. J, Howdle. S. M, and Shakesheff. K. M, "Interconnectivity and permeability of supercritical fluid-foamed scaffolds and the effect of their structural properties on cell distribution", *Polymer.* Vol. 55, No. 1, (2014), 435-444, DOI: 10.1016/j.polymer.2013.09.041
8. Viana. T, Biscaia. S, Almeida. H. A, and Bártolo. P. J, "Permeability evaluation of lay-down patterns and pore size of PCL scaffolds", *Procedia Engineering.*, Vol. 59, (2013), 255-262, DOI: 10.1016/j.proeng.2013.05.119
9. Botchwey. E. A, Dupree. M. A, Pollack. S. R, Levine. E. M, and Laurencin. C. T, "Tissue engineered bone: Measurement of nutrient transport in three-dimensional matrices", *Journal of Biomedical Materials Research Part A: An Official Journal of the Society for Biomaterials*, The Japanese Society for Biomaterials, and The Australian Society for Biomaterials and the Korean Society for Biomaterials, Vol. 67, No. 1, (2003), 357-367, DOI: 10.1002/jbm.a.10111
10. Chan. B. P, and Leong. K. W, "Scaffolding in tissue engineering: general approaches and tissue-specific considerations", *European Spine Journal.*, Vol. 17, No. 4, (2008), 467-479, DOI: 10.1007/s00586-008-0745-3
11. Pennella. F, Cerino. G, Massai. D, Gallo. D, Labate. G. F. D. U, Schiavi. A, Deriu. M. A, Audenino. A, and Morbiducci. U, "A survey of methods for the evaluation of tissue engineering scaffold permeability", *Annals of Biomedical Engineering.*, Vol. 41, No. 10, (2013), 2027-2041, DOI: 10.1007/s10439-013-0815-5
12. Rakovsky. A, Gotman. I, Rabkin. E, and Gutmanas. E. Y, "β-TCP-poly lactide composite scaffolds with high strength and enhanced permeability prepared by a modified salt leaching method", *Journal of the Mechanical Behavior of Biomedical Materials.*, Vol. 32, (2014), 89-98, DOI: 10.1016/j.jmbm.2013.12.022
13. Serpooshan. V, Quinn. T. M, Muja. N, and Nazhat. S. N, "Hydraulic permeability of multilayered collagen gel scaffolds under plastic compression-induced unidirectional fluid flow", *Acta Biomaterialia.*, Vol. 9, No. 1, (2013), 4673-4680, DOI: 10.1016/j.actbio.2012.08.031
14. Sharma. B, and Elisseeff. J. H, "Engineering structurally organized cartilage and bone tissues", *Annals of Biomedical Engineering.*, Vol. 32, No. 1, (2004), 148-159, DOI: 10.1023/B:ABME.0000007799.60142.78
15. Amirkhani. S, Bagheri. R, and Yazdi. A. Z, "Effect of pore geometry and loading direction on deformation mechanism of rapid prototyped scaffolds", *Acta Materialia.*, Vol. 60, No. 6-7, (2012), 2778-2789, DOI: 10.1016/j.actamat.2012.01.044
16. Hollister. S. J, "Porous scaffold design for tissue engineering", *Nature Materials.*, Vol. 4, No. 7, (2005), 518-524, DOI: 10.1038/nmat1421
17. Syahrom. A, Kadir. M. R. A, Abdullah. J, and Öchsner. A, "Permeability studies of artificial and natural cancellous bone structures", *Medical Engineering & Physics.*, Vol. 35, No. 6, (2013), 792-799, DOI: 10.1016/j.medengphy.2012.08.011
18. Truscello. S, Kerckhofs. G, Van Bael. S, Pyka. G, Schrooten. J, and Van Oosterwyck. H, "Prediction of permeability of regular scaffolds for skeletal tissue engineering: a combined computational and experimental study", *Acta Biomaterialia.*, Vol. 8, No. 4, (2012), 1648-1658, DOI: 10.1016/j.actbio.2011.12.021
19. Gross. K. A, and Rodriguez-Lorenzo. L. M, "Biodegradable composite scaffolds with an interconnected spherical network for bone tissue engineering", *Biomaterials.*, Vol. 25, No. 20, (2004), 4955-4962, DOI: 10.1016/j.biomaterials.2004.01.046
20. Hutmacher. D. W, Schantz. J. T, Lam. C. X. F, Tan. K. C, and Lim. T. C, "State of the art and future directions of scaffold-based bone engineering from a biomaterials perspective", *Journal of Tissue Engineering and Regenerative Medicine.*, Vol. 1, No. 4, (2007), 245-260, DOI: 10.1002/term.24
21. Karageorgiou. V, and Kaplan. D, "Porosity of 3D biomaterial scaffolds and osteogenesis", *Biomaterials.*, Vol. 26, No. 27, (2005), 5474-5491, DOI: 10.1016/j.biomaterials.2005.02.002
22. Murphy. C. M, Haugh. M. G, and O'Brien. F. J, "The effect of mean pore size on cell attachment, proliferation and migration in collagen-glycosaminoglycan scaffolds for bone tissue engineering", *Biomaterials.*, Vol. 31, No. 3, (2010), 461-466, DOI: 10.1016/j.biomaterials.2009.09.063
23. O'Brien. F. J, Harley. B. A, Yannas. I. V, and Gibson. L. J, "The effect of pore size on cell adhesion in collagen-GAG scaffolds", *Biomaterials.*, Vol. 26, No. 4, (2005), 433-441, DOI: 10.1016/j.biomaterials.2004.02.052
24. Hollister. S. J, Liao. E. E, Moffitt. E. N, Jeong. C. G, and Kempainen. J. M, "Defining design targets for tissue engineering scaffolds", *In Fundamentals of Tissue Engineering and Regenerative Medicine.*, (2009), 521-537, DOI: 10.1007/978-3-540-77755-7_38
25. Grimm. M. J, and Williams. J. L, "Measurements of permeability in human calcaneal trabecular bone", *Journal of Biomechanics.*, Vol. 30, No. 7, (1997), 743-745, DOI: 10.1016/S0021-9290(97)00016-X
26. Jones. A. C, Arns. C. H, Hutmacher. D. W, Milthorpe. B. K, Sheppard. A. P, and Knackstedt. M. A, "The correlation of pore morphology, interconnectivity and physical properties of 3D ceramic scaffolds with bone ingrowth", *Biomaterials.*, Vol. 30, No. 7, (2009), 1440-1451, DOI: 10.1016/j.biomaterials.2008.10.056
27. Mitsak. A. G, Kempainen. J. M, Harris. M. T, and Hollister. S. J, "Effect of polycaprolactone scaffold permeability on bone regeneration in vivo", *Tissue Engineering Part A.*, Vol. 17, No. 13-14, (2011), 1831-1839, DOI: 10.1089/ten.tea.2010.0560
28. Sandino. C, Krolczek. P, McErlain. D. D, and Boyd. S. K, "Predicting the permeability of trabecular bone by micro-computed tomography and finite element modeling", *Journal of Biomechanics.*, Vol. 47, No. 12, (2014), 3129-3134, DOI: 10.1016/j.jbiomech.2014.06.024
29. Sell. S, Barnes. C, Simpson. D, and Bowlin. G, "Scaffold permeability as a means to determine fiber diameter and pore size of electrospun fibrinogen", *Journal of Biomedical Materials Research Part A: An Official Journal of the Society for Biomaterials*, The Japanese Society for Biomaterials, and the Australian Society for Biomaterials and the Korean Society for Biomaterials, Vol. 85, No. 1, (2008), 115-126, DOI: 10.1002/jbm.a.31556

30. Yang, X, Lu, T. J, and Kim, T, "An analytical model for permeability of isotropic porous media", *Physics Letters A*, Vol. 378, No. 30-31, (2014), 2308-2311, DOI: 10.1016/j.physleta.2014.06.002
31. Li, S, de Wijn, J. R, Li, J, Layrolle, P, and de Groot, K, "Macroporous biphasic calcium phosphate scaffold with high permeability/porosity ratio", *Tissue Engineering*, Vol. 9, Issue. 3, (2003), 535-548, DOI: 10.1089/107632703322066714
32. Bear, J, "Dynamics of fluids in porous media", Courier Corporation, (2013), ISBN-13: 978-0-486-65675-5
33. Biswas, R, and Strawn, R. C, "Tetrahedral and hexahedral mesh adaptation for CFD problems", *Applied Numerical Mathematics*, Vol. 26, No. 1-2, (1998), 135-151, DOI: 10.1016/S0168-9274(97)00092-5
34. Reza Kashyzadeh, K, Farrahi, G. H, Shariyat, M, and Ahmadian, M. T, "Experimental and finite element studies on free vibration of automotive steering knuckle", *International Journal of Engineering. Transaction B: Applications*, Vol. 30, No. 11, (2017), 1776-1783, DOI: 10.5829/ije.2017.30.11b.20
35. Reza Kashyzadeh, K, "Effects of axial and multiaxial variable amplitude loading conditions on the fatigue life assessment of automotive steering knuckle", *Journal of Failure Analysis and Prevention*, Vol. 20, (2020), 455-463, DOI: 10.1007/s11668-020-00841-w
36. Farrahi, G. H, Reza Kashyzadeh, K, Minaei, M, Sharifpour, A, and Riazi, S, "Analysis of resistance spot welding process parameters effect on the weld quality of three-steel sheets used in automotive industry: experimental and finite element simulation", *International Journal of Engineering. Transaction A: Basics*, Vol. 33, No. 1, (2020), 148-157, DOI: 10.5829/ije.2020.33.01a.17
37. Andersson, L, Jones, A. C, Knackstedt, M. A, and Bergström, L, "Permeability, pore connectivity and critical pore throat control of expandable polymeric sphere templated macroporous alumina", *Acta Materialia*, Vol. 59, No. 3, (2011), 1239-1248, DOI: 10.1016/j.actamat.2010.10.056
38. O'Brien, F. J, Harley, B. A, Waller, M. A, Yannas, I. V, Gibson, L. J, and Prendergast, P. J, "The effect of pore size on permeability and cell attachment in collagen scaffolds for tissue engineering", *Technology and Health Care*, Vol. 15, No. 1, (2007), 3-17, DOI: 10.3233/THC-2007-15102

Persian Abstract

چکیده

استفاده از داربست‌های ریزساختار برای پیوند بافت استخوان به طور گسترده‌ای مورد توجه قرار گرفته است. در میان ویژگی‌های داربست، نفوذپذیری نقش مهمی در انتقال مواد مغذی، اکسیژن و مواد معدنی دارد. این یک پارامتر کلیدی است که شامل ویژگی‌های مختلف هندسی مانند شکل و اندازه منافذ و اتصال متقابل، تخلخل و مساحت ویژه است. هدف اصلی این پژوهش توصیف نفوذپذیری داربست‌های ریزساختار از نظر اندازه‌ی منافذ مختلف و تخلخل است. برای این منظور، منافذ با هندسه‌های استوانه‌ای شکل مدل شده و با استفاده از مقادیر سرعت و افت فشار و با به‌کارگیری قانون داری ضریب نفوذپذیری محاسبه شد. فرایند اعتبارسنجی نتایج عددی با مقایسه با داده‌های تجربی انجام شد. در این راستا، یک آزمایش ساده بر اساس روش سر ثابت ارائه شد. داربست‌ها با استفاده از فنون ساخت جامد فرم-آزاد (SFF) ساخته شدند. نتایج نشان داد که افزایش تخلخل منجر به افزایش نفوذپذیری می‌شود. علاوه بر این، با افزایش اندازه‌ی منافذ، نفوذپذیری نیز افزایش می‌یابد. در نهایت، کاهش قطر منافذ تأثیر قابل توجهی بر جریان، و در پی آن نفوذپذیری دارد (به عنوان مثال، کاهش ۲۰ درصدی قطر منجر به کاهش ۷۶ درصدی نفوذپذیری می‌شود).



Reliability Evaluation of a Disaster Airflow Emergency Control System Based on Bayesian Networks

J. Zhang, Z. Ai*, L. Guo, X. Cui

College of Mining Engineering, North China University of Science and Technology, Tangshan, PR China

PAPER INFO

Paper history:

Received 29 April 2020

Received in revised form 16 August 2020

Accepted 03 September 2020

Keywords:

Bayesian Network

Conditional Probability

Emergency Airflow Control System

Fault Diagnosis

Reliability

ABSTRACT

This study proposed a novel method for system failure reasoning based on Bayesian networks to solve emergency airflow control system reliability problems. A system fault tree model was established to identify the logical relationship between the units, which was then transformed into a Bayesian network fault analysis model to determine network node states and the conditional probability table, as well as to carry out diagnostic reasoning on the system node branches. The reliability analysis of the model based on Netica Bayesian tool shows that the probability of system failure caused by substation communication node is the highest under normal conditions, and data monitoring and central station communication nodes have a greater impact on intelligent control. By predicting and diagnosing system faults, the optimization of system design is realized on the framework of Bayesian network to improve the reliability, and there by establishing a theoretical foundation for future disaster prevention research.

doi: 10.5829/ije.2020.33.11b.32

NOMENCLATURE

CPT	Conditional probability table	FMEA	Failure mode and effect analysis
FTA	Fault tree analysis	BN	Bayesian networks

1. INTRODUCTION

The diffusion of smoke flow along the roadway after a mine fire is critical to ensure mine disaster prevention. By adjusting the damper switch in the disaster area, the air volume can be modulated to ensure the safety of underground personnel during disasters [1, 2]. This emergency control system has been greatly popularized and applied. It is of great significance to improve disaster relief efficiency and reduce system failure rate through reliability evaluation.

Commonly used reliability analysis methods include failure mode and effect analysis (FMEA), fault tree analysis (FTA), and others. Lo and liou [3] proposed a new FMEA risk assessment method based on multi-criteria decision making. Hyun et al. [4] used fault tree analysis (FTA) and analytic hierarchy processes (AHP) to conduct risk assessment during tunnel construction.

Peeters et al. [5] improved the efficiency of fault analysis by combining FTA and FMEA through recursion. However, these methods do not account for the connection between various failure modes and are not suitable to characterize uncertain casual relationships. Current equipment failure diagnosis strategies do not meet the requirements for failure diagnosis under complex catastrophe scenarios. Therefore, it is the direction of current scientific research to establish a judgment model through artificial intelligence for independent evaluation. Dynamic process fault detection and diagnosis based on a combined approach of hidden Markov and Bayesian network model [6]. It presents a novel technique using artificial neural network learning for automated diagnosis of localized faults in rolling element bearings [7]. Predictions of tool wear in hard turning of AISI4140 steel through artificial neural network, fuzzy logic and regression models, the results

*Corresponding Author Institutional Email: aizibo@stu.ncst.edu.cn (Z. Ai)

reveal that the artificial neural network (ANN) provides better accuracy when compared to regression analysis [8]. A new hybrid decision tree (DT) technique based on two artificial neural networks (ANN), namely multilayer perceptron (MLP) and radial basis function (RBF), is proposed to predict sediment transport in clean pipes [9].

Bayesian networks were developed to address uncertainty in artificial intelligence research, and have been widely used in artificial intelligence, pattern recognition, and other fields. In fact, learning structures of interval-based Bayesian networks in probabilistic generative model for human complex activity recognition is discussed in literature [10]. A new stability-based dynamic Bayesian network method for dynamic systems represented by their time series [11]. Given that Bayesian networks have a solid theoretical foundation, analysis ability, and a capacity to describe uncertainty, this approach has begun to be applied in recent years in medical diagnosis, risk and safety assessment, fault diagnosis, reliability analysis and assessment, among other fields. Comparison of automatic and guided learning for Bayesian networks to analyze pipe failures in the water distribution system [12]. A comparative study between discrete and continuous time Bayesian networks demonstrates clinical time series data with irregularity [13]. A novel scoring function based on family transfer entropy for Bayesian networks learning and its application to industrial alarm systems is discussed [14]. Copula-based Bayesian network model for process system risk assessment is discussed [15]. Bayesian networks are supported by mathematical theory and can be implemented through a variety of reasoning models and algorithms with good learning performance.

The FMEA method has a comprehensive analysis of failure modes, but it has insufficient analysis of the causes of failures and cannot reflect the logical relationship between various factors. FTA analyzes the causes of failures comprehensively and can reflect simple logical relationships, but it is easy to miss failure modes. It can be seen that these two methods have a certain degree of complementarity. Bayesian networks can reflect the characteristics of complex systems such as polymorphism, failure correlation, and uncertainty in logical relations. It has the ability to deal with uncertainties that FMEA and FTA do not have, and it can conduct bidirectional analysis, which is stronger reasoning and analysis ability. However, the disadvantage of Bayesian networks is that modeling is difficult. Especially when there is a lack of data, it is difficult to build Bayesian networks using data learning methods. Therefore, it is an effective method to use the information provided by FMEA and FTA to build a Bayesian network model to solve the problem of lack of data.

Aiming at the reliability problem of disaster airflow emergency control system, the reliability model of

Bayesian network is constructed by integrating the reliability related information of FMEA and FTA. Determine the fault nodes of the entire control system, apply the fault data to the autonomous learning of the Bayesian network, and propose a reliability evaluation method for the disaster airflow emergency control system based on the Bayesian network. Carry out precise reasoning on the cause and result of the failure, determine the main failure factors, and provide reliability guidance for the disaster airflow emergency control system.

To address emergency control system reliability problems, Bayesian networks can be employed in conjunction with fault diagnosis models to determine the fault node of the entire control system, after which the fault data can be used for Bayesian network autonomous learning, thereby determining the main failure factors for disaster emergency control.

2. MODEL

2.1. Bayesian Network Bayesian networks, also known as directed acyclic graphs (DAG), were first proposed by Pearl in 1986. Bayesian networks are composed of individual nodes, and the conditional probability between each node constitutes the conditional probability table (CPT) of the Bayesian network, which connects the whole network for reasoning diagnosis through the causal relationship between nodes and conditional dependence.

The reasoning of Bayesian network is to use the Bayesian network structure and its conditional probability table to calculate the posterior probability distribution of some non-evidence nodes under the value state of the set of known evidence nodes. Bayesian network reasoning algorithms are divided into exact reasoning and approximate reasoning, both of which are NP-hardness [16].

Bayesian networks can be represented as $B = \langle G, P \rangle = \langle \langle V, E \rangle, P \rangle$, which includes two parts: $G = \langle V, E \rangle$ represents the directed acyclic graph (DAG), where the elements in node set V represent variables, the directed edge E between nodes represents the association between variables, and P represents the conditional probability table (CPT). An example of a Bayesian network is shown in Figure 1. Node A is the parent of node B, and the prior probabilities of nodes B and C depend on the distribution probability of A.

According to Bayes theorem, the conditional probability formula is obtained as Equation (1):

$$P(A|B) = \frac{P(B|A)P(A)}{P(B)} \quad (1)$$

Suppose a directed acyclic graph of a Bayesian network $G = \langle V, E \rangle$, where the elements in node set V represents variables $X_1, X_2, X_3, \dots, X_n$, the directed edge E

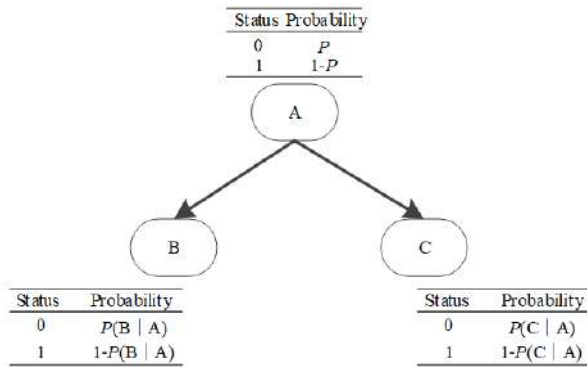


Figure 1. Basic framework of a Bayesian network

between nodes represents the correlation between variables, and the multiplication of conditional distributions of each node is the joint probability distribution such as Equation (2):

$$P(X_1, X_2, \dots, X_i) = \prod_{i=1}^n P(X_i | X_{\pi(i)}) \tag{2}$$

When performing system reliability analysis, a Bayesian network model can be established. Suppose the model has n nodes X_0, X_1, \dots, X_{n-1} . X_0 represents a system failure node, X_1-X_{n-1} represents other failure causes and failure mode nodes. The actual state value of node X_i ($0 \leq i \leq n-1$) is represented by x_i , which can take two state values of 0 and 1. 0 means no occurrence, and 1 means occurrence. Afterward, the probability of failure of the whole system can be directly calculated by using the joint probability distribution such as Equation (3):

$$P(X_0 = 1) = \sum_{x_1 \dots x_{n-1}} P(X_0 = 1, X_1 = x_1, \dots, X_{n-1} = x_{n-1}) \tag{3}$$

Taking the failure cause event as the root node, the failure mode event as the intermediate node, and the failure impact event of the entire system failure as the leaf node, a Bayesian network model is constructed. Suppose that after the occurrence of a node X_j , the previous probability of other events can be expressed as Equation (4):

$$P(X_i = 1 | X_j = 1) = \frac{P(X_j=1 | X_i=1)P(X_i=1)}{P(X_j=1)} \tag{4}$$

2. 2. Reliability Model

In the event of system data imperfections, the study of system failure effect analysis can effectively determine system failure mode and failure cause, after which failure effect analysis of the fault tree structure can determine the logical relationship between various influencing factors. Finally, the fault tree can be converted into Bayesian networks, and the uncertainty of using Bayesian network problems to handle capacity reliability of the system can be analyzed. The block diagram of this method is shown in Figure 2.

First, make the system definition. Clarify the working principle of the system, analyze the function of the system, and determine the content and scope of the research object.

The second step starts with the basic unit of the system, analyzes the possible causes of the failure of each unit, the failure mode and the influence of the failure mode on the unit, and compiles the FMEA table.

The third step is to convert the FMEA form into FTA. Taking the fault effect of the basic unit as the top event, the fault mode as the middle event, and the fault cause as the basic event, the logical relationship between each event is analyzed, and the fault subtree is formed by connecting logic gates. Connect the fault subtree corresponding to each basic unit to the upper level system with appropriate logic gates to form a complete FTA.

The fourth step is to transform FTA into Bayesian network. Take the top event of the fault tree as the root node of the Bayesian network, the intermediate event of the fault tree as the intermediate node of the Bayesian network, and the basic event of the fault tree as the leaf node of the Bayesian network. Convert the logical relationship of the fault tree into the corresponding conditional probability table, and use statistical data or expert opinions to obtain the basic probability information of the root node.

Finally, reliability analysis is carried out. The reliability analysis work such as fault diagnosis reasoning is carried out by using the bidirectional analysis ability of Bayesian network.

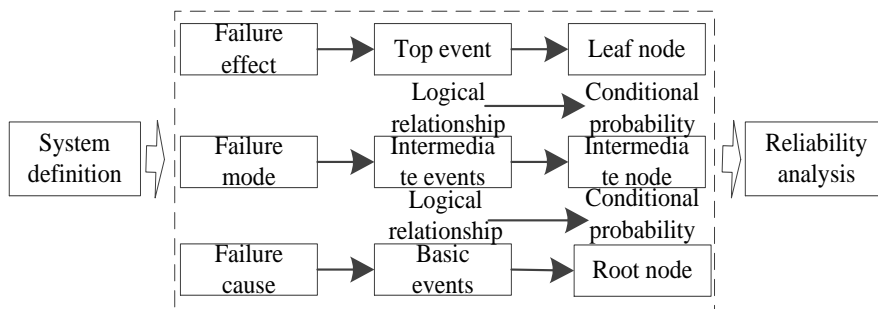


Figure 2. Reliability analysis block diagram

3. BAYESIAN NETWORK DETERMINATION

3. 1. Disaster Wind Emergency Control System

According to the characteristics of the mine ventilation system and the law of smoke flow after a fire, a multi-channel electronically controlled pneumatic disaster relief damper was preset in each ventilation connection lane and its switching state was remotely controlled from the ground monitoring center, forming the disaster emergency rescue system. After a fire occurs in a mine, emergency control of remote airflow is carried out to adjust the air volume by adjusting the damper switch in the disaster area so that the polluted airflow enters the return air lane and is discharged, while fresh airflow is maintained in the densely populated area. The flow chart of a disaster airflow emergency control system is shown in Figure 3.

3. 2. System Failure Impact Analysis According to the definition of a disaster airflow emergency control system, failure mode influence analysis was carried out from three perspectives: fault cause, fault mode, and fault influence. The results are summarized in Table 1.

3. 3 System Fault Tree Analysis According to failure impact analyses, the system fault tree diagram was drawn with the catastrophic control fault as the top event

TABLE 1. System failure impact analysis

Unit (U)	Failure cause (C)	Failure model (M)	Fault effect (E)
Upper machine	C1 data troubleshooting failure	M1 upper computer software control failure	E1 intelligent control fault
	C2 disaster monitoring failure		
Ground central base station	C3 communication system failure	M2 center station hardware control failure	
	C4 control system failure		
Controller station	C5 control system failure	M3 controller substation failure	E2 remote control failure
	C6 communication system failure		
Damper	C7 data acquisition failure	M4 damper failure	
	C8 starter failure		
	C9 power system failure		
	C10 mechanical system failure		

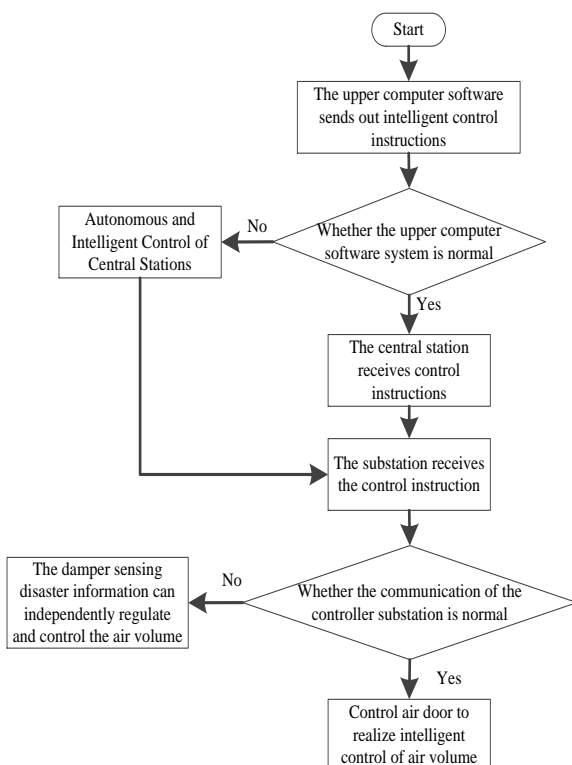


Figure 3. Flow chart of a disaster airflow emergency control system

of the fault tree. Afterward, each fault subtree was connected, and the logical relationship between each event was determined, as shown in Figure 4. Any failure of the remote control and intelligent control will result in the failure of the top catastrophic control event, the failure of upper computer software control and center station hardware control will affect intelligent control fault, and any failure of the controller sub-station and damper will result in remote control fault. The control of upper computer software is affected by data solution and disaster monitoring; the control of central station hardware is affected by the communication system and control system of the central station; the fault of the controller sub-station is affected by the control system, communication system, and data acquisition of the sub-station; the failure of the damper is affected by the damper start-up device, power system, and mechanical system.

3. 4. Bayesian Network Construction

3. 4. 1. Bayesian Node Determination According to the system fault tree model, 17 Bayesian network nodes were determined to represent the fault of the remote control system from cause to effect. The classification of all nodes and states was described as follows:

Data solution (state: normal/abnormal): this node indicates that the upper computer software reads the disaster information of each sub-station underground, studies and analyzes the ventilation parameters and environmental parameters during the disaster period, and

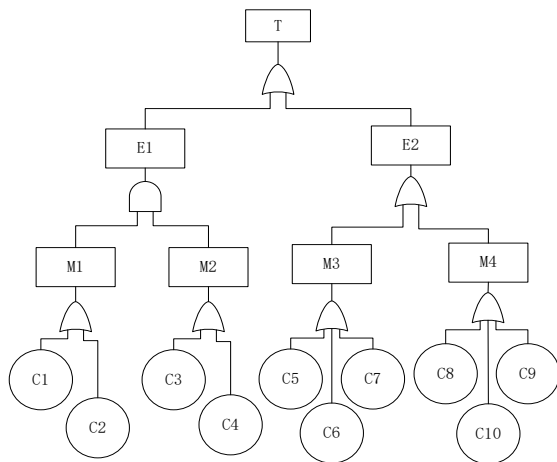


Figure 4. System fault tree analysis

generates the intelligent control scheme during the disaster period.

Disaster monitoring (status: normal/abnormal): this node represents the real-time acquisition of monitoring data of each sensor in the controller sub-station by the host computer and the ground central station.

Communication system of ground central station (state: normal/abnormal): this node represents the communication equipment between the ground center station and the host computer and the controller sub-station, which is composed of optical fiber and a communication interface.

Ground central station control system (state: normal/abnormal): this node indicates that the ground central station receives the instructions from the host computer or the autonomic control instructions and performs intelligent control of underground sub-stations through a programmable logic controller (PLC).

Communication system of the controller sub-station (state: normal/abnormal): this node represents the communication equipment between each sub-station and the central station and is composed of optical fiber and a communication interface.

Controller sub-station control system (state: normal/abnormal): this node represents that each branch station receives control instructions from the central station or directly reads control instructions from the upper computer and conducts intelligent control of the damper through a PLC.

Data collection of controller station (state: normal/abnormal): this node represents the real-time acquisition of downhole disaster monitoring data by each sub-station and the feedback to the upper computer and the ground central station.

Damper start device (state: normal/abnormal): this node represents the start switch of the damper power system after the damper receives the sub-station control command.

Damper power system (state: normal/abnormal): this node represents the high-pressure gas transported from the ground to the underground and the standby high-pressure gas cylinder as the power source of the damper, driving the cylinder to drive the active door.

Damper mechanical system (state: normal/abnormal): this node represents the mechanical structure of the damper; a steel wire rope is used to bypass the pulley to connect the driven door so that the two doors can be opened synchronously.

Control failure of upper computer software (state: normal/abnormal): the failure of any node in data calculation and disaster monitoring can cause the control failure of upper computer software.

Center station hardware control failure (state: normal/abnormal): the failure of any disaster monitoring node in the central station control system and communication system causes the failure of central station hardware control.

Control fault of the controller sub-station (state: normal/abnormal): any sub-station control system node failure of the communication system and data acquisition will cause control failure of the controller sub-station.

Damper failure (state: normal/abnormal): damper failure occurs at any node of the damper starter, power system, and mechanical system.

Intelligent control fault (state: normal/abnormal): the upper computer software control and the center station hardware control implement double insurance intelligent control, and accept the underground sub-station to collect the information for intelligent solutions. When both of them fail at the same time, an intelligent control fault will occur.

Remote control fault (state: normal/abnormal): remote control failure occurs when the downhole controller sub-station and damper malfunction, and the sub-station starts the automatic induction disaster relief mode.

Catastrophic control fault (state: intelligent fault/Remote fault) Catastrophic control faults include intelligent control faults and remote control faults.

3.4.2. Conditional Probability Table for Bayesian Nodes

Historical data is typically used in Bayesian network learning algorithms as the prior probability of each node, and some comprehensive decision-making methods, such as the Delphi method [17] and fuzzy analytic hierarchy process [18] are adopted to consult expert opinions. The prior probability table and conditional probability table of the Bayesian network can be determined through systematic test statistics and expert advice, providing data support for Bayesian network process learning. Due to the subjectivity of human decision making, multiple groups of learning should be carried out based on debugging sample data to minimize error. The conditional probability table (CPT)

is the core foundation of Bayesian reasoning, which can be obtained through parametric learning of historical records and statistics, as well as the experience of industry experts themselves. In this section, Bayesian network reasoning is performed for the "controller station fault" node branch. The fault tree bottom events "substation control system failure," "substation communication system failure," and "Data acquisition failure" root nodes are converted into the Bayesian network C5 "substation control system," C6 "substation communication system," C7 "data acquisition," and the top event "controller substation fault" leaf node is converted into the Bayesian network M3 "controller substation." Figure 5 shows the branches of the Bayesian network corresponding to the nodes of the "controller substation failure."

According to Table 1, if the controller station node M3 fails, the probability of failure caused by C5 node is $P(C5=1 | M3=1)=11.4\%$, the probability of failure caused by C6 node is $P(C6=1 | M3=1)=68.2\%$, and the probability of failure caused by C7 is $P(C7=1 | M3=1)=22.7\%$. The failure rate of C6 after calculating node M3 is $P(C6=1 | M3=1, C5=0)=76.1.6\%$. Similarly, $P(C5=1 | M3=1, C6=0)=33.6\%$.

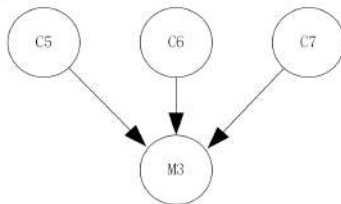
3. 4. 3. Emergency Control System Bayesian Network Based on the equipment downhole test statistics and fault information in the accident database, the root node historical information is obtained, as shown in Table 2.

The probabilistic inference was based on the Netica Bayesian network analysis tools. Each node of the system includes two states, "Y" means normal and "N" means failure. Through the prior probability of the root node and

TABLE 2. Prior information of the root node

Node name	Node state	Transcendental probability
data decoding	normal	0.99
	failure	0.01
disaster monitoring	normal	0.95
	failure	0.05
Central station communication	normal	0.92
	failure	0.08
Central station control	normal	0.98
	failure	0.02
Substation communication	normal	0.99
	failure	0.01
Substation control	normal	0.94
	failure	0.06
data collection	normal	0.98
	failure	0.02
start device	normal	0.99
	failure	0.01
Power system	normal	0.96
	failure	0.04
Mechanical systems	normal	0.95
	failure	0.05

C5 P(C5)		C6 P(C6)		C7 P(C7)	
0	99%	0	94%	0	98%
1	1%	1	6%	1	2%



(a) Bayesian network branch

C5	C6	C7	P(M3)
0	0	0	0
0	0	1	1
0	1	0	1
1	0	0	1
0	1	1	1
1	0	1	1
1	1	0	1
1	1	1	1

(b) Conditional probability table
Figure 5. Bayesian network analysis

the conditional probability of each node, the initial Bayesian network of the disaster airflow emergency control system was established, as shown in Figure 6.

4. RELIABILITY ASSESSMENT

Air volume adjustment has a vital role in normal system operation during emergencies and disaster periods, the regulation process and control system structure are complex, especially the unit logical relationships.

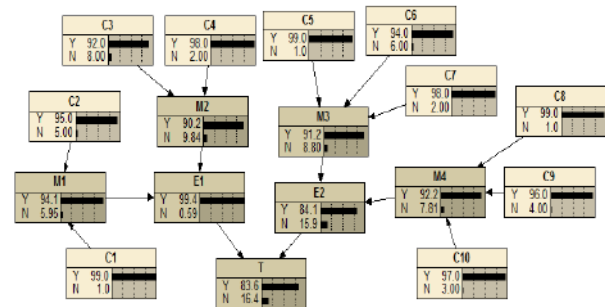


Figure 6. Bayesian network of a disaster airflow emergency control system

Regulation failure mechanisms can often be unclear, however, through the construction of a Bayesian network, reliable system evaluation can be performed based on the causal relationship between all nodes, allowing for the use of causal reasoning mechanisms to determine the system failure probability via the collaborative relationship between the units of the system. All of this in conjunction provides a theoretical basis for system reliability assessment.

4. 1. Emergency Control Fault Analysis

The reliability analysis was conducted according to the initial emergency control system Bayesian network. If the system failed, node T was assumed to be 100% in the N state, as shown in Figure 7(a). The intelligent control of node E1 failure probability was 3.6%, the remote control node E2 failure probability was 97%, the visible intelligent control in double insurance was under the action of high reliability; therefore, the analysis of the remote control node E2 to the next level node, as shown

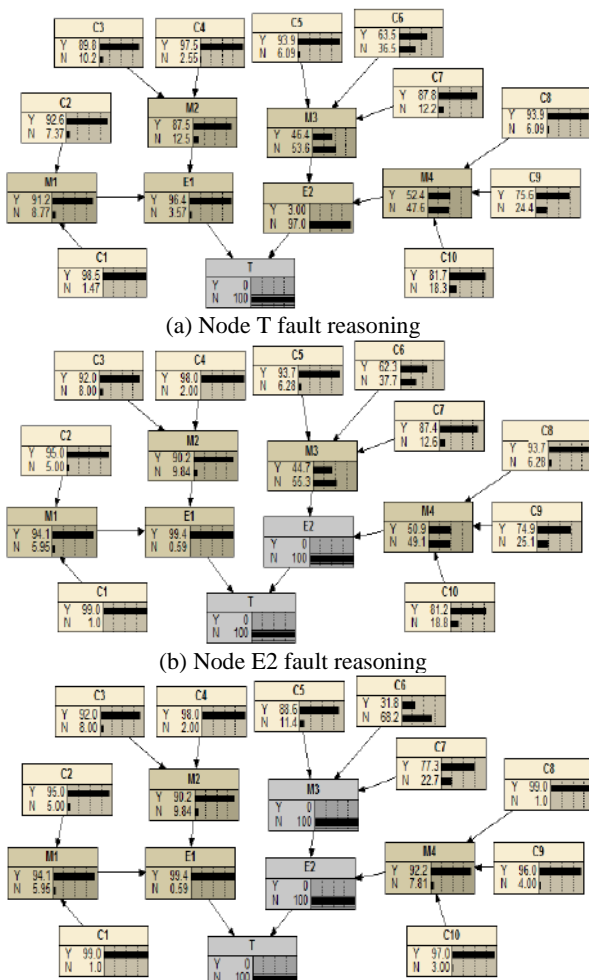


Figure 7. Node M3 fault reasoning

in Figure 7(b), determined that the controller sub-station node M3 failure rate was 55.3% and the damper node M4 failure rate was 49.1%. After comparison, the lower level analysis of the controller substation node M3 was conducted, as shown in Figure 7(c), and the communication node C6 failure rate of the sub-station was 68.2%, the control node C7 failure rate of the sub-station was 11.4%, and the data acquisition node C5 failure rate was 22.7%. The analysis shows that the probability of fault caused by sub-station communication was the highest under normal fault condition.

4. 2. Intelligent Control Fault Analysis

The emergency control system of catastrophic wind flow obtains the airflow control parameters of each branch through intelligent calculation of underground data collection, thus realizing intelligent control of fire smoke flow, which is the key of the emergency control system. The intelligent control system examined herein was made up of upper machine and ground centers in parallel, which could simultaneously read intelligent control commands sent to relief sub-station data information and conduct intelligent double insurance control. When the emergency air control system fails, assuming that the remote control node E2 is in a normal state, the intelligent control node E1 will fail, so as to conduct reliability reasoning on each cause node.

At this point, as shown in Figure 8, both the upper computer node M1 and the ground central station node M2 fail simultaneously. The failure rate of node C1 is 16.8%, the failure rate of node C2 is 84%, the failure rate of node C3 is 81.3%, and the failure rate of node C4 is 20.3%. Analysis shows that the data monitoring node C2 and the communication node C3 of the central station are more likely to cause intelligent control faults, so as to conduct troubleshooting.

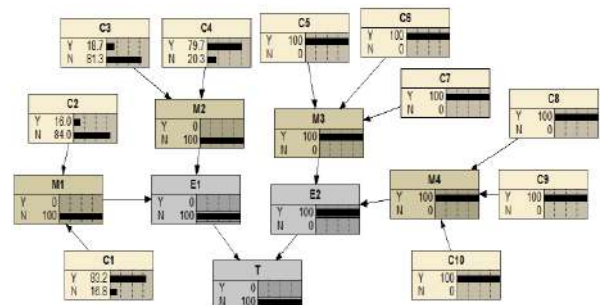


Figure 8. Fault analysis of intelligent control

5. CONCLUSION

Given the lack of perfect system data, a reliability evaluation model from failure impact analysis and fault impact analysis to Bayesian network was established to

analyze the reliability of the system by using the uncertainty processing ability of Bayesian networks.

The structural process of the emergency control system was analyzed, the system reliability analysis model was established, and 17 Bayesian network nodes and states were determined. Based on the prior probability of the root node and the conditional probability of each node, the initial Bayesian network of a disaster airflow emergency control system was established.

Based on the Netica Bayesian learning software, the reliable diagnosis of the disaster airflow emergency control system was carried out, and the diagnosis results showed that the probability of failure caused by substation communication node was the highest under normal circumstances. Through the analysis of the intelligent control of the system, it was concluded that the data monitoring node and the central station communication node have a greater impact on the intelligent control and are prone to failure. Predict and diagnose system failures, analyze the weak links of the system, guide operation and maintenance, and realize the optimization of system design.

6. ACKNOWLEDGEMENTS

This research work was supported by the National Key Research and Development Plan of China (2018YFC0808100), the National Natural Science Foundation of China (grant number 51874012).

7. REFERENCES

- Wang, K., Haiqing, H., Jiang, S. G., Wu, Z. Y., and Shao, H., "Research on regional linkage and intelligent control system of mine fire wind and smoke flow." *Industry and Mine Automation*, Vol. 45, No. 7, (2019), 21–27. <https://doi.org/10.13272/j.issn.1671-251x.17440>
- Wang, K., Jiang, S. G., Zhang, W. Q., Wu, Z. Y., and Shao, H., "Numerical simulation and application research of mine fire emergency rescue system." *Journal of China Coal Society*, Vol. 37, No. 5, (2012), 857–862. Retrieved from <https://www.ingentaconnect.com/content/jccs/jccs/2012/00000037/00000005/art00025>
- Lo, H. W., and Liou, J. J. H., "A novel multiple-criteria decision-making-based FMEA model for risk assessment." *Applied Soft Computing Journal*, Vol. 73, (2018), 684–696. <https://doi.org/10.1016/j.asoc.2018.09.020>
- Hyun, K. C., Min, S., Choi, H., Park, J., and Lee, I. M., "Risk analysis using fault-tree analysis (FTA) and analytic hierarchy process (AHP) applicable to shield TBM tunnels." *Tunnelling and Underground Space Technology*, Vol. 49, (2015), 121–129. <https://doi.org/10.1016/j.tust.2015.04.007>
- Peeters, J. F. W., Basten, R. J. I., and Tinga, T., "Improving failure analysis efficiency by combining FTA and FMEA in a recursive manner." *Reliability Engineering and System Safety*, Vol. 172, (2018), 36–44. <https://doi.org/10.1016/j.res.2017.11.024>
- Galagedarage Don, M., and Khan, F., "Dynamic process fault detection and diagnosis based on a combined approach of hidden Markov and Bayesian network model." *Chemical Engineering Science*, Vol. 201, (2019), 82–96. <https://doi.org/10.1016/j.ces.2019.01.060>
- Attaran, B., Ghanbarzadeh, A., and Moradi, S., "A Novel Intelligent Fault Diagnosis Approach for Critical Rotating Machinery in the Time-frequency Domain." *International Journal of Engineering - Transactions A: Basics*, Vol. 33, No. 4, (2020), 668–675. <https://doi.org/10.5829/IJE.2020.33.04A.18>
- Rajeev, D., Dinakaran, D., Kanthavelkumaran, N., and Austin, N., "Predictions of Tool Wear in Hard Turning of AISI4140 Steel through Artificial Neural Network, Fuzzy Logic and Regression Models." *International Journal of Engineering - Transactions A: Basics*, Vol. 31, No. 1, (2018), 32–37. <https://doi.org/10.5829/ije.2018.31.01a.05>
- Ebtehaj, I., Bonakdari, H., and Zaji, A. H., "A new hybrid decision tree method based on two artificial neural networks for predicting sediment transport in clean pipes." *Alexandria Engineering Journal*, Vol. 57, No. 3, (2018), 1783–1795. <https://doi.org/10.1016/j.aej.2017.05.021>
- Liu, L., Wang, S., Hu, B., Qiong, Q., Wen, J., and Rosenblum, D. S., "Learning structures of interval-based Bayesian networks in probabilistic generative model for human complex activity recognition." *Pattern Recognition*, Vol. 81, (2018), 545–561. <https://doi.org/10.1016/j.patcog.2018.04.022>
- Naili, M., Bourahla, M., Naili, M., and Tari, A. K., "Stability-based Dynamic Bayesian Network method for dynamic data mining." *Engineering Applications of Artificial Intelligence*, Vol. 77, (2019), 283–310. <https://doi.org/10.1016/j.engappai.2018.09.016>
- Tang, K., Parsons, D. J., and Jude, S., "Comparison of automatic and guided learning for Bayesian networks to analyse pipe failures in the water distribution system." *Reliability Engineering and System Safety*, Vol. 186, (2019), 24–36. <https://doi.org/10.1016/j.res.2019.02.001>
- Liu, M., Stella, F., Hommersom, A., Lucas, P. J. F., Boer, L., and Bischoff, E., "A comparison between discrete and continuous time Bayesian networks in learning from clinical time series data with irregularity." *Artificial Intelligence in Medicine*, Vol. 95, (2019), 104–117. <https://doi.org/10.1016/j.artmed.2018.10.002>
- Meng, Q. Q., Zhu, Q. X., Gao, H. H., He, Y. L., and Xu, Y., "A novel scoring function based on family transfer entropy for Bayesian networks learning and its application to industrial alarm systems." *Journal of Process Control*, Vol. 76, (2019), 122–132. <https://doi.org/10.1016/j.jprocont.2019.01.013>
- Guo, C., Khan, F., and Imtiaz, S., "Copula-based Bayesian network model for process system risk assessment." *Process Safety and Environmental Protection*, Vol. 123, (2019), 317–326. <https://doi.org/10.1016/j.psep.2019.01.022>
- Dagum, P., and Luby, M., "Approximating probabilistic inference in Bayesian belief networks is NP-hard." *Artificial Intelligence*, Vol. 60, No. 1, (1993), 141–153. [https://doi.org/10.1016/0004-3702\(93\)90036-B](https://doi.org/10.1016/0004-3702(93)90036-B)
- Tong, X., Fang, W., Yuan, S., Ma, J., and Bai, Y., "Application of Bayesian approach to the assessment of mine gas explosion." *Journal of Loss Prevention in the Process Industries*, Vol. 54, (2018), 238–245. <https://doi.org/10.1016/j.jlp.2018.04.003>
- Ping, P., Wang, K., Kong, D., and Chen, G., "Estimating probability of success of escape, evacuation, and rescue (EER) on the offshore platform by integrating Bayesian Network and Fuzzy AHP." *Journal of Loss Prevention in the Process Industries*, Vol. 54, (2018), 57–68. <https://doi.org/10.1016/j.jlp.2018.02.007>

Persian Abstract

چکیده

این مطالعه یک روش جدید برای استدلال خرابی سیستم مبتنی بر شبکه‌های بیزی برای حل مشکلات قابلیت اطمینان سیستم کنترل جریان هوای اضطراری ارائه داده است. یک مدل درخت خطای سیستم برای شناسایی رابطه منطقی بین واحدها ایجاد شد که سپس به مدل تجزیه و تحلیل خطای شبکه بیزی برای تعیین حالت‌های گره شبکه و جدول احتمال شرطی و همچنین انجام استدلال‌های تشخیصی در شاخه‌های گره سیستم تبدیل شد. تجزیه و تحلیل قابلیت اطمینان مدل مبتنی بر ابزار **Netica Bayesian** نشان می‌دهد که احتمال خرابی سیستم ناشی از گره ارتباطی پست در شرایط عادی بیشترین است و نظارت بر داده و گره‌های ارتباطی ایستگاه مرکزی تأثیر بیشتری در کنترل هوشمند دارند. با پیش‌بینی و تشخیص خطاهای سیستم، بهینه‌سازی طراحی سیستم در چارچوب شبکه بیزی برای بهبود قابلیت اطمینان و در آنجا با ایجاد یک بنیان نظری برای تحقیقات پیشگیری از بلایای آبی تحقق می‌یابد.



Interaction Effect of Depth of Cut, Back Rake Angle and Rock Properties on Temperature of Single Polycrystalline Diamond Compact Cutter

A. H. Abdullah^a, M. A. Maoinser^{*b}, E. A. Rahim^c

^a Department of Petroleum Engineering, Universiti Teknologi PETRONAS, 32610 Bandar Seri Iskandar, Perak Darul Ridzuan, Malaysia

^b Department of Mechanical Engineering, Universiti Teknologi PETRONAS, 32610 Bandar Seri Iskandar, Perak Darul Ridzuan, Malaysia

^c Manufacturing and Industry Engineering Department, Universiti Tun Hussein Onn, 86400 Batu Pahat, Johor Darul Takzim, Malaysia

PAPER INFO

Paper history:

Received 20 July 2020

Received in revised form 28 August 2020

Accepted 03 September 2020

Keywords:

Analysis of Variance

Back Rake Angle

Depth of Cut

Polycrystalline Diamond Compact Cutter

Rock Properties

ABSTRACT

The single polycrystalline diamond compact (PDC) cutter's performance is affected by temperature during rock cutting process. The study towards understanding the factors and its interaction affecting the cutter's temperature is essential prior to cutting process optimization. Thus, this study aims to investigate the effect of various cutting parameters and its interaction on the temperature of a single PDC cutter. A series of test was conducted in a lathe machine which utilized facing operation to cut the rock samples at 0.5 to 1.5 mm depth of cut and back rake angle of 5° to 15°. Two types of rock being tested in this study were Indiana limestone and Carthage marble. The analysis of variance (ANOVA) output indicated that cutting parameters and rock properties and its interaction have a significant effect on cutter's temperature except for interaction between back rake angle and rock properties. Increasing the depth of cut and decreasing back rake angle has resulted in increasing temperature. The temperature of the single PDC cutter is higher when cutting Carthage marble than Indiana limestone. Combination of low back rake angle and high depth of cut producing maximum temperature. It is also validated that the data developed from the mathematical model having a difference of 5% as compared to the experimental data obtained using similar parameters which indicates that the results are reliable and can be forwarded in the future study.

doi: 10.5829/ije.2020.33.11b.33

NOMENCLATURE

mD	Millidarcy	s	second
MPa	Megapascal	T_{cm}	Temperature for Carthage marble
mm	Millimetre	T_{il}	Temperature for Indiana limestone
°C	Degree Celcius		

1. INTRODUCTION

Polycrystalline diamond compact (PDC) cutter brazing onto the PDC's bit and cut the rock formation during a drilling operation in the oil and gas industry. Rate of penetration, weight on bit and torque are the parameters that were controlled and affecting the bit's performance [1]. On the other hand, the depth of cut, back rake angle, cutting speed and spindle rate are the parameters affecting the performance of single PDC cutter that directly correlates with PDC bit. It has been proven that

the rock cutting theories produced in single PDC cutter study which was verified through analytical and numerical models applied in industry and improved the drilling operation [2]. The temperature which is one of the uncontrolled factors affecting the bit's performance suggested to be considered when conducting a single PDC cutter study, respectively.

The generated temperature at the cutter-rock interface during rock cutting affecting the cutting performance of a single PDC cutter [3, 4]. Various studies have been conducted by researchers to investigate the relationship

*Corresponding Author Institutional Email:
mazuwan.maoinser@utp.edu.my (M. A. Maoinser)

between rock cutting process with rock properties discussed in literature [5-9]; but, did not evaluate the temperature response. Meanwhile, studies to evaluate the effect of various cutting parameters on temperature have been conducted using experimental work and simulation analysis [2-4]. However, one can find that the data obtained from the experiment are more accurate as compared to the calculated temperature from the simulation [4]. The inaccuracy of the results happened due to simplification of calculation solution which is unacceptable in the complicated circumstance in the 'real' rock cutting. Thus, it is essential to employ the best temperature measuring technique in order to improve the accuracy and reliability of the temperature measurement in the experiment [2].

During rock cutting, the temperature of single PDC cutter was measured using thermocouple due to the principle of the Seebeck where dissimilar metals such as copper and iron are connected between one end to the other [10]. The wire is connected from thermocouple to the signal conditioning circuitry. The voltage is produced when the area between the measurement and reference junction is heated [11]. The magnitude of the produced voltage indicates the difference between the temperature at the junction with the thermocouple connectors and the data logged in the computer software [12].

Che et al. [3] used a thermocouple technique to measure the temperature of a single PDC cutter by placing the thermocouple at five locations on the PDC cutter surface to increase the accuracy of the measurement. The same technique is also used by Wilson and Vorono [13]. Both studies [3, 13] agreed that the temperature was the highest when the thermocouple is positioned at the edge of the PDC cutter (the interface area between cutter and rock). These findings proved that the heat was mainly generated at the cutter rock interface and suggested to be the area of measurement for this study. However, these studies did not include the effect of a parameter such as rock properties on the temperature response of a single PDC cutter.

In the previous literature [13-16] depth of cut, back rake angle and rock properties are reported to have a significant effect on single PDC cutter performance such as cutting force and mechanical specific energy. However, the effect of these parameters on temperature is not much explored. Thus, it is the objective of this study to evaluate the effect of various cutting parameters on the temperature of single PDC cutter during rock cutting process.

This article is organized as follows: Section 2 described the materials; rock sample and cutter, experimental setup and design of experiment used in this study. Section 3 portrayed the obtained result and analysis of temperature mechanism in single PDC cutter test, analysis of variance, the effect of various cutting parameters on temperature and validation of the

mathematical model, followed by brief conclusion drawn in section 4.

2. MATERIALS AND METHODS

2. 1. Research Methodology Figure 1 shows the flowchart of this study which is divided into three sections. The first section involves the development of experimental setup and the selection of the materials consist of PDC cutters and rock samples; Carthage marble and Indiana limestone, and cutting parameters consist of depth of cut, back rake angle and rock properties based on comprehensive literature review.

The second section includes the application of design of experiment in lathe rock cutting to obtain the temperature responses. The final section involves the analysis of the interaction effect between cutting parameters on temperature. Finally, the mathematical models obtained from an ANOVA output were validated. The experimental result was compared to the predicted result from the obtained mathematical model.

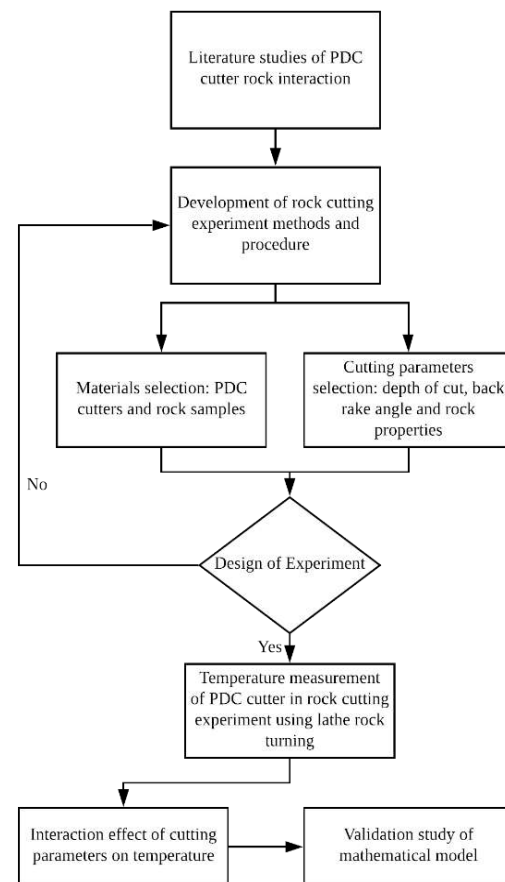


Figure 1. Research flowchart

2. 2. Materials

In this experiment, Indiana limestone and Carthage marble of cylindrical shape with 101.6 mm diameter and height are used as rock samples as shown in Figure 2. The samples provided by Kocurek Industries Inc. with physical properties given in Table 1. The selection of these rocks based on distinguished strength and hardness and expected to be one of the factors affecting the temperature of single PDC cutter. The hardness of these rocks is classified by Wang et al. [17] where Indiana limestone and Carthage marble are fairly hard and hard rock, respectively.

PDC cutters used in this study were manufactured by Glynn Technical Diamonds had a dimension of 13.4 mm diameter and 8.0 mm height as shown in Figure 3. The single PDC cutter built by 6 mm thick carbide substrate and 2 mm thick diamond (chamfered at 45° chamfered with 0.6 mm length).

2. 3. Experimental Setup

Figure 4 shows the single PDC cutter test conducted using electronic centre lathe 2-axis by Harrison A400 Alpha having 7.5 kW spindle and a maximum spindle speed of 2500 rpm.

In this study, the temperature of the PDC cutter is measured using K-type thermocouple which connected to DAQ system instruments consist of DEWESoft®



Figure 2. One of the rock samples for Indiana limestone (left) and Carthage marble (right) used in rock cutting experiment

TABLE 1. Physical properties of the two rock samples

Property	Indiana Limestone	Carthage Marble
Formation	Mississippian	Permian
Permeability (mD)	4.000	0.007
Porosity (%)	14	5
Unconfined compressive strength (MPa)	34.47	137.90
Rock hardness classification [17]	Fairly hard rock	Hard rock



Figure 3. Single polycrystalline diamond compact (PDC) cutter

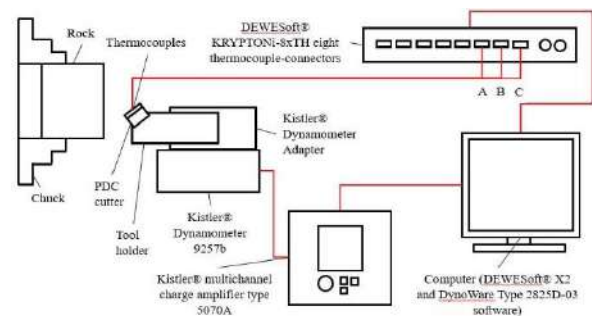


Figure 4. Schematic diagram of temperature measurement

KRYPTONI-8xTH multichannel charge amplifier and DEWESoft® X2 software. This thermocouple can measure a range of temperature between -200°C to 1372°C. The measurement of PDC cutter temperature started when the thermocouple heated during the cutting process. Then, the thermocouple sends the signal to the amplifier to be processed by setting the maximum sampling rate, 100 Hz, to produce more temperature data points. Thus, the higher accuracy of temperature measurement can be obtained. The software is used to visualize the temperature reading in time (s) vs temperature (°C) graph.

2. 4. Design of Experiment

Design of experiment has been numerously utilized by researchers to study the significant effect of parameters on interest response output as discussed in literature [18-21]. Analysis tool such as ANOVA is beneficial to validate the adequacy of the mathematical model and the corresponding significance of each tested parameters under the assumption of 95% confidence [22]. In this study, the two-level factorial design was employed to study the significant effect of depth of cut, back rake angle and rock properties while setting the temperature of PDC cutter as a response. The parameters design and range of depth of cut, back rake angle and rock properties are summarized in Table 2.

Other parameters such as spindle speed and feed rate were kept constant at 750 rpm and 0.15 mm/rev, respectively. It should be notable that the constant

TABLE 2. Parameters design in single PDC cutter

Factors	Symbol	Coded Level	
		Low (-1)	High (+1)
Depth of Cut (mm)	A	0.5	1.5
Back Rake Angle (°)	B	5	15
Rock Properties	C	Indiana limestone	Carthage marble

surface speed mode is not applied in this facing operation due to the limitation of the lathe machine. The constant surface speed mode is used to ensure constant cutting speed throughout the cutting process. When it is not applied, the cutting speed is changing during the rock cutting process as the diameter of the rock sample being cut is reduced, which can be proved by using cutting speed formula as shown in Equation (1). This is in agreement with a similar finding reported by Che et al. [3].

$$V_c = \frac{\pi * D * n}{1000} \quad (1)$$

Where V_c represents the cutting speed (m/min), D represents the diameter of the rock sample (mm) and n represent spindle speed (rev/min).

These selected ranges of parameters are made by considering of comprehensive literature of previous study [13-16]. Thus, the lower range depth of cut and back rake angle is selected. Design expert software is used to develop the design of the experiment of this study.

3. RESULTS AND DISCUSSION

A set of single PDC cutter test was performed at low depth of cut and back rake angle by cutting different rock properties consist of Indiana limestone and Carthage marble rock samples. The set of tests were randomized and repeated thrice in order to perform a significance test, increase the sensitivity of the statistical test, and ensure the independence of experimental errors [23]. Overall, there were 24 sets of runs to complete the matrix and the suggested combinations of the run, as well as the temperature result, is portrayed in Table 3.

This section starts with the discussion on mechanism of temperature during this rock cutting experiment. After all the results are obtained, ANOVA approach is used to evaluate the relation effects between factors on temperature [14]. It is also used to obtain mathematical models in predicting the response [24]. Then, the interaction effect between depth of cut, back rake angle and rock properties on temperature are analyzed. Supplementary rock cutting experiment was performed to validate predicted models and discussed in section 3.4.

3. 1 Discussion on Temperature Mechanism of Single PDC Cutter Test

The mechanism of temperature during PDC cutter cutting rock samples was analyzed from temperature (°C) vs time (s) graph as shown in Figure 5. It was found that a similar trend in the graph but with different magnitude was captured for all sets of the tests.

The mechanism of temperature is analyzed according to the two phases identified in this study. In phase 1, the temperature rises approximately after 12 seconds which show the rock cutting has started. Approximately after 17 seconds, the temperature reached its maximum value at 118.98 °C.

Based on the rock cutting principle, when the cutter starts to cut the rock sample, the heat generated from the friction of cutter-rock interaction was dissipated to both cutter and rock sample including the chips removed [2]. This condition caused the temperature rises rapidly and the maximum temperature was recorded. During this period, there is more volume of chips removed due to high cutting speed and the majority of the heat dissipated to the chips.

In phase 2, when the cutter moved towards the centre of the rock sample, the cutting speed is reduced and there was less volume of rock to be cut. Subsequently, the cutting process is completed and there is no more rock sample to be cut. Thus, it is understood that all the heat generated dissipated only at the PDC cutter where the thermocouple was placed to measure the temperature. After the maximum point, the temperature decline gradually which indicated that the PDC cutter began to

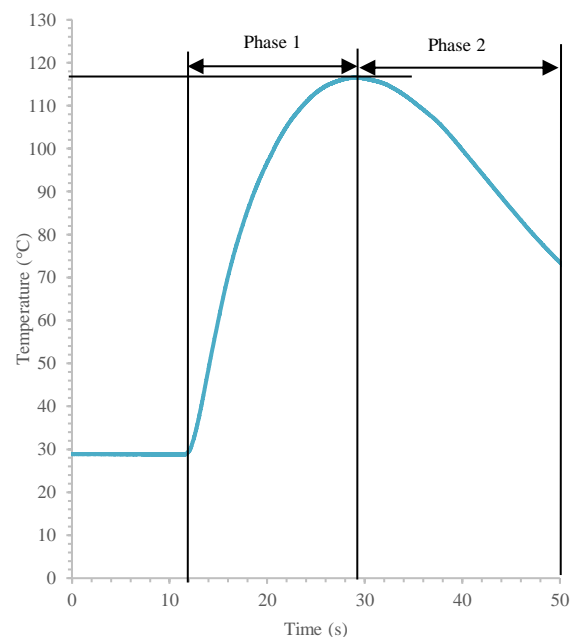


Figure 5. Temperature (°C) vs Time (s) graph captured from DEWESoft® X2 software

TABLE 3. Temperature result of design parameters applied in single PDC cutter test

Run	Depth of Cut (mm), A	Back Rake Angle (°), B	Rock Properties, C	Temperature (°C)
1	1.5	5	Carthage marble	214.68
2	1.5	5	Carthage marble	209.91
3	0.5	15	Carthage marble	121.02
4	0.5	15	Indiana limestone	66.96
5	0.5	5	Carthage marble	130.21
6	1.5	15	Indiana limestone	100.86
7	0.5	5	Indiana limestone	94.19
8	0.5	15	Indiana limestone	69.58
9	1.5	15	Carthage marble	179.38
10	1.5	5	Indiana limestone	120.25
11	1.5	5	Carthage marble	205.66
12	0.5	5	Carthage marble	131.52
13	0.5	5	Indiana limestone	92.04
14	1.5	5	Indiana limestone	118.98
15	0.5	5	Carthage marble	135.91
16	0.5	15	Carthage marble	124.63
17	1.5	15	Indiana limestone	105.88
18	1.5	15	Carthage marble	180.29
19	1.5	15	Indiana limestone	100.13
20	0.5	15	Carthage marble	125.38
21	0.5	15	Indiana limestone	62.83
22	1.5	5	Indiana limestone	119.52
23	0.5	5	Indiana limestone	80.53
24	1.5	15	Carthage marble	178.28

cool down until it returns to the ambient temperature. The result obtained agreed with previous work carried out by [3] where the temperature tends to decrease at the end of the cutting process as the interaction between cutter and rock decrease.

3. 2. Statistical Analysis ANOVA is used to analyze the interaction and significant effect between depth of cut, back rake angle and rock properties on temperature. Table 4 shows the ANOVA for temperature response. In ANOVA, factors with Prob > F less than 0.05 and large F-value are considered significant [25, 26].

Based on Table 4, Factors A, B, C, AB, AC and ABC are significant as Prob > F is 0.0001 while factors BC is insignificant because Prob > F is 0.9845. This means that only the interaction between back rake angle and rock properties did not have a significant effect on temperature.

Based on F value, the significance of the sequence of parameters and their interaction effects on the temperature response can be conveyed as: C > A > B > AC > AB > ABC > BC. Combining the interaction between factors and evaluating the effect of the interaction on temperature is considered more reliable as compared to the previous experiment [3, 13] that conducted using one factor at a time.

The model highly fitted the data and validated as the adjusted R-squared is 0.9931. The model of this study is considered acceptable when the adjusted R-squared value is approaching 1 [27]. The mathematical models for temperature response also have been obtained with a 95% confidence level. The linear regression expressions are the output of ANOVA and presented in Equations (2) and (3). This equation illustrates that the interaction between cutting parameters has a critical impact on the determination of temperature in a single PDC cutter experiment [28].

TABLE 4. ANOVA for temperature response of single PDC cutter test

Source	Sum of Squares	DF	Mean Square	F Value	Prob > F
Model	46370.9	7	6624.41	475.47	< 0.0001
A	14951	1	14951	1073.12	< 0.0001
B	2363.74	1	2363.74	169.659	< 0.0001
C	27009.1	1	27009.1	1938.59	< 0.0001
AB	104.918	1	104.918	7.53055	0.0144
AC	1667.33	1	1667.33	119.674	< 0.0001
BC	0.0054	1	0.0054	0.00039	0.9845
ABC	274.727	1	274.727	19.7187	0.0004
Pure Error	222.917	16	13.9323		
Cor Total	46593.8	23			

$$T_{cm} = 92.7392 + 88.4850A + 0.2078B - 2.1897AB \quad (2)$$

$$T_{il} = 86.1125 + 28.0783A - 2.5048B + 0.5170AB \quad (3)$$

Where T_{cm} and T_{il} represent the temperature (°C) for Carthage marble and Indiana limestone, respectively while A is depth of cut (mm) and B is back rake angle (°).

3. 3 Effect of Cutting Parameters and Rock Properties on Temperature

Figures 6 and 7 shows the interaction effect between the back rake angle and depth of cut on temperature. Interaction effect of depth of cut on temperature is not included in other single PDC cutter studies as they used a constant depth of cut [3, 13]. It can be observed that temperature increased when the depth of cut increase from 0.5 to 1.5 mm. Based on Figure 6, a steep increase in temperature is observed using 5° and 15° back rake angle with increasing depth of cut. A similar trend was found in Figure 7.

The higher the depth of cut, the larger the contact length between the PDC cutter and the rock sample as illustrated in Figure 8. Larger contact length leads to a larger contact area between cutter-rock resulted in higher friction and increasing temperature. Energy consumption to break a fragile material is commensurate with the amount of new surface created [11]. Thus, at 1.5 mm depth of cut, more volume of rock is needed to be cut as compared to 0.5 mm depth of cut. The temperature increase as the depth of cut increase due to the increasing cross-sectional area of cut and generate more frictional heat [11]. Similar finding can be found in a study conducted by Rajabov et al. [15] where mechanical specific energy is analysed. As the depth of cut increase, the area of cut increased and put higher stresses on a PDC cutter. This significantly affects the temperature response by generating more heat at a cutter-rock interaction area of a single PDC cutter. It should be mentioned that high correlation of force to the temperature was observed in a

study conducted by Wilson and Vorono [13]. Thus, the changes in magnitude of cutting force is directly proportional to the temperature changes.

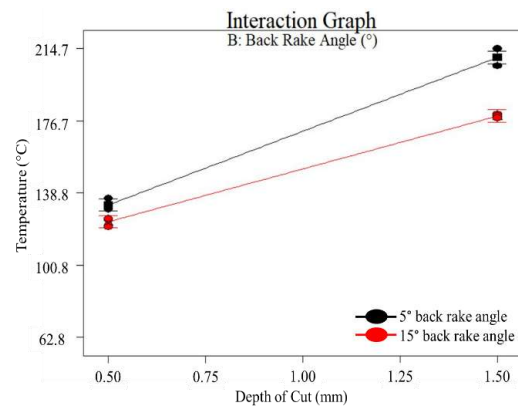


Figure 6. Interaction effect of depth of cut and back rake angle on temperature for Carthage marble

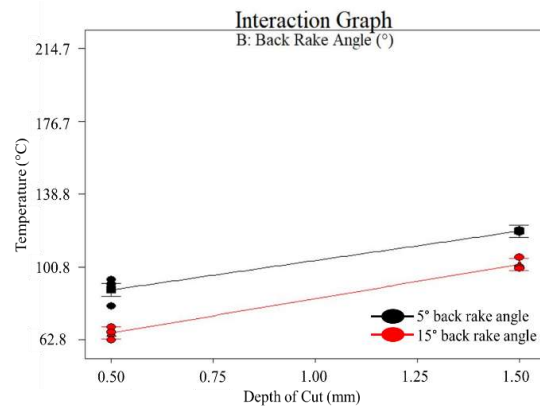


Figure 7. Interaction effect of depth of cut and back rake angle on temperature for Indiana limestone

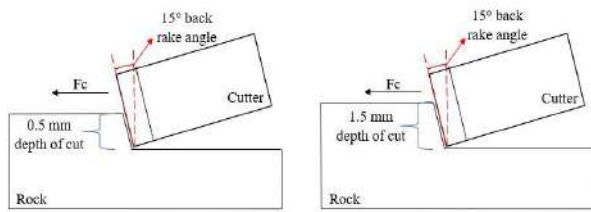


Figure 8. The cutting condition of 0.5 mm and 1.5 mm depth of cut

The interaction effect between the depth of cut and rock properties are presented in Figures 9 and 10. The temperature increases sharply when cutting Carthage marble and Indiana limestone with increasing depth of cut. It is also observed that temperature is higher when cutting Carthage marble as compared to Indiana limestone. Classified as very hard rock based on unconfined compressive strength (Table 1), the higher cutting force required to cut Carthage marble and possibly generate more heat which resulted in higher temperature as compared to cutting Indiana limestone, respectively.

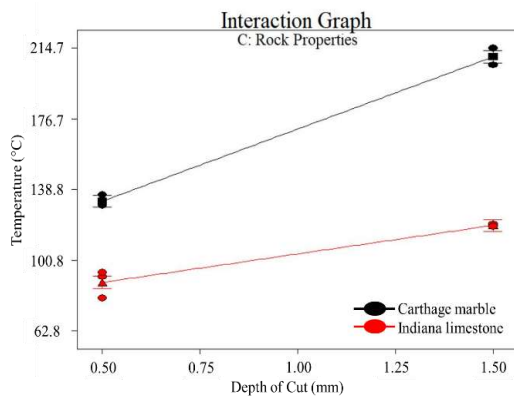


Figure 9. Interaction effect of back rake angle and rock properties on temperature for 0.5 mm depth of cut

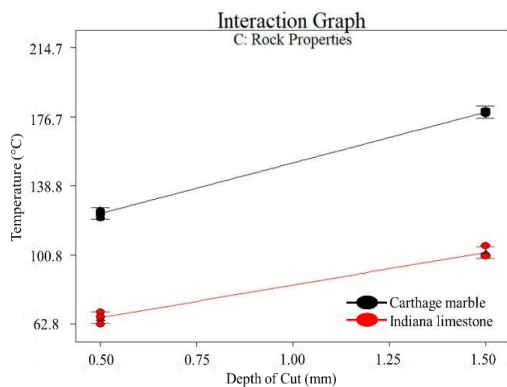


Figure 10. Interaction effect of back rake angle and rock properties on temperature for 1.5 mm depth of cut

On the other hand, Rajabov et al. [15] and Cheng et al. [29] suggested that the analysis of rock cutting cannot depend solely on the UCS of the rock and must also support with the analysis on the sedimentology of rock including rock type and its formation characteristic. Hence, the formation characteristic of Carthage marble and Indiana limestone were identified.

Carthage marble originated from a metamorphic type of rock which is formed through the alteration of existing rocks at the same environment of high pressure and temperature [15, 29]. This condition produced homogeneous behaviour where grains are well cemented and interaction forces between these grains are very high. Hence, the rock becomes harder and required a larger force and induce more heat to cut through this rock.

Meanwhile, Indiana limestone created from a sedimentary type of rock formed by deposition of materials in different environments over hundreds of years [30]. This condition leads to heterogeneous behaviour of this rock where it had poor cementation between grains. Therefore, the temperature generated in cutting this rock is much lower than Carthage marble.

The interaction effect between the back rake angle and rock properties are portrayed in Figures 11 and 12. The temperature trend in these figures indicates an inverse relationship between temperature and back rake angle. But hardly any changes of temperature are observed when cutting Carthage marble and Indiana limestone with increasing back rake angle. This is possibly due to the use of a low range of back rake angle. The results show in agreement with ANOVA output of Prob>F is higher than 0.05 where interaction between rock properties and back rake angle has no significant effect on temperature.

This is possibly due to the action of frictional impact between the rock and the cutter's rake face. Increment of back rake angle leads to the decrease of force component tangent to the rake face [31]. In addition, a study conducted by Akbari et al. [32] also indicates that at

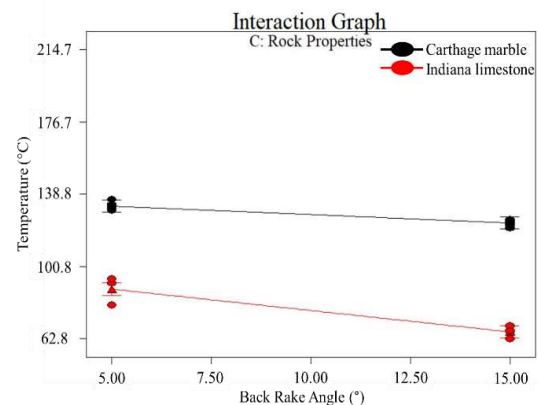


Figure 11. Interaction effect of back rake angle and rock properties on temperature for 0.5 mm depth of cut

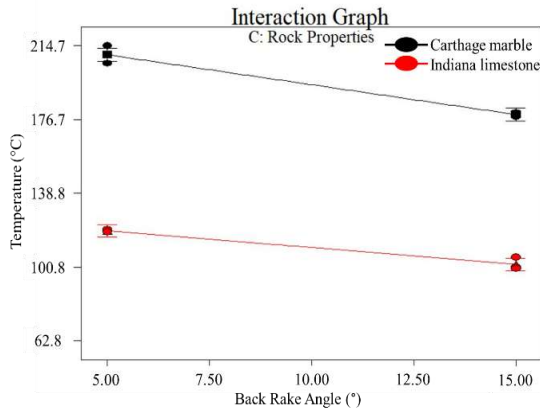


Figure 12. Interaction effect of back rake angle and rock properties on temperature for 1.5 mm depth of cut

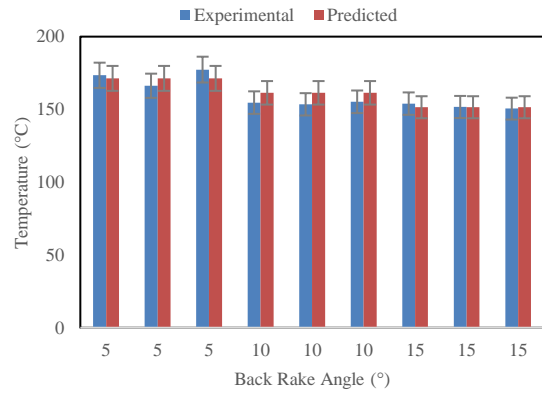


Figure 13. The experimental and predicted temperature values at a constant 1.0 mm depth of cut in Carthage marble cutting

low back rake angle, the friction between cutter and rock is higher than cutting at high back rake angle. These findings explain the higher cutting force at lower back rake angle.

In general, Figures 6-12 show that the result is more reliable when the interaction between factors are included in the study. For example, increasing depth of cut is obvious on temperature changes when using 5° back rake angle as compared to 15° back rake angle.

This result is in agreement with Akbari et al. [32] where at low back rake angle, the friction between cutter and rock is higher than cutting at high back rake angle. Meanwhile, larger depth of cut causes the cutter to cut more cutting surface area as compared to the low depth of cut [15, 33]. Combination of the high depth of cut and low back rake angle causes the cutter's edge to cut the rock in the larger cutting area and higher friction.

3. 4. Validation of Predicted Temperature Model

The predicted values for temperature using 1.0 mm depth of cut and 10° back rake angle for Carthage marble and Indiana limestone was calculated using the linear model through Equations (2) and (3). Experimental results for Carthage marble and Indiana limestone cutting are compared with the predicted results and shown in Figures 13 to Figure 16.

It was observed that the experimental and predicted results are overlapping each other with 5% error bars and indicate the accuracy of the linear models [34]. the linear models predict the temperature of single PDC cutter with a high degree of accuracy. From these results, it can be deemed that the proposed linear model can be applied to predict the temperature of a single PDC cutter in cutting Carthage marble and Indiana limestone at low depth of cut between 0.5 to 1.5 mm and low back rake angle between 5 to 15°.

Figure 17 has portrayed the experimental data obtained in this study to show the interaction effects between depth of cut, back rake angle and rock properties

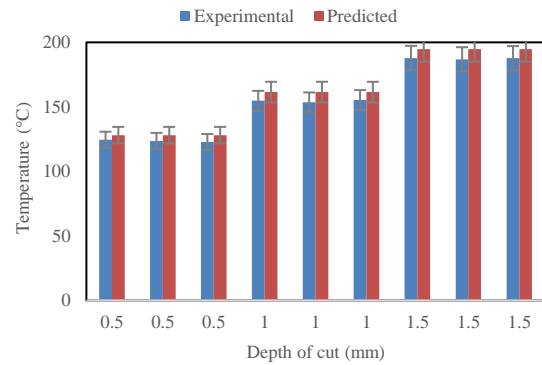


Figure 14. The experimental and predicted temperature values at a constant 10° back rake angle in Carthage marble cutting

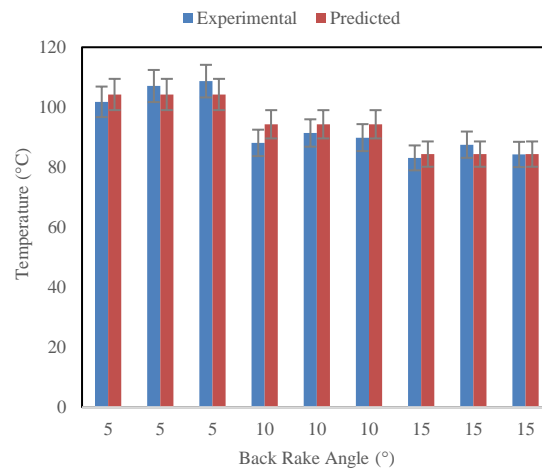


Figure 15. The experimental and predicted temperature values at a constant 1.0 mm depth of cut in Indiana limestone cutting

on temperature. The graphs show that the temperature increased linearly with increasing depth of cut which was in agreement with Shao et al. [11]. It was also concluded

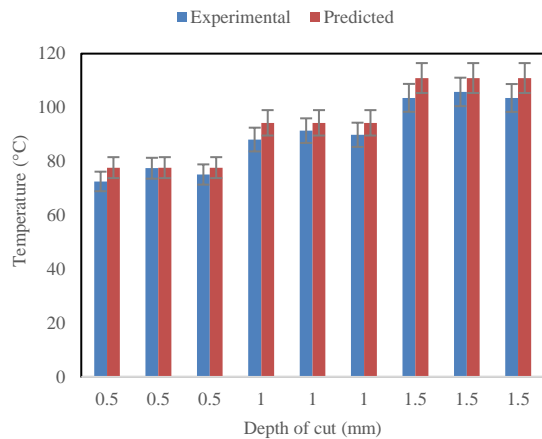


Figure 16. The experimental and predicted temperature values at constant 10° back rake angle in Indiana limestone cutting

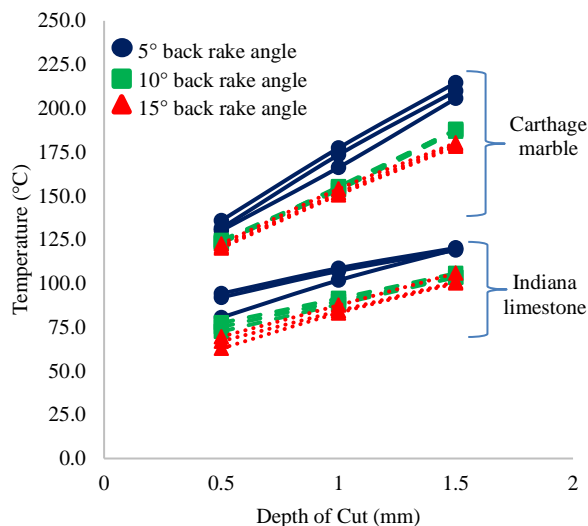


Figure 17. The comparison of all experimental interaction effects between depth of cut, back rake angle and rock properties on temperature

that the temperature exhibit by Carthage marble cutting is much higher than Indiana limestone due to different properties of Carthage marble and Indiana limestone [11, 15].

4. CONCLUSION

The rock cutting experiment was successfully conducted to evaluate the effect of back rack angle, depth of cut and rock properties and its interaction on temperature. This study contributed to the literature where the effect of low back rake angle (0.5-1.5 mm) and depth of cut (5-15°) did not evaluate in previous single PDC cutter study. It can be concluded that the depth of cut, back rake angle and

rock properties have a significant effect on the temperature where $\text{Prob} > F$ is lower than 0.05. The interaction between depth of cut and back rake angle also shows a significant effect on temperature. Another interaction between factors (depth of cut and rock properties) also indicate significant effect towards temperature. However, the interaction between back rake angle and rock properties imply insignificant changes on temperature. Nonetheless, the interaction between all factors provides a significant effect on temperature. A validation study has also been performed where a small difference (5%) between experimental and predicted data were observed. This study was limited to different formation type of rock samples; Carthage marble from metamorphic rock while Indiana limestone from sedimentary rock. The effect of different rock properties between similar formation type on temperature response is yet to be explored. Thus, it is suggested to conduct a single PDC cutter study of various rock samples from the same formation type such as sedimentary rocks.

5. REFERENCES

- Elkatatny, S., "New approach to optimize the rate of penetration using artificial neural network", *Arabian Journal for Science and Engineering*, Vol. 43, No. 11, (2018), 6297-6304. 10.1007/s13369-017-3022-0: 10.1007/s13369-017-3022-0.
- Che, D., Han, P., Guo, P. and Ehmman, K., "Issues in polycrystalline diamond compact cutter-rock interaction from a metal machining point of view—part I: Temperature, stresses, and forces", *Journal of Manufacturing Science and Engineering*, Vol. 134, No. 6, (2012). 10.1115/1.4007468: 10.1115/1.4007468.
- Che, D., Ehmman, K. and Cao, J., "Analytical modeling of heat transfer in polycrystalline diamond compact cutters in rock turning processes", *Journal of Manufacturing Science and Engineering*, Vol. 137, No. 3, (2015), 031005. 10.1115/1.4029653: 10.1115/1.4029653.
- Appl, F., Wilson, C.C. and Lakshman, I., "Measurement of forces, temperatures and wear of pdc cutters in rock cutting", *Wear*, Vol. 169, No. 1, (1993), 9-24. 10.1016/0043-1648(93)90386-Z: 10.1016/0043-1648(93)90386-Z.
- Dormishi, A., Ataei, M., Mikaeil, R. and Kakaie, R.K., "Relations between texture coefficient and energy consumption of gang saws in carbonate rock cutting process", *Civil Engineering Journal*, Vol. 4, No. 2, (2018), 413-421. 10.28991/cej-0309101: 10.28991/cej-0309101.
- Suryo, S.H., Bayuseno, A., Jamari, J. and Wahyudi, A.I., "Analysis of rake angle effect to stress distribution on excavator bucket teeth using finite element method", *Civil Engineering Journal*, Vol. 3, No. 12, (2018), 1222-1234. 10.28991/cej-030952: 10.28991/cej-030952.
- Mohammadi, J., Ataei, M., Kakaie, R.K., Mikaeil, R. and Haghshenas, S.S., "Prediction of the production rate of chain saw machine using the multilayer perceptron (mlp) neural network", *Civil Engineering Journal*, Vol. 4, No. 7, (2018), 1575-1583. 10.28991/cej-0309196: 10.28991/cej-0309196.
- Wang, Z., Chen, X., Xue, X., Zhang, L. and Zhu, W., "Mechanical parameter inversion in sandstone diversion tunnel and stability analysis during operation period", *Civil Engineering Journal*, Vol. 5, No. 9, (2019), 1917-1928. 10.28991/cej-2019-03091382: 10.28991/cej-2019-03091382.

9. Bednarik, R.G., "Rock metamorphosis by kinetic energy", *Emerging Science Journal*, Vol. 3, No. 5, (2019), 293-302. 10.28991/esj-2019-01192: 10.28991/esj-2019-01192.
10. Duff, M. and Towey, J., "Two ways to measure temperature using thermocouples feature simplicity, accuracy, and flexibility", *Analog Dialogue*, Vol. 44, No. 10, (2010), 1-6.
11. Shao, W., Li, X., Sun, Y., Huang, H. and Tang, J., "An experimental study of temperature at the tip of point-attack pick during rock cutting process", *International Journal of Rock Mechanics and Mining Sciences*, Vol. 107, No., (2018), 39-47. 10.1016/j.ijrmms.2018.04.044: 10.1016/j.ijrmms.2018.04.044.
12. Goldsmid, H.J., *The thermoelectric and related effects*, in *Introduction to thermoelectricity*, S.S.i.M. Science, Editor. 2016, Springer, Berlin, Heidelberg, 1-7.
13. Wilson, C. and Vorono, O., "Diamond turning of granite", in *Key Engineering Materials*, Trans Tech Publ. Vol. 250, No., (Year), 138-146.
14. Akbari, B. and Miska, S.Z., "Relative significance of multiple parameters on the mechanical specific energy and frictional responses of polycrystalline diamond compact cutters", *Journal of Energy Resources Technology*, Vol. 139, No. 2, (2017), 022904. 10.1115/1.4034291: 10.1115/1.4034291.
15. Rajabov, V., Miska, S.Z., Mortimer, L., Yu, M. and Ozbayoglu, M.E., "The effects of back rake and side rake angles on mechanical specific energy of single pdc cutters with selected rocks at varying depth of cuts and confining pressures", in *IADC/SPE Drilling Conference and Exhibition*, Society of Petroleum Engineers. (2012). DOI: <https://doi.org/10.2118/151406-MS>
16. Che, D. and Ehmann, K., "Experimental study of force responses in polycrystalline diamond face turning of rock", *International Journal of Rock Mechanics and Mining Sciences*, Vol. 72, No., (2014), 80-91. 10.1016/j.ijrmms.2014.08.014: 10.1016/j.ijrmms.2014.08.014.
17. Wang, H., Lin, H. and Cao, P., "Correlation of ucs rating with schmidt hammer surface hardness for rock mass classification", *Rock Mechanics and Rock Engineering*, Vol. 50, No. 1, (2017), 195-203. 10.1007/s00603-016-1044-7: 10.1007/s00603-016-1044-7.
18. Kazemian, M.E. and Gandjalikhan Nassab, S.A., "Thermodynamic analysis and statistical investigation of effective parameters for gas turbine cycle using the response surface methodology", *International Journal of Engineering*, Vol. 33, No. 5, (2020), 894-905. 10.5829/IJE.2020.33.05B.22: 10.5829/IJE.2020.33.05B.22.
19. Jaafarian, M., Ebrahimi-Nejad R, S. and Kazemian, M., "Experimental investigation of energy consumption and performance of reverse osmosis desalination using design of experiments method", *International Journal of Engineering, Transactions A: Basics*, Vol. 31, No. 1, (2018), 79-87. 10.5829/ije.2018.31.01a.12: 10.5829/ije.2018.31.01a.12.
20. Noorossana, R. and Alemzad, H., "Quality improvement through multiple response optimization", *International Journal of Engineering, Transactions B: Applications*, Vol. 16, No. 1, (2003), 49-58.
21. Kadhodayan, M., "An investigation into the deep drawing of fiber-metal laminates based on glass fiber reinforced polypropylene", *International Journal of Engineering, Transactions C: Aspects*, Vol. 27, No. 3, (2014), 349-358. 10.5829/idosi.ije.2014.27.03c.01
22. Ranjbari, G. and Doniavi, A., "Prediction and optimization of mechanical properties of st52 in gas metal arc weld using response surface methodology and anova", *International Journal of Engineering, Transactions C: Aspects*, Vol. 29, No. 9, (2016), 1307-1313. 10.5829/idosi.ije.2016.29.09c.17: 10.5829/idosi.ije.2016.29.09c.17.
23. Hough, J.C.L., "The effect of back rake angle on the performance of small-diameter polycrystalline diamond rock bits: Anova tests", *Journal of Energy Resources Technology*, Vol. 108, No. 4, (1986), 305-309. 10.1115/1.3231281: 10.1115/1.3231281.
24. Chamoli, S., "Ann and rsm approach for modeling and optimization of designing parameters for a v down perforated baffle roughened rectangular channel", *Alexandria Engineering Journal*, Vol. 54, No. 3, (2015), 429-446. 10.1016/j.aej.2015.03.018: 10.1016/j.aej.2015.03.018.
25. Wang, H., Sun, J., Li, J., Lu, L. and Li, N., "Evaluation of cutting force and cutting temperature in milling carbon fiber-reinforced polymer composites", *The International Journal of Advanced Manufacturing Technology*, Vol. 82, No. 9-12, (2016), 1517-1525. 10.1007/s00170-015-7479-2: 10.1007/s00170-015-7479-2.
26. Song, C., Li, X., Wang, L. and Shi, W., "Fabrication, characterization and response surface method (rsm) optimization for tetracycline photodegradation by bi 3.84 w 0.16 o 6.24-graphene oxide (bwo-go)", *Scientific reports*, Vol. 6, No., (2016), 37466. 10.1038/srep37466: 10.1038/srep37466.
27. Miles, J., *R squared, adjusted r squared*, in *Wiley StatsRef: Statistics Reference Online*, T.C. N. Balakrishnan, B. Everitt, W. Piegorisch, F. Ruggeri and J.L. Teugels, Editor. 2014, John Wiley & Sons.
28. Tan, Y.H., Abdullah, M.O., Nolasco-Hipolito, C. and Zauzi, N.S.A., "Application of rsm and taguchi methods for optimizing the transesterification of waste cooking oil catalyzed by solid ostrich and chicken-eggshell derived cao", *Renewable Energy*, Vol. 114, (2017), 437-447. 10.1016/j.renene.2017.07.024: 10.1016/j.renene.2017.07.024.
29. Cheng, Z., Sheng, M., Li, G., Huang, Z., Wu, X., Zhu, Z. and Yang, J., "Imaging the formation process of cuttings: Characteristics of cuttings and mechanical specific energy in single pdc cutter tests", *Journal of Petroleum Science and Engineering*, Vol. 171, (2018), 854-862. 10.1016/j.petrol.2018.07.083: 10.1016/j.petrol.2018.07.083.
30. Greensmith, J., *Petrology of the sedimentary rocks*, Springer Science & Business Media, (2012).
31. Che, D., Zhang, W. and Ehmann, K., "Chip formation and force responses in linear rock cutting: An experimental study", *Journal of Manufacturing Science and Engineering*, Vol. 139, No. 1, (2017), 011011. 10.1115/1.4033905: 10.1115/1.4033905.
32. Akbari, B., Miska, S., Yu, M. and Rahmani, R., "The effects of size, chamfer geometry, and back rake angle on frictional response of pdc cutters", in *48th US Rock Mechanics/Geomechanics Symposium*, American Rock Mechanics Association. (2014).
33. Gerbaud, L., Menand, S. and Sellami, H., "Pdc bits: All comes from the cutter rock interaction", in *IADC/SPE Drilling Conference*. DOI: <https://dx.doi.org/10.2118/98988-MS>
34. Pratap, T. and Patra, K., "Micromilling of ti-6al-4v titanium alloy using ball-end tool", in *IOP Conference Series: Materials Science and Engineering*, IOP Publishing. Vol. 229, No. 1, (2017), 012011.

Persian Abstract

چکیده

عملکرد برش یکپارچه الماس چند بلوری (PDC) تحت تأثیر دما در طی فرآیند برش سنگ است. قبل از بهینه سازی فرآیند برش، مطالعه در مورد درک عوامل و تأثیر متقابل آن بر دمای برش ضروری است. بنابراین، این مطالعه با هدف بررسی تأثیر پارامترهای مختلف برش و اثر متقابل آن بر دمای یک برش PDC منفرد انجام می شود. یک سری آزمایش در دستگاه تراشکاری انجام شد که با استفاده از عمل روبرو، نمونه های سنگ را در عمق 0.5 تا 1.5 میلی متر برش و زاویه شیب عقب 5 درجه تا 15 درجه برش داد. دو نوع سنگ مورد آزمایش در این مطالعه سنگ آهک هندی و سنگ مرمر کارتاژ است. تجزیه و تحلیل واریانس (ANOVA) خروجی نشان داد که پارامترهای برش و خصوصیات سنگ و اثر متقابل آن تأثیر قابل توجهی بر روی درجه حرارت برش دارد به جز برهم کنش بین زاویه شیب عقب و خصوصیات سنگ. افزایش عمق برش و کاهش زاویه شیب عقب منجر به افزایش دما می شود. دمای برش PDC منفرد هنگام برش سنگ مرمر کارتاژ بیشتر از سنگ آهک هندی است. ترکیبی از زاویه شیب کم پشت و عمق زیاد برش که حداکثر دما را تولید می کند. همچنین تأیید شده است که داده های حاصل از مدل ریاضی با اختلاف 5٪ در مقایسه با داده های آزمایشی به دست آمده با استفاده از پارامترهای مشابه نشان می دهد که نتایج قابل اعتماد هستند و می توانند در مطالعه آینده استفاده شوند.

AIMS AND SCOPE

The objective of the International Journal of Engineering is to provide a forum for communication of information among the world's scientific and technological community and Iranian scientists and engineers. This journal intends to be of interest and utility to researchers and practitioners in the academic, industrial and governmental sectors. All original research contributions of significant value focused on basics, applications and aspects areas of engineering discipline are welcome.

This journal is published in three quarterly transactions: Transactions A (Basics) deal with the engineering fundamentals, Transactions B (Applications) are concerned with the application of the engineering knowledge in the daily life of the human being and Transactions C (Aspects) - starting from January 2012 - emphasize on the main engineering aspects whose elaboration can yield knowledge and expertise that can equally serve all branches of engineering discipline.

This journal will publish authoritative papers on theoretical and experimental researches and advanced applications embodying the results of extensive field, plant, laboratory or theoretical investigation or new interpretations of existing problems. It may also feature - when appropriate - research notes, technical notes, state-of-the-art survey type papers, short communications, letters to the editor, meeting schedules and conference announcements. The language of publication is English. Each paper should contain an abstract both in English and in Persian. However, for the authors who are not familiar with Persian, the publisher will prepare the latter. The abstracts should not exceed 250 words.

All manuscripts will be peer-reviewed by qualified reviewers. The material should be presented clearly and concisely:

- *Full papers* must be based on completed original works of significant novelty. The papers are not strictly limited in length. However, lengthy contributions may be delayed due to limited space. It is advised to keep papers limited to 7500 words.
- *Research notes* are considered as short items that include theoretical or experimental results of immediate current interest.
- *Technical notes* are also considered as short items of enough technical acceptability with more rapid publication appeal. The length of a research or technical note is recommended not to exceed 2500 words or 4 journal pages (including figures and tables).

Review papers are only considered from highly qualified well-known authors generally assigned by the editorial board or editor in chief. Short communications and letters to the editor should contain a text of about 1000 words and whatever figures and tables that may be required to support the text. They include discussion of full papers and short items and should contribute to the original article by providing confirmation or additional interpretation. Discussion of papers will be referred to author(s) for reply and will concurrently be published with reply of author(s).

INSTRUCTIONS FOR AUTHORS

Submission of a manuscript represents that it has neither been published nor submitted for publication elsewhere and is result of research carried out by author(s). Presentation in a conference and appearance in a symposium proceeding is not considered prior publication.

Authors are required to include a list describing all the symbols and abbreviations in the paper. Use of the international system of measurement units is mandatory.

- On-line submission of manuscripts results in faster publication process and is recommended. Instructions are given in the IJE web sites: www.ije.ir-www.ijeir.info
- Hardcopy submissions must include MS Word and jpg files.
- Manuscripts should be typewritten on one side of A4 paper, double-spaced, with adequate margins.
- References should be numbered in brackets and appear in sequence through the text. List of references should be given at the end of the paper.
- Figure captions are to be indicated under the illustrations. They should sufficiently explain the figures.
- Illustrations should appear in their appropriate places in the text.
- Tables and diagrams should be submitted in a form suitable for reproduction.
- Photographs should be of high quality saved as jpg files.
- Tables, Illustrations, Figures and Diagrams will be normally printed in single column width (8cm). Exceptionally large ones may be printed across two columns (17cm).

PAGE CHARGES AND REPRINTS

The papers are strictly limited in length, maximum 6 journal pages (including figures and tables). For the additional to 6 journal pages, there will be page charges. It is advised to keep papers limited to 3500 words.

Page Charges for Papers More Than 6 Pages (Including Abstract)

For International Author ***	\$55 / per page
For Local Author	100,000 Toman / per page

AUTHOR CHECKLIST

- Author(s), bio-data including affiliation(s) and mail and e-mail addresses).
- Manuscript including abstracts, key words, illustrations, tables, figures with figure captions and list of references.
- MS Word files of the paper.



THOMSON REUTERS

WEB OF SCIENCE



Scopus®



CAS®

A DIVISION OF THE
AMERICAN CHEMICAL SOCIETY



Scientific Indexing Services

Google
Scholar